A STUDY OF THE ENTRAINMENT AND TURBULENCE IN A PLANE BUOYANT JET

by
Nikolas E. Kotsovinos

W. M. Keck Laboratory of Hydraulics and Water Resources
Division of Engineering and Applied Science
CALIFORNIA INSTITUTE OF TECHNOLOGY
Pasadena, California

Report No. KH-R-32

August 1975

A STUDY OF THE ENTRAINMENT AND TURBULENCE IN A PLANE BUOYANT JET

by

Nikolas E. Kotsovinos

Project Supervisor:

E. John List
Associate Professor of
Environmental Engineering

Supported by
National Science Foundation
Grant No. ENG75-02985

W. M. Keck Laboratory of Hydraulics and Water Resources
Division of Engineering and Applied Science
California Institute of Technology
Pasadena, California

Report No. KH-R-32

August 1975

ACKNOWLEDGMENTS

I wish to express my deepest appreciation and gratitude to my advisor, Professor Ericson John List, whose inspired guidance, insight, perspicacious criticism and enthusiasm were invaluable to this research.

I am greatly indebted to Professors Norman H. Brooks and Donald Coles, whose advice and interest in this research continuously stimulated and inspired me. I am grateful to Dr. Robert C. Y. Koh for numerous discussions, and to Dr. Jörg Imberger for his personal interest, encouragement and friendship during the incipient period of my graduate studies. I wish also to express my deepest respect and appreciation to Professor Vito Vanoni for his kind interest and encouragement throughout my research.

I gratefully acknowledge that the enthusiastic teaching of Professor Themis Xanthopoulos provided me with the necessary stimulation to pursue graduate studies.

I thank the California Institute of Technology for providing me with financial support through Graduate Teaching and Research Assistantships, and for its superb research environment facilities. Financial assistance provided by the National Science Foundation, under Grant ENG75-02985, is greatly appreciated.

I am indebted to Mr. Elton F. Daly and Mr. Joseph Fontana for their invaluable assistance in the construction of the laboratory equipment, and Mr. Bob Shultz for the preparation of the graphs. I thank also Mrs. Joan Mathews for her patience in typing this manuscript.

Finally, I thank my wife, Kathy, whose love, support and understanding were essential during the course of this work.

This report was submitted by the writer in May 1975 as a thesis with the same title to the California Institute of Technology in partial fulfillment of the requirements for the degree of Doctor of Philosophy.

ABSTRACT

The entrainment and mixing processes in a two-dimensional vertical turbulent buoyant (heated) jet in its transition state from a pure jet to a pure plume have been studied. The ambient fluid is of uniform density and non-flowing except for the flow induced by the jet. Density variations are assumed small.

The equations of motion integrated across the jet have been carefully examined and it has been found that the kinematic buoyancy flux of a heated plume and the kinematic momentum flux of a pure jet are not in general conserved. It has been proven that the flow in a two-dimensional pure jet is not self-preserving.

A systematic set of experiments was carried out to examine turbulent buoyant jet behavior for a wide range of initial Richardson numbers (or densimetric Froude numbers). Values of the Richardson number, which describes the relative importance of buoyancy in a jet, extended from the value appropriate for a pure jet (zero) to that appropriate for a plume (approximately 0.6). The buoyant jet temperature and velocity fields were measured using calibrated fast response thermistors and a laser Doppler velocimeter respectively. The velocity and temperature data obtained were recorded magnetically in digital form and subsequently processed to extract both mean and fluctuating values of temperature and velocity.

The structure of the mean flow (including the spreading rate of the mean velocity and temperature profiles, velocity and temperature distribution along jet axis, and the heat flux profile), the turbulence structure

(including the profile of turbulence intensity and turbulent heat transfer, probability density distribution of temperature and velocity, skewness and flatness factor of temperature fluctuations) and the large scale motions (intermittency, profile of maximum and minimum temperature, frequency of crossing of hot/cold, cold/hot interface) of a buoyant jet were investigated as a function of the jet Richardson number. It was determined that the turbulent heat transfer and the turbulent intensity increase with increasing the Richardson number. The spreading rate of the transverse mean velocity and temperature profiles were found to be independent of the Richardson number. The turbulent buoyancy flux in a fully developed buoyant jet has been found to be a significant fraction (38%) of the axial buoyancy flux.

TABLE OF CONTENTS

Part	Title	Page
	NOMENCLATURE	1
1.	INTRODUCTION	7
1.1	Introductory note	7
1.2	A review of previous theories	7
	Entrainment coefficient approach	12
	Dimensional analysis	17
1.3	A review of previous experiments	18
	I. Pure jet	18
	II. Pure plume	22
	III. Buoyant jet	24
1.4	Scope of this work	24
2.	THE MECHANICS OF JETS	25
2.0	Basic definitions and assumptions	25
2.1	The mechanics of the two-dimensional pure jet	30
2.2	The mechanics of the two-dimensional pure plume	39
2.3	The mechanics of the two-dimensional buoyant jet	46
2.4	Numerical solution of the buoyant jet problem	52
3.	EXPERIMENTAL PROBLEMS AND OBJECTIVES	53
3.0	Introduction	53
3.1	Temperature measurements	53
	Thermistors	53
	A/D sampling rate	58
3.2	Velocity measurements	62
	I. Description of the laser Doppler velocimeter	62
	II. Derivation of the Doppler shift frequency formula	64
	III. Signal processing	68
3.3	Velocity-temperature cross correlations measurements	71
3.4	Experimental set-up	73
3.5	Data collection and processing	77
	Program I	81
	Program II	86

Part		Title	Page
4.		TEMPERATURE MEASUREMENT RESULTS	88
	4.0	Basic experimental parameters and initial data	88
	4.1	Mean temperature	90
	4.2	Turbulence intensity	106
	4.3	Cross sectional profile of maximum and minimum temperature	120
	4.4	Intermittency	125
	4.5	Frequency of crossing of the hot/cold interface	130
	4.6	The frequency distribution of temperature	135
	4.7	Skewness and flatness factor	135
5.		VELOCITY MEASUREMENT RESULTS	142
	5.0	Basic experimental parameters and initial data	142
	5.1	Mean velocity profile	144
	5.2	On the conservation of the momentum and on the decay of the centerline velocity of a pure jet	157
	5.3	Centerline velocity of a plume	166
	5.4	The frequency distribution of the velocity	167
	5.5	Turbulence intensity	167
6.		VELOCITY-TEMPERATURE RESULTS	174
	6.0	Basic experimental parameters-initial data	174
	6.1	Mean velocity and mean temperature profile	175
	6.2	Profiles of $\overline{uT}$ and $\overline{u'T'}$	184
7.		COMPARISON OF THE THEORY WITH THE EXPERIMENTAL RESULTS	203
	7.0	Introduction	203
	7.1	Comparison of the theory with the experimental results	203
	7.2	Comparison of the theory with the experimental results of temperature	204
8.		ON THE SELF-PRESERVATION OF A PURE JET	210
9.		SUMMARY OF MAIN RESULTS AND CONCLUSIONS	228
	9.0	Introductory note	228
	9.1	Summary of the main results	228
		I. The mean flow structure	228
		II. The turbulence structure	231

Part	Title	Page
	III. The structure of the large eddies	232
9.2	Conclusions	234
APPENDIX A	Pictures of the flow	236
APPENDIX B	Mean temperature profiles for all the experimental runs	244
APPENDIX C	Test of the two-dimensionality of the flow	288
REFERENCES		300

LIST OF FIGURES

Figure		Page
1.2.1	Geometry of a buoyant jet.	8
2.0.1	Definition of jet boundary.	29
2.1.1	Geometry of a jet.	30
2.1.2	Flow towards a line distribution of sinks of strength given by Eq. 2.1.10.	36
2.1.3	Schematic of the assumed induced flow and virtual origin of a real plane jet.	36
2.2.1	Thermal expansion coefficient of water as a function of temperature.	42
2.2.2	Induced flow towards a line plume on a horizontal plane.	43
3.1.1	Close photograph of the thermistor probe. One subdivision is one millimeter.	55
3.1.2	The bridge circuit used for the measurement of the temperature.	56
3.1.3	Typical thermistor calibration curve.	57
3.1.4	Mean temperature as a function of sampling rate (length of sample 50 sec).	60
3.1.5	Mean temperature as a function of sampling time (sample rate 10 samples/second).	60
3.2.1.a	Optics of laser Doppler velocimeter.	63
3.2.1.b	Signal processing of laser Doppler velocimeter.	63
3.2.2	Scattering light from a moving particle.	65
3.2.3	Spectrum analysis of the signal given by Eq. 3.2.4	67
3.2.4	Schematic of a spectrum analyser.	70
3.3.1	Schematic for temperature-velocity measurement.	72
3.3.2	Schematic for the measurement of the correlation $\overline{uT}$.	74
3.4.1.b	Cross section of the chamber of the emerging jet.	75

LIST OF FIGURES (Cont'd)

Figure		Page
3.4.2	Overall experimental set-up.	76
3.4.3	First instrumental set-up.	78
3.4.4.a	Front view of the second instrumental set-up.	79
3.4.4.b	Plane view of the second instrumental set-up.	80
3.5.1	Typical intermittent signal.	84
4.1.1.a	Mean temperature profile for a turbulent jet at x/D = 10.0.	91
4.1.1.b	Mean temperature profile for a turbulent jet at x/D = 20.0.	91
4.1.1.c	Mean temperature profile for a turbulent jet at x/D = 30.4.	92
4.1.1.d	Mean temperature profile for a turbulent jet at x/D = 51.0.	92
4.1.2	Non-dimensional temperature half-width of a turbulent jet plotted against non-dimensional distance along the jet axis.	93
4.1.3	Non-dimensional mean temperature profile of a jet plotted against non-dimensional distance from jet axis.	94
4.1.4.a	Mean temperature profile for a turbulent plume at x/D = 6.0.	95
4.1.4.b	Mean temperature profile for a turbulent plume at x/D = 14.0.	95
4.1.4.c	Mean temperature profile for a turbulent plume at x/D = 30.2.	96
4.1.4.d	Mean temperature profile for a turbulent plume at x/D = 36.0.	96
4.1.5	Temperature half-width of a plume as a function of distance from plume orifice.	97
4.1.6	Non-dimensional mean temperature profile for a plume.	100
4.1.7	Temperature distribution along jet axis.	101

LIST OF FIGURES (Cont'd)

Figure		Page
4.1.8	Temperature distribution along plume axis.	102
4.1.9	Temperature distribution along plume axis.	103
4.2.1	Profile of the intensity of turbulent fluctuations of plume temperature plotted against non-dimensional distance from jet axis.	107
4.2.2	Profile of the intensity of turbulent fluctuations of jet temperature against non-dimensional distance from plume axis.	108
4.2.3	Intensity of turbulent fluctuations of temperature on jet axis as a function of non-dimensional distance from jet orifice and initial Richardson number.	112
4.2.4	Intensity of turbulent fluctuations of temperature on jet axis normalized by the local mean temperature as a function of non-dimensional distance from jet orifice.	113
4.2.5	Sketch of an intermittent temperature signal.	117
4.2.6	Profiles of turbulence intensities $\overline{T'^2}$, $\overline{T'^2_{hot}}$, $\overline{T'^2_{cold}}$ for a turbulent plume.	118
4.2.7	Profiles of turbulence intensities $\overline{T'^2}$, $\overline{T'^2_{hot}}$, and $\overline{T'^2_{cold}}$ for a turbulent plume.	119
4.3.1	Maximum and minimum temperature for a turbulent jet as a function of distance from jet axis.	122
4.3.2	Maximum and minimum temperature for a turbulent plume as a function of distance from plume axis.	123
4.3.3	Distribution of maximum and minimum temperature along jet axis as a function of initial Richardson number.	124
4.4.1	Temperature intermittency for a turbulent jet plotted against non-dimensional distance from jet axis.	126
4.4.2	Temperature intermittency for a turbulent plume plotted against non-dimensional distance from plume axis.	127
4.4.3	Profile of the velocity intermittency for a turbulent jet (based on data by Hanum [40]).	128

LIST OF FIGURES (Cont'd)

Figure		Page
4.4.4	Temperature intermittency for a turbulent plume plotted against non-dimensional distance from plume axis.	129
4.5.1	Profile of frequency of hot/cold, cold/hot interface crossing for a turbulent plume.	131
4.5.2	Profile of frequency of hot/cold, cold/hot interface crossing for a turbulent jet.	132
4.5.3	Profile of frequency of hot/cold, cold/hot, interface crossing for a turbulent jet.	132
4.5.4	The Strouhal number, based on the peak frequency of hot/cold, cold/hot interface crossing profile against distance from jet orifice.	134
4.5.5	Average duration of hot bursts in a turbulent plume.	136
4.5.6	Average duration of hot bursts in a turbulent jet.	136
4.6.1.a	Probability density of the temperature of a turbulent plume at $y/x' = 0.005$.	137
4.6.1.b	Probability density of the temperature of a turbulent plume at $y/x' = 0.055$.	137
4.6.1.c	Probability density of the temperature of a turbulent plume at $y/x' = 0.098$.	138
4.6.1.d	Probability density of the temperature of a turbulent plume at $y/x' = 0.148$.	138
4.7.1	Skewness factor of temperature fluctuations of a buoyant jet as a function of distance from the jet axis.	139
4.7.2	Flatness factor of temperature fluctuations of a buoyant jet as a function of distance from jet axis.	140
5.1.1.a	Mean velocity profile for a turbulent jet at $X/D = 20.8$.	145
5.1.1.b	Mean velocity profile for a turbulent jet at $X/D = 33.3$.	145
5.1.1.c	Mean velocity profile for a turbulent jet at $X/D = 37.0$.	146
5.1.1.d	Mean velocity profile for a turbulent jet at $X/D = 54.2$.	146

LIST OF FIGURES (Cont'd)

Figure		Page
5.1.1.e	Mean velocity profile for a turbulent jet at X/D = 58.75.	147
5.1.1.f	Mean velocity profile for a turbulent jet at X/D = 74.50.	147
5.1.2	Non-dimensional velocity half-width for a turbulent jet as a function of distance from jet orifice.	148
5.1.3	Non-dimensional mean velocity profile for a turbulent jet.	149
5.1.4.a	Mean velocity profile for a turbulent plume at X/D = 9.0.	150
5.1.4.b	Mean velocity profile for a turbulent plume at X/D = 14.0.	150
5.1.4.c	Mean velocity profile for a turbulent plume at X/D = 19.0.	151
5.1.4.d	Mean velocity profile for a turbulent plume at X/D = 28.8.	151
5.1.4.e	Mean velocity profile for a turbulent plume at X/D = 33.6.	152
5.1.4.f	Mean velocity profile for a turbulent plume at X/D = 39.1.	152
5.1.5	Non-dimensional velocity half-width of a turbulent plume plotted against non-dimensional distance from jet orifice.	153
5.1.6	Non-dimensional mean velocity profile for a turbulent plume.	156
5.2.1	Experimental values for the kinematic momentum flux m(x) of a turbulent jet (R_o = 0) as a function of distance from jet orifice.	159
5.2.2	Velocity distribution along jet axis (R_o = 0).	161
5.2.3	Kinematic momentum flux m(x) of a two-dimensional turbulent jet (R_o = 0) as a function of distance ℓ_{max}/D and jet geometry.	164
5.2.4	Schematic of the induced flow by a two dimensional pure jet.	165

LIST OF FIGURES (Cont'd)

Figure		Page
5.3.1	Velocity distribution along plume axis.	168
5.4.1	Probability density of the velocity for a turbulent plume as a function of distance from jet axis.	169
5.4.2	Probability density of the velocity of a turbulent jet as a function of distance from jet axis.	170
5.5.1	Profile of the intensity of turbulent fluctuations of the velocity in a turbulent jet.	172
5.5.2	Profile of the intensity of turbulent fluctuations of the velocity in a turbulent plume.	173
6.1.1.a	Non-dimensional mean velocity profile in a turbulent jet ($R_o = 0$).	176
6.1.1.b	Non-dimensional mean temperature profile in a turbulent jet ($R_o = 0$).	176
6.1.2.a	Velocity half-width of a jet ($R_o \approx 0$) as a function of distance along the jet.	177
6.1.2.b	Temperature half-width of a jet ($R_o \approx 0$) as a function of distance along the jet.	177
6.1.3.a	Non-dimensional mean velocity profile in a turbulent plume.	178
6.1.3.b	Non-dimensional mean temperature profile in a turbulent plume.	178
6.1.4.a	Velocity half-width of a plume as a function of distance along the plume.	179
6.1.4.b	Temperature half-width of a plume as a function of distance along the plume.	179
6.1.5	Turbulent heat flux in a buoyant jet normalized by the heat flux at the jet orifice, as a function of distance along the jet.	185
6.1.6	Turbulent heat flux in a buoyant jet, normalized by the heat flux at the jet orifice, as a function of the local Richardson number.	186
6.2.1	Schematic of the fluctuations of the temperature $T'(x,y,t)$ and vertical velocity $u'(x,y,t)$; (a) plume (b) jet.	188

LIST OF FIGURES (Cont'd)

Figure		Page
6.2.2.a	Profile of the correlation $\rho c_p R(\Delta x,0)$ in a turbulent jet at x/D = 20.8.	191
6.2.2.b	Profile of the correlation $\rho c_p R(\Delta x,0)$ in a turbulent jet at x/D = 37.0.	191
6.2.2.c	Profile of the correlation $\rho c_p R(\Delta x,0)$ in a turbulent jet at x/D = 58.75.	192
6.2.2.d	Profile of the correlation $\rho c_p R(\Delta x,0)$ in a turbulent jet at x/D = 93.75.	192
6.2.3	Profile of the correlation $\rho c_p R(\Delta x,0)$ in a turbulent plume at x/D = 19.0.	193
6.2.4	Heat flux half-width for a turbulent jet as a function of distance along the jet axis.	194
6.2.5	Non-dimensional heat flux profile in a turbulent jet.	195
6.2.6	Profile of turbulent heat flux in a jet.	198
6.2.7	Profile of turbulent heat flux in a plume.	199
6.2.8	Jet correlation coefficient of velocity and temperature as a function of distance from the jet axis.	201
6.2.9	Plume correlation coefficient of velocity and temperature as a function of distance from the jet axis.	202
7.1.1	Comparison of the model with the experimental results for the kinematic mass flux.	205
7.1.2	Comparison of the model with the experimental results of the kinematic momentum flux.	206
7.1.3	Comparison of the model with the experimental results for the kinematic buoyancy flux.	207
7.2.1	Comparison of the model with the experimental results for the mean temperature distribution on the jet axis.	209
8.1	Hypothesis concerning the nonlinear spread of the mean velocity profile of a turbulent jet.	212
8.2	Correlation of spreading rate K_{1u} and non-dimensional virtual origin K_{2u}.	213

LIST OF FIGURES (Cont'd)

Figure		Page
8.3	Spreading rate K_{1u} as a function of non-dimensional distance ℓ_{max}/D.	214
8.4	Non-dimensional virtual origin K_{2u} as a function of non-dimensional distance ℓ_{max}/D.	215
8.5	Nonlinear spread of half-width b_u of mean velocity profile of a two-dimensional turbulent pure jet.	217
8.6	Correlation of spreading rate K_{1T} and non-dimensional virtual origin K_{2T}.	218
8.7	Spreading rate K_{1T} of mean temperature profile as a function of distance ℓ_{max}/D.	219
8.8	Non-dimensional virtual origin K_{2T} as a function of distance ℓ_{max}/D.	220
8.9	Nonlinear spread of temperature half-width b_T of a two-dimensional pure plume.	221
8.10	Velocity ratio $\overline{u}_o^2/\overline{u}_M(x)$ as a nonlinear function of non-dimensional distance x/D.	223
8.11	Velocity ratio $\overline{u}_o^2/\overline{u}_M(x)$ as a nonlinear function of non-dimensional distance x/D. Data from several investigators.	224
8.12	Correlation of coefficients C_{1u} and C_{2u}.	225
8.13	Coefficient C_{1u} as a function of non-dimensional distance ℓ_{max}/D.	226
8.14	Coefficient C_{2u} as a function of non-dimensional distance ℓ_{max}/D.	227
A.1	Short time (0.01 seconds) exposure photograph of a turbulent two-dimensional plume ($R_o \approx 0.5$).	237
A.2	Short time (0.01 seconds) exposure photograph of a turbulent two-dimensional plume ($R_o \approx 0.5$).	238
A.3	Medium time (2 seconds) exposure photograph of a turbulent two-dimensional plume ($R_o \approx 0.5$).	239
A.4	Short time (0.01 seconds) exposure photograph of a turbulent two-dimensional jet ($R_e \approx 2500$, $R_o = 0$).	240
A.5	Medium time (2 seconds) exposure photograph of a turbulent two-dimensional jet ($R_e \approx 2500$, $R_o = 0$).	241

LIST OF FIGURES (Cont'd)

Figure		Page
A.6	Hypothetical instantaneous picture of a plume.	242
A.7	Schematic to explain the production of large waves in a plume.	243
C.1	Distribution of mean temperature in a direction parallel to the slot.	290
C.2	Distribution of mean temperature in a direction parallel to the slot.	291
C.3	Distribution of mean temperature in a direction parallel to the slot.	292
C.4	Distribution of mean temperature in a direction parallel to the slot.	293
C.5	Distribution of turbulence intensity in a direction parallel to the slot.	294
C.6	Distribution of turbulence intensity in a direction parallel to the slot.	295
C.7	Distribution of intermittency in a direction parallel to the slot.	296
C.8	Distribution of maximum and minimum temperature (see Section 4.3) in a direction parallel to slot.	297
C.9	Distribution of f_R (see Section 4.5) in a direction parallel to the slot.	298
C.10	Schematic of the induced flow profile between the two confining walls.	299

LIST OF TABLES

Table		Page
1.3.1	Review of previous experiments for a two-dimensional pure jet.	20
3.1.1	Thermistor characteristics.	53
4.0.1	Basic experimental parameters and initial data of the temperature measurements.	89
4.1.1	Linear approximation of the growth of the temperature half-width and the centerline dilution.	98
4.1.2	Experimental values for temperature half-width and temperature distribution along jet axis for turbulent jets and plumes.	105
4.2.1	Tabulated experimental values for the intensity of turbulent fluctuations of temperature along jet axis for turbulent jets and plumes.	114
5.0.1	Basic experimental parameters and initial data of the velocity measurements.	143
5.1.1	Linear approximation of the growth of the velocity half-width.	154
5.1.2	Tabulated experimental values for volume, kinematic momentum and buoyancy fluxes for turbulent jets and plumes.	158
5.2.1	The kinematic momentum flux of a plane pure jet.	163
6.0.1	Basic parameters of velocity-temperature measurement.	174
6.1.1	Velocity temperature basic results.	180

NOMENCLATURE

Arabic Notation

b_u = $b_u(x)$, half-width of the time averaged mean velocity profile (see Eq. 1.2.15.a)

b_T = $b_T(x)$, half-width of the time averaged mean temperature or concentration profile (see Eq. 1.2.15.b)

$B(x)$ = boundary of the jet (see Eq. 2.0.3)

C = invariant of a buoyant jet ($C \approx 0.55$, see Eq. 2.0.1 and Section 5.1)

C_{1u}, C_{2u} = coefficients for the distribution of the mean velocity along the jet axis (see Eq. 1.3.3)

C_{1T}, C_{2T} = coefficients for the distribution of the mean temperature along the jet axis (see Eq. 1.3.4)

c_p = specific heat of water, 1 cal/gr °C

D = slot thickness

E_1 = C/2, experimental constant (see Eq. 2.1.10)

f_o = frequency of the laser beam

f_R = frequency (in Hz) of the hot/cold, cold/hot interface crossings (see Eq. 3.5.3)

g = gravitational acceleration (981 cm/sec^2)

G_r = Grashof number, $\beta x^3/\nu$ (see Section 2.2)

h = h(R), buoyancy function (see Eq. 2.3.6)

h_o, h_1 = coefficients (see Eq. 2.3.10)

H_o = heat flux at the orifice of the jet, $\alpha_o u_o T_o D$

H_M = transport of heat by mean flow (see Eq. 6.1.5)

H_T = turbulent heat transfer (see Eq. 6.1.6)

H_c = see Eq. 6.2.4

$I(x,y,t)$ = characterizes the presence (I = 1) or absence (I = 0) of the temperature field of the jet at a point (x,y) at time t (see Section 2.0)

K_{1T} = spreading rate of the mean temperature profile (see Eq. 4.1.2)

K_{2T} = non-dimensional virtual origin of the mean temperature profile (see Eq. 4.1.2)

K_{1u} = spreading rate of the mean velocity profile (see Eq. 5.1.2)

K_{2u} = non-dimensional virtual origin of the mean velocity profile (see Eq. 5.1.2)

ℓ_{min} = distance of the closest measurement to the jet orifice (see Figure 5.2.4)

ℓ_{max} = distance of the most distant (from jet orifice) measurement (see Figure 5.2.4)

m = $m(x)$, kinematic momentum flux (see Eq. 2.1.20)

m_o = kinematic momentum flux at the jet orifice, $u_o^2 D$

Max T = Max $T(x,y,t)$, maximum temperature excess at a point (x,y) during the sampling time τ (see Section 4.3)

Max T_M = Max $T(x,0,t)$

Min T = Min $T(x,y,t)$, minimum temperature excess at a point (x,y) during the sampling time τ (see Section 4.3)

Min T_M = Min $T(x,0,t)$

p = $p(x,y,t)$, instantaneous pressure deviation above the hydrostatic ambient pressure

$\overline{p}$ = $\overline{p}(x,y)$, time averaged mean pressure

q = $q(R)$, entrainment function (see Eq. 2.3.7)

q_o, q_1 = coefficients (see Eq. 2.3.10)

R_e = Reynolds number

R_o = Richardson number at the jet orifice (for a pure jet $R_o \approx 0$ and for a pure plume $R_o \approx 0.62$, see Section 2.3)

R = $R(x)$, local Richardson number (see Eq. 2.3.1)

R_p = Richardson number of a pure plume ($R_p \approx 0.62$, see Section 5.1)

$R(\Delta x,0)$ = see Eq. 6.2.3

R_M = value of $R(\Delta x,0)$ on the jet axis

R_f = flux Richardson number (see Eq. 2.2.16)

T = $T(x,y,t)$, instantaneous temperature excess (above the ambient) at a point (x,y) at time t

$\overline{T}$ = $\overline{T}(x,y)$, time averaged mean temperature excess (above the ambient) at a point (x,y)

T_a = ambient temperature

$\overline{T}_c(x)$ = cross sectional mean excess temperature (see Eq. 2.3.3)

$\overline{T}_M$ = $\overline{T}_M(x)$, time averaged mean temperature on the jet axis

T' = $T'(x,y,t)$, turbulent component of the temperature, $T' = T - \overline{T}$

$\overline{T'^2}$ = $\overline{T'^2}(x,y)$, intensity of turbulent fluctuations of temperature (see Eq. 4.2.2)

$\overline{T'^2_{hot}}$ = $\overline{T'^2_{hot}}(x,y)$, turbulence intensity associated with the small eddies (see Eq. 4.2.12)

$\overline{T'^2_{cold}}$ = $\overline{T'^2_{cold}}(x,y)$, turbulence intensity associated with the large eddies (see Eq. 4.2.11)

$\overline{T}_o$ = excess (above the ambient) temperature at the jet orifice

u = $u(x,y,t)$, instantaneous vertical velocity at a point (x,y)

$\overline{u}$ = $\overline{u}(x,y)$, time averaged mean vertical velocity at a point (x,y)

$\overline{u}_M$ = $\overline{u}_M(x)$, time averaged mean vertical velocity on the jet axis.

u' = $u'(x,y,t)$, turbulent component of the vertical velocity, $u' = u - \overline{u}$

$\overline{u'^2}$ = $\overline{u'^2}(x,y)$, turbulence intensity

$\overline{u}_o$ = velocity at the orifice of the jet

v = $v(x,y,t)$, instantaneous horizontal velocity at a point (x,y)

$\bar{v}$ = $\bar{v}(x,y,t)$, time averaged mean horizontal velocity

v' = $v'(x,y,t)$, turbulent component of the horizontal velocity, $v' = v - \bar{v}$

x = coordinate axis in vertical direction, same direction as gravitation (see Figure 2.1.1)

X = distance along jet axis (i.e. $X = x$)

x_o = virtual origin (see Figure 2.1.3)

x_{oT} = virtual origin of the mean temperature profile (see Section 4.1)

x_{ou} = virtual origin of the mean velocity profile (see Section 5.1)

x' = distance from the virtual origin along jet axis

X' = same as x'

y = coordinate axis in horizontal direction (see Figure 2.1.1)

Y = distance from jet axis (i.e. $Y = y$)

Greek Notation

α_o = thermal expansion coefficient at the jet orifice (see Eq. 2.2.5)

α = $\alpha(x)$, thermal expansion coefficient (see Section 2.3, Eq. 2.3.3)

α_e = universal entrainment coefficient

α_j = entrainment coefficient for a pure jet

α_p = entrainment coefficient for a pure plume

β_o = kinematic buoyancy flux at the jet orifice (see Eq. 2.2.7)

β = $\beta(x)$, kinematic buoyancy flux (see Eq. 2.3.9)

γ = $\gamma(x,y)$, intermittency (or intermittency factor) of the temperature signal (see Section 2.0.1 for definition)

$\delta(x)$ = Dirac delta function

δ_u = $\ell n 2/K_{1u}^2$, experimental coefficient

$\Delta\rho$ = $\Delta\rho(x,y) = \rho(x,y)-\rho_a$, density deficiency

$\Delta\rho_o$ = $\rho_o - \rho_a$

$\Delta\rho_M$ $\overline{\rho}_M(x) - \rho_a$

η = non-dimensional distance from the jet axis, $\eta = y/x'$

μ_o = volume flux at the jet orifice, $u_o D$

μ = $\mu(x)$, volume flux (see Eq. 2.1.9)

ν_o = kinematic viscosity at the jet orifice

$\overline{\rho}$ = $\overline{\rho}(x,y)$, time averaged mean density

ρ_a = density of the ambient fluid

ρ_o = density at the orifice of the jet

$\overline{\rho}_M$ = $\overline{\rho}_M(x) = \overline{\rho}(x,0)$, time averaged mean density on the jet axis

σ_u = experimental constant (see Eq. 2.2.13)

σ_T = experimental constant (see Eq. 2.2.14)

Σ = normalized turbulence intensity (see Eq. 4.2.7)

τ = sampling time (see section 3.1)

ϕ = angle between the y-axis and the induced flow streamlines (see Figure 2.1.2)

ψ = $\psi(x,y)$, stream function of the induced flow (see Figure 2.1.2)

Subscripts

a = quantities of the ambient fluid

m,M = quantities on the jet axis

o = quantities at the jet orifice

Superscripts

$\overline{\quad}$	= time averaged mean value
$'$	= fluctuating component

Mathematical Symbols

exp A	= e^A, exponential function
$\ell n 2$	= Naperian logarithm of 2 ($\approx 0.693....$)
π	= 3.141.....
$\sim$	= is proportional to
E{X}	= expectation of variable X

INTRODUCTION

1.1 INTRODUCTORY NOTE

The interest in the mechanics of buoyant jets has been accelerated by the increased demand for shore-sited power plants which use cold ocean water for cooling. Such plants discharge warm water back to the ocean and it has been suggested that a fast dilution of the warm effluent will minimize the disruption of the ecological balance. Rapid dilution can be accomplished with a multiport diffuser structure in which jets from numerous ports spaced along the ocean outfall merge and form a two-dimensional buoyant jet. Hence the understanding of the entrainment and mixing process in a two-dimensional buoyant jet is necessary for the optimal solution of the warm water disposal problem and for an effective design of the diffuser.

Apart from this particular problem, the mechanics of jets is important to a wide range of problems, from jet propulsion of airplanes and submarines, to jet pumps. From a more fundamental point of view, the investigation of two-dimensional buoyant jets will contribute to the understanding of free turbulence phenomena.

1.2 A REVIEW OF PREVIOUS THEORIES

Previous theories of two-dimensional pure jets, pure plumes, and buoyant jets will be described briefly with a view to examining the principal assumptions and results of each theory.

The flow configuration and geometry are shown diagrammatically in Figure (1.2.1). The ambient fluid will be assumed to be of uniform

density ρ_a and motionless, except for flows induced by the jets. The difference between the time averaged local fluid density at any point, $\bar{\rho}(x,y)$, and the ambient density, ρ_a, will be small, so that

$$-(\bar{\rho}(x,y) - \rho_a)/\rho_a << 1 \ ,$$

in the buoyant jet. Thus, there will be little error in using the ambient density ρ_a to replace the local density $\bar{\rho}(x,y)$ in the description of the inertia forces. However, the difference $\bar{\rho}(x,y) - \rho_a$ will be important in the description of the gravitational body forces (Boussinesq approximation).

It is further assumed that the flow is fully turbulent and that the viscous and molecular transport of momentum and heat respectively can be neglected relative to the turbulent transports.

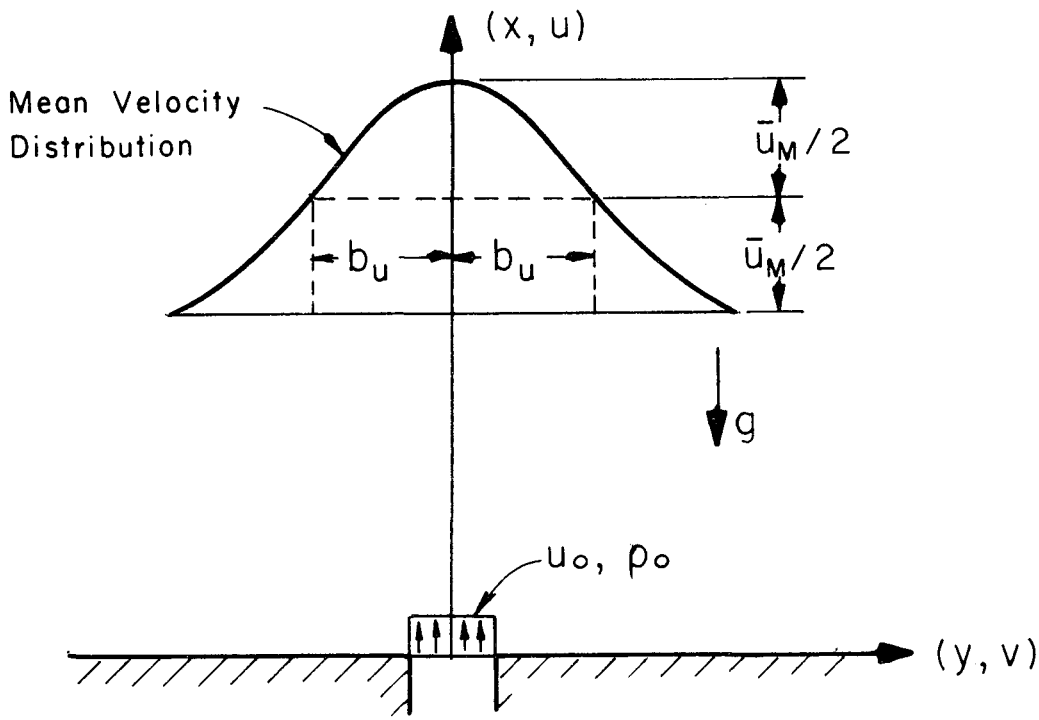

Figure 1.2.1. Geometry of a buoyant jet

Under these conditions, the time-averaged Boussinesq equations for the two-dimensional incompressible motion of a turbulent fluid with density variations are:

(i) conservation of volume flux

$$\frac{\partial \bar{u}}{\partial x} + \frac{\partial \bar{v}}{\partial y} = 0 \ , \tag{1.2.1}$$

(ii) conservation of momentum

$$\bar{u}\frac{\partial \bar{u}}{\partial x} + \bar{v}\frac{\partial \bar{u}}{\partial y} = -\frac{1}{\rho_a}\frac{\partial \bar{p}}{\partial x} - \frac{(\bar{\rho}-\rho_a)}{\rho_a} g - \frac{\partial \overline{u'^2}}{\partial x} - \frac{\partial \overline{u'v'}}{\partial y} \ , \tag{1.2.2}$$

$$\bar{u}\frac{\partial \bar{v}}{\partial x} + \bar{v}\frac{\partial \bar{v}}{\partial y} = -\frac{1}{\rho_a}\frac{\partial \bar{p}}{\partial y} - \frac{\partial \overline{u'v'}}{\partial x} - \frac{\partial \overline{v'^2}}{\partial y} \ , \tag{1.2.3}$$

where u', and v' are the deviations in velocity from the time-averaged mean values of u and v respectively, and $\bar{p}$ the deviation from hydrostatic pressure.

(iii) conservation of tracer

$$\bar{u}\frac{\partial \bar{c}}{\partial x} + \bar{v}\frac{\partial \bar{c}}{\partial y} = -\frac{\partial \overline{u'c'}}{\partial x} - \frac{\partial \overline{v'c'}}{\partial y} \ , \tag{1.2.4}$$

where $\bar{c}$ is the time-averaged tracer concentration and c' the deviation from this mean value. An equation must also be provided for the relation between the density and the tracer concentration. The linear form

$$\frac{\bar{\rho}(x,y) - \rho_a}{\rho_a} = \alpha_o \, \bar{c}(x,y) \ , \tag{1.2.5}$$

is assumed, where α_o is taken to be constant.

The above system of five equations (1.2.1) to (1.2.5) has ten

unknowns $\bar{u}$, $\bar{v}$, $\overline{u'^2}$, $\bar{c}$, $\overline{c'^2}$, $\overline{v'^2}$, $\bar{p}$, $\overline{u'c'}$, $\overline{v'c'}$, $\bar{\rho}$, and therefore cannot be solved even if the appropriate boundary conditions were provided and this is the fundamental problem of turbulent fluid mechanics.

An extremely large number of methods of dealing with this general problem has been proposed but the existing work on two-dimensional free shear flows (jets, plumes, wakes, etc.) can be classified into one of two schools of thought. The first school tries to derive a constitutive equation, i.e., a relation (not necessarily linear) between the Reynolds stress tensor and the deformation tensor of the fluid. The early workers in this school assumed, in addition, self-preservation for the mean and fluctuating quantities (see, for example, Tollmien [45], G. I. Taylor [46], or the textbook by Schlichting [47], pp. 590-613). More recent workers use more complex constitutive equations and solve numerically the appropriate system of equations (see, for example, Saffman [48]). The validity of this approach has been criticized by a growing number of investigators, including Laufer [49] and Coles [50]. Batchelor [51] also pointed out the defects of the early models of this school.

A second group of investigators integrates the equations of motion across the jet and derives conservation integrals for the mass, momentum and buoyancy fluxes (see Corrsin and Uberoi [52], Morton et al [20], Brooks and Koh [53], List and Imberger [23]). For a two-dimensional buoyant jet in uniform and still environment this approach leads to equations of the form:

(i) conservation of volume flux

$$\frac{d}{dx} \int_{-\infty}^{\infty} \bar{u}(x,y)dy = -2 \lim_{y\to+\infty} \bar{v}(x,y) \ , \tag{1.2.6}$$

(ii) conservation of momentum

$$\frac{d}{dx} \int_{-\infty}^{\infty} (\bar{u}^2 + \overline{u'^2} + \frac{\bar{p}}{\rho_a})dy = -\int_{-\infty}^{\infty} \frac{\bar{\rho}(x,y)-\rho_a}{\rho_a} g dy - 2 \lim_{y\to+\infty} [\bar{u}\,\bar{v} + \overline{u'v'}] \tag{1.2.7}$$

(iii) conservation of tracer

$$\frac{d}{dx} \int_{-\infty}^{\infty} [\bar{u}\,\bar{c} + \overline{u'c'}]dy = -2 \lim_{y\to+\infty} [\bar{c}\,\bar{v} + \overline{c'v'}] \tag{1.2.8}$$

The following assumptions are then generally made:

(i) The integration is assumed to be extended to infinity, hence it is argued that

$$\lim_{y\to+\infty} [\bar{u}\,\bar{v} + \overline{u'v'}] = 0$$

$$\lim_{y\to+\infty} [\bar{c}\,\bar{v} + \overline{c'v'}] = 0$$

(ii) It is assumed that the turbulent tracer transfer $\overline{u'c'}$ is negligible in comparison with $\bar{u}\,\bar{c}$.

(iii) It is assumed that $\overline{u'^2} + \frac{\bar{p}}{\bar{\rho}} << \bar{u}^2$. This has been justified by the experimental work of Miller and Comings [12].

These assumptions then lead to the following set of equations:

(i) conservation of mass

$$\frac{d}{dx} \int_{-\infty}^{\infty} \bar{u}(x,y)dy = -2 \lim_{y\to+\infty} \bar{v}\ (x,y) \ , \tag{1.2.9}$$

(ii) conservation of kinematic momentum flux

$$\frac{d}{dx}\int_{-\infty}^{\infty}\overline{u}^2(x,y)dy = -\int_{-\infty}^{\infty}\frac{\overline{\rho}(x,y)-\rho_a}{\rho_a}gdy \ , \tag{1.2.10}$$

(iii) conservation of kinematic buoyancy flux (from Eq. (1.2.8) and Eq. (1.2.5))

$$\frac{d}{dx}\int_{-\infty}^{\infty}\frac{\overline{\rho}(x,y)-\rho_a}{\rho_a}g\overline{u}dy = 0 \ . \tag{1.2.11}$$

A more accurate description of the basic jet mechanics than represented by the above equations and assumptions will be presented in Chapter 2, where the deficiencies of Eq. (1.2.10) and Eq. (1.2.11) will be discussed in more detail.

The Eqs. (1.2.9), (1.2.10) and (1.2.11) have provided the basic framework for almost all the previous investigations of jets, plumes and buoyant jets. From this point, two further approaches have been used to obtain the basic jet behavior.

I. Entrainment Coefficient Approach

The entrainment coefficient approach (Brooks and Koh [53], Morton et al [20], Morton [24], Fan [58], Fan and Brooks [22]) is based on the hypothesis of G. I. Taylor [20] that the entrainment should be proportional to some characteristic velocity of the jet, i.e.

$$-\lim_{y\to+\infty} 2\overline{v}(x,y) = 2\alpha_e\overline{u}_M(x) \ , \tag{1.2.12}$$

where the entrainment coefficient α_e was assumed by Morton [24] to be a universal constant with the same value for jets, plumes, and

buoyant jets. Similarity of the velocity and temperature profiles has also been assumed and, on the basis of the experimental evidence, they have been given by the Gaussian curves

$$\bar{u}(x,y) = \bar{u}_M(x) \exp[-\ell n2 \ (y/b_u)^2] \ , \tag{1.2.13}$$

$$\bar{\rho}(x,y)-\rho_a = (\bar{\rho}_M(x)-\rho_a) \exp[-\ell n2 \ (y/b_T)^2] \ , \tag{1.2.14}$$

where $b_u(x)$ and $b_T(x)$ are the characteristic lengths of the velocity and temperature profiles respectively, and are defined by the relations

$$\bar{u}(x,\pm b_u(x)) = \bar{u}(x,0)/2 \ , \tag{1.2.15.a}$$

$$\bar{\rho}(x,\pm b_T(x)) = \bar{\rho}(x,0)/2 \ , \tag{1.2.15.b}$$

and where $\bar{u}_M(x) = \bar{u}(x,0)$ and $\bar{\rho}_M(x) = \bar{\rho}(x,0)$. One further assumption has been that

$$\frac{b_T(x)}{b_u(x)} = \lambda \tag{1.2.16}$$

where λ is supposed a universal constant.

Under these assumptions the system of equations (1.2.9), (1.2.10) and (1.2.11) becomes

$$\frac{d}{dx} [\bar{u}_M b_u] = 2\alpha_e \bar{u}_M (\ell n2/\pi)^{1/2} \tag{1.2.17}$$

$$\frac{d}{dx} [\bar{u}_M^2 b_u] = -\sqrt{2} \ g \ \frac{\overline{\Delta\rho}_M}{\rho_a} \ b_T \tag{1.2.18}$$

$$\frac{d}{dx}\left[\frac{\overline{\Delta\rho}_M \bar{u}_M b_u}{\rho_a (1+\lambda^2)^{1/2}}\right] = 0 \qquad (1.2.19)$$

where $\overline{\Delta\rho}_M(x) = \bar{\rho}_M(x) - \rho_a$. The system of the ordinary differential Equations (1.2.17), (1.2.18), and (1.2.19) with appropriate initial conditions can be solved numerically (see Fan and Brooks [22]) to find the evolution of $\bar{u}_M(x)$, $\bar{b}_u(x)$, and $\overline{\Delta\rho}_M(x)$.

It seems worthy to examine closely the two particular cases of a pure jet and of a pure plume, where analytical solutions can be obtained for the equations (1.2.17), (1.2.18) and (1.2.19). For a pure jet $\bar{\rho}(x,y) = \rho_a$, hence the kinematic momentum flux is conserved, i.e.

$$(\pi/2\ell n2)^{1/2}\, \bar{u}_M^2(x) b_u(x) = \bar{u}_o^2\, D \qquad (1.2.20)$$

where $\bar{u}_o$ the exit velocity and D is the width of the jet at the orifice. Then the system of Equations (1.2.17) and (1.2.20) can be solved explicitly to give

$$\frac{db_u}{dx} = K_{1u} = (16\ \ell n2/\pi)^{1/2}\ \alpha_j \qquad (1.2.21)$$

where K_{1u} a constant and α_j is the entrainment coefficient for a pure jet.

The equation (1.2.21) can be written

$$\frac{b_u}{D} = K_{1u}\left(\frac{x}{D} + K_{2u}\right)$$

The decay of the centerline velocity is then given by Eq. (1.2.20) as

$$\left(\frac{\overline{u}_o}{\overline{u}_M}\right)^2 = \sqrt{\frac{\Pi}{2\ell n2}}\,(\frac{x}{D} + K_{2u})K_{1u} \tag{1.2.22}$$

and the centerline dilution of a passive tracer is given by

$$\left(\frac{\overline{T}_o}{\overline{T}_M}\right)^2 = \sqrt{\frac{\Pi}{\ell n2}}\;\frac{1}{1+\left(\frac{b_u}{b_T}\right)^2}\;K_{1u}(\frac{x}{D} + K_{2u})\ , \tag{1.2.23}$$

where $\overline{T}_o$ and $\overline{T}_M(x)$ are the excess tracer concentrations above ambient at the jet exit, and on the jet axis, respectively.

For a plume it is easy to verify that the system of Equations (1.2.17), (1.2.18) and (1.2.19) admits the following solution (see Lee and Emmons [27])

$$\overline{u}_M(x) = A_o\beta_o^{1/3} \sim \text{constant}\ , \tag{1.2.24}$$

$$\frac{\overline{\Delta\rho}_M(x)}{(\rho_o-\rho_a)} = A_1 x^{-1}\ , \tag{1.2.25}$$

and

$$\frac{db_u}{dx} = (4\ell n2/\Pi)^{1/2}\;\alpha_p\ , \tag{1.2.26}$$

where A_0, A_1, are constants which can be easily determined. α_p is the entrainment coefficient for a plume and

$$\beta_o = \frac{\rho_a - \rho_o}{\rho_a} g \bar{u}_o D ,$$

the initial kinematic buoyancy flux if ρ_o is the density of the jet at the orifice.

Since the basic assumption of this approach is that the entrainment coefficient is constant, i.e.

$$\alpha_j = \alpha_p = \alpha_e$$

it is concluded from (1.2.21) and (1.2.26) that the jet half-width b_u should be twice the plume half-width. This is indicated also in the numerical solution of Fan and Brooks ([22], Figure 17(e)). Brooks [67] adopted the value $\alpha_e = 0.14$ since he believed that the flows of interest to him were more plume-like than jet-like, hence

$$\frac{db_u}{dx} = K_{1u} = 0.26 \qquad \text{for a jet,}$$

and

$$\frac{db_u}{dx} = K_{1u} = 0.13 \qquad \text{for a plume.}$$

The experimental results of this investigation for pure jets and plumes have shown that the coefficient K_{1u} is approximately the same for both jets and plumes (see Section 5.1 and Chapters 8 and 9). The assumption of a universal entrainment coefficient is therefore incorrect and in reality

$$\alpha_j = \frac{\alpha_p}{2}$$

II. Dimensional Analysis

Dimensional analysis can be used to find the basic characteristics of the jets and plumes. For a pure jet in uniform environment, Eq. (1.2.10) implies that the kinematic momentum flux is conserved, i.e.

$$\overline{u}_M^2(x) b_u(x) = \text{constant}.$$

Dimensional analysis then gives for a pure jet (Landau and Lifshitz [63])

$$b_u \sim x \quad ,$$

$$\overline{u}_M^2 \sim x^{-1} \quad .$$

For a plume, dimensional analysis gives (see Batchelor [54])

$$\overline{u}_M \sim \beta_o^{1/3} \sim \text{constant} \quad ,$$

$$b_u(x) \sim x \quad ,$$

$$\overline{\Delta\rho}_M(x) \sim x^{-1} \quad .$$

List and Imberger [23] used dimensional analysis to write the integrated equations of motion in the form

$$\frac{d\mu}{dx} = \frac{m}{\mu} q(R,C) \qquad (1.2.27)$$

$$\frac{dm}{dx} = \frac{\mu\beta}{m} h(R,C) \qquad (1.2.28)$$

$$\frac{d\beta}{dx} = 0 \qquad (1.2.29)$$

where $$R = \frac{\mu^3\beta}{m^3}, \qquad C = \frac{\mu}{(mx)^{1/2}},$$

and $$\mu = \int_{-\infty}^{\infty} \overline{u}(x,y)\, dy, \qquad m = \int_{-\infty}^{\infty} \overline{u}^2(x,y)\, dy,$$

$$\beta = -\int_{-\infty}^{\infty} \frac{\overline{\rho}-\rho_a}{\rho_a} g\, \overline{u} dy .$$

Their approach was to find the leading terms of the functions q(R,C) and h(R,C). Their basic idea has been extended in this investigation (see Section 2.3).

1.3 REVIEW OF PREVIOUS EXPERIMENTS

I. Pure jet

Usually an experimenter measures the mean velocity and concentration profile at different distances from the exit, he plots the growth of the half-widths of mean velocity and temperature profile, the centerline decay of mean velocity and the centerline dilution and finds that

$$\frac{b_u}{D} = K_{1u}\left(\frac{x}{D} + K_{2u}\right), \tag{1.3.1}$$

$$\frac{b_T}{D} = K_{1T}\left(\frac{x}{D} + K_{2T}\right), \tag{1.3.2}$$

$$\left(\frac{\overline{u}_o}{\overline{u}_m}\right)^2 = C_{1u}\left(\frac{x}{D} + C_{2u}\right), \tag{1.3.3}$$

$$\left(\frac{\overline{T}_o}{\overline{T}_m}\right)^2 = C_{1T}\left(\frac{x}{D} + C_{2T}\right). \tag{1.3.4}$$

The coefficients K_{1u}, K_{2u}, K_{1T}, K_{2T}, C_{1u}, C_{2u}, C_{1T}, C_{2T} are then usually empirically determined. Alternatively some investigators report the fitting of their mean velocity results in the form

$$\frac{\bar{u}(x,y)}{\bar{u}_m(x,y)} = e^{-\delta_u (\frac{y}{x})^2} , \qquad (1.3.5)$$

without determining the location of any virtual origin. In this case the coefficient K_{1u} can be calculated by

$$K_{1u} = \sqrt{\frac{\ell n 2}{\delta_u}} .$$

Table (1.3.1) summarizes the principal parameters and results for the mean velocity and mean temperature found by other investigators. The coefficients K_{1u}, K_{2u}, C_{1u}, C_{2u} for Forthmann's [3] experiments were calculated from his graphs by the present investigator. The experimental investigation of Heskestad [5] was good but the mean velocity at the jet exit, $\bar{u}_o$, was not reported. However, it can be estimated from the reported Reynolds number, so the coefficients C_{1u} and C_{2u} were calculated by the present investigator using an inferred value for $\bar{u}_o$, (they were also calculated by Flora et al [4]). Mih's [11] experiments were carried out by discharging the jet into a diffusion chamber which was too small to ensure a "free" jet. To overcome this problem, he pumped water out of the diffusion chamber which produced a current in the chamber, thereby violating the assumption that the ambient flow be a jet-induced flow only. The centerline velocity decay (Figure 7, [11]) is apparently incorrect because all of his experimental points indicate that he measured more

Experimenter	$\frac{X}{D}$ from	$\frac{X}{D}$ to	Aspect Ratio	$R_e \times 10^3$	K_{1u}	K_{2u}	C_{1u}	C_{2u}	K_{1T}	K_{2T}	C_{1T}	C_{2T}	Reference
Miller	0	40	40	20	0.096	1.15	0.181 0.163	-0.62 1.05	--	--	--	--	[12] [39]
Heskestad	47	155	120	34	0.11	-4.2	0.27	-10.0	--	--	--	--	[5]
Zijnen	10 10	40 35	20 25	13 13	0.096 0.099	0.6 1.7	0.162 0.205	0.6 1.7	0.141 --	0.6 --	0.25 --	0.6 --	[16] [38]
Forthmann	0	25	21	10	0.098	0.33	0.18	0.11	--	--	--	--	[3]
Jenkins	10 10 10	60 60 60	24 24 24	14 14 14	0.088 0.091 0.096	4.5 3.0 2.5	0.16 -- --	4 -- --	0.123 0.128 0.137	4.8 3.6 3.2	-- -- --	-- -- --	[8] [8] [8]
Knystautas	50	295	50	40	0.106	-1.5	0.18	-1.4	--	--	--	--	[7]
Gartshore	100	100	130	20	0.115 0.102	-- -2.0	-- 0.164	-- -2.0	--	--	--	--	[9] [37]
Flora	0	90	50	20	0.109	0.0	--	--	--	--	--	--	[4]
Goldschmidt	15	67	15	16	0.099	0.66	0.207	-5.83	--	--	--	--	[10]
Bradbury	15	70	48	30	0.109	--	--	--	--	--	--	--	[2]
Mih	6	300	58	20	0.116	--	0.175	--	--	--	--	--	[11]
Albertson	1	2000	300	10	0.126	--	0.192	--	--	--	--	--	[1]
Reichardt	0	100	21	24	0.108	--	--	--	0.17	--	--	--	[13]
Vulis	0	15	15	80	0.109	0.64	--	--	--	--	--	--	[14]
Hetsroni	10	30	26	8	0.128	--	--	--	--	--	--	--	[6]
Nakaguchi	10	100	133	10	0.106	-0.3	0.189	-0.3	--	--	--	--	[37]
Tailland	10	100		20	0.10	0.0	--	--	--	--	--	--	[42]
Householder			16		0.091	1.46	0.193	-6.98	--	--	--	--	[4] [44]
Bicknell	15	125	60	30	0.115	-2.7	0.112	6.7	0.17	-2.0	--	--	[57]

Table 1.3.1. Review of previous experiments for a two-dimensional pure jet

momentum than the jet had originally (of the order 25% at x/D = 15). The opinion of this investigator is that his coefficients C_{1u}, C_{2u} should be discounted. He also did not calculate the location of the virtual origin.

The experiments by Miller et al [12] can be considered of high quality. They verified experimentally that $\overline{u'^2}$ and $\frac{\overline{p}}{\rho}$ are of the same order and of opposite sign. Their experimental results are tabulated in Miller's Ph.D. thesis ([39], Table 18) from where this writer calculated C_{1u}, C_{2u}. The writer also calculated the coefficients K_{1u}, K_{2u} for the experiments by Vulis et al [14] but these should also probably be discounted because of the limited accuracy involved in estimating the half-width from their very small published figures.

The variation of the coefficients K_{1u}, K_{1T}, found by Jenkins et al [8] is, in this investigator's opinion, due to minor instrumentation problems rather than to the argument presented by them that K_{1u}, K_{1T} increased with increasing the exit temperature. It seems unlikely that this is the case when the initial Richardson number was of the order 10^{-5} ($\sim$ pure jet), and the measurements were in the same region (10 to 60 diameters from exit). Jenkins et al [8] claim that the centerline temperature $\overline{T}_m$ decays like x^{-2}, which is not in agreement with any other theory or experiments. Hestroni et al [6] did not calculate the location of the virtual origin and probably this is the reason why their K_{1u} is large. Reichardt [13] did not calculate the virtual origin nor the centerline velocity decay. The writer calculated the coefficients K_{1u}, K_{2u} from Knystautas' [7] experimental results presented in his Figure 6 and the coefficients C_{1u}, C_{2u} from his Figure 8. The

coefficients C_{1u}, C_{2u} from Flora et al [4] should probably be discounted because they calculated the exit velocity from the measured momentum of the jet at a downstream position and assumed conservation of the kinematic momentum flux, an assumption that will be shown to be questionable (see Chapter 2.1). Bradbury [2] investigated a plane jet in a slow secondary current hence his coefficients C_{1u}, C_{2u} are not appropriate to this study. The coefficient K_{1u} for Tailland et al's [42] experiments was calculated by the present investigator from their Figure 3.

The writer calculated the coefficients K_{1u}, K_{2u}, C_{1u}, C_{2u} from Bicknell's [57] experimental results presented in his Figure 8, and the coefficients K_{1T}, K_{2T} from his Figures 12, 13 and 14.

Turbulence intensity studies have been reported by Miller [12], Heskestad [5], Zijnen [17], Bradbury [2], and Vulis [14]. The turbulence energy balance was investigated by Heskestad [5] and Bradbury [2]. Intermittency measurements were reported by Heskestad [5] and Hannum [40].

II. Pure plume

Rouse et al [21] considered experimentally the pure two-dimensional plume, simulated in their investigation by a line gas burner. This kind of experiment is very delicate because small convection currents in the ambient air usually exist and the assumption of a motionless environment is most probably violated. Their experimental measurements of velocity show substantial scatter either because of inadequate instrumentation or because of existing ambient air currents. They found

$$\overline{u}(x,y) = \overline{u}_m \, e^{-32(\frac{y}{x})^2} \quad , \quad \overline{T}(x,y) = \overline{T}_m \, e^{-41(\frac{y}{x})^2}$$

which give $K_{1u} = 0.147$ and $K_{1T} = 0.130$. They did not know the input heat flux a priori, but calculated it from the measured mean velocity and temperature profile assuming implicitly that $\overline{u'T'} << \bar{u}\,\bar{T}$. It will be shown later that this is a questionable assumption (see Chapter 6 on temperature-velocity results). Kotsovinos and List [25] measured directly the entrainment in a pure plume, simulated by a heater in a water tank. The input heat flux was known and, although the velocity and temperature profiles were not measured, the results can be combined with the results of the present investigation to give $K_{1u} = 0.11$.

Ellison et al [26] measured an entrainment coefficient for the half-plume equal to 0.112, which may be used with (1.2.18), to give $K_{1u} = 0.105$. Lee's Ph.D. thesis [55] is the basis of the Lee and Emmons [27] publication. They measured temperature profiles above a line gas burner, from which the coefficients K_{1T} and K_{2T} can be calculated as 0.130 and 0.9 respectively (see [55], Figure 5-2). Velocities were not measured, but they tried to estimate the entrainment coefficient α_p and the growth of the velocity half-width K_{1u} from temperature measurement alone which, in principle, is not possible without any implicit or explicit assumptions. In their case, they assumed implicitly, that the turbulent heat transfer $\int_{-\infty}^{\infty} \overline{u'T'}\, dy$ was negligible with respect to the mean heat transfer $\int_{-\infty}^{\infty} \bar{u}\,\bar{T}\, dy$, which will be shown to be incorrect (see Chapter 6). The conclusion of their calculations (not measurements) that $\alpha_p = 0.16$ and $K_{1T}/K_{1u} = 0.88$ should therefore be discounted.

The experimental measurements of concentration by Anwar [62] show substantial scatter. He did not determine the location of the virtual origin. He suggested $K_{1T} = 0.13$.

III. Buoyant jet

To the best of the knowledge of this writer, no experiments have been reported concerning a two-dimensional buoyant jet in transition from a jet to a plume.

1.4 SCOPE OF THIS WORK

The scope of this work is the systematic study of the entrainment and mixing processes in a two-dimensional buoyant jet in its transition from a pure jet to a pure plume. For this purpose an organized set of experiments over a wide range of initial Richardson number has been carried out to improve the understanding of the buoyant jet mechanics and to make possible the development of a theoretical model which is based on correct physical assumptions. The practical outcome of this investigation is to provide a definite input for the design of two-dimensional buoyant jet type diffusers. From a broader point of view, the attitude is to study the jet problem in a rigorous way with the hope that the understanding of the fundamental laws of free turbulence flows will be improved.

2. THE MECHANICS OF JETS

2.0 BASIC DEFINITIONS AND ASSUMPTIONS

The two-dimensional turbulent pure jet, pure plume and buoyant jet problem will be studied. The fluid (in this investigation, water) is assumed to be incompressible. The ambient fluid is assumed to be motionless, except for the movements induced by the jet, and of uniform density ρ_a. The pure jet, plume, or buoyant jet is assumed to be turbulent and therefore viscosity and molecular diffusivity will be neglected. Density variations will be assumed small, so that the density difference is important only in the gravitational body force term in the equations of motion.

A pure jet is defined as a source of kinematic momentum flux, m_o and/or kinematic mass flux μ_o; a pure plume is a source of kinematic buoyancy flux β_o only. A buoyant jet is a source of kinematic mass flux μ_o, kinematic momentum flux m_o, and kinematic buoyancy flux β_o. Using dimensional analysis, it can shown that each buoyant jet has effectively two characteristic length scales. One, μ_o^2/m_o, defines the importance of the initial volume flux (or kinematic mass flux), and the other $m_o/\beta_o^{2/3}$ defines the importance of the initial momentum flux relative to the buoyancy. The ratio of these two scales is the non-dimensional number

$$R = \frac{\mu_o^3 \beta_o}{m_o^3}$$

which expresses the ratio of the distance at which kinematic momentum flux is important relative to kinematic buoyancy flux, to that at which

kinematic momentum flux is important relative to kinematic mass flux. The non-dimensional number, R, is called the Richardson number of the jet. The Richardson number, calculated at the jet origin, assuming uniform velocity and temperature profiles, can be written

$$R_o = \frac{\frac{\overline{\Delta\rho}}{\rho_o} g D}{\overline{u}_o^2} ,$$

i.e., the Richardson number is the square of the inverse of the densimetric Froude number. For a pure plume, the local Richardson number

$$R_p = \frac{\mu^3(x)\beta}{m^3(x)}$$

will be shown (see Chapters 2.2 and 5.1) to be a constant ($\approx$0.6), while for a pure jet it is equal to zero. A buoyant jet with an exit Richardson number $R_o << R_p$, can be considered to be a pure jet for a distance $x < m_o/\beta_o^{2/3}$ (where x is the distance from exit). However, since the local Richardson number continuously increases, eventually, for $x >> m_o/\beta_o^{2/3}$, it will approximate the constant value of the plume Richardson number R_p. The conclusion from this discussion is that a buoyant jet is always in transition towards a pure plume.

Another important invariant of a buoyant jet is the non-dimensional ratio C defined by (see Section 5.1)

$$C = \frac{\mu(x)}{\sqrt{m(x)\ (x-x_o)}} \qquad (2.0.1)$$

where x_o is the location of a virtual origin. The invariant C, which is

a measure of the angle expansion of the buoyant jet, has been found to be almost constant at the same value (0.55) for jets, plumes, and buoyant jets. The virtual origin is then defined by applying Eq. 2.0.1 at the orifice of the jet, i.e., at x = 0 so that

$$x_o = - \frac{\mu_o^2}{m_o C^2} = - \frac{D}{C^2} \approx - 3.3\ D\ . \qquad (2.0.2)$$

This definition of the virtual origin is quite different from the virtual origins x_{ou}, x_{oT} of the mean velocity and temperature profiles respectively defined from the relations

$$x_{ou} = -K_{2u} D\ ,$$

$$x_{oT} = -K_{2T} D\ .$$

The virtual origin defined by Eq. 2.0.2 is always upstream of the jet orifice; the experimentally determined virtual origins x_{ou}, x_{oT} were found (see Table 1.3.1) to be upstream or downstream of the jet orifice. This present study will explain that these variations are due to the non-self-preserving character of the jet.

In its initial stage of development, (5-6 characteristic lengths for a pure jet), a plane jet consists of two plane mixing layers. After the two mixing layers have merged for some distance, the jet becomes fully developed. Viewed instantaneously an irregular and sharp interface separates the jet fluid which is turbulent from the ambient fluid which is irrotational. If the jet or ambient fluid has a tracer, this sharp interface also divides fluid of different concentration (see Coles [43]).

The difference that can be seen in a short exposure photograph and time exposure photograph of a jet is dramatic (see Werlé [36] plates A, B). In a time exposure of a jet, a fictitious interface (a plane) appears which separates fluid that is sometimes turbulent from fluid that is never turbulent. This plane will be called the boundary of the jet.

It seems necessary to clarify the idea of the boundary of a jet. For this purpose, first the intermittency $\gamma_A(x,y)$ of a quantity A of jet will be defined as

$$\gamma_A(x,y) = \lim_{t\to\infty} \frac{1}{t} \int_o^t I_A(x,y,t') \, dt'$$

where

$$I_A(x,y,t) = \begin{cases} 1 \text{ if quantity A is present at } x,y \text{ at time } t \\ 0 \text{ otherwise} \end{cases}$$

The vorticity of the fluid or the presence of tracer is usually used to characterize the presence of the jet at any point (x,y) at time t. The boundaries of the jet can then be defined by the two lines

$$y = \pm B(x) \ , \qquad (2.0.3)$$

where $2B(x)$ is the width of the intermittency profile $\gamma(x,y)$ when $\gamma \approx 0$. The experimental determination of γ for values close to zero is difficult and depends on the chosen threshold level for the quantity A. Although an estimation of B(x) for practical purposes can be obtained (see Figure 4.4.1 and 4.4.2), this estimate must necessarily be a function of the threshold level. The profile of maximum temperature can also be used to estimate B(x) (see Section 4.3).

Therefore, given any threshold level by which to determine the intermittency, the boundaries of the jet $y = \pm B(x)$ describe an inherent property of the jet, which is quite different from the width $y = \pm b(x)$, which is defined by

$$\overline{T}(x, \pm b(x)) = \frac{\overline{T}(x,o)}{N} \quad . \tag{2.0.4}$$

N can be any real number larger than one but it usually has the value two, in which case b(x) is called the half-width.

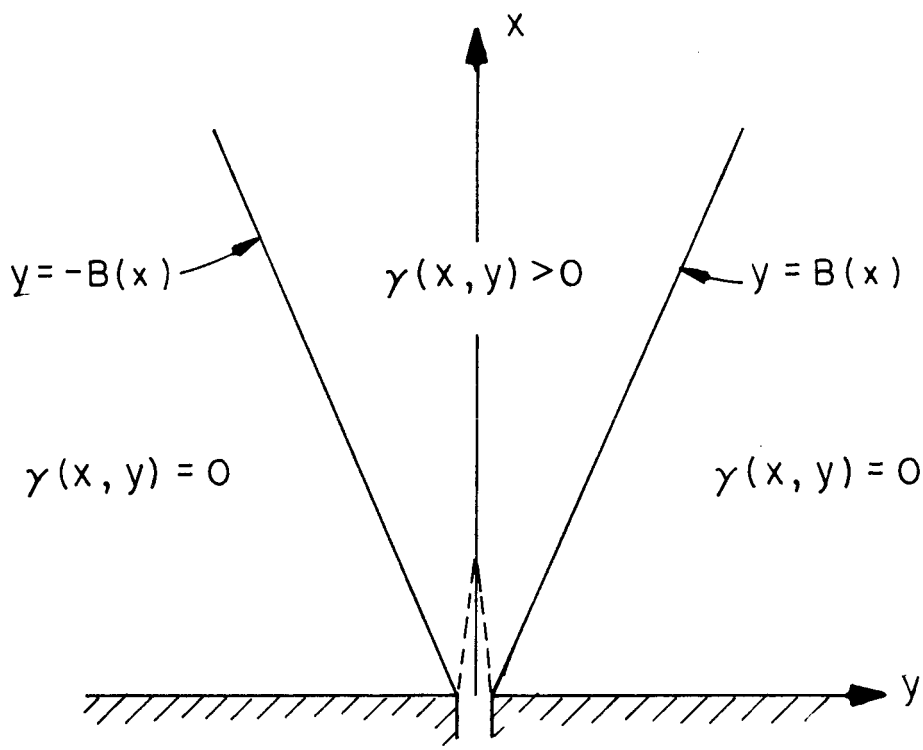

Figure 2.0.1. Definition of jet boundary

2.1 THE MECHANICS OF THE TWO-DIMENSIONAL PURE JET

A pure jet is defined here as a steady source which delivers kinematic mass flux μ_o, and kinematic momentum flux m_o, through a slot of thickness D to an ambient fluid. The geometry and the axes of coordinates of Figure 2.1.1, indicating a jet out of a wall, will be considered.

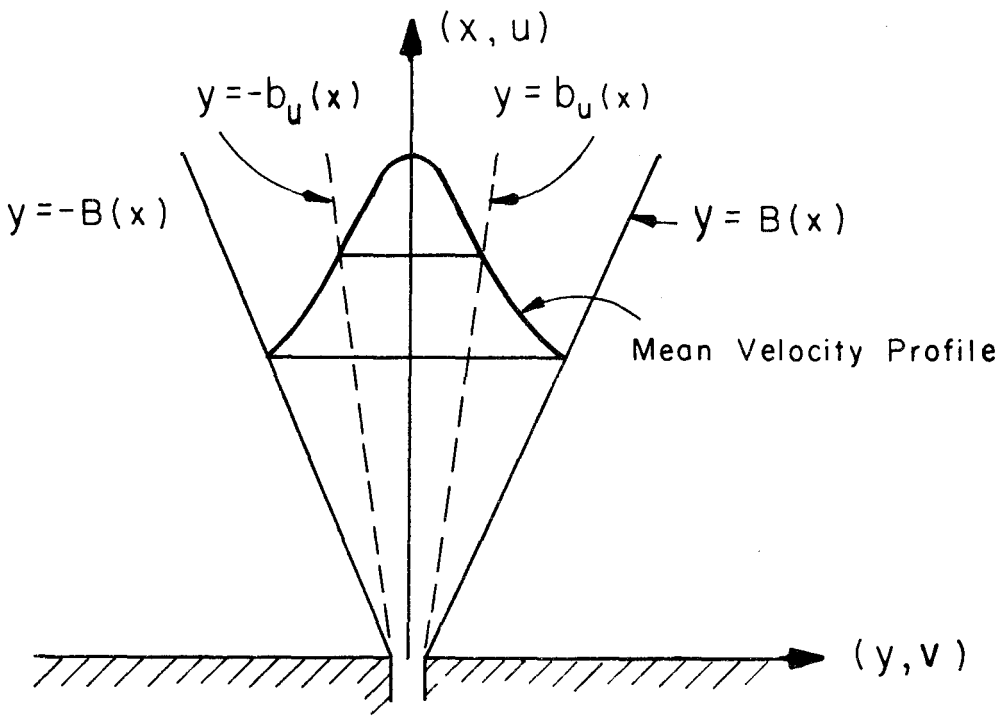

Figure 2.1.1. Geometry of a jet

The jet will be assumed turbulent, which according to Sato et al [66] requires a Reynolds number at the exit greater than 500. The equations are the

continuity equation

$$\frac{\partial \bar{u}}{\partial x} + \frac{\partial \bar{v}}{\partial y} = 0 \quad , \tag{2.1.1}$$

and momentum equations,

$$\frac{\partial}{\partial x}\left[\bar{u}^2 + \overline{u'^2} + \frac{\bar{p}}{\rho}\right] + \frac{\partial}{\partial y}\left[\bar{u}\,\bar{v} + \overline{u'v'}\right] = 0 \ , \tag{2.1.2}$$

$$\frac{\partial}{\partial x}\left(\bar{u}\,\bar{v} + \overline{u'v'}\right) + \frac{\partial}{\partial y}\left(\bar{v}^2 + \overline{v'^2} + \frac{\bar{p}}{\rho}\right) = 0 \ . \tag{2.1.3}$$

The turbulent fluctuations are zero at the boundaries of the jet, so that

$$\overline{u'v'}(x, \pm B(x)) = \overline{u'^2}(x, \pm B(x)) = \overline{v'^2}(x, \pm B(x)) = 0 \tag{2.1.4}$$

It is not possible to solve the Reynolds equations with the present state of the art of free turbulence; the Equations (2.1.1), (2.1.2), (2.1.3) are therefore integrated across the jet using the boundary conditions (2.1.4) to give

$$\frac{d}{dx}\int_{-B(x)}^{B(x)} \bar{u}(x,y)\,dy + 2\bar{v}(x, B(x)) = 2\frac{dB(x)}{dx}\,\bar{u}(x,B(x)) \tag{2.1.5}$$

$$\frac{d}{dx}\int_{-B(x)}^{B(x)}\left[\bar{u}^2 + \overline{u'^2} + \frac{\bar{p}}{\rho}\right] dy + \left[\bar{u}\,\bar{v}\right]_{-B(x)}^{B(x)} = 2\frac{dB(x)}{dx}\left[\bar{u}^2(x,B(x)) + \frac{\bar{p}}{\rho}\right] \tag{2.1.6}$$

$$\frac{d}{dx}\int_{-B(x)}^{B(x)}\left(\bar{u}\,\bar{v} + \overline{u'v'}\right) dy - 2\frac{dB(x)}{dx}\,\bar{u}(x,B(x))\,\bar{v}(x,B(x)) = 0$$

Now consider each of the terms in equation 2.1.6 in turn. The term

$$\frac{d}{dx} \int_{-B(x)}^{B(x)} (\overline{u}^2 + \overline{u'^2} + \frac{\overline{p}}{\rho}) \, dy$$

is what Benjamin [68] has termed the flow force of the jet and represents the rate of change of the total flux of momentum and the pressure force along the jet. Miller and Comings [12] (Figures 7 and 8), and Bradbury [2] (Figures 8, 9, 10, and 11) have investigated the contributions from turbulent momentum flux and the pressure, and have shown that these contributions are approximately equal in magnitude and opposite in sign. Their experimental results indicate a weak positive pressure gradient on the jet axis and this will tend to reduce the momentum flux of the jet. We will therefore ignore these contributions to the integral. The second term

$$\left[\overline{u}\ \overline{v}\right]_{-B(x)}^{B(x)}$$

represents the flux of axial momentum into the jet from the outer flow entrained into the jet.

Morton et al [19] and Corrsin and Uberoi [52] ignored this term by assuming that axial component of velocity $\overline{u}(x)$ vanished outside the jet. The term on the right-hand side

$$2\frac{dB(x)}{dx}\left[\overline{u}^2(x,B(x) + \frac{\overline{p}}{\rho}\,(x,B(x))\right]$$

represents the flux of vertical momentum and the component of axial

pressure force that act on the sloping side of the jet as defined by $y = \pm B(x)$. The pressure component is small and, as Miller and Comings [12] show, represents a decelerating component of force and it will be ignored in the subsequent analysis because it is difficult to characterize. However, recognizing that it is a decelerating component, we can recognize its influence. The momentum flux term is also small but can easily be incorporated into the analysis later as will be shown.

We believe that an improvement can be achieved by examining the error involved in neglecting the above terms associated with the induced flow field, and which have been ignored by previous investigators. The procedure will be to assume first that the terms usually neglected are negligible. From this we will obtain an approximate solution, and then we will determine the correction to this approximation. The equations (2.1.5), (2.1.6) are now written as

$$\frac{d\mu}{dx} = -2\overline{v}(x, B(x)) ,$$

$$\frac{dm}{dx} = m_o \, \delta(x) , \qquad (2.1.8)$$

where

$$\mu(x) = \int_{-B(x)}^{B(x)} \overline{u}(x,y) \, dy ,$$

$$m(x) = \int_{-B(x)}^{B(x)} \overline{u}^2 \, dy \qquad (2.1.9)$$

and m_o is the kinematic momentum flux at the exit of the jet. From

(2.1.8) $m(x) = m_o$ so that using dimensional analysis

$$\frac{d\mu}{dx} = f(m,x) = f(m_o,x) = E_1 m_o^{1/2} x^{-1/2} , \qquad (2.1.10)$$

where E_1 is a constant to be determined experimentally, ($E_1 = 0.28$, as will be shown in Section 5.1). Hence the kinematic mass flux increases as $x^{+1/2}$ and a flow in the region where the intermittency is zero must be induced towards the jet. The ambient fluid therefore sees the jet as a distribution of planar sinks of strength $E_1 m_o^{1/2} x^{-1/2}$. The induced flow is irrotational (since at $y = \pm\infty$ the vorticity is zero and a slip condition is assumed). Lippisch [29] has an illustrative picture of such a flow induced by a jet out of a wall.

Now, for the ideal case of a series of sinks in a straight line from $x = 0$ to infinity (see Figure 2.1.2) of strength given by Eq. 2.1.10, the streamlines $\psi(x,y)$ of the induced flow, which satisfy the Laplace equation $\nabla^2\psi(x,y) = 0$ and the boundary conditions

$$\psi(0,y) = 0$$

$$\frac{d}{dx}\left(\psi(x,0)\right) = E_1 m_o^{1/2} x^{-1/2} , \qquad (2.1.11)$$

were calculated by G. I. Taylor [28] to be

$$\psi(x,y) = E_1 m_o^{1/2} (x^2 + y^2)^{1/4} \left(1 - \frac{y}{\sqrt{x^2+y^2}}\right)^{1/2} . \qquad (2.1.12)$$

Clearly these streamlines represent parabolas with slope $\phi = 45°$ at

$y = 0$, (see Figure 2.1.2). For the case of a real jet out of a wall, the flow field depicted schematically in Figure 2.1.3 will be assumed. Specifically it will be assumed that the jet originates as a source of kinematic momentum flux (only) m_o at a distance $x_o = \mu_o/C^2 m_o \approx 3.3$ D upstream from the jet orifice (see Eq. 2.0.2 and Figure 2.1.3), and that sinks of intensity given by Eq. 2.1.10 are distributed on the x'-axis from the virtual origin 0' to infinity. The angle ϕ (see Figure 2.1.3) will be assumed constant at a value $\pi/4$. The existence of the potential core is neglected in this approximation.

The procedure now will be to consider the momentum Eq. 2.1.6 and to discuss the terms which were previously neglected. From Figure 2.1.3

$$\overline{u}(x, B(x)) = \tan \phi \, \overline{v}(x, B(x))$$

Hence
$$[\overline{u}\,\overline{v}]_{-B(x)}^{B(x)} = 2 \tan \phi \, \overline{v}^2(x, B(x)) \, , \qquad (2.1.14)$$

and combining (2.1.14) and (2.1.5), it is seen that

$$[\overline{u}\,\overline{v}]_{-B(x)}^{B(x)} = \frac{1}{2} \tan \phi \left(\frac{d\mu}{dx}\right)^2 / (1 - \frac{dB(x)}{dx} \tan \phi)^2 \qquad (2.1.15)$$

Physically, Eq. 2.1.15 represents the x-component of the momentum of the induced flow. The momentum equation (2.1.6) now becomes

$$\frac{dm}{dx} = m_o \delta(x) - \frac{1}{2} \tan \phi \left(\frac{d\mu}{dx}\right)^2 / (1 - K_B \tan \phi)^2$$

$$+ 2K_B \overline{u}^2(x, B(x)) \qquad \text{or}$$

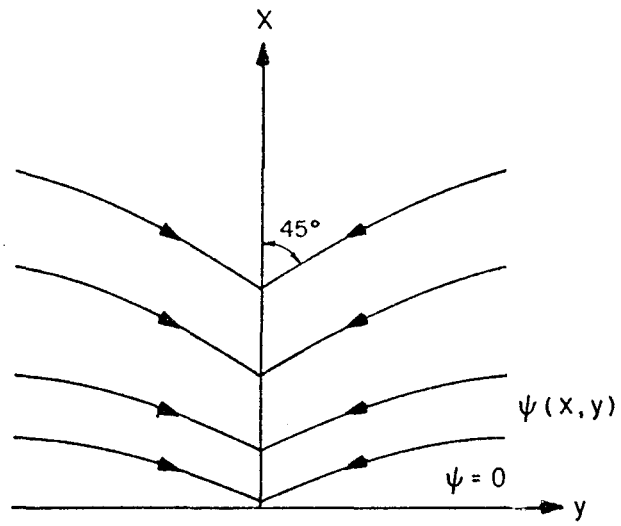

Figure 2.1.2. Flow towards a line distribution of sinks of strength given by Eq. 2.1.10.

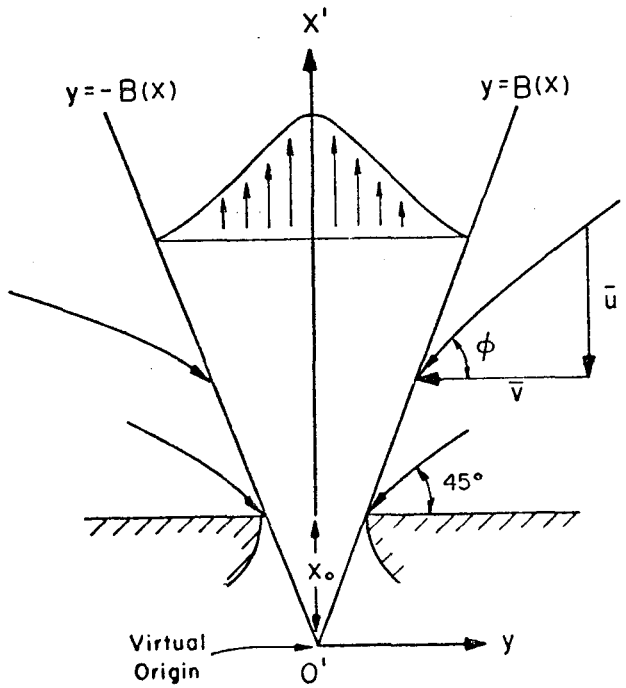

Figure 2.1.3. Schematic of the assumed induced flow and virtual origin of a real plane jet.

$$\frac{dm}{dx} = m_o \delta(x) - \frac{1}{2} \tan \phi \left(\frac{d\mu}{dx}\right)^2 / (1 - K_B \tan \phi) \qquad (2.1.16)$$

where

$$K_B = \frac{dB(x)}{dx} \approx 0.25 \quad \text{(see Section 4.3).}$$

We observe that the momentum of the induced flow (second term of the R.H.S. of the Eq. 2.1.16) tends to reduce the kinematic momentum flux defined by Eq. 2.1.9.

A solution which would predict precisely the kinematic momentum flux m(x) appears to be very difficult. However, a rough estimation of the reduction of the kinematic momentum flux due to the opposing momentum of the induced flow can be obtained using the simplified flow shown schematically in Figure 2.1.3.

Again using dimensional analysis, we write

$$\frac{d\mu}{dx} = E_1 m^{1/2} x^{-1/2} , \qquad (2.1.17)$$

and substitution of (2.1.17) in (2.1.16) gives

$$\frac{dm}{dx} = m_o \delta(x) - \frac{1}{2} E_1^2 \tan \phi \, x^{-1} m / (1 - K_B \tan \phi) \qquad (2.1.18)$$

Considering that induced flow exists only for $x' \geq x_o$, Eq. 2.1.18 implies, with x replaced by x', that

$$\frac{m(x)}{m_o} = \left(\frac{x_o}{x+x_o}\right)^{\frac{E_1^2}{2(1-K_B)}}$$

$$= \left(\frac{3.3}{\frac{x}{D}+3.3}\right)^{0.0522} \qquad (2.1.19)$$

where $E_1 = \frac{C}{2} \approx 0.28$ and x is the distance from the jet orifice.

For example, at x/D = 100, we obtain $m(x)/m_o = 0.83$, i.e., the opposing momentum of the induced flow reduces the initial kinematic momentum flux by 17%.

It will be shown in Section 5.2, where the experimental results of previous investigators are examined, that this estimation of the reduction of the initial kinematic momentum flux is conservative and that most investigators of a pure plane jet out of a wall experienced a much greater reduction of the kinematic momentum flux. This can be explained if we assume that the decelerating pressure gradient existing along the jet axis has a larger negative contribution to the flow force than the increase resulting from the turbulent momentum flux. However, this aspect of the problem, although investigated to some extent by Miller and Comings [12] and Bradbury [2], needs further study.

2.2 THE MECHANICS OF THE TURBULENT PURE PLUME

The convection flow generated by a steady line source of heat is called a two-dimensional plume. In the analysis that follows, it is assumed that the ambient fluid has only the motion induced by the plume and is of uniform density ρ_a, and that density variations from ρ_a are small. According to Forstrom et al [31] a fully turbulent plume is characterized by a modified Grashof number G_r greater than 5×10^9 where

$$G_r = \frac{\alpha g H_o x^3}{\rho_a c_p \nu^3} \quad ,$$

where H_o is the input heat flux per unit length,

α is the thermal expansion coefficient,

x is the distance from the heat source,

g is the gravitational acceleration (981 cm^2/sec),

ρ_a is the density of the ambient fluid,

c_p is the specific heat,

ν is the kinematic viscosity.

The Reynolds equations of motion integrated across the turbulent plume are

(i) volume conservation

$$\frac{d}{dx}\int_{-B(x)}^{B(x)} \bar{u}(x,y)\, dy = -2\bar{v}(x, B(x)) + 2\frac{dB(x)}{dx}\bar{u}(x, B(x)) \quad (2.2.1)$$

This equation was derived from integrating the incompressibility equation and assuming that small volume changes arising from the transfer of mass by diffusion are neglected (see List [32]).

(ii) kinematic momentum flux

$$\frac{d}{dx}\int_{-B(x)}^{B(x)} (\overline{u}^2 + \overline{u'^2} + \frac{\overline{p}}{\overline{\rho}})\, dy = -\int_{-B(x)}^{B(x)} (\frac{\overline{\rho}-\rho_a}{\rho_a})g\,dy + [\overline{u}\ \overline{v}]_{-B(x)}^{B(x)} , \quad (2.2.2)$$

(iii) conservation of heat flux

$$\int_{-B(x)}^{B(x)} (\overline{u}\ \overline{T} + \overline{u'T'})\, dy = \frac{H_o}{\rho_a c_p} , \quad (2.2.3)$$

where $\overline{T}(x,y)$ is the excess (above the ambient) temperature and $\overline{p}$ is the pressure deviation from the hydrostatic ambient pressure.

It will be shown that the experimental results of this investigation indicate that $\overline{u'T'}$ cannot be neglected (see Chapter 6). Density variations are related with the temperature variations by the equation

$$\frac{1}{\rho(\theta)}\frac{d\rho(\theta)}{d\theta} = -\alpha(\theta) \quad (2.2.4)$$

where $\rho(\theta)$ is the density at temperature θ, (°C),

$\alpha(\theta)$ is the thermal expansion coefficient (1/°C) at temperature θ.

For pure water and for 5°C $<\theta<$ 50°C the following algebraic expression was obtained using values of α given by Batchelor [33]

$$\alpha(\theta) = (-0.773 + 0.19\ \theta - 0.0027\ \theta^2 + 0.000021\ \theta^3)\ \times 10^{-4} \qquad (2.2.5)$$

(see also Figure 2.2.1). The kinematic buoyancy flux β is defined as

$$\beta = -\int_{-B(x)}^{B(x)} \frac{g}{\rho_a} \overline{(\rho-\rho_a)u}\ dy\ ,$$

or for small temperature increments,

$$\beta = \int_{-B(x)}^{B(x)} \alpha g\ \overline{Tu}\ dy\ , \qquad (2.2.6)$$

where T is the excess temperature increment above ambient. It is obvious from (2.2.6) that the kinematic buoyancy flux cannot be conserved since it depends, implicitly, through the thermal expansion coefficient, on the temperature field of the plume. However, in order to derive the basic features of the two-dimensional plume, the thermal expansion coefficient will be assumed constant, which leads to

$$\beta = \alpha g \int_{-B(x)}^{B(x)} \overline{uT}\ dy = \frac{\alpha g H_o}{\rho_a c_p}\ , \qquad (2.2.7)$$

i.e., the kinematic buoyancy flux is conserved if α is constant.

The basic character of the line pure plume can be found using dimensional analysis. In particular, it can be shown that

$$\frac{d\mu}{dx} = \varepsilon_1 \beta^{1/3}\ , \qquad (2.2.8)$$

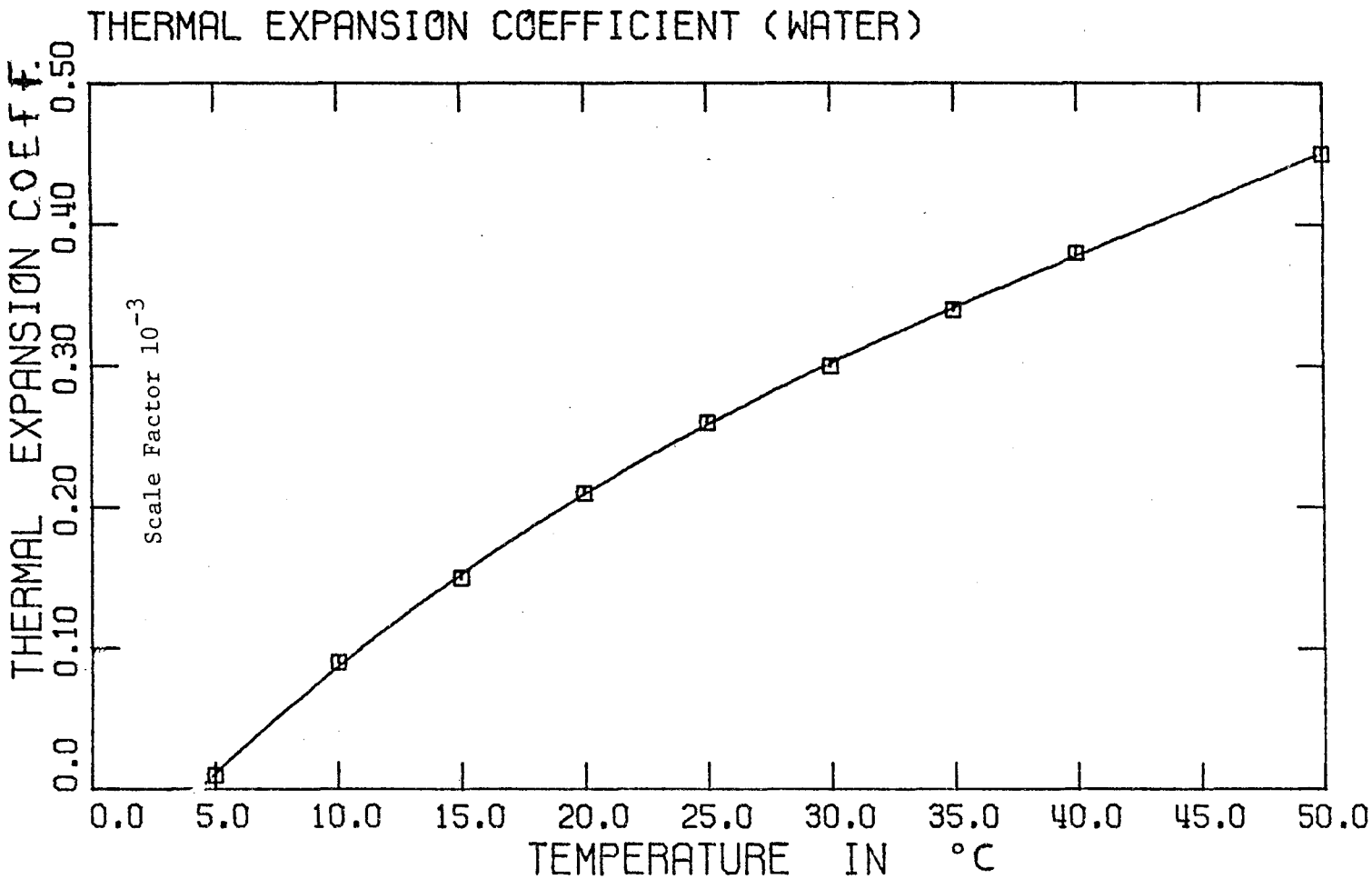

Figure 2.2.1. Thermal expansion coefficient of water as a function of temperature.

$$\frac{dm}{dx} = \varepsilon_2 \beta^{2/3} , \qquad (2.2.9)$$

where ε_1, ε_2 are experimental constants, and

$$\mu(x) = \int_{-B(x)}^{B(x)} \bar{u}(x,y)\, dy ,$$

$$m(x) = \int_{-B(x)}^{B(x)} \bar{u}^2\, dy$$

The conclusion from (2.2.8) is that the ambient fluid sees the two-dimensional plume as a distribution of sinks of constant strength $\varepsilon_1 \beta^{1/3}$. Hence for a plume on a half horizontal plane the induced flow will have streamlines orthogonal to the axis of the plume as in Figure (2.2.2) and an entrainment velocity equal to $\frac{\epsilon_1}{2} \beta^{1/3}$, i.e., independent of x.

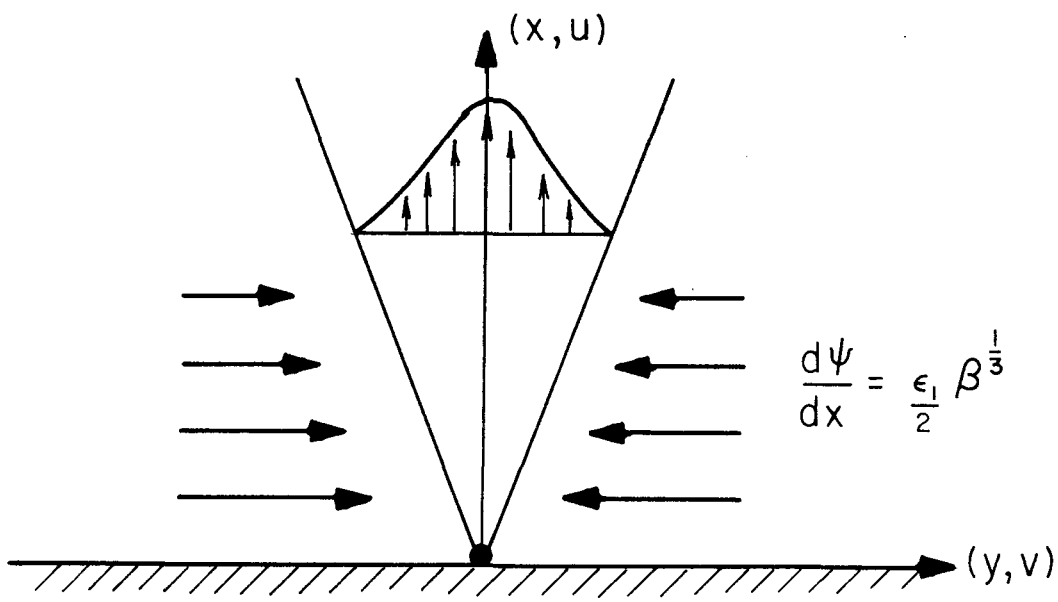

Figure 2.2.2. Induced flow towards a line plume on a horizontal plane

This observation was used by Kotsovinos and List [25] to measure the entrainment velocity using a flow visualization technique. The second term of the right-hand side of Equation (2.2.2) is then zero. It can then be shown from Equations (2.2.8) and (2.2.9) that

$$\frac{d\mu}{dx} = (\varepsilon_1 \varepsilon_2^{-1/2})\, m^{1/2}\, x^{-1/2}, \tag{2.2.10}$$

which is quite similar to the relation (2.1.17) for a pure jet, except that here the kinematic momentum flux, m, increases as x. Two important non-dimensional ratios can be obtained from (2.2.8) and (2.2.9):

$$C_p = \frac{\mu(x)}{\sqrt{m(x)(x-x_o)}} = \frac{\varepsilon_1}{\sqrt{\varepsilon_2}} = \text{constant}\ , \tag{2.2.11}$$

$$R_p = \frac{\mu^3 \beta}{m^3} = \left(\frac{\varepsilon_1}{\varepsilon_2}\right)^3 = \text{constant}\ . \tag{2.2.12}$$

The non-dimensional ratio C_p is a measure of the plume angle and R_p is the Richardson number of the plume. Again using dimensional analysis, two useful relations for the centerline velocity and temperature can be obtained:

$$\overline{u}_M = \sigma_u\, \beta^{1/3}\ , \tag{2.2.13}$$

$$\overline{T}_M = \frac{\beta^{2/3}}{\alpha g (x-x_o) \sigma_T}\ , \tag{2.2.14}$$

where σ_u, σ_T are experimental constants, and x_o locates the virtual origin. It will be shown that the experimental results of this investigation give

$$\sigma_u \approx 1.66 \qquad \text{and} \qquad \sigma_T \approx 0.42$$

(see Section 5.3 and 4.1 respectively).

The turbulence-energy equation is in this case

$$\frac{d}{dt}(\overline{q'^2}) = \underbrace{-\overline{u'v'}\frac{\partial \bar{u}}{\partial y}}_{(I)} + \underbrace{\alpha g\,\overline{u'T'}}_{(II)} \underbrace{-(\overline{u'^2}-\overline{v'^2})\frac{\partial \bar{u}}{\partial x}}_{(III)} \underbrace{-\frac{\partial}{\partial y}\overline{v'(\frac{p'}{\rho}+\frac{q'^2}{2})}}_{(IV)} - \text{Dissipation} \qquad (2.2.15)$$

where $\overline{q'^2} = \overline{u'^2} + \overline{v'^2} + \overline{w'^2}$

Each term of (2.2.15) represents a rate of change of the turbulent energy per unit mass, specifically:

The total time derivative of the turbulence kinetic energy (left-hand side) is equal to production of turbulent energy by shearing stress (I), plus production by buoyancy forces (II), plus production by normal stress (III), plus diffusion by turbulence (IV), plus the dissipation per unit of mass by the turbulent motion (see [34], [35]). The ratio of buoyant production of turbulent energy to shearing stress production of turbulent kinetic energy is called the flux Richardson number R_f (see [69])

$$R_f = \frac{\alpha g \overline{u'T'}}{\overline{u'v'} \frac{\partial \overline{u}}{\partial y}} \quad . \tag{2.2.16}$$

From Equation (2.2.13) $u \sim \beta^{1/3}$ and $T \sim \beta^{2/3}$, hence u' and T' are very well correlated, i.e., $\overline{u'T'} > 0$. Also $\overline{u'v'} \frac{\partial \overline{u}}{\partial y} < 0$, hence the flux Richardson number R_f is negative and indicates that the turbulent kinetic energy is increased. The centerline turbulence intensity of a plume is expected to be larger than the intensity of a pure jet, because for a pure jet the main production term, the shearing stress, is zero at the center, while for the plume the production by buoyancy should dominate. It will be shown that this was verified by the experimental results of this investigation (see Chapter 4).

2.3 THE MECHANICS OF THE TWO-DIMENSIONAL BUOYANT JET

A buoyant jet is defined as a source of kinematic mass flux μ_o, kinematic momentum flux m_o and kinematic buoyancy flux β_o. Using dimensional analysis, it can be found that each buoyant jet has effectively two characteristic length scales. One, μ_o^2/m_o, defines the importance of the initial volume flux (or kinematic mass flux), and the other $m_o/\beta_o^{2/3}$ defines the importance of the initial momentum flux. As noted previously the ratio of these two scales yields the Richardson number

$$R = \frac{\mu_o^3 \beta_o}{m_o^3} \quad , \tag{2.3.1}$$

which relates the distances at which kinematic momentum flux is important relative to kinematic buoyancy flux, to the distance at which kinematic momentum flux is important relative to kinematic mass flux.

For a pure plume, the local Richardson number

$$R(x) = \frac{\mu^3(x)\beta(x)}{m^3(x)} \tag{2.3.1}$$

was shown (see Chapters 2.2 and 5.1) to be a constant (equal ~ 0.6), while for a pure jet it is equal to zero. A buoyant jet with an exit Richardson number $R_o << R_p$ can be considered a pure jet for a distance $x < m_o/\beta_o^{2/3}$ (where x is the distance from jet orifice). But given any significant distance to develop, any slightly heated jet will eventually become a plume, because the initial momentum will be a small fraction of the momentum which will be gained by the continuous action of the buoyancy forces. The local Richardson number continuously increases, so that for $x >> m_o/\beta_o^{2/3}$ it will approximate the constant value of the plume Richardson number R_p. On the basis of this, transition to a plume is assured at any point, x, for which

$$\frac{x\beta_o^{2/3}}{m_o} > 10 .$$

The conclusion from this discussion is that a buoyant jet is always in a transition towards a pure plume.

Further reiterating, it should be noted that another important invariant of a buoyant jet is the non-dimensional ratio C defined by

$$C = \frac{\mu(x)}{\sqrt{m(x)(x-x_o)}} \tag{2.3.2}$$

where x_o the location of the virtual origin; this invariant C, which is a measure of the angle expansion of the buoyant jet has been found to have almost the same value (0.55) for jets, plumes and buoyant jets.

The thermal expansion coefficient α which appears in the buoyancy flux term (Eq. 2.2.6) is, implicitly, a function of the coordinates x,y, but for simplicity it will be assumed that α is a function only of x, and that its value at a given cross section is given by

$$\alpha(x) = \alpha(T_a + \bar{T}_c(x))$$

where T_a is the ambient temperature, and

$\bar{T}_c$ is the cross sectional mean excess temperature defined by

$$\bar{T}_c(x) = \frac{H_o}{\rho_a c_p \mu(x)} \quad . \tag{2.3.3}$$

The time-averaged integral equations of motion are Equations (2.2.1), (2.2.2), and (2.2.3) with initial conditions

$$\mu(0) = \mu_o \ ,$$

$$m(0) = m_o \ ,$$

$$\beta(0) = \beta_o = \frac{\alpha_o g H_o}{\rho c_p} \quad .$$

From (2.1.14)

$$[\overline{u}\ \overline{v}]_{-B(x)}^{B(x)} = \frac{1}{2} \tan\phi \left(\frac{d\mu}{dx}\right)^2 / (1-K_B \tan\phi)^2, \qquad (2.3.4)$$

where ϕ, now a function of local Richardson number, $\phi(R)$, is the angle of the induced flow streamlines with the jet boundaries (or approximately with the jet axis). Using dimensional analysis we can write according to List and Imberger [23]

$$-2\overline{v}(x, B(x)) = m\, q(R)/(1-K_B \tan\phi)\mu \ , \qquad (2.3.5)$$

and

$$\int_{-B(x)}^{B(x)} \frac{\overline{\Delta\rho}}{\rho} g\, dy = \frac{\mu\beta}{m} h(R) \ . \qquad (2.3.6)$$

The governing equations then become

$$\frac{d\mu}{dx} = \frac{m}{\mu} q(R) \ , \qquad (2.3.7)$$

$$\frac{dm}{dx} = \frac{\mu\beta}{m} h(R) - \frac{\tan\phi}{2} \frac{m^2}{\mu^2} \frac{q^2(R)}{(1-K_B \tan\phi)} \ , \qquad (2.3.8)$$

$$\beta(x) = \frac{\alpha[T_a + \overline{T}_c(x)]gH_o}{\rho c_p} \ . \qquad (2.3.9)$$

The objective is to then find the linear part of the functions q(R) and h(R). An expansion of q(R) h(R), ϕ(R) gives

$$q(R) = q_o + q_1 R + 0(R^2)$$

$$h(R) = h_o + h_1 R + 0(R^2) \qquad (2.3.10)$$

$$\phi(R) = \phi_o + \phi_1 R + 0(R^2)$$

The coefficients ϕ_o, ϕ_1 can be calculated immediately considering that $\phi(0) = \phi_o = \pi/4$ and $\phi(R_p) = \pi/4 + \phi_1 R_p = 0$,

hence

$$\phi(R) = \pi/4 \ (1 - \frac{R}{R_p})$$

Using Equations (2.3.7), (2.3.8) and (2.3.9), it can be shown that

$$\frac{dR}{dx} = \frac{3R}{xC^2}\left[q - Rh + \frac{C}{2}\ \frac{q^2 \tan\phi}{1-K_B \tan\phi}\right] + \frac{\mu^3}{m^3}\frac{d\beta}{dx} \qquad (2.3.11)$$

$$\frac{dC}{dx} = \frac{1}{Cx}\left[q - \frac{C^2}{2} - \frac{Rh}{2} + \frac{q^2 \tan\phi}{4(1-K_B \tan\phi)}\right] \qquad (2.3.12)$$

where R and C are given by Eq. 2.3.1 and Eq. 2.3.2 respectively.

For the case of a pure jet R = 0, $\phi = \pi/4$, and (2.3.12) gives

$$q_o - \frac{C^2}{2} + \frac{q_o^2}{4(1-K_B)} = 0$$

or

$$q_o = \sqrt{4(1-K_B)^2 + 2C^2(1-K_B)} \ -2(1-K_B) \qquad (2.3.13)$$

For a pure plume $R = R_p$, $\phi = 0$ and (2.3.11) and (2.3.12) give

$$q_c + q_1 R_p - R_p h_o + O(R^2) = 0 \quad , \tag{2.3.14}$$

$$q_o + q_1 R_p - \frac{C^2}{2} - \frac{R_p h_o}{2} + O(R^2) = 0 \quad , \tag{2.3.15}$$

or

$$h_o = \frac{C^2}{R_p} \quad , \tag{2.3.16}$$

$$q_1 = \frac{C^2}{R_p} - \frac{q_o}{R_p} \quad . \tag{2.3.17}$$

Hence the governing equations become

$$\frac{d\mu}{dx} = (q_o + q_1 R) \frac{m}{\mu} \quad , \tag{2.3.18}$$

$$\frac{dm}{dx} = \frac{\mu\beta}{m} h_o - \frac{\tan\phi}{2} \frac{m^2}{\mu^2} \frac{q_o^2 + 2q_o q_1 R}{1 - K_B \tan\phi} \quad ,$$

$$\frac{d\beta}{dx} = -[0.19 - 0.0054(T_a + \frac{H_o}{\rho_o c_p \mu}) + 0.000063(T_a + \frac{H_o}{\rho_o c_p \mu})^2]$$

$$\frac{g H_o^2}{(\rho_o c_p)^2} \frac{1}{\mu^2} \frac{d\mu}{dx} \quad ,$$

with initial conditions

$$\mu(0) = \mu_o \quad ,$$

$$m(0) = m_o \quad ,$$

$$\beta(0) = \beta_o \quad .$$

On the basis of the experimental results of this investigation (see Sections 4.3 and 5.1)

$$q_o = 0.146, \qquad q_1 = 0.252 ,$$

$$h_o = 0.48 , \qquad K_B = 0.25 .$$

2.4 NUMERICAL SOLUTION OF THE BUOYANT JET PROBLEM

The theoretical analysis developed in the previous Section 2.3 results in a system of ordinary differential equations.

The numerical solution and the stability of such systems is well established. The solution was obtained by direct step by step integration using a subroutine "MODDEQ/Differential equation solver" available at Caltech's computer center. The subroutine was based on the Runge-Kutta-Gill method with automatic control of truncation error. The solution of this model which gives the growth of the kinematic mass, momentum and buoyancy fluxes will be presented in Chapter 7 with the experimental results from this investigation.

3. EXPERIMENTAL PROBLEMS AND OBJECTIVES

3.0 INTRODUCTION

The objective of this investigation was to study the mechanics of a two-dimensional turbulent buoyant jet for a wide range of initial Richardson numbers. Values of the Richardson number, which describes the relative importance of buoyancy in a jet, extended from the value appropriate for a pure jet (zero) to that appropriate for a pure plume (approximately 0.6). Jet buoyancy was produced by increasing the temperature of the jet discharge over the temperature of the ambient fluid and the buoyant jet temperature and velocity fields were measured using calibrated fast-response thermistors and a laser Doppler velocimeter respectively. The velocity and temperature data obtained were recorded magnetically in digital form and subsequently processed to extract both mean and fluctuating values of temperature and velocity. A variety of other data such as intermittencies, frequencies, minima and maxima, and so forth, were also obtained. Conditional sampling was a significant feature of the data processing.

3.1 TEMPERATURE MEASUREMENTS

Thermistors

Six small bead thermistors were used for temperature measurements and their characteristics are given in Table 3.1.1.

Type	Bead Diameter	Dissipation Constant-Still Water at 25°C	Time Constant in Moving Water	Resistance at 25°C
Small bead Veco thermistors type 52A26	0.35 mm	0.75 mw/°C	27 milli-seconds	~200 kΩ

Table 3.1.1. Thermistor characteristics.

Each bead thermistor was insulated and mounted on a stainless steel tube thereby forming a temperature probe as shown in Figure 3.1.1. The thermistor temperature response was measured with a bridge circuit as shown in Figure 3.1.2. The resistors used in the bridge were precision wire wound resistors (1% tolerance) and an integrated circuit operational amplifier (741) was used to reduce the impedance of the output signal to a few ohms to match the input characteristics of the analog-to-digital converter. The electrical current passing through the thermistor was approximately 5×10^{-6} Amperes, the ohmic dissipation of the thermistor was approximately 6×10^{-6} Watts, hence the self-heating of the thermistor due to the ohmic dissipation can be calculated using the dissipation constant given in Table 3.1.1 to be less than 0.008 °C. The drift of the thermistor circuit for an extended period of time (3 hours) was of the order one millivolt resulting in an absolute accuracy of the temperature measurement of the order 0.01 °C.

Each thermistor was individually calibrated and a third order polynomial fitted to the set of calibration points in the least squares sense

$$T = A_o + A_1 V + A_2 V^2 + A_3 V^3 \ ,$$

where T is the temperature in °C, V the analog output from the bridge in volts (see Fig. 3.1.3), and A_o, A_1, A_2, A_3 regression coefficients.

Each analog output V was fed into one channel of an eight channel analog-to-digital data acquisition system (manufactured by Digital Data Systems) which digitized the information and packed it on magnetic tape

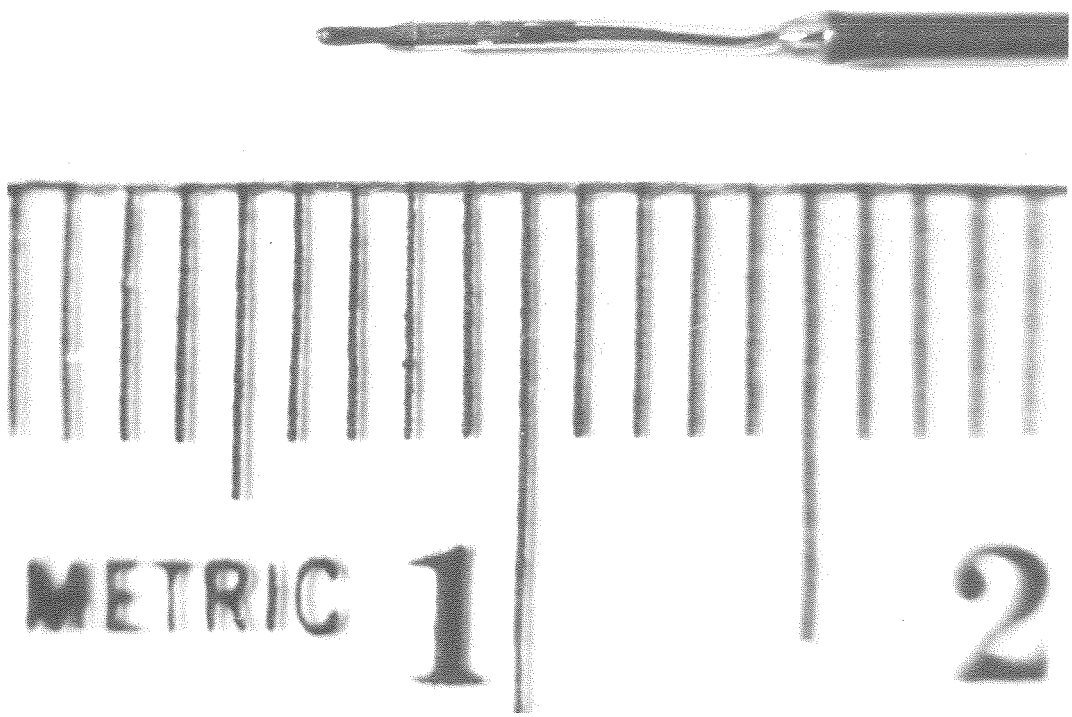

Figure 3.1.1. Close photograph of the thermistor probe. One subdivision is one millimeter.

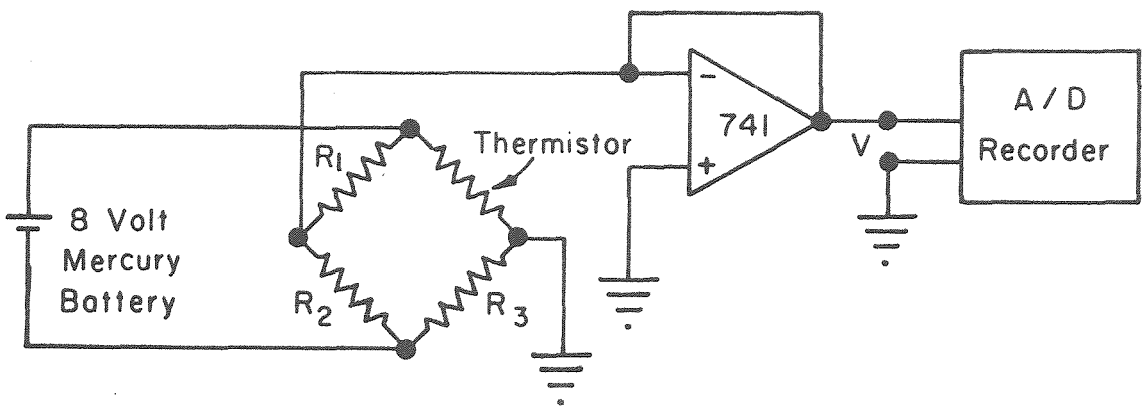

$R_1 = 200\ K\Omega$, $R_2 = R_3 = 1.2\ M\Omega$

Figure 3.1.2. The bridge circuit used for the measurement of the temperature.

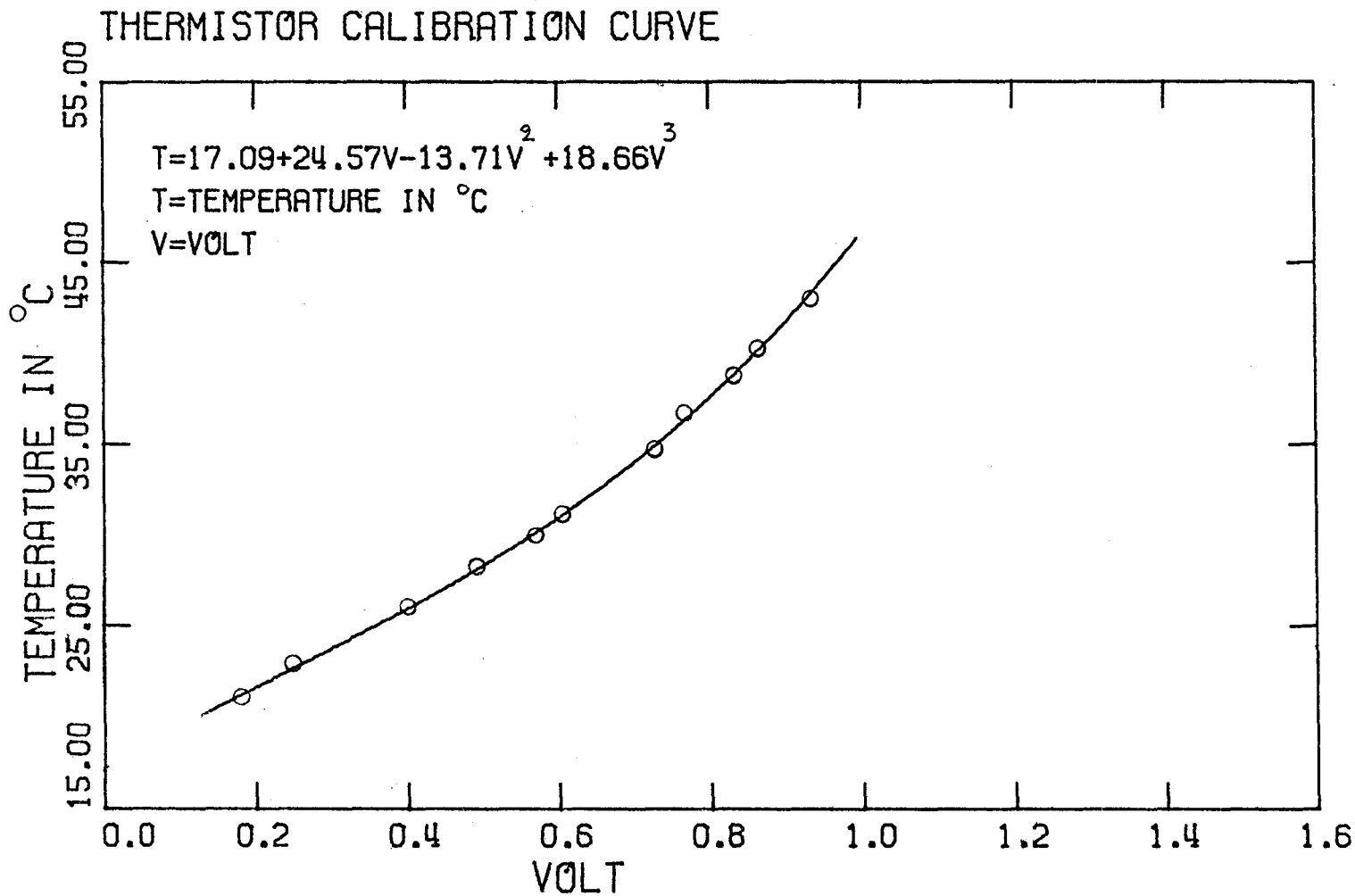

Figure 3.1.3. Typical thermistor calibration curve.

compatible with the IBM 360/75 high speed digital computer in Booth Computing Center. The digitizing resolution was one millivolt, and the sampling rate could be varied from 0.01 to 1600 samples per second. The thermistor time constant was determined by moving a thermistor quickly from air into a hot water tank (simulation of a step function) and recording the response of the thermistor. The time required to obtain 63% of the final reading was found to be 27 msec for one thermistor with special insulation and 45 msec for the five others.

A/D Sampling Rate

An investigation was carried out to determine the lowest sampling rate and sampling time for the A/D converter that would give a time-averaged temperature $\overline{T}$ with a standard deviation of ± 0.02 °C from the expected exact one $\overline{T}_E$. Ideally, if T(x,y,t) is the temperature at any point (x,y) at time t, then

$$\overline{T}_E = \lim_{\tau \to \infty} \frac{1}{\tau} \int_o^\tau T(x,y,t)\, dt \ ,$$

but what is measured is

$$\overline{T} = \frac{1}{N} \sum_{i=1}^{N} T(x,y,t_i) \ ,$$

where

τ = sampling time (sec),

N = total number of samples during τ seconds,

$\frac{N}{\tau}$ = sampling rate (samples/sec),

$t_i = \frac{\tau}{N} i$, i = 1, 2, N.

The question is to determine the minimum sampling time τ and the minimum sampling rate, $\frac{N}{\tau}$, such that

$$\sqrt{E\{(\overline{T}_E - \overline{T})^2\}} \lesssim 0.02\ ^\circ C\ .$$

The sampling rate was determined by first forming a temperature file data at a sampling rate much faster (400 samples/sec) than necessary to determine a good spectrum, then calculating the mean using every sample, every second sample and so on, i.e.,

$$\overline{T}_M(x,y) = \frac{1}{M} \sum_{i=1}^{M} T(x,y,jt_i)$$

where $j = 1, 2, \ldots\ldots\ldots 100$

$N = 400\ \tau$, the total number of the recorded samples during the sampling time τ.

M = the integer part of the quotient N/j, $\frac{N}{100} < M < N$.

$i = 1,2,\ldots\ldots\ldots N$, the first, second, etc., sample

t_i = time in seconds of the ith recorded sample

$t_1 = 0$

τ = sampling time for the file in seconds (fixed)

$\overline{T}_M(x,y)$ as a function of the sampling rate M/τ is shown in Figure 3.1.4.

From Figure 3.1.4 it can be seen that a reasonable minimum sampling rate is of the order of 10 samples/sec, which indicates that the cut-off frequency is probably about 20 Hz. In order to determine the minimum sampling time (length of record) a 10 minute file was taken at a fixed sampling rate 10 samples/sec, i.e., an array was generated with elements

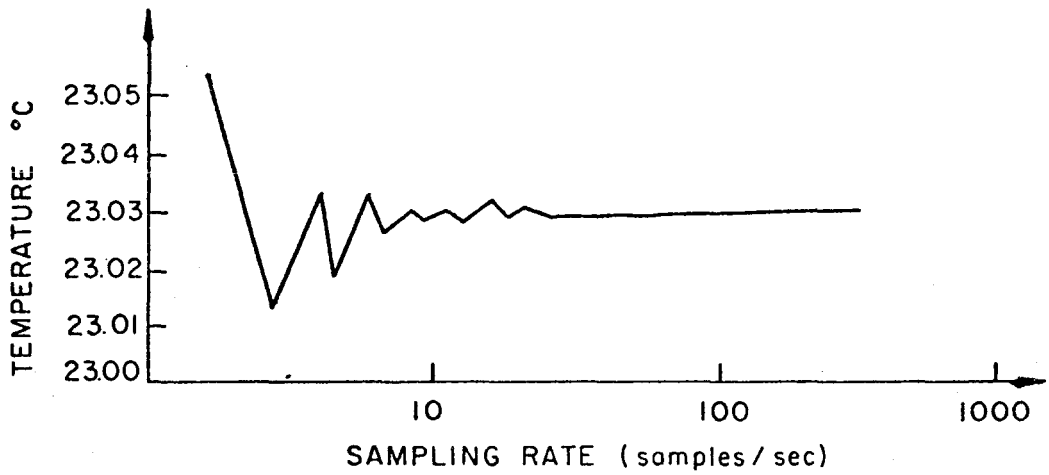

Figure 3.1.4. Mean temperature as a function of sampling rate (length of sample 50 sec).

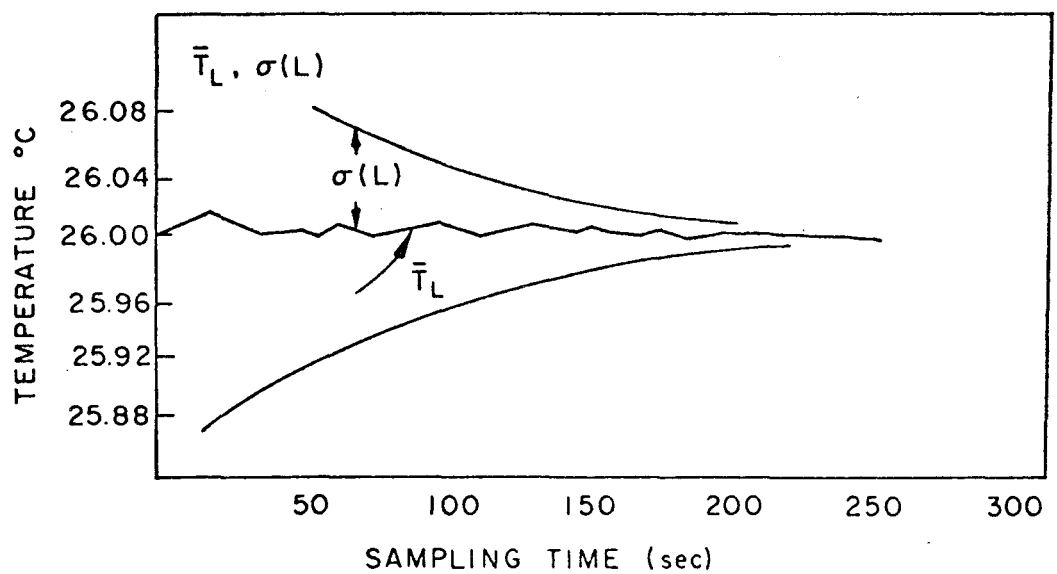

Figure 3.1.5. Mean temperature as a function of sampling time (sample rate 10 samples/second).

$T(x,y,t_i)$ where

$T(x,y,t_i)$ is the temperature at a point (x,y) in a plume at time t_i

$i = 1,2,.....6000$, the first, second, etc., sample

$t_1 = 0$

t_i = time in seconds of the ith recorded sample, i.e., $t_i = i/10$

A matrix S was then calculated with elements found by the running mean S_{jL} as follows

$$S_{jL} = (1/L) \sum_{\ell=1}^{L} T(x,y,t_j + t_\ell)$$

where

$L = 50,100,150,200,.....,6000.$ (number of samples),

$\ell = 1,2,3,.....L,$

$j = 0,10,20,30,.....,J,$

$J+L < 6000,$

$t_1 = 0,$

$t_j = j/10$ seconds (determines the beginning of the file),

$t_L = L/10$, sampling time in seconds, t.

Then the mean $\overline{T}_L$ of all the means S_{jL}

$$\overline{T}_L = 1/M \sum_{j=1}^{M} S_{jL}$$

where M = J/10 is the number of the means with sampling time L/10.

The variance

$$\sigma^2(L) = 1/M \sum_{j=1}^{M} (\overline{T}_L - S_{jL})^2$$

and the mean $\overline{T}_L$ have been plotted in Figure 3.1.5 versus the sampling time t_L. On the basis of Figure 3.1.5 the sampling time was chosen to be 150 to 200 seconds.

3.2 VELOCITY MEASUREMENTS

I. Description of the laser Doppler velocimeter

A laser Doppler velocimeter, with direction sensitivity and capable of measuring the velocity of a free turbulent flow of high turbulence intensity was developed and used in this experiment (Figure 3.2.1.a and b). A Spectra-Physics Model 120, 5 mw Helium-Neon laser was the source of the laser beam which had wavelength 0.6328 micron (in air). The intensity of the light of the laser beam has a Gaussian distribution and the diameter, where the intensity is $1/e^2$ (e = 2.718...) of the center-line intensity of 0.65 mm.

The laser beam was first passed through a rotating radial diffraction grating disk (manufactured by the Dynamics Research Corporation). This grating disk, which had 2048 lines was mounted directly on the shaft of a synchronous motor (Hurst Corporation, Model Minibee) rotating at 1800 revolutions per minute (r.p.m.). The zeroth order diffracted laser light has the frequency of the laser beam f_o and the kth order diffracted order beam has a frequency

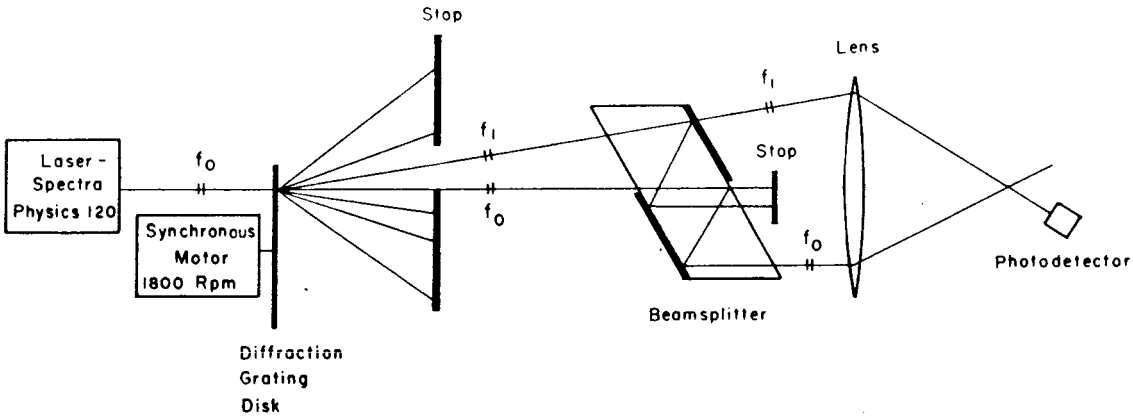

Figure 3.2.1.a. Optics of laser Doppler velocimeter.

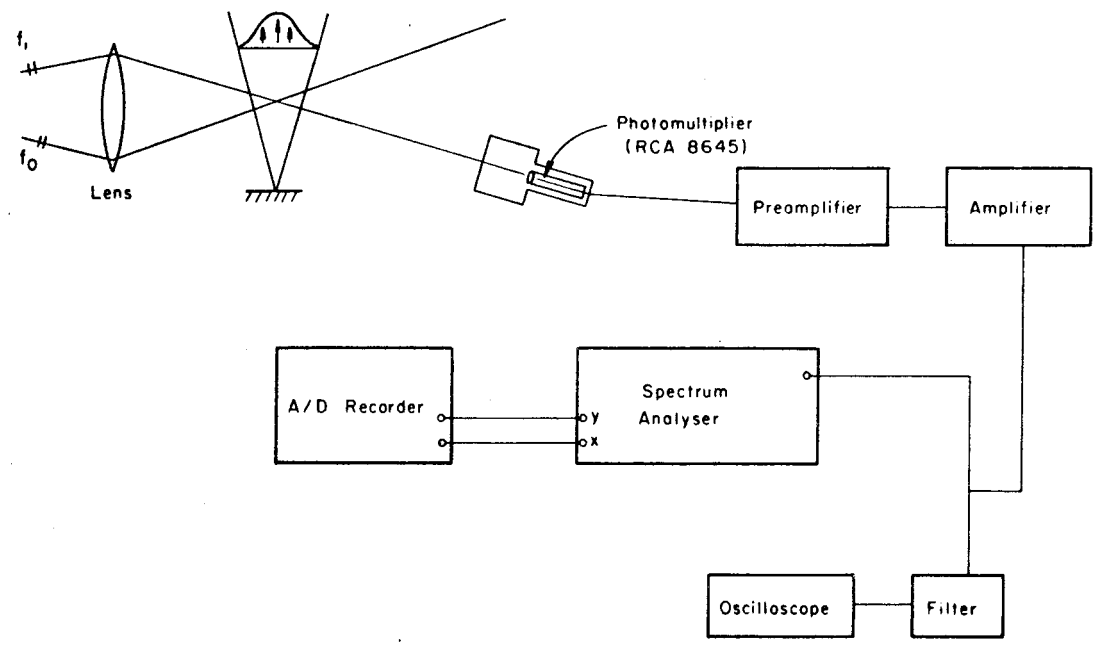

Figure 3.2.1.b. Signal processing of laser Doppler velocimeter.

$$f_k = f_o \pm \frac{M\,N}{60}\,k = f_o \pm 61.440\,k\ , \qquad (3.2.1)$$

where N is speed of rotation of the radial diffraction grating (1800 rpm),

M is number of lines on the radial diffraction grating (2048),

k is the diffraction order.

Thus a rotating diffraction grating provides a convenient way for optically shifting the frequency of the laser light (Stevenson [64]). It was observed in this investigation that some laser light of frequency f_o was also propagated in the direction of the light of frequency f_k and this caused some problems with the frequency demodulation equipment which will be discussed subsequently. The basic technique for use of the laser velocimeter is shown diagrammatically in Figures 3.2.1.a and b. The zeroth f_o and first f_1 order diffracted light was passed through a beam splitter in order to increase their separation; all other diffracted light was masked. A lens focused the two beams of frequencies f_o and f_1 into the flow field and a photodetector (RCA 8645 photomultiplier tube) was aligned with the beam f_1 ("reference beam") after it passed through the flow. The photomultiplier also collected light of frequency f_o that was scattered by particles (of the order 1 micron) existing in abundance in the flow field. The heterodyning of the scattered light with the reference beam formed the basis of the velocity measurement system as will be described in more detail subsequently.

II. Derivation of the Doppler shift frequency formula

Consider a particle which is moving with velocity $\vec{U}$ and which is

irradiated with a laser beam of frequency f_o in the direction $\vec{e}_o$ (Figure 3.2.2). Light scattered by the moving particle will have a frequency f_p given by

$$f_p = f_o\left(1 - n\frac{\vec{e}_o \cdot \vec{U}}{c}\right) \qquad (3.2.2)$$

where n is the index of refraction of the medium,

c is velocity of light in a vacuum.

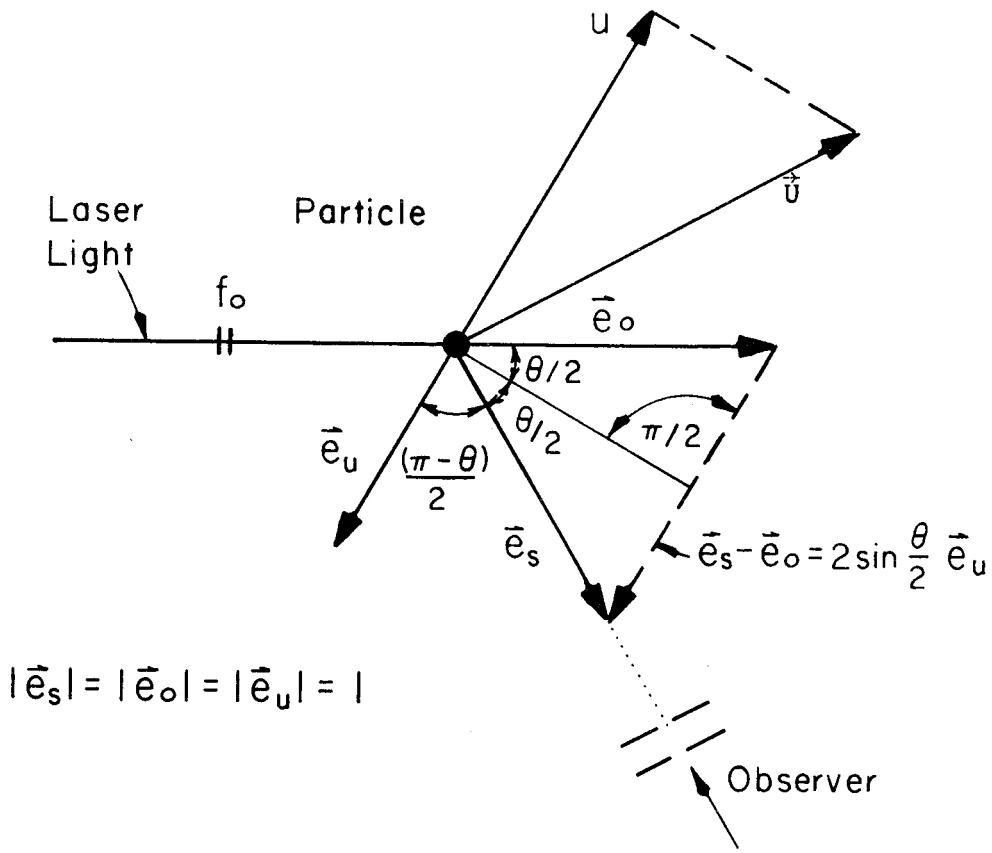

Figure 3.2.2. Scattering light from a moving particle.

Light scattered from the same particle in the direction $\vec{e}_s$ will have the frequency (when viewed in the laboratory)

$$f_s = f_p(1 + n\frac{\vec{e}_s\cdot\vec{U}}{c}) = f_o(1 - n\frac{\vec{e}_o\cdot\vec{U}}{c})(1 + n\frac{\vec{e}_s\cdot\vec{U}}{c}) =$$

$$= f_o + \frac{n\vec{U}f_o}{c}\cdot(\vec{e}_s - \vec{e}_o) + 0(\frac{1}{c^2}) \approx$$

$$\approx f_o + \frac{n\ u\ \sin(\theta/2)}{\lambda} \qquad (3.2.3)$$

where θ is the angle between $\vec{e}_s$, $\vec{e}_o$ in the medium of index of refraction n,

u is component of the vector velocity $\vec{U}$ in the plane of $\vec{e}_o$, $\vec{e}_s$ and perpendicular to their bisectrice,

λ is the wave length of laser light in a vacuum.

The cathode of the photomultiplier superimposes the following electrical fields

(i) $A_s(t)\ \sin 2\pi f_s t$, the scattered light,

(ii) $A_1 \sin 2\pi f_1 t$, the reference beam,

(iii) $A_o \sin 2\pi f_o t$, unwanted scattered light from the rotating disk,

where $|A_1| >> |A_s(t)| >> |A_o|$.

Assuming that all the above components have the same polarization direction, the output current, i, from the photomultiplier (which is a square law detector) is proportional to the total received intensity so that

$$i = c[A_1 \sin 2\pi f_1 t + A_s(t)\ \sin 2\pi f_s t + A_o \sin 2\pi f_o t]^2$$

$$= A_1 A_s(t)\ \cos 2\pi(f_s - f_1)t + A_1 A_o \cos 2\pi(f_1 - f_o)t$$

$$+ A_o A_s(t)\ \cos 2\pi(f_s - f_o)t + \text{D.C. terms} +$$

+ terms oscillating at a very high frequency (order $f_o = 10^{14}$ Hz) that exceeds the response of photomultiplier. (3.2.4)

A spectrum analysis of the signal given by (3.2.4) will have the form of Figure 3.2.3.

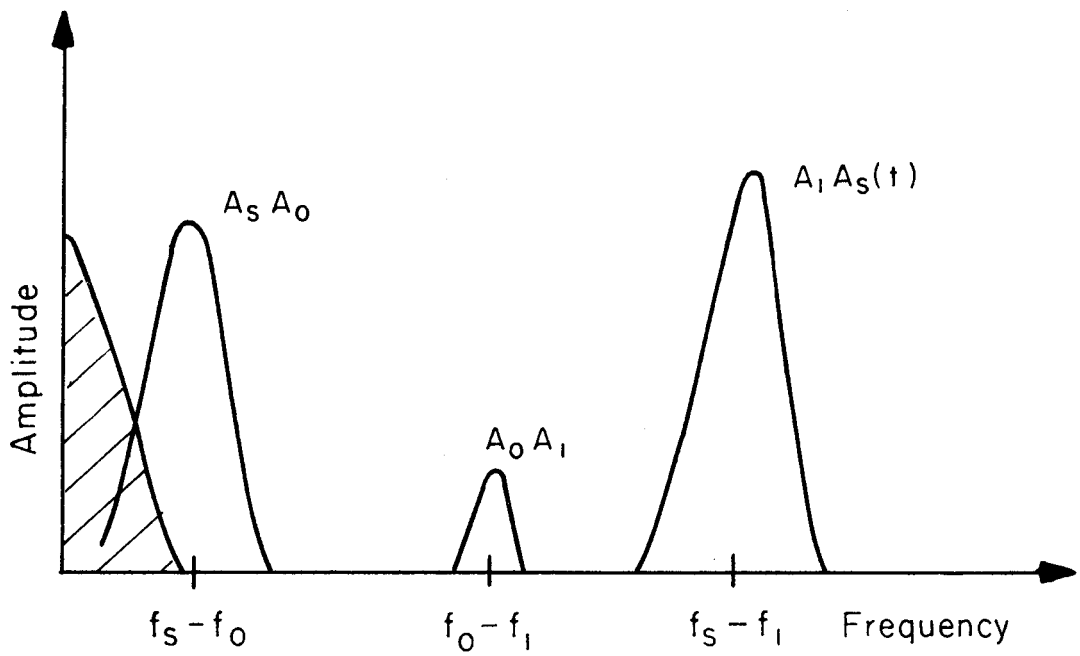

Figure 3.2.3. Spectrum analysis of the signal given by Eq. 3.2.4

For this investigation from Equation 3.2.1 it can be seen that for a first order scattering beam $f_1 = f_o$ - 61,440 Hz, and this has been verified experimentally to be correct within ± 3 Hz. Then from Equation

3.2.3 the component u of the vector velocity $\vec{U}$ (Figure 3.2.2) can be calculated using the linear relation

$$f_s - f_1 = 61440 + \frac{n\ u\ \sin(\theta/2)}{\lambda} \qquad (3.2.5)$$

The problem then becomes how to measure $f_s - f_1$ experimentally. It can be done in a time-averaged way by using a standard spectrum analyser. On such an instrument the spectral peaks can easily be determined. However, instantaneous demodulation of the photomultiplier output signal is complicated by the presence of the other spectral peaks.

Apart from the demodulation problem which has been introduced by these additional spectral peaks it can be seen that the presence of the rotating radial diffraction grating shifts the zero velocity Doppler frequency away from zero. There are two distinct advantages to this in that it becomes possible to measure very low velocities and also to gain directional sensitivity.

III. Signal processing

There are three basic methods for signal processing, (a) spectrum analysis, (b) frequency tracking, and (c) period timing (counting). Period timing is proper for flows with a low particle content where individual signal "bursts" from a single scattering particle are detected and the time between zero crossings of the signal can be measured. Frequency tracking or phase-lock-loop techniques are convenient for most applications but are inadequate for flows with wide or rapid excursions in velocity such as in the intermittent flow that occurs at a jet boundary. Spectrum analysis, which has been used in this investigation,

is appropriate for flows with a high turbulence intensity or intermittency.

The function of a spectrum analyser (Figure 3.2.4) will be described briefly. A local oscillator (V.C.O.) delivers a signal whose frequency f_{vco} increases linearly with time between a minimum f_L and a maximum f_H.

Consider the case wherein the Doppler signal is $A\cos 2\pi f_D t$ where f_D is constant (e.g. laminar flow). As the V.C.O. is swept from f_L to f_H the output signal S(t) from the mixer varies

$$S_L(t) \leqslant S(t) \leqslant S_H(t)$$

where (see Magrab et al [56])

$$S(t) = \frac{A}{2}[\cos 2\pi(f_{vco} + f_c - f_D)t + \cos 2\pi(f_{vco} + f_c + f_D)t]$$

$$S_L(t) = \frac{A}{2}[\cos 2\pi(f_L + f_c - f_D)t + \cos 2\pi(f_L + f_c + f_D)t]$$

$$S_H(t) = \frac{A}{2}[\cos 2\pi(f_H + f_c - f_D)t + \cos 2\pi(f_H + f_c + f_D)t]$$

Since the narrow constant bandwidth filter has a center frequency f_c and a bandwidth Δf_c there is no output from it except when $|f_D - f_{vco}| < \Delta f_c$. Thus the amplitude of the spectrum analyser display would be zero until the swept frequency equaled that of the input Doppler signal. In the case of a random input Doppler signal $f_D(t_i)$ (turbulent flow) there is an output of the constant bandwidth filter only for those input Doppler frequencies that are centered in the band $|f_D(t_i) - f_{vco}(t_i)| < \Delta f_c$.

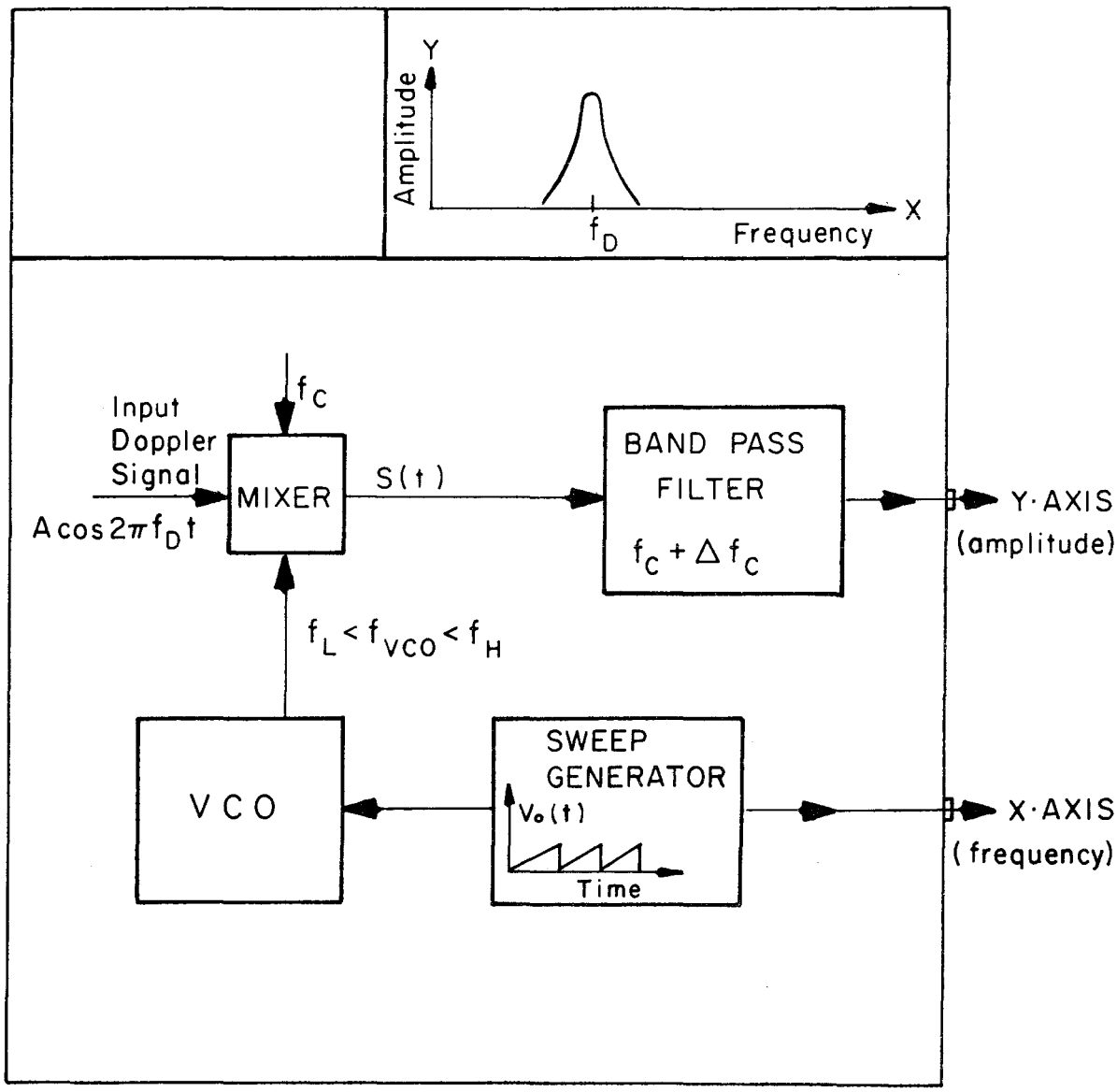

Figure 3.2.4. Schematic of a spectrum analyser.

The available adjustments of a spectrum analyser are:

(i) Bandwidth Δf_c of Band pass filter (Hz)

(ii) Sweep rate of V.C.O. frequency (Hz/second), $\frac{df_{vco}}{dt}$.

(iii) Minimum f_L and maximum f_H of scan (Hz).

Typical settings in the experiments performed were

$$\Delta f_c = 100 \text{ Hz},$$

$$\frac{df_{vco}}{dt} = 200 \text{ Hz/sec},$$

$$f_L = 55 \text{ KHz}, \qquad f_H = 75 \text{ KHz}.$$

A 8553L-RF section, 8552A-IF section Hewlett-Packard spectrum analyser was used in the investigation.

The Y-axis output (amplitude) and the X-axis output (frequency) of the spectrum analyser were fed into the A/D data acquisition system (A/D) described in Section 3.1. Typical sampling time for data acquisition was 10 minutes with a sample rate of 40 samples per second. This resulted in a reasonably smooth probability density distribution for the velocity.

3.3 VELOCITY-TEMPERATURE CROSS CORRELATIONS MEASUREMENTS

A technique was developed to measure the product

$$\overline{uT} = \frac{1}{N} \sum_{i=1}^{N} u(x,y,t_i)T(x',y,t_i) \quad ,$$

where

$u(x',y,t_i)$ is the instantaneous velocity at (x',y) at time t_i

$T(x,y,t_i)$ is the instantaneous temperature at (x,y) at time t_i.

A small diameter (0.35 mm), fast response (time constant 27 msec), bead thermistor placed near the focal volume of the laser Doppler velocimeter (Figure 3.3.1) so that $x - x' \approx 2$ mm was used to measure temperature and the spectrum analyser was used to provide an array of instantaneous but not necessarily continuous, velocity measurements.

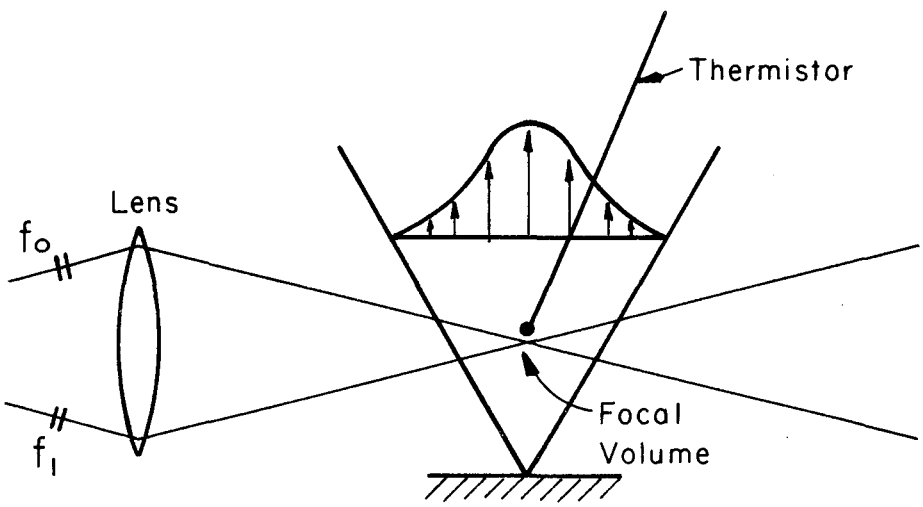

Figure 3.3.1. Schematic for temperature-velocity measurement

The A/D was used to record (i) the instantaneous frequency of the spectrum analyser scan, $f_{vco}(t_i)$(X-axis), (ii) the instantaneous amplitude $A(t_i)$, (Y-axis), of the spectrum analyser, and (iii) the analog signal for the temperature $T(t_i)$. Now if $f_D(t_i)$ is the instantaneous Doppler frequency at time t_i, then defining

$$A(t_i) = \begin{cases} 0 & \text{if } |f_D - f_{vco}| > \Delta f_c \\ 1 & \text{if } |f_D - f_{vco}| < \Delta f_c. \end{cases}$$

the instantaneous velocity $u(t_i)$ is calculated from the instantaneous Doppler frequency $f_D(t_i)$ only when $A(t_i) = 1$. The scheme is depicted in Figure 3.3.2. It is obvious that this array $u(t_i)$ of the instantaneous velocities cannot be used for power spectra of velocity fluctuations, but it can be used to construct the product $\overline{uT}$.

3.4 EXPERIMENTAL SET-UP

The two-dimensional buoyant jet was generated by hot water emerging from a chamber combining flow straightening elements and then discharging through a slot 13 cm long and D cm wide (D could vary from 0.2 to 2 cm). The jet discharged into tank 4.0 by 4.0 meters by one meter deep filled with tap water. The jet was confined by two plexiglas walls 13 cm apart in order to maintain the two-dimensionality of the jet (Figure 3.4.1.a and Figure 3.4.1.b). A constant head tank was used to provide the necessary pressure to drive the jet flow and a precision bore Flowmeter (tube No. B6-27-10/27 manufactured by Fischer Corporation) was used to regulate the flow with an accuracy of 1%. The overall experimental set-up is shown schematically in Figure 3.4.2. A first series of experiments

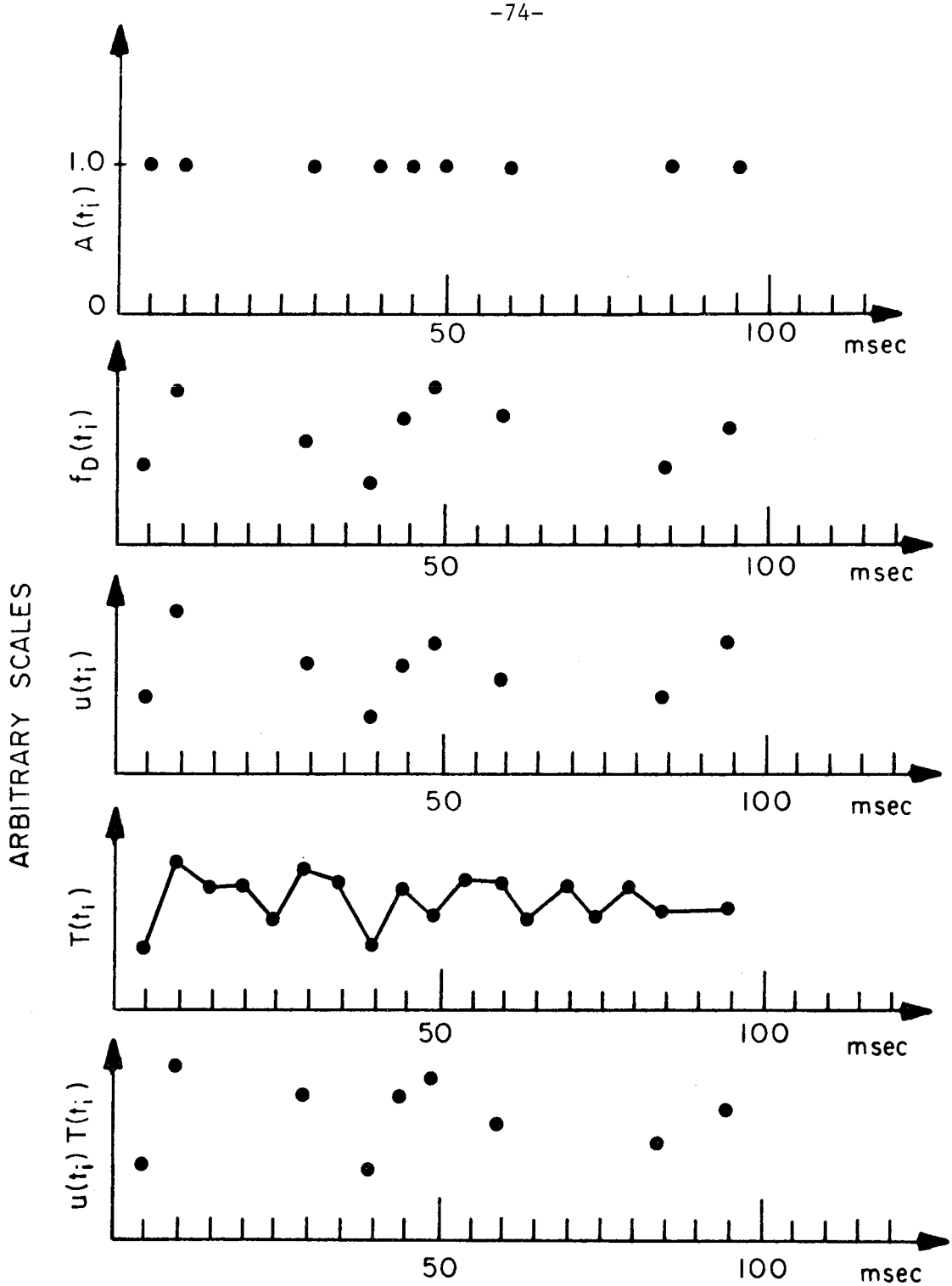

Figure 3.3.2. Schematic for the measurement of the correlation $\overline{uT}$.

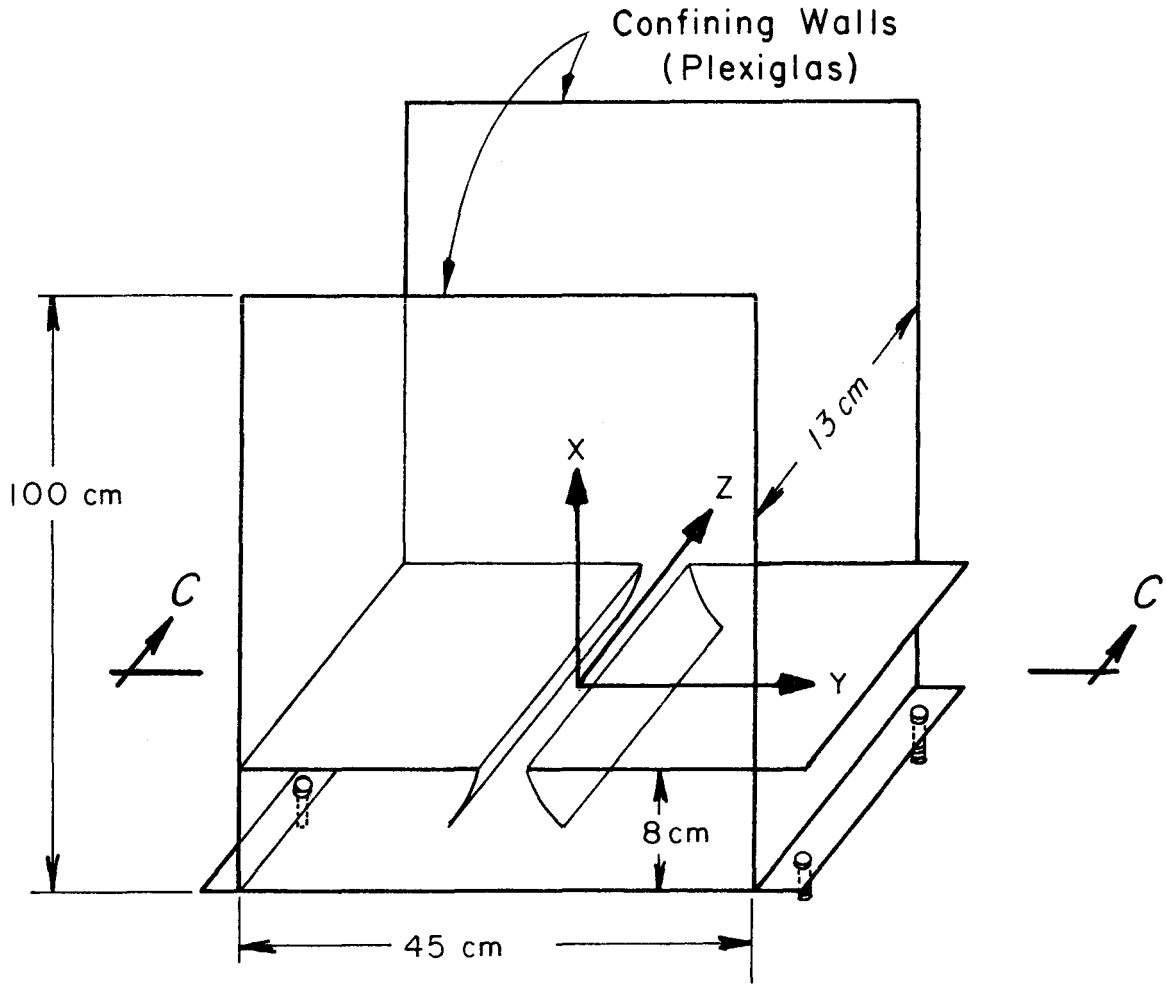

Figure 3.4.1.a. Perspective view of the chamber of the emerging jet.

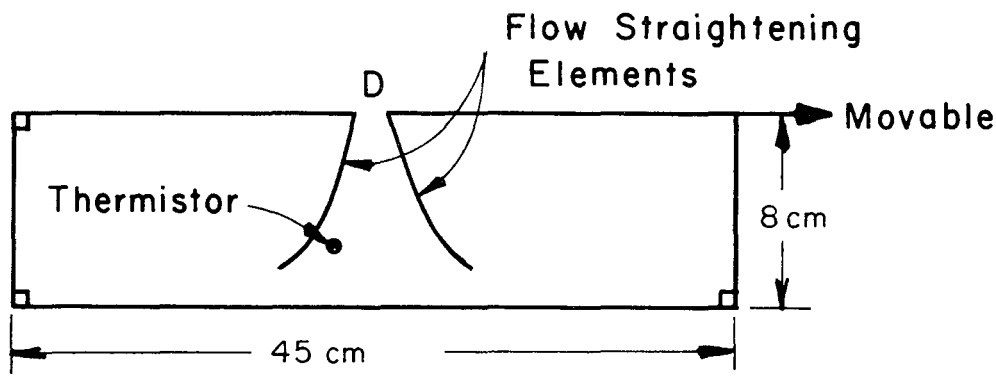

Figure 3.4.1.b. Cross section of the chamber of the emerging jet.

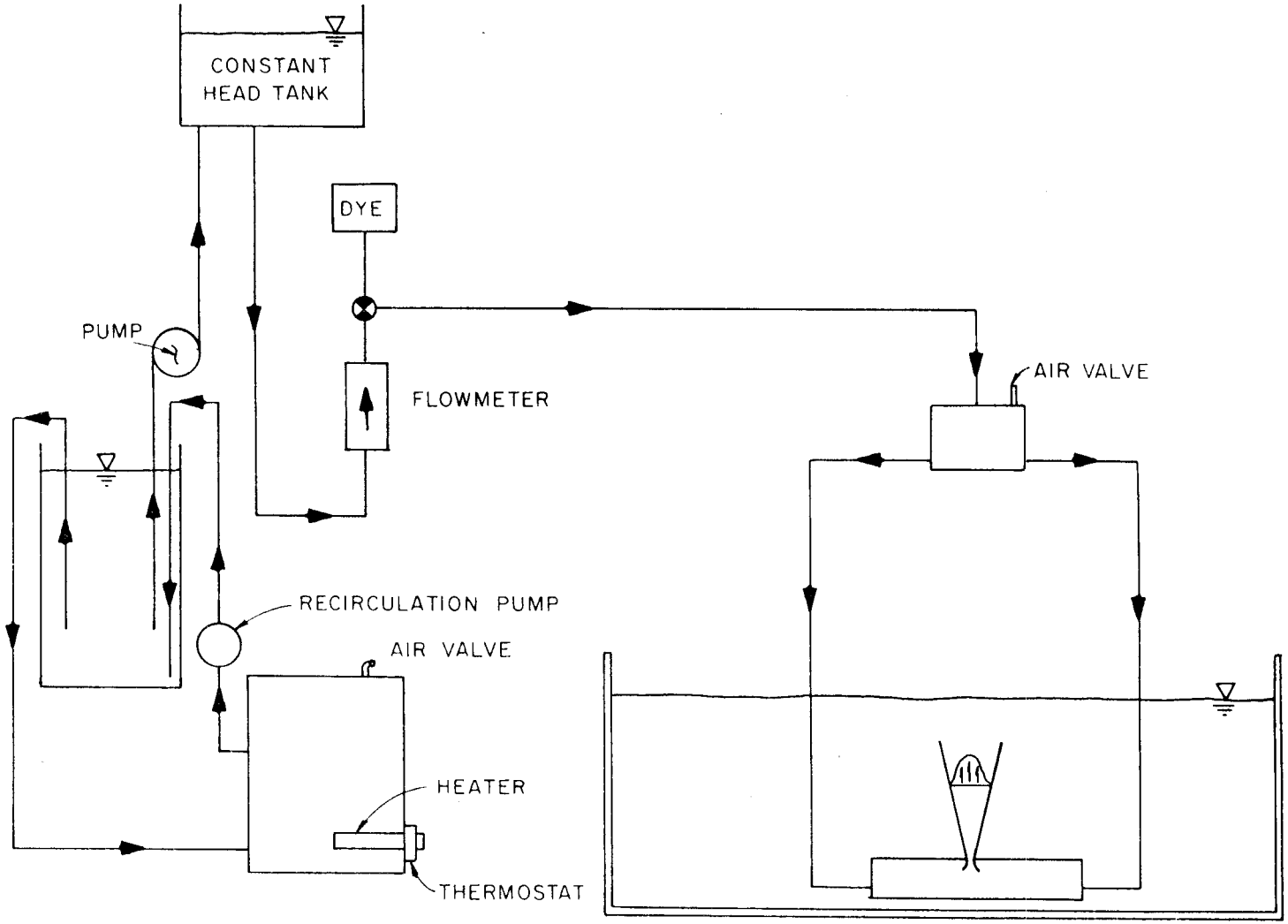

Figure 3.4.2. Overall experimental set-up.

were performed in which only temperatures were measured and the instrumental set-up for these tests is shown in Figure 3.4.3. Five thermistors each at a different elevation and located in the middle plane parallel to the two confining walls were used for temperature measurement. All the thermistors could be simultaneously traversed across the jet by means of a single support carriage. The carriage was connected to a potentiometer and mercury battery so that a voltage was obtained that was proportional to the position (Y) of the carriage (resolution 0.01 mm). The A/D was used to record the temperature at the exit of the jet, the temperatures from the five thermistors, and the Y-position. The jet chamber was placed on the floor of the 4 m x 4 m tank and adjusted to make the plane of the exit slot horizontal. For the second series of tests in which both velocities and temperatures were measured, the instrumental set-up used is shown in Figure 3.4.4.a and b. A laser Doppler velocimeter was used to measure the velocities and a small thermistor (0.35 mm) about 2 mm above the focal volume of the laser was used to measure temperature. The focal volume was located in the jet midway between the two confining walls. In these experiments the jet chamber and confining walls were mounted on the carriage and the thermistor and laser held fixed. The laser Doppler velocimeter was aligned and focused and then the transverse velocity profile was measured by placing the jet at different Y-positions. The purpose of the mirror (Figure 3.4.4.a) was to reduce to path of the laser light into the water tank.

3.5 DATA COLLECTION AND PROCESSING

The analog outputs of the thermistor circuits, spectrum analyser,

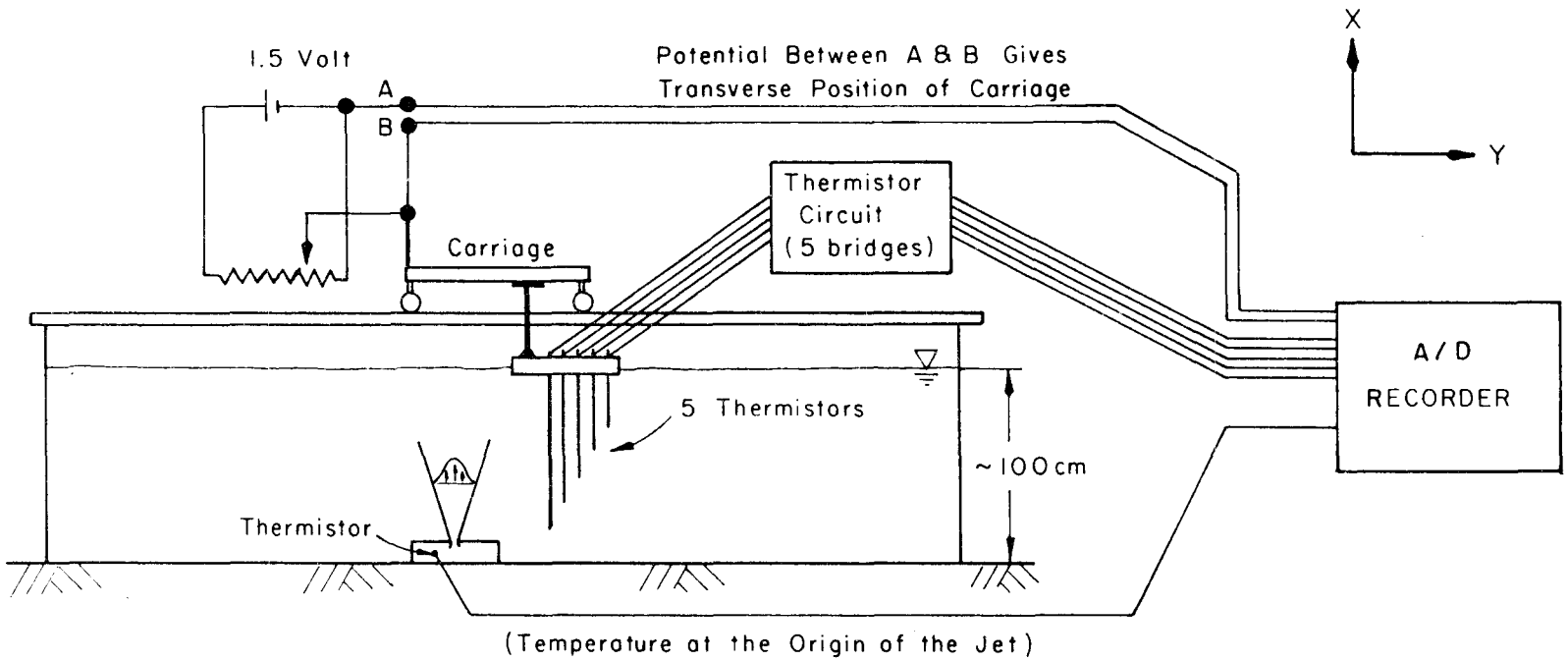

Figure 3.4.3. First instrumental set-up.

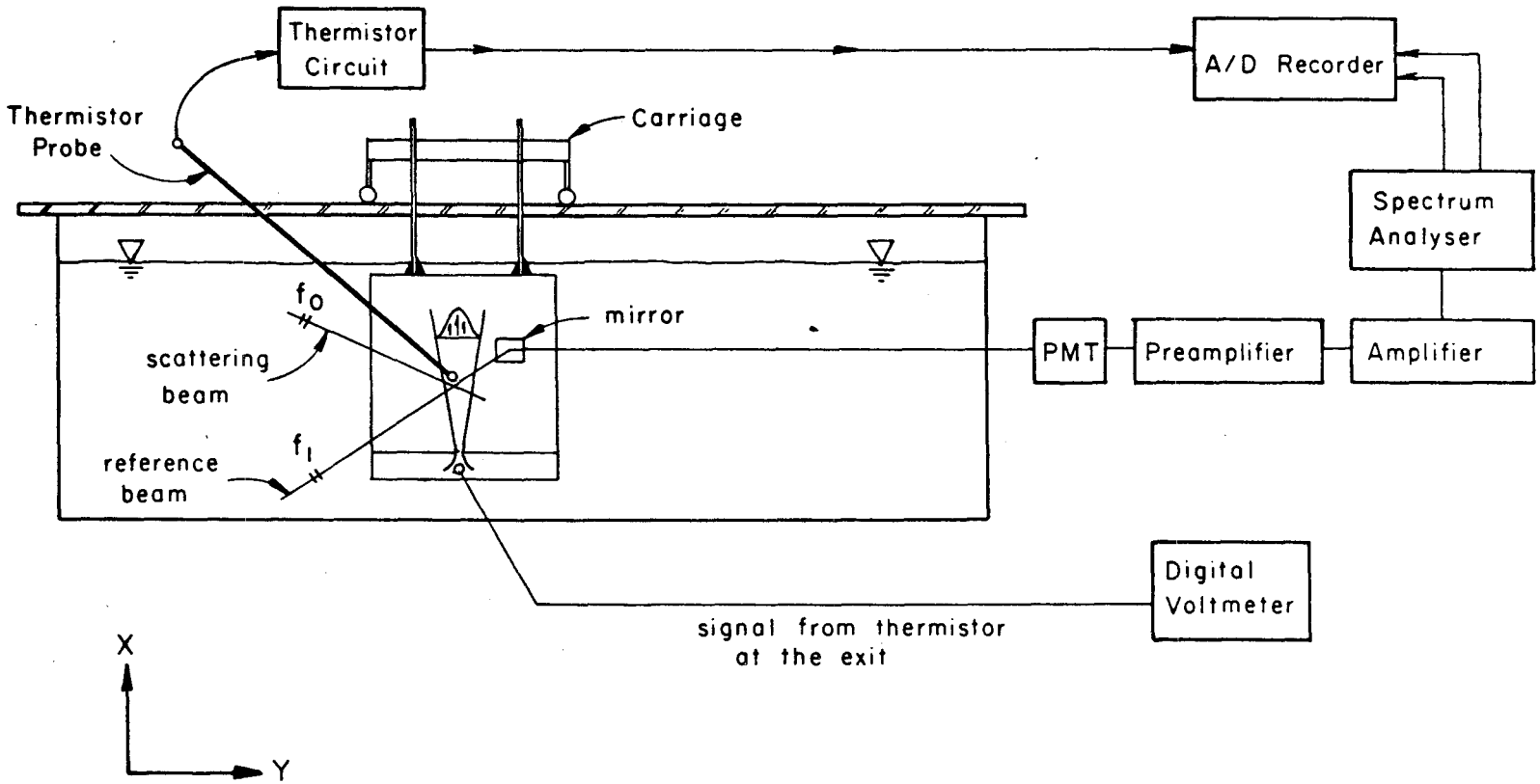

Figure 3.4.4.a. Front view of the second instrumental set-up.

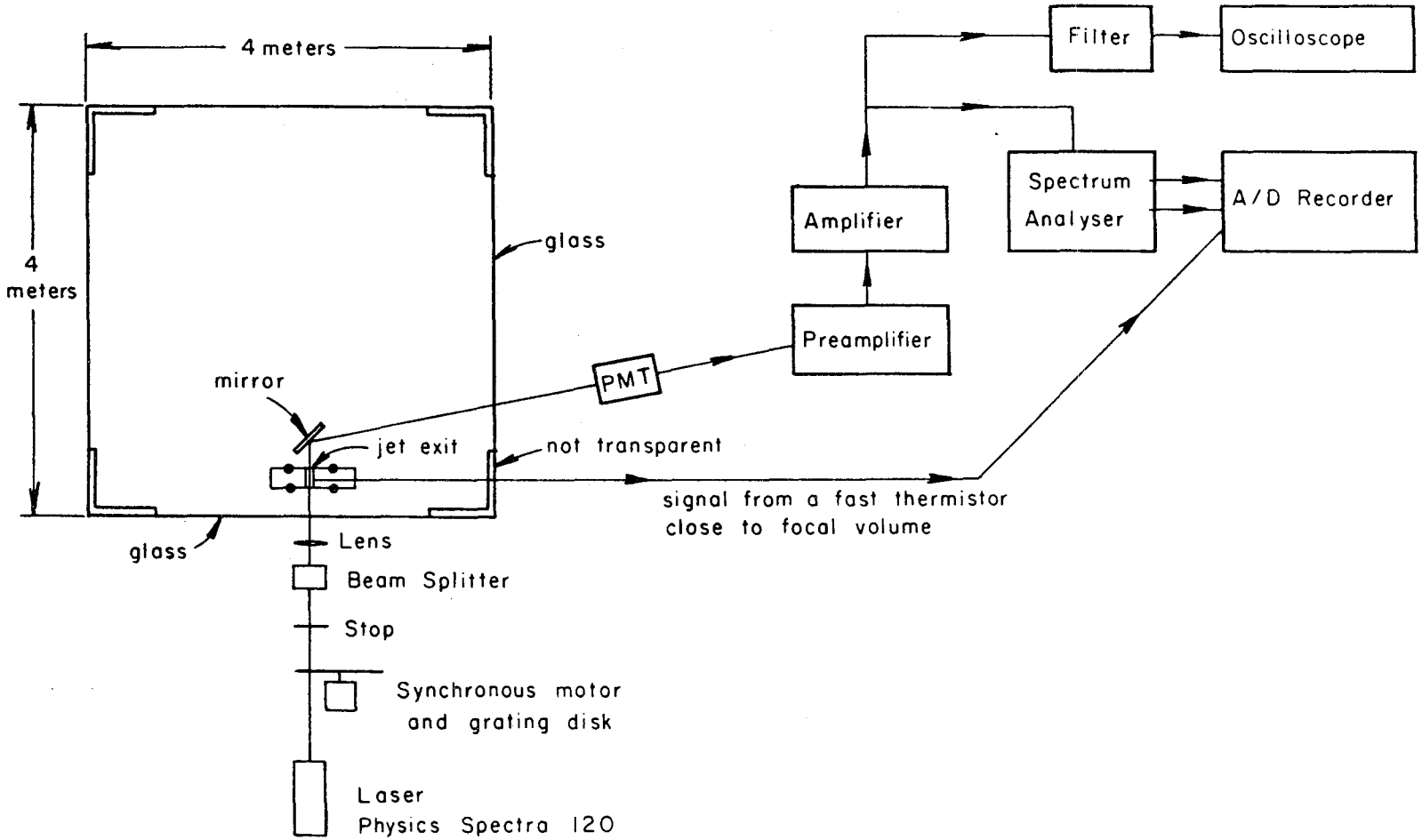

Figure 3.4.4.b. Plan view of the second instrumental set-up.

and potentiometer were digitized continuously by the A/D data acquisition system and packed onto a magnetic tape compatible with the IBM 360/75 high speed digital computer in Booth Computing Center. Two main programs were written to process the recorded information. The first (Program I) was applicable to the first instrumental set-up where only temperatures were measured across the jet using the five thermistors at five different elevations. The second program (Program II) was used for the second instrumental set-up when the laser Doppler velocimeter was used to measure velocities and one thermistor was used to measure temperature close to the focal volume.

Program I

Each of the six thermistors was characterized by its calibration polynomial

$$T = A(i) + B(i)V + C(i)V^2 + D(i)V^3,$$

where $i = 1,2,.....6$ (six thermistors),

and V is analog signal from bridge circuit,

T is temperature in °C .

The coefficients B(i), C(i), D(i), were practically constant for an extended period of time (3 months) but the coefficient A(i) did change slightly with the time (order 1 week), possibly due to the ageing of the thermistors or the temperature variations of the ambient air (affecting the precision resistors of the bridge). Thus a calibration of the coefficient A(i) was necessary prior to each run. The first file of the

magnetic tape (for every run) represented the analog outputs V_i of the six thermistors at ambient water temperature T_a. Then A(i) was calculated from the relation

$$A(i) = T_a - B(i)V_i - C(i)V_i - D(i)V_i , \qquad i = 1,2,.....6.$$

Measurements of the same temperature from the six thermistors had an accuracy ± 0.01 °C. Each of the next files then contained the conditional sampling of the signal from the six thermistor circuits and the signal from the potentiometer (transverse position Y). The main steps of the program were as follows:

1. Read a file from the tape.
2. Calculate the instantaneous temperature

$$T_k(x_k,y,t_i) = A(k) + B(k)V_k(x_k,y,t_i) + C(k)V_k^2(x_k,y,t_i) + D(k)V_k^3(x_k,y,t_i) ,$$

for $k = 1,2,.....5$, (five thermistors at five elevations)

and $k = 6$ (thermistor at the exit).

3. Calculate the mean temperature at x_k,y,

$$\overline{T}_k(x_k,y) = \frac{\sum_{i=1}^{N} T_k(x_k,y,t_i)}{N} ,$$

where $k = 1,2,.....6$ (thermistors at different elevations and at exit).

4. Calculate standard deviation of the temperature fluctuations

$$\sqrt{\overline{T_k'^2}} = \sqrt{\overline{(T_k - \bar{T}_k)^2}} \quad ,$$

$k = 1,2,.....5$.

5. Calculate $I(x_k,y,t_i)$ where

$$I(x_k,y,t_i) = \begin{cases} 1 & \text{if } T(x_k,y,t_i) > T_a + 0.04\ ^\circ C \ , \\ 0 & \text{if } T(x_k,y,t_i) < T_a + 0.04\ ^\circ C \ , \end{cases} \tag{3.5.1}$$

where T_a the temperature of the ambient water.

6. Calculate the intermittency $\gamma_k(x_k,y)$ where

$$\gamma_k(x_k,y) = \frac{\sum_{i=1}^{N} I(x_k,y,t_i)}{N} \quad . \tag{3.5.2}$$

7. Calculate the intensity of the temperature fluctuations with respect to the mean $\overline{T}(x_k,y)$ defined in step 3 but subtracting the contribution to the signal when the temperature is below the threshold defined in (5) above ,

$$\overline{T'^2_{hot}} = \frac{1}{N} \sum_{i=1}^{N} [T(x_k,y,t_i) - \overline{T}(x_k,y)]^2 \ I(x_k y,t_i) \quad .$$

8. Calculate the intensity of the temperature fluctuations with respect to the mean $\overline{T}(x_k,y)$ taking into account only the signal below the threshold,

$$\overline{T'^2_{cold}} = \frac{1}{N} \sum_{i=1}^{N} [T(x_k,y,t_i) - \overline{T}(x_k,y)]^2 \ [1 - I(x_k,y,t_i)] \ .$$

9. Calculate the frequency of the conditionally sampled intermittent signal (Figure 3.5.1).

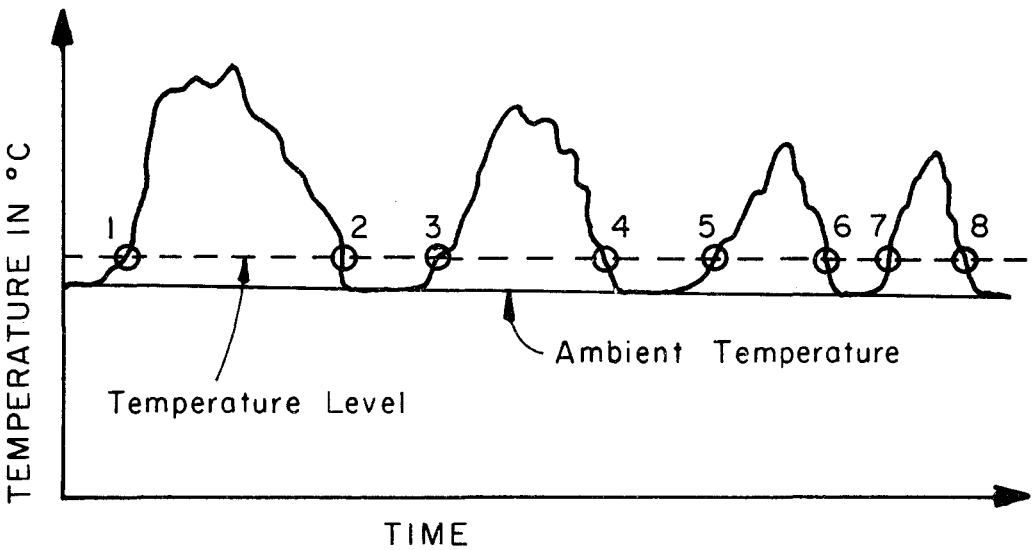

Figure 3.5.1. Typical intermittent signal.

In order to count the threshold crossings, a temperature level T_L was chosen such that $T_L = T_a + 0.04$ °C (where T_a = ambient temperature). Then the product is formed

$$Z(t_i) = [T_k(x_k,y,t_i) - T_L]\cdot[T_k(x_k,y,t_{i+1}) - T_L],$$

and defining $F(t_i)$ as

$$F(t_i) = \begin{cases} 0 & \text{if } Z(t_i) > 0, \\ 1 & \text{if } Z(t_i) < 0, \end{cases}$$

the frequency of threshold crossings f_R is given as

$$f_R = \frac{\sum_{i=1}^{N} F(t_i)}{2(t_N - t_1)} \quad . \tag{3.5.3}$$

Another way to find f_R is to construct a function $M(x_k,y,t_i)$ such that

$$M(x_k,y,t_i) = \begin{cases} 0 & \text{if } [I(x_k,y,t_i) + I(x_k,y,t_{i+1})] = 0 \text{ or } 2 \ , \\ 1 & \text{if } [I(x_k,y,t_i) + I(x_k,y,t_{i+1})] = 1 \ , \end{cases}$$

then

$$f_R = \frac{\sum_{i=1}^{N} M(x_k,y,t_i)}{2(t_N - t_1)} \quad .$$

10. Determine the maximum temperature Max T,

Max T = maximum $\{T(x_k,y,t_i)$, for $0 < t_i < \tau\}$ where τ = sampling time .

11. Determine the minimum temperature Min T.

Min T = minimum $\{T_k(x_k,y,t_i)$, $0 < t_i < \tau\}$ where τ = sampling time.

12. Determine the skewness factor

$$\frac{\overline{T_k'^3}}{(\overline{T_k'^2})^{3/2}} \quad \text{where } \overline{T_k'^3} = \overline{[T_k(x_k,y,t_i) - \bar{T}_k(x_k,y)]^3} \ .$$

13. Determine the flatness factor

$$\overline{(T_k')^4} / (\overline{T_k'^2})^2 \ ,$$

where $\overline{T_k'^4} = \overline{[T_k(x_k,y,t_i) - \bar{T}_k(x_k,y)]^4}$,

(For a Gaussian distribution the flatness factor is 3.)

14. Plot the transverse mean temperature profile.

Program II

This program had all the features of program I with some additions. Briefly the steps of this program were

1
2
.
.
.
14

} as in program 1 .

15. The frequency histogram of temperature was calculated and plotted.

16. The frequency histogram of the velocity was calculated and plotted.

17. The mean velocity $\bar{u}(x,y)$ was calculated from the velocity histogram.

18. The standard deviation $\overline{u'^2}$ was calculated from the velocity

histogram.

19. The product $\overline{uT}$ was calculated.

4. TEMPERATURE MEASUREMENT RESULTS AND DISCUSSION

4.0 BASIC EXPERIMENTAL PARAMETERS AND INITIAL DATA

Complete information regarding the basic parameters and the initial data of the experimental runs is given in Table 4.0.1. An explanation of the data columns is as follows:

Column 1 gives the name of the run. The series of runs June or July, corresponds to the experiments in which only temperature was measured; while the series PLVT corresponds to the experiments in which both temperatures and velocities were measured.

Column 2 gives the width of the jet (in cm) at the orifice.

Column 3 gives the aspect ratio of the jet at the orifice.

Column 4 gives the exit velocity of the jet.

Column 5 gives the temperature of the ambient water in °C.

Column 6 gives the excess (above ambient) temperature at the jet orifice in °C.

Column 7 gives the kinematic viscosity (cm^2/sec multiplied by 10^2) at the jet orifice.

Column 8 gives the thermal expansion coefficient (1/°C multiplied by 1000), calculated at the jet orifice.

Column 9 gives the Reynolds number at the jet orifice

$$R_e = \bar{u}_o D/\nu_o \ .$$

Column 10 gives the Richardson number calculated at the jet orifice

$$R_o = \frac{\alpha_o g \bar{T}_o D}{\bar{u}_o^2} \ .$$

Run	D cm	Aspect ratio	$\bar{u}_o$ cm/sec	$\bar{T}_o$ °C	T_a °C	ν_o x 10^2	α_o x 10^3	R_e	R_o
1	2	3	4	5	6	7	8	9	10
PLVT2-F	0.24	54.20	62.93	3.30	21.80	0.90	0.25	1633.38	0.00005
PLVT2-Z	0.24	54.20	62.93	5.40	21.80	0.85	0.27	1777.09	0.00006
PLVT2-H	0.24	54.20	64.20	3.80	22.20	0.87	0.26	1762.78	0.00005
PLVT2-A	0.24	54.20	62.90	6.85	23.25	0.60	0.30	1697.30	0.00012
JUNE-3	0.50	26.00	43.40	11.20	20.00	0.78	0.31	2794.28	0.00090
JUNE-3	0.50	26.00	43.40	11.20	20.00	0.78	0.31	2794.28	0.00090
JUNE-3	0.50	26.00	43.40	11.20	20.00	0.78	0.31	2794.28	0.00090
JUNE-3	0.50	26.00	43.40	11.20	20.00	0.78	0.31	2794.28	0.00090
JUNE-7	0.50	26.00	30.58	6.60	19.85	0.86	0.27	1767.87	0.00094
JUNE-7	0.50	26.00	30.58	6.60	19.85	0.86	0.27	1767.87	0.00094
JUNE-7	0.50	26.00	30.58	6.60	19.85	0.86	0.27	1767.87	0.00094
JUNE-7	0.50	26.00	30.58	6.60	19.85	0.86	0.27	1767.87	0.00094
JUNE-7	0.50	26.00	30.58	6.60	19.85	0.86	0.27	1767.87	0.00094
PLVT3-A	0.24	54.20	19.00	9.20	22.50	0.77	0.31	593.61	0.00189
PLVT3-A	0.24	54.20	19.00	10.40	23.20	0.74	0.32	618.17	0.0022
JULY-3	1.00	13.00	15.29	5.10	21.40	0.86	0.27	1769.95	0.0058
JULY-3	1.00	13.00	15.29	5.10	21.40	0.86	0.27	1769.95	0.0058
JULY-3	1.00	13.00	15.29	5.10	21.40	0.86	0.27	1769.95	0.0058
JULY-3	1.00	13.00	15.29	5.10	21.40	0.86	0.27	1769.95	0.0058
JULY-3	1.00	13.00	15.29	5.10	21.40	0.86	0.27	1769.95	0.0058
JULY-5	1.00	13.00	15.29	4.50	21.20	0.88	0.26	1736.93	0.0050
JULY-5	1.00	13.00	15.29	4.50	21.20	0.88	0.26	1736.93	0.0050
JULY-5	1.00	13.00	15.29	4.50	21.20	0.88	0.26	1736.93	0.0050
JULY-5	1.00	13.00	15.29	4.50	21.20	0.88	0.26	1736.93	0.0050
JULY-5	1.00	13.00	15.29	4.50	21.20	0.88	0.26	1736.93	0.0050
JULY-25	1.00	13.00	15.29	18.30	23.00	0.63	0.38	2407.91	0.0297
JULY-25	1.00	13.00	15.29	18.30	23.00	0.63	0.38	2407.91	0.0297
JULY-25	1.00	13.00	15.29	18.30	23.00	0.63	0.38	2407.91	0.0297
JULY-25	1.00	13.00	15.29	18.30	23.00	0.63	0.38	2407.91	0.0297
JULY-25	1.00	13.00	15.29	18.30	23.00	0.63	0.38	2407.91	0.0297
JUNE-6	0.50	26.00	12.23	23.50	19.70	0.61	0.39	995.64	0.0308
JUNE-6	0.50	26.00	12.23	23.50	19.70	0.61	0.39	995.64	0.0308
JUNE-6	0.50	26.00	12.23	23.50	19.70	0.61	0.39	995.64	0.0308
JUNE-6	0.50	26.00	12.23	23.50	19.70	0.61	0.39	995.64	0.0308
JUNE-6	0.50	26.00	12.23	23.50	19.70	0.61	0.39	995.64	0.0308
JULY-10	1.00	13.00	9.18	15.10	22.10	0.69	0.35	1338.73	0.062
JULY-10	1.00	13.00	9.18	15.10	22.10	0.69	0.35	1338.73	0.062
JULY-10	1.00	13.00	9.18	15.10	22.10	0.69	0.35	1338.73	0.062
JULY-10	1.00	13.00	9.18	15.10	22.10	0.69	0.35	1338.73	0.062
JULY-10	1.00	13.00	9.18	15.10	22.10	0.69	0.35	1338.73	0.062
PLVT1-F	1.00	13.00	4.55	11.50	21.50	0.75	0.32	809.05	0.177
PLVT1-D	1.00	13.00	4.55	11.55	21.60	0.74	0.32	810.99	0.176
PLVT1-Z	1.00	13.00	4.55	11.00	22.00	0.75	0.32	809.05	0.169
PLVT1-C	1.00	13.00	4.55	10.90	22.00	0.75	0.32	807.76	0.167
PLVT1-K	1.00	13.00	4.55	11.15	23.00	0.73	0.33	823.93	0.176
PLVT1-A	1.00	13.00	4.55	11.00	22.00	0.75	0.32	809.05	0.169
PLVT1-H	1.00	13.00	4.55	11.40	23.00	0.73	0.33	827.17	0.181
JUNE-28	1.00	13.00	6.11	20.90	21.30	0.62	0.39	977.70	0.216
JUNE-28	1.00	13.00	6.11	20.90	21.30	0.62	0.39	977.70	0.216
JUNE-28	1.00	13.00	6.11	20.90	21.30	0.62	0.39	977.70	0.216
JUNE-28	1.00	13.00	6.11	20.90	21.30	0.62	0.39	977.70	0.216
JUNE-28	1.00	13.00	6.11	20.90	21.30	0.62	0.39	977.70	0.216
JULY-1	1.00	13.00	6.11	21.85	21.65	0.61	0.40	999.94	0.231
JULY-1	1.00	13.00	6.11	21.85	21.65	0.61	0.40	999.94	0.231
JULY-1	1.00	13.00	6.11	21.85	21.65	0.61	0.40	999.94	0.231
JULY-1	1.00	13.00	6.11	21.85	21.65	0.61	0.40	999.94	0.231
JULY-1	1.00	13.00	6.11	21.85	21.65	0.61	0.40	999.94	0.231
JUNE-26	2.00	6.50	7.60	21.90	20.60	0.62	0.39	2445.06	0.294
JUNE-26	2.00	6.50	7.60	21.90	20.60	0.62	0.39	2445.06	0.294
JUNE-26	2.00	6.50	7.60	21.90	20.60	0.62	0.39	2445.06	0.294
JUNE-26	2.00	6.50	7.60	21.90	20.60	0.62	0.39	2445.06	0.294
JULY-29	1.00	13.00	4.59	21.70	24.10	0.59	0.41	780.40	0.423
JULY-29	1.00	13.00	4.59	21.70	24.10	0.59	0.41	780.40	0.423
JULY-29	1.00	13.00	4.59	21.70	24.10	0.59	0.41	780.40	0.423
JULY-29	1.00	13.00	4.59	21.70	24.10	0.59	0.41	780.40	0.423
JULY-29	1.00	13.00	4.59	21.70	24.10	0.59	0.41	780.40	0.423

Table 4.0.1. Basic experimental parameters and initial data of the temperature measurements.

4.1 MEAN TEMPERATURE

The mean temperature $\overline{T}(x,y)$ in °C for a particular distance from the exit x, was plotted versus the transverse distance y (in cm), and a Gaussian curve was fitted of the form

$$\overline{T}(x,y) = \overline{T}_M \exp[-\ell n2 \ (y/b_T)^2] \ , \qquad (4.1.1)$$

where b_T is the half-width of the temperature profile, as in Figures 4.1.1.a to 4.1.1.d and 4.1.4.a to 4.1.4.d. The temperature half-widths, $b_T(x)$, for a particular run were plotted versus the distance from the exit as in Figure 4.1.2 and 4.1.5, and a straight line

$$\frac{b_T}{D} = K_{1T} \ (\frac{x}{D} + K_{2T}) \qquad (4.1.2)$$

was fitted to the data, where D is the width of the jet at the origin (jet exit). The virtual origin of the mean temperature profile is then given by

$$x_{oT} = -K_{2T} \ D \ .$$

The coefficients K_{1T}, K_{2T} from all the runs are tabulated in Table 4.1.1 from where it can be observed that there is no apparent variation of K_{1T}, K_{2T} with the initial Richardson number R_o. But it is interesting to note that the coefficients K_{1T}, K_{2T} for runs PLVT2 and June 7 are quite different, although they both correspond to jet Richardson numbers appropriate to a pure jet. The explanation of this appears to be that the true character of the jet half-width is non-self-preserving, i.e., the assumption of linear growth of the half-width although

(text continues on page 99)

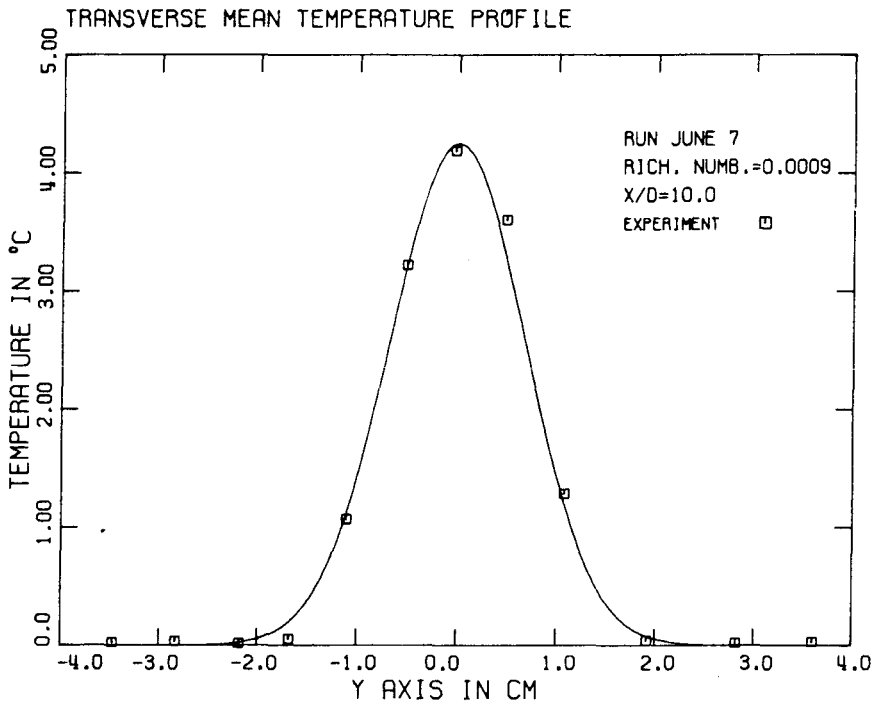

Figure 4.1.1.a. Mean temperature profile for a turbulent jet at x/D = 10.0.

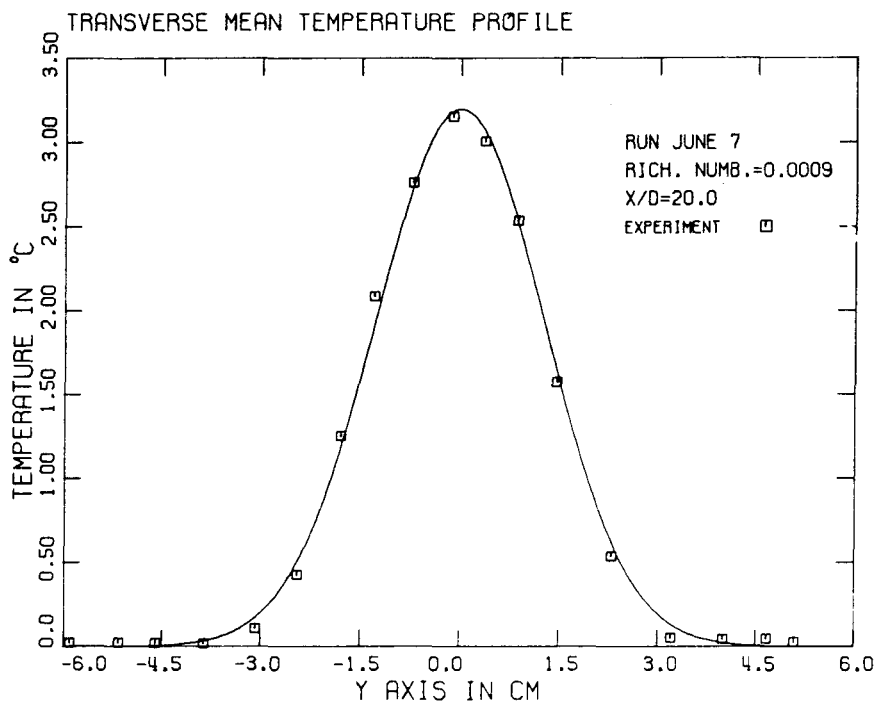

Figure 4.1.1.b. Mean temperature profile for a turbulent jet at x/D = 20.0.

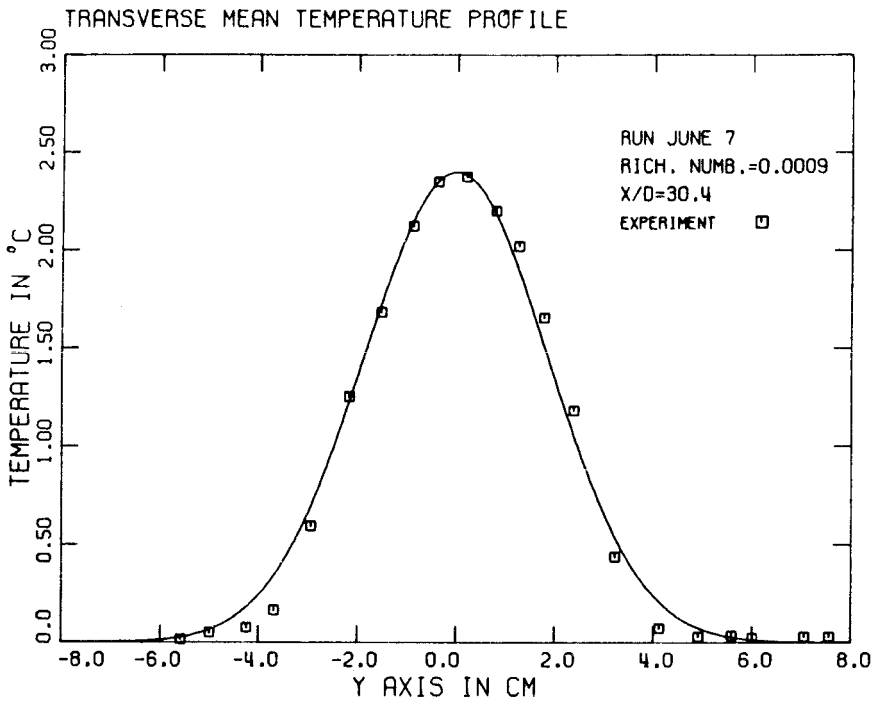

Figure 4.1.1.c. Mean temperature profile for a turbulent jet at x/D = 30.4.

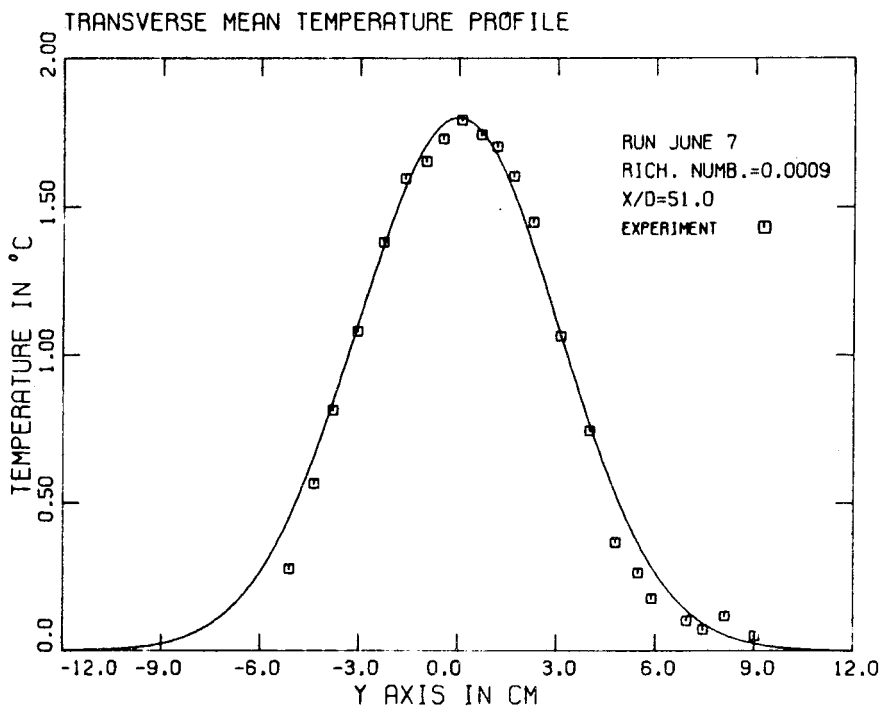

Figure 4.1.1.d. Mean temperature profile for a turbulent jet at x/D = 51.0.

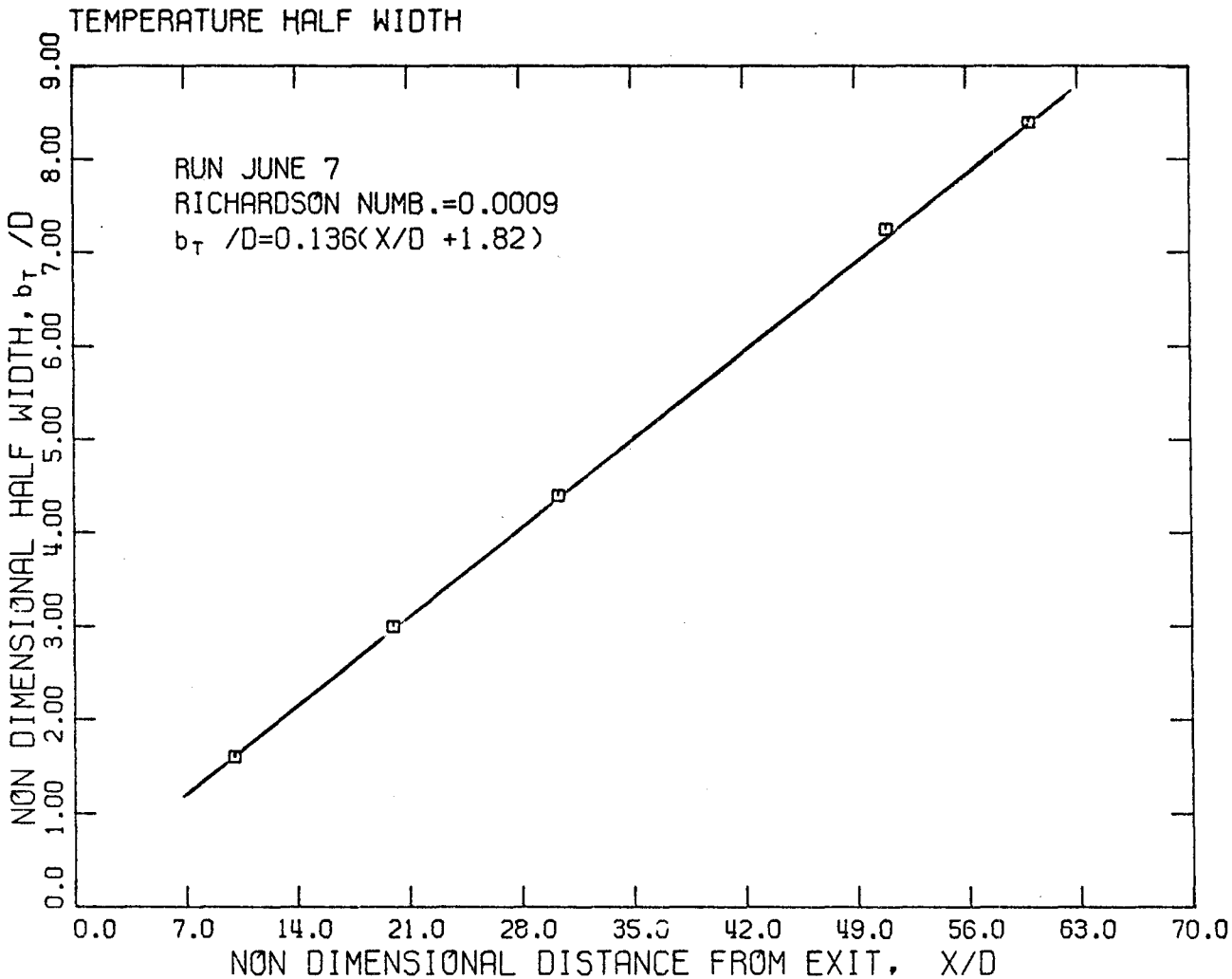

Figure 4.1.2. Non-dimensional temperature half-width of a turbulent jet plotted against non-dimensional distance along the jet axis.

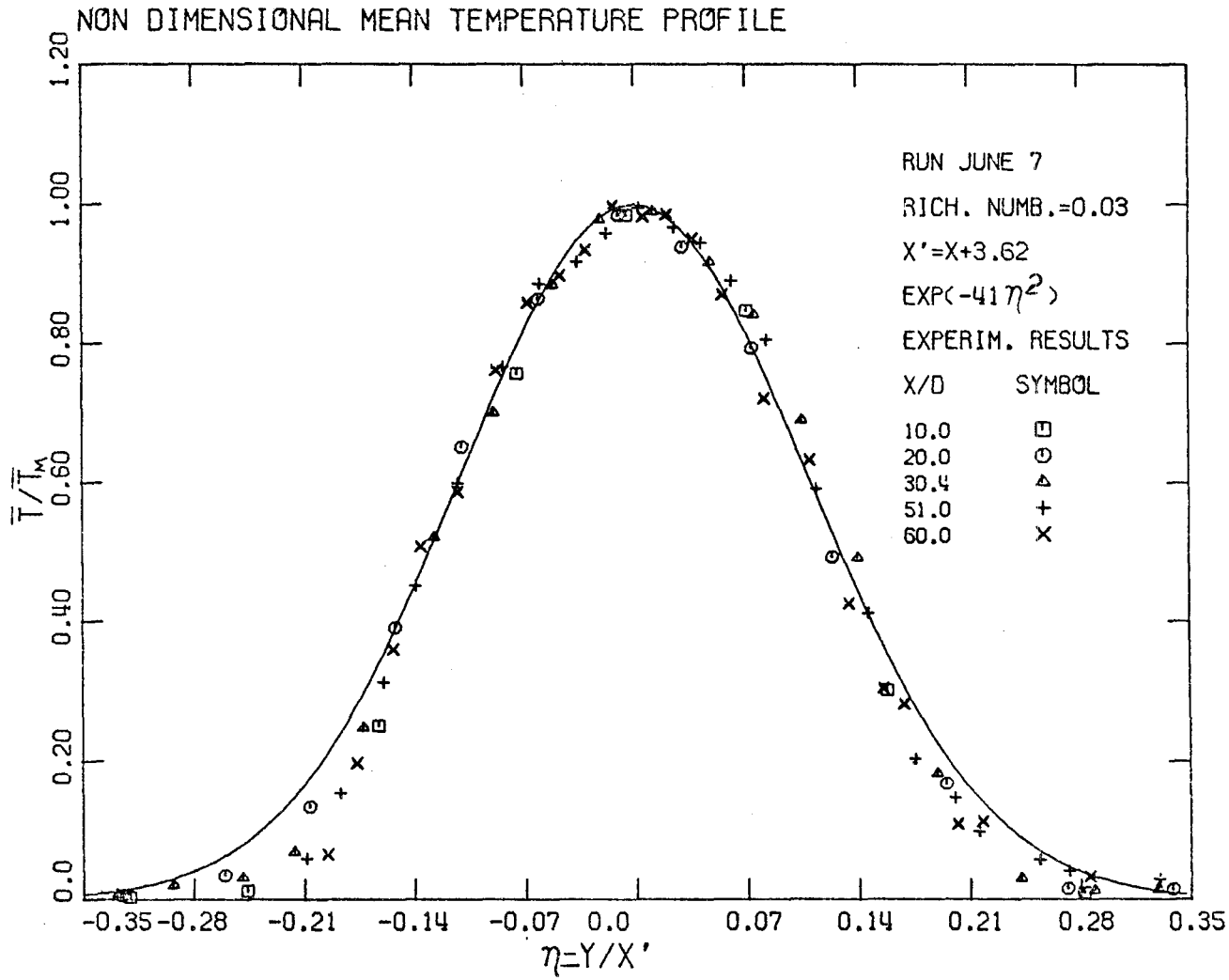

Figure 4.1.3. Non-dimensional mean temperature profile of a jet plotted against non-dimensional distance from jet axis.

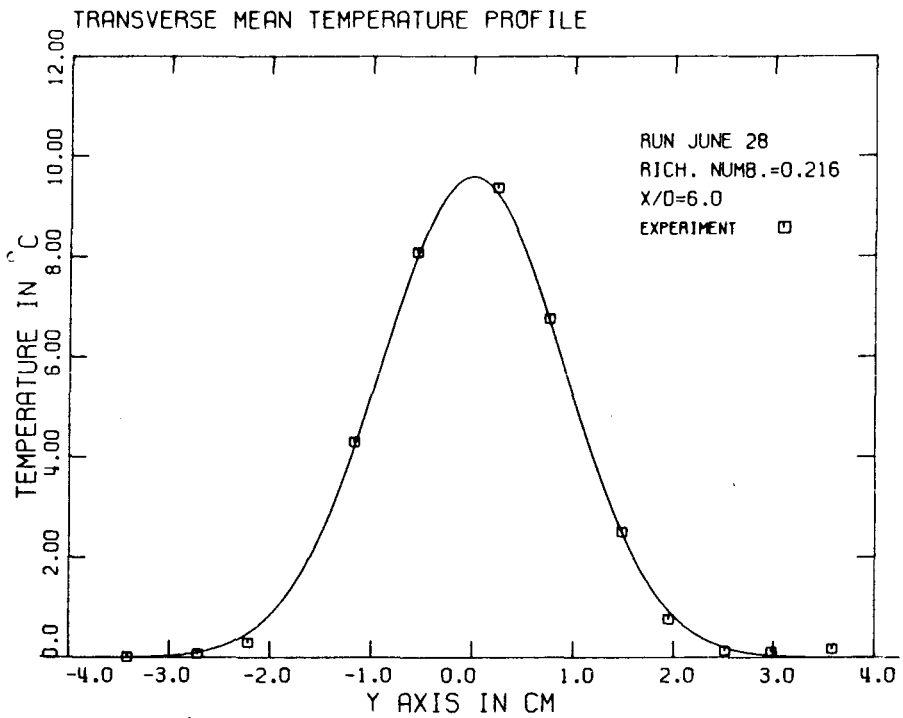

Figure 4.1.4.a. Mean temperature profile for a turbulent plume at x/D = 6.0.

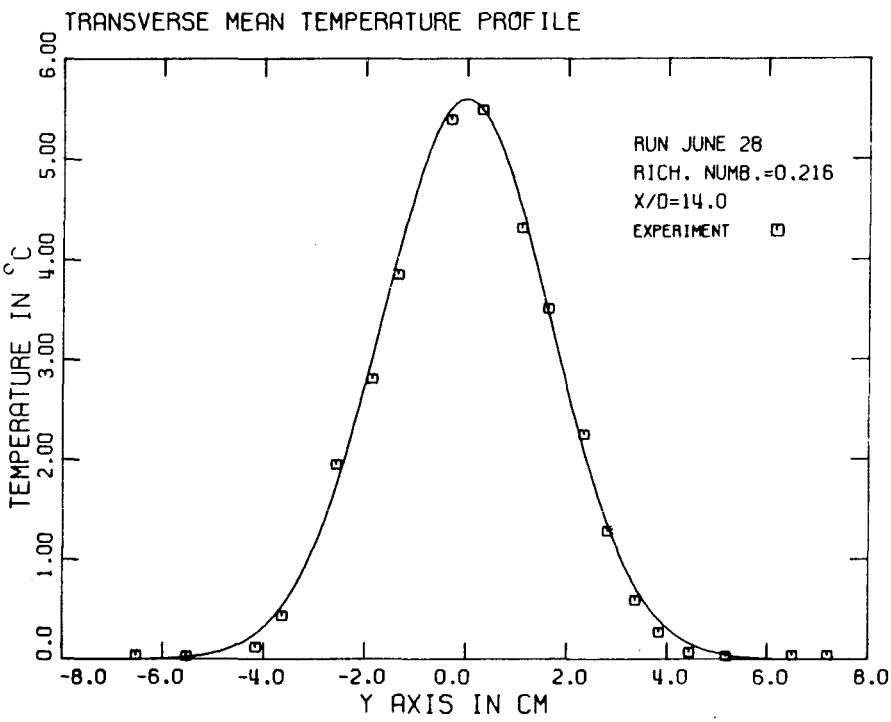

Figure 4.1.4.b. Mean temperature profile for a turbulent plume at x/D = 14.0.

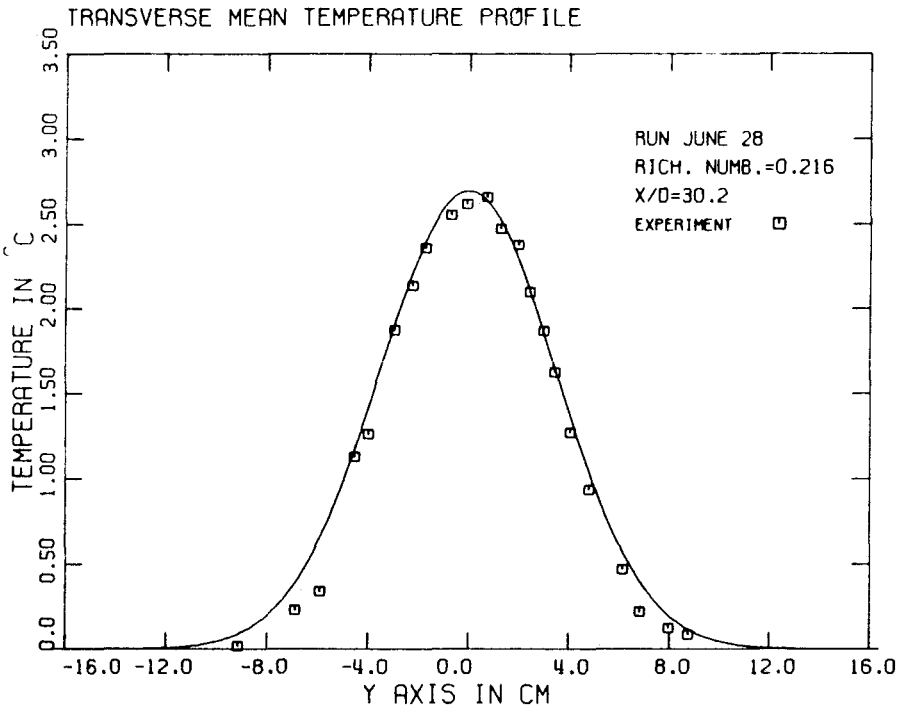

Figure 4.1.4.c. Mean temperature profile for a turbulent plume at x/D = 30.2.

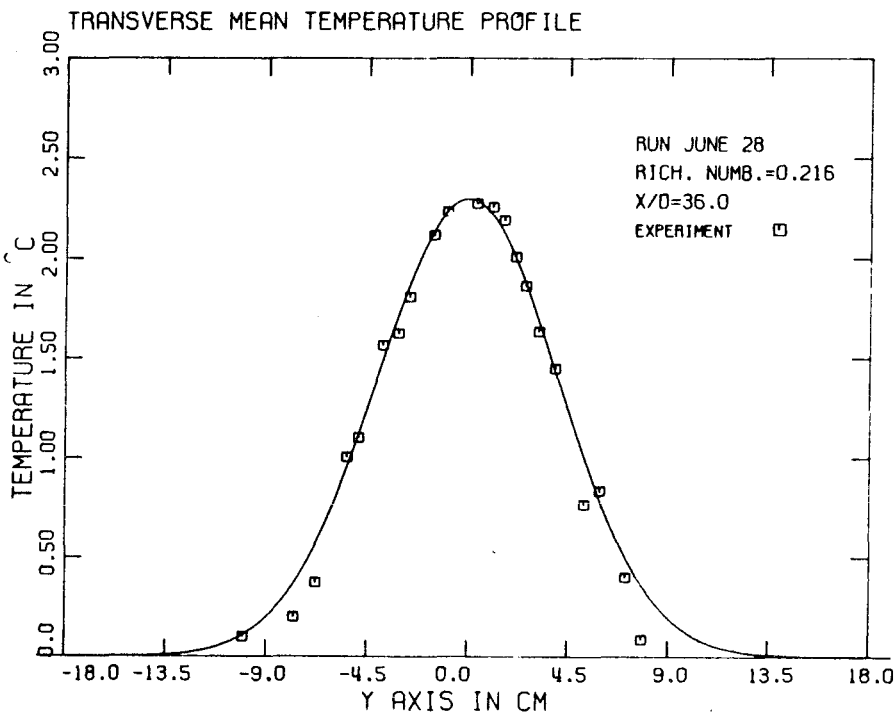

Figure 4.1.4.d. Mean temperature profile for a turbulent plume at x/D = 36.0.

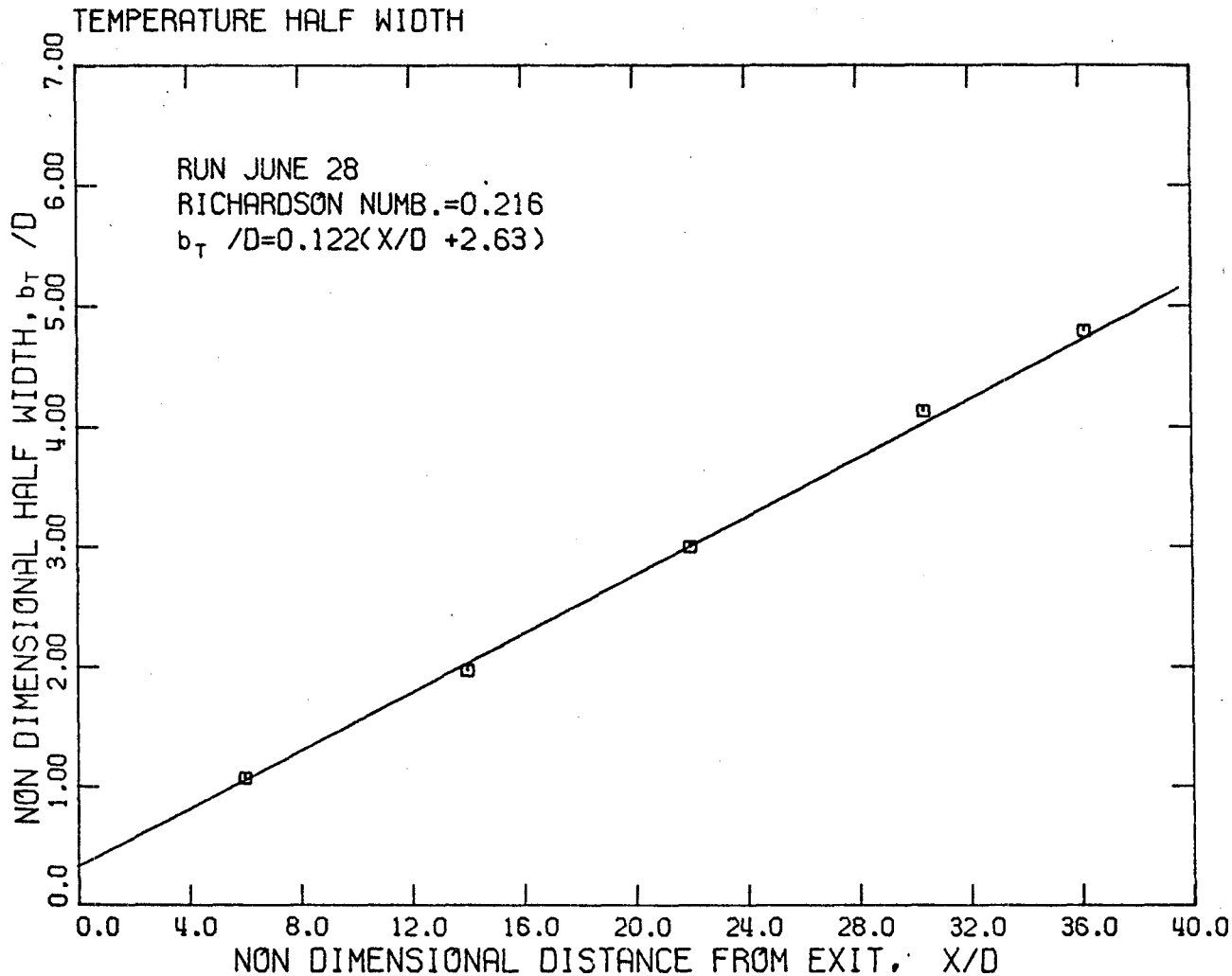

Figure 4.1.5. Temperature half-width of a plume as a function of distance from plume orifice.

Run	R_o	X/D from	X/D to	K_{1T}	K_{2T}	C_{1T}	C_{2T}
1	2	3	4	5	6	7	8
PLVT2	0.00008	20.80	93.75	0.167	-1.56	0.20	-2.44
June 3	0.00091	10.0	50.00	0.130	3.90	0.27	-1.0
June 7	0.00094	10.0	60.0	0.136	1.82	0.27	-1.0
PLVT3	0.002	33.75	93.75	0.141	-2.12	0.31	-4.70
July 3	0.0058	6.0	36.0	0.125	4.35	0.35	-0.1
July 5	0.0050	6.0	36.2	0.121	4.46	0.35	-0.1
July 25	0.0297	6.0	36.0	0.123	2.3	--	--
June 6	0.031	10.0	60.0	0.120	3.3	--	--
July 10	0.063	6.0	36.0	0.118	3.3	--	--
PLVT1	0.17	9.0	39.0	0.120	2.10	--	--
June 28	0.216	6.0	36.2	0.122	2.63	--	--
July 1	0.231	6.0	36.0	0.121	2.87	--	--
June 26	0.294	6.0	18.0	0.113	4.0	--	--
July 29	0.424	6.0	36.0	0.112	4.42	--	--

Table 4.1.1. Linear approximation of the growth of the temperature half-width and the centerline dilution.

providing a convenient way of plotting and fitting data which is compatible with the overall accuracy of a particular run is not strictly valid. This will be clarified in Chapter 8.

The mean temperature $\overline{T}$ normalized by the mean temperature on the jet axis $\overline{T}_M$ has been plotted versus the non-dimensional distance y/x' (where $x' = x - x_{oT}$) for two representative cases of Richardson number. Figure 4.1.3 gives $\overline{T}/\overline{T}_M$ for a jet and Figure 4.1.6 for a plume. The Gaussian curve which is plotted on these figures is defined by

$$\frac{\overline{T}}{\overline{T}_M} = \exp[-\ell n2\ (y/K_{1T}x')^2] \ . \qquad (4.1.3)$$

Similar plots for the other experimental runs are presented in Appendix B.

The centerline dilution, defined as $\overline{T}_o/\overline{T}_M$ has been plotted in Figure 4.1.7 for the case of a pure jet ($R_o \approx 0.0009$) and a line

$$\left(\frac{\overline{T}_o}{\overline{T}_M}\right)^2 = C_{1T}\left(\frac{x}{D} + C_{2T}\right) \ , \qquad (4.1.4)$$

fitted to the data. In Figure 4.1.8 it can be seen that for a pure plume the centerline mean temperature $\overline{T}$ decays as x^{-1}, and not as $x^{-1/2}$ as occurs for a jet (Figure 4.1.7). The centerline temperature for many runs with initial Richardson number greater than 0.15 (case of a plume) has been plotted in Figure 4.1.9 in a fashion suggested by the non-dimensional number (see Eq. 2.2.14)

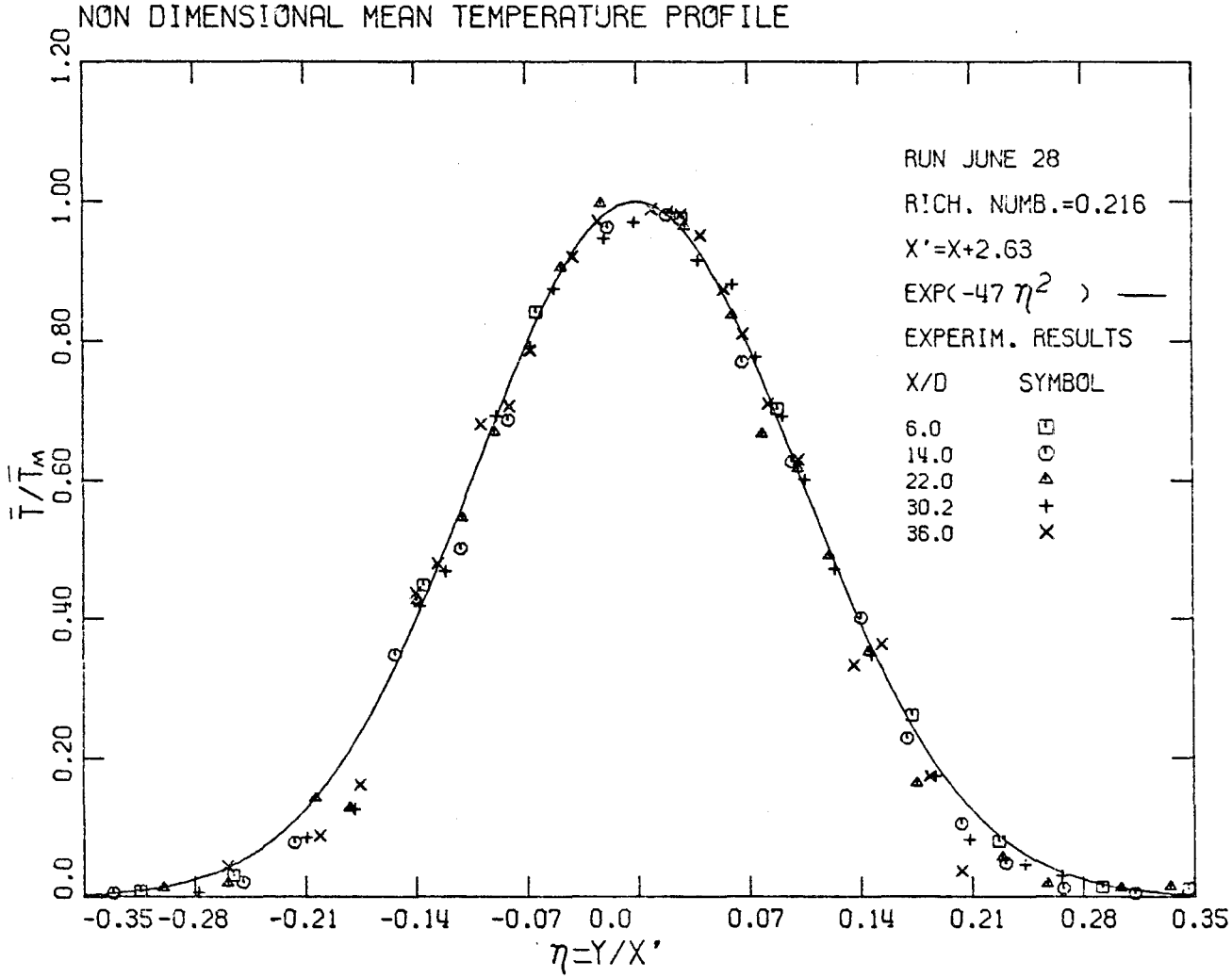

Figure 4.1.6. Non-dimensional mean temperature profile for a plume.

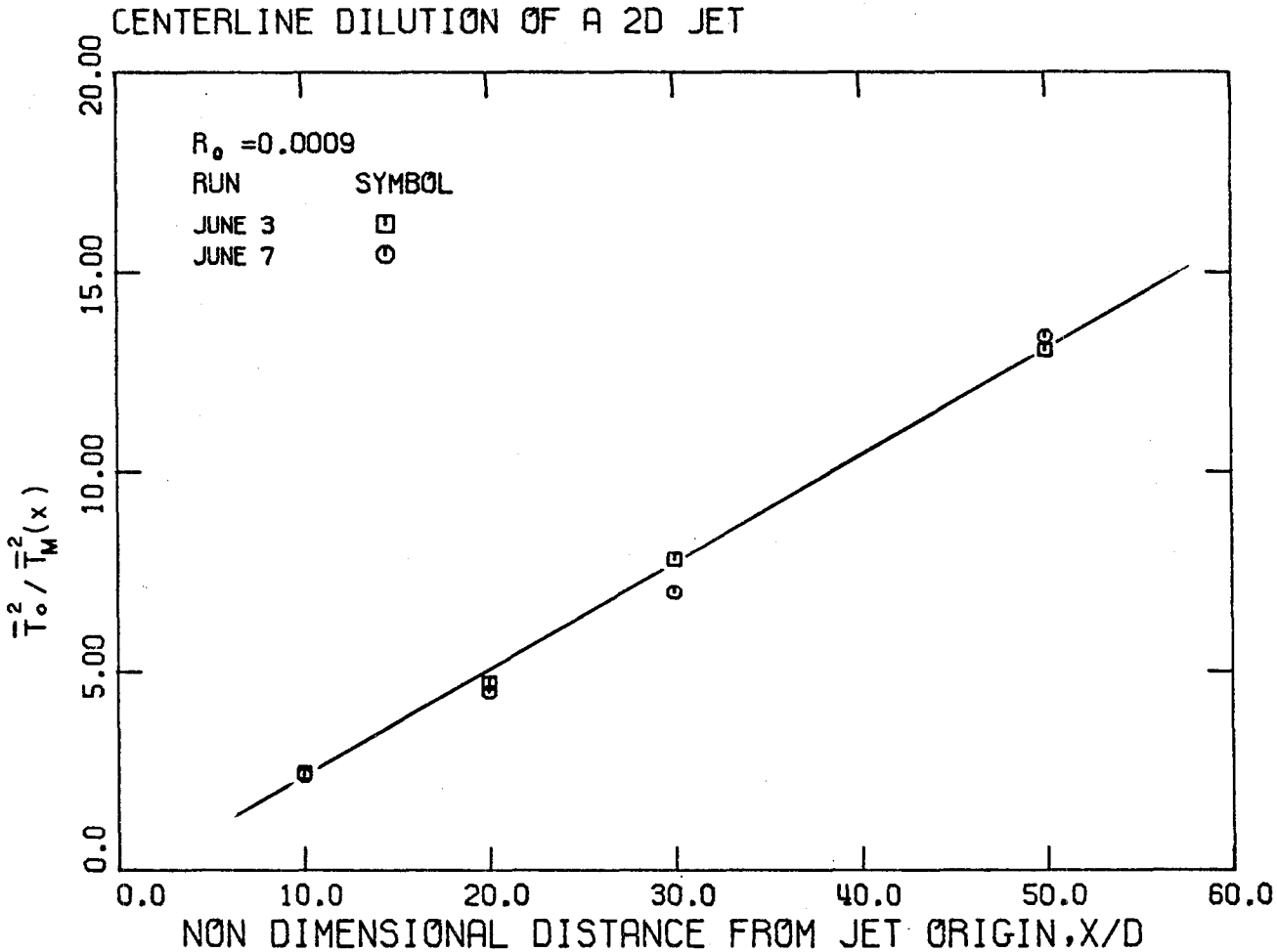

Figure 4.1.7. Temperature distribution along jet axis.

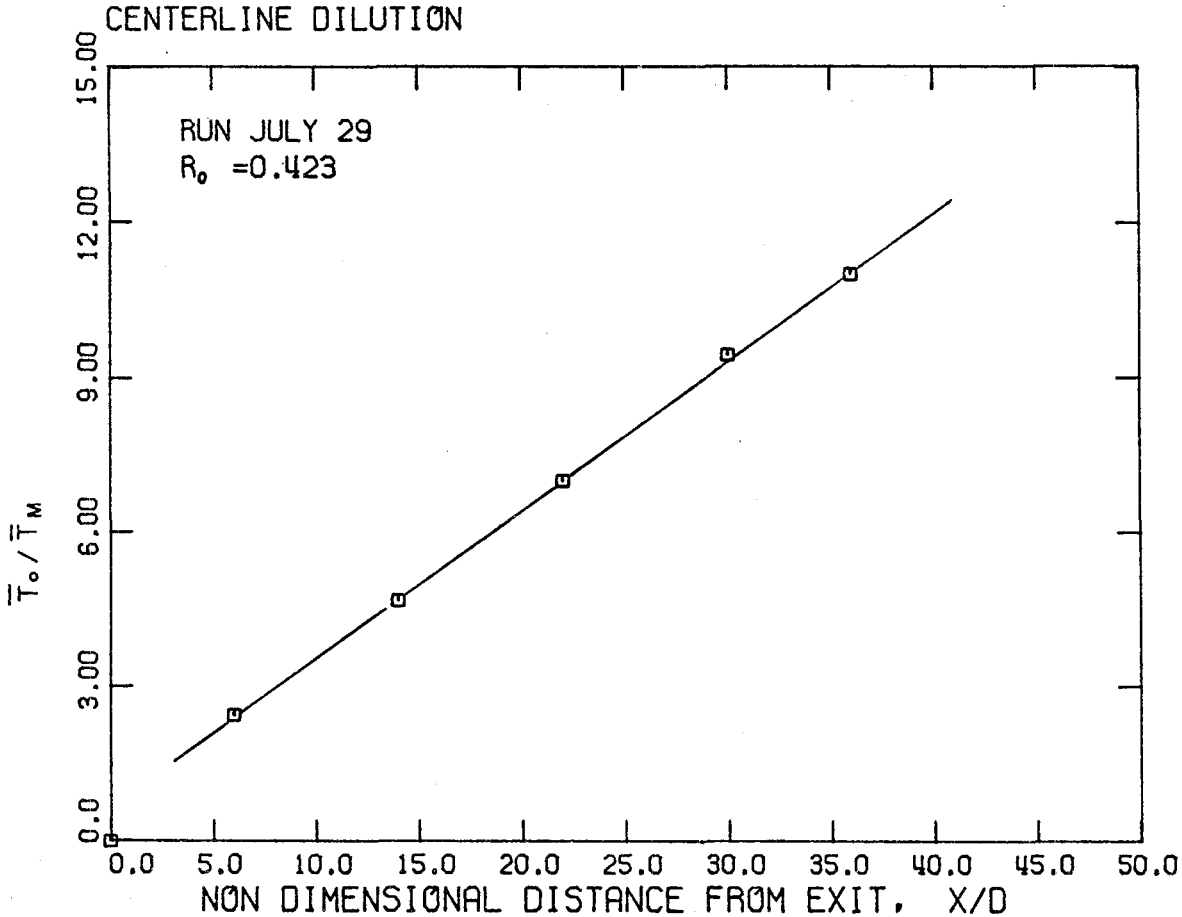

Figure 4.1.8. Temperature distribution along plume axis.

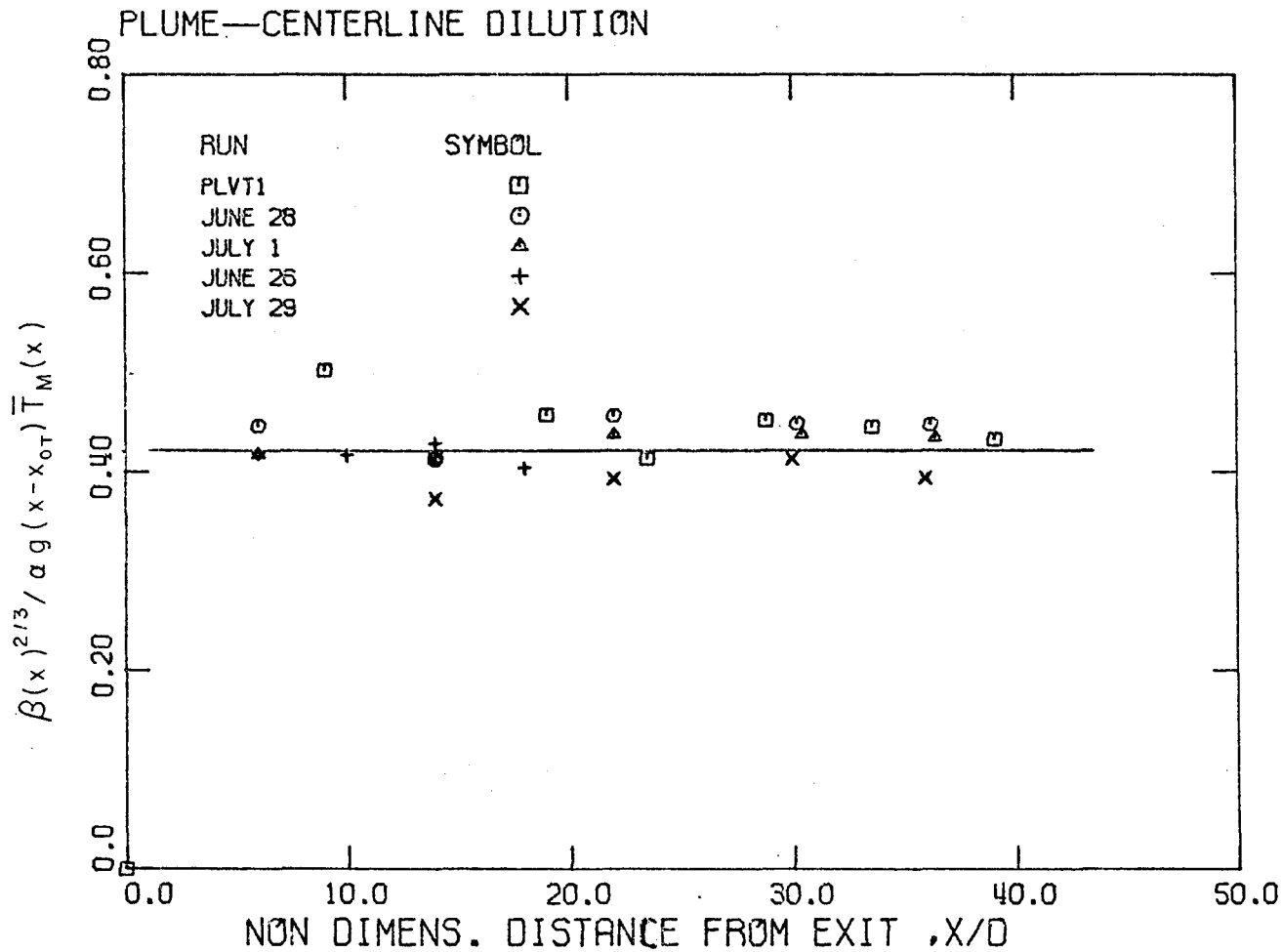

Figure 4.1.9. Temperature distribution along plume axis.

$$\sigma_T = \frac{\beta(x)^{2/3}}{\alpha(x) g \ (x-x_{oT}) \ \overline{T}_M(x)} \quad , \tag{4.1.5}$$

where the thermal expansion coefficient $\alpha(x)$ is calculated from Eq. (2.2.5) at a temperature $T_a + \overline{T}_M(x)$ and the kinematic buoyancy flux $\beta(x)$ is calculated from the relation

$$\beta(x) = \frac{\alpha(x) g H_o}{\rho c_p} \quad , \tag{4.1.6}$$

where H_o the heat flux at the origin of the jet. The mean value for σ_T suggested by the results tabulated in Table 4.1.2 is $\sigma_T \approx 0.42$ with a standard deviation of 0.02. Since

$$\alpha(x) \ \overline{T}_M(x) = (\rho_o - \overline{\rho}_M(x))/\rho_o \quad ,$$

where $\overline{\rho}_M(x)$ is the mean density on the jet axis at a distance x from the jet origin, then using Eq. 4.1.5 it is apparent that

$$\frac{\rho_o}{\rho_o - \overline{\rho}_M(x)} = 0.42 \ g \ (x - x_{oT}) \beta(x)^{-2/3} \quad . \tag{4.1.7}$$

This value for σ_T is higher than the value $\sigma_T \approx 0.38$ suggested by Koh and Brooks (60), or by Lee (55).

The mean centerline temperature $\overline{T}_M(x)$ and the temperature half-width $b_T(x)$ for each measured temperature profile are given in Table 4.1.2.

Run	R_o	D cm	x cm	$\bar{T}_o$ °C	$\bar{T}_M$ °C	b_T cm	σ_T
1	2	3	4	5	6	7	8
PLVT2-E	0.000051	0.240	5.000	3.300	1.750	0.790	2.660
PLVT2-I	0.000089	0.240	9.900	5.400	2.020	1.400	1.722
PLVT2-H	0.000058	0.240	14.100	3.800	1.160	2.040	1.501
PLVT2-A	0.000123	0.240	22.500	6.850	1.800	3.300	0.858
JUNE-3	0.000309	0.500	5.000	11.200	7.100	0.900	1.157
JUNE-3	0.000909	0.500	10.000	11.200	5.150	1.530	0.961
JUNE-3	0.000900	0.500	15.300	11.200	4.060	2.210	0.889
JUNE-3	0.000930	0.500	25.300	11.200	3.100	3.500	0.734
JUNE-7	0.000940	0.500	5.000	6.600	4.250	0.800	1.174
JUNE-7	0.000940	0.500	10.000	6.600	3.200	1.500	0.911
JUNE-7	0.000940	0.500	15.200	6.600	2.500	2.200	0.818
JUNE-7	0.000940	0.500	25.500	6.600	1.800	3.620	0.714
JUNE-7	0.000940	0.500	30.000	6.600	1.740	4.200	0.635
PLVT3-B	0.001854	0.240	8.100	9.200	3.050	1.160	0.800
PLVT3-A	0.002242	0.240	22.500	10.400	1.780	3.100	0.518
JULY-3	0.005821	1.000	6.000	5.100	3.680	1.290	0.705
JULY-3	0.005821	1.000	14.000	5.100	2.430	2.300	0.625
JULY-3	0.005821	1.000	22.000	5.100	1.760	3.200	0.612
JULY-3	0.005821	1.000	30.400	5.100	1.560	4.200	0.527
JULY-3	0.005821	1.000	36.000	5.100	1.430	4.800	0.497
JULY-5	0.005001	1.000	6.000	4.500	3.000	1.270	0.838
JULY-5	0.005001	1.000	14.000	4.500	2.150	2.200	0.669
JULY-5	0.005001	1.000	22.000	4.500	1.560	3.330	0.649
JULY-5	0.005001	1.000	30.400	4.500	1.370	4.200	0.562
JULY-5	0.005001	1.000	36.200	4.500	1.250	4.900	0.529
JULY-25	0.029741	1.000	6.000	18.300	12.000	1.130	0.607
JULY-25	0.029741	1.000	14.000	18.300	7.250	2.000	0.532
JULY-25	0.029741	1.000	22.000	18.300	5.250	3.000	0.502
JULY-25	0.029741	1.000	30.000	18.300	4.150	4.050	0.483
JULY-25	0.029741	1.000	36.000	18.300	3.550	4.700	0.479
JUNE-6	0.030897	0.500	5.000	23.500	12.700	0.800	0.467
JUNE-6	0.030897	0.500	10.000	23.500	7.800	1.430	0.455
JUNE-6	0.030897	0.500	15.000	23.500	5.500	2.030	0.463
JUNE-6	0.030897	0.500	25.000	23.500	3.750	3.220	0.434
JUNE-6	0.030897	0.500	30.300	23.500	3.400	3.770	0.405
JULY-10	0.062853	1.000	6.300	15.100	8.300	1.100	0.509
JULY-10	0.062853	1.000	14.000	15.100	5.250	2.070	0.445
JULY-10	0.062853	1.000	22.000	15.100	3.450	3.000	0.473
JULY-10	0.062853	1.000	30.400	15.100	3.000	3.830	0.410
JULY-10	0.062853	1.000	36.200	15.100	2.500	4.670	0.422
PLVT1-E	0.177563	1.000	9.300	11.500	3.870	1.700	0.503
PLVT1-D	0.178673	1.000	14.300	11.550	3.250	2.340	0.416
PLVT1-I	0.165843	1.000	19.000	11.000	2.200	2.550	0.458
PLVT1-C	0.167867	1.000	23.500	10.900	2.000	3.250	0.414
PLVT1-K	0.176845	1.000	28.900	11.150	1.530	3.750	0.452
PLVT1-B	0.169843	1.000	33.600	11.000	1.350	4.400	0.446
PLVT1-H	0.181941	1.000	39.100	11.400	1.220	4.950	0.433
JUNE-28	0.216254	1.000	6.000	20.900	9.600	1.070	0.447
JUNE-28	0.216254	1.000	14.000	20.900	5.600	1.970	0.413
JUNE-28	0.216254	1.000	22.000	20.900	3.500	3.000	0.457
JUNE-28	0.216254	1.000	30.200	20.900	2.700	4.130	0.449
JUNE-28	0.216254	1.000	36.200	20.900	2.300	4.800	0.448
JULY-1	0.231431	1.000	6.000	21.850	10.200	1.070	0.418
JULY-1	0.231431	1.000	14.000	21.850	5.650	1.970	0.414
JULY-1	0.231431	1.000	22.000	21.850	3.700	2.870	0.438
JULY-1	0.231431	1.000	30.400	21.850	2.800	4.000	0.438
JULY-1	0.231431	1.000	36.400	21.850	2.400	4.700	0.435
JUNE-26	0.294518	2.000	12.000	21.900	8.500	2.260	0.419
JUNE-26	0.294518	2.000	20.000	21.900	6.250	3.320	0.417
JUNE-26	0.294518	2.000	28.000	21.900	4.800	4.000	0.429
JUNE-26	0.294518	2.000	36.000	21.900	4.200	5.000	0.404
JULY-29	0.423977	1.000	6.000	21.700	9.000	1.170	0.328
JULY-29	0.423977	1.000	14.000	21.700	4.650	2.070	0.374
JULY-29	0.423977	1.000	22.000	21.700	3.120	2.950	0.394
JULY-29	0.423977	1.000	30.000	21.700	2.300	3.850	0.414
JULY-29	0.423977	1.000	36.000	21.700	2.060	4.900	0.365

Table 4.1.2. Experimental values for temperature half-width and temperature distribution along jet axis for turbulent jets and plumes.

4.2 TURBULENCE INTENSITY

The intensity of turbulent temperature fluctuations, defined as

$$\overline{T'^2} = \lim_{t'\to\infty} \frac{1}{t'} \int_0^{t'} [T(x,y,t) - \overline{T}(x,y)]^2 dt , \qquad (4.2.1)$$

or, when conditional sampling is performed, as

$$\overline{T'^2} = \frac{1}{N} \sum_{i=1}^{N} [T(x,y,t_i) - \overline{T}(x,y)]^2 , \qquad (4.2.2)$$

is plotted in Figure 4.2.1 (representative case for a plume) and in Figure 4.2.2 (representative case for a jet). It is interesting to notice the dramatic difference in the structure of the turbulence intensity profile for the above two cases. The reason for this is probably the production of turbulent energy by the buoyancy forces (see Eq. 2.2.15). The turbulent energy equation (see Eq. 2.2.15) has the form

$$\frac{\overline{dq'^2}}{dt} = \alpha g \overline{u'T'} + \text{production by Reynolds stresses + diffusion and dissipation terms} , \qquad (4.2.3)$$

where $\overline{q'^2} = \overline{u'^2} + \overline{v'^2} + \overline{w'^2}$ and $\alpha g \overline{u'T'}$ is the production of turbulent energy by the buoyancy forces. The production of turbulent energy on the jet cross section is obtained by integrating Eq. (4.2.3) across the jet:

$$\int_{-B(x)}^{B(x)} \alpha(x) g \, \overline{u'T'} dy ,$$

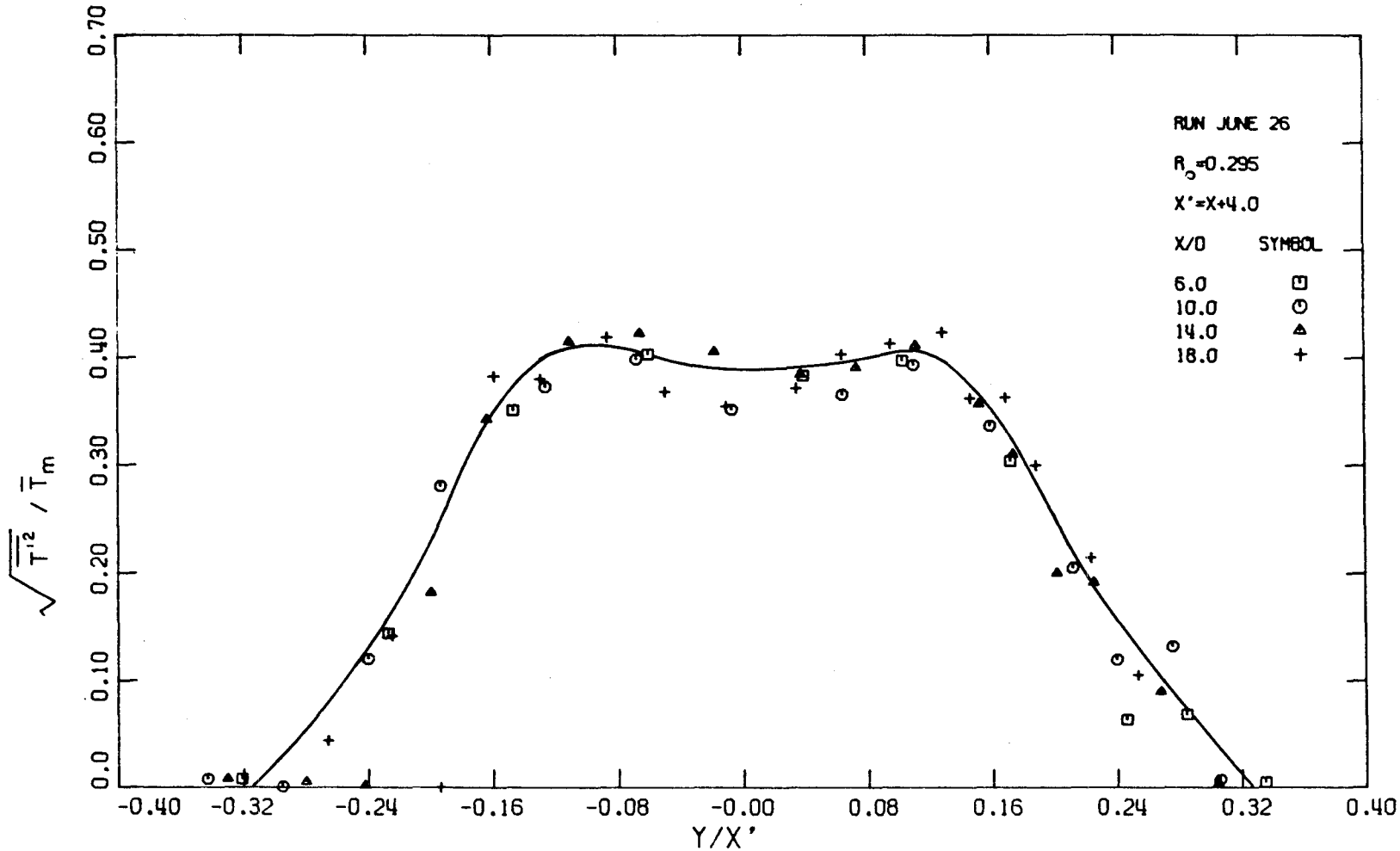

Figure 4.2.1. Profile of the intensity of turbulent fluctuations of plume temperature plotted against non-dimensional distance from jet axis.

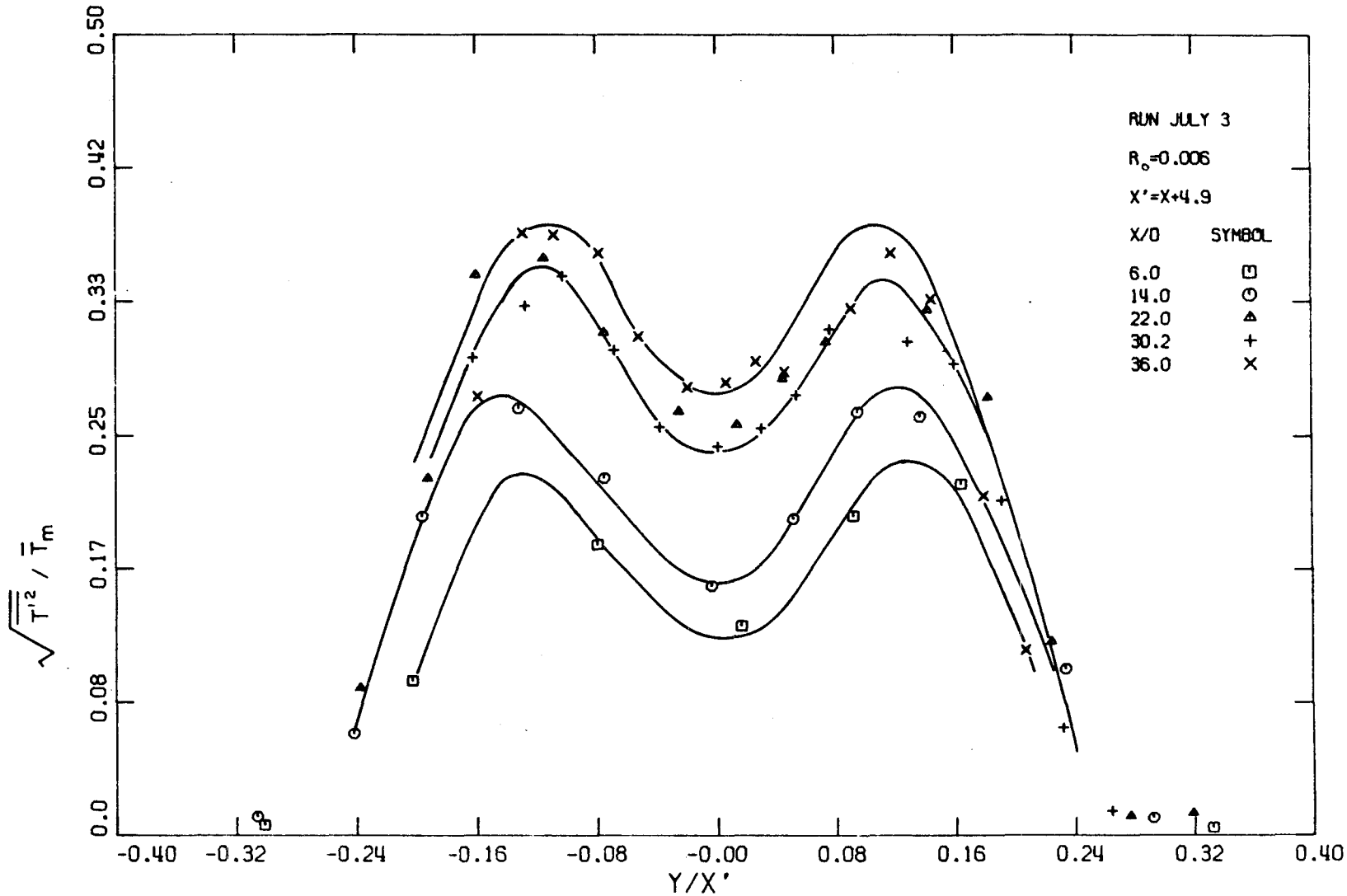

Figure 4.2.2. Profile of the intensity of turbulent fluctuations of jet temperature against non-dimensional distance from plume axis.

where the thermal expansion coefficient $\alpha(x)$ is calculated from Eq. (2.2.5) at a temperature $T_a + \overline{T}_M(x)$. However, the kinematic buoyancy flux

$$\beta(x) = \int_{-B(x)}^{B(x)} \alpha(x) g \overline{u(x,y)T(x,y)} dy ,$$

$$= \int_{-B(x)}^{B(x)} \alpha(x) g \overline{u}(x,y)\ \overline{T}(x,y) dy + \int_{-B(x)}^{B(x)} \alpha(x) g \overline{u'T'} dy , \qquad (4.2.4)$$

so that the production of turbulent energy by the buoyancy forces is equal to the turbulent contribution to the buoyancy flux. Assuming that $\overline{u}(x,y)$ and $\overline{T}(x,y)$ are approximated by the Gaussian curves Eq. 4.1.3 and Eq. 5.1.3 respectively, and considering that for a plume

$$\overline{u}_M = \sigma_u \beta^{1/3} ,$$

(see Section 2.2) it is found that

$$\int_{-B(x)}^{B(x)} \frac{\alpha(x) g \overline{u}(x,y) \overline{T}(x,y)}{\beta} dy \sim \frac{\alpha g (x - x_{oT}) \overline{T}_M(x)}{\beta^{2/3}} , \qquad (4.2.5)$$

i.e., the non-dimensional number Eq. (4.1.5) can be regarded as the ratio of the kinematic buoyancy flux of the mean motion to the total kinematic buoyancy flux.

Further, assuming that the distribution of the turbulent energy flux is self-similar, it is possible to write

$$\overline{u'T'} = (\overline{u'T'})_M \, f(\tfrac{y}{x}) \ ,$$

where $(\overline{u'T'})_M$ the value of $\overline{u'T'}$ on the jet axis, so that

$$\int_{-B(x)}^{B(x)} \alpha(x) g \overline{u'T'} dy \sim \alpha g x (\overline{u'T'})_M \ .$$

For a plume, u(x,y,t) and T(x,y,t) are well correlated (see Section 6.2), so that it is possible to write

$$(\overline{u'T'})_M \sim \beta^{1/3} \sqrt{\overline{T'^2}} \ .$$

Using this result, it then becomes possible to write

$$\int_{-B(x)}^{B(x)} \frac{\alpha(x) g \overline{u'(x,y)T'(x,y)}}{\beta(x)} dy \sim \frac{\alpha(x) g (x-x_{oT}) \sqrt{\overline{T'^2}}}{\beta(x)^{2/3}} \ , \qquad (4.2.6)$$

where $\beta(x)$ is calculated by Eq. (4.1.6).

We can therefore conclude from Eqs. (4.2.5) and (4.2.6) that Eq. 4.2.4 can be rewritten as

$$A \frac{\alpha(x) g (x-x_{oT}) \overline{T}_M(x)}{\beta^{2/3}} + B \frac{\alpha(x) g (x-x_{oT}) \sqrt{\overline{T'^2}}}{\beta^{2/3}} = 1 \ ,$$

for some constants A and B. Furthermore, since the first term is constant in a turbulent plume (see Figure 4.1.9), it is apparent that the second term should also be constant.

The centerline turbulence intensity for many runs was scaled according to Eq. (4.2.6) and the results are plotted in Figure (4.2.3) versus the non-dimensional distance from exit X/D. Two important conclusions can be drawn. First the right-hand side of Eq. (4.2.6) is constant for a plume and it is approximately equal to 1.0, i.e.

$$\Sigma = \frac{\alpha(x) g (x-x_{oT}) \sqrt{\overline{T'^2}}}{\beta(x)^{2/3}} \approx 1.0 \quad . \tag{4.2.7}$$

Second, the turbulence intensity increases as the initial or local Richardson number increases, and tends asymptotically to the turbulence intensity of the plume. Combining (4.2.6) and (4.1.5) it is seen that for a plume

$$\frac{\sqrt{\overline{T'^2}}}{\overline{T}_M} \approx 0.42 \, . \tag{4.2.8}$$

The effect of the initial Reynolds number on the turbulence intensity (see for example Heskestad (5)), which should be relevant in the cases of $R_o << R_p$, was of second order in this investigation because the initial Reynolds number for all the experiments remained essentially constant. The centerline turbulence intensity is plotted again in Figure 4.2.4 where it is non-dimensionalized using the local centerline mean temperature $\overline{T}_M(x)$. Basic parameters and experimental results regarding the centerline turbulence intensity are given in Table 4.2.1; column 3 is the Grashof number, defined as $\beta x^3/\nu^3$, and column 10 is the non-dimensional ratio given by Eq. 4.2.7. The profile of turbulence intensity, as defined by Eq. (4.2.1) gives the gross picture of the

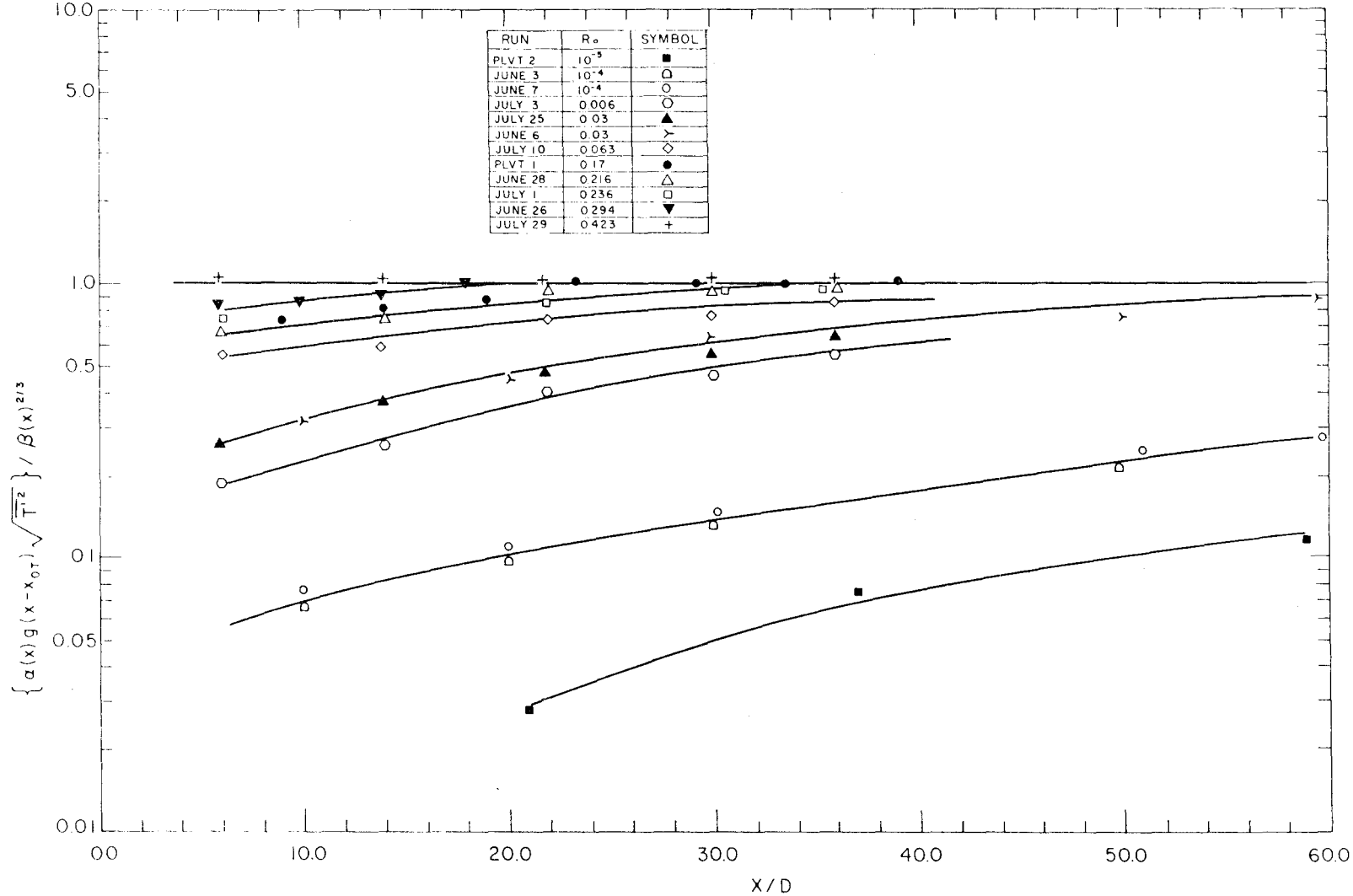

Figure 4.2.3. Intensity of turbulent fluctuations of temperature on jet axis as a function of non-dimensional distance from jet orifice and initial Richardson number.

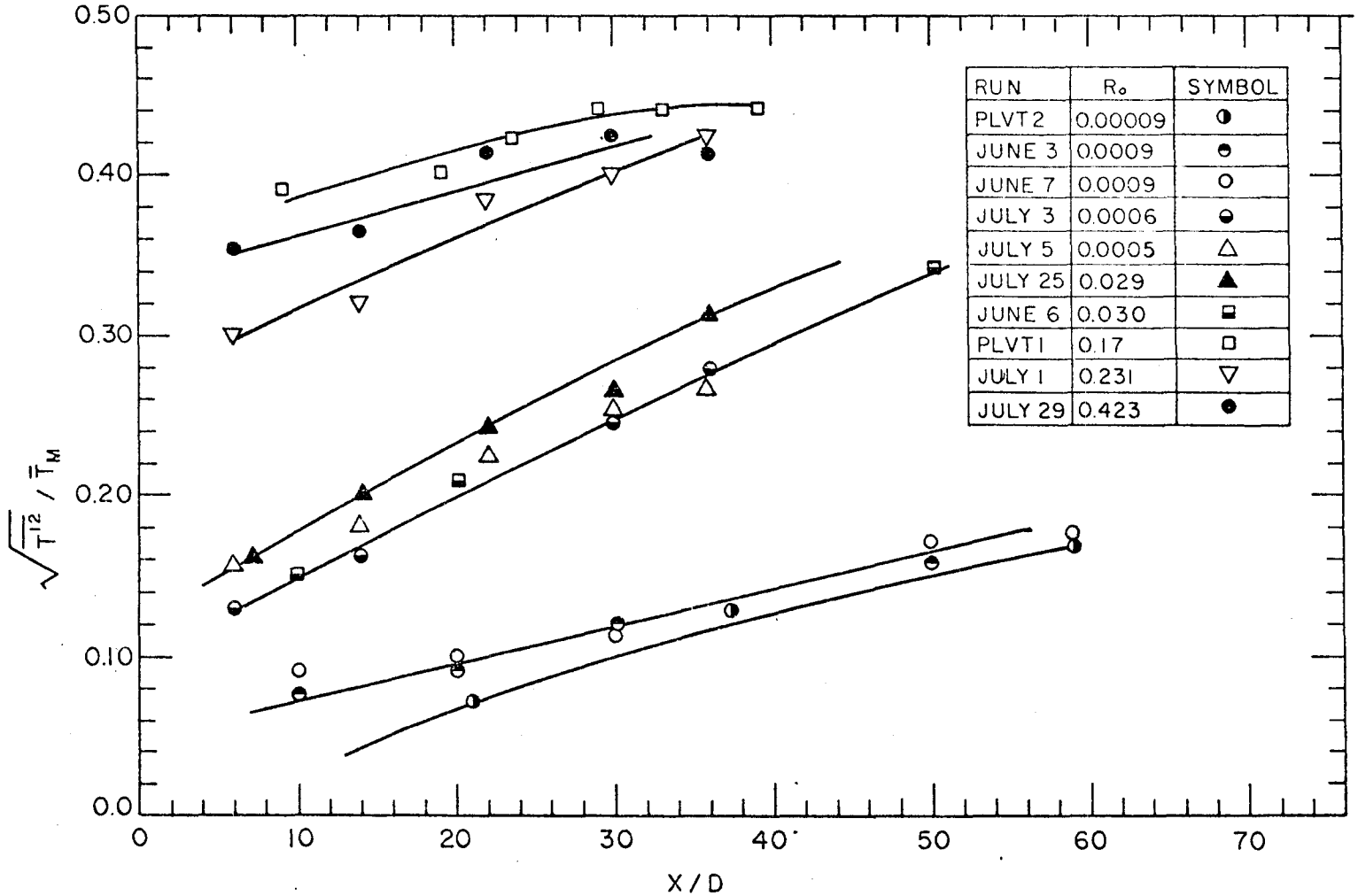

Figure 4.2.4. Intensity of turbulent fluctuations of temperature on jet axis normalized by the local mean temperature as a function of non-dimensional distance from jet orifice.

Run	R_o	G_r x 10^{10}	x cm	$\bar{T}_o$ °C	$\bar{T}_M$ °C	$\sqrt{\overline{T'^2}}$ °C	$\frac{\sqrt{\overline{T'^2}}}{\bar{T}_M}$	$\frac{\sqrt{\overline{T'^2}}}{\bar{T}_o}$	Σ
1	2	3	4	5	6	7	8	9	10
PLVT2-E	0.000051	0.184	5.000	3.300	1.750	0.130	0.074	0.039	0.028
PLVT2-Z	0.000089	1.787	8.900	5.400	2.020	0.260	0.129	0.048	0.075
PLVT2-H	0.000058	4.947	14.100	3.800	1.160	0.200	0.172	0.053	0.115
PLVT2-A	0.000123	41.670	22.500	6.850	1.800	0.340	0.189	0.050	0.220
JUNE-3	0.000209	1.337	5.000	11.200	7.190	0.560	0.079	0.050	0.068
JUNE-3	0.000909	8.732	10.000	11.200	5.150	0.480	0.093	0.043	0.057
JUNE-3	0.000909	26.013	15.000	11.200	4.000	0.480	0.120	0.043	0.135
JUNE-3	0.000909	108.903	25.000	11.200	3.100	0.490	0.158	0.044	0.215
JUNE-7	0.000940	0.404	5.000	6.600	4.250	0.382	0.090	0.058	0.077
JUNE-7	0.000940	2.878	10.000	6.600	3.200	0.320	0.100	0.048	0.110
JUNE-7	0.000940	9.324	15.200	6.600	2.500	0.290	0.116	0.044	0.142
JUNE-7	0.000940	40.560	25.500	6.600	1.800	0.315	0.175	0.048	0.245
JUNE-7	0.000940	65.576	30.000	6.600	1.740	0.300	0.172	0.045	0.271
PLVT3-B	0.001956	0.836	8.100	9.200	3.050	0.0	0.0	0.0	0.204
PLVT3-A	0.002242	15.059	22.500	10.400	1.780	0.630	0.354	0.061	0.683
JULY-3	0.005821	0.601	6.000	5.100	3.680	0.480	0.130	0.094	0.185
JULY-3	0.005821	6.660	14.000	5.100	2.430	0.395	0.163	0.077	0.260
JULY-3	0.005821	23.974	22.000	5.100	1.760	0.450	0.256	0.088	0.418
JULY-3	0.005821	61.835	30.400	5.100	1.560	0.380	0.244	0.075	0.462
JULY-3	0.005821	101.177	36.000	5.100	1.430	0.400	0.280	0.078	0.563
JULY-5	0.005001	0.482	6.000	4.500	3.000	0.480	0.160	0.107	0.191
JULY-5	0.005001	5.569	14.000	4.500	2.150	0.390	0.181	0.087	0.271
JULY-5	0.005001	20.212	22.000	4.500	1.560	0.350	0.224	0.078	0.346
JULY-5	0.005001	52.177	30.400	4.500	1.370	0.340	0.248	0.076	0.441
JULY-5	0.005001	86.890	36.200	4.500	1.250	0.330	0.264	0.073	0.499
JULY-25	0.029741	5.499	6.000	18.300	12.000	1.920	0.160	0.105	0.264
JULY-25	0.029741	45.905	14.000	18.300	7.250	1.450	0.200	0.079	0.376
JULY-25	0.029741	147.052	22.000	18.300	5.250	1.260	0.240	0.069	0.478
JULY-25	0.029741	334.140	30.000	18.300	4.150	1.100	0.265	0.060	0.549
JULY-25	0.029741	543.131	36.000	18.300	3.550	1.120	0.315	0.061	0.658
JUNE-6	0.030897	1.306	5.000	23.500	12.700	1.900	0.150	0.081	0.320
JUNE-6	0.030897	6.584	10.000	23.500	7.800	1.630	0.209	0.069	0.460
JUNE-6	0.030897	17.519	15.000	23.500	5.500	1.650	0.300	0.070	0.648
JUNE-6	0.030897	66.983	25.000	23.500	3.750	1.280	0.341	0.054	0.787
JUNE-6	0.030897	111.267	30.000	23.500	3.400	1.200	0.353	0.051	0.872
JULY-10	0.062853	1.815	6.000	15.100	8.300	2.280	0.275	0.151	0.540
JULY-10	0.062853	17.166	14.000	15.100	5.250	1.360	0.259	0.090	0.582
JULY-10	0.062853	55.333	22.000	15.100	3.450	1.230	0.357	0.081	0.754
JULY-10	0.062853	139.179	30.400	15.100	3.000	0.910	0.303	0.060	0.740
JULY-10	0.062853	227.688	36.200	15.100	2.500	0.910	0.364	0.060	0.862
PLVT1-E	0.177563	1.403	9.000	11.500	3.870	1.500	0.388	0.130	0.771
PLVT1-D	0.178073	5.017	14.000	11.550	3.250	1.100	0.338	0.095	0.813
PLVT1-Z	0.169943	11.129	19.000	11.000	2.200	0.890	0.405	0.081	0.883
PLVT1-C	0.167897	20.412	23.500	10.900	2.000	0.850	0.425	0.078	1.027
PLVT1-K	0.176845	40.730	28.500	11.150	1.530	0.680	0.444	0.061	0.984
PLVT1-B	0.169943	56.004	33.600	11.000	1.350	0.600	0.444	0.055	0.997
PLVT1-H	0.181841	100.740	39.100	11.400	1.220	0.540	0.443	0.047	1.022
JUNE-28	0.216254	1.752	6.000	20.900	9.600	2.950	0.307	0.141	0.688
JUNE-28	0.216254	15.110	14.000	20.900	5.600	1.700	0.304	0.081	0.735
JUNE-28	0.216254	47.054	22.000	20.900	3.500	1.480	0.423	0.071	0.925
JUNE-28	0.216254	111.546	30.200	20.900	2.700	1.130	0.419	0.054	0.932
JUNE-28	0.216254	183.772	36.200	20.900	2.300	1.000	0.435	0.048	0.971
JULY-1	0.231431	1.997	6.000	21.850	10.200	3.060	0.300	0.140	0.717
JULY-1	0.231431	16.450	14.000	21.850	5.650	1.810	0.320	0.083	0.774
JULY-1	0.231431	52.175	22.000	21.850	3.700	1.420	0.384	0.065	0.876
JULY-1	0.231431	124.964	30.400	21.850	2.800	1.120	0.400	0.051	0.914
JULY-1	0.231431	205.324	36.400	21.850	2.400	1.020	0.425	0.047	0.978
JUNE-26	0.294518	30.837	12.000	21.900	8.500	2.890	0.340	0.132	0.811
JUNE-26	0.294518	114.249	20.000	21.900	6.250	2.250	0.360	0.103	0.864
JUNE-26	0.294518	269.629	28.000	21.900	4.800	1.800	0.375	0.082	0.875
JUNE-26	0.294518	537.451	36.000	21.900	4.200	1.680	0.400	0.077	0.991
JULY-29	0.423977	1.664	6.000	21.700	9.000	3.200	0.356	0.147	1.082
JULY-29	0.423977	14.165	14.000	21.700	4.650	1.700	0.366	0.076	0.979
JULY-29	0.423977	47.241	22.000	21.700	3.120	1.300	0.417	0.060	1.057
JULY-29	0.423977	110.170	30.000	21.700	2.300	0.980	0.426	0.045	1.029
JULY-29	0.423977	185.703	36.000	21.700	2.060	0.850	0.413	0.039	1.045

Table 4.2.1. Tabulated experimental values for the intensity of turbulent fluctuations of temperature along jet axis for turbulent jets and plumes.

phenomenon but there is a lot of additional information which is important and should be considered when intermittent flows are investigated. Specifically the turbulence intensity $\overline{T'^2}$ can be analyzed as the sum of two terms as follows

$$\overline{T'^2} = \lim_{t'\to\infty} \frac{1}{t'} \int_o^{t'} [T(x,y,t) - \overline{T}(x,y)]^2 dt ,$$

$$= \lim_{t'\to\infty} \frac{1}{t'} \int_o^{t'} [T(x,y,t) - \overline{T}(x,y)]^2 [1 - I(x,y,t)] dt ,$$

$$+ \lim_{t'\to\infty} \frac{1}{t'} \int_o^{t'} [T(x,y,t) - \overline{T}(x,y)]^2 \, I(x,y,t) dt , \qquad (4.2.9)$$

where

$$\overline{T}(x,y) = \lim_{t'\to\infty} \frac{1}{t'} \int_o^{t'} T(x,y,t) dt , \qquad (4.2.10)$$

and

$$I(x,y,t) = \begin{cases} 1 \text{ if } T(x,y,t) > T_a + 0.05°C, \\ 0 \text{ otherwise.} \end{cases}$$

Hence $\overline{T'^2} = \overline{T'^2_{cold}} + \overline{T'^2_{hot}}$,

where

$$\overline{T'^2_{cold}} = \lim_{t'\to\infty} \frac{1}{t'} \int_o^{t'} [T(x,y,t) - \overline{T}(x,y)]^2 [1 - I(x,y,t)] dt , \qquad (4.2.11)$$

and

$$\overline{T'^2_{hot}} = \lim_{t'\to\infty} \frac{1}{t'} \int_o^{t'} [T(x,y,t) - \overline{T}(x,y)]^2 \, I(x,y,t)dt \, . \qquad (4.2.12)$$

Clearly, if $I(x,y,t) = 1$ for all the time t (which means $\gamma(x,y) = 1$) then $\overline{T'^2_{cold}} = 0$ and $\overline{T'^2} = \overline{T'^2_{hot}}$. If $I(x,y,t) = 0$ for all the time t (which means the temperature probe is always in the cold ambient water) then

$$\overline{T'^2_{hot}} = \overline{T'^2_{cold}} = \overline{T'^2} = 0 \, .$$

Figure 4.2.5 (where an intermittent temperature signal is sketched) can be used to clarify the physical meaning of each of the two components $\overline{T'^2_{cold}}$ and $\overline{T'^2_{hot}}$. The turbulence intensity (see Eq. 4.2.1) is the moment of the whole signal $T(x,y,t)$ (the continuous and the dotted line) with respect to the mean temperature $\overline{T}(x,y)$ (defined by Eq. 4.2.10). $\overline{T'^2_{hot}}(x,y)$ is the moment of the continuous line with respect to the mean $\overline{T}(x,y)$ (again defined by Eq. 4.2.10) and the $\overline{T'^2_{cold}}$ is the moment of the dotted line with respect the mean $\overline{T}(x,y)$ (again defined by Eq. 4.2.10). Hence the term $\overline{T'^2_{cold}}$ can be considered as an apparent turbulence intensity generated by the intermittency, i.e., by cold bursts or puffs. The presence of the term $\overline{T'^2_{cold}}$ does not necessarily imply turbulence (it can even exist in the case of an unstable laminar jet). An intrinsic look at the profile of turbulence intensity can be obtained from Figures 4.2.6 (~ pure jet) and 4.2.7 (~ plume) where $\overline{T'^2}$, $\overline{T'^2_{cold}}$, $\overline{T'^2_{hot}}$ are plotted, and from which some interesting conclusions can be drawn. The two peaks in the profile of the turbulence intensity $\overline{T'^2}$ of a pure

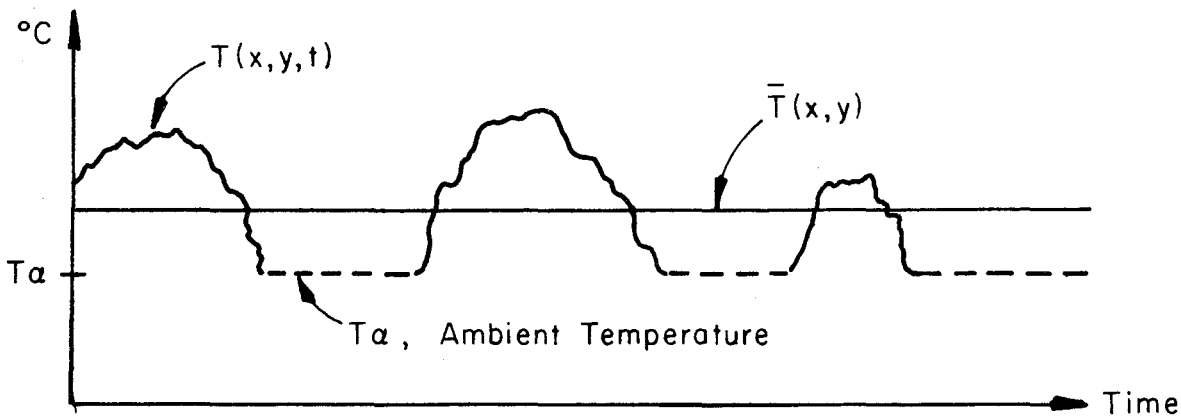

Figure 4.2.5. Sketch of an intermittent temperature signal.

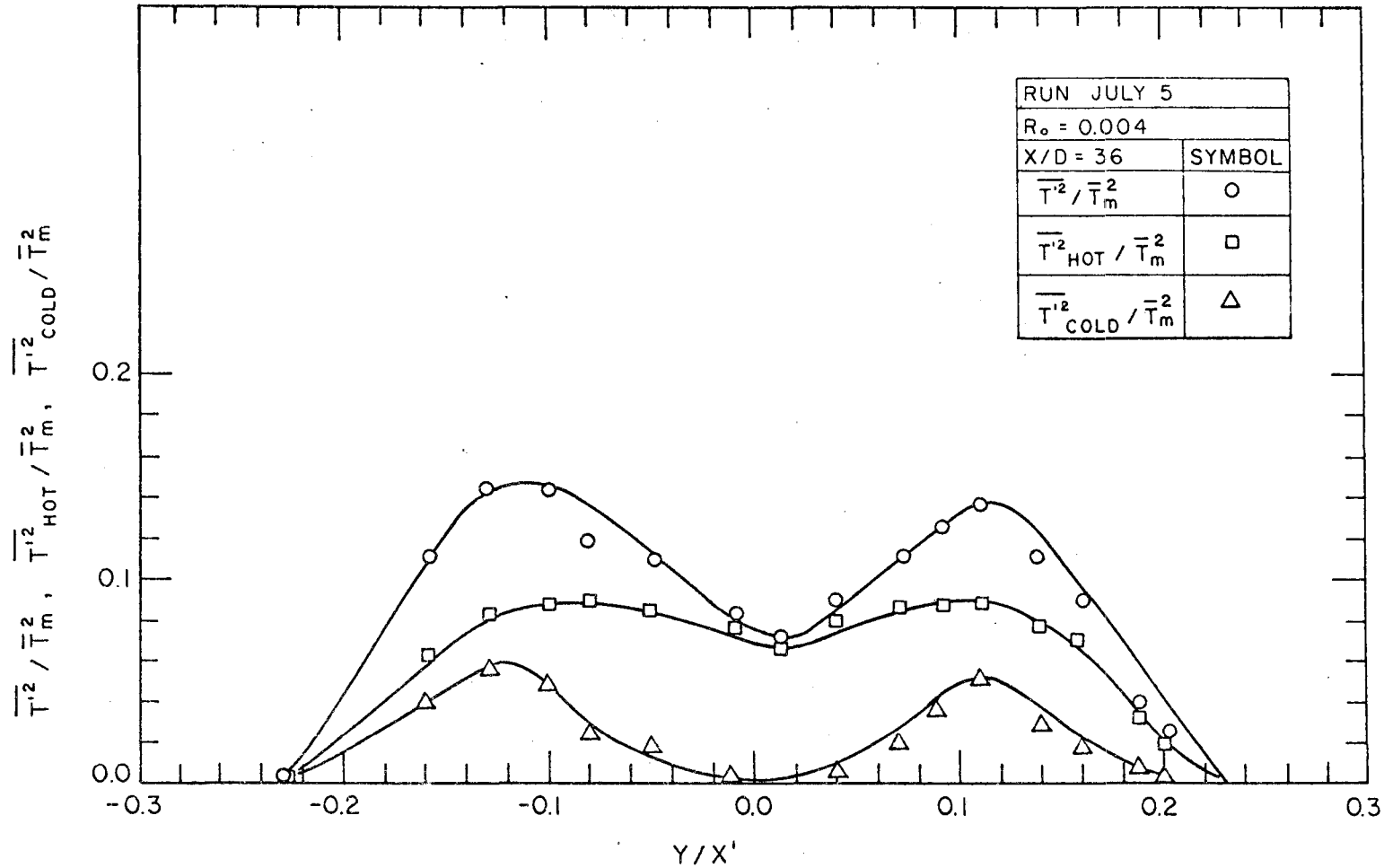

Figure 4.2.6. Profiles of turbulence intensities $\overline{T'^2}$, $\overline{T'^2}_{hot}$, $\overline{T'^2}_{cold}$ for a turbulent jet.

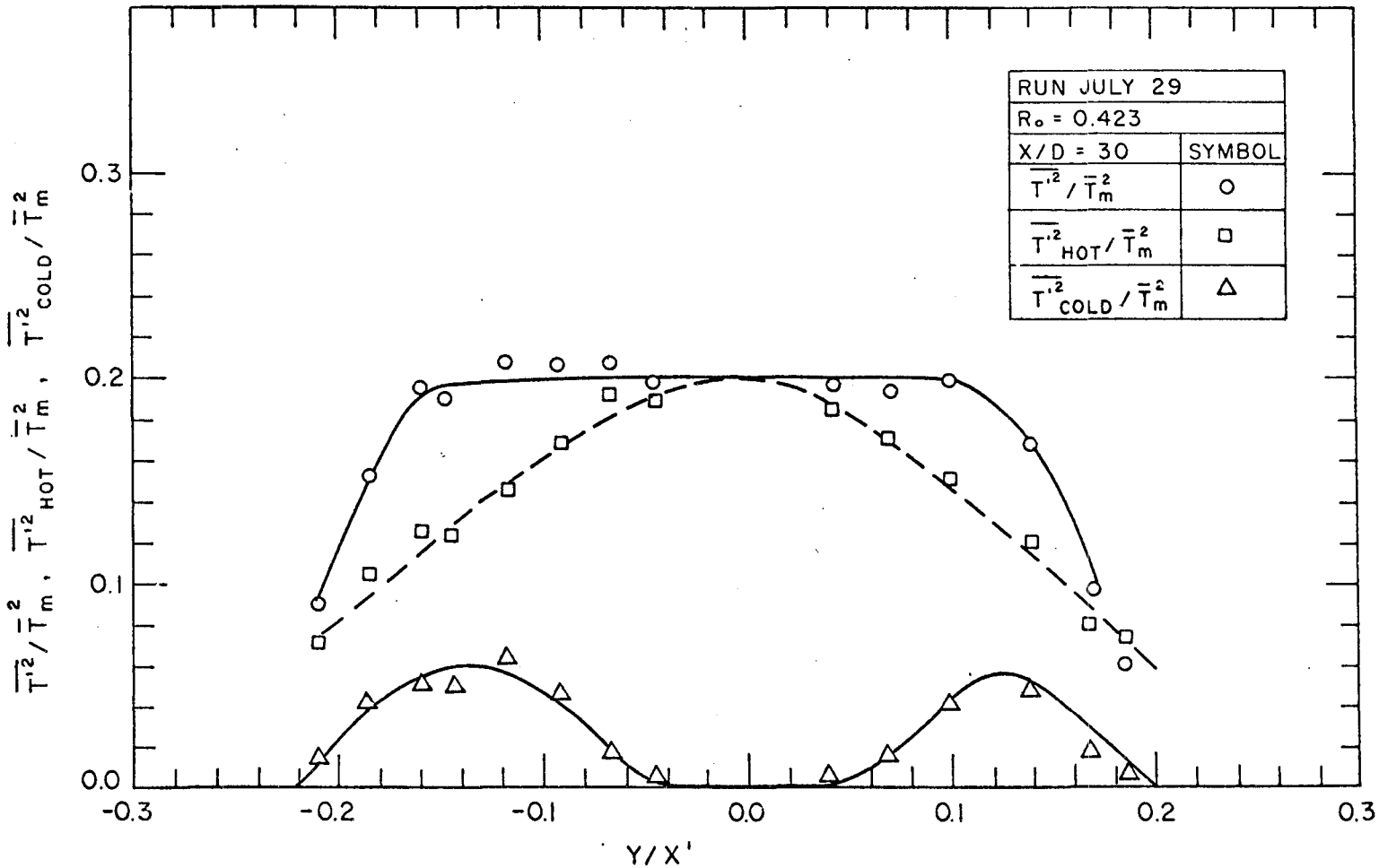

Figure 4.2.7. Profiles of turbulence intensities $\overline{T'^2}$, $\overline{T'^2_{hot}}$, and $\overline{T'^2_{cold}}$ for a turbulent plume.

jet (Figure 4.2.6) are mainly generated by the large cold bursts (which may be irrotational), i.e., by $\overline{T'^2_{cold}}$. The Reynolds equations and the energy equation, where all phase information is lost by averaging, cannot be used to predict $\overline{T'^2_{cold}}$. It was found previously (Section 2.2, or Figure 4.2.3) that the normalized turbulent intensity $\sqrt{\overline{T'^2}}/\overline{T}_M$ is greater for a plume than for a jet due to the action of buoyancy forces. Since $\overline{T'^2}$ was analyzed into two components $\overline{T'^2_{hot}}$ (hot vortices) and $\overline{T'^2_{cold}}$ (cold bursts) the question is which component in particular the buoyancy forces feed. The answer to this question can be obtained from Figures 4.2.6 and 4.2.7 from where it can be observed that the non-dimensional profile $\overline{T'^2_{cold}}/\overline{T}^2_M$ (apparent intensity due to cold bursts) is almost the same in magnitude and shape for both jet and plume. However, the profile $\overline{T'^2_{hot}}$ is much bigger for the plume. It can be observed also that on the jet axis

$$\overline{T'^2_{cold}} \approx 0, \qquad \overline{T'^2} \approx \overline{T'^2_{hot}} ,$$

for both jet and plume and that

$$\left(\frac{\overline{T'^2}}{\overline{T}^2_M}\right)_{plume} > \left(\frac{\overline{T'^2}}{\overline{T}^2_M}\right)_{jet} .$$

Hence it seems that the buoyancy forces intensify the $\overline{T'^2_{hot}}$ term, i.e., they feed mainly the hot vortices.

4.3 CROSS-SECTIONAL PROFILE OF MAXIMUM AND MINIMUM TEMPERATURE

The maximum and minimum temperature occurring at a given point (x,y)

during a sampling time, and made non-dimensional using the mean centerline temperature $\overline{T}_M(x)$, are plotted in Figures 4.3.1 and 4.3.2 for the two typical cases of $R_o \approx 0.005$ (jet) and $R_o \approx 0.4$ (plume). The boundaries of the jet can be defined as the distance y/x' at which the profile of maximum recorded temperature drops abruptly to zero, i.e., the equation

$$y = \pm B(x) \approx \pm\ 0.25\ (x - x_{oT})\ ,$$

can be considered as defining the boundaries of the jet (Figure 4.3.1). For the same experiment the equation of half-width of temperature profile is given by $y = \pm 0.121\ (x - x_{oT})$ and the equation of standard deviation by $y = \pm 0.103\ (x - x_{oT})$. Hence the boundary as defined by the maximum temperature profile is approximately at 2.4 standard deviations from the axis. The centerline maximum and minimum temperatures are plotted in the Figure 4.3.3 for many initial Richardson numbers. The conclusion from Figure 4.3.3 is that the non-dimensional centerline maximum temperature Max $T_M/\overline{T}_M$ and the non-dimensional centerline minimum temperature Min $T_M/\overline{T}_M$ depend on the Richardson number, R. Specifically Max $T_M/\overline{T}_M$ increases with R and tends to an asymptotic value equal to 2.5 for $R \approx R_p$ while Min $T_M/\overline{T}_M$ decreases with increasing R and becomes zero for $R \approx R_p$. This is consistent with the results of Section 4.2, i.e., that the turbulence intensity increases with R. The interesting result Min $T_M/\overline{T}_M = 0$ for a plume implies that the intermittency of the temperature at the center of the plume is not one, and cold ambient water can reach the axis of the plume.

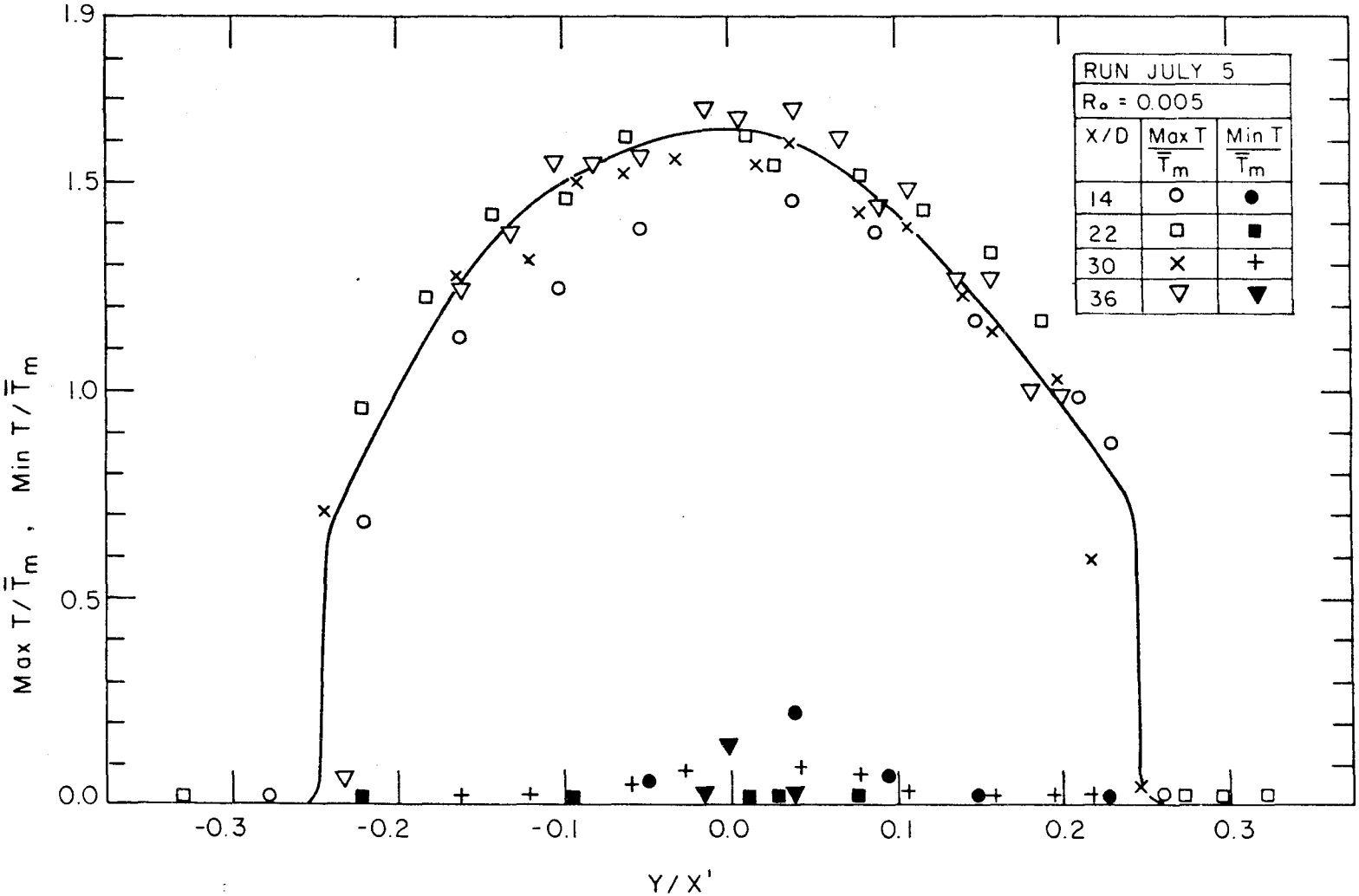

Figure 4.3.1. Maximum and minimum temperature for a turbulent jet as a function of distance from jet axis.

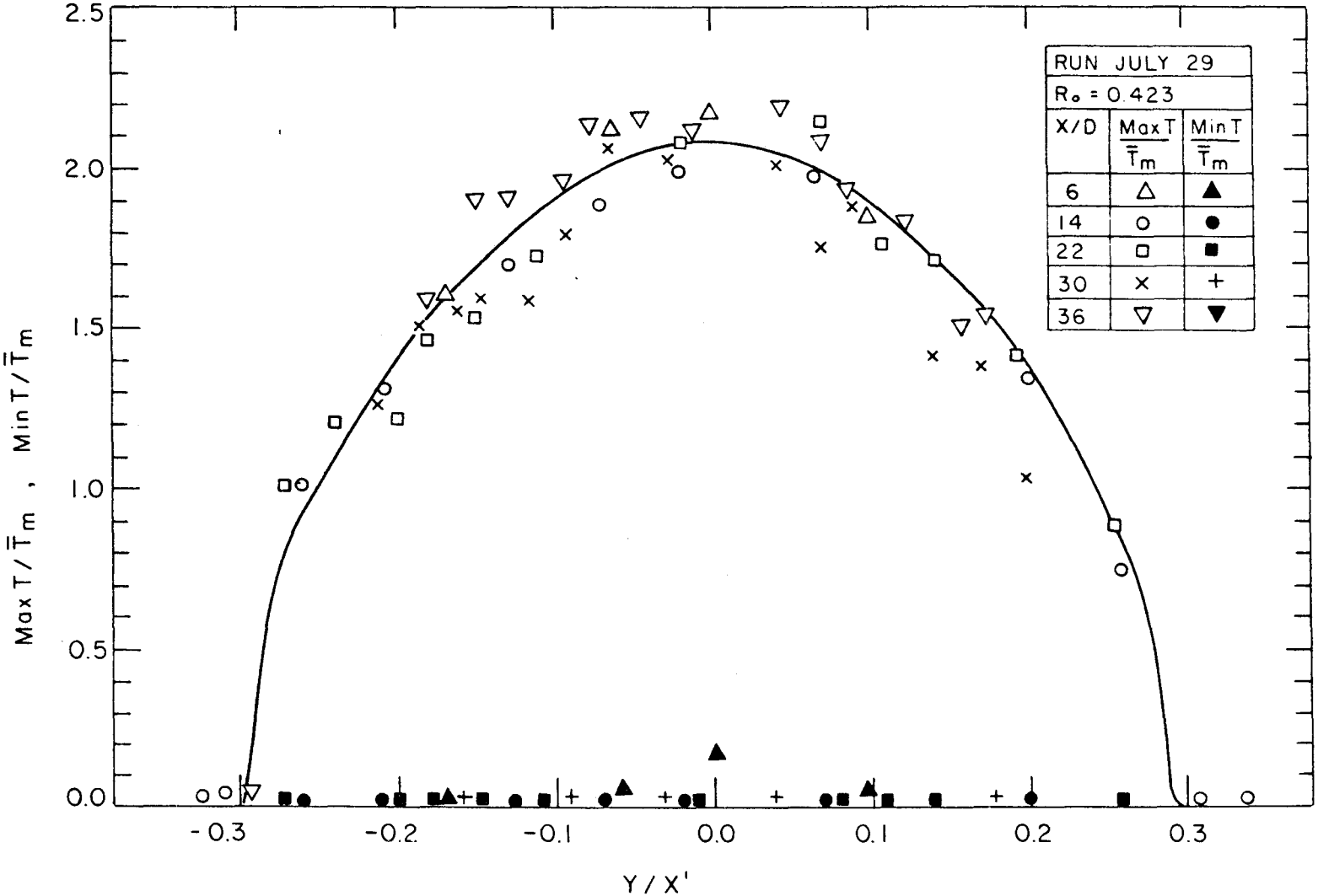

Figure 4.3.2. Maximum and minimum temperature for a turbulent plume as a function of distance from plume axis.

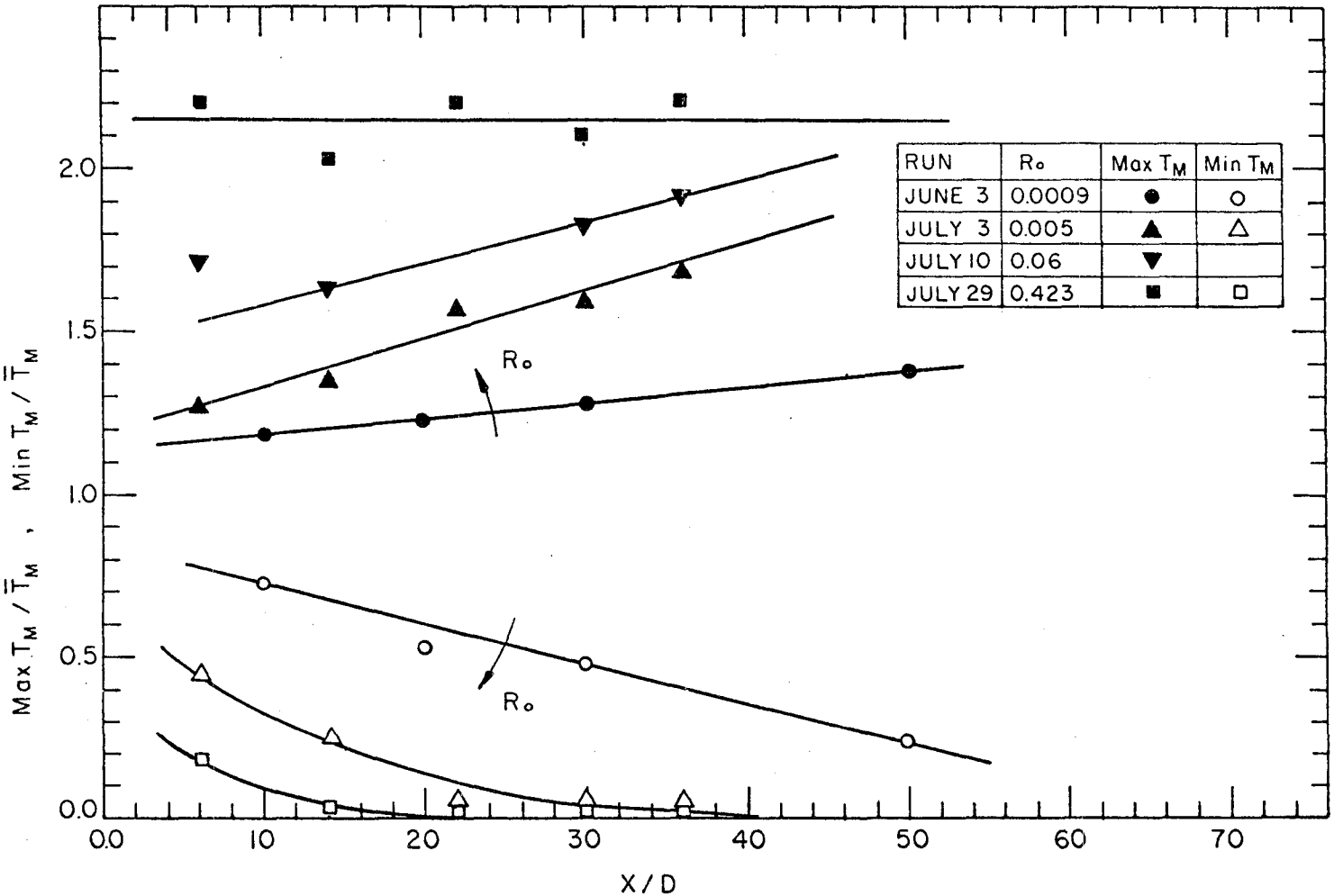

Figure 4.3.3: Distribution of maximum and minimum temperature along jet axis as a function of initial Richardson number.

4.4 INTERMITTENCY

The intermittency γ of the temperature was defined as

$$\gamma(x,y) = \lim_{t'\to\infty} \frac{1}{t'} \int_0^{t'} I(x,y,t)dt \ ,$$

where

$$I(x,y,t) = \begin{cases} 1 \text{ if } T(x,y,t) - T_a > 0.05°C \ , \\ 0 \text{ otherwise} \ , \end{cases}$$

where T_a is the ambient temperature. The intermittency profile is plotted in Figure 4.4.1 for an almost pure jet and in Figure 4.4.2 for an almost pure plume. The intermittency at the center of the plume-like buoyant jet was found to be of the order 0.985 to 0.999, which is consistent with the profile of minimum recorded temperatures (Figure 4.3.2). An interesting conclusion for an almost pure jet (Figure 4.4.1) is that the intermittency at a given y/x' location, where $x' = x - x_{oT}$, depends on the distance x from the exit. There is no previous experimental investigation of the intermittency profile of temperature with which to compare the above results, but there is an experimental investigation of the intermittency profile of velocity by Hanum [40]. By replotting his Figure 2 in new coordinates, (γ versus y/x), it can be seen that the same pattern is revealed, i.e., at a given location y/x the intermittency decreases with increasing x, (see Figure 4.4.3). Hanum [40, or 61] did not report the location of the virtual origin x_o in his experiments so it has been arbitrarily chosen as zero. From his replotted results (Figure 4.4.3) it can be obtained that $\gamma(x,y) \approx 0.6$

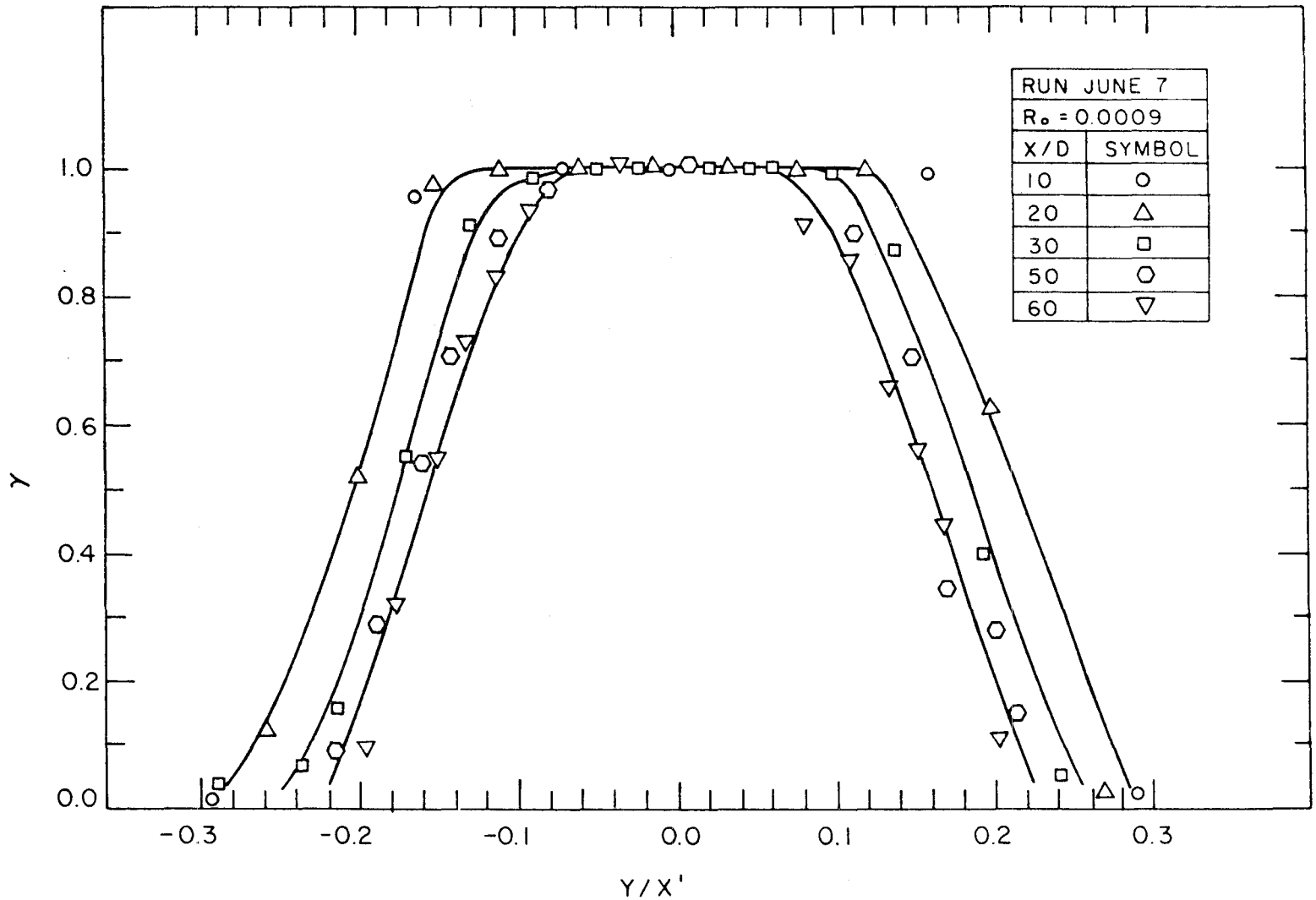

Figure 4.4.1. Temperature intermittency for a turbulent jet plotted against non-dimensional distance from jet axis.

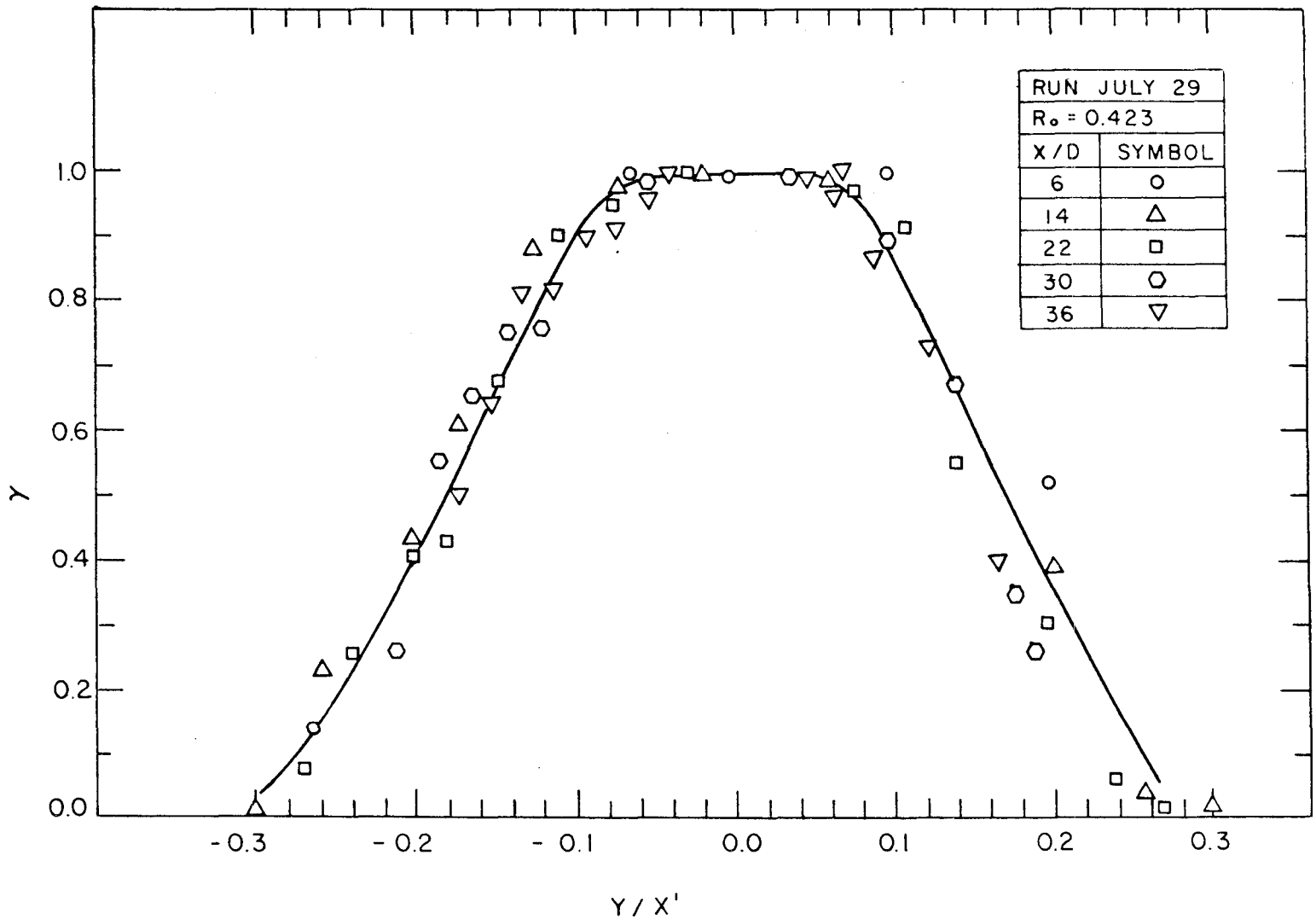

Figure 4.4.2. Temperature intermittency for a turbulent plume plotted against non-dimensional distance from plume axis.

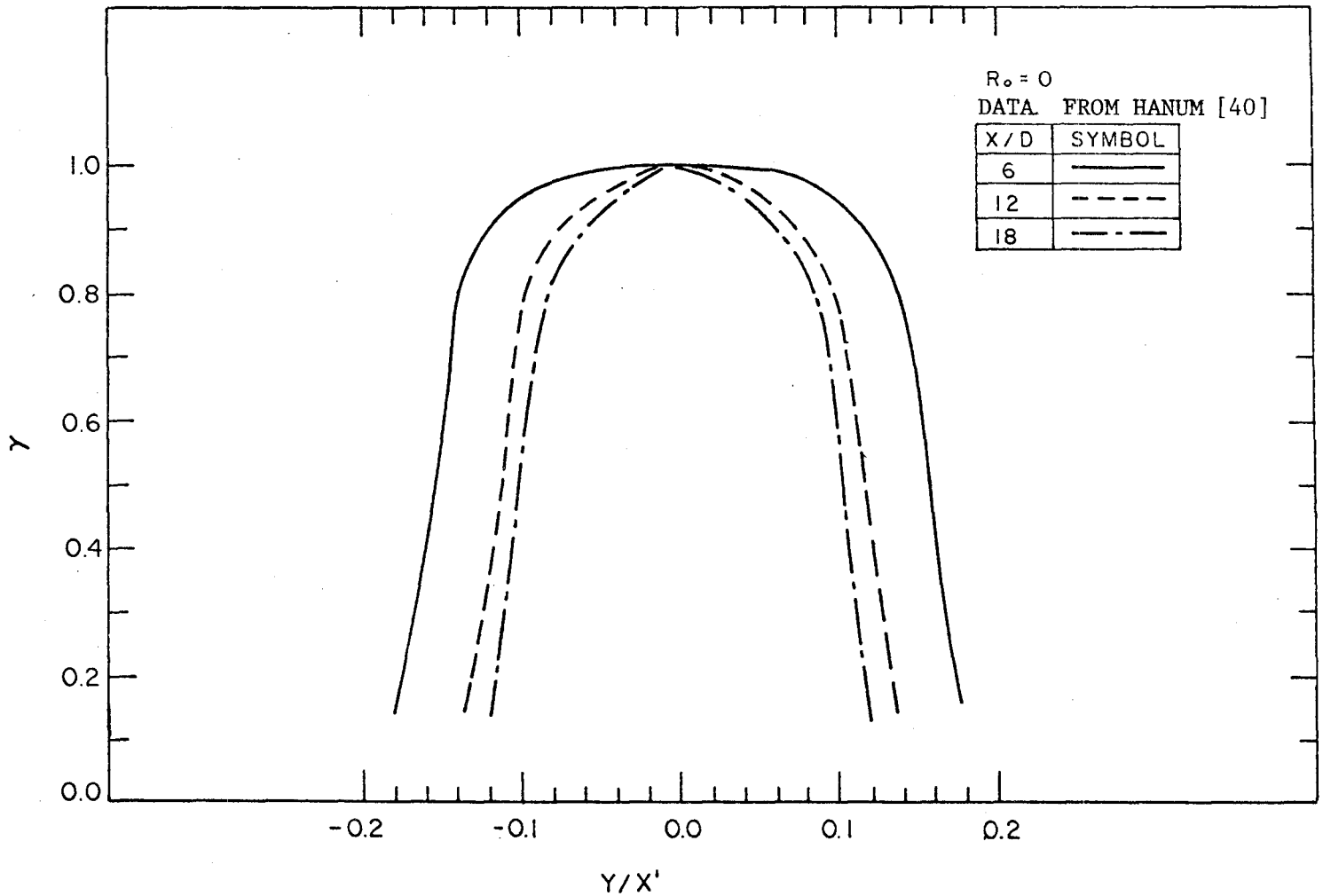

Figure 4.4.3. Profile of the velocity intermittency for a turbulent jet (based on data by Hanum [40]).

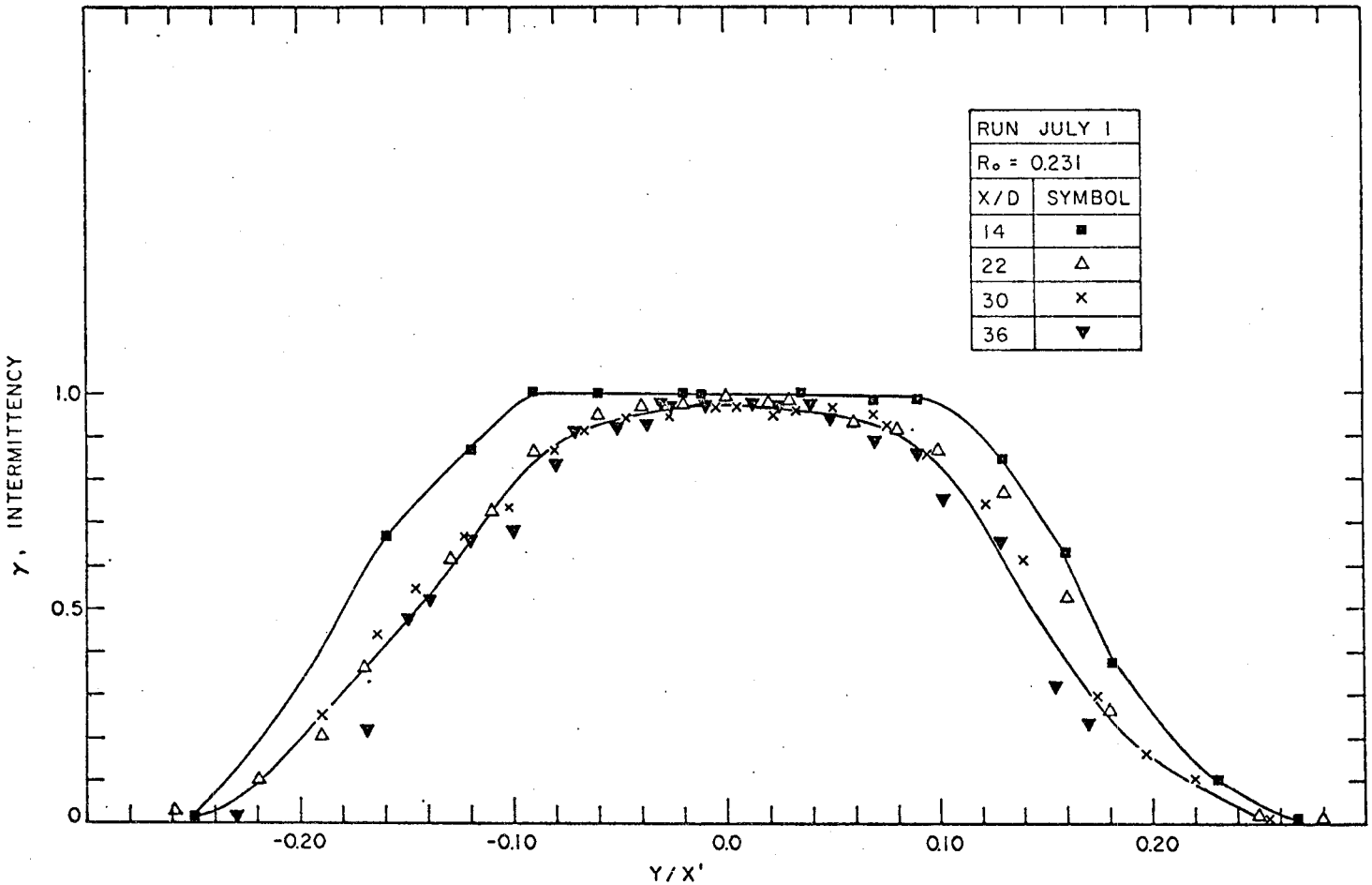

Figure 4.4.4. Temperature intermittency for a turbulent plume plotted against non-dimensional distance from plume axis.

at y/x = 0.10 at x/D = 18, which seems too low compared with the temperature intermittency results of this investigation or with the results of velocity intermittency of Heskestad [5], who reported only one intermittency profile at x/D = 102 and who found $\gamma(x,y) \approx 0.92$ at $y/x' = 0.10$. The temperature (or concentration) intermittency γ_H can be measured more precisely than the velocity intermittency γ_u (where the vorticity should be detected to distinguish the turbulent from the irrotational fluid).

4.5 FREQUENCY OF CROSSING OF THE HOT/COLD INTERFACE

The frequency of interface crossing f_R in Hz is given by

$$f_R = \frac{\sum_{i=1}^{N} M(x,y,t_i)}{2(t_N - t_1)} \quad ,$$

where

$$M(x,y,t_i) = \begin{cases} 0 & \text{if } [I(x,y,t_i) + I(x,y,t_{i+1})] = 0 \text{ or } 2 \quad , \\ 1 & \text{if } [I(x,y,t_i) + I(x,y,t_{i+1})] = 1 \quad , \end{cases}$$

(see Figure 3.5.1) was plotted in Figure 4.5.1 for the case of an almost pure plume, and in Figures 4.5.2, 4.5.3 for the case of an

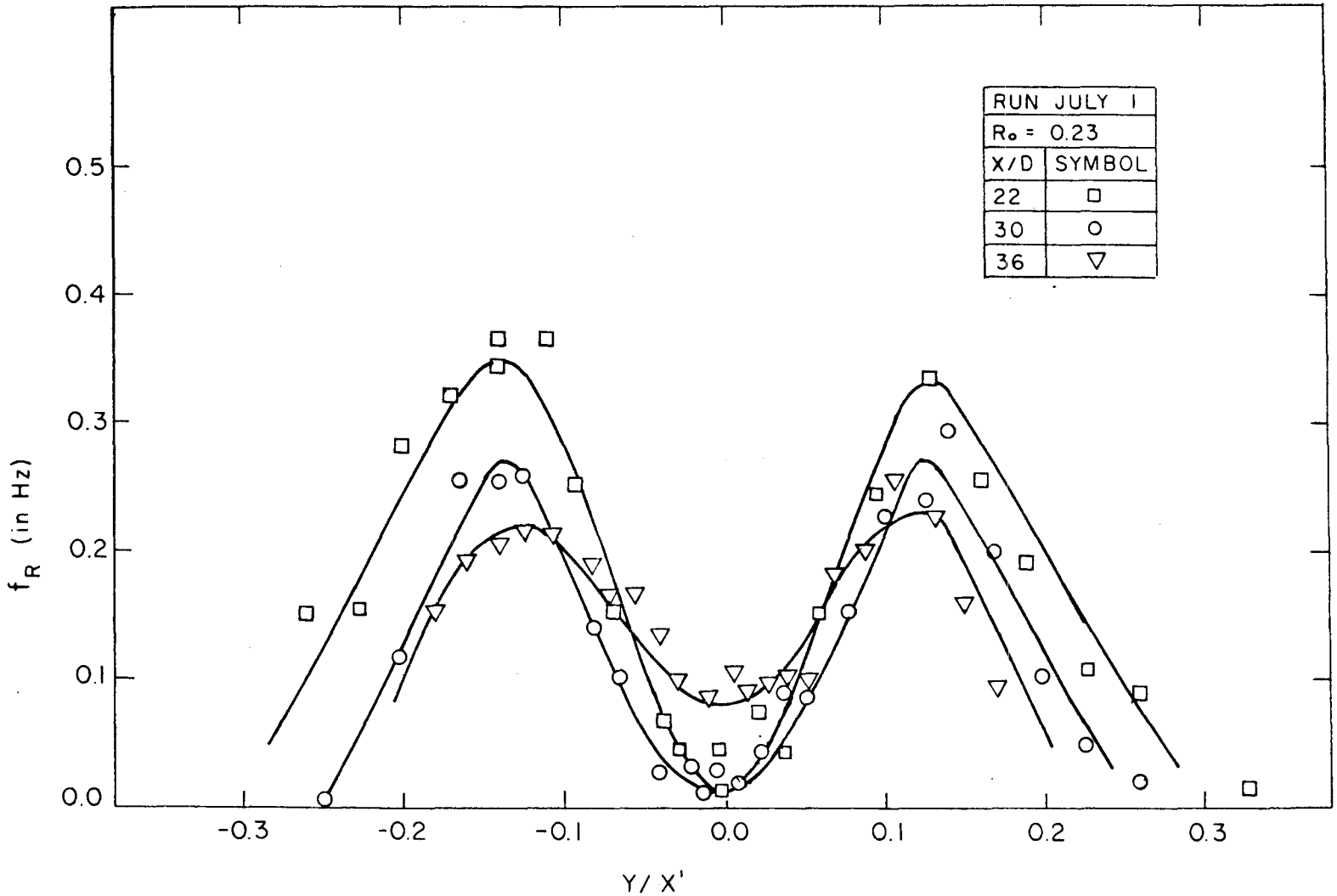

Figure 4.5.1. Profile of frequency of hot/cold, cold/hot interface crossing for a turbulent plume.

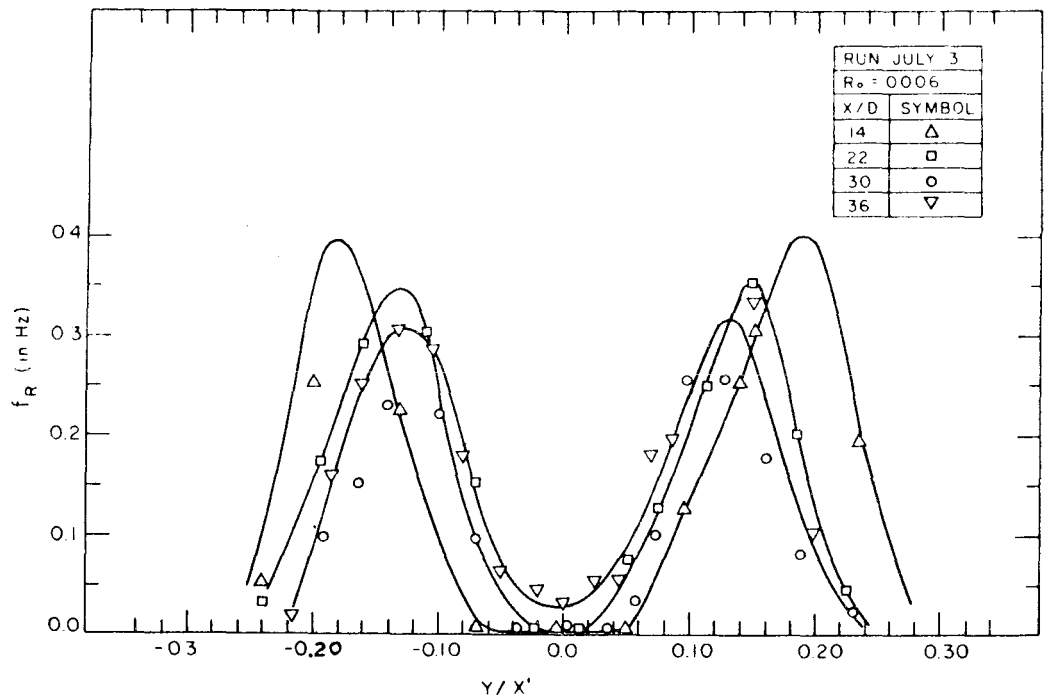

Figure 4.5.2. Profile of frequency of hot/cold, cold/hot interface crossing for a turbulent jet.

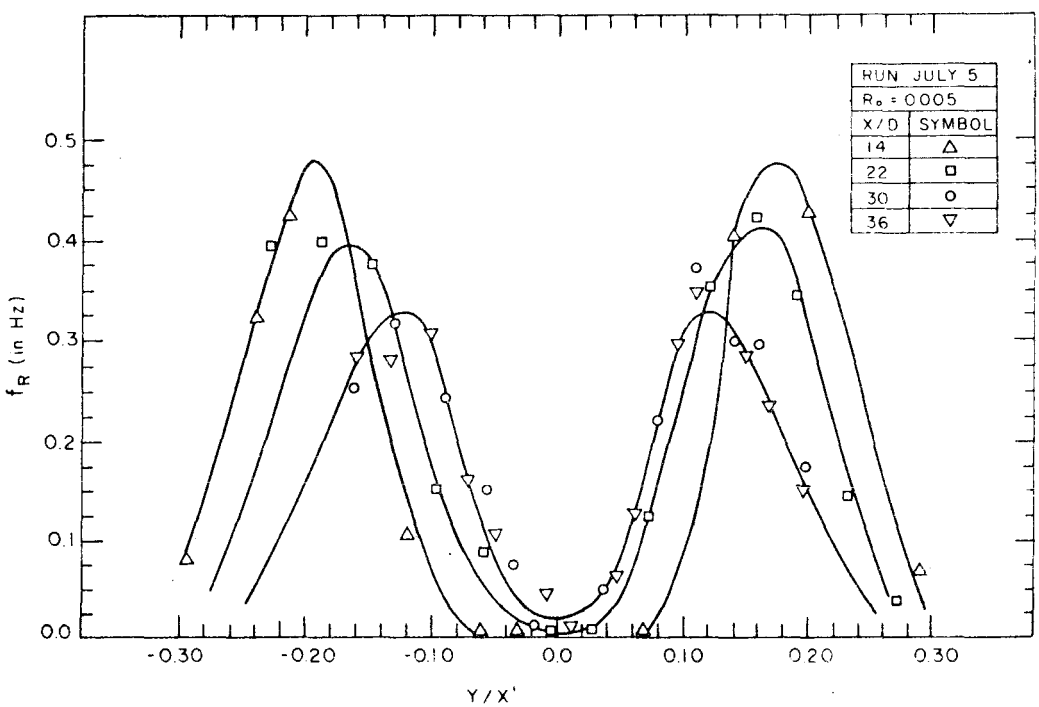

Figure 4.5.3. Profile of frequency of hot/cold, cold/hot interface crossing for a turbulent jet.

almost pure jet. The same general structure was revealed in all experiments performed.

It should be noted that the nature of these measurements relies essentially on the formation of the test function I(x,y,t) (see Eq. 2.0.1) which depends on the threshold level T_L, i.e.,

$$I(x,y,t) = \begin{cases} 1 \text{ if } T(x,y,t) > T_L \ , \\ 0 \text{ otherwise} \ . \end{cases}$$

In this investigation $T_L \approx T_a + 0.05°C$. The absolute value of the f_R depends on the value of the threshold level chosen (T_L), but a systematic investigation of this dependence was not made. The important point is that keeping T_L constant for a particular experiment resulted in the same structure being revealed. A feeling of the reproducibility and of the effect of the threshold T_L can be obtained from Figures 4.5.2 and 4.5.3 which represent the results from two experiments with almost identical initial Richardson and Reynolds number, but with slightly different thresholds, i.e., $T_L = T_a + 0.04°C$, for experiment "July 3" (Figure 4.5.2), and $T_L = T_a + 0.07°C$, for experiment "July 5" (Figure 4.5.3). As should be expected, the level $T_L = T_a + 0.04°C$ gives slightly lower values than the level $T_L = T_a + 0.07°C$. The peak frequency can be used to form a Strouhal number based on the half-width and on the exit velocity and it is plotted in Figure 4.5.4 where some results by Bradbury [2] are also plotted. From the intermittency and the frequency of interface crossing the average duration of a hot burst at a point (x,y) (time between two successive cold/hot, hot/cold interface crossings) can be found.

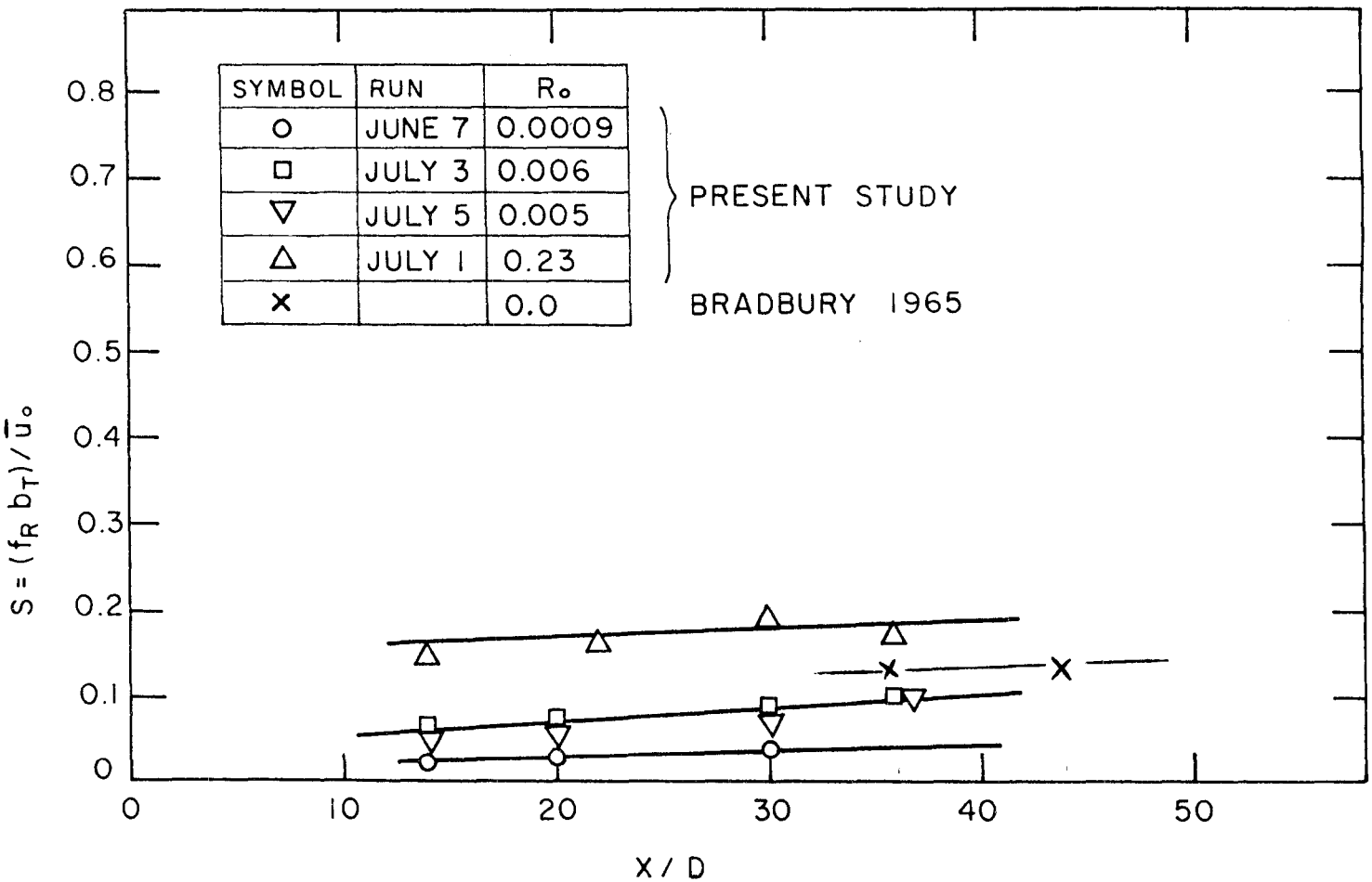

Figure 4.5.4. The Strouhal number, based on the peak frequency of hot/cold, cold/hot interface crossing profile against distance from jet orifice.

$$\frac{\gamma(x,y)}{f_R(x,y)} \quad \text{(in seconds)}$$

and is plotted in Figure 4.5.5 and 4.5.6.

4.6 THE FREQUENCY DISTRIBUTION OF TEMPERATURE

The frequency distribution of the conditionally sampled instantaneous temperature is plotted in Figure 4.6.1.a-d for four typical positions across the jet. It is clear that the turbulence is not homogeneous (because the shape of the frequency distribution depends on the non-dimensional position y/x'). The intermittency $\gamma(x,y)$ is defined (see Section 4.4) as the fraction of the time for which the temperature of the flow is above some level T_L (where T_L is close to zero, i.e. $T_L \approx 0.05 - 0.10°C$). Hence $1 - \gamma(x,y)$ is the fraction of the time for which the temperature of the flow is below the level T_L. Now, the peak located near zero temperature (see Figures 4.6.1.b-d) is due to the intermittency of the flow. Since the whole area under the frequency distribution is unity, the area of the peak around zero temperature is approximately $1 - \gamma(x,y)$.

4.7 SKEWNESS AND FLATNESS FACTOR FOR THE TEMPERATURE DISTRIBUTION

The skewness factor, defined as

$$\overline{T'^3}/(\overline{T'^2})^{3/2} ,$$

is plotted in Figure 4.7.1, and the flatness factor defined as

$$\overline{T'^4}/(\overline{T'^2})^2 ,$$

is plotted in Figure 4.7.2.

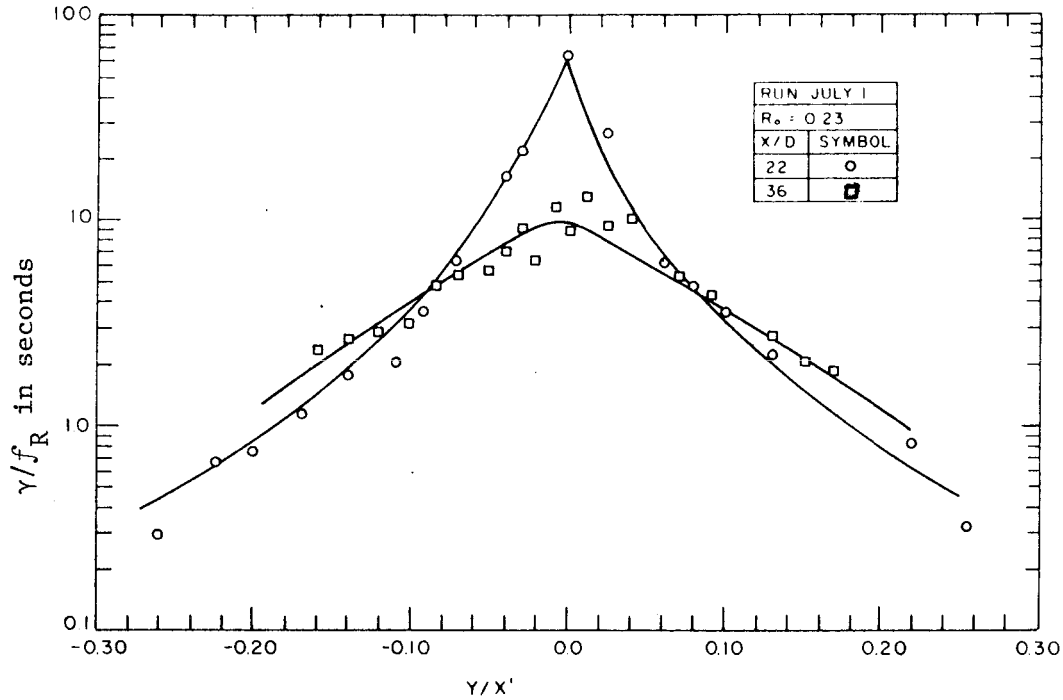

Figure 4.5.5. Average duration of hot bursts in a turbulent plume.

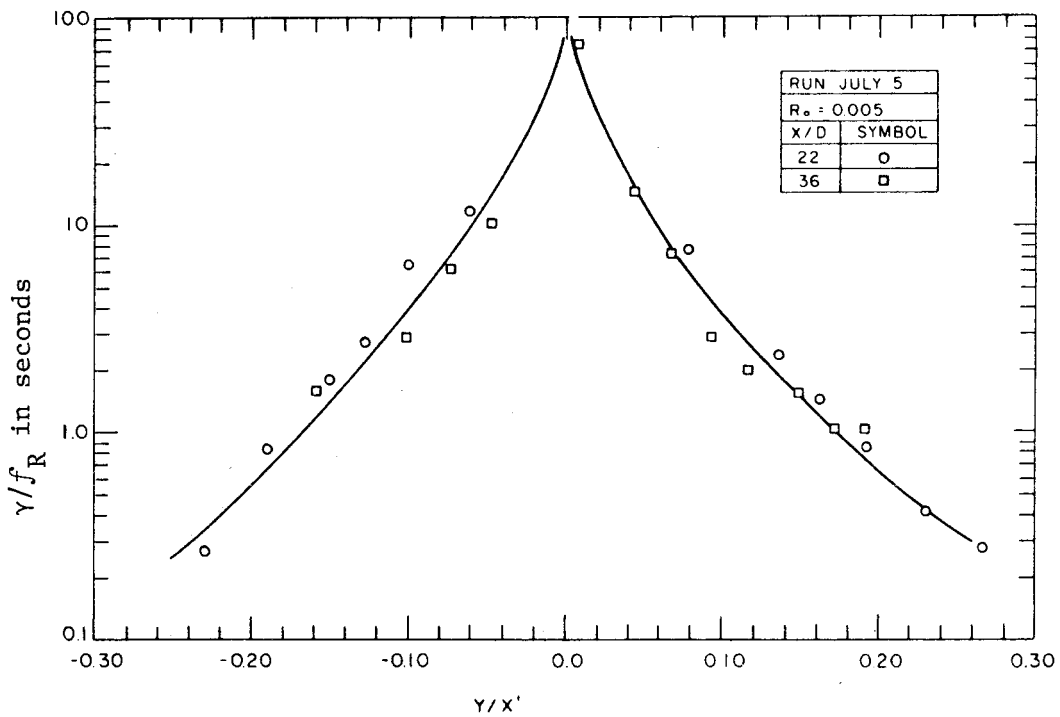

Figure 4.5.6. Average duration of hot bursts in a turbulent jet.

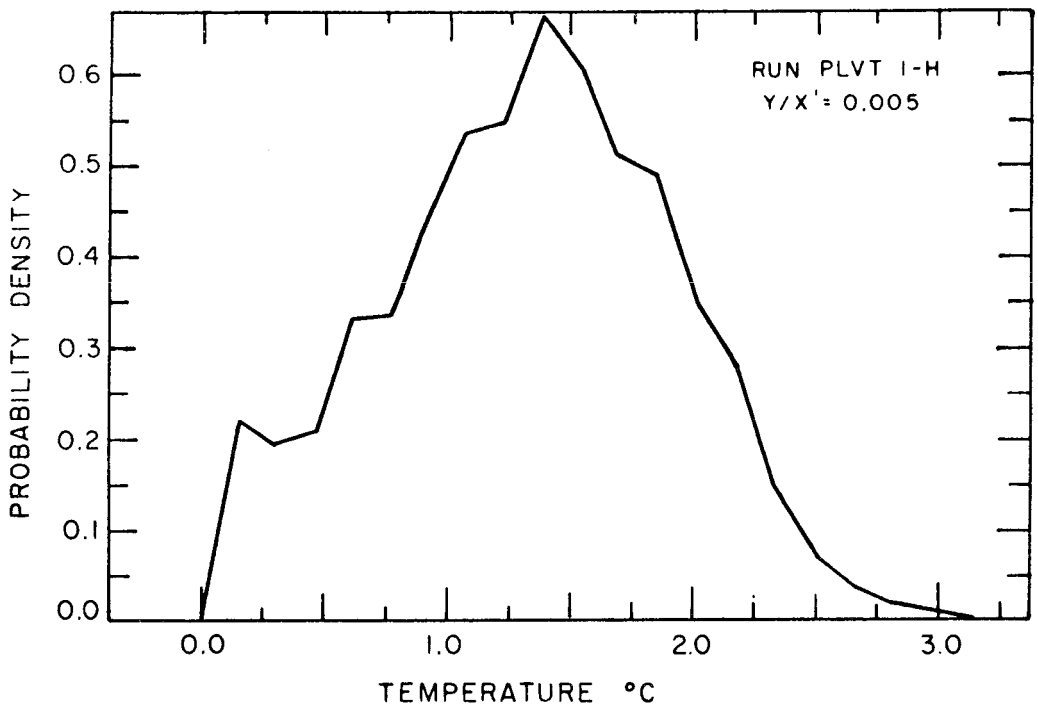

Figure 4.6.1.a. Probability density of the temperature of a turbulent plume at y/x' = 0.005.

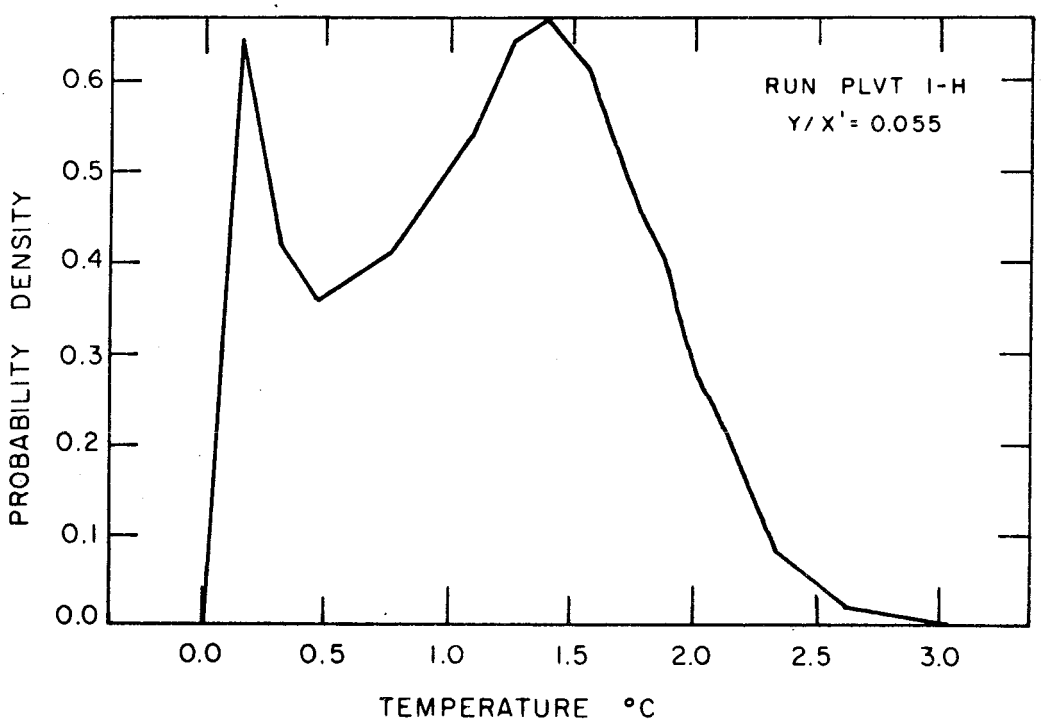

Figure 4.6.1.b. Probability density of the temperature of a turbulent plume at y/x' = 0.055.

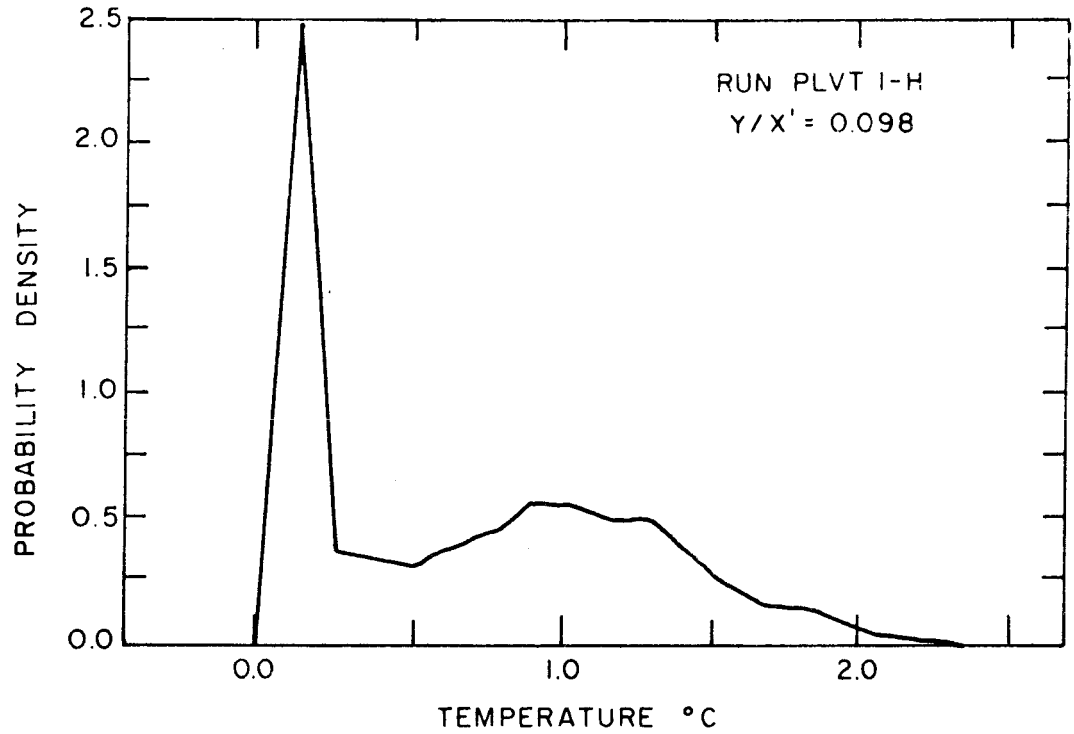

Figure 4.6.1.c. Probability density of the temperature of a turbulent plume at y/x' = 0.098.

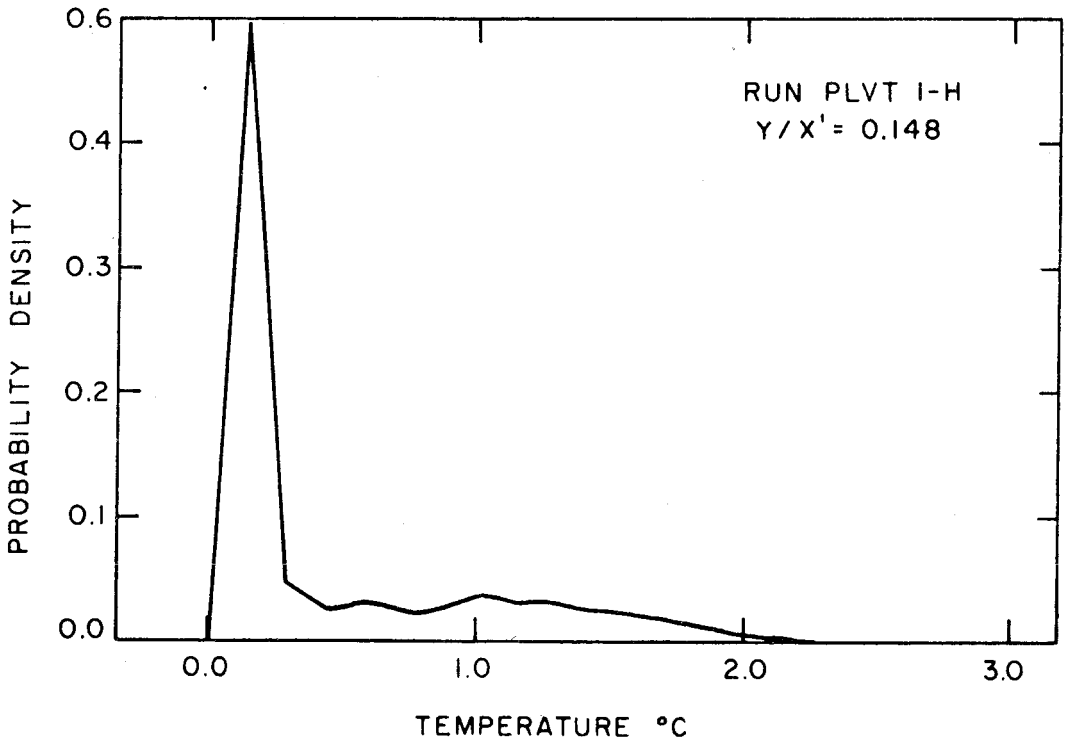

Figure 4.6.1.d. Probability density of the temperature of a turbulent plume at y/x' = 0.148.

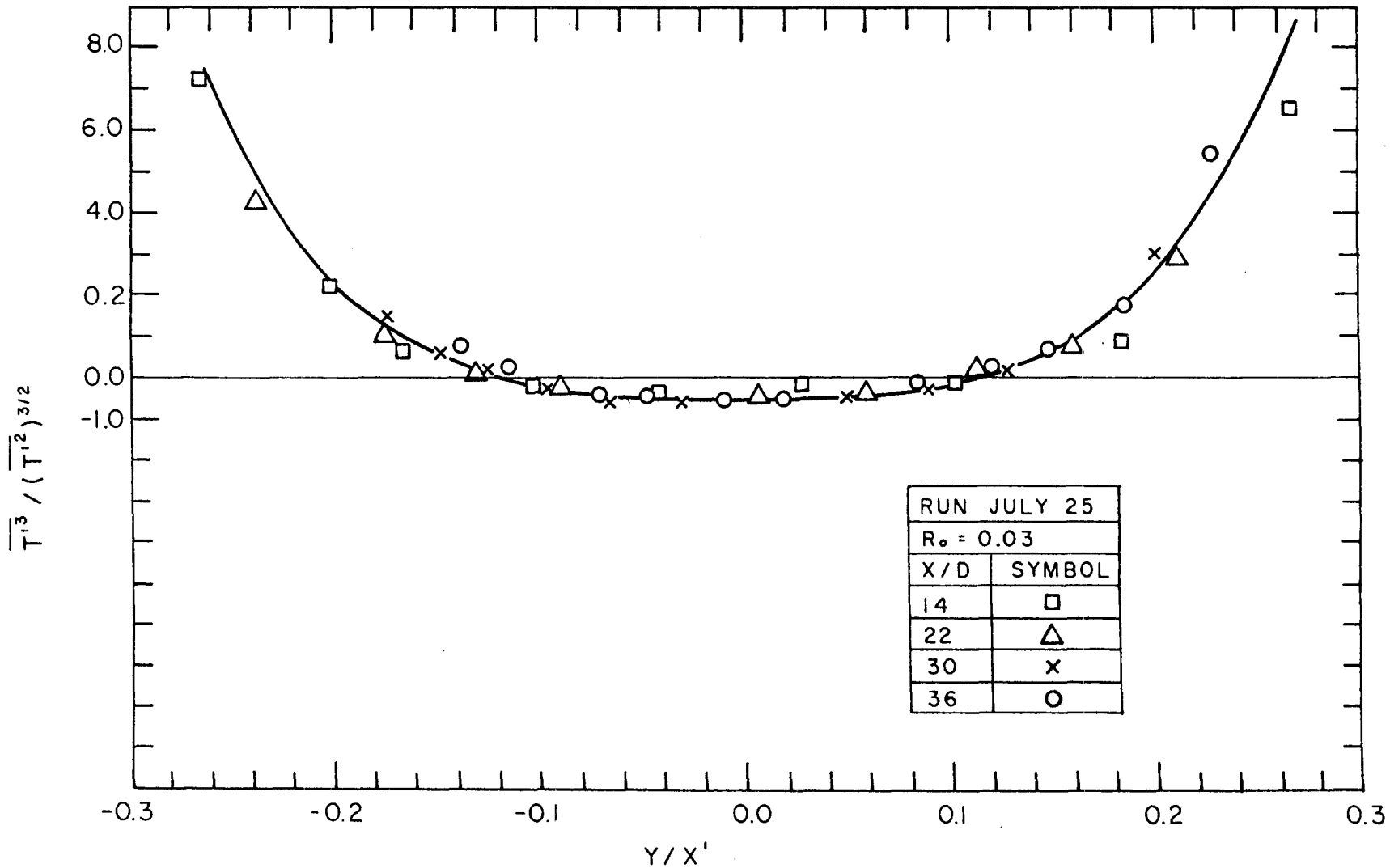

Figure 4.7.1. Skewness factor of temperature fluctuations of a buoyant jet as a function of distance from the jet axis.

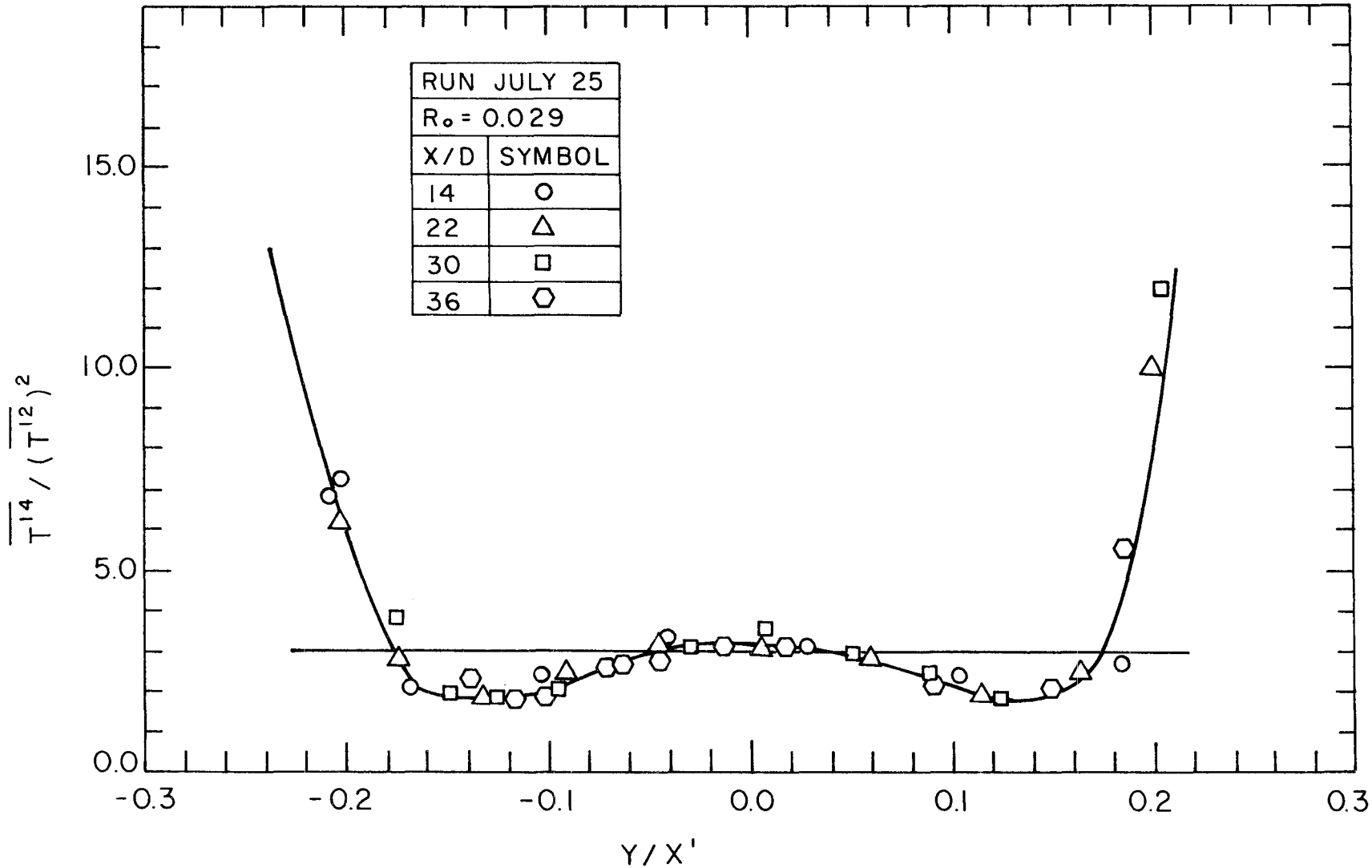

Figure 4.7.2. Flatness factor of temperature fluctuations of a buoyant jet as a function of distance from jet axis.

For a Gaussian curve the skewness factor is zero and the flatness factor is 3.0. The conclusion from these figures is consistent with the results of the previous chapter, i.e., the turbulence is not homogeneous.

5. VELOCITY MEASUREMENT RESULTS

5.0 BASIC EXPERIMENTAL PARAMETERS AND INITIAL DATA

Complete information regarding the basic parameters and the initial data of the experimental runs is given in Table 5.0.1. An explanation of the data columns is as follows:

Column 1 gives the name of the experimental run. The mean transverse velocity profile was measured for all the runs except the runs Center, Cent 1 and Cent 2 where only the centerline mean velocity was measured.

Column 2 gives the width of the jet (in cm) at the orifice.

Column 3 gives the aspect ratio of the jet at the orifice.

Column 4 gives the exit velocity (in cm/sec) of the jet.

Column 5 gives the temperature of the ambient water in °C.

Column 6 gives the excess (above the ambient) temperature at the jet orifice in °C.

Column 7 gives the kinematic viscosity in cm^2/sec at the jet orifice and multiplied by 100.

Column 8 gives the thermal expansion coefficient (1/°C) of the discharge calculated at the jet orifice and multiplied by 1000.

Column 9 gives the Reynolds number of the jet at the orifice.

Column 10 gives the Richardson number of the jet calculated at the orifice.

$$R_o = \frac{\alpha_o g \bar{T}_o D}{\bar{u}_o^2}$$

Run	D	Aspect ratio	$\bar{u}_o$ cm/sec	$\bar{T}_o$ °C	T_a °C	ν_o x 10^2	α_o x 10^3	R_e	R_o
1	2	3	4	5	6	7	8	9	10
PLVT2-F	0.24	54.20	62.93	3.30	21.60	0.90	0.25	1683.38	0.000051
PLVT2-B	0.24	54.20	62.00	0.0	23.00	0.94	0.23	1584.12	0.0
PLVT2-Z	0.24	54.20	62.93	5.40	21.80	0.85	0.27	1777.09	0.000089
PLVT2-C	0.24	54.20	62.63	0.0	23.00	0.94	0.23	1600.22	0.0
PLVT2-H	0.24	54.20	64.20	3.80	22.20	0.87	0.26	1762.78	0.000058
PLVT2-D	0.24	54.20	62.93	0.0	23.00	0.94	0.23	1607.88	0.0
PLVT2-A	0.24	54.20	62.90	6.85	23.25	0.80	0.30	1897.30	0.000123
P-7A	1.00	13.00	18.10	0.01	24.99	0.90	0.25	2022.22	0.000008
P-7B	1.00	13.00	18.10	0.01	24.99	0.90	0.25	2022.22	0.000008
PLVT3-B	0.24	54.20	19.00	9.20	22.50	0.77	0.31	593.61	0.001894
PLVT3-A	0.24	54.20	19.00	10.40	23.20	0.74	0.32	618.17	0.002242
P-2B	1.00	13.00	7.56	14.10	24.00	0.67	0.36	1121.90	0.068
P-2A	1.00	13.00	7.56	16.90	22.00	0.66	0.36	1139.13	0.107
P-3A	1.00	13.00	15.11	20.00	22.00	0.63	0.38	2409.36	0.033
P-4B	1.00	13.00	15.10	10.00	24.00	0.73	0.33	2064.19	0.014
P-4A	1.00	13.00	15.10	11.10	22.00	0.75	0.32	2025.55	0.015
P-4C	1.00	13.00	15.10	10.00	24.00	0.73	0.33	2064.19	0.014
PLVT1-F	1.00	13.00	4.55	11.00	22.00	0.75	0.32	609.05	0.169
PLVT1-D	1.00	13.00	4.55	11.15	22.00	0.74	0.32	610.99	0.172
PLVT1-Z	1.00	13.00	4.55	11.00	22.00	0.75	0.32	609.05	0.169
PLVT1-C	1.00	13.00	4.55	10.90	22.00	0.75	0.32	607.76	0.167
PLVT1-K	1.00	13.00	4.55	11.15	23.00	0.73	0.33	623.93	0.176
PLVT1-B	1.00	13.00	4.55	11.00	22.00	0.75	0.32	609.05	0.169
PLVT1-H	1.00	13.00	4.55	11.40	23.00	0.73	0.33	627.17	0.181
P-1D	1.00	13.00	4.53	17.00	24.00	0.64	0.38	709.56	0.313
P-1C	1.00	13.00	4.53	17.00	24.00	0.64	0.38	709.56	0.313
P-1?	1.00	13.00	4.53	17.00	24.00	0.64	0.38	709.56	0.313
P-1B	1.00	13.00	4.53	17.00	24.00	0.64	0.38	709.56	0.313
P-1A	1.00	13.00	4.53	17.00	24.00	0.64	0.38	709.56	0.313
P-5B	1.00	13.00	6.04	30.40	24.70	0.51	0.48	1175.99	0.400
P-5A	1.00	13.00	6.04	32.30	23.50	0.51	0.49	1186.88	0.439
P-5D	1.00	13.00	6.04	30.10	23.80	0.52	0.47	1157.25	0.388
P-5C	1.00	13.00	6.04	30.20	24.00	0.52	0.47	1161.94	0.392
P-6B	1.00	13.00	4.53	30.50	24.00	0.52	0.46	874.97	0.707
P-6A	1.00	13.00	4.53	30.40	24.70	0.51	0.48	881.99	0.712
P-6C	1.00	13.00	4.53	30.10	24.10	0.52	0.47	871.45	0.694
CENTER	0.24	54.20	62.00		21.00	1.00		1488.00	0.0
CENTER	0.24	54.20	62.00		21.00	1.00		1488.00	0.0
CENTER	0.24	54.20	62.00		21.00	1.00		1488.00	0.0
CENTER	0.24	54.20	62.00		21.00	1.00		1488.00	0.0
CENTER	0.24	54.20	62.00		21.00	1.00		1488.00	0.0
CENTER	0.24	54.20	62.00		21.00	1.00		1488.00	0.0
CENT1	0.24	54.20	81.87		21.00	1.00		1964.88	0.0
CENT1	0.24	54.20	50.40		21.00	1.00		1209.60	0.0
CENT1	0.24	54.20	50.40		21.00	1.00		1209.60	0.0
CENT1	0.24	54.20	81.87		21.00	1.00		1964.88	0.0
CENT1	0.24	54.20	81.87		21.00	1.00		1964.88	0.0
CENT1	0.24	54.20	62.90		21.00	1.00		1509.60	0.0
CENT1	0.24	54.20	50.40		21.00	1.00		1209.60	0.0
CENT1	0.24	54.20	31.50		21.00	1.00		756.00	0.0
CENT1	0.24	54.20	31.50		21.00	1.00		756.00	0.0
CENT1	0.24	54.20	81.87		21.00	1.00		1964.88	0.0
CENT1	0.24	54.20	81.87		21.00	1.00		1964.88	0.0
CENT2	0.24	54.20	81.87		21.00	1.00		1964.88	0.0
CENT2	0.24	54.20	62.98		21.00	1.00		1511.52	0.0
CENT2	0.24	54.20	62.98		21.00	1.00		1511.52	0.0
CENT2	0.24	54.20	31.58		21.00	1.00		757.92	0.0
CENT2	0.24	54.20	31.58		21.00	1.00		757.92	0.0
CENT2	0.24	54.20	81.87		21.00	1.00		1964.88	0.0
CENT2	0.24	54.20	81.87		21.00	1.00		1964.88	0.0
CENT2	0.24	54.20	81.87		21.00	1.00		1964.88	0.0

Table 5.0.1. Basic experimental parameters and initial data of the velocity measurements.

5.1 MEAN VELOCITY PROFILE

For every experimental run the mean velocity profile $\bar{u}(x,y)$ in cm/sec was plotted versus the transverse distance y(in cm), the half-width b_u was calculated, and a Gaussian curve defined as

$$\bar{u}(x,y) = \bar{u}_M(x) \exp[-\ell n2 \ (y/b_u)^2] \qquad (5.1.1)$$

was plotted as in Figures 5.1.1.a-f (representative case for a pure jet), and 5.1.4.a-f (representative case of an almost pure plume). The velocity half-widths $b_u(x)$ for a particular run were plotted versus the distance from the exit as in Figures 5.1.2 (jet) and 5.1.5 (plume) and a straight line

$$\frac{b_u}{D} = K_{1u}(\frac{x}{D} + K_{2u}) \ , \qquad (5.1.2)$$

was fitted to the data. The virtual origin of the mean velocity profile is given by $x_{ou} = -K_{2u} D$. The coefficients K_{1u}, K_{2u} for all the runs are given in Table 5.1.1 from where it can be observed that there is no correlation of the variation of these coefficients with the initial Richardson number. However, it is interesting to notice that the coefficients K_{1u}, K_{2u} of the runs PLVT2 (~pure jet) and P-7 (~pure jet) are quite different. An explanation for this is the apparent non-self-preserving character of the pure two-dimensional jet and it will be discussed in detail in Chapter 8.

The mean velocity $\bar{u}(x,y)$, normalized by the mean velocity $\bar{u}_M(x)$ on the jet axis, has been plotted against the non-dimensional distance y/x' (where $x' = x - x_{ou}$) for the case of a jet, Figure 5.1.3 and the

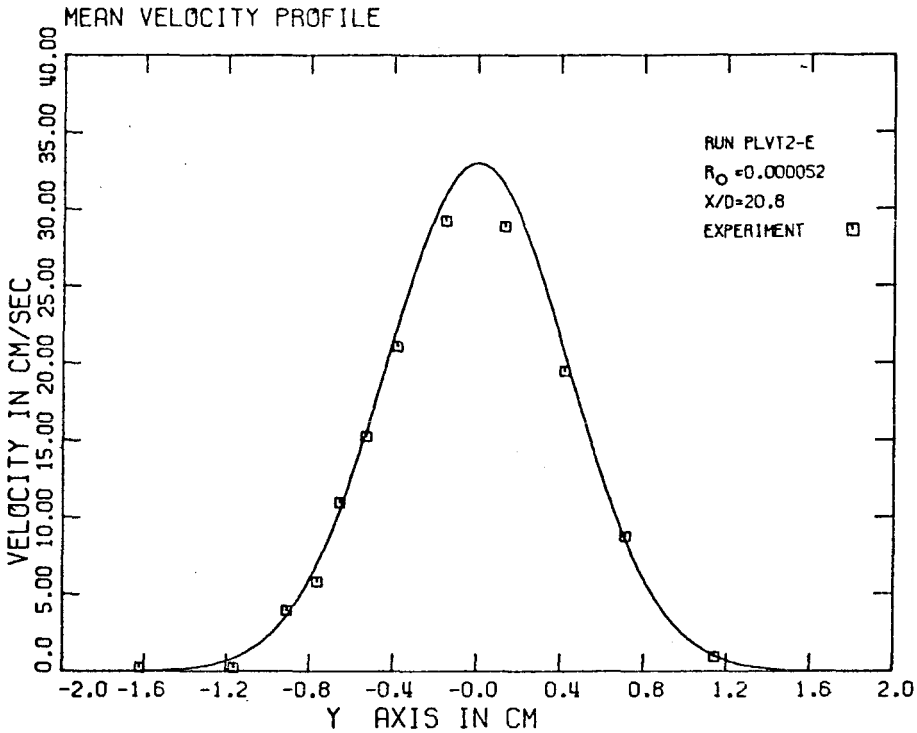

Figure 5.1.1.a. Mean velocity profile for a turbulent jet at X/D = 20.8

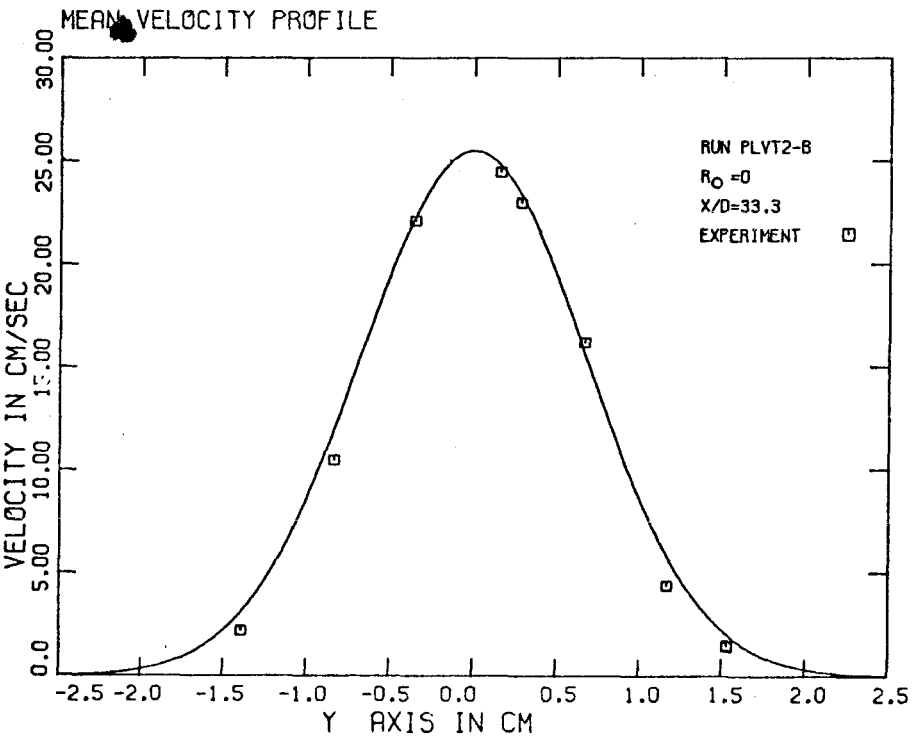

Figure 5.1.1.b. Mean velocity profile for a turbulent jet at X/D = 33.3.

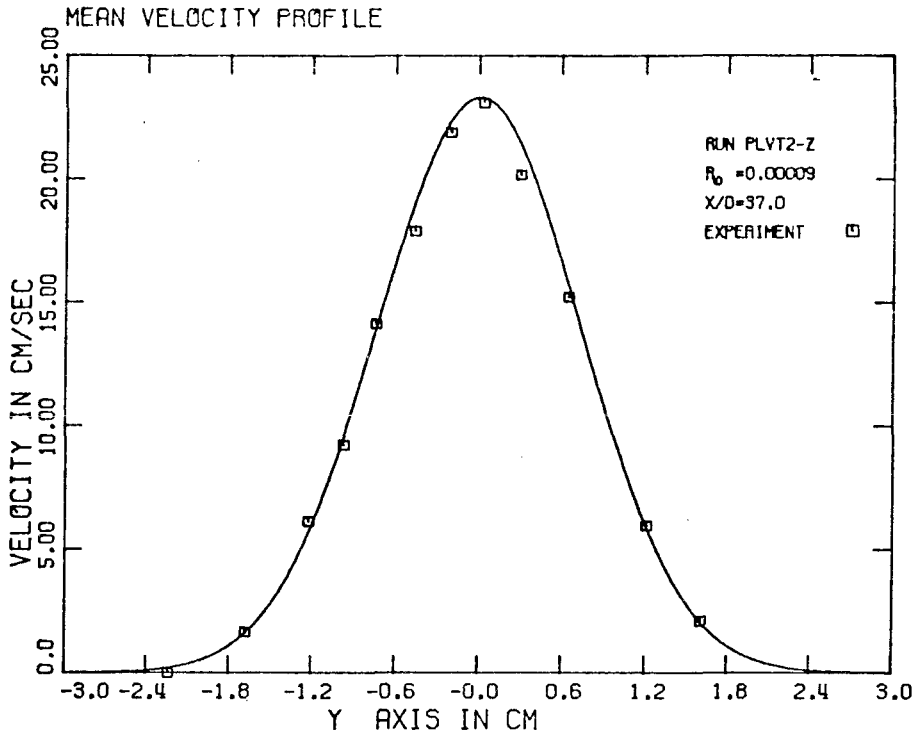

Figure 5.1.1.c. Mean velocity profile for a turbulent jet at X/D = 37.0

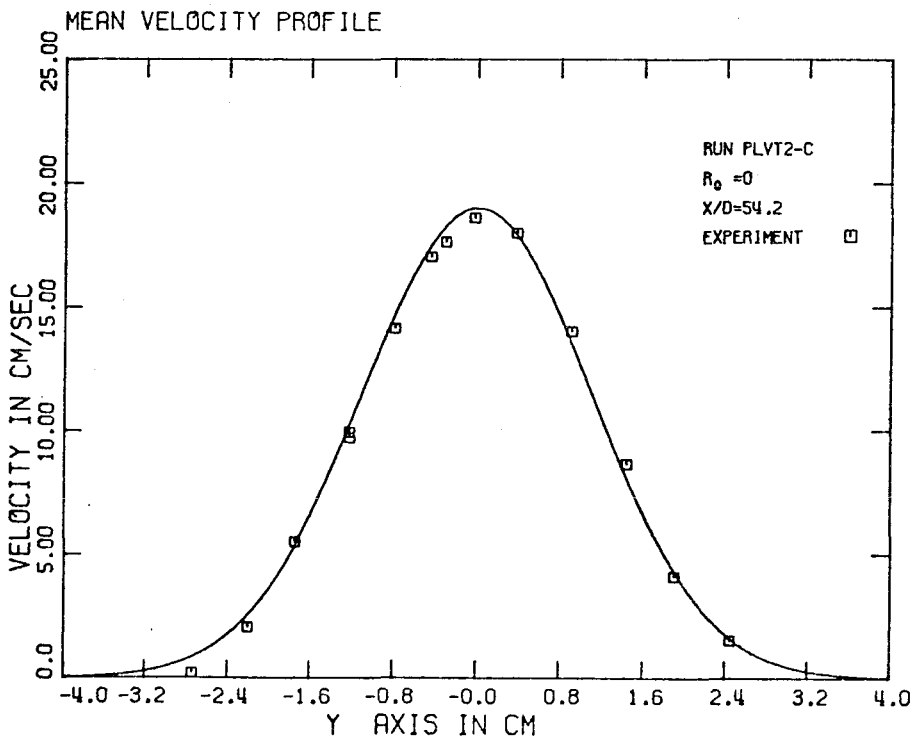

Figure 5.1.1.d. Mean velocity profile for a turbulent jet at X/D = 54.2

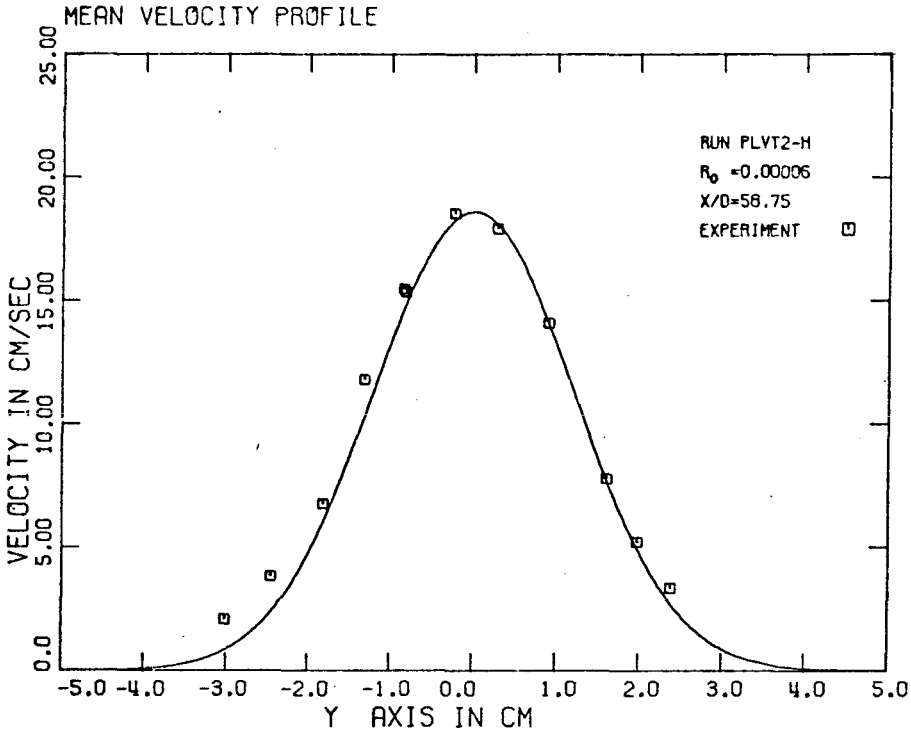

Figure 5.1.1.e. Mean velocity profile for a turbulent jet at X/D = 58.75

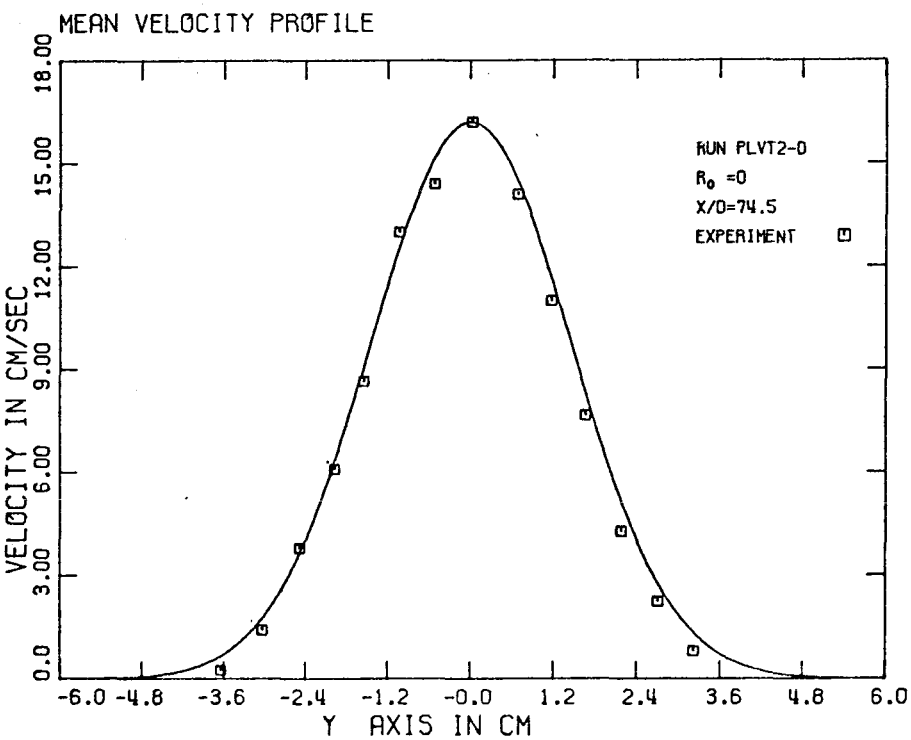

Figure 5.1.1.f. Mean velocity profile for a turbulent jet at X/D = 74.50

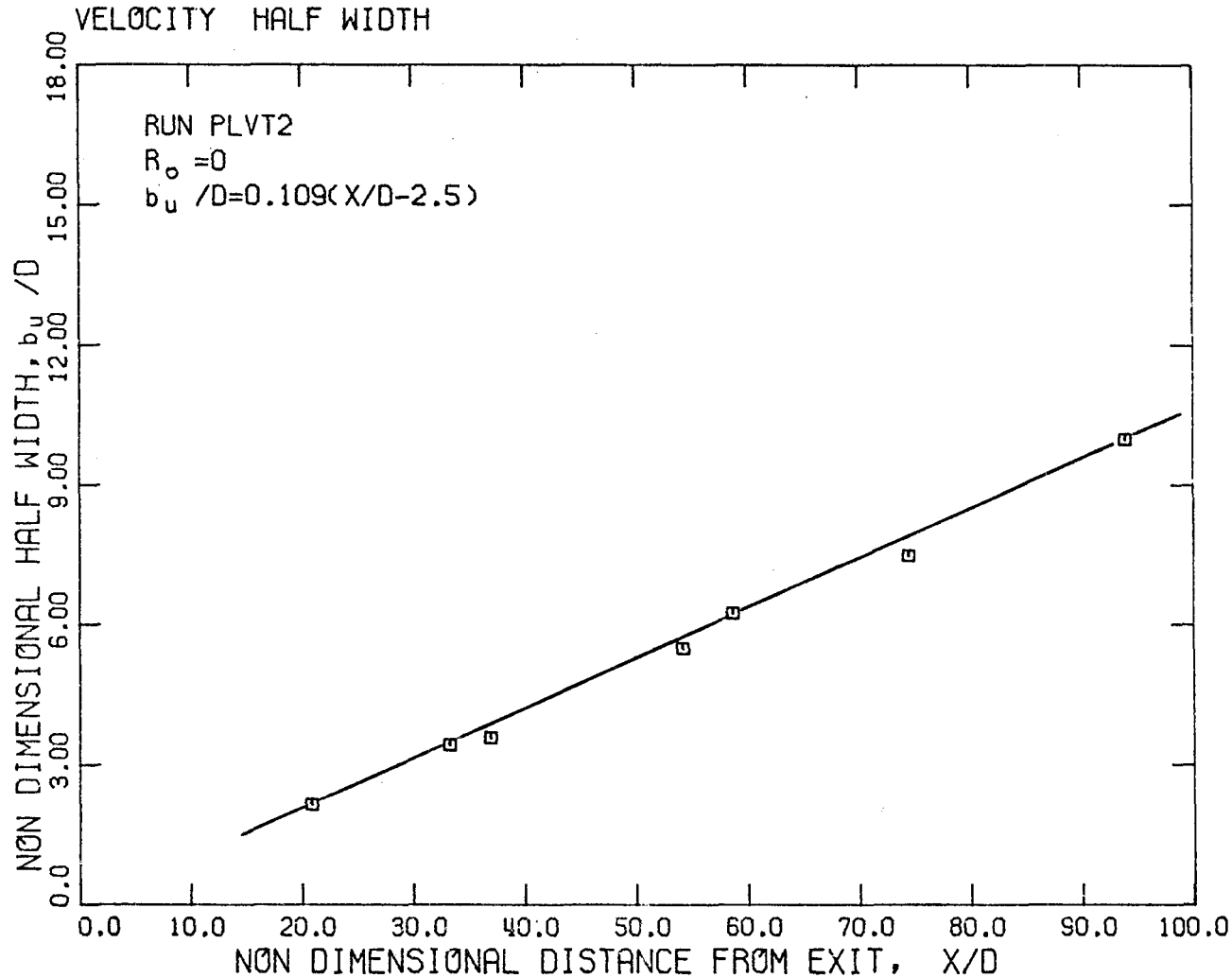

Figure 5.1.2. Non-dimensional velocity half-width for a turbulent jet as a function of distance from jet orifice.

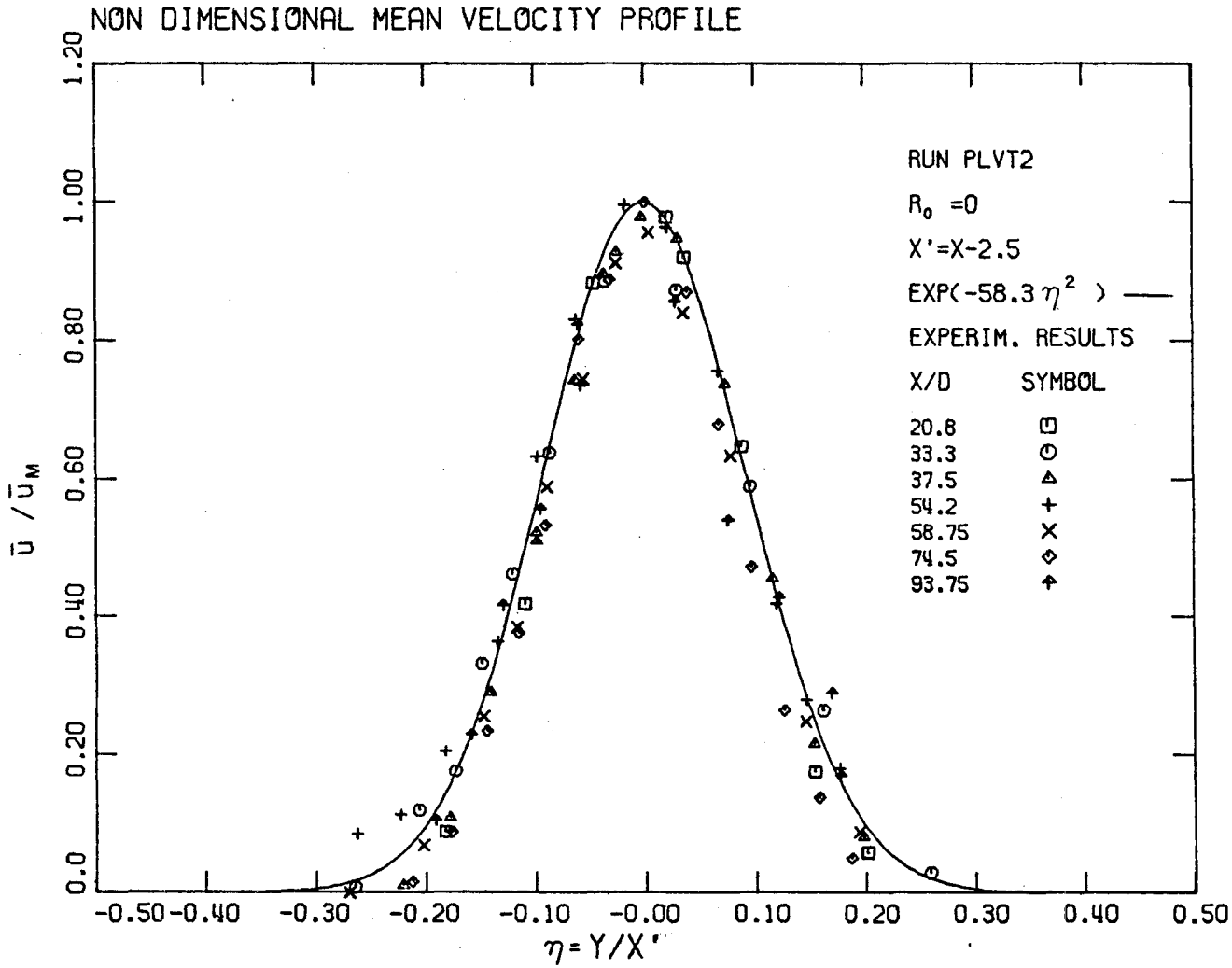

Figure 5.1.3. Non-dimensional mean velocity profile for a turbulent jet.

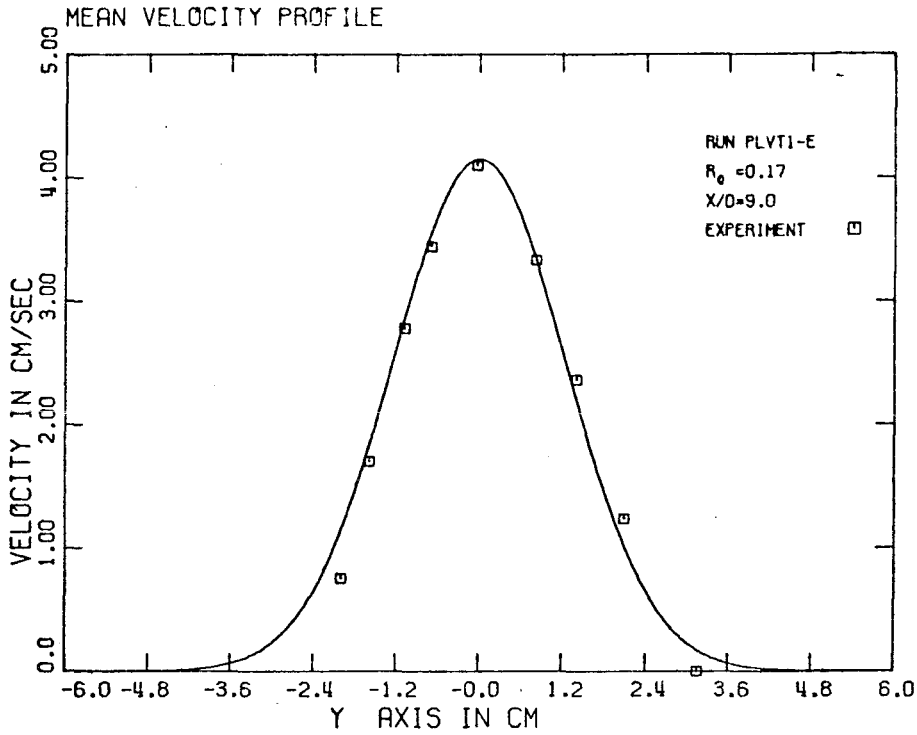

Figure 5.1.4.a. Mean velocity profile for a turbulent plume at X/D = 9.0

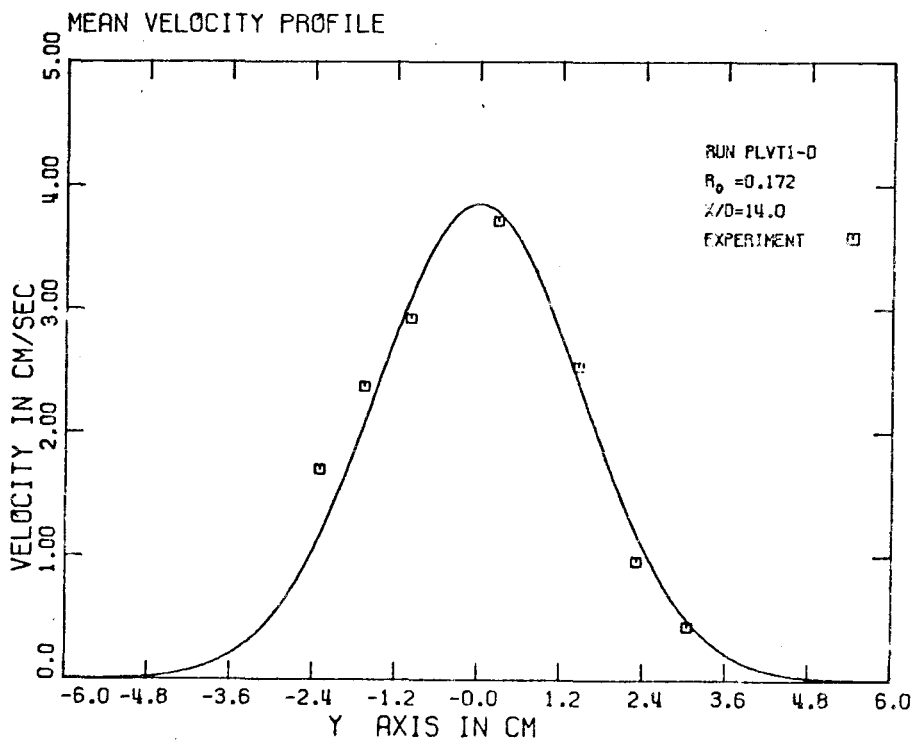

Figure 5.1.4.b. Mean velocity profile for a turbulent plume at X/D = 14.0

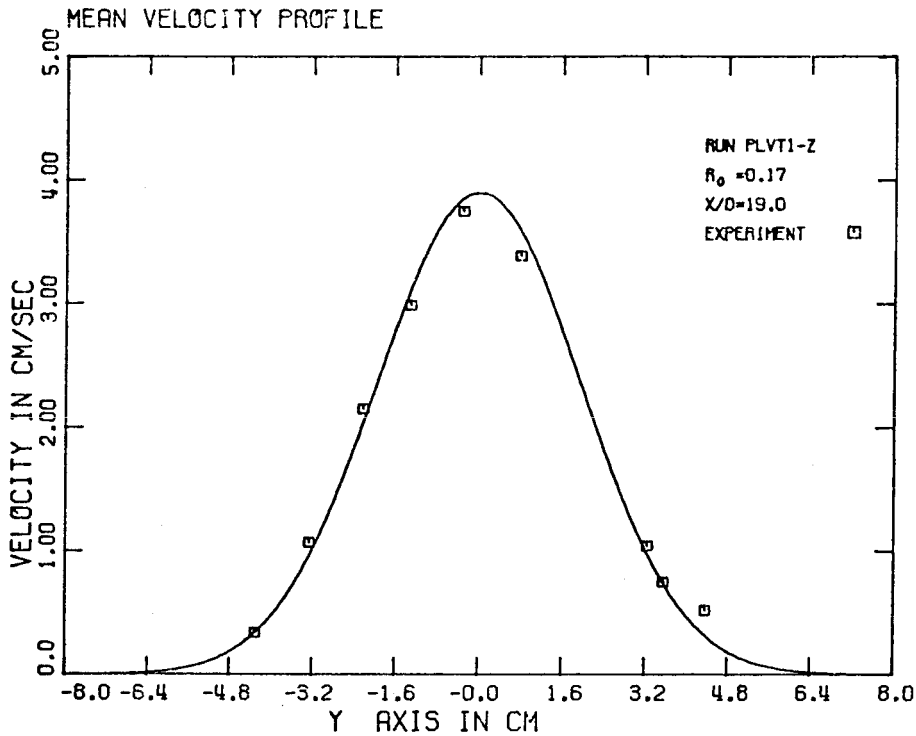

Figure 5.1.4.c. Mean velocity profile for a turbulent plume at X/D = 19.0

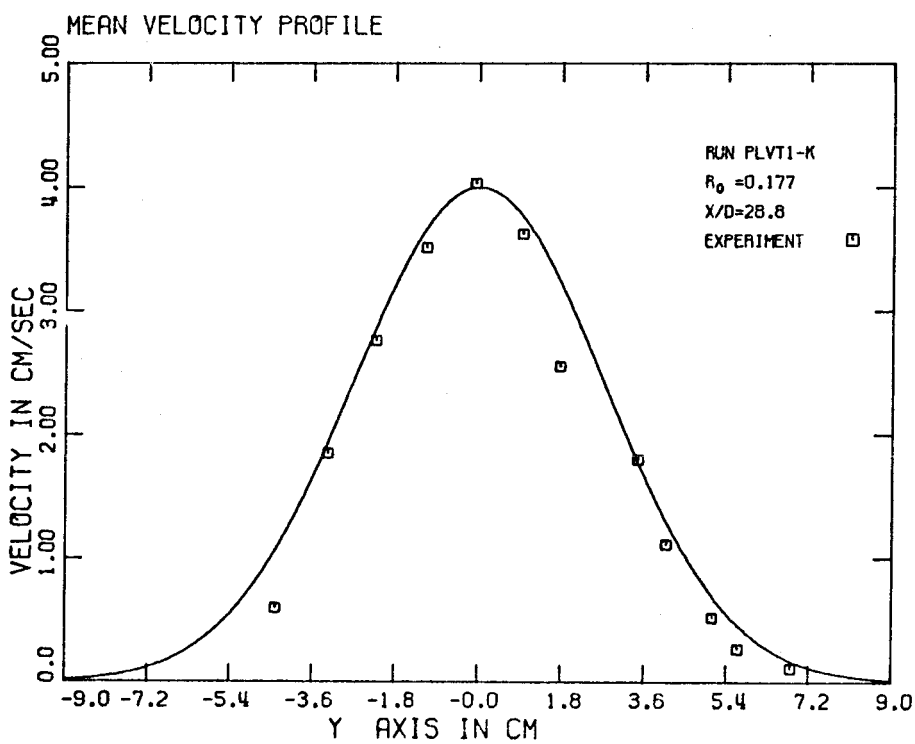

Figure 5.1.4.d. Mean velocity profile for a turbulent plume at X/D = 28.8

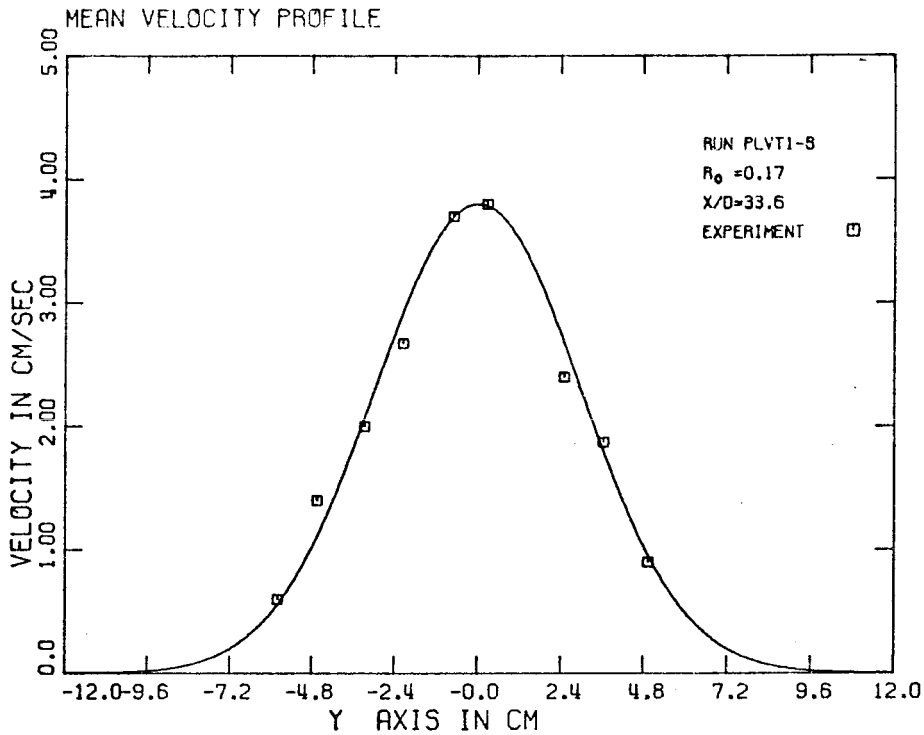

Figure 5.1.4.e. Mean velocity profile for a turbulent plume at X/D = 33.6

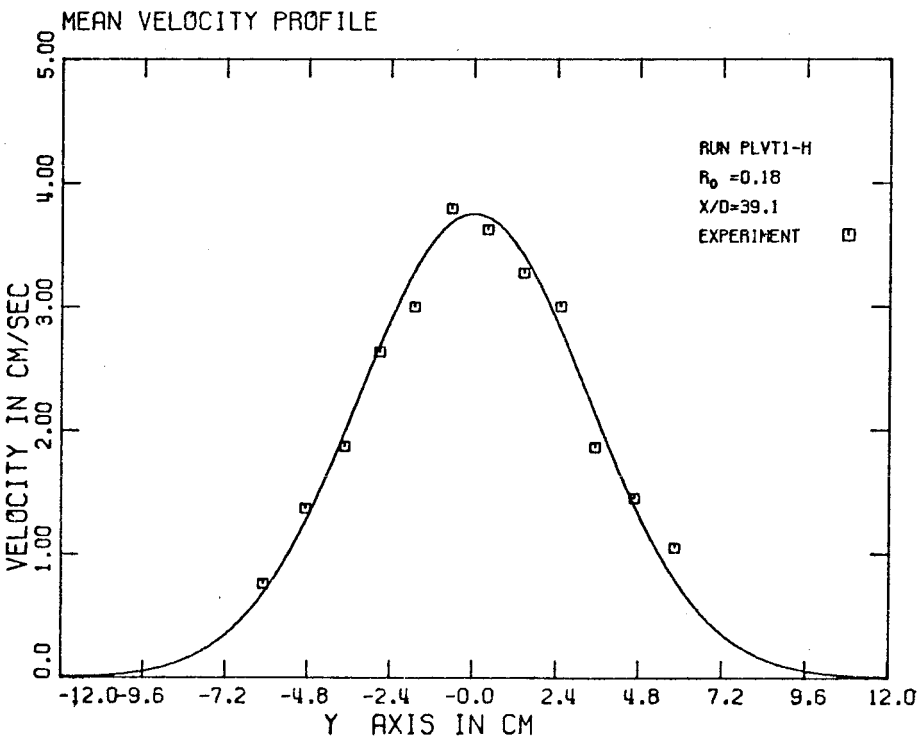

Figure 5.1.4.f. Mean velocity profile for a turbulent plume at X/D = 39.1

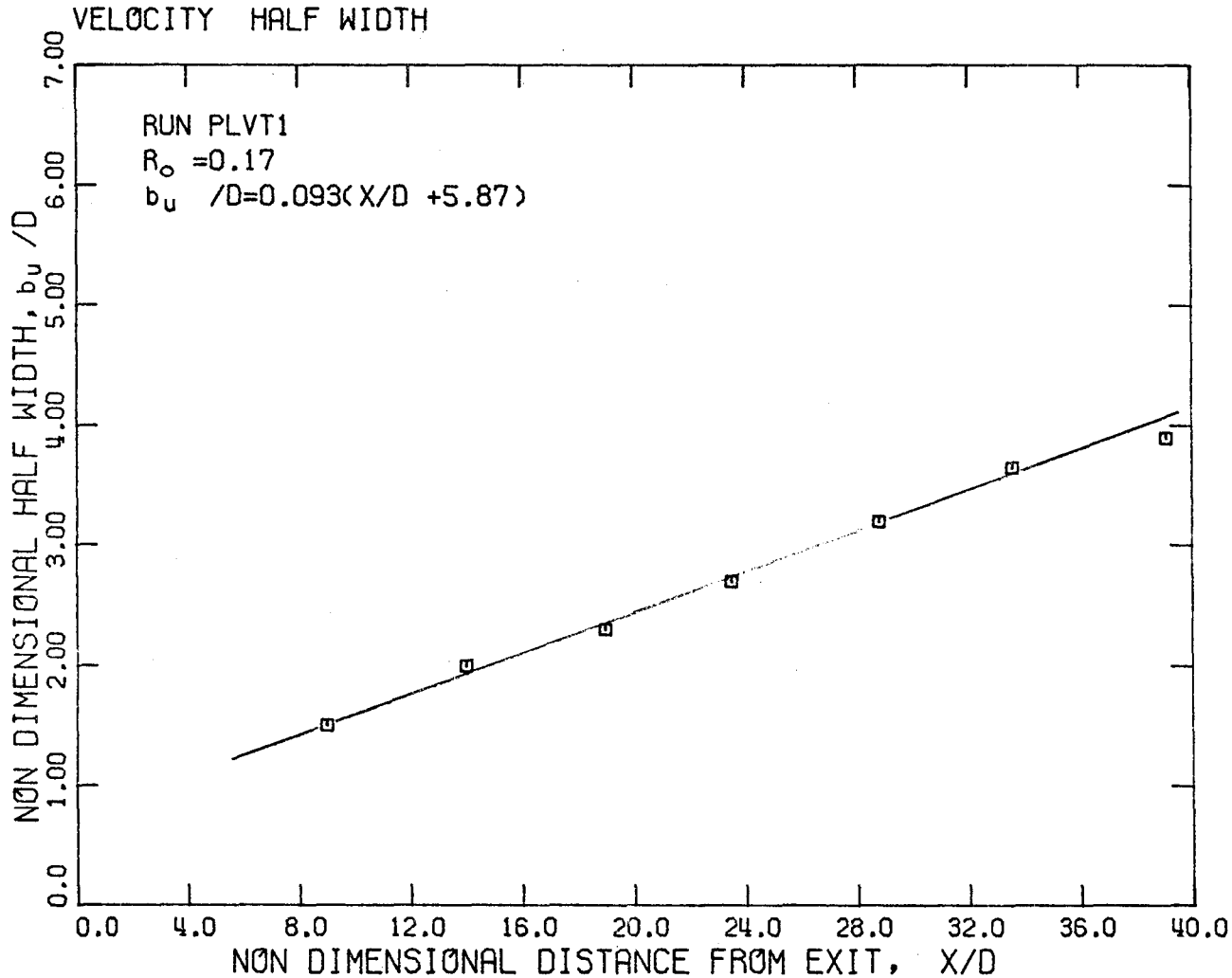

Figure 5.1.5. Non-dimensional velocity half-width of a turbulent plume plotted against non-dimensional distance from jet orifice.

Run	R_o	X/D from	X/D to	K_{1u}	K_{2u}
1	2	3	4	5	6
P-7	0.0	14.0	37.0	0.087	6.7
PLVT-2	~0.0	20.8	93.7	0.109	-2.5
PLVT-3	0.002	33.7	94.0	0.106	-3.1
P-4	0.015	14.0	37.0	0.087	5.6
P-2	0.10	14.0	24.0	0.09	3.8
PLVT-1	0.17	9.0	39.1	0.093	5.87
P-1	0.31	12.5	43.0	0.095	4.85
P-5	0.40	14.0	37.2	0.104	1.78
P-6	0.70	14.0	37.2	0.093	4.20

Table 5.1.1. Linear approximation of the growth of the velocity half-width.

case of a plume, Figure 5.1.6. The Gaussian curves in Figures 5.1.3 and 5.1.6 are defined by

$$\frac{\overline{u}(x,y)}{\overline{u}_M(x)} = \exp\left[-\ell n2\ (y/K_{1u}x')^2\right], \tag{5.1.3}$$

where $x' = x - x_{ou}$.

The kinematic mass flux $\mu(x)$ and the kinematic momentum flux $m(x)$ were calculated for each profile using the Gaussian curve given by Eq. 5.1.1 as a reasonable approximation to the measurements so that

$$\mu(x) = \sqrt{\frac{\Pi}{\ell n2}}\, b_u(x)\ \overline{u}_M(x)\ , \tag{5.1.4}$$

$$m(x) = \sqrt{\frac{\Pi}{2\ell n2}}\, b_u(x)\ \overline{u}_M^2(x)\ . \tag{5.1.5}$$

The kinematic buoyancy flux $\beta(x)$ was calculated from the relation

$$\beta(x) = \alpha g H_o/\rho c_p\ , \tag{5.1.6}$$

where the thermal expansion coefficient α is calculated from Eq. 2.2.5 for a temperature $T_a + \overline{T}_c$ where $\overline{T}_c = H_o/\rho c_p \mu(x)$, i.e., $\overline{T}_c$ is the mean cross sectional temperature. The two non-dimensional numbers, the jet angle

$$C = \mu(x)/[m(x)(x-x_{ou})]^{1/2}\ ,$$

and the Richardson number

$$R(x) = \mu^3(x)\beta(x)/m^3(x)\ ,$$

were calculated for each cross section. The basic experimental results

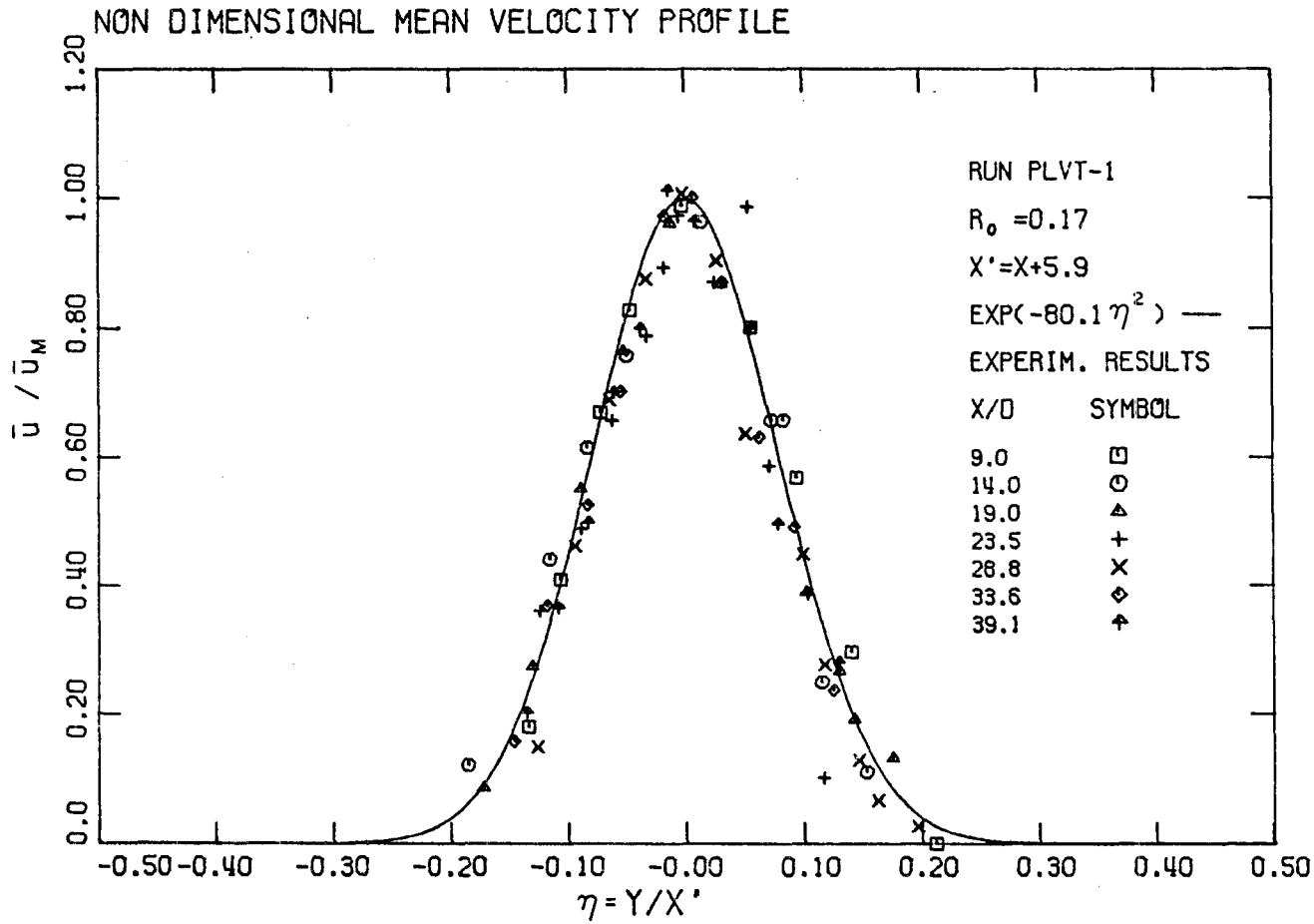

Figure 5.1.6. Non-dimensional mean velocity profile for a turbulent plume.

from each cross section, i.e., $\bar{u}_M(x)$, $b_u(x)$, $\mu(x)/\mu_o$, $m(x)/m_o$, $\beta(x)/\beta_o$, C, R(x), are given in Table 5.1.2 where $\mu_o = \bar{u}_c D$, $m_o = \bar{u}_o^2 D$ and $\beta_o = \alpha_o g \bar{u}_o \bar{T}_o D$.

It can be observed from Table 5.1.2 that the Richardson number R(x), which is identically zero for a pure jet, tends to a constant value R_p for an almost pure plume. The mean value, suggested for runs with $R_o > 0.15$ is $R_p = 0.63$ with a standard deviation 0.05. Hence it seems that the Richardson number of a pure plume is a constant, not only in the case of conserved kinematic buoyancy flux (see Eq. 2.2.12), but also in the case of a variable thermal expansion coefficient (not conserved kinematic buoyancy flux). It can be observed also from Table 5.1.2 that the non-dimensional number C (see Eq. 5.1.7) is a constant for a wide range of initial Richardson numbers, from R = 0 (pure jet) to $R \approx 0.63$ (pure plume), with a mean value C = 0.54 and a standard deviation 0.02.

5.2 ON THE CONSERVATION OF MOMENTUM AND ON THE DECAY OF THE CENTERLINE VELOCITY OF A PURE JET

The kinematic momentum flux m(x) at a distance x from the exit, normalized by the initial kinematic momentum flux $m_o = \bar{u}_o^2 D$ (see Table 5.1.2), has been plotted versus the distance from the exit x/D in Figure 5.2.1 for the run PLVT2 and P-7 (case of a pure jet). The interesting conclusion is that the kinematic momentum flux is not conserved in the case of a pure jet out of a wall, but it decreases as the distance from the exit increases, in qualitative agreement with the theoretical prediction made in Chapter 2.1 and given by the continuous line of Figure 5.2.1. The same conclusion can be drawn from Figure

Run	x cm	$\bar{u}_M$ cm sec	b_u cm	$\frac{\mu(x)}{\mu_o}$	$\frac{m(x)}{m_o}$	$\frac{\beta(x)}{\beta_o}$	C	R(x)
1	2	3	4	5	6	7	8	9
PLVT2-E	5.00	33.00	0.515	2.396	0.868	0.943	0.580	0.001
PLVT2-B	8.10	25.50	0.800	2.919	0.849	1.000	0.559	0.000
PLVT2-Z	8.90	24.50	0.850	2.935	0.808	0.889	0.549	0.004
PLVT2-C	13.00	19.00	1.300	3.498	0.750	1.000	0.557	0.000
PLVT2-H	14.10	18.60	1.430	3.675	0.753	0.908	0.561	0.006
PLVT2-D	17.80	16.20	1.700	3.852	0.706	1.000	0.542	0.001
PLVT2-A	22.50	13.00	2.400	4.400	0.643	0.855	0.572	0.034
P-7A	14.00	10.50	1.800	2.223	0.912	1.000	0.512	0.000
P-7B	37.60	6.90	3.760	3.052	0.822	1.000	0.506	0.000
PLVT3-B	8.10	8.10	0.840	3.177	0.957	0.835	0.586	0.058
PLVT3-A	22.50	5.65	2.500	6.595	1.386	0.781	0.588	0.189
P-2B	14.00	6.30	1.600	2.839	1.672	0.805	0.520	0.347
P-2A	24.00	5.50	2.500	3.872	1.991	0.732	0.520	0.577
P-3A	24.00	7.90	2.900	3.228	1.193	0.731	0.603	0.488
P-4B	14.00	10.30	1.700	2.469	1.190	0.856	0.512	0.110
P-4A	24.00	7.40	2.620	2.733	0.947	0.821	0.517	0.308
P-4C	37.00	7.30	3.700	3.912	1.374	0.817	0.512	0.271
PLVT1-E	9.00	4.25	1.500	2.983	1.970	0.817	0.558	0.482
PLVT1-D	14.00	3.85	2.000	3.603	2.155	0.793	0.556	0.640
PLVT1-Z	19.00	3.90	2.300	4.197	2.543	0.770	0.532	0.588
PLVT1-C	23.50	3.80	2.700	4.801	2.834	0.766	0.530	0.625
PLVT1-K	28.80	3.80	3.200	5.690	3.359	0.754	0.530	0.648
PLVT1-B	33.60	3.80	3.650	6.490	3.832	0.744	0.530	0.614
PLVT1-H	39.10	3.75	3.900	6.843	3.987	0.746	0.513	0.686
P-1D	12.50	4.65	1.650	3.606	2.617	0.756	0.535	0.619
P-1E	24.50	4.65	2.550	5.573	4.044	0.719	0.512	0.589
P-1Z	32.00	4.55	3.500	7.484	5.314	0.701	0.535	0.613
P-1B	38.00	4.55	3.950	8.446	5.997	0.695	0.527	0.608
P-1A	43.00	4.50	4.550	9.622	6.757	0.689	0.535	0.623
P-5B	14.00	6.00	1.650	3.489	2.450	0.671	0.561	0.777
P-5A	24.00	6.20	2.800	6.119	4.440	0.588	0.572	0.663
P-5D	32.00	6.40	3.600	8.121	6.083	0.584	0.567	0.541
P-5C	37.20	6.15	4.200	9.104	6.553	0.578	0.570	0.608
P-6B	14.00	5.60	1.600	4.211	3.660	0.643	0.515	0.682
P-6A	24.00	5.80	2.500	6.814	6.108	0.602	0.517	0.578
P-6C	37.20	5.50	3.850	9.951	8.541	0.575	0.529	0.632
CENTER	10.50	19.60						0
CENTER	10.50	19.52						0
CENTER	11.80	19.52						0
CENTER	11.80	18.67						0
CENTER	14.50	17.46						0
CENTER	14.50	16.98						0
CENT1	11.50	25.40						0
CENT1	11.50	15.28						0
CENT1	8.00	18.93						0
CENT1	8.00	30.49						0
CENT1	14.40	22.97						0
CENT1	14.40	17.68						0
CENT1	14.40	14.48						0
CENT1	14.40	8.78						0
CENT1	14.40	8.78						0
CENT1	11.90	25.02						0
CENT1	12.00	25.40						0
CENT2	16.70	21.10						0
CENT2	16.70	16.05						0
CENT2	16.70	16.22						0
CENT2	16.70	7.92						0
CENT2	19.00	7.40						0
CENT2	19.00	19.59						0
CENT2	19.00	19.41						0
CENT2	17.80	20.51						0

Table 5.1.2. Tabulated experimental values for volume, kinematic momentum and buoyancy fluxes for turbulent jets and plumes.

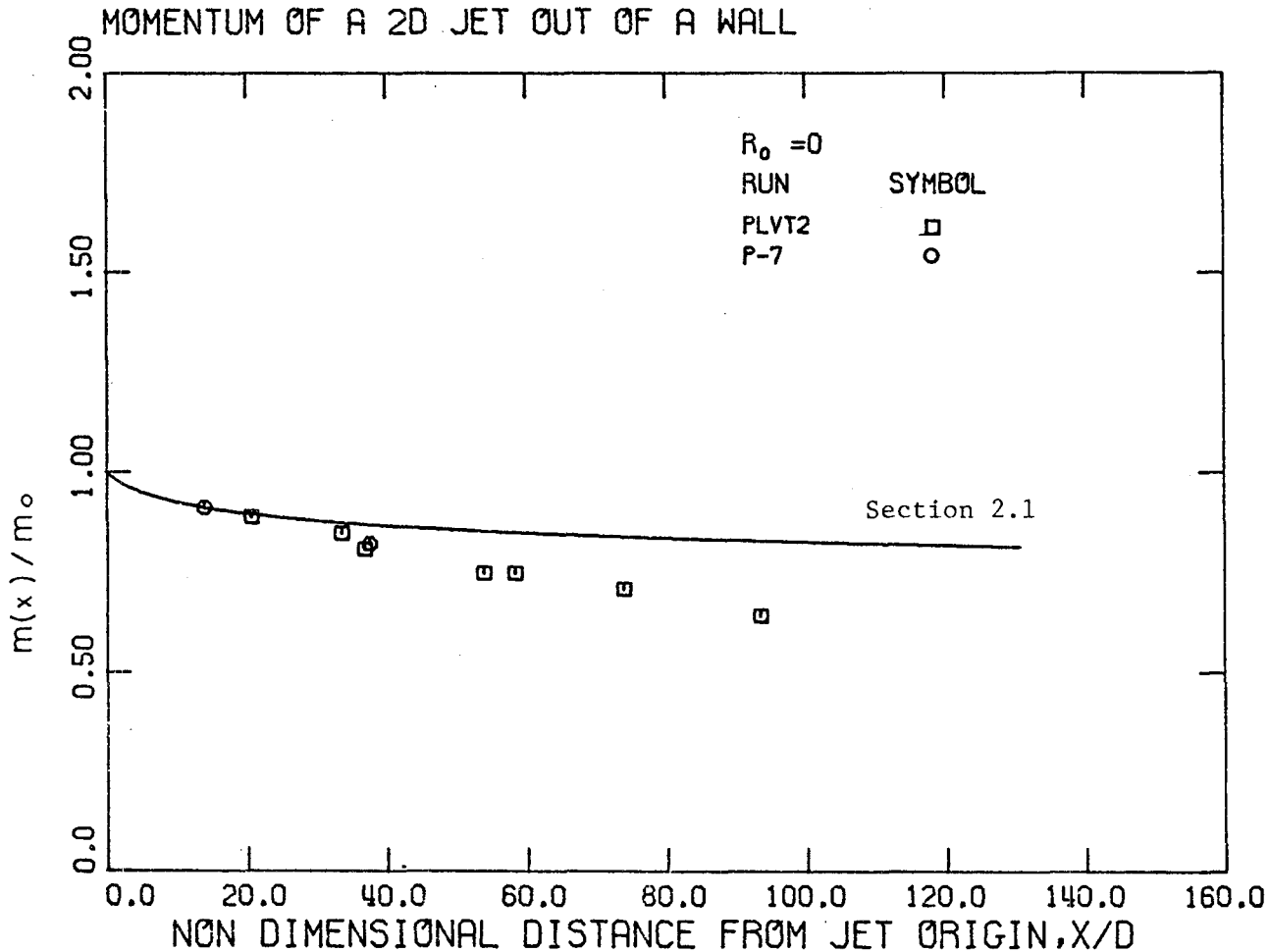

Figure 5.2.1. Experimental values for the kinematic momentum flux m(x) of a turbulent jet (R_o = 0) as a function of distance from jet orifice.

5.2.2, where the centerline velocity is plotted versus the distance from the exit x/D. If the kinematic momentum flux is really conserved, then the decay of the centerline velocity should be given by the relation

$$\left(\frac{\bar{u}_o}{\bar{u}_M(x)}\right)^2 = K_{1u}\sqrt{\frac{\pi}{2\ell n 2}}\left(\frac{x}{D} + K_{2u}\right), \qquad (5.2.1)$$

which is represented by the dotted line plotted in Figure 5.2.2. It can be seen that all the experimental points are well above the dotted line. This means that the centerline velocity decays faster than is predicted from the conservation of the kinematic momentum flux, i.e., the kinematic momentum flux is not conserved. The straight line which fits the experimental data (Figure 5.2.2) has the form

$$\left(\frac{\bar{u}_o}{\bar{u}_M(x)}\right)^2 = C_{1u}\left(\frac{x}{D} + C_{2u}\right), \qquad (5.2.2)$$

where C_{1u}, C_{2u} are the coefficients given in Table 5.2.1. A discussion of Eq. 5.2.2 will be given in Chapter 8.

Using the relation Eq. 5.1.5, it can be shown that

$$\frac{m(x)}{m_o} = \sqrt{\frac{\pi}{2\ell n 2}}\ \frac{K_{1u}\left(\frac{x}{D} + K_{2u}\right)}{C_{1u}\left(\frac{x}{D} + C_{2u}\right)}, \qquad (5.2.3)$$

or for x/D much greater than K_{2u}, C_{2u}

$$\frac{m(x)}{m_o} = \sqrt{\frac{\pi}{2\ell n 2}}\ \frac{K_{1u}}{C_{1u}}. \qquad (5.2.4)$$

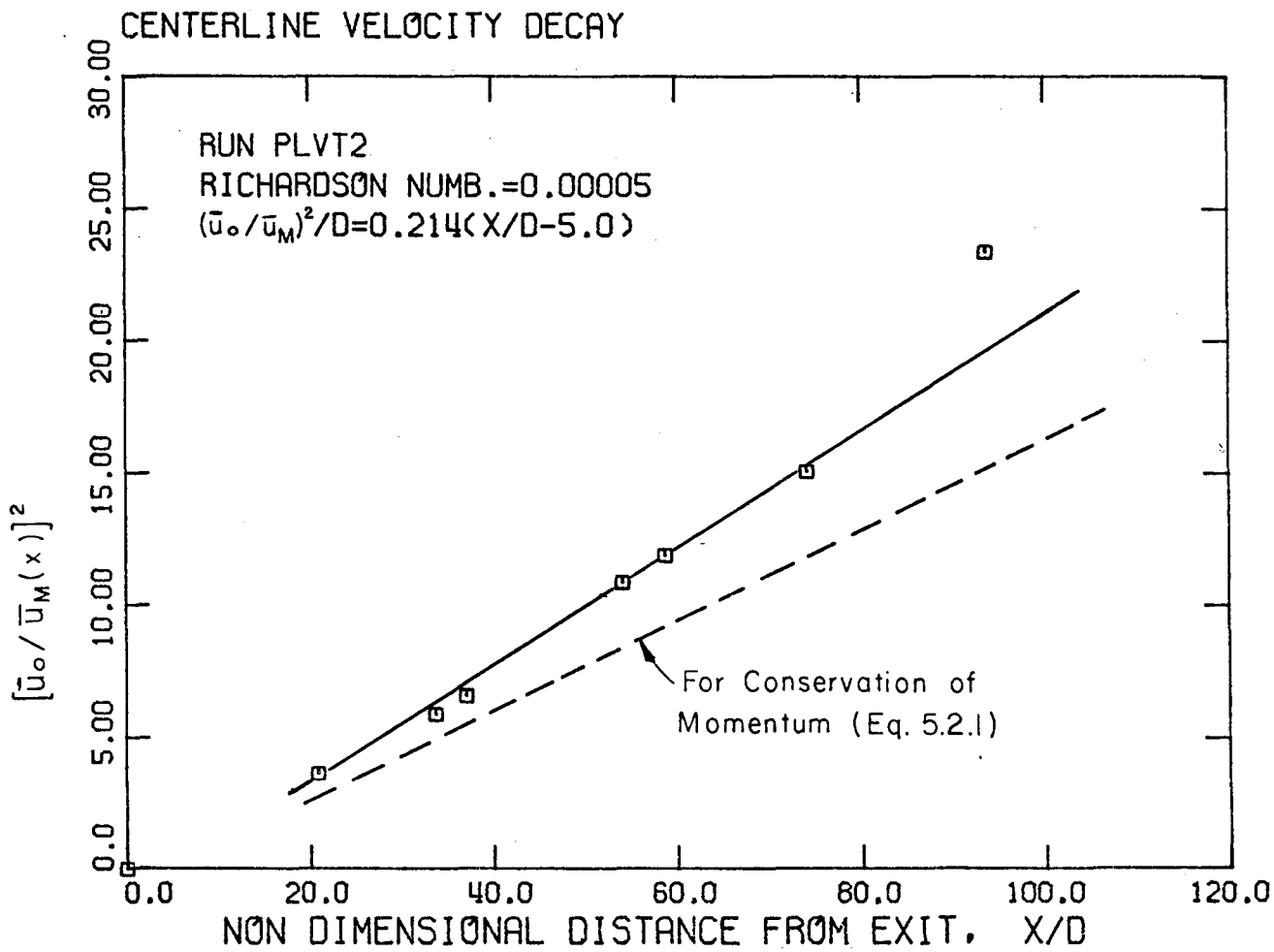

Figure 5.2.2. Velocity distribution along jet axis (R_o = 0).

The results obtained by several previous investigators are given in Table 5.2.1. An explanation of the data of the columns is as follows:

Column 1 gives the name of the investigator while the number in parentheses refers to the reference number.

Column 2 gives the geometrical configuration of the jet, i.e., out of a wall or without a wall (see Figure 5.2.4).

Column 3 gives the distance of the closest measurement to the exit, ℓ_{min} (see Figure 5.2.4).

Column 4 gives the distance of the most distant (from the exit) measurement, ℓ_{max} (see Figure 5.2.4).

Columns 5 and 6 give the coefficients K_{1u}, K_{2u} (see Eq. 5.1.2).

Columns 7 and 8 give the coefficients C_{1u}, C_{2u} (see Eq. 5.2.2).

Column 9 gives the ratio Eq. 5.2.3 for $x = \ell_{max}$.

$$\frac{m(\ell_{max})}{m_o} = \sqrt{\frac{\Pi}{2\ell n 2}} \; \frac{K_{1u}\left(\frac{\ell_{max}}{D} + K_{2u}\right)}{C_{1u}\left(\frac{\ell_{max}}{D} + C_{2u}\right)} \quad . \tag{5.2.5}$$

Column 10 gives the ratio $m(x)/m_o$ for $\frac{x}{D} >> 1$, i.e., Eq. 5.2.4.

A careful examination of the ratio $m(x)/m_o$ (Table 5.2.1) for the experimental results of many experimenters who investigated a pure two-dimensional jet out of a wall confirms the failure of the conservation of momentum argument. It is believed that the reason why the coefficients C_{1u}, C_{2u}, K_{1u}, K_{2u} and the ratio $m(x)/m_o$ varies considerably from investigator to investigator, is the non-self-preserving character of the two-dimensional pure jet, as will be clarified in

Experimenter	Geometry of the Jet	$\frac{\ell_{min}}{D}$	$\frac{\ell_{max}}{D}$	K_{1u}	K_{2u}	C_{1u}	C_{2u}	$\frac{m(\ell_{max})}{m_o}$	$\frac{m(x)}{m_o}$
1	2	3	4	5	6	7	8	9	10
Miller et al [12]	Out of a wall	1	40	0.096	1.57	0.181 0.163	-0.62 1.05	0.83 0.89	0.79 0.88
Heskestad [5]	>>	47	155	0.110	-4.2	0.27	-10.0	0.63	0.61
Goldshmidt [10]	>>	15	67	0.099	0.66	0.207	-5.8	0.80	0.72
Jenkins-Goldshmidt [8]	>>	10	60	0.088	4.5	0.16	4.0	0.83	0.83
Zijnen [38]	>>	10 10	40 35	0.096 0.099	0.6 1.7	0.162 0.205	0.6 1.7	0.89 0.72	0.89 0.72
Forthmann [3]	>>	0	25	0.096	0.50	0.18	0.11	0.88	0.80
Nakaguchi [37],[59]	>>	10	100	0.106	-0.3	0.189	-0.3	0.84	0.84
Knystautas [7]	>>	50	295	0.106	-1.5	0.18	-1.4	0.88	0.88
Householder [44]	>>	?	?	0.091	1.46	0.193	-6.98	0.70(?)	0.70
Bicknell [57]	No wall	15	126	0.115	-2.70	0.112	6.70	1.45	1.53
Present Study Run P-7	Out of a wall	14	37	0.087	6.7	0.17	1.72	0.87	0.77
Present Study Run PLVT2	>>	20	94	0.109	-2.5	0.214	-5.0	0.77	0.76

Table 5.2.1. The kinematic momentum flux of a plane pure jet.

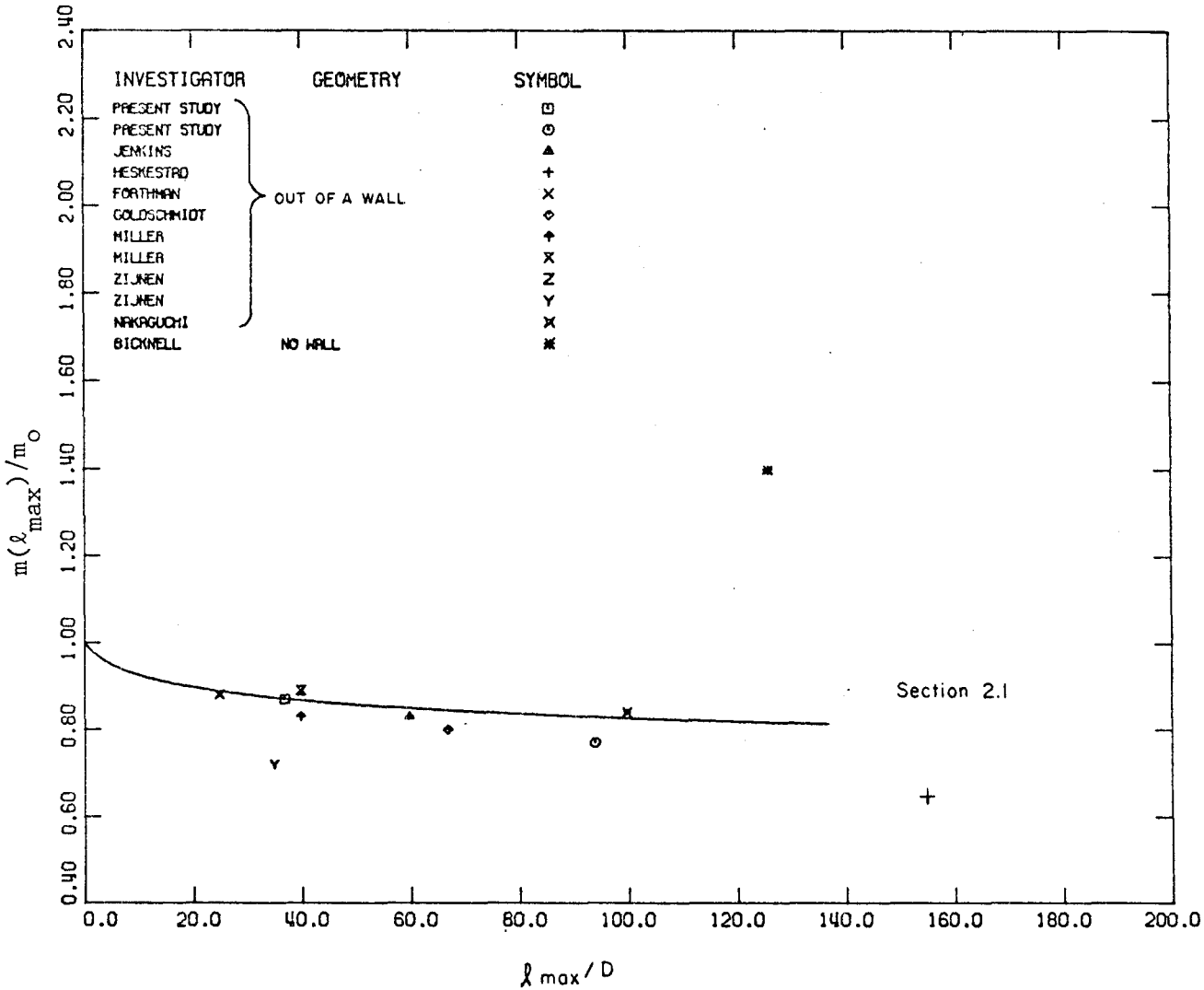

Figure 5.2.3. Kinematic momentum flux m(x) of a two-dimensional turbulent jet (R_o = 0) as a function of distance ℓ_{max}/D and jet geometry.

Chapter 8. The Figure 5.2.3 demonstrates essentially that the momentum ratio $m(\ell_{max})/m_o$ from different investigators is correlated with ℓ_{max}/D (where ℓ_{max} is the most distant measurement of the centerline velocity from the jet exit). In fact, it can be seen that $m(x)/m_o$ decreases as x increases.

It is interesting to notice that Bicknell (see Table 5.2.1), who investigated a pure two-dimensional jet without a wall, obtained the result that the ratio $m(x)/m_o$ is greater than one, i.e., the momentum flux in the jet increased. This agrees with the theory proposed in Section 2.1 because the momentum of the induced flow is now in the same direction with the input momentum, see Figure 5.2.4.

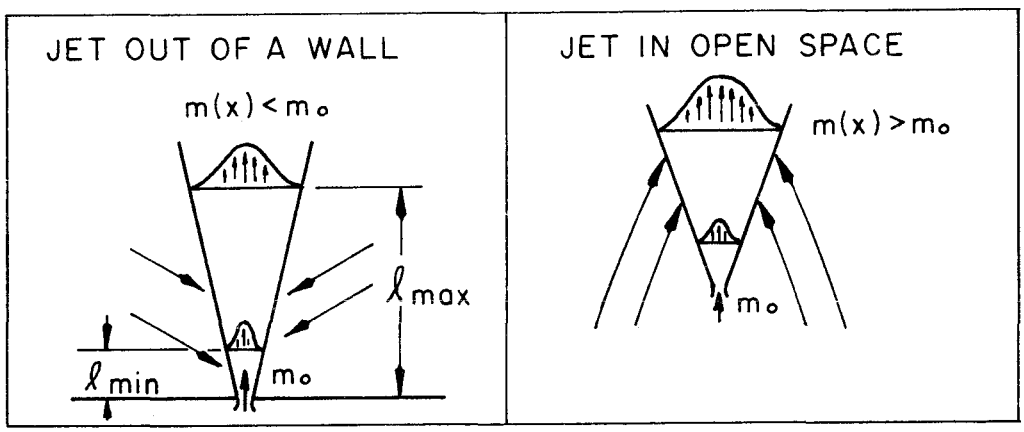

Figure 5.2.4 Schematic of the induced flow by a two-dimensional pure jet.

It can be observed from Figures 5.2.1 and 5.2.3 that the solution of the mathematical model developed in Chapter 2.1 underestimates the decay of the kinematic momentum flux. A definite explanation for this is not presently available but one possible cause is that the

theoretical prediction is based on a first approximation with external streamlines meeting the axis of the jet at $\phi = \pi/4$ for all x. A second order approximation should find that the angle ϕ should increase as x increases. This can be observed in the interesting picture of Lippisch ([29], his Figure 22). When ϕ increases the rate of decrease of the kinematic momentum flux increases, as is obvious from Eq. 2.1.16.

5.3 CENTERLINE VELOCITY OF A PLUME

It was shown in Chapter 2.2 that for a pure plume the centerline mean velocity $\overline{u}_M$ is related to the kinematic buoyancy flux $\beta(x)$ by

$$\overline{u}_M = \sigma_u \beta(x)^{1/3} , \qquad (5.3.1)$$

where σ_u is an experimental constant. The kinematic buoyancy flux $\beta(x)$ is given by

$$\beta(x) = \frac{\alpha(x) g H_o}{\rho_o c_p} , \qquad (5.3.2)$$

where the thermal expansion coefficient $\alpha(x)$ is calculated from the algebraic relation Eq. 2.2.5 at a temperature

$$\theta = T_a + \overline{T}_c , \qquad (°C)$$

and where

$$\overline{T}_c = \frac{H_o}{\rho_o c_p \mu(x)} .$$

$\overline{T}_c$ can be considered as a cross sectional mean temperature.

The basic experimental results for the centerline mean velocity

$\overline{u}_M$ (cm/sec), and the kinematic buoyancy flux $\beta(x)/\beta_o$ (where $\beta_o = \alpha_o g H_o/\rho_o c_p$) are given in Table 5.1.2. The value of σ_u calculated from the values of $\overline{u}_m$ and $\beta(x)$ given in Table 5.1.2 is plotted in Figure 5.3.1. σ_u was found to be constant with the value

$$\sigma_u = \frac{\overline{u}_M}{\beta^{1/3}} = 1.66 \pm 0.04 \qquad (5.3.3)$$

5.4 THE FREQUENCY DISTRIBUTION OF THE VELOCITY

The frequency distribution of the velocity was generated by taking many sweeps of the spectrum analyser using the process described in Chapter 3.2, part III. Two representative cases of the frequency distribution of the velocity are plotted in Figure 5.4.1 (plume) and Figure 5.4.2 (jet).

The occurrence of "negative" velocities (i.e., velocities with direction opposite to the jet flow) was observed on the oscilloscope of the spectrum analyser while an estimation of their probability can be obtained from the figures. There are two possible mechanisms for the generation of such negative velocities. First, large vortices produced at the edge of the jet near the exit could contain velocities larger than the advection velocity of the vortex. Second, the external induced flow has a reverse component as can be seen in the flow visualization experiments by Lippisch [29].

5.5 TURBULENCE INTENSITY

An estimation of the turbulent intensity of the velocity fluctuations $\overline{u'^2}$ can be obtained from the frequency distribution of the

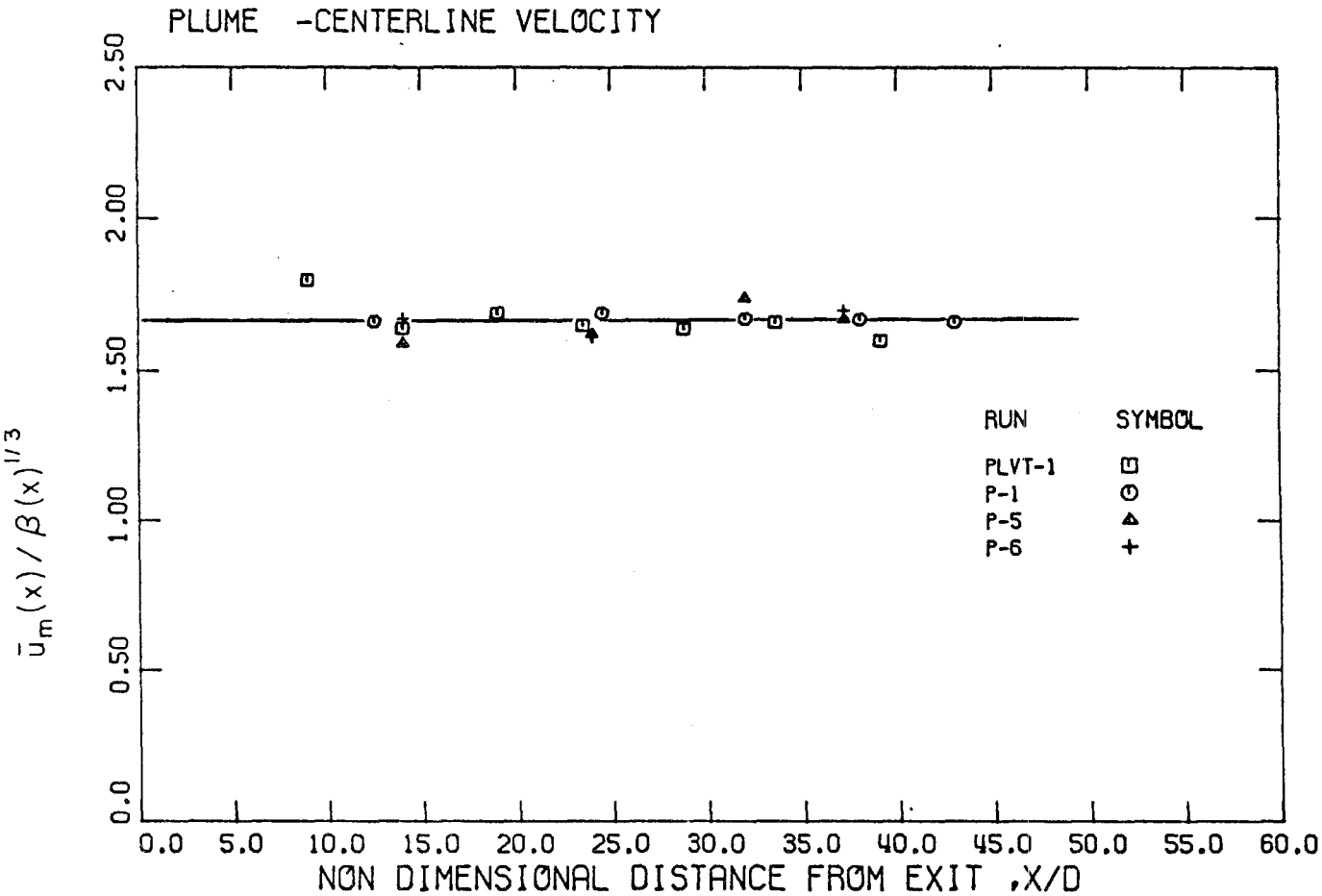

Figure 5.3.1. Velocity distribution along plume axis.

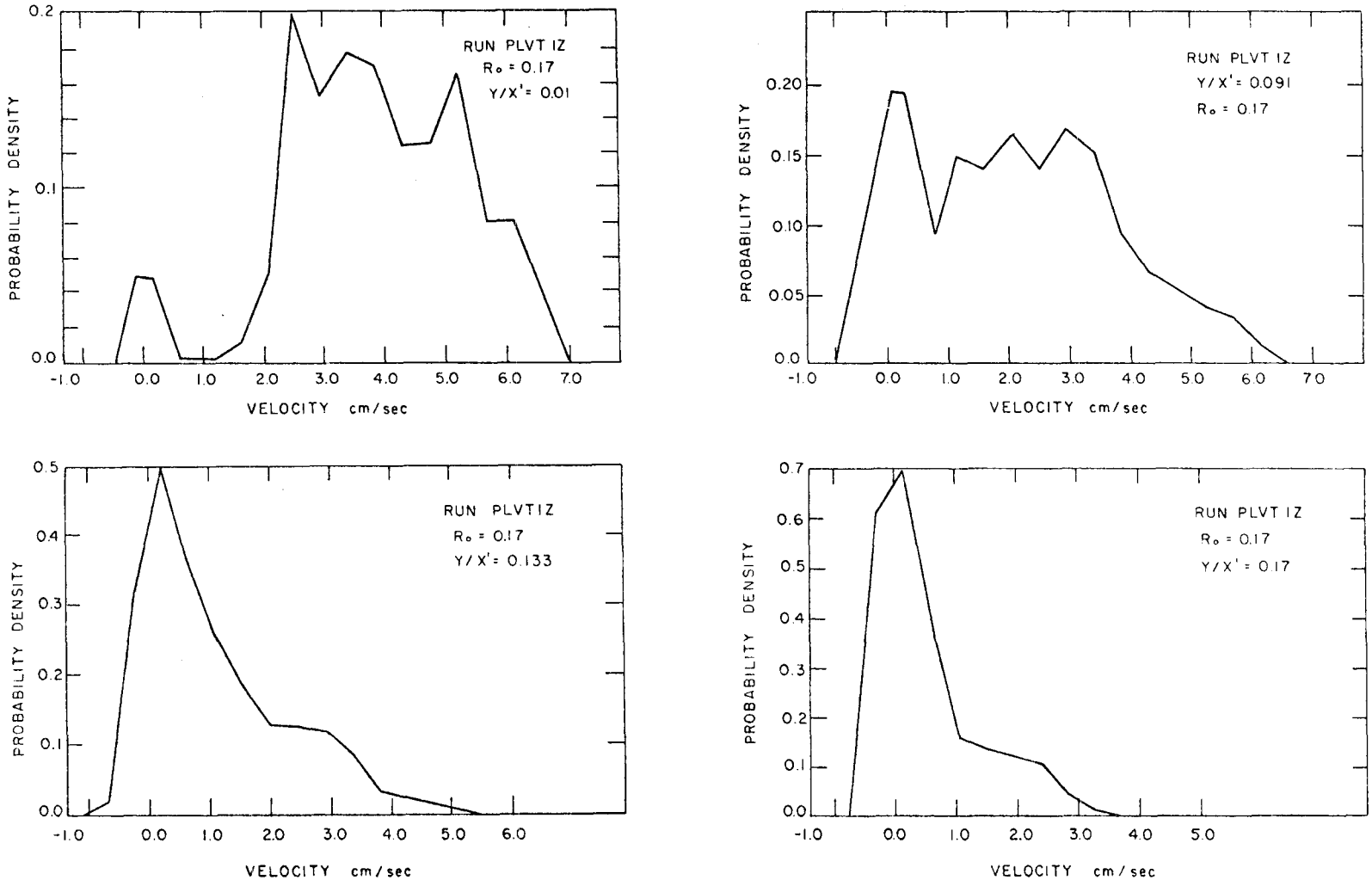

Figure 5.4.1. Probability density of the velocity for a turbulent plume as a function of distance from jet axis.

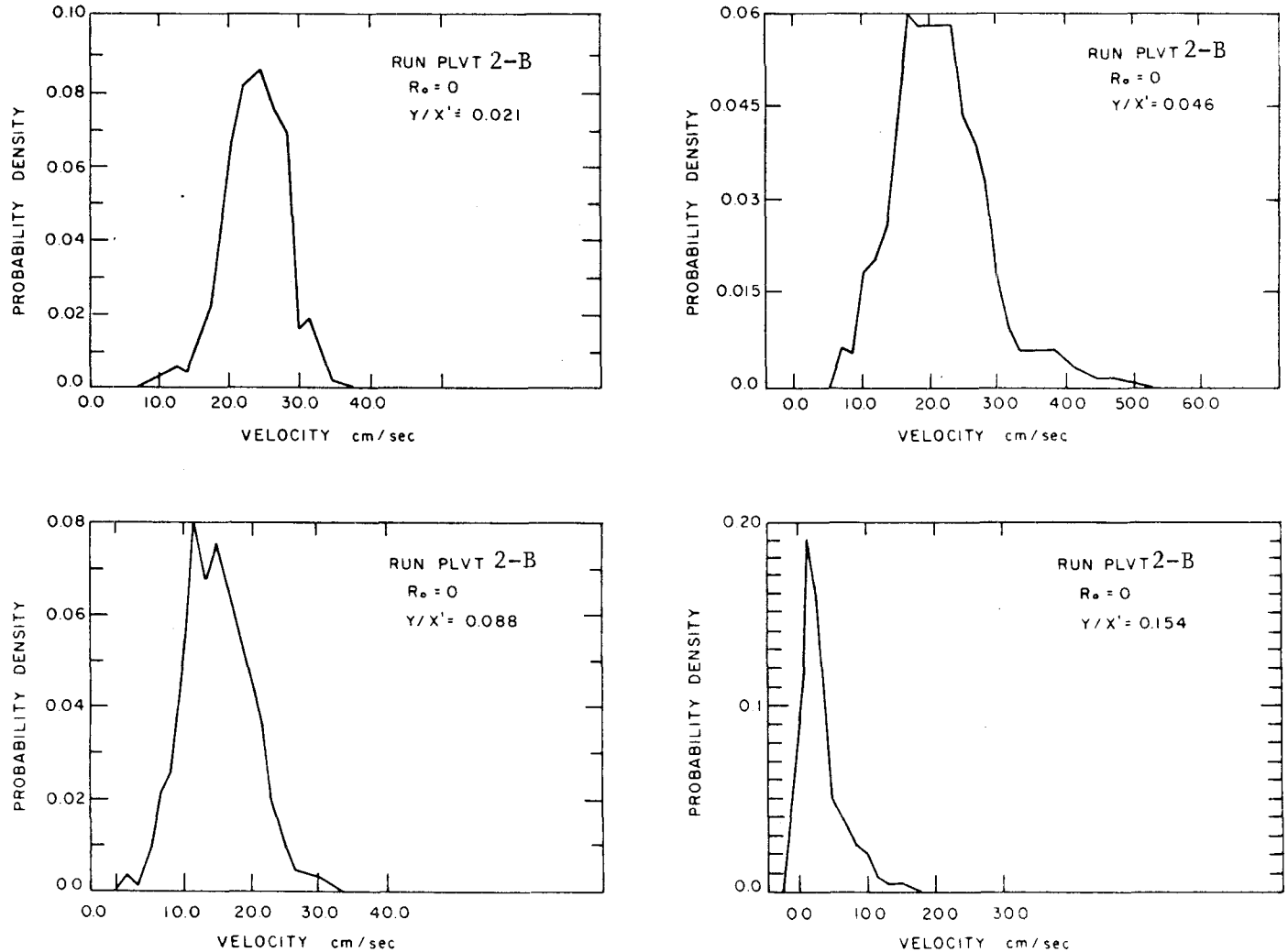

Figure 5.4.2. Probability density of the velocity of a turbulent jet as a function of distance from jet axis.

velocity. The turbulence intensity $\overline{u'^2}$, normalized by the mean velocity on the jet axis, is plotted against y/b_u (where b_u the velocity half-width) in Figure 5.5.1 for the case of a pure jet, and in Figure 5.5.2 for the case of a plume. It can be observed that the effect of the buoyancy is an increase in the relative turbulent intensity. Similar results concerning the turbulent intensity of the temperature fluctuations were described in Chapter 4.2.

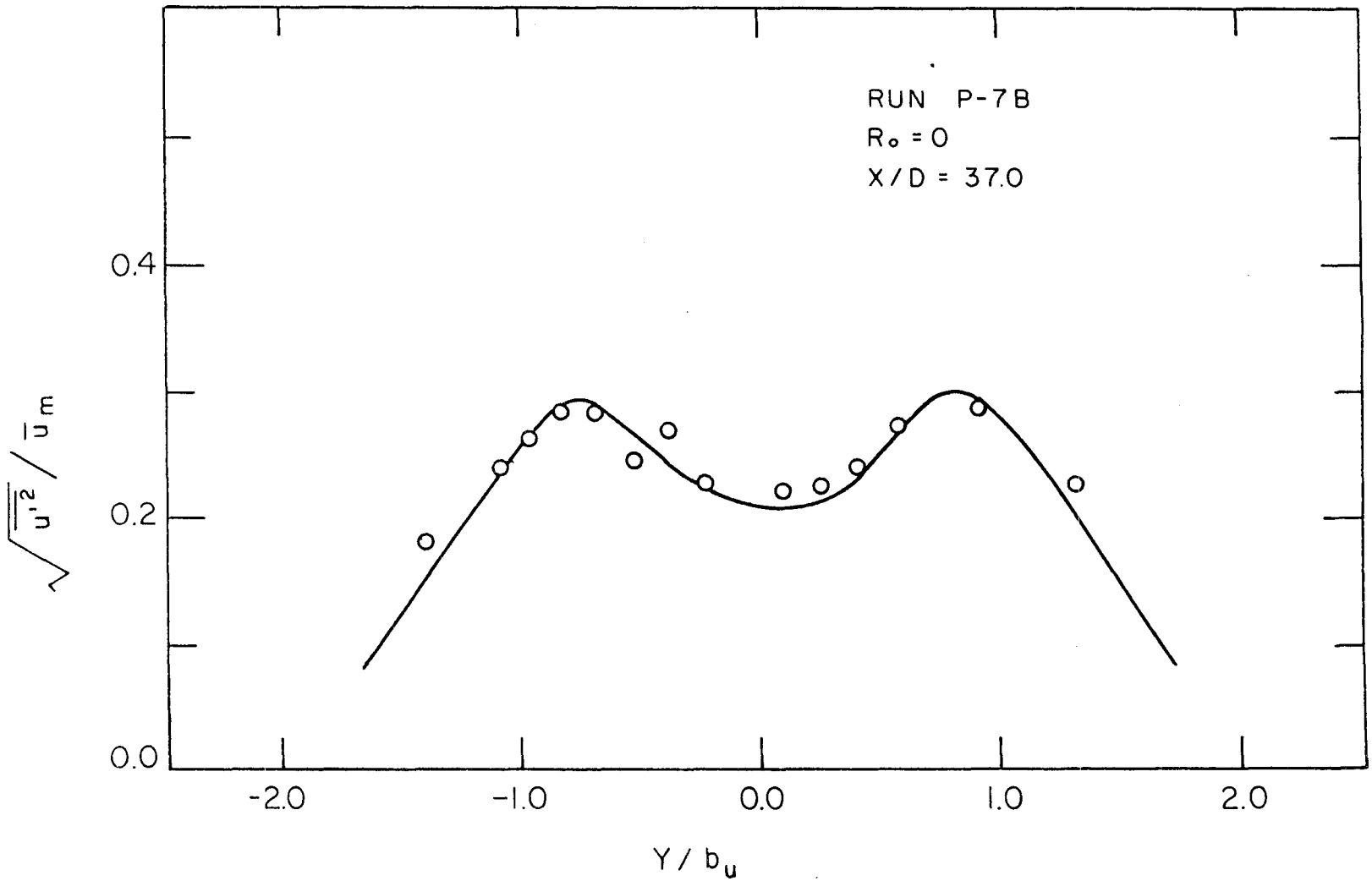

Figure 5.5.1. Profile of the intensity of turbulent fluctuations of the velocity in a turbulent jet.

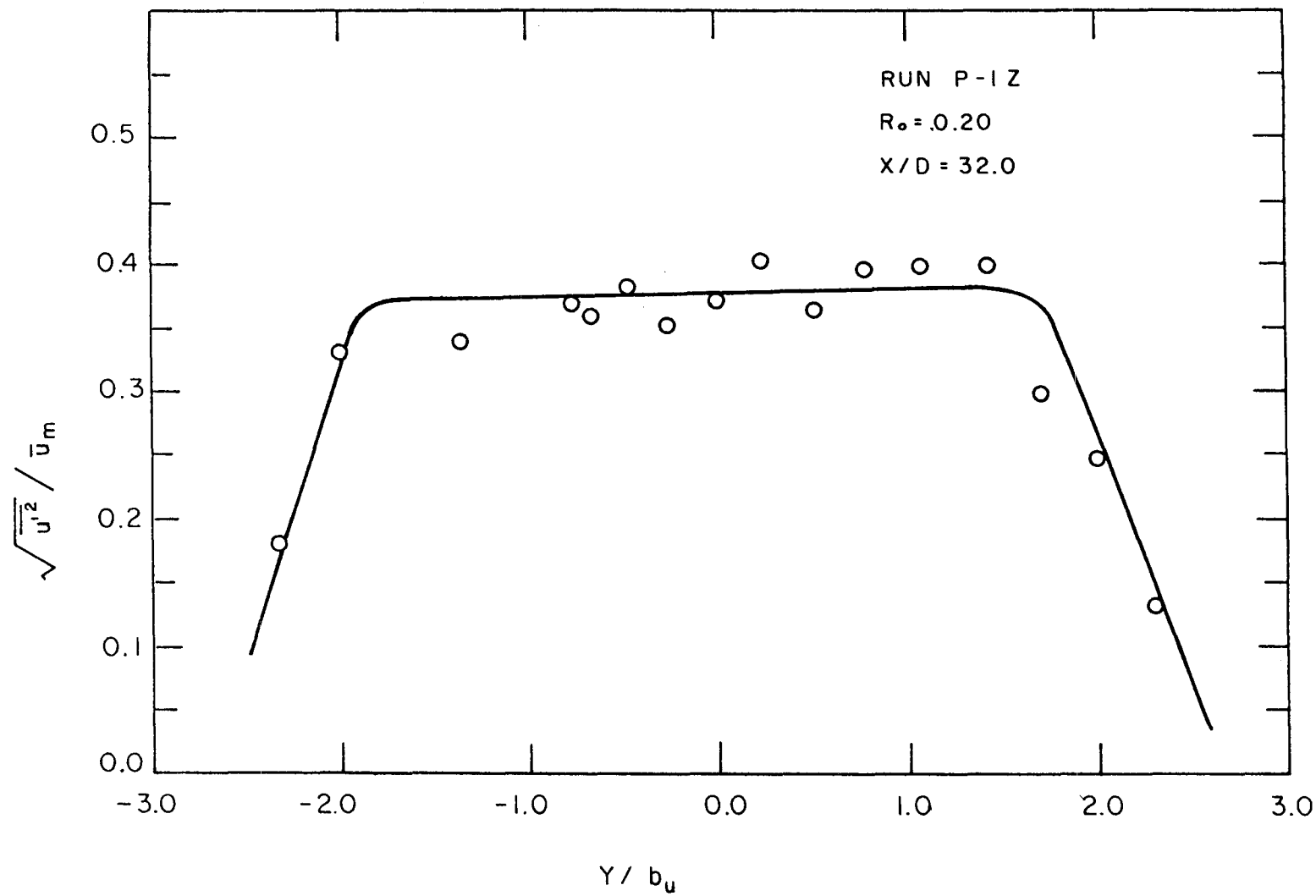

Figure 5.5.2. Profile of the intensity of turbulent fluctuations of the velocity in a turbulent plume.

6. VELOCITY-TEMPERATURE EXPERIMENTAL RESULTS AND DISCUSSION

6.0 BASIC EXPERIMENTAL PARAMETERS-INITIAL DATA

The velocity and the temperature were measured simultaneously using the instrumental set-up described in Chapter 3.4 (Figures 3.4.4.a-c). Complete information concerning the basic experimental parameters is given in Table 6.0.1.

TABLE 6.0.1 Basic parameters of velocity-temperature measurement

Run	D cm	Aspect ratio	$\bar{u}_o$ cm/sec	$\bar{T}_o$ °C	T_a °C	R_e	R_o
PLVT2-E	0.24	54.2	62.93	3.45	21.6	1680	0.00005
PLVT2-Z	0.24	54.2	62.0	5.40	21.8	1780	0.00009
PLVT2-H	0.24	54.2	62.93	3.80	22.2	1760	0.00006
PLVT2-A	0.24	54.2	62.63	6.85	23.25	1900	0.0001
PLVT3-B	0.24	54.2	64.20	9.20	23.2	593	0.0019
PLVT3-A	0.24	54.2	62.93	10.40	24.0	620	0.0022
PLVT1-E	1.0	13.0	19.0	11.0	22.0	610	0.17
PLVT1-D	1.0	13.0	19.0	11.15	22.0	610	0.17
PLVT1-Z	1.0	13.0	4.55	11.0	22.0	610	0.17
PLVT1-C	1.0	13.0	4.55	10.90	22.0	610	0.17
PLVT1-K	1.0	13.0	4.55	11.15	23.0	620	0.17
PLVT1-B	1.0	13.0	4.55	11.0	22.0	610	0.17
PLVT1-H	1.0	13.0	4.55	11.40	23.0	630	0.17

6.1 MEAN VELOCITY AND MEAN TEMPERATURE PROFILE

The non-dimensional velocity and temperature profiles and the half-widths b_u and b_T are plotted in Figures 6.1.1 and 6.1.2 for a pure jet, and in Figures 6.1.3 and 6.1.4 for a plume. The basic experimental results from each temperature or velocity profile were given previously in Tables 4.1.1, 4.1.2 and Tables 5.1.1, 5.1.2. In Table 6.1.1 the ratio of the temperature half-width b_T to the velocity half-width b_u, and the ratio K_{1T}/K_{1u}, are given for each profile. The interesting conclusion that can be drawn from Figures 6.1.1, 6.1.3 and Table 6.1.1, is that the temperature profile is wider than the velocity profile for a wide range of Richardson numbers ($R \sim 0 \sim 0.6$). Thus the suggestion of Rouse et al [21], that the velocity profile of a pure plume is wider than the temperature profile, is not supported by this investigation. At the present moment, it is not clear what is the mechanism which makes the mean temperature profile wider than the mean velocity profile. The statement which is used by some investigators (see Hinze [34], p.426) that "the spread of heat is much greater than the momentum" should be avoided because the terms "spread of heat" and "spread of momentum" are not well defined for a free turbulent flow. As a matter of fact, a particular mass of cold irrotational fluid without any axial momentum that is engulfed by the jet acquires axial momentum much faster than it is heated. The large vortices which are produced at the edge of the jet contain velocities larger and of opposite direction than the advection velocity of the vortex and may be partially responsible for narrowing the velocity profile.

The heat transport by the mean flow, H_M, can be calculated

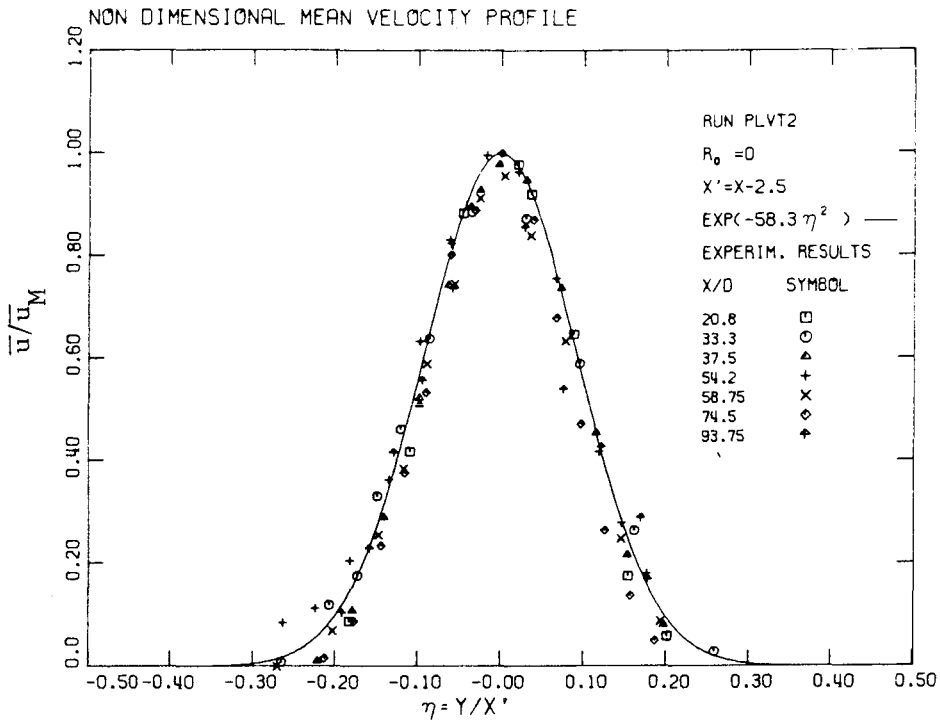

Figure 6.1.1.a. Non-dimensional mean velocity profile in a turbulent jet (R_o = 0).

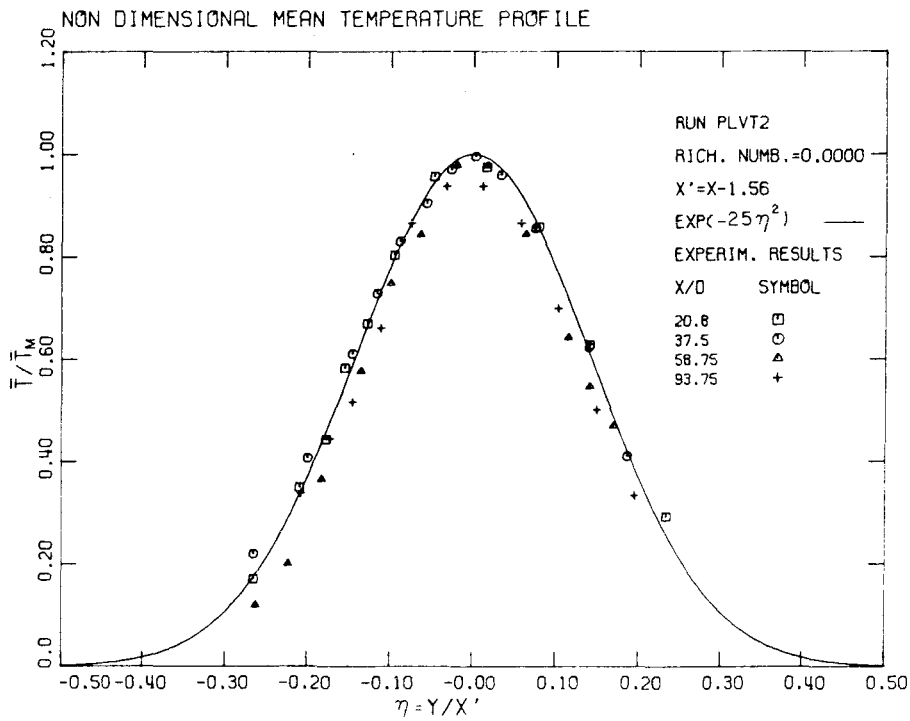

Figure 6.1.1.b. Non-dimensional mean temperature profile in a turbulent jet (R_o = 0).

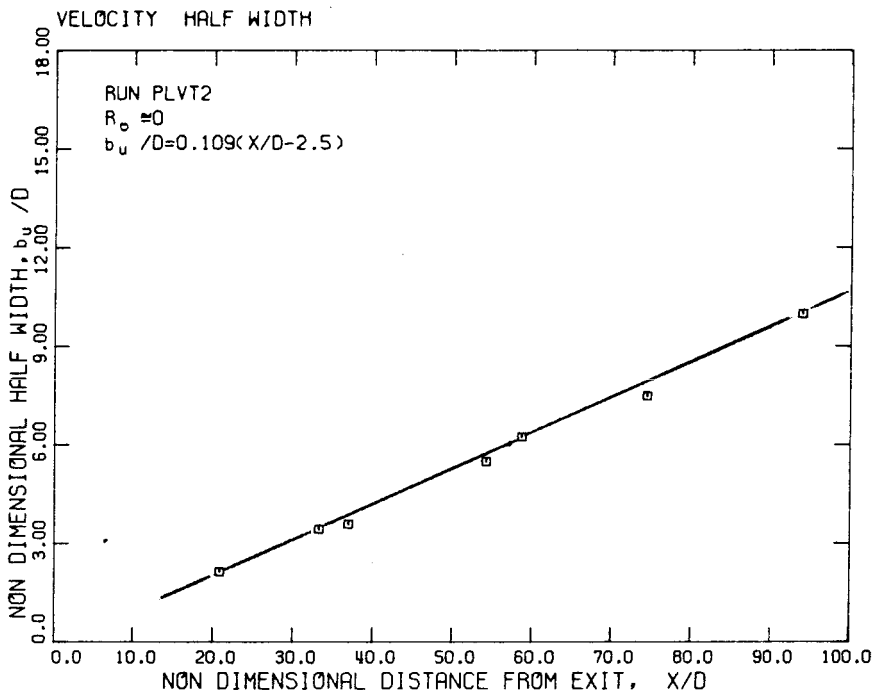

Figure 6.1.2.a. Velocity half-width of a jet ($R_o \approx 0$) as a function of distance along the jet.

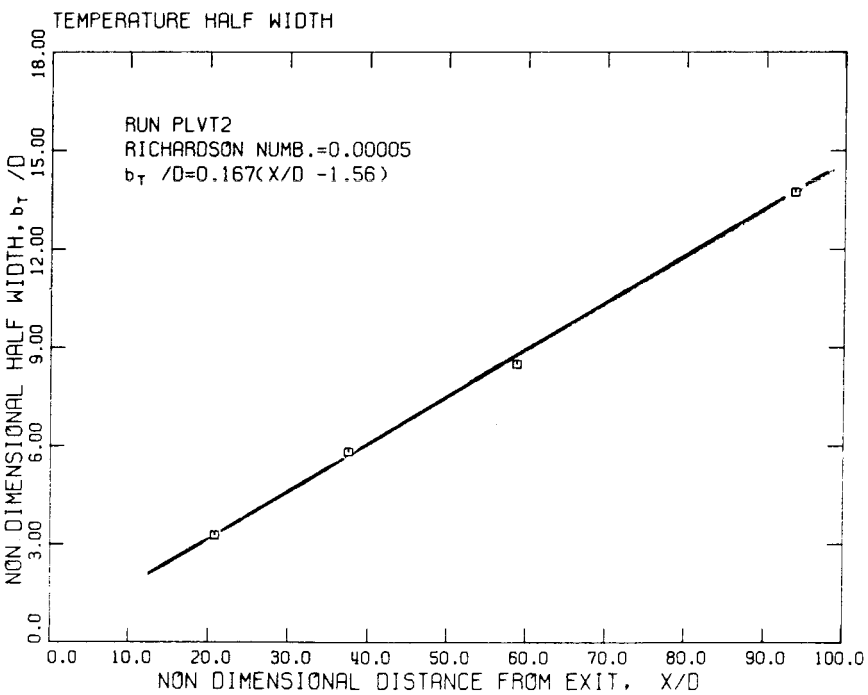

Figure 6.1.2.b. Temperature half-width of a jet ($R_o \approx 0$) as a function of distance along the jet.

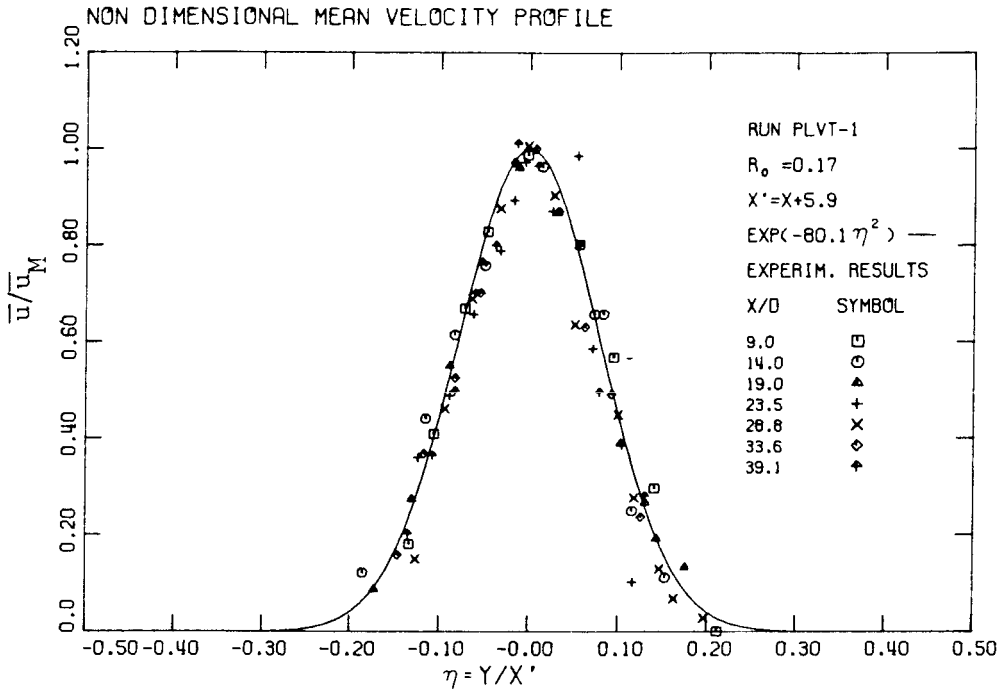

Figure 6.1.3.a. Non-dimensional mean velocity profile in a turbulent plume.

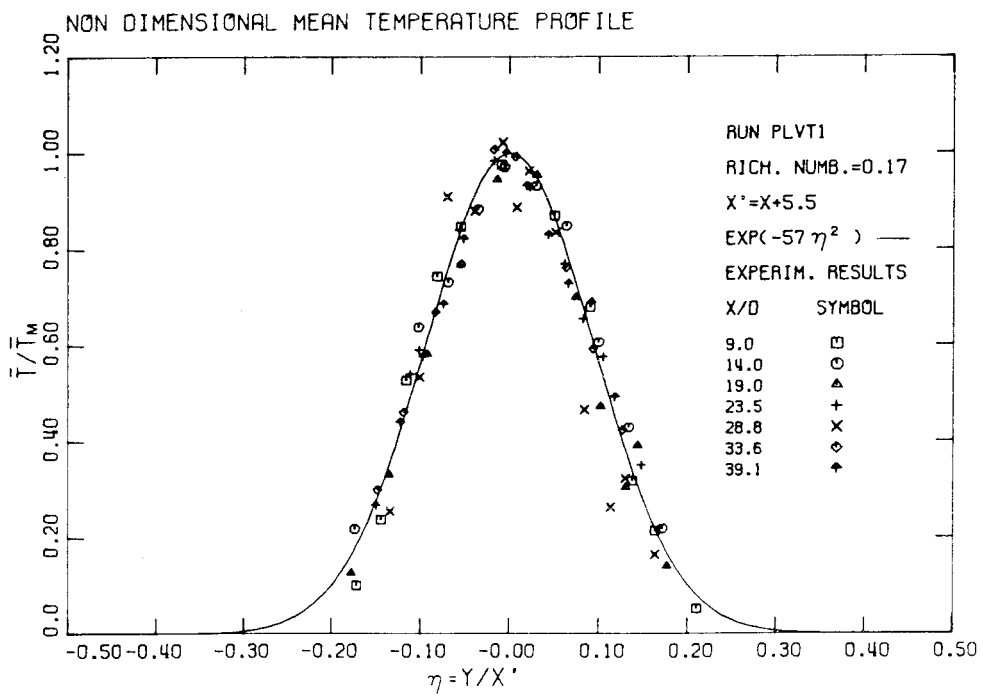

Figure 6.1.3.b. Non-dimensional mean temperature profile in a turbulent plume.

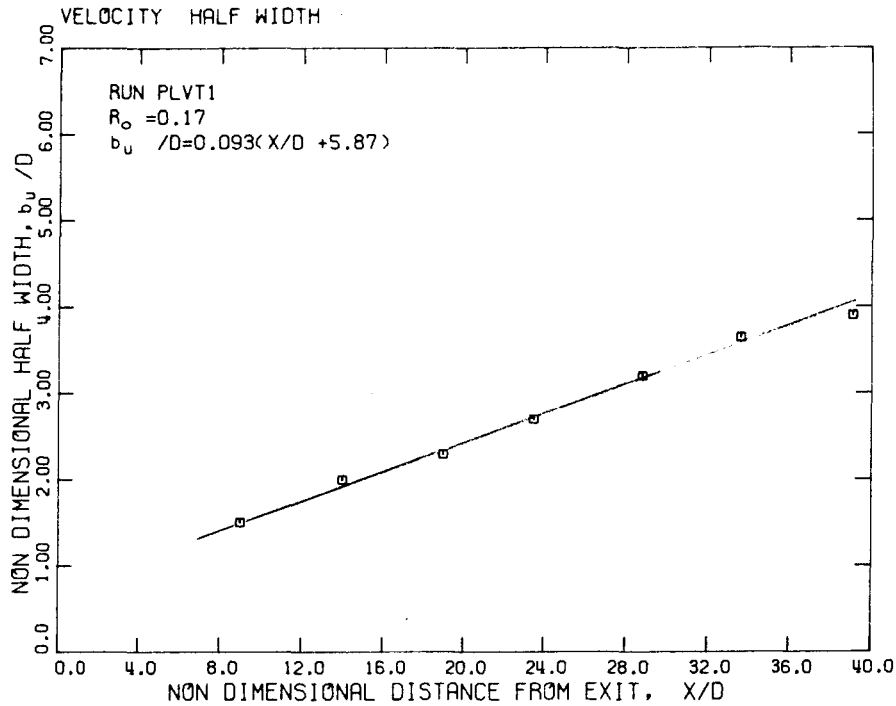

Figure 6.1.4.a. Velocity half-width of a plume as a function of distance along the plume.

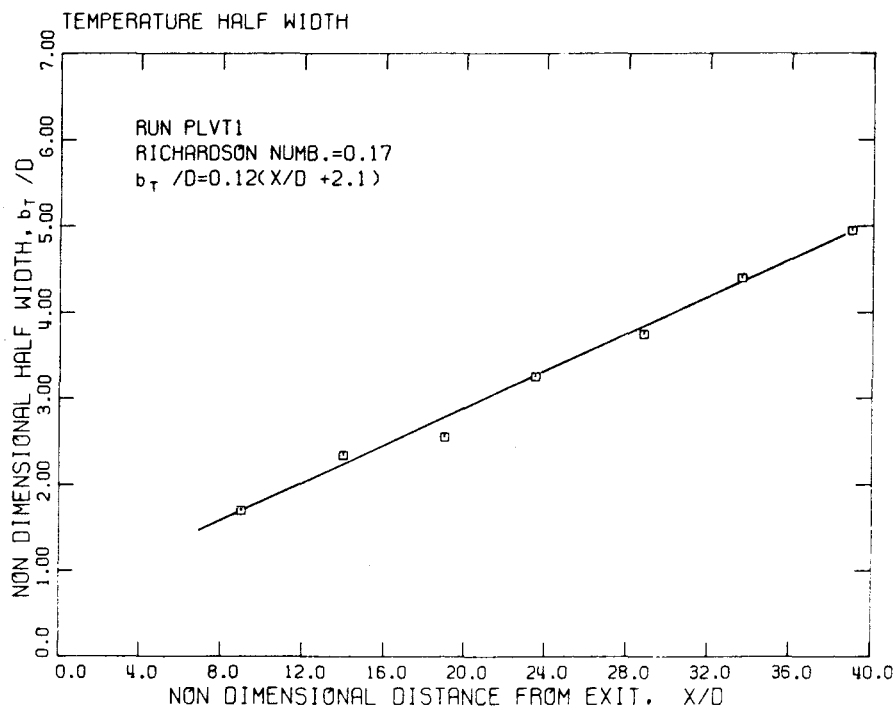

Figure 6.1.4.b. Temperature half-width of a plume as a function of distance along the plume.

Run	R(X)	$\frac{X}{D}$	$\frac{b_T}{b_u}$	$\frac{K_{1T}}{K_{1u}}$	$\frac{H_T}{H_o}$
PLVT2-E	0.001	20.8	1.54	1.53	0.06
PLVT2-Z	0.004	37.0	1.65	1.53	0.06
PLVT2-H	0.006	58.7	1.43	1.53	0.08
PLVT2-A	0.034	93.7	1.38	1.53	0.06
PLVT3-B	0.058	33.7	1.38	1.33	0.10
PLVT3-A	0.189	93.7	1.24	1.33	0.12
PLVT1-E	0.482	9.0	1.13	1.29	0.21
PLVT1-D	0.64	14.0	1.17	1.29	0.24
PLVT1-Z	0.59	19.0	1.10	1.29	0.38
PLVT1-C	0.62	23.5	1.20	1.29	0.32
PLVT1-K	0.64	28.8	1.17	1.29	0.44
PLVT1-B	0.61	33.6	1.20	1.29	0.41
PLVT1-H	0.68	39.1	1.27	1.29	0.42

Table 6.1.1. Velocity-temperature basic results.

for each measured velocity and temperature profile by using the Gaussian curves Eq. (5.1.1) and Eq. (4.1.1) as a reasonable fit to the experimental results. In this case

$$H_M = \rho c_p \int_{-B(x)}^{B(x)} \overline{u}(x,y)\overline{T}(x,y)dy =$$

$$\rho c_p \int_{-\infty}^{\infty} \overline{u}_M(x)\ \exp[-\ell n2\ (y/b_u)^2]\ \overline{T}_M(x)\exp[-\ell n2\ (y/b_T)^2]dy$$

$$= \frac{\rho c_p\ \overline{u}_M(x)\ \overline{T}_M(x)\ b_u(x)(\pi)^{1/2}}{(\ell n2)^{1/2}(1 + (b_u/b_T)^2)^{1/2}} \cdot \qquad (6.1.1)$$

Hence the cross sectional heat transport by the turbulence is

$$H_T = \rho c_p \int_{-B(x)}^{B(x)} \overline{u'T'}dy = H_o - H_M \ , \qquad (6.1.2)$$

where H_o the conserved input heat flux. The local Richardson number R(x), see section 5.1, and the ratio $H_T(x)/H_o$ for each experiment are given in Table 6.1.1. The interesting point brought out by these results is that the fraction of heat transported by the turbulence H_T, increases as the local Richardson number increases. For a low local Richardson number $R(x) < 0.01$ (jet)

$$\int_{-B(x)}^{B(x)} \overline{u'T'}dy \approx 0.06 \int_{-B(x)}^{B(x)} \overline{uT}\ dy \ , \qquad (6.1.3)$$

i.e., the turbulent heat transport is a negligible fraction of the longitudinal heat transport for a jet. But for a local Richardson number $R(x) \sim 0.6$ (plume)

$$\int_{-B(x)}^{B(x)} \overline{u'T'} \approx 0.38 \int_{-B(x)}^{B(x)} \overline{uT}\, dy \ ,$$

or

$$\int_{-B(x)}^{B(x)} \overline{u'T'}\, dy \approx 0.6 \int_{-B(x)}^{B(x)} \overline{u}\,\overline{T}\, dy \ . \qquad (6.1.4)$$

Now, given significant distance to develop, any slightly heated jet will eventually become a plume because the initial momentum will be a small fraction of the momentum which will be gained by the continuous action of the buoyancy forces. It was found in Section 2.3 that the importance of the initial kinematic momentum flux relative to the kinematic buoyancy flux is given by the length scale,

$$m_o/\beta_o^{2/3} \ ,$$

which is infinite for a pure jet and zero for a pure plume. A heated jet with low Richardson number at the jet orifice ($R_o << 0.6$), becomes a plume at a distance

$$x >> m_o/\beta_o^{2/3} \ .$$

On the basis of this investigation transition to a plume is assured at any point for which

$$x\beta_o^{2/3}/m_o \geq 10 \ .$$

The turbulent heat transport will increase with the distance x, or the local Richardson number R(x), and eventually for

$$x\beta_o^{2/3}/m_o >> 1 \ ,$$

will be comparable with the heat transport by the mean motion.

Hence, the assumption made by previous investigators ((21), (27), (24), (20)) concerning a pure plume, that

$$\overline{u'T'} \ll \overline{u}\,\overline{T} ,$$

has no physical basis, and the turbulent heat transfer (and consequently the turbulent kinematic buoyancy flux) should not be neglected when a plume is investigated. It should be noted that for a pure plume the transport of heat by the mean flow H_M can be calculated using the expressions

$$\overline{u}_M = 1.66\ \beta(x)^{1/3},$$

for the mean velocity, (see Eq. 5.3.3),

$$\overline{T}_M = 2.4\ \beta(x)^{2/3}/\alpha(x)\ g\ (x - x_{oT}) ,$$

for the mean temperature, (see Eq. 4.1.5), to give

$$H_M = \rho c_p \int_{-B(x)}^{B(x)} \overline{u}(x,y)\ \overline{T}(x,y)dy =$$

$$\rho c_p\ \overline{u}_M\overline{T}_M(x - x_{oT}) \int_{-\infty}^{\infty} \exp\left[-\ell n2\left(1 + \frac{K_{1T}^2}{K_{1u}^2}\right)\left(\frac{y}{K_{1T}x'}\right)^2\right] d\left(\frac{y}{x'}\right)$$

(where $x' = x - x_{oT}$), then using $K_{1T}/K_{1u} \approx 1.3$, $K_{1T} = 0.12$ (see Tables 6.1.1 and 4.1.1)

$$H_M = 0.62\ \rho c_p\ \beta(x)/\alpha(x)g = 0.62\ H_o . \qquad (6.1.5)$$

The ratio H_T/H_o, given in Table 6.1.1, is plotted in Figure 6.1.5. Assuming $H_T = \xi(R)H_o$, expanding $\xi(R) = \xi_o + \xi_1 R + O(R^2)$, neglecting the terms $O(R^2)$, and considering that for a pure jet $\xi(0) = 0.06$, and for a pure plume $\xi(R_p) \approx 0.38$, the turbulent heat transfer as a function of the local Richardson number R(x) is obtained as

$$H_T = (0.06 + 0.51\ R(x))\ H_o\ . \qquad (6.1.6)$$

Hence, the turbulent heat transfer H_T normalized by the initial heat flux H_o can be represented by the following empirical function of the local Richardson number

$$H_T/H_o = 0.06 + 0.51\ R(x)\ , \qquad (6.1.7)$$

which is plotted in Figure 6.1.6 together with experimental results. It follows also from Eq. 6.1.5 that for a plume

$$\int_{-B(x)}^{B(x)} \overline{u'T'}\ dy \approx 0.6 \int_{-B(x)}^{B(x)} \overline{u}\ \overline{T}\ dy\ .$$

6.2 PROFILES OF $\overline{uT}$ AND $\overline{u'T'}$

The purpose of these measurements was to find the profile of the advective heat flux

$$\overline{u(x,y,t)\ T(x,y,t)}\ ,$$

and then to derive the profile of the turbulent heat flux from the relation

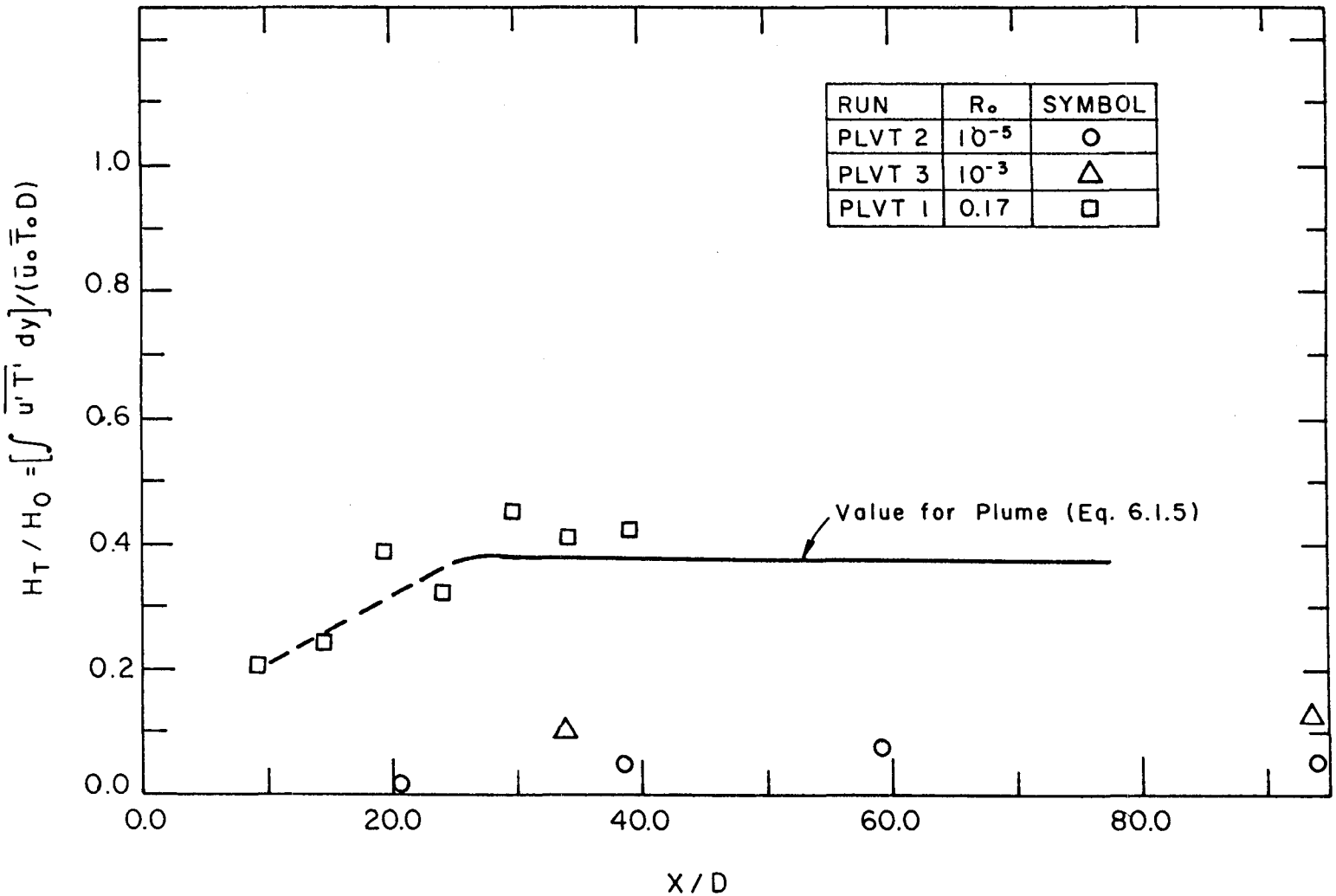

Figure 6.1.5. Turbulent heat flux in a buoyant jet normalized by the heat flux at the jet orifice, as a function of distance along the jet.

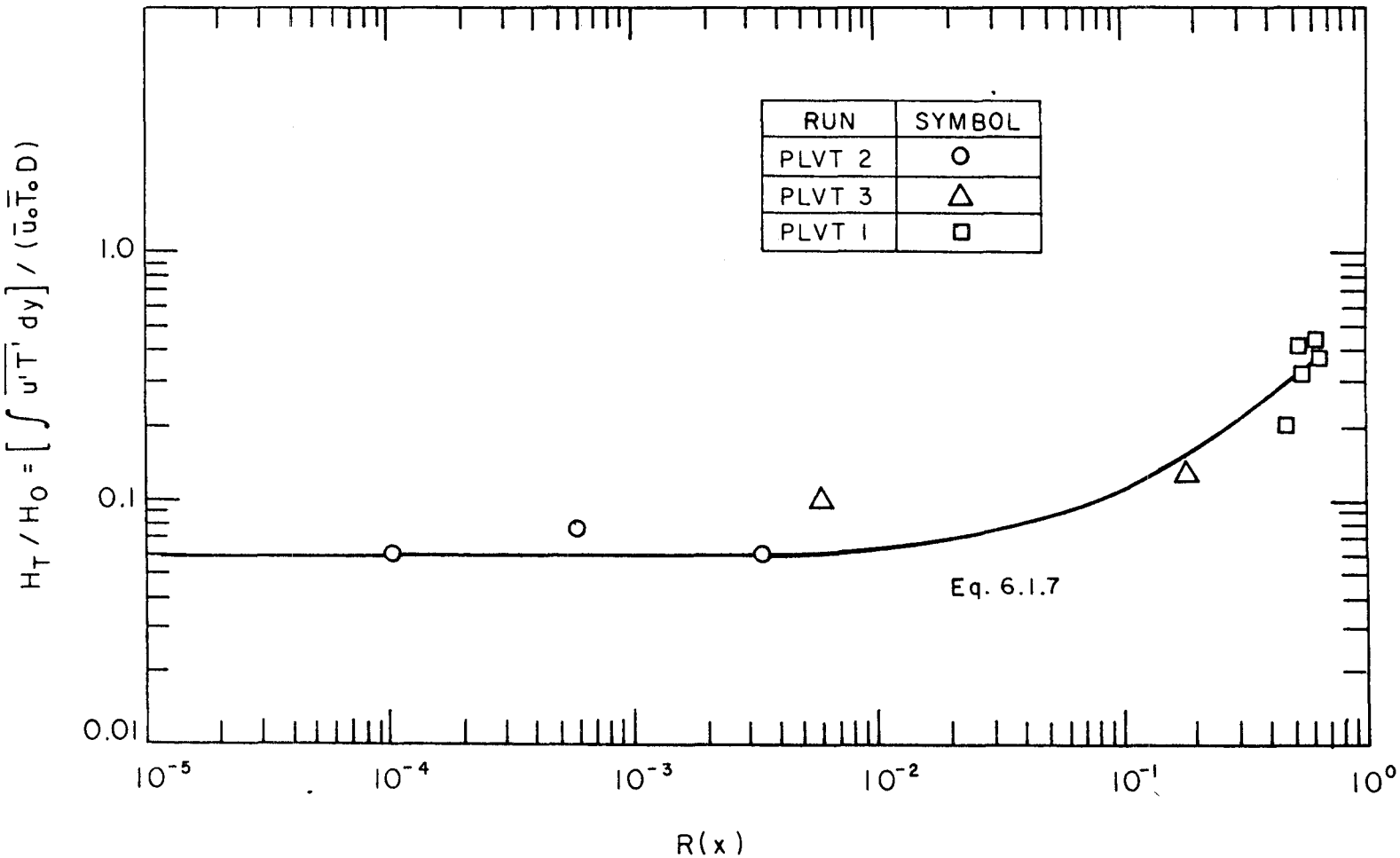

Figure 6.1.6. Turbulent heat flux in a buoyant jet, normalized by the heat flux at the jet orifice, as a function of the local Richardson number.

$$\overline{u'(x,y,t)T'(x,y,t)} = \overline{u(x,y,t)T(x,y,t)} - \overline{u}(x,y)\overline{T}(x,y) \ . \qquad (6.2.1)$$

Ideally one would like to measure

$$R(0,0) = \lim_{t\to\infty} \frac{1}{t} \int_0^t u(x,y,t')T(x,y,t')dt' \ , \qquad (6.2.2)$$

without disturbing the flow (without inserting probes), but this has not yet become possible. In this investigation the velocity was measured at the focal volume (x,y) of two focused beams of a laser Doppler velocimeter, while the temperature was measured with a small (0.4 mm diameter) fast response thermistor located at a point (x+Δx,y). The distance Δx was chosen to be 1-2 mm, the criterion being that the thermistor bead should be close to the focal volume of the laser beams, but not so close as to block the laser light or to disturb the flow. Hence the correlation

$$R(\Delta x,0) = \overline{u(x,y,t)T(x+\Delta x,y,t)} =$$

$$\lim_{t\to\infty} \frac{1}{t} \int_0^t u(x,y,t')T(x+\Delta x,y,t')dt' \ , \qquad (6.2.3)$$

was measured.

The interesting question is how the correlations R(0,0) and R(Δx,0) are related. To the best knowledge of this writer, the correlation R(Δx,0) as a function of Δx has not been examined in a buoyant jet. For a plume the instantaneous velocity u(x,y,t) at a point (x,y) should depend upon the instantaneous buoyancy forces at (x,y) and since the instantaneous buoyancy forces at (x,y) depend upon

the instantaneous temperature $T(x,y,t)$, it follows that the velocity $u(x,y,t)$ and the temperature $T(x,y,t)$ should be very well correlated. Hence the correlation

$$R(0,0) = \lim_{t\to\infty} \frac{1}{t} \int_o^t u(x,y,t)T(x,y,t)dt \quad ,$$

in a pure plume should be larger than the correlation

$$R(\Delta x,0) = \lim_{t\to o} \frac{1}{t} \int_o^t u(x,y,t)T(x+\Delta x,y,t)dt \quad ,$$

because the signals $u(x,y,t)$ and $T(x + \Delta x,y,t)$ are not necessarily well correlated, and

$$\overline{T}(x + \Delta x,y) \approx \overline{T}(x,y) \quad ,$$

(strictly $\overline{T}(x + \Delta x,y) < \overline{T}(x,y)$).

For a pure jet, where the heat behaves as a passive tracer, the fluctuations of the signals of the velocity $u(x,y,t)$ and of the temperature $T(x,y,t)$ should not exhibit any strong correlation, as the experimental results of Corrsin and Uberoi [52] have demonstrated. The schematic of Figure 6.2.1.a-b is expected for the correlation of the fluctuation u', T' for a plume and a jet respectively.

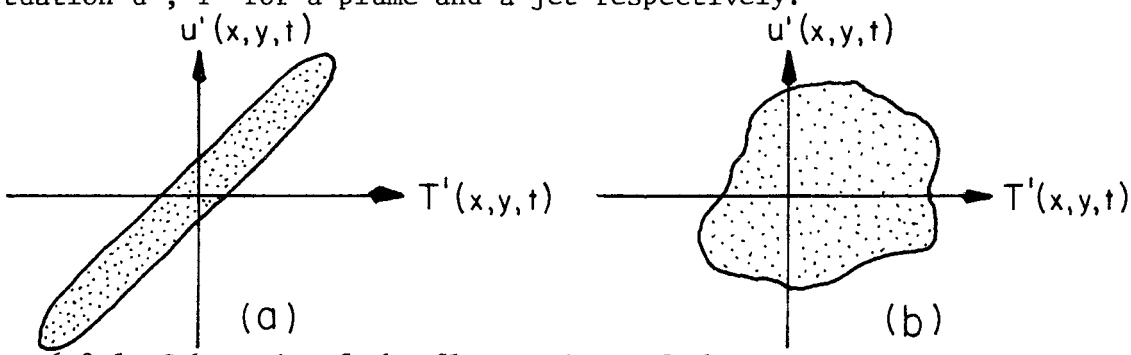

Figure 6.2.1 Schematic of the fluctuations of the temperature $T'(x,y,t)$ and vertical velocity $u'(x,y,t)$; (a) plume (b) jet.

Hence it is expected that for a plume $R(\Delta x,0) < R(0,0)$, but for a jet $R(\Delta x,0) \sim R(0,0)$.

A direct measurement of $R(0,0)$ and comparison with the $R(\Delta x,0)$ was not possible in this investigation. However, a reasonable understanding can be obtained by calculating the integral of $R(\Delta x,0)$ across the jet

$$H_c = \rho c_p \int_{-B(x)}^{B(x)} R(\Delta x,0)dy \ , \tag{6.2.4}$$

and comparing it with the input heat flux H_o. The conservation of the heat flux gives

$$H_o = \rho c_p \int_{-B(x)}^{B(x)} R(0,0)dy \ , \tag{6.2.5}$$

and any deviation from this relation should be attributed to experimental errors (if radiation effects are absent). Since in general $R(\Delta x,0) \neq R(0,0)$ it is expected that

$$H_c \neq H_o \ .$$

It seems reasonable then to assume that

$$\frac{R(0,0)}{R(\Delta x,0)} \approx \frac{\int_{-B(x)}^{B(x)} R(0,0)dy}{\int_{-B(x)}^{B(x)} R(\Delta x,0)dy} \ . \tag{6.2.6}$$

Keeping these preliminary results in mind, the experimental results as they were obtained will be presented, some observations will be made, and then the profile of $\overline{u'T'}$ will be derived. The profile of

the correlation $\rho c_p R(\Delta x,0)$ in cal/sec is plotted in Figures 6.2.2.a-d (jet) and 6.2.3 (plume). The half-width $b_{\overline{uT}}$ was calculated for each profile and a Gaussian curve given by

$$R(\Delta x,0) = R_M \exp[-\ell n2 \ (y/b_{\overline{uT}})^2] \ , \qquad (6.2.7)$$

fitted to the data, where R_M is the value of $R(\Delta x,0)$ on the jet axis. The half-widths $b_{\overline{uT}}(x)$ of the $R(\Delta x,0)$ profiles of a jet were plotted in Figure 6.2.4 and a straight line

$$b_{\overline{uT}}/D = K_{1\overline{uT}}(\frac{x}{D} + K_{2\overline{uT}}) \ ,$$

was fitted. The values of $K_{1\overline{uT}} = 0.105$ and $K_{2\overline{uT}} = -5.0$ were found. The profile of $R(\Delta x,0)$, normalized by R_M was plotted against y/x' in Figure 6.2.5 and a Gaussian curve given by

$$R(\Delta x,0) = R_M \exp[-\ell n2 \ (y/K_{1\overline{uT}}x')^2] \ ,$$

(where $x' = x + K_{2\overline{uT}} \ D$) was fitted. The integral of the correlation $R(\Delta x,0)$ across the jet or plume can be calculated for each profile by

$$H_c = \rho c_p \int_{-B(x)}^{B(x)} R(\Delta x,0)dy \approx \rho c_p \int_{-\infty}^{\infty} R_M \exp[-\ell n2 \ (y/b_{\overline{uT}})^2]dy$$

$$= \rho c_p R_M b_{\overline{uT}} \ (\pi/\ell n2)^{1/2} \ . \qquad (6.2.8)$$

The ratio

$$\frac{H_c}{H_o} \ ,$$

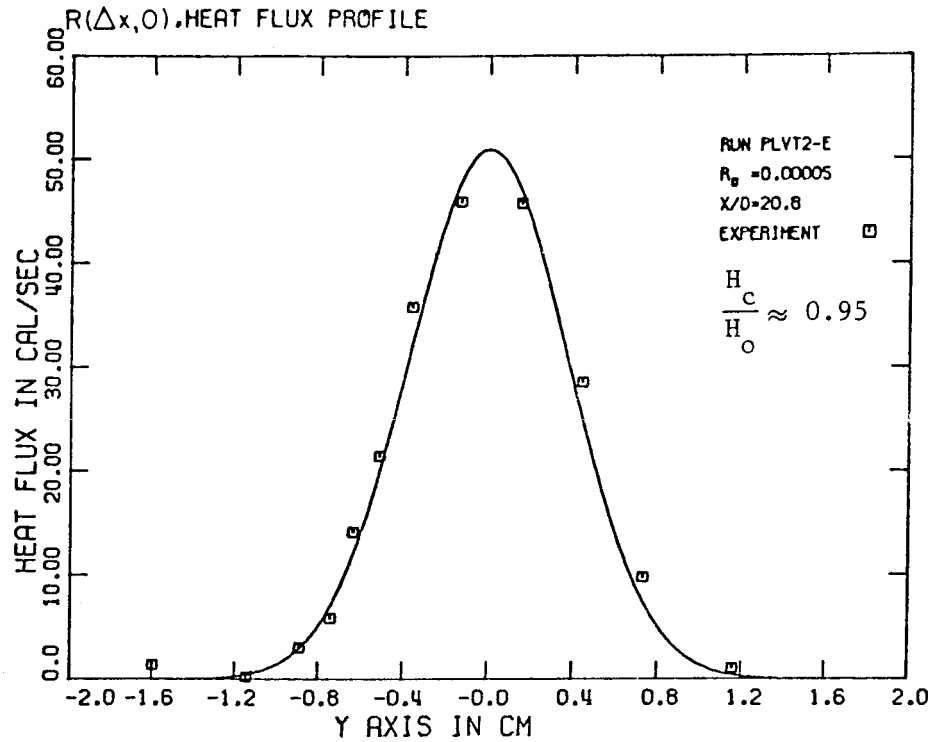

Figure 6.2.2.a. Profile of the correlation $\rho c_p R(\Delta x,0)$ in a turbulent jet at x/D = 20.8.

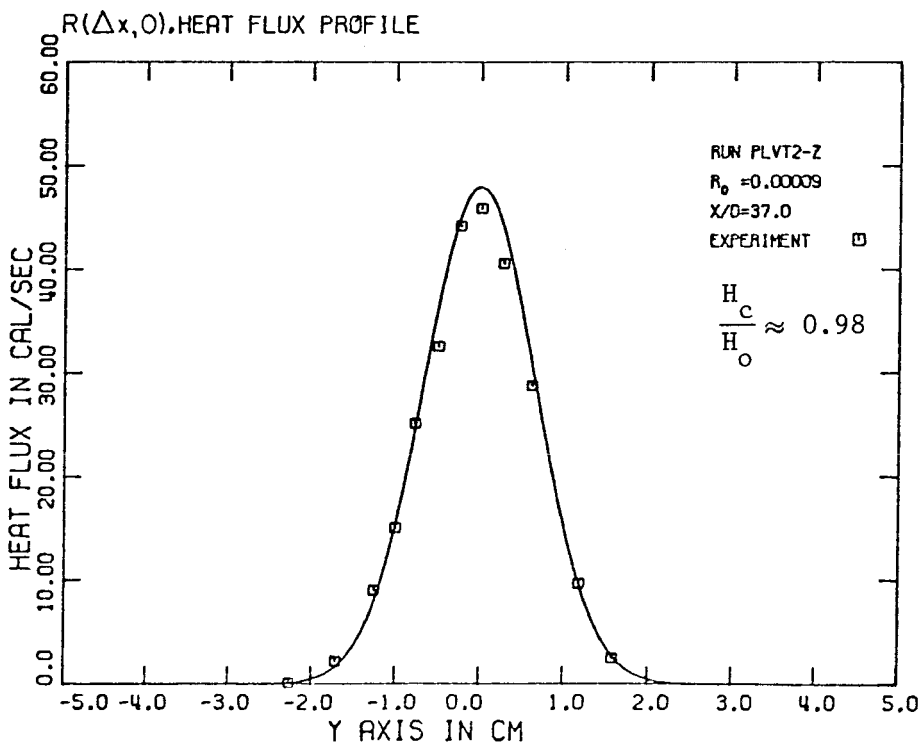

Figure 6.2.2.b. Profile of the correlation $\rho c_p R(\Delta x,0)$ in a turbulent jet at x/D = 37.0.

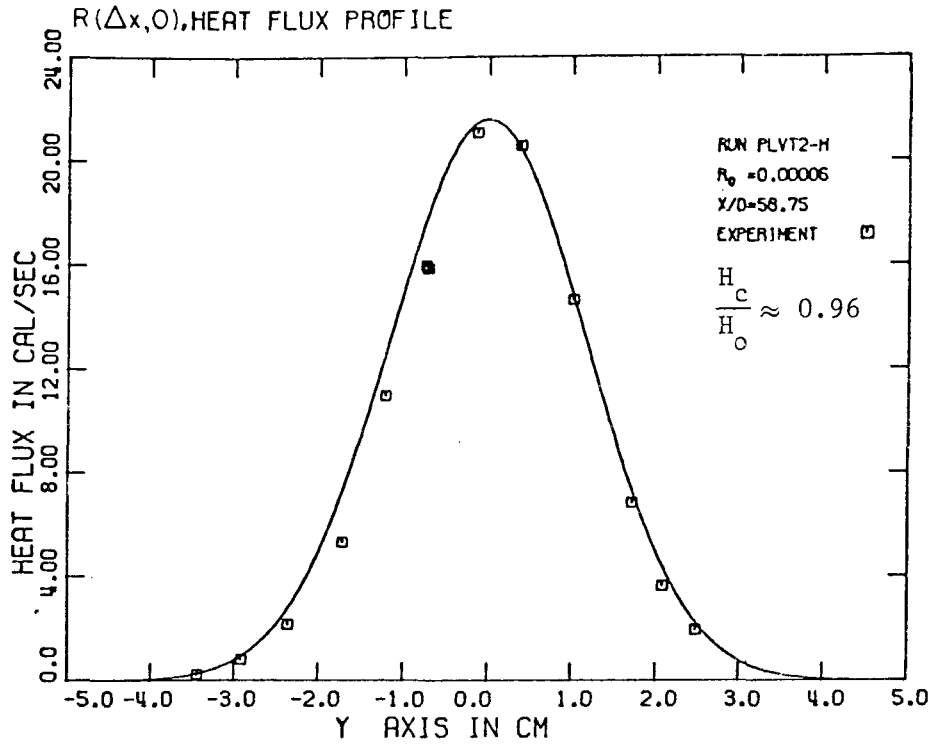

Figure 6.2.2.c. Profile of the correlation $\rho c_p R(\Delta x,0)$ in a turbulent jet at x/D = 58.75.

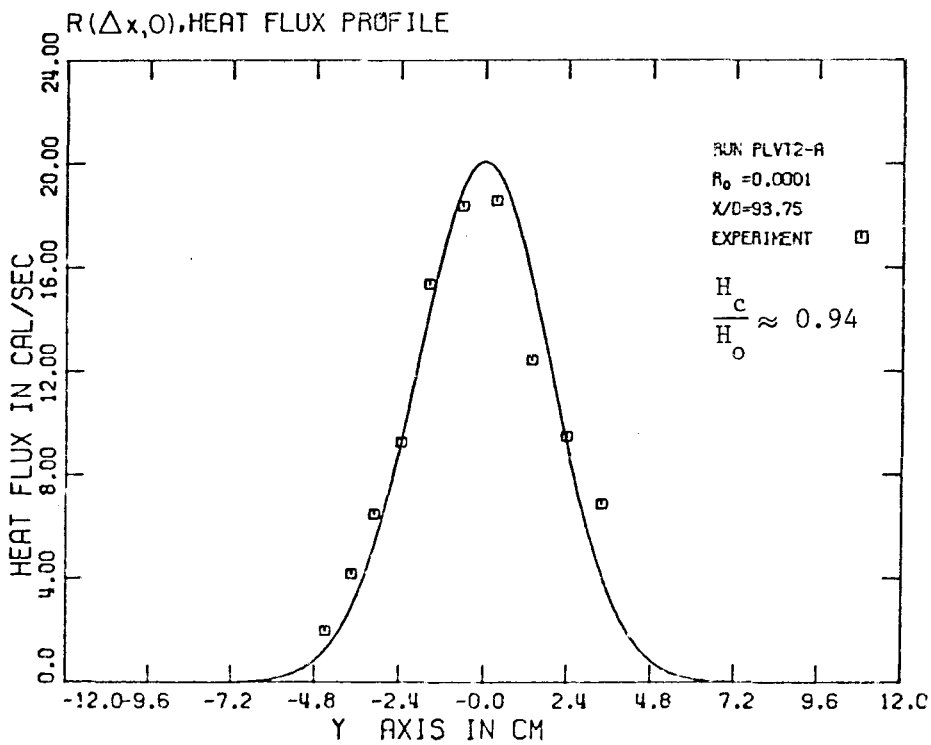

Figure 6.2.2.d. Profile of the correlation $\rho c_p R(\Delta x,0)$ in a turbulent jet at x/D = 93.75.

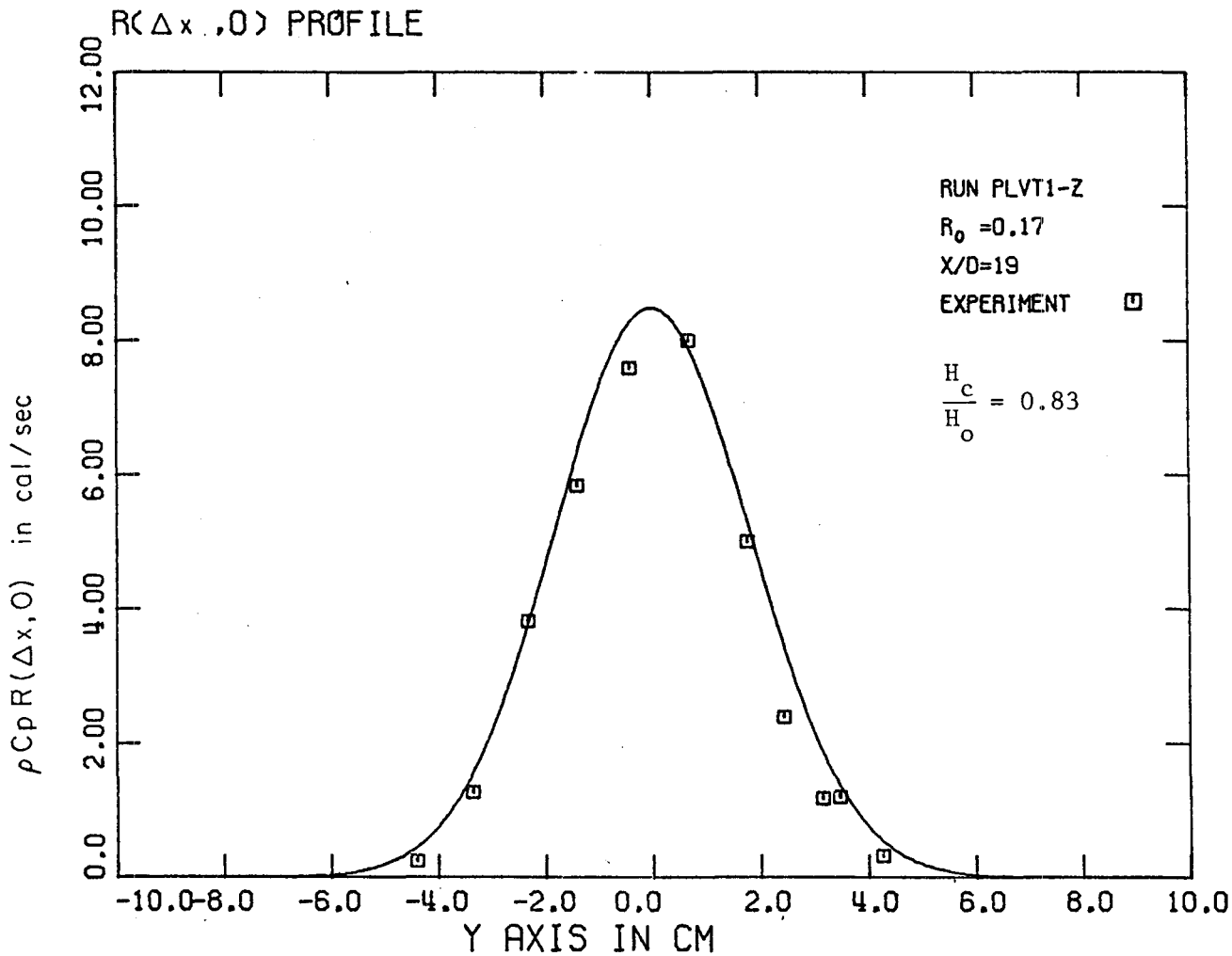

Figure 6.2.3. Profile of the correlation $\rho c_p R(\Delta x,0)$ in a turbulent plume at x/D = 19.0.

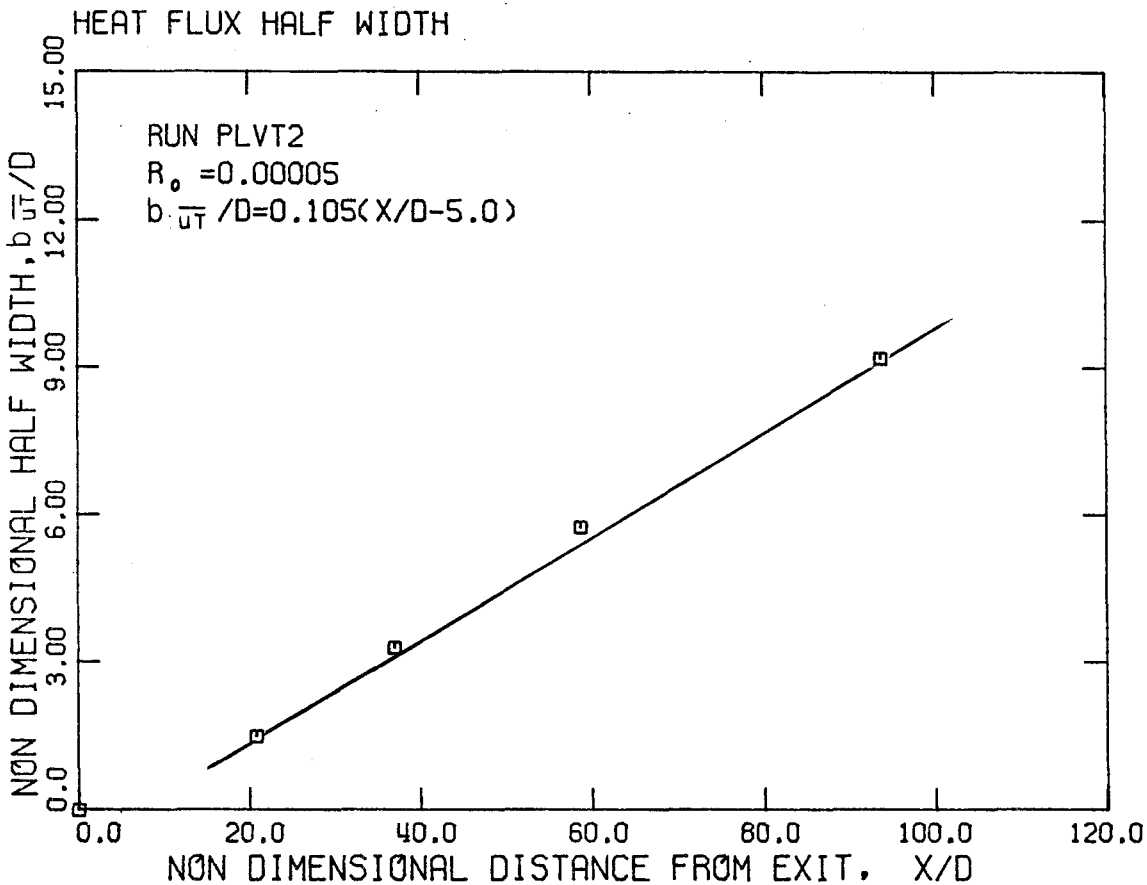

Figure 6.2.4. Heat flux half-width for a turbulent jet as a function of distance along the jet axis.

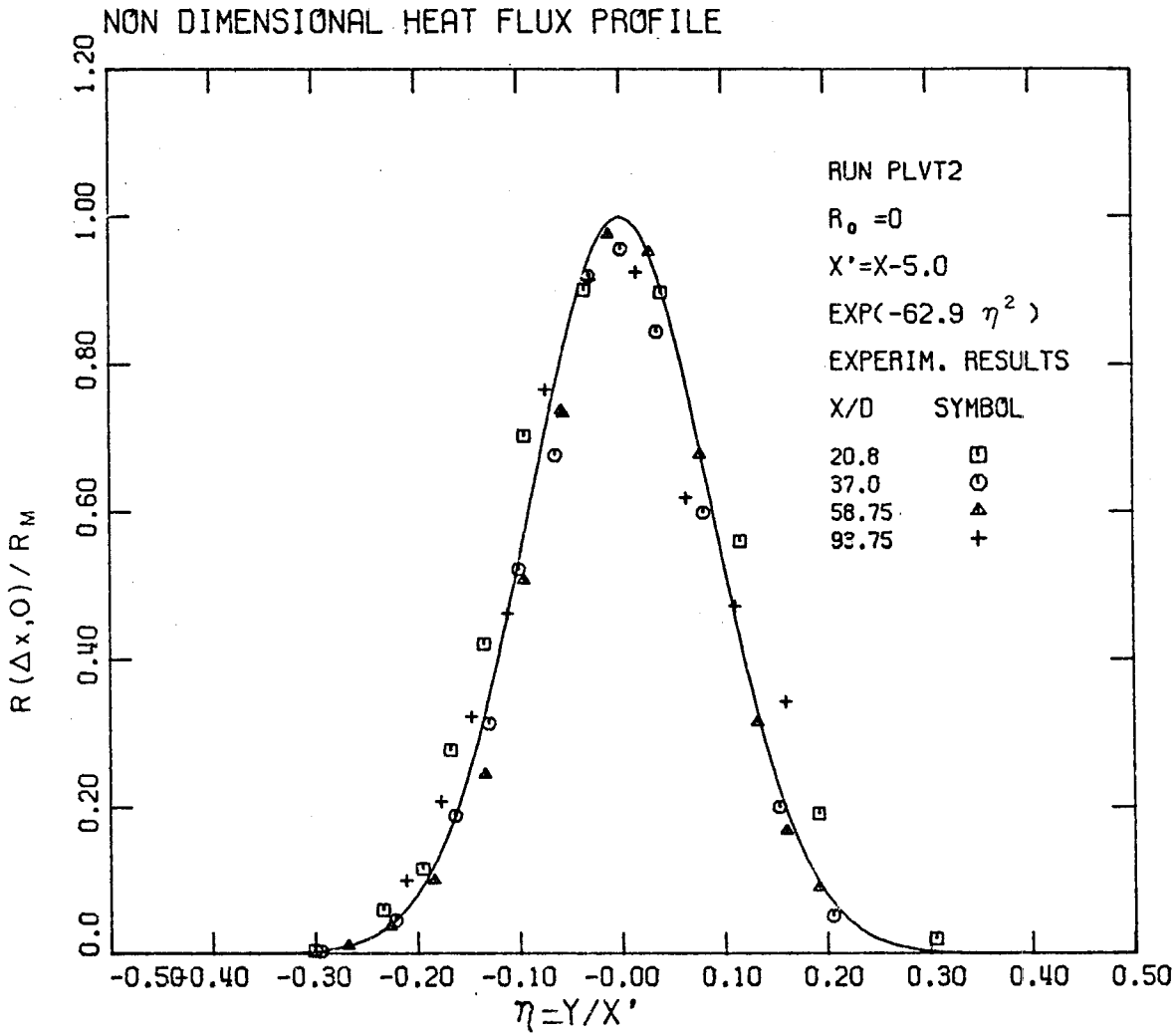

Figure 6.2.5. Non-dimensional heat flux profile in a turbulent jet.

is indicated in Figures 6.2.2.a-d and 6.2.3. It can be observed that for a jet the ratio H_c/H_o was found to be between 0.9 and 0.98, i.e., H_c is approximately equal to the input heat flux H_o. This implies that for this particular experiment for a pure jet

$$R(\Delta x,0) \approx R(0,0) \text{ for } \Delta x \approx 1\text{-}2 \text{ mm} .$$

The experimental result $H_c \sim H_o$ for a pure jet can be considered, also as an overall check of the velocity and temperature measurements.

For the case of a plume, it was found that (see Figure 6.2.3)

$$\frac{H_c}{H_o} = \frac{\int_{-B(x)}^{B(x)} R(\Delta x,0)\,dy}{\int_{-B(x)}^{B(x)} R(0,0)\,dy} \approx 0.83. \qquad (6.2.9)$$

The reason for this probably is that the correlation $R(\Delta x,0)$ is less than $R(0,0)$ for a plume.

The turbulence heat flux $\overline{u'T'}$ ideally must be calculated from the relation

$$\overline{u'(x,y,t)T'(x,y,t)} = R(0,0) - \bar{u}(x,y)\bar{T}(x,y). \qquad (6.2.10)$$

During this investigation the quantities $R(\Delta x,0)$, $\bar{u}(x,y)$ and $\bar{T}(x + \Delta x,y)$ were measured. For $\Delta x/x << 1$ it can be assumed $\bar{T}(x + \Delta x,y) = \bar{T}(x,y)$. The correlation product $R(\Delta x,0)$ can substitute $R(0,0)$ only when $R(\Delta x,0) \approx R(0,0)$ or presumably only when

$$\int_{-B(x)}^{B(x)} R(\Delta x,0)\,dy = \int_{-B(x)}^{B(x)} R(0,0)\,dy ,$$

which was appropriate for a jet. The profile of $\overline{u'T'}$ for a jet

calculated from the relation

$$\overline{u'T'} = R(\Delta x,0) - \overline{u}\,\overline{T} ,$$

and normalized by the local mean velocity $\overline{u}_M(x)$ and temperature $\overline{T}_M(x)$ on the jet axis, is plotted in Figure 6.2.6. For a plume $R(\Delta x,0) < R(0,0)$, hence an adjustment is necessary in order to obtain a meaningful profile of $\overline{u'T'}$. It is assumed, according to the discussion in the beginning of this section, that

$$R(0,0) = R(\Delta x,0)\ H_o/H_c . \qquad (6.2.11)$$

Hence the product $\overline{u'T'}$ is calculated from the relation

$$\overline{u'T'} = \frac{H_o}{H_c} R(\Delta x,0) - \overline{u}(x,y)\overline{T}(x,y) . \qquad (6.2.12)$$

The adjustment given by the Eq. 6.2.11 gives the correct balance of the Eq. 6.2.12 integrated across the plume

$$\rho c_p \int_{-B(x)}^{B(x)} \overline{u'T'}\, dy = \frac{H_o}{H_c}\ \rho c_p \int_{-B(x)}^{B(x)} R(\Delta x,0)dy - \rho c_p \int \overline{u}\,\overline{T}\, dy =$$

$$H_o - \rho c_p \int_{-B(x)}^{B(x)} \overline{u}\,\overline{T}\, dy .$$

The profile of $\overline{u'T'}$ for a plume calculated using the Eq. 6.2.12 and normalized using the local mean velocity $\overline{u}_M(x)$ and temperature $\overline{T}_M(x)$ on the jet axis is plotted in Figure 6.2.7. It is interesting to notice the dramatic difference both in magnitude and shape of the normalized profile of $\overline{u'T'}$ for a jet and for a plume. This is consistent with the

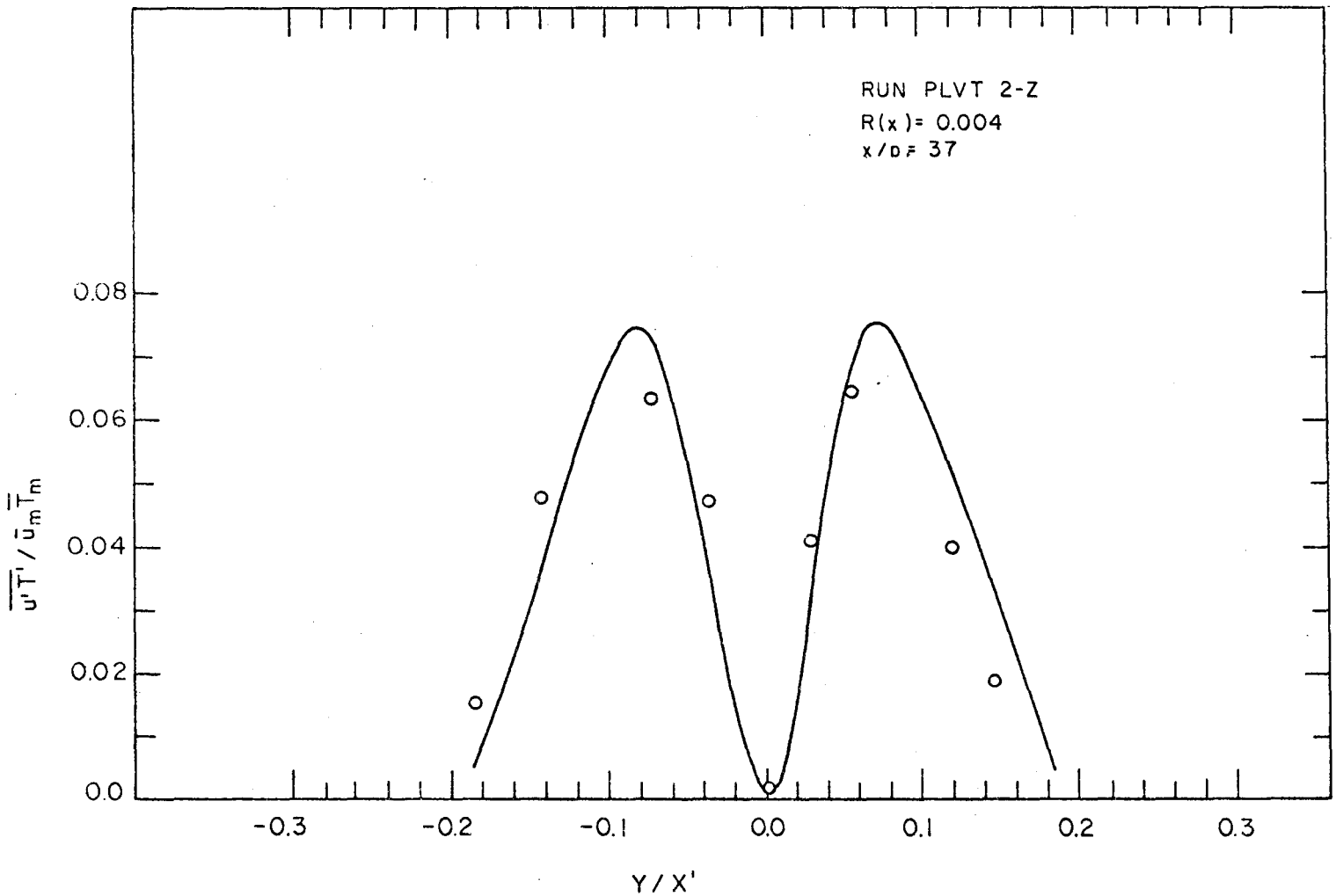

Figure 6.2.6. Profile of turbulent heat flux in a jet.

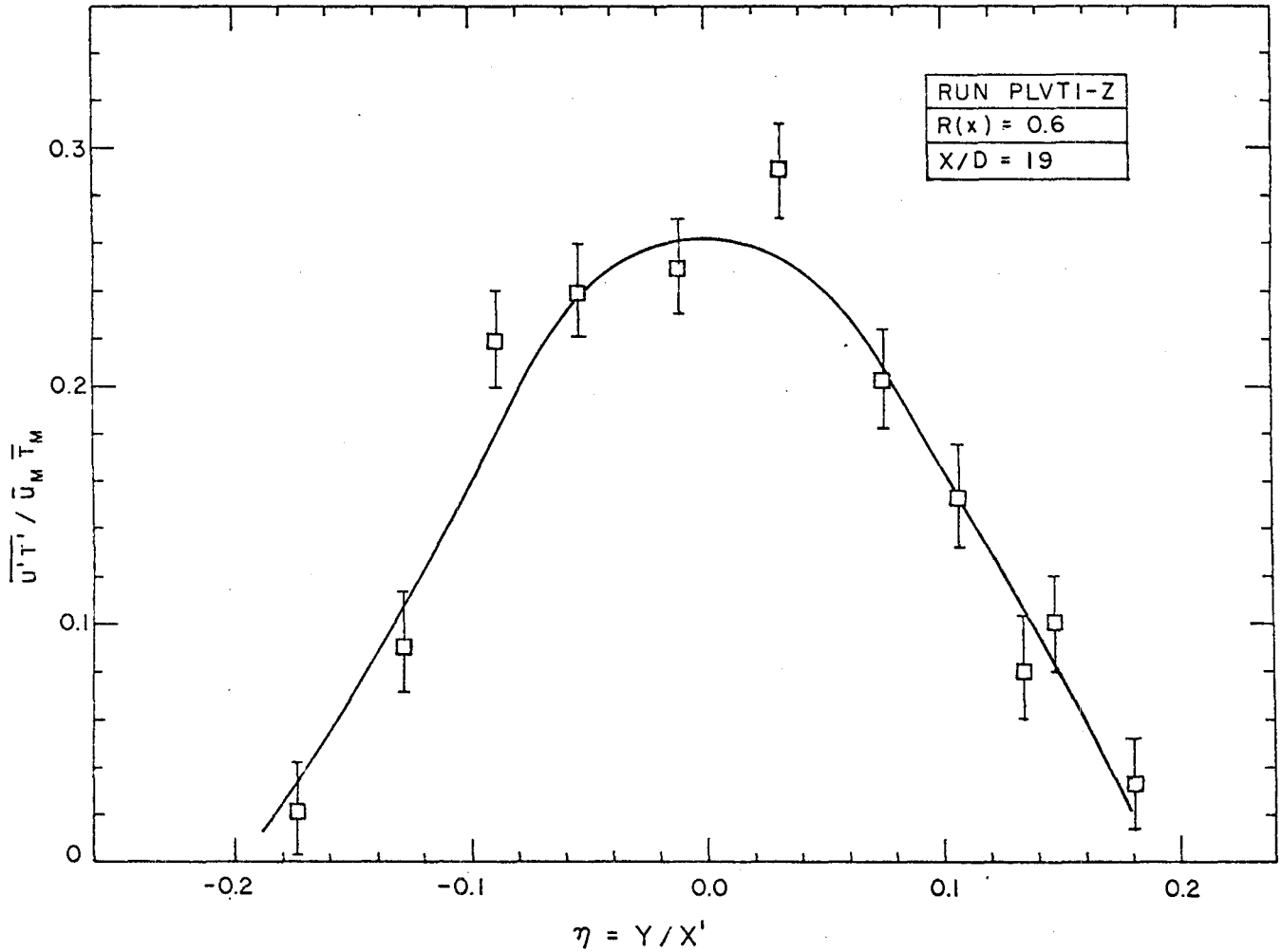

Figure 6.2.7. Profile of turbulent heat flux in a plume.

previous discussions concerning the turbulence intensity (see Section 4.2) and the turbulent heat flux (see Section 6.1). Although jets and plumes share some common characteristics (for example, the jet angle expansion given by the non-dimensional number C, see Section 5.1, is almost the same for both jets and plumes) they are radically different with respect to the forces which drive or maintain their growth, the plume is driven by gravitational forces and the jet by the input inertia forces; as a result their turbulence structure is entirely different.

Finally, the correlation coefficient

$$R_{\overline{uT}} = \frac{\overline{u'T'}}{\sqrt{\overline{u'^2}}\sqrt{\overline{T'^2}}}$$

is plotted in Figure 6.2.8 for a jet and in Figure 6.2.9 for a plume.

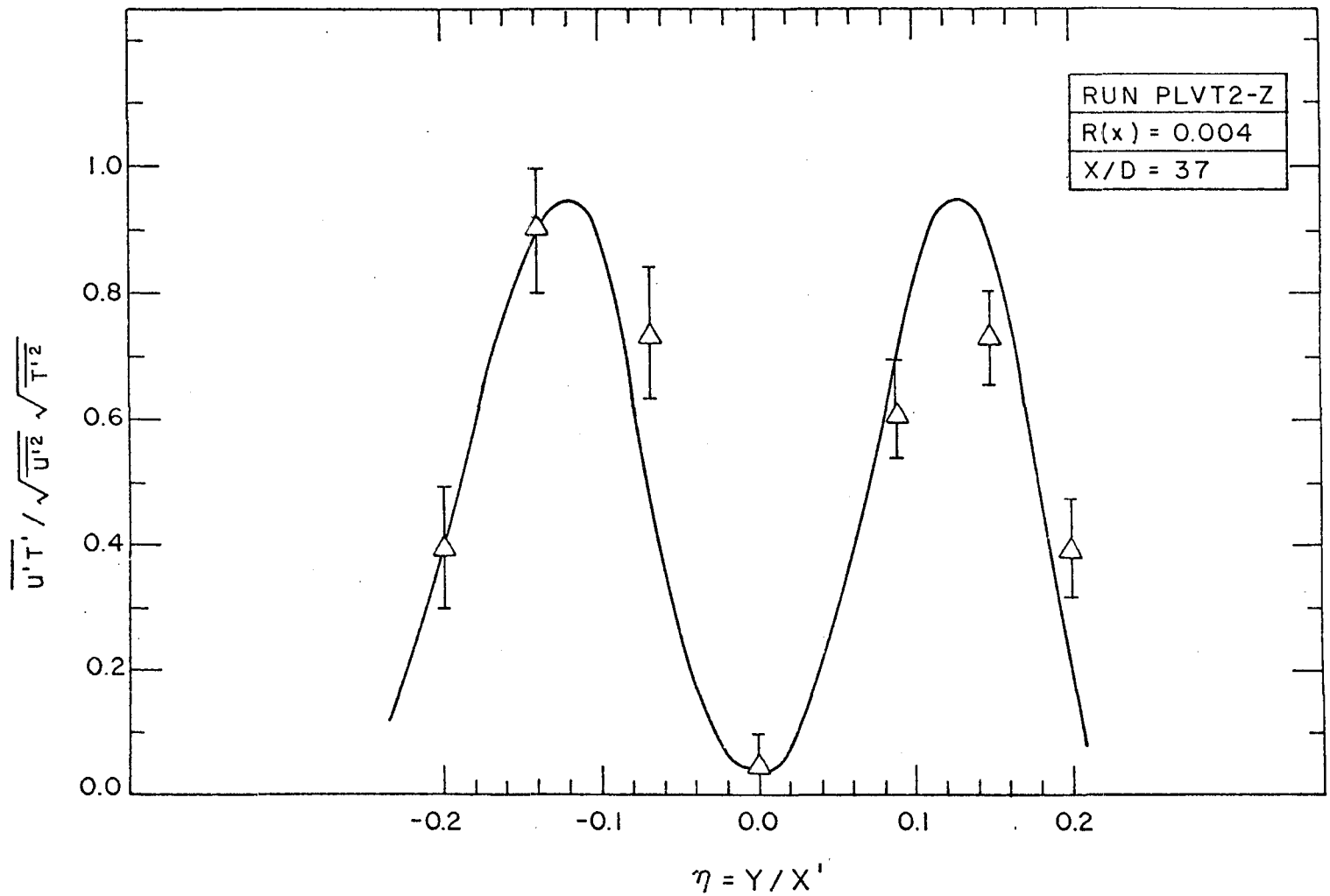

Figure 6.2.8. Jet correlation coefficient of velocity and temperature as a function of distance from the jet axis.

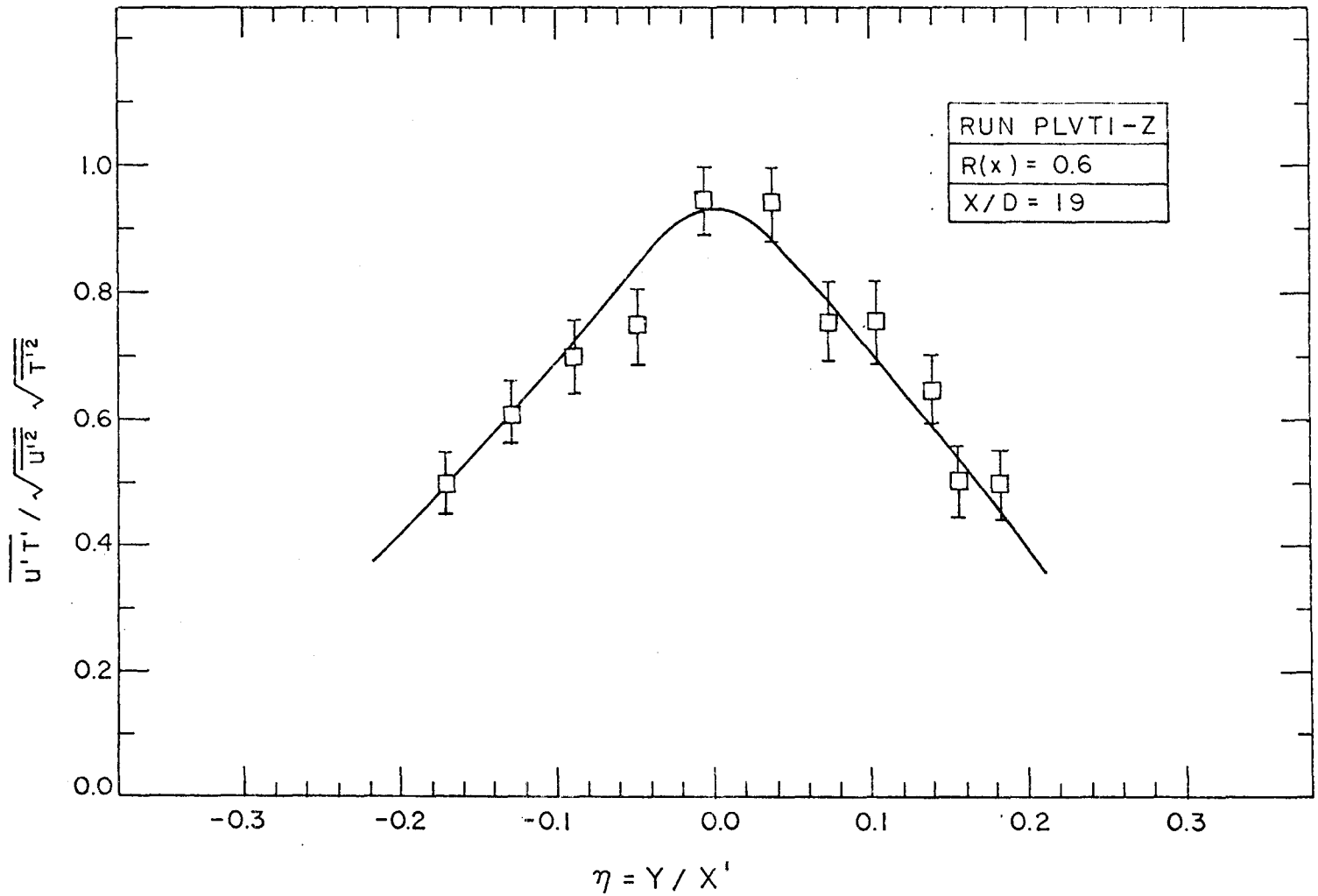

Figure 6.2.9. Plume correlation coefficient of velocity and temperature as a function of distance from the jet axis.

7. COMPARISON OF MODEL PREDICTION WITH THE EXPERIMENTAL RESULTS

7.0 INTRODUCTION

The mathematical model developed in Chapter 2.3 predicts the evolution of the kinematic mass flux $\mu(x)$, kinematic momentum flux $m(x)$, and the kinematic buoyancy flux $\beta(x)$. Hence the experimental results of Chapter 5, where the above quantities were measured, can be compared with the model. However, the experimental results of Chapter 4, where only temperatures were measured, cannot be used for a direct comparison with the model, but the centerline dilution $\bar{T}_o/\bar{T}_M$ can be used to predict the mean dilution $\frac{\mu(x)}{\mu_o}$ (see Section 7.2).

7.1 COMPARISON OF THE MODEL WITH THE EXPERIMENTAL RESULTS

The basic experimental results obtained from the velocity measurements are given in Table 5.1.2, where $\mu_o = \bar{u}_o D$ is the initial volume flux, $m_o = \bar{u}_o^2 D$ is the initial kinematic momentum flux, and $H_o = \rho_o c_p \bar{u}_o \bar{T}_o D$ is the initial heat flux. $\beta_o = \frac{\alpha_o g H}{\rho_o c_p}$ the initial kinematic buoyancy flux and the kinematic buoyancy flux at any location along the jet is calculated by the relation

$$\beta(x) = \frac{\alpha g H_o}{\rho c_p} ,$$

where the thermal expansion coefficient is calculated at a temperature $T_a + \bar{T}_c$. $\bar{T}_c = H_o/\rho c_p \mu(x)$ is the cross-sectional mean temperature. Hence the apparently unjustified approximation that the buoyancy flux is conserved, i.e., $\beta(x) = \beta_o$ is avoided.

The experimental results for the kinematic mass, momentum and buoyancy fluxes are plotted in Figures 7.1.1, 7.1.2, 7.1.3 respectively. The theoretical prediction, which is the solution of the system of the differential equations given in Chapter 2.3, is also plotted on these Figures for purposes of comparison.

7.2 COMPARISON OF THE MODEL WITH EXPERIMENTAL RESULTS OF TEMPERATURE

The experimental results for temperature give the centerline dilution $\overline{T}_o/\overline{T}_M$, but the model (Section 2.3) predicts the mean dilution $\mu(x)/\mu_o$. Hence a relation should be found between $\overline{T}_o/\overline{T}_M$ and $\mu(x)/\mu_o$ in order to extend the application of the model to cases where the centerline dilution is desired. Using the Gaussian fit to the experimental data, the heat flux by the mean motion is given by

$$H_M = \rho c_p \int_{-B(x)}^{B(x)} \overline{u}.\overline{T}\, dy = \rho c_p \overline{u}_M(x)\overline{T}_M(x) \frac{x\sqrt{\pi}\, K_{1u}}{\sqrt{\ell n 2}\sqrt{1+\left(\frac{K_{1u}}{K_{1T}}\right)^2}} \qquad (7.2.1)$$

and the kinematic mass flux is given by

$$\mu(x) = \frac{\overline{u}_M(x)\, x\sqrt{\pi}\, K_{1u}}{\sqrt{\ell n 2}} \qquad (7.2.2)$$

so that

$$H_M = \frac{\rho c_p \mu(x)\overline{T}_M(x)}{\left(1+\left(\frac{K_{1u}}{K_{1T}}\right)^2\right)^{1/2}} \qquad (7.2.3)$$

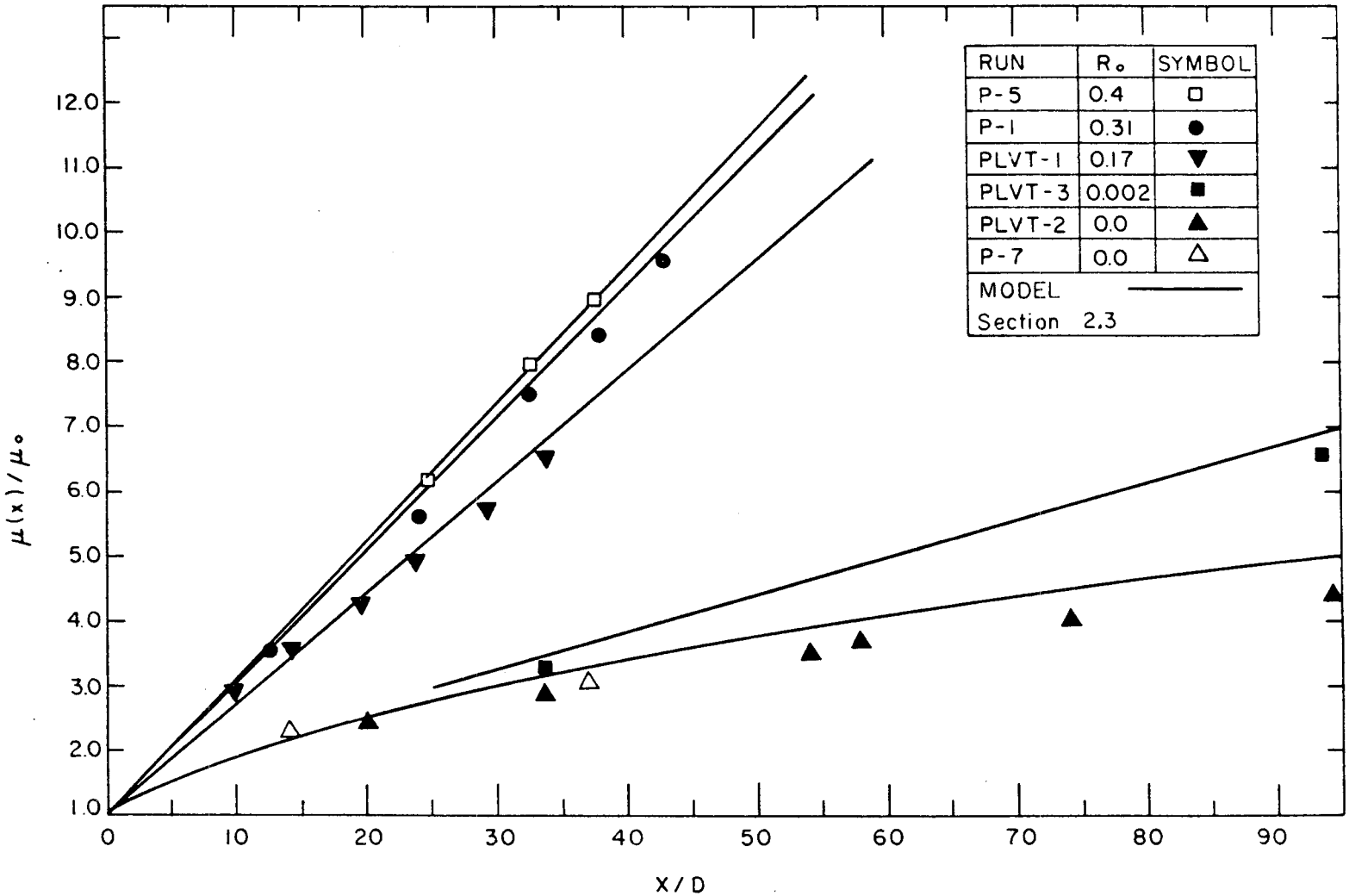

Figure 7.1.1. Comparison of the model with the experimental results for the kinematic mass flux.

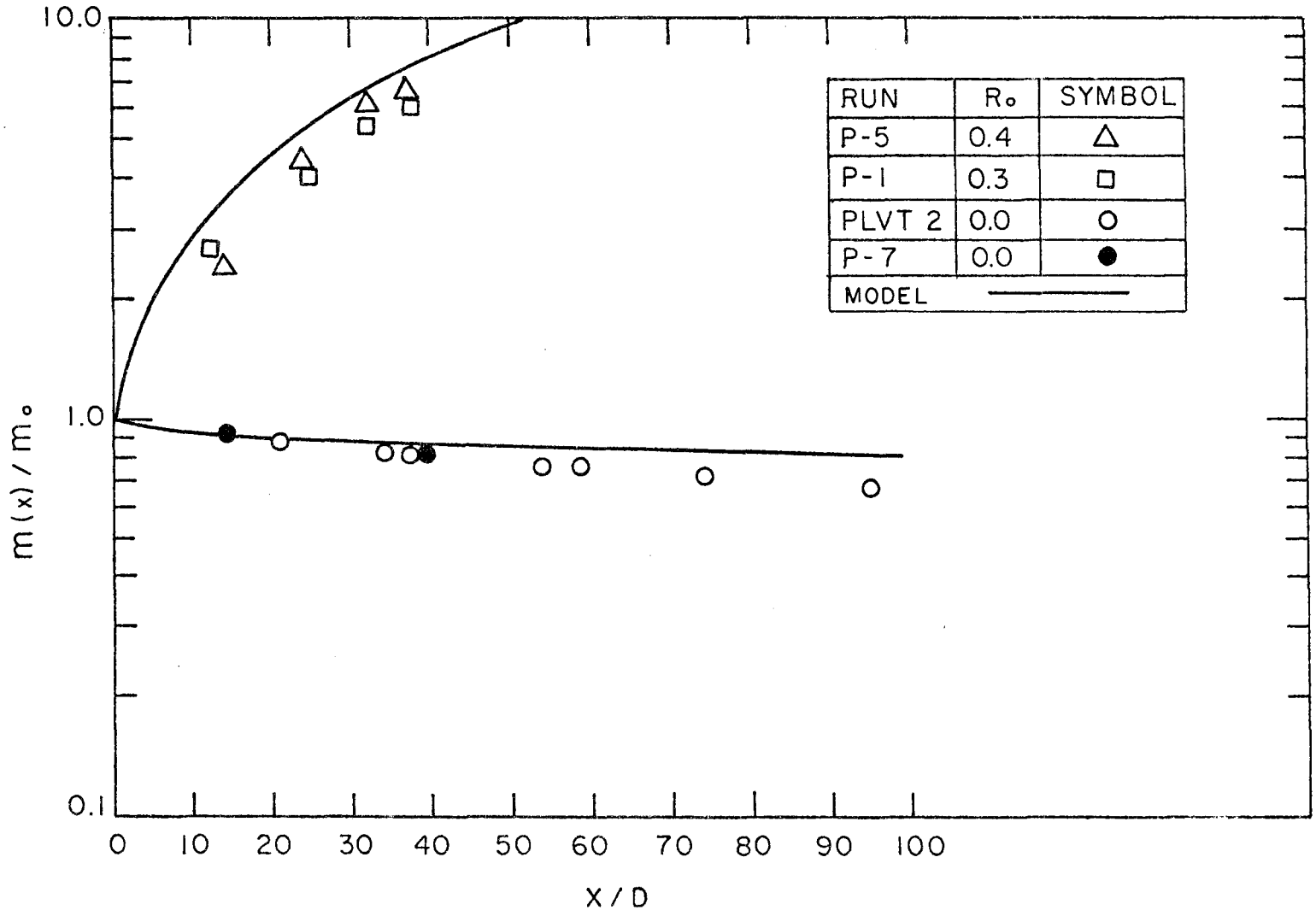

Figure 7.1.2. Comparison of the model with the experimental results of the kinematic momentum flux.

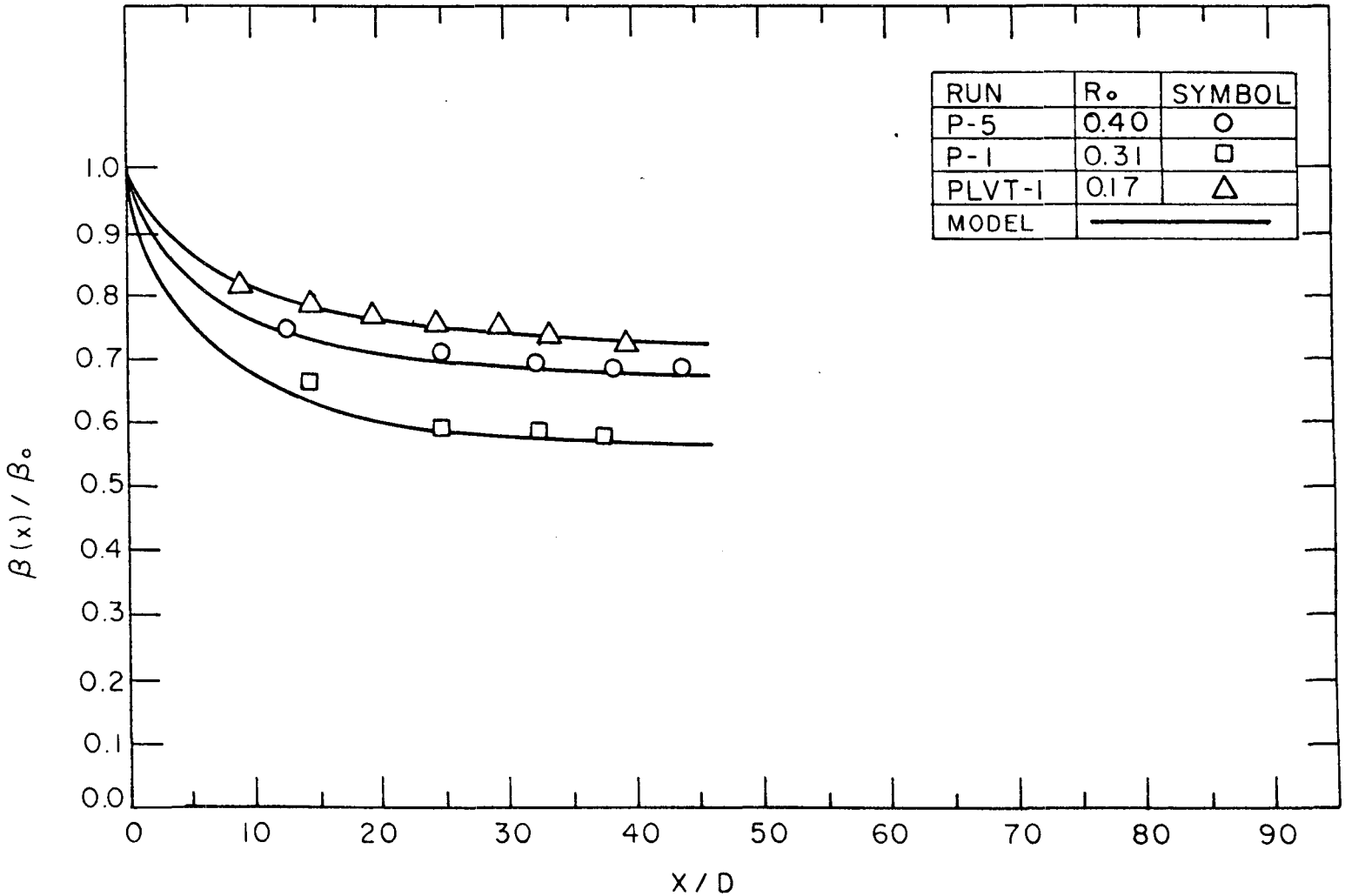

Figure 7.1.3. Comparison of the model with the experimental results for the kinematic buoyancy flux.

Combining Eqs. (7.2.3) and (6.1.7) it is found that

$$\frac{\bar{T}_o}{\bar{T}_M(x)} = \frac{1.064 + 0.85 \cdot R(x)}{\sqrt{1+\left(\frac{K_{1u}}{K_{1T}}\right)^2}} \frac{\mu(x)}{\mu_o} \tag{7.2.4}$$

and for $K_{1u}/K_{1T} \approx 0.8$, it is found that

$$\frac{\bar{T}_o}{\bar{T}_M(x)} = [0.83 + 0.66\ R(x)]\ \frac{\mu(x)}{\mu_o} \tag{7.2.5}$$

Then the mean dilution $\frac{\mu(x)}{\mu_o}$ can be calculated from the centerline dilution $\bar{T}_o/\bar{T}_M$ using Eq. (7.2.5) (see Table 4.1.2). Both the experimental results and the prediction based on the model (Section 2.3) are plotted in Figure 7.2.1.

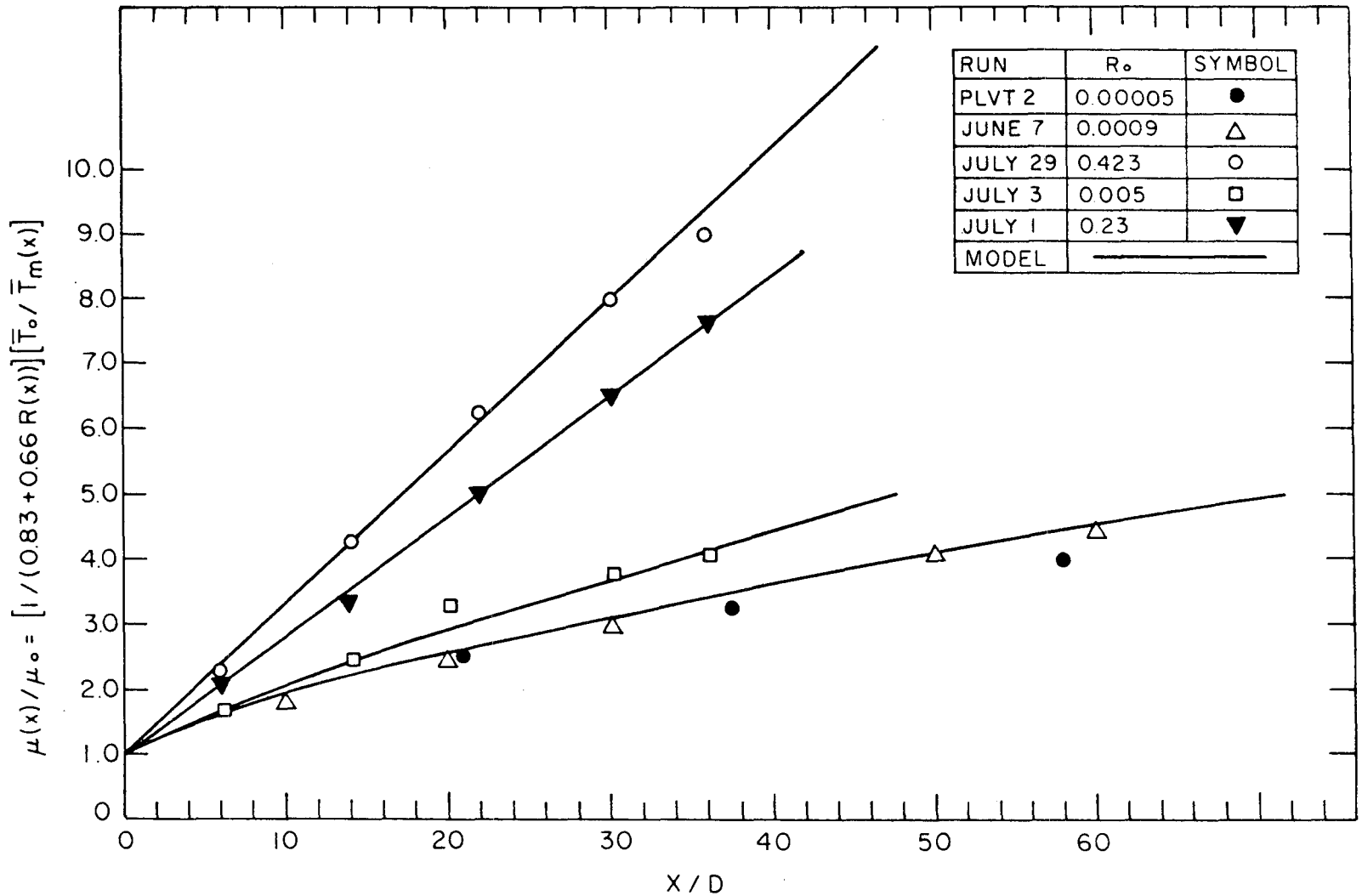

Figure 7.2.1. Comparison of the model with the experimental results for the mean temperature distribution on the jet axis.

8. ON THE SELF-PRESERVATION OF A PURE JET

The self-preservation of the velocity or temperature profile of a pure two-dimensional jet has been assumed by previous investigators (Townsend (18), Reichardt (13), Miller et al (12)). A consequence of this assumption is that velocity b_u and temperature b_T half-widths were thought to depend linearly on the distance x from exit, and equations of the form

$$\frac{b_u}{D} = K_{1u}(\frac{x}{D} + K_{2u}) \quad , \tag{8.1}$$

$$\frac{b_T}{D} = K_{1T}(\frac{x}{D} + K_{2T}) \quad , \tag{8.2}$$

were used to describe the half-widths. The coefficients K_{1u}, K_{2u}, K_{1T}, K_{2T} were thought to be unique for all the experimental results concerning two-dimensional pure jets. However, the variations of these coefficients from investigator to investigator were not negligible (see Table 1.3.1). Some investigators found the location of the virtual origin $x_o = -K_{2u}\, D$ to be positive, others negative.

In the past, these variations were attributed to experimental errors. The opinion of this writer is that although the linear assumption is probably valid locally, these variations are most likely due to the fact that the growth of the jet is not linear on a larger scale. The self-preservation argument which leads to the linear approximation for jet growth should therefore be reexamined. Keeping in mind the results in Chapter 2, a hypothesis was therefore made that the true

growth of the velocity half-width has the shape as in Figure 8.1. The Experimenters A and B would fit straight lines to their experimental results thus indicating linear growth. Possibly Experimenter A could not extend his region of experiments to a greater X/D, perhaps because he was restricted by the aspect ratio of the slot and the requirement of two-dimensionality. Experimenter B could possibly not extend his region of experiments closer to origin because the physical dimensions of the jet profile (say in mm) would be too small to ensure accurate experimental results. Obviously, Experimenter A finds smaller slope (i.e., smaller coefficient K_{1u}) and a negative virtual origin whereas Experimenter B would find a positive virtual origin.

The preceding discussion indicates that if the hypothesis of a non-self-preserving two-dimensional jet is correct, a correlation should be found between the experimental results K_{1u}, K_{2u} of different experimenters and ℓ_{max}/D, where ℓ_{max} is the distance of the more distant cross section from the origin for each investigator. The coefficients K_{1u} from each jet investigator are plotted versus the coefficient K_{2u} in Figure 8.2. The coefficient K_{1u} is plotted versus ℓ_{max}/D in Figure 8.3, and the coefficient K_{2u} is plotted versus ℓ_{max}/D in Figure 8.4. It is interesting to notice in Figure 8.2 that the coefficients K_{1u}, K_{2u} do not vary randomly from investigator to investigator but vary as predicted by the hypothesis, i.e., when K_{1u} increases, K_{2u} decreases and becomes negative, giving a positive virtual origin $x_{ou} = -K_{2u} D$. Also the coefficient K_{1u} increases as ℓ_{max}/D increases and K_{2u} decreases as ℓ_{max}/D increases, as predicted. The coefficients

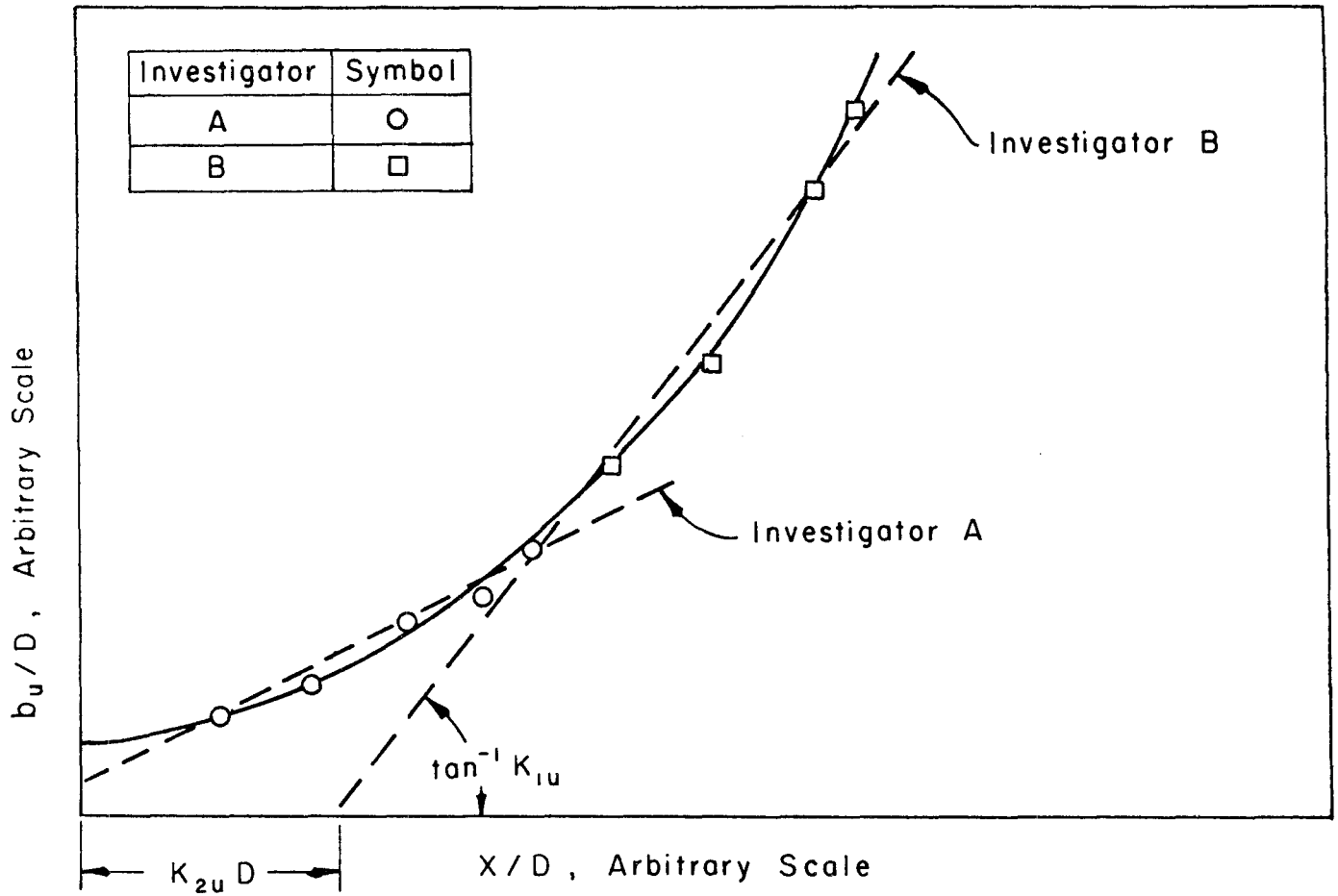

Figure 8.1. Hypothesis concerning the nonlinear spread of the mean velocity profile of a turbulent jet.

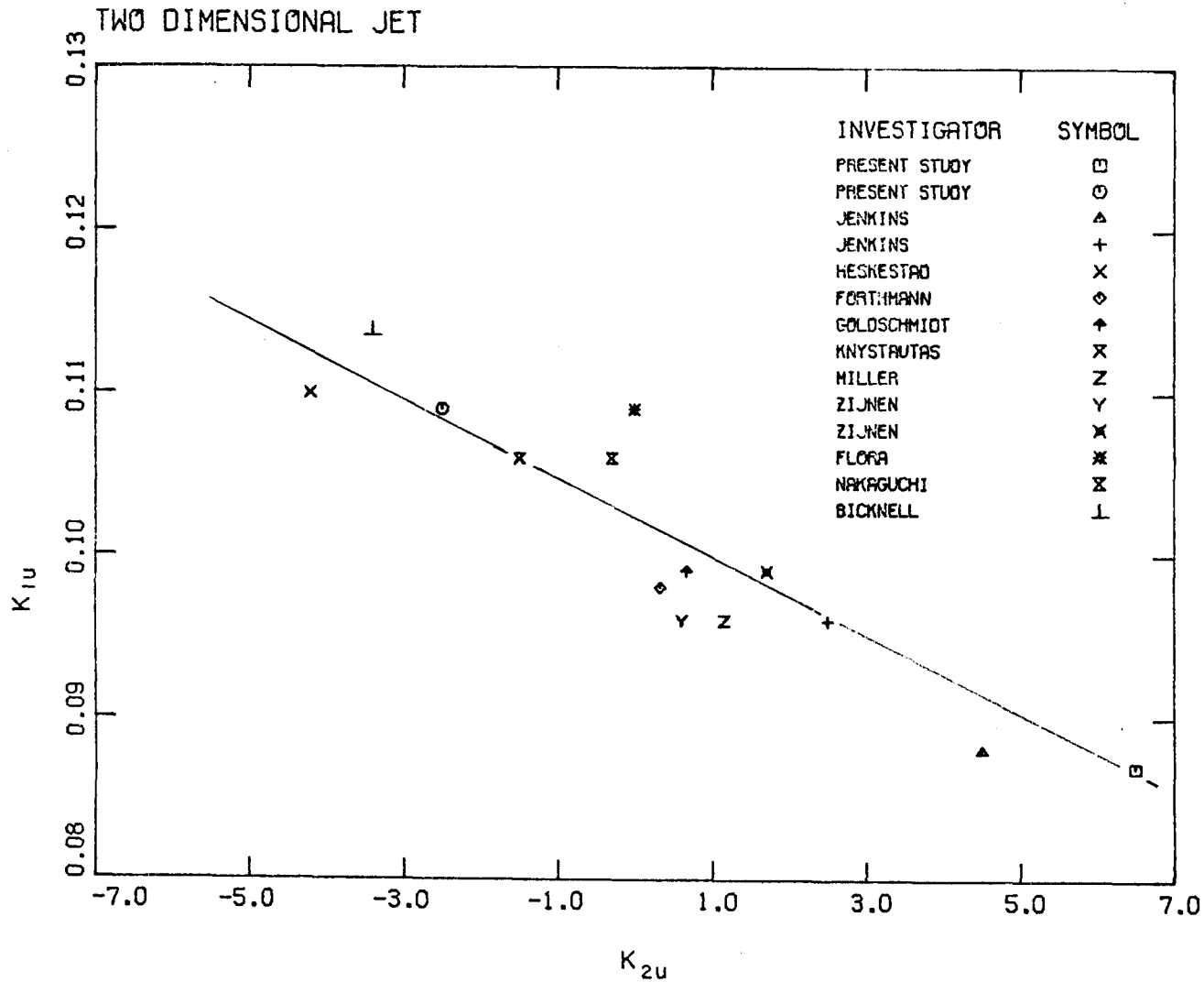

Figure 8.2. Correlation of spreading rate K_{1u} and non-dimensional virtual origin K_{2u}.

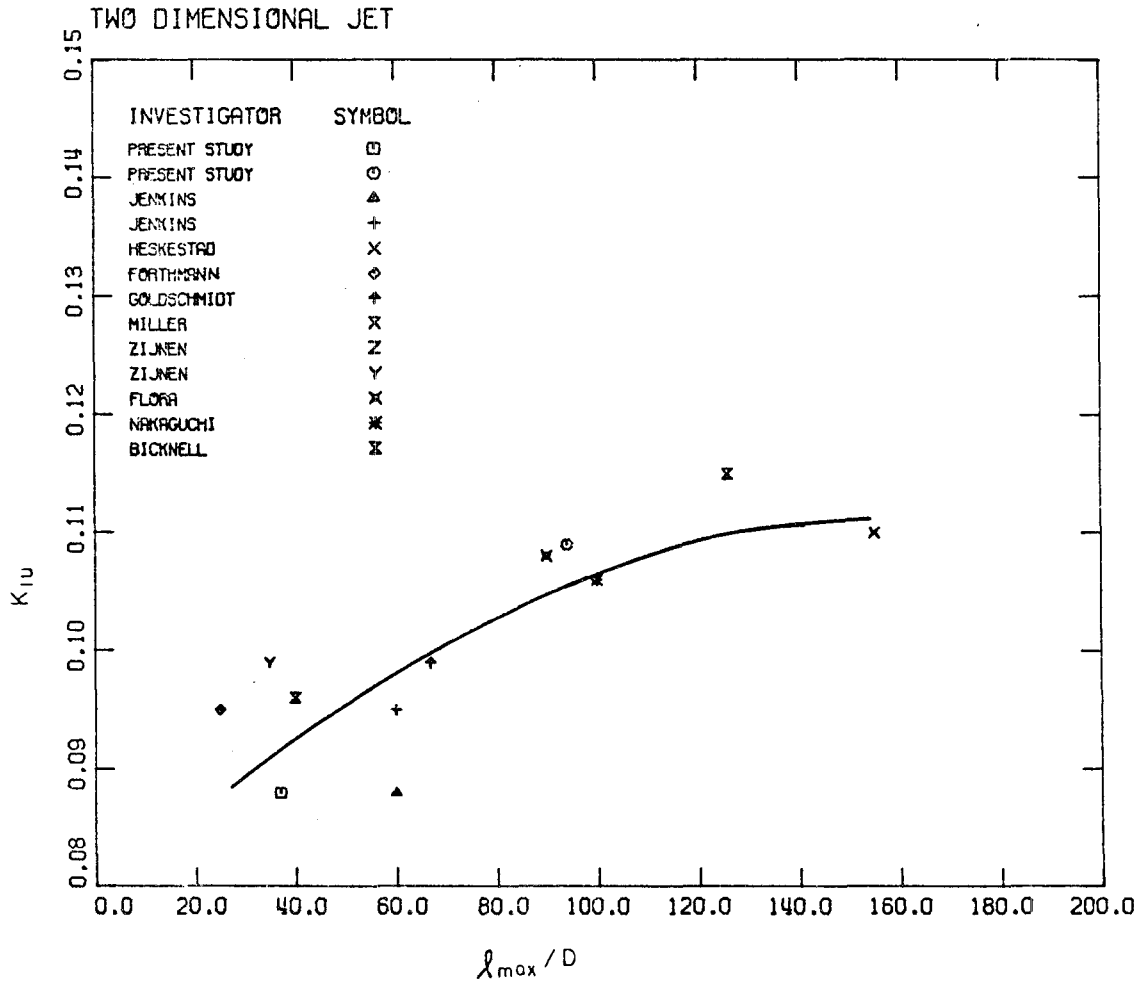

Figure 8.3. Spreading rate K_{1u} as a function of non-dimensional distance ℓ_{max}/D.

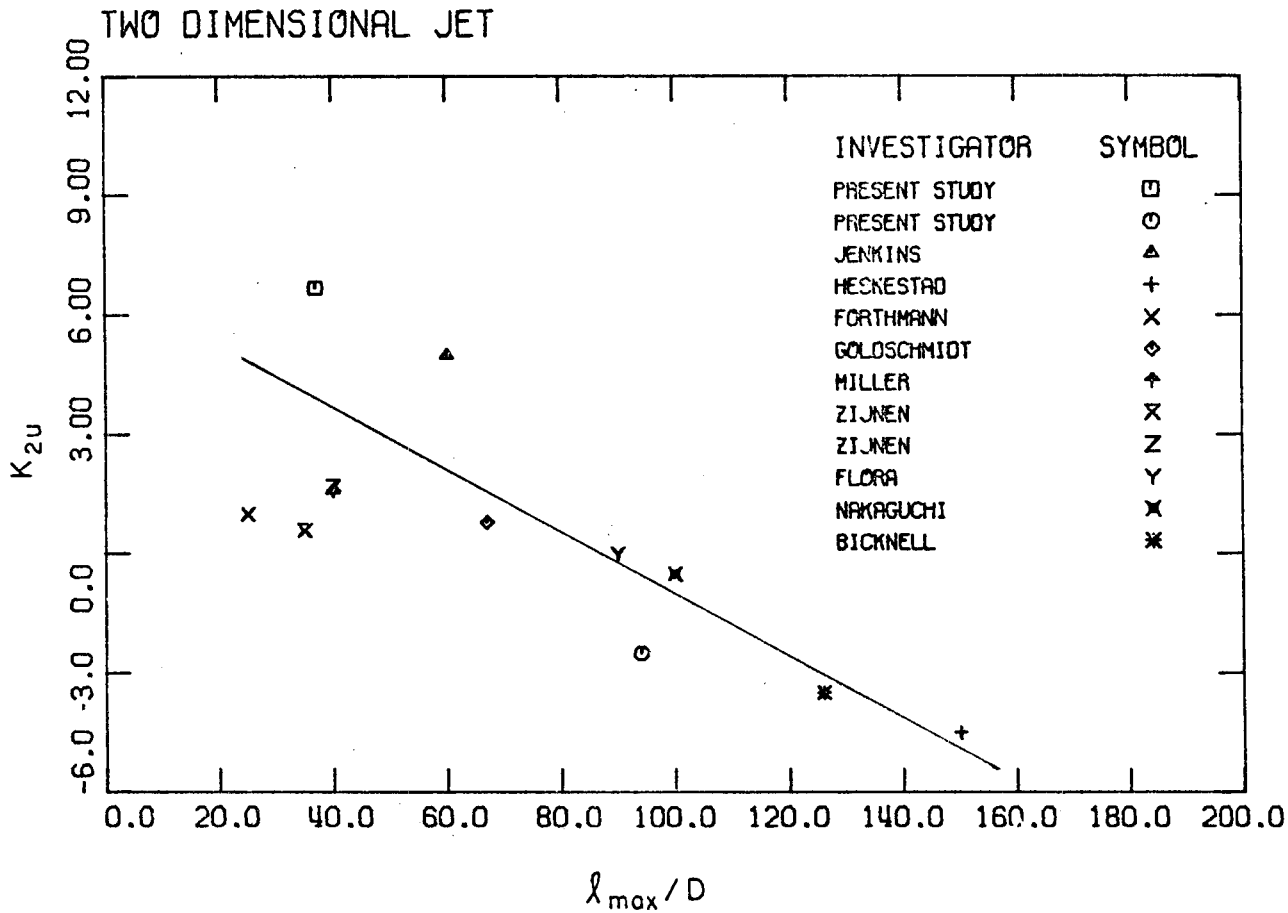

Figure 8.4. Non-dimensional virtual origin K_{2u} as a function of non-dimensional distance ℓ_{max}/D.

K_{1u}, K_{2u} given by any experimenter, should therefore, apparently be viewed as the best linear approximation, for each experimenter, of the growth of the half-width in the region $\frac{\ell_{min}}{D} < \frac{x}{D} < \frac{\ell_{max}}{D}$ (where ℓ_{min} is the closest to origin measurement). Equation 8.1, with coefficients so determined, should not be extrapolated outside this region.

Using the above results the jet half-width b_u/D was plotted versus the distance x/D from different investigators (Figure 8.5) from which it is easy to observe that b_u/D is not a linear function of x.

The interesting conclusion is that the velocity profile of a two-dimensional pure jet is not self-preserving. Similar arguments show that the temperature profile is not self-preserving either, as the Figures 8.6, 8.7, 8.8, 8.9 demonstrate.

The self-preservation of the pure two-dimensional jet, and the conservation of the kinematic momentum flux, require that

$$\bar{u}_M^2 \sim x^{-1} ,$$

and previous investigators (see Table 1.3.1) and this writer (see Table 5.2.1), give the decay of the centerline velocity in the form

$$\left(\frac{\bar{u}_o}{\bar{u}_M} \right)^2 = C_{1u}\left(\frac{x}{D} + C_{2u}\right) . \qquad (8.3)$$

The above relation should be viewed as a linear approximation to some

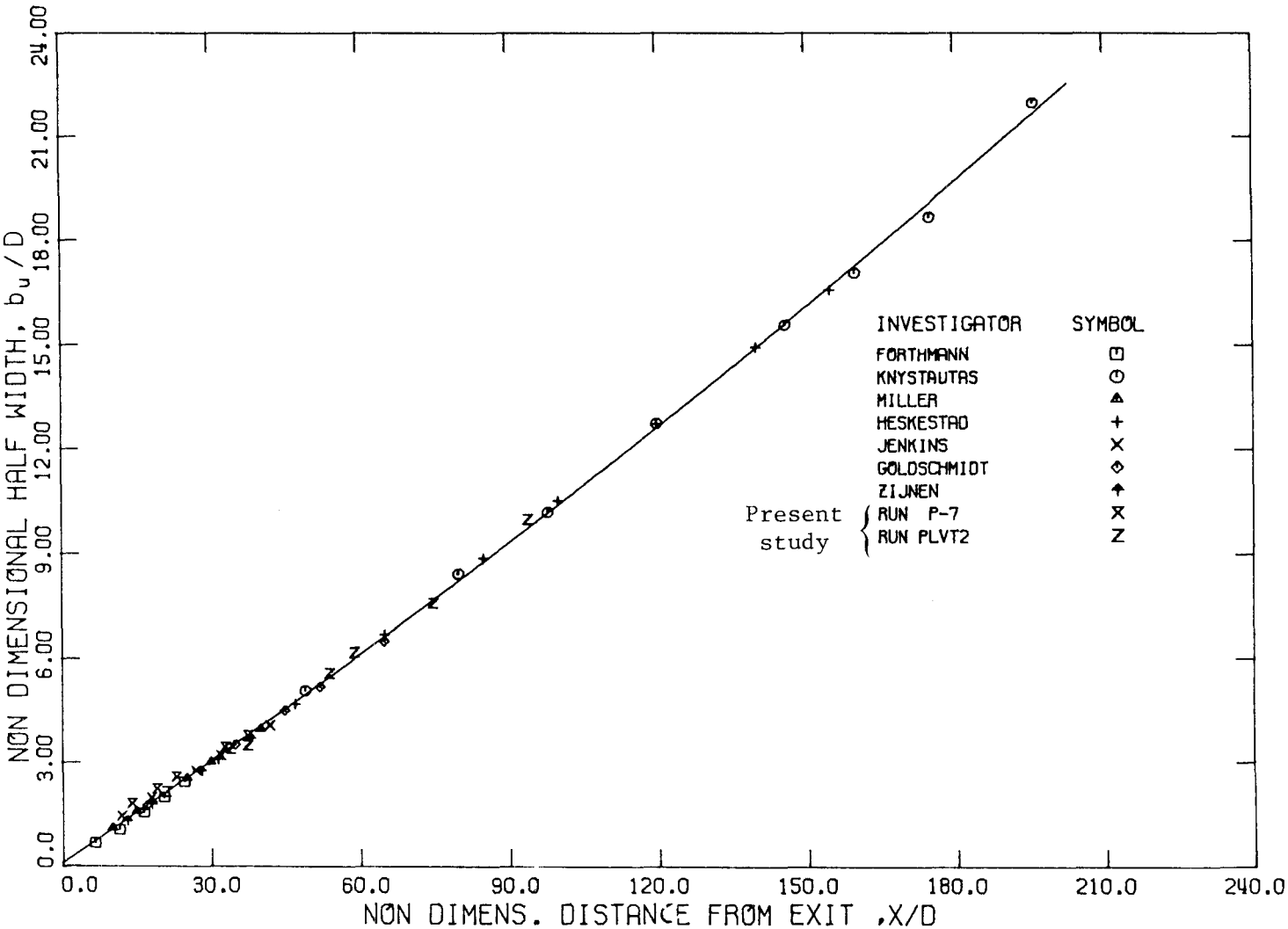

Figure 8.5. Nonlinear spread of half-width b_u of mean velocity profile of a two-dimensional turbulent pure jet.

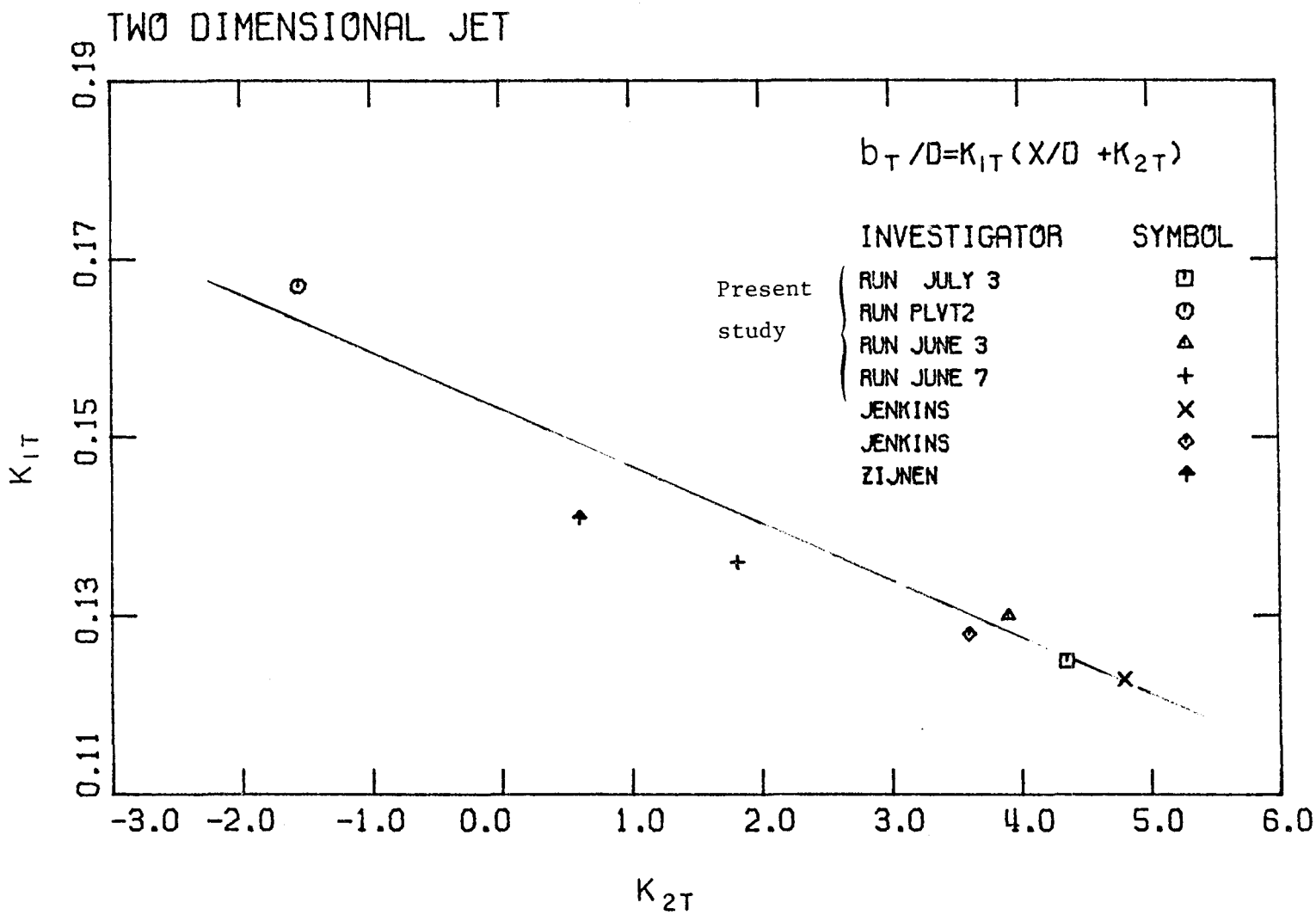

Figure 8.6. Correlation of spreading rate K_{1T} and non-dimensional virtual origin K_{2T}.

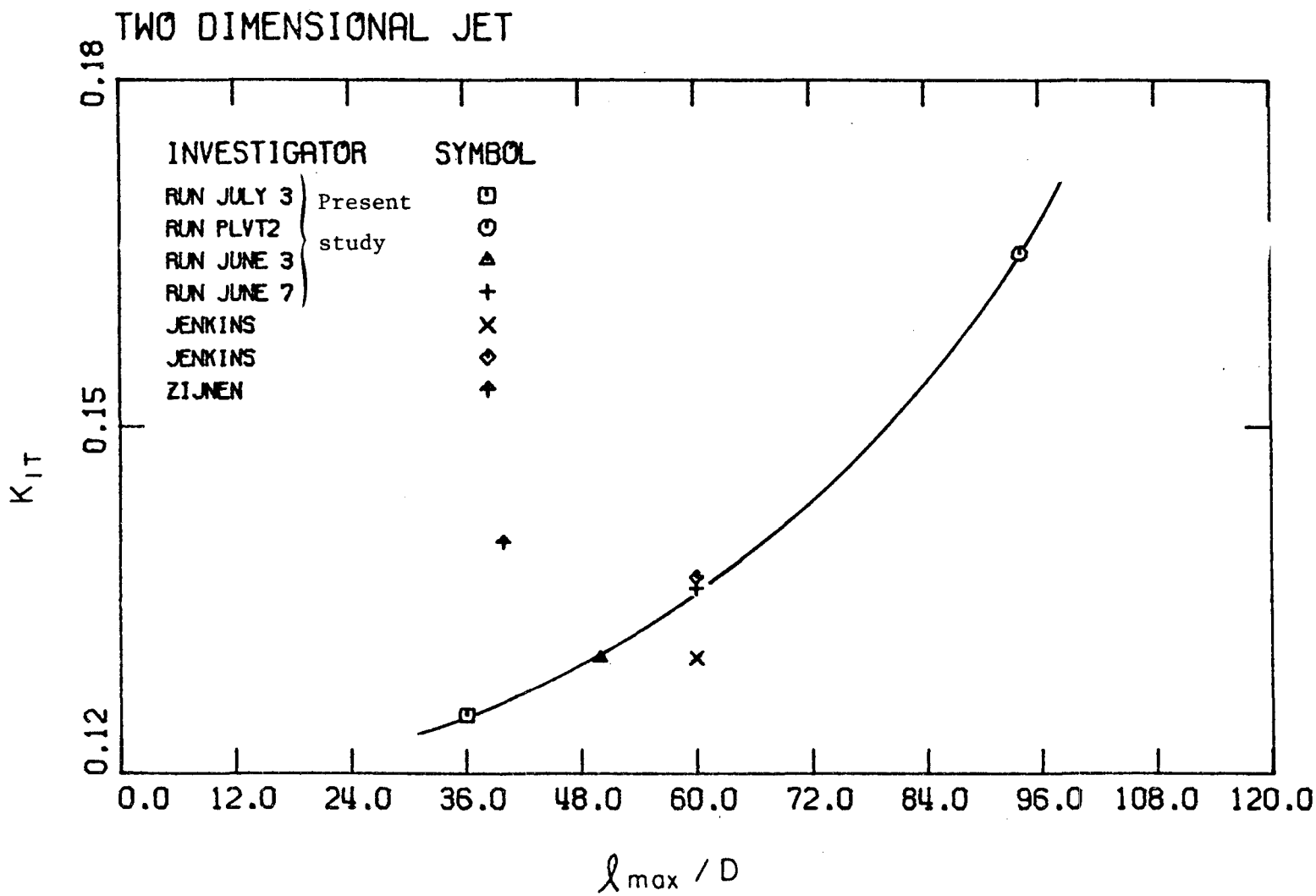

Figure 8.7. Spreading rate K_{1T} of mean temperature profile as a function of distance ℓ_{max}/D.

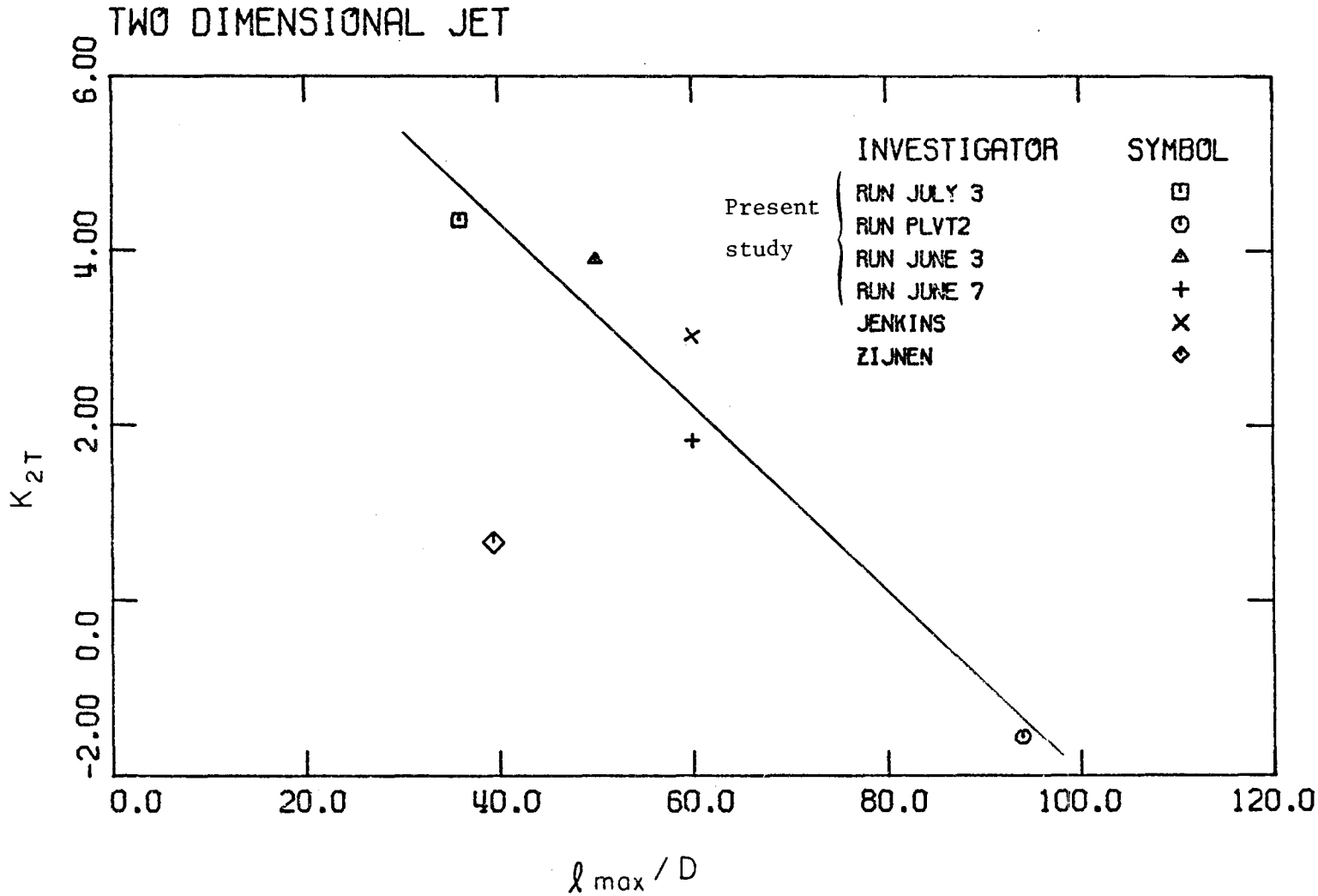

Figure 8.8. Non-dimensional virtual origin K_{2T} as a function of distance ℓ_{max}/D.

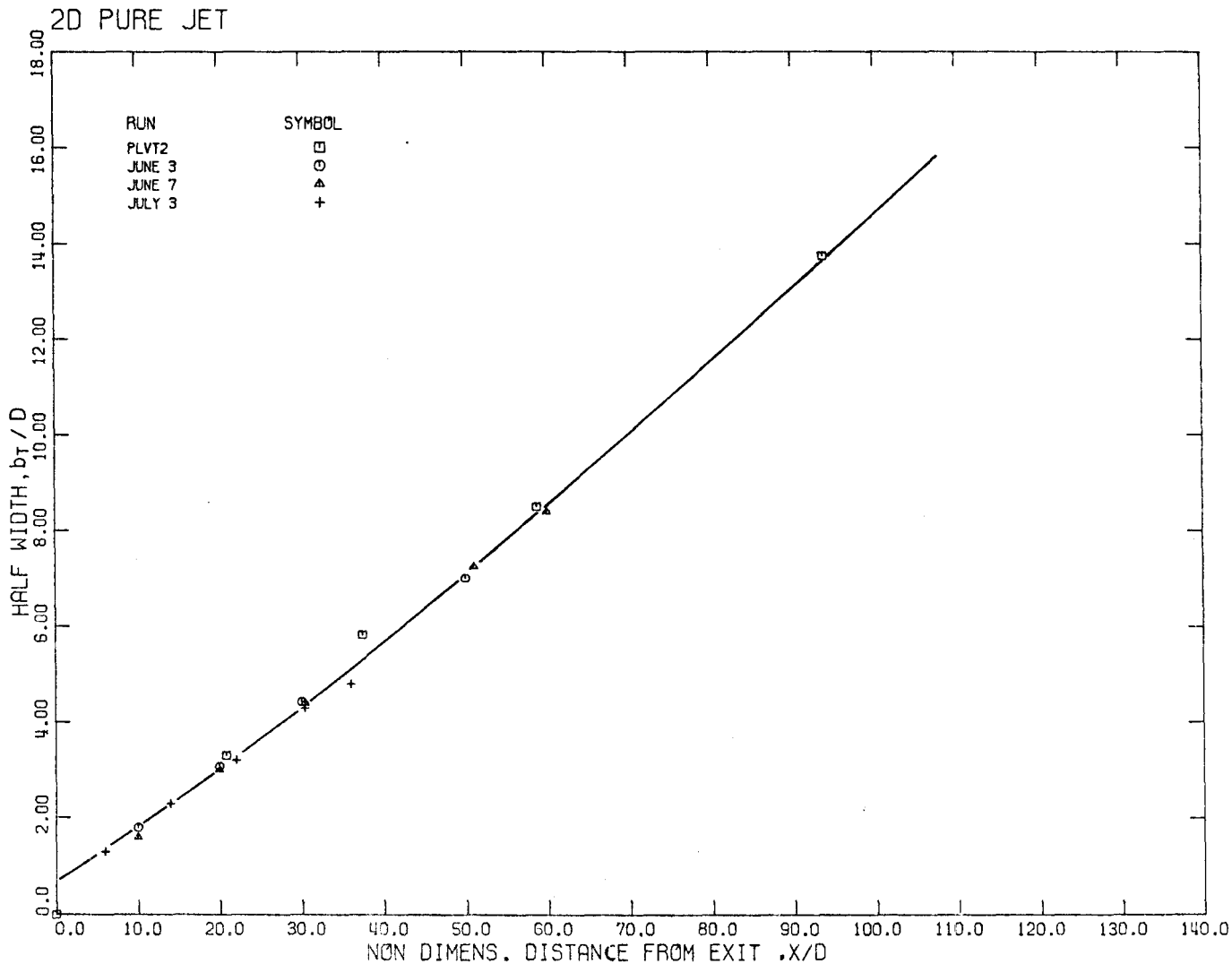

Figure 8.9. Nonlinear spread of temperature half-width b_T of a two-dimensional pure jet.

nonlinear decay of the centerline velocity. This becomes clear if the non-dimensional centerline velocity $\left(\frac{\bar{u}_o}{\bar{u}_M}\right)^2$ is plotted versus X/D from many experiments by this writer (Figure 8.10) or from the results of numerous other experimenters (Figure 8.11).

The coefficient C_{1u} versus C_{2u} is plotted in Figure 8.12; the coefficient C_{1u} versus ℓ_{max}/D in Figure 8.13; and the coefficient C_{2u} versus ℓ_{max}/D in Figure 8.14. The results all indicate a similar behavior to the rate of decay of centerline velocity.

The above results concerning the decay of the centerline velocity and temperature for a pure two-dimensional jet out of a wall, are consistent with the analysis of Sections 2.1 and 5.2, where it was found that the kinematic momentum flux of a pure jet out of a wall is not conserved.

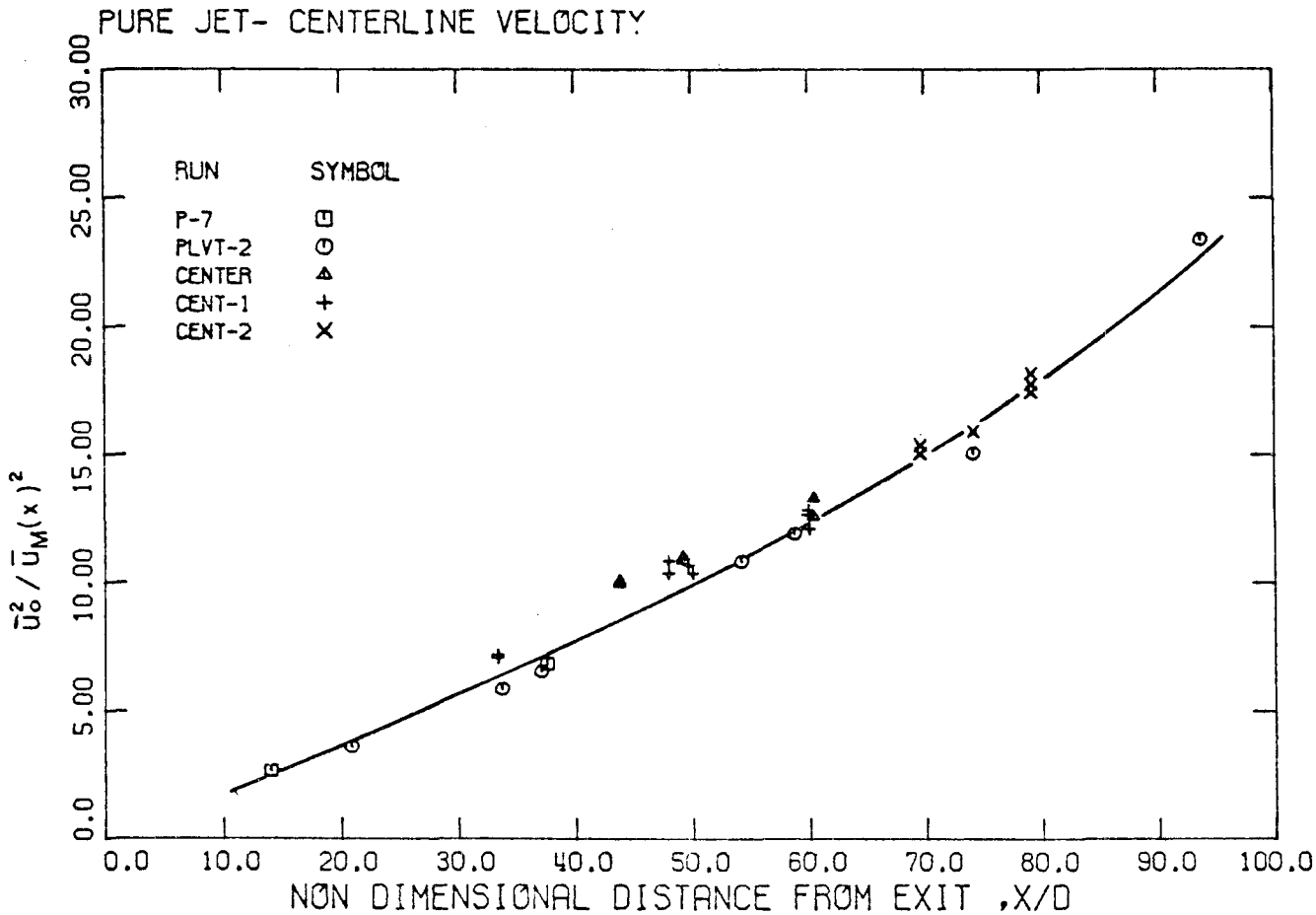

Figure 8.10. Velocity ratio $\bar{u}_o^2/\bar{u}_M(x)$ as a nonlinear function of non-dimensional distance x/D.

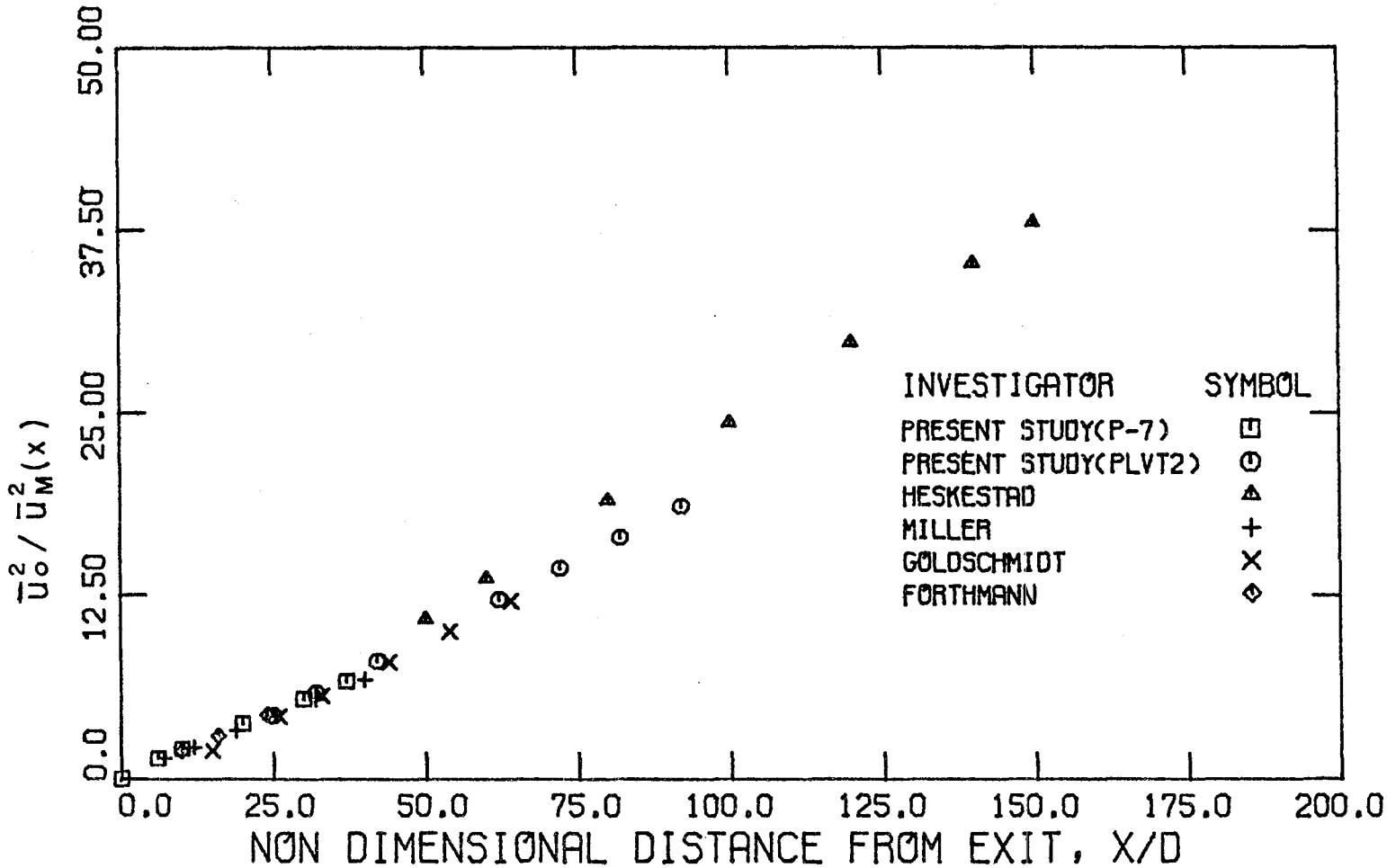

Figure 8.11. Velocity ratio $\bar{u}_o^2/\bar{u}_M(x)$ as a nonlinear function of non-dimensional distance x/D. Data from several investigators.

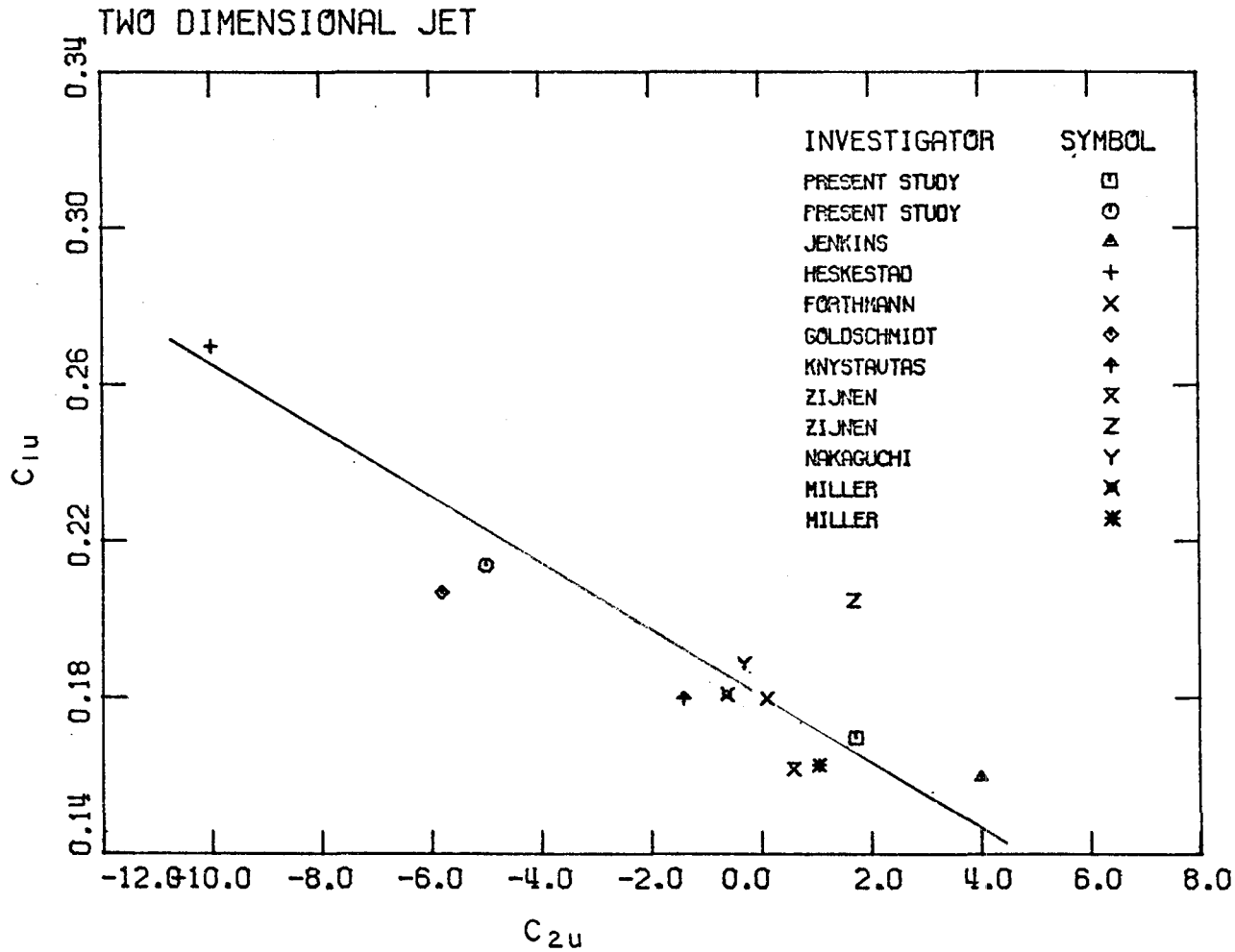

Figure 8.12. Correlation of coefficients C_{1u} and C_{2u}.

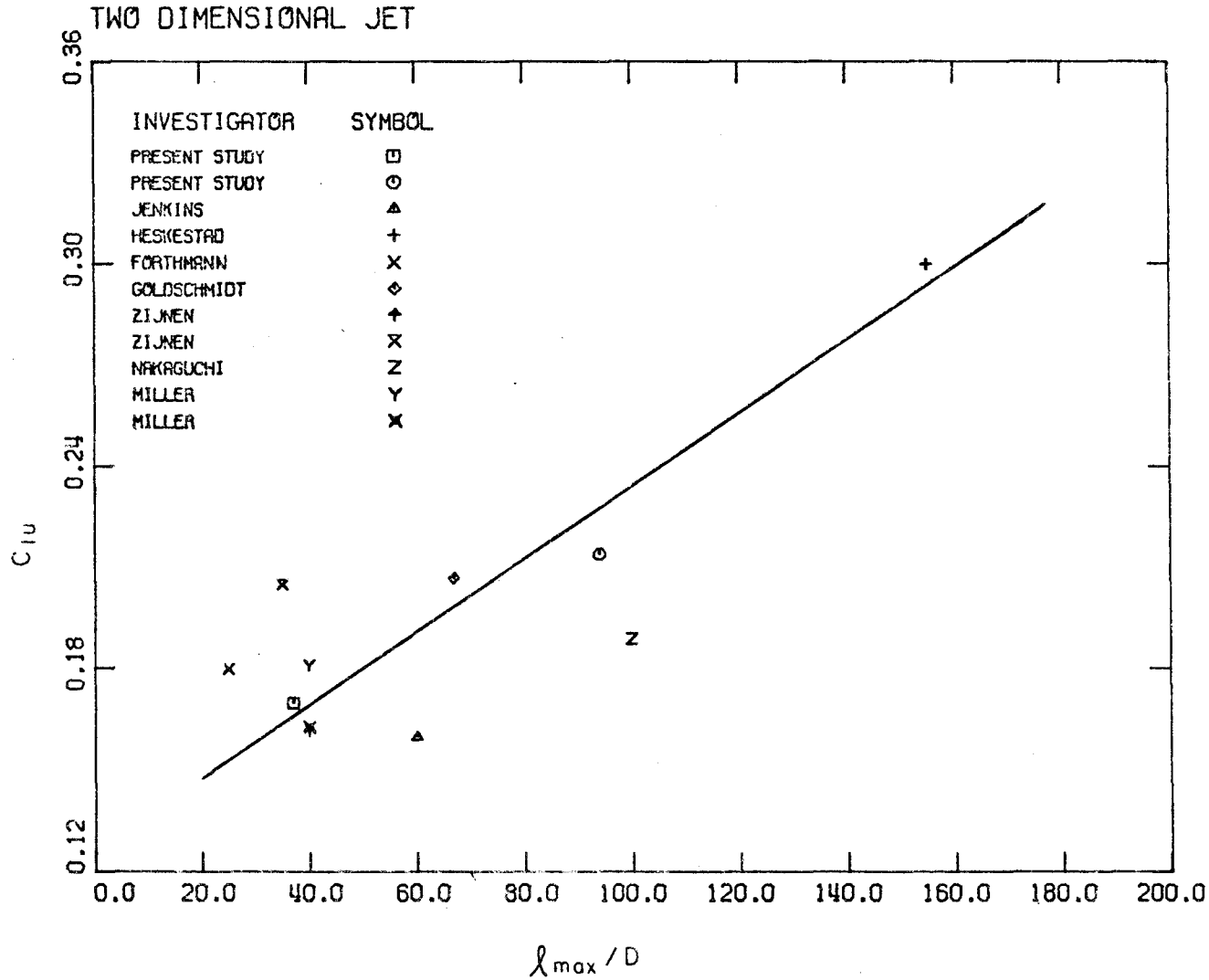

Figure 8.13. Coefficient C_{1u} as a function of non-dimensional distance ℓ_{max}/D.

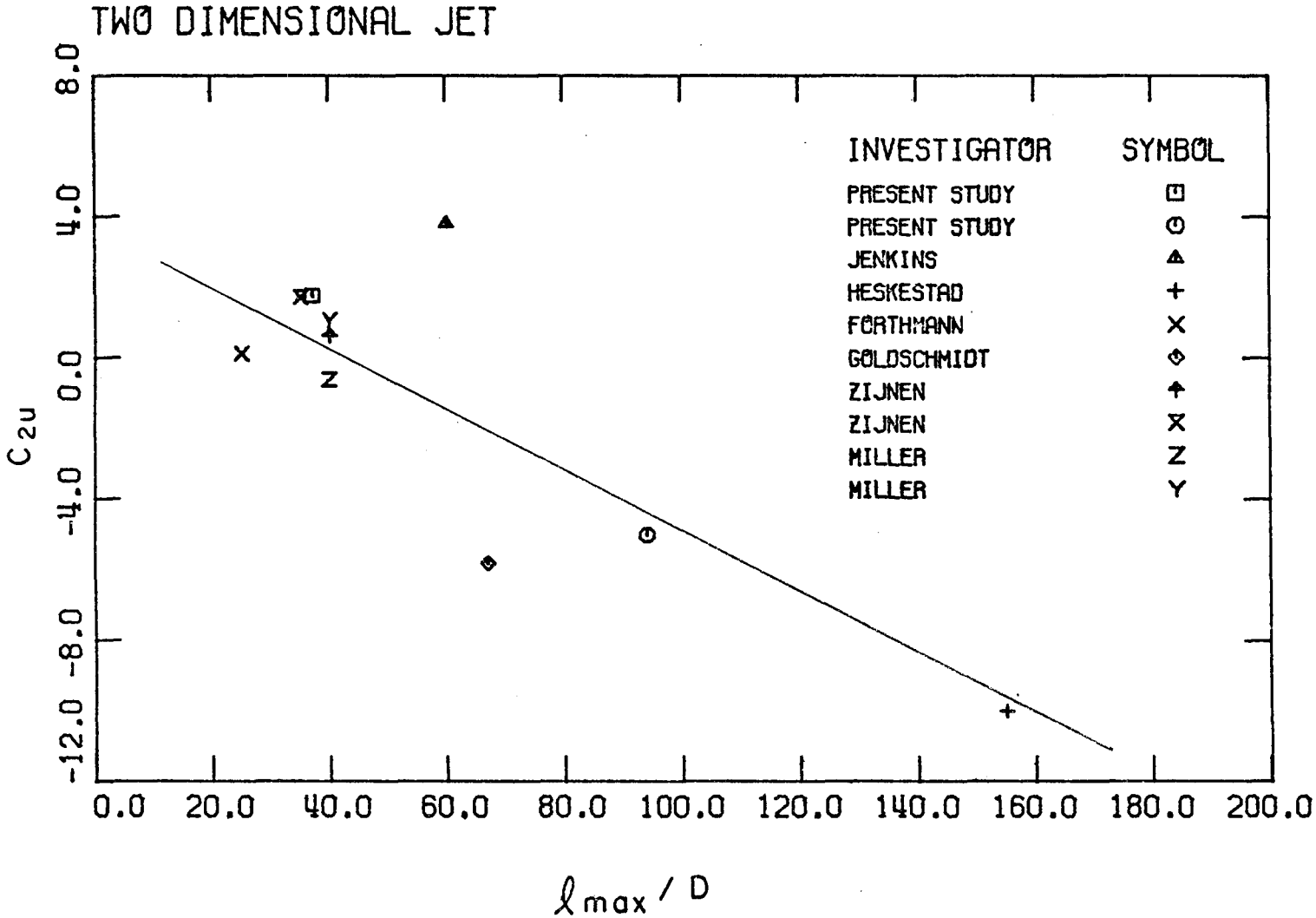

Figure 8.14. Coefficient C_{2u} as a function of non-dimensional distance ℓ_{max}/D.

9. SUMMARY OF MAIN RESULTS AND CONCLUSIONS

9.0 INTRODUCTORY NOTE

The present study contributes to the understanding of the mechanics of a vertical two-dimensional turbulent buoyant jet in its transition-state from a pure jet to a pure plume. The structure of the mean flow, the turbulence structure, and the structure of the large scale motion of a buoyant jet as a function of the Richardson number are examined. Several interesting results have been brought out and numerous conclusions can be drawn.

9.1 SUMMARY OF THE MAIN RESULTS

I. The mean flow structure

The integrated equations of motion (i.e., the equations for the conservation of the kinematic mass, momentum, and buoyancy fluxes) were examined in a rigorous way and the basic assumptions made by previous investigators were critically reviewed.

The concept of the jet boundary was clarified and its usefulness was demonstrated in Section 2.1.

The conservation of the kinematic momentum flux of a pure jet in a uniform non-flowing environment has been accepted as a valid assumption by almost all previous investigators. This study has shown, however, that the kinematic momentum flux is not conserved, but it decreases or increases (depending on the external geometry of the flow) due to the flow induced by the jet (see Sections 2.1, 5.2).

The conservation of the kinematic buoyancy flux of a buoyant (heated) jet or pure plume in a homogeneous environment was thought to be an exact

statement by previous investigators. This study has demonstrated, however, that the dependence of thermal expansion coefficient upon the temperature (see Sections 2.2 and 7.1) leads to the kinematic buoyancy flux being not conserved.

Previous investigators had assumed that the kinematic buoyancy flux $\beta(x)$ of a plume could be written as

$$\beta(x) = \int_{-B(x)}^{B(x)} \alpha(x) g \overline{u}(x,y)\ \overline{T}(x,y)\ dy\ ,$$

but the experimental results of this study have shown that this is not justified because the turbulent buoyancy flux term for a plume (see Section 6.1)

$$\int_{-B(x)}^{B(x)} \overline{u'T'}\ dy \approx 0.6 \int_{-B(x)}^{B(x)} \overline{u}\ \overline{T}\ dy\ .$$

It was found that the angle expansion of a buoyant jet, given by the non-dimensional number C (see Section 2.3), or by the growth of the half-widths, b_u and b_T, of the velocity and temperature profiles respectively, (see Sections 5.1 and 4.1), is essentially independent of the Richardson number, i.e., it is the same for both jets and plumes. For an accurate description of the growth of a turbulent jet the non-self-preserving character of velocity profile should be taken into account (see Chapter 8). Suggested values for the linear part of the growth of the profile of a buoyant jet are

$$C = \frac{u(x)}{\sqrt{m(x)(x-x_{ou})}} = 0.55 \ ,$$

$$\frac{db_u}{dx} = K_{1u} = 0.10 \ ,$$

$$\frac{db_T}{dx} = K_{1T} = 0.14 \ .$$

The entrainment coefficient can be calculated for a pure jet by using Equation (1.2.11) to give

$$\alpha_j = \frac{K_{1u}}{4} \left(\frac{\Pi}{\ell n 2}\right)^{1/2} \approx 0.055 \ ,$$

and for a plume, using Equation (1.2.18),

$$\alpha_p = \frac{K_{1u}}{2} \left(\frac{\Pi}{\ell n 2}\right)^{1/2} \approx 0.11 \ .$$

It was found that the time-averaged mean temperature profile is wider than the mean velocity profile for both jets and plumes (see Section 6.1).

The centerline dilution of a pure plume was found to be (see Section 4.1)

$$\frac{\rho_o}{\rho_o - \overline{\rho}_M(x)} = 0.42 \ gx\beta^{-2/3}(x) \ .$$

The centerline velocity of a pure plume was found to be

$$\overline{u}_M = 1.66\ \beta(x)^{1/3} .$$

It was an open question in the literature as to why the virtual origin of the mean velocity profile, defined as $x_{ou} = -DK_{2u}$, was sometimes found upstream and sometimes downstream of the jet orifice. Furthermore, the jet angle expansion (given by $\tan^{-1}K_{1u}$) has varied from investigator to investigator. This study has proved that this is mainly because the mean flow for a two-dimensional pure jet out of a wall is not self-preserving (see Chapter 8). The nonlinear growth of the jet velocity half-width can be empirically approximated by the algebraic equation

$$\frac{b_u}{D} = 0.0937 + 0.097\ (\frac{x}{D}) + 0.000052\ (\frac{x}{D})^2 ,$$

where $6 < x/D < 200$.

II. The turbulence structure of jets and plumes

Turbulent jets and plumes share some common characteristics; their expansion angle (given by the growth of the half-width of velocity profile) is approximately the same. Time exposure pictures of jets and plumes are amazingly alike. An extrapolation of these similarities of jets and plumes in their turbulent structure is, however, not justified, because the forces which drive or maintain their motion are radically different. A pure jet is maintained by the input inertia forces whereas a pure plume is driven by the buoyancy forces. For a pure plume the velocity u(x,y,t) at any point (x,y) depends upon the buoyancy at time t, which depends on the temperature T(x,y,t) which implies that u(x,y,t) and T(x,y,t) are well correlated. Combining this observation with the turbulence energy

equation (see Section 2.2) we concluded that the turbulence intensity and the turbulent heat transfer should increase with the local Richardson number. These conclusions were verified by the experimental results of this investigation (see Sections 4.2, 6.2).

It was found that the profiles of the turbulence intensity of a plume and of a jet are quite different and that the normalized turbulence intensity on the jet axis increased with the Richardson number and became constant for a plume (see Section 4.2). Similarly, it was found that the turbulent heat transfer $\overline{u'T'}$ increases with the local Richardson number (see Section 6.1). Hence the turbulence structure of jets and plumes is entirely different.

To the best knowledge of this writer there is no previously published investigation of the turbulence structure of a buoyant jet as a function of the Richardson number. It is believed that similar results should be obtained for a round buoyant jet.

III. The structure of the large eddies of jets and plumes

The mechanics of the buoyant jets can be described adequately by the mean flow and the turbulence structure, but the characteristics of the phase information of the intermittent velocity and temperature signals are of vital significance for a better understanding and explanation of jet behavior. In this investigation the large eddy structure of the temperature field was investigated as a function of the Richardson number. The intermittency was studied and it was found that the intermittency is not unity on the axis of a plume (i.e., ambient unmixed water does reach the axis of the plume). For an almost pure jet the

intermittency was found to be unity on the jet axis, but the intermittency profile was found to narrow with increasing distance from the jet exit (see Section 4.4).

The intensity of the turbulent fluctuations of the temperature, $\overline{T'^2}$, was separated into two distinct components, one associated with the hot vortices of the buoyant jet and the other associated with the cold bursts. It was found that the normalized profile of the turbulence intensity associated with the cold bursts is essentially the same for both jets and plumes and that the cold bursts are mainly responsible for the two maxima in the distribution of the intensity of turbulent fluctuations $\overline{T'^2}$ across a pure jet (see Section 4.2).

The frequency with which the hot/cold and cold/hot interface passed through any given point was studied and it was found that the occurrence of the hot vortices has an orderly structure. The profiles of the average duration of a hot burst (defined as the time between two successive cold/hot and hot/cold crossings) was obtained (see Section 4.5).

The profiles of the maximum and minimum temperatures were studied as a function of the Richardson number. The profile of the maximum temperature provides an accurate way to determine the boundaries of the jet. It was found that there is a finite probability of finding jet fluid at the jet boundaries with temperature approximately equal to the mean temperature on the jet axis. This suggests that for some applications the buoyant jet should be viewed from a probabilistic rather than a deterministic point of view (see Section 4.3).

The frequency distribution of the turbulent fluctuations of

temperature and velocity are in general skewed (see Section 4.6 and 5.4). The skewness factor is approximately zero (appropriate for symmetric distribution) only on the jet axis and the flatness factor is approximately 3.0 (appropriate for Gaussian distribution) again only on the jet axis (see Section 4.7).

9.2 CONCLUSIONS

The main conclusion from the study is that the nature of turbulent jets and plumes are quite different because the nature of the forces which act upon them is quite different. A pure jet is maintained by the input inertia forces and a pure plume is driven by buoyancy forces. This difference explains why the evolution of the volume flux, the centerline mean temperature and mean velocity, the intensity of turbulent fluctuations of temperature and velocity, and the turbulent heat transfer, are entirely different for a plume and for a jet. However, the shape and the spreading rate of the mean velocity profiles are approximately the same for both jets and plumes. Hence we can conclude that the shape of the mean velocity profile and its spreading rate are independent of the nature of the driving force. This conclusion is also supported by the fact that similar results were found for a round jet (Corrsin and Uberoi [52]) and a round plume (Rouse et al [21]).

Previous mathematical models (see Section 1.2) used to predict the evolution of mean quantities in a turbulent buoyant jet, were found to be lacking in two basic respects. Future models of the evolution of mean quantities in a buoyant jet should consider that the turbulent kinematic buoyancy flux is not negligible for a plume, and that the kinematic

momentum flux of a pure jet in a uniform nonflowing environment is not conserved. The assumption of a universal entrainment coefficient α_e for both jets and plumes is not correct (see Section 1.2). Previous mathematical models based on this concept and used for design should be replaced by more reasonable models that recognize the variation of the entrainment coefficient.

The increase of the intensity of turbulent fluctuations and of the turbulent heat transfer with the Richardson number leads to the conclusion that the turbulent mixing is much more effective for plumes than for jets. In particular, for a given ratio of the volume flux $\mu(x)$ to the initial volume flux μ_o, the centerline dilution $\overline{T}_o/\overline{T}_M(x)$ is much bigger for a plume than for a jet (see Section 7.2).

Finally, the large scale motion of buoyant jets is not chaotic but has a structure and an order which is essential to the understanding and explanation of some of the basic jet features.

APPENDIX A

A few photographs are presented here to illustrate that the short time exposure photographs of turbulent jets and plumes are entirely different. Figure A.1 and A.2 are short exposure pictures (1/100 of a second) and Figure A.3 is a medium exposure picture ($\sim$2 seconds) of a turbulent two-dimensional plume in a uniform nonflowing (except for the external induced flow) environment. Figure A.4 is a short exposure picture (1/100 of a second) and picture A.5 is a medium exposure ($\sim$2 seconds) of a pure two-dimensional turbulent jet in nonflowing (except for the external induced flow) environment. A feeling for the flow induced by a jet or a plume can be obtained from the Figures A.3, A.4, and A.5.

It is interesting to observe the large scale waving motion of the plume. A detailed stability analysis will not be presented here, but the basic mechanism which produces these large scale waves can be explained as follows.

Assume that at some time t_o a plume achieves the configuration of Figure A.6 and consider the volume V_{AB} which is included between the cross sections AA and BB. Now, the temperature on the plume axis decreases and the density increases as the distance x from the plume orifice increases. Hence the center of the mass of the volume V_{AB} will be above the center of the pressure forces. Two external forces are acting on the mass m_{AB} of the volume V_{AB}, (i) the gravitational force, with absolute value

$$G = m_{AB}\, g$$

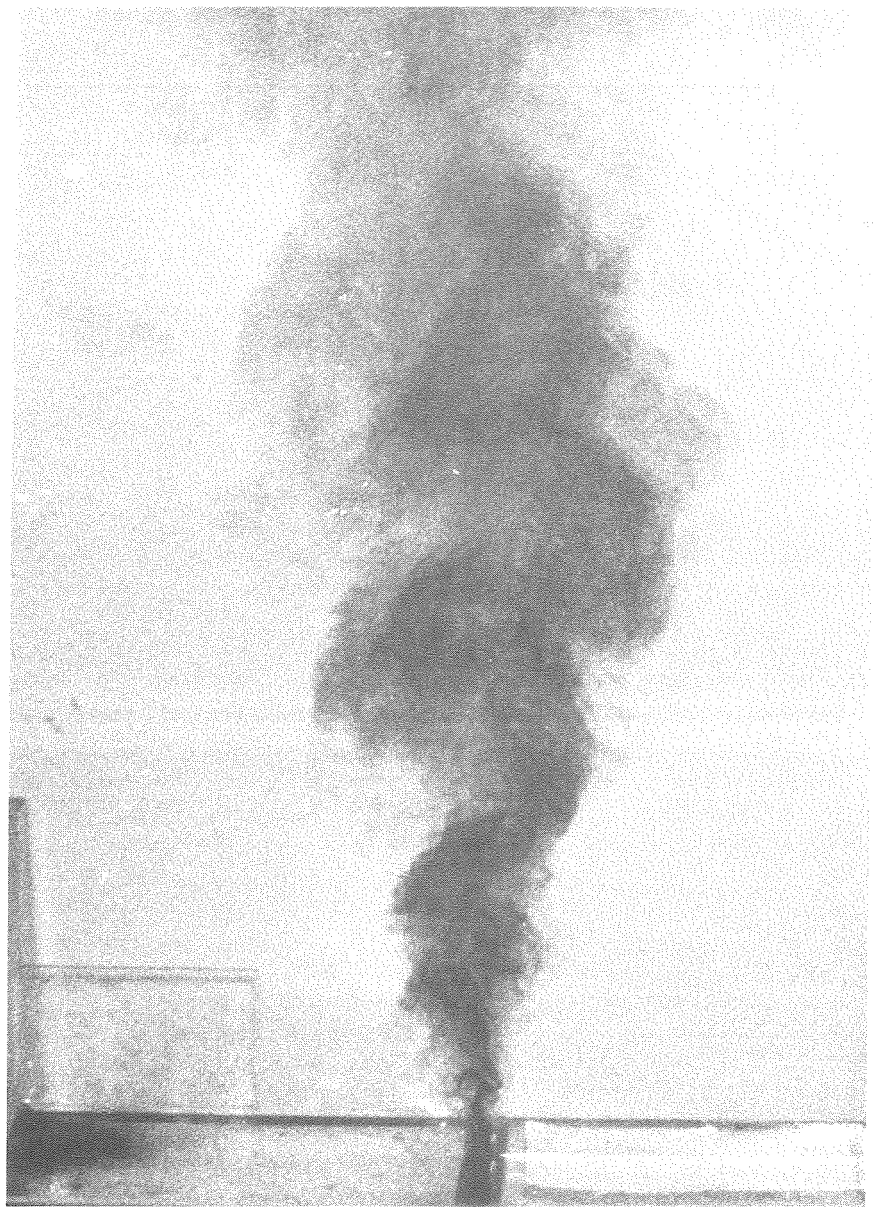

Figure A.1. Short time (0.01 seconds) exposure photograph of a turbulent two-dimensional plume ($R_o \approx 0.5$).

Figure A.2. Short time (0.01 seconds) exposure photograph of a turbulent two-dimensional plume ($R_o \approx 0.5$).

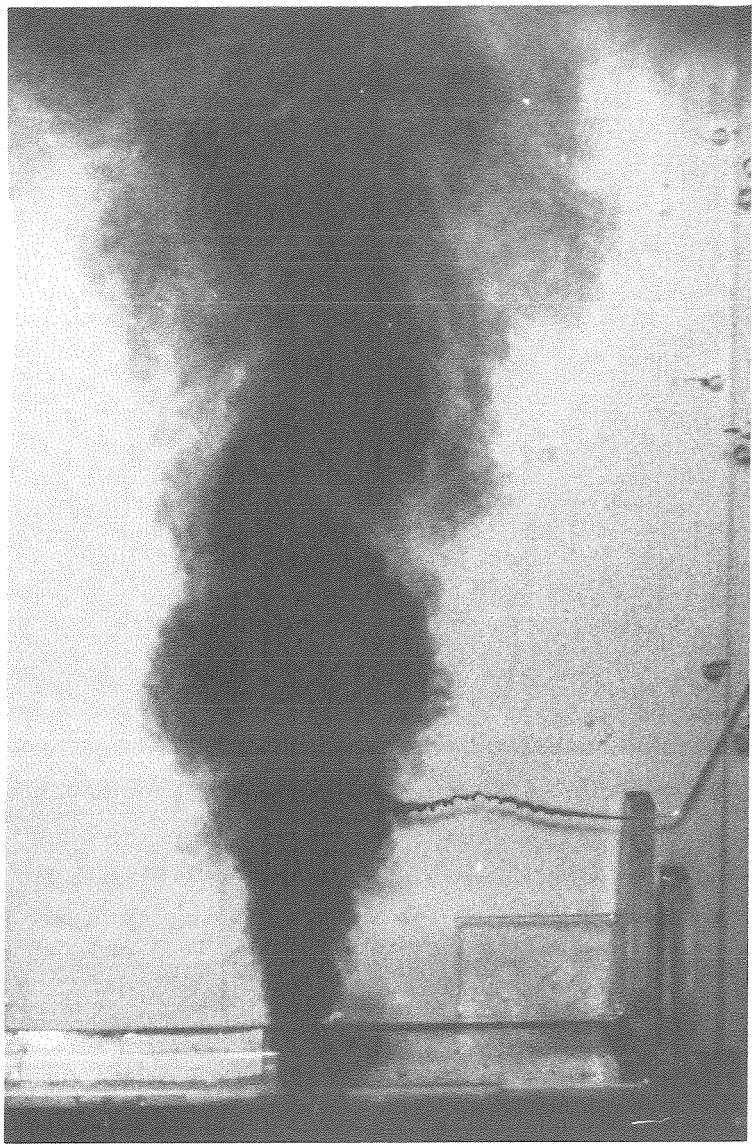

Figure A.3. Medium time (2 seconds) exposure photograph of a turbulent two-dimensional plume ($R_o \approx 0.5$).

Figure A.4. Short time (0.01 seconds) exposure photograph of a turbulent two-dimensional jet ($R_e \approx 2500$, $R_o = 0$).

Figure A.5. Medium time (2 seconds) exposure photograph of a turbulent two-dimensional jet ($R_e \approx 2500$, $R_o = 0$).

which acts at the center of mass of m_{AB}, and (ii) the Archimedian force, with absolute value

$$R = V_{AB}\rho_a g$$

(where ρ_a the density of the ambient fluid), which acts at the center of pressure forces. If the Figure A.6 is slightly perturbed, then the Figure A.7 is obtained from where we can observe that the moment between the forces R and G tends to overturn the volume V_{AB}, and probably this is the mechanism which is responsible for the large scale waves which are observed in a plume.

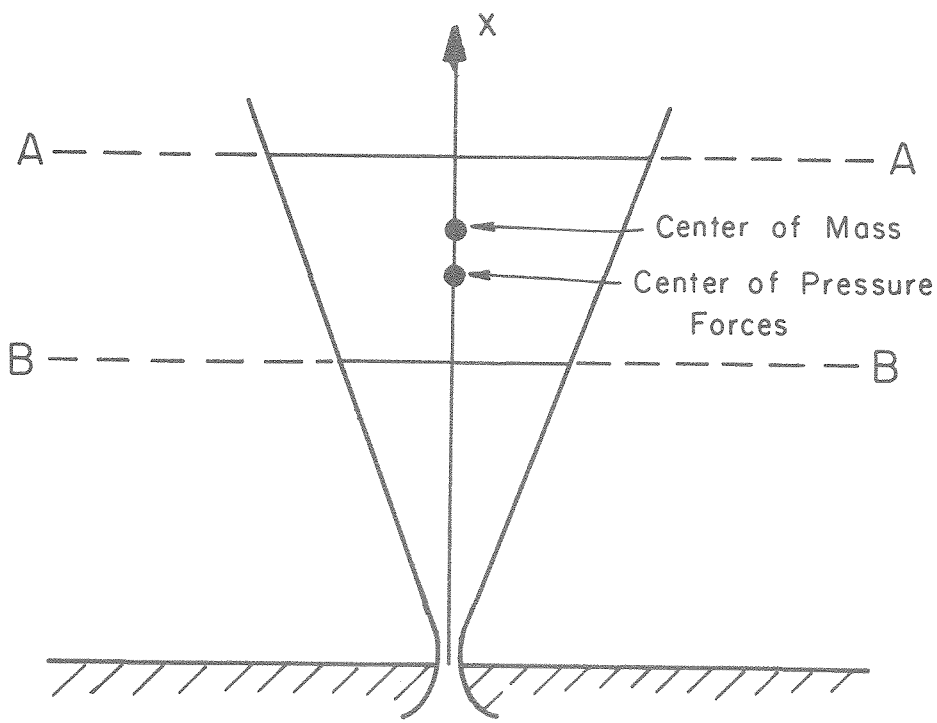

Figure A.6. Hypothetical instantaneous picture of a plume

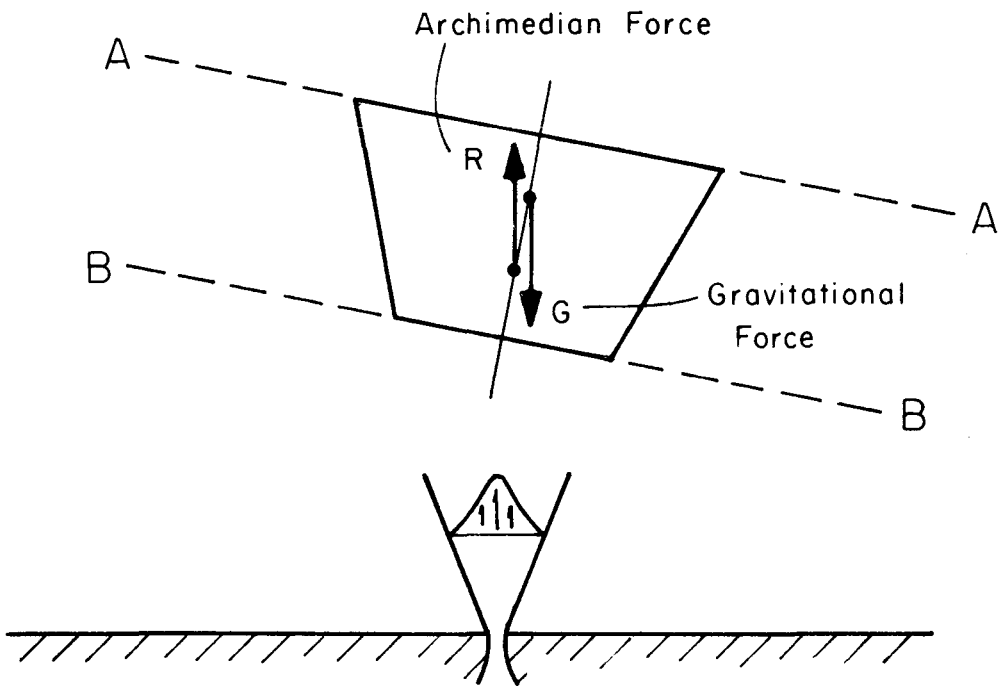

Figure A.7. Schematic to explain the production of large waves in a plume.

APPENDIX B

The experimental results concerning the mean temperature profile for all the runs are presented here. For every experimental run the mean temperature profile $\overline{T}(x,y)$ in °C was plotted versus the distance from the jet axis in cm, the temperature half-width b_T were calculated and a Gaussian curve defined by Equation 4.1.1 was fitted. The half-widths $b_T(x)$ for each particular run were plotted versus the distance from the exit and the spreading rate K_{1T} was calculated according to Equation 4.1.2. The mean temperature $\overline{T}(x,y)$ normalized by the mean temperature on the jet axis, $\overline{T}_M(x)$, was plotted against the non-dimensional distance from the jet axis y/x' (where $x = x - x_{0T}$) for each particular run and a Gaussian curve defined by Equation 4.1.3 was fitted. The experimental values for the half-width b_T and for the temperature on the jet axis $\overline{T}_M(x)$ for each run were presented previously in Table 4.1.2.

Since all the necessary information concerning each experiment is indicated in each figure, no titles will be given in the figures of Appendix B.

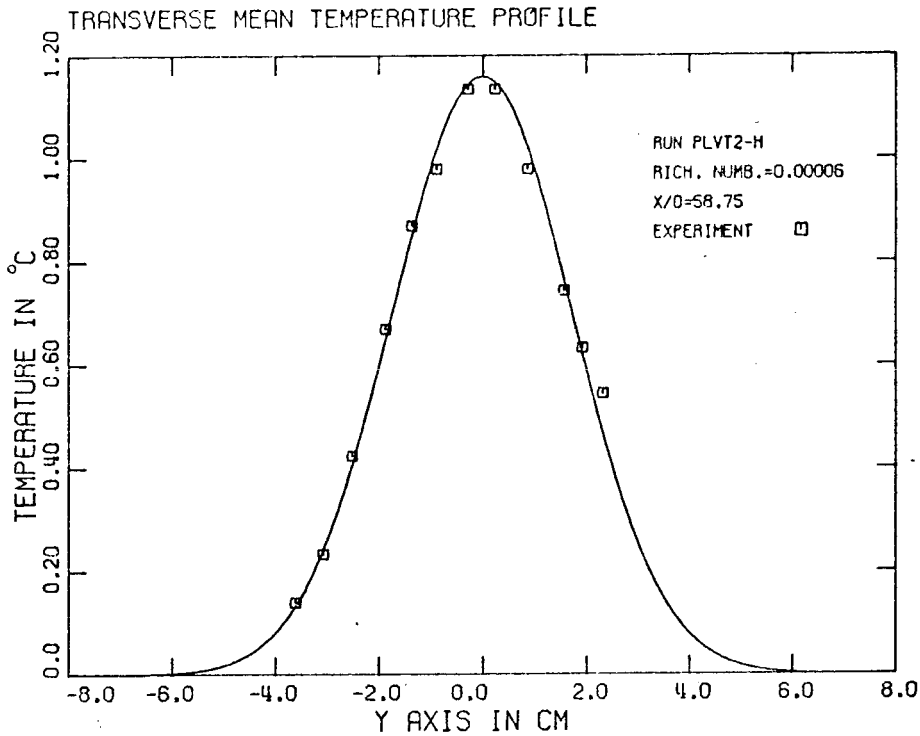
TRANSVERSE MEAN TEMPERATURE PROFILE
RUN PLVT2-H
RICH. NUMB.=0.00006
X/D=58.75
EXPERIMENT
TEMPERATURE IN °C
0.0
0.20
0.40
0.60
0.80
1.00
1.20
-8.0
-6.0
-4.0
-2.0
0.0
2.0
4.0
6.0
8.0
Y AXIS IN CM

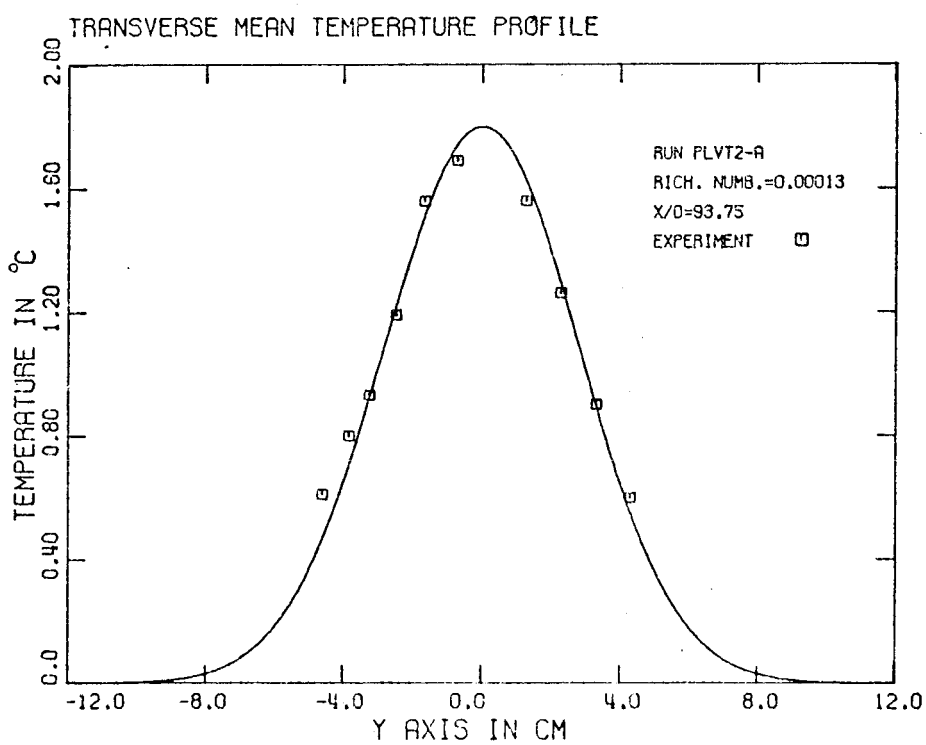
TRANSVERSE MEAN TEMPERATURE PROFILE
RUN PLVT2-A
RICH. NUMB.=0.00013
X/D=93.75
EXPERIMENT
TEMPERATURE IN °C
0.0
0.40
0.80
1.20
1.60
2.00
-12.0
-8.0
-4.0
0.0
4.0
8.0
12.0
Y AXIS IN CM

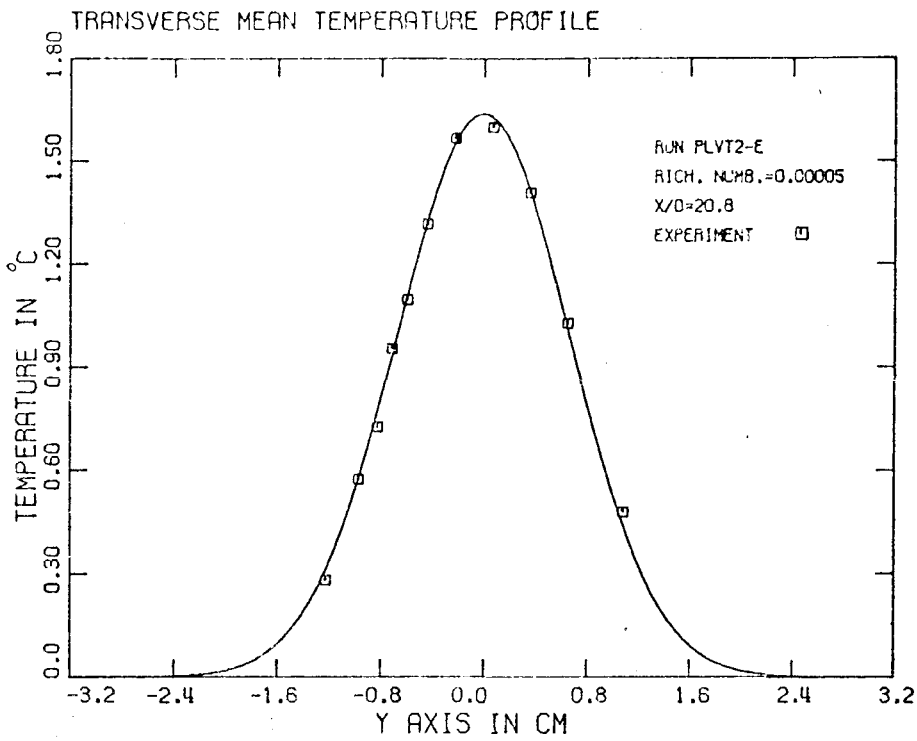
TRANSVERSE MEAN TEMPERATURE PROFILE
RUN PLVT2-E
RICH. NUMB.=0.00005
X/D=20.8
EXPERIMENT
TEMPERATURE IN °C
Y AXIS IN CM
0.0
0.30
0.60
0.90
1.20
1.50
1.80
-3.2
-2.4
-1.6
-0.8
0.0
0.8
1.6
2.4
3.2

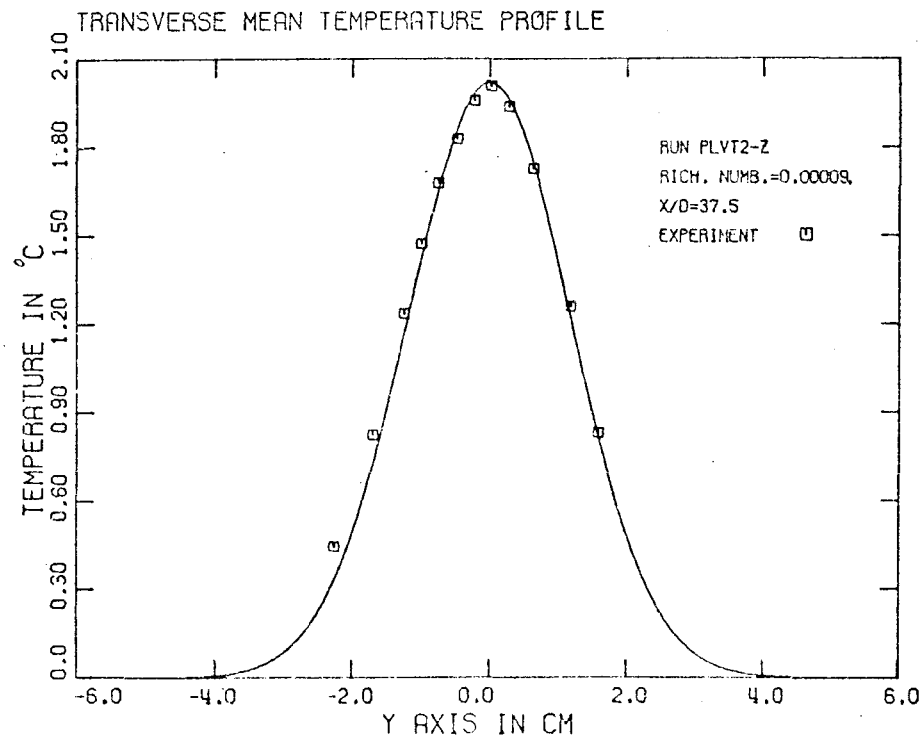
TRANSVERSE MEAN TEMPERATURE PROFILE
RUN PLVT2-Z
RICH. NUMB.=0.00009
X/D=37.5
EXPERIMENT
TEMPERATURE IN °C
Y AXIS IN CM
0.0
0.30
0.60
0.90
1.20
1.50
1.80
2.10
-6.0
-4.0
-2.0
0.0
2.0
4.0
6.0

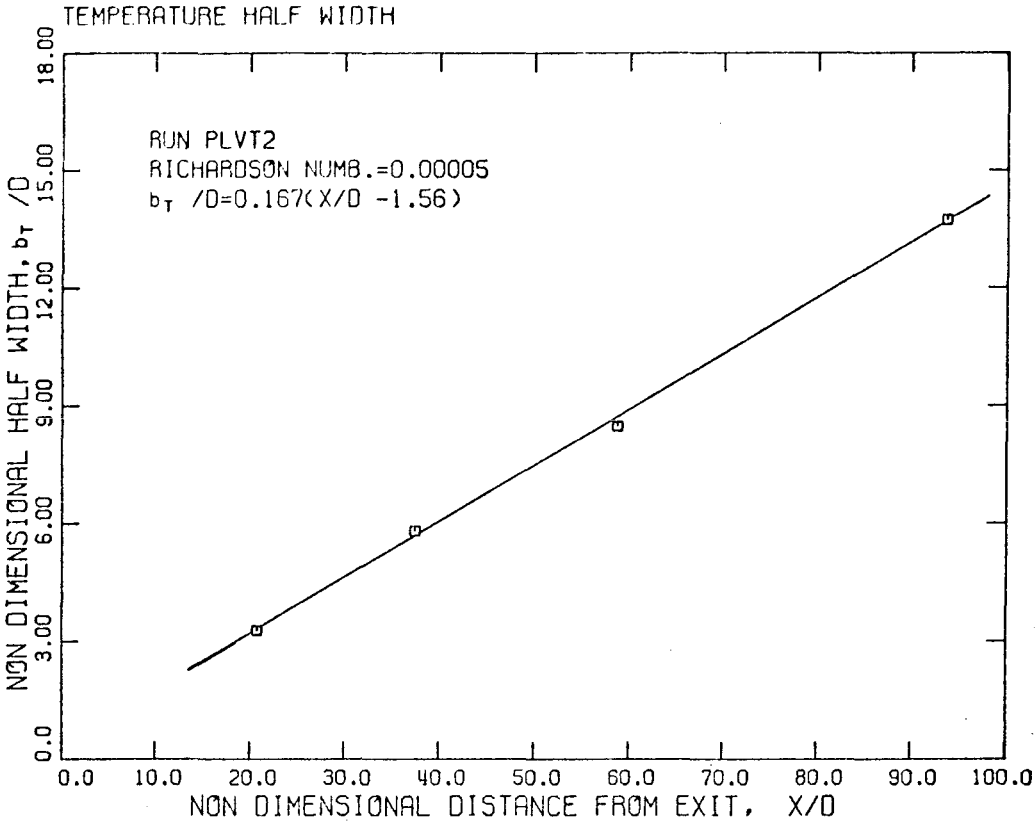
TEMPERATURE HALF WIDTH
RUN PLVT2
RICHARDSON NUMB.=0.00005
b_T /D=0.167(X/D -1.56)
NON DIMENSIONAL HALF WIDTH, b_T /D
0.0
3.00
6.00
9.00
12.00
15.00
18.00
0.0
10.0
20.0
30.0
40.0
50.0
60.0
70.0
80.0
90.0
100.0
NON DIMENSIONAL DISTANCE FROM EXIT, X/D

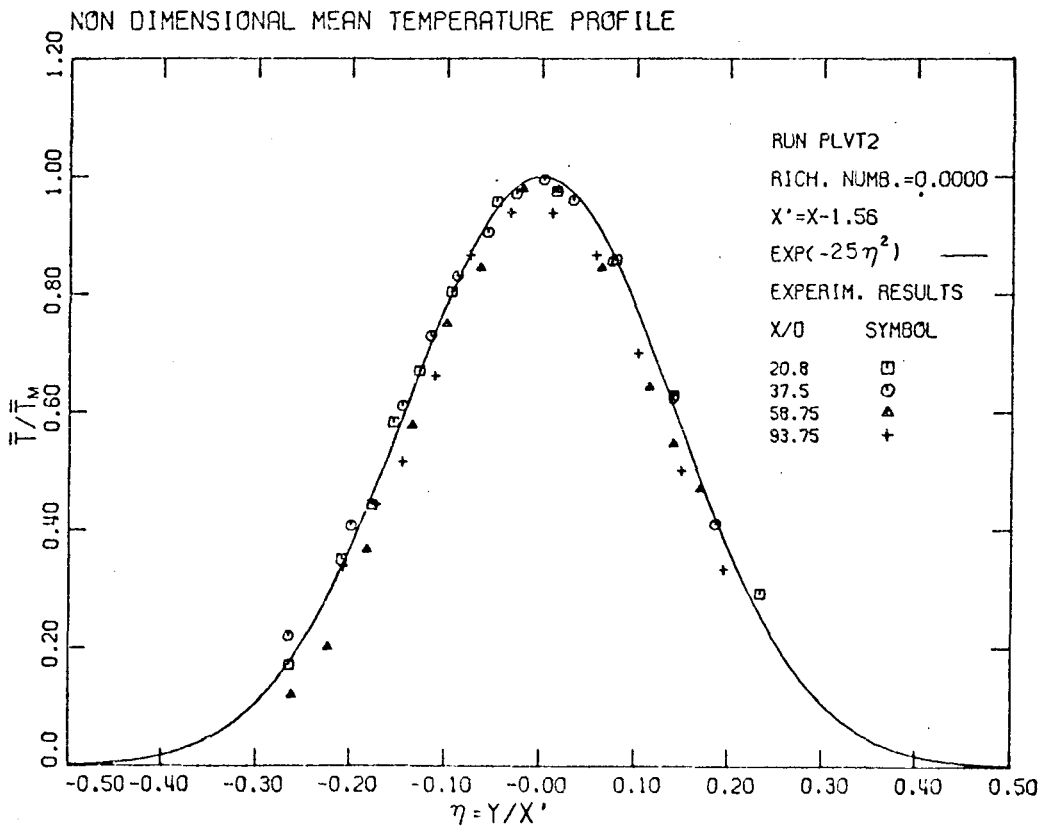
NON DIMENSIONAL MEAN TEMPERATURE PROFILE
RUN PLVT2
RICH. NUMB.=0.0000
X'=X-1.56
EXP(-25η^2)
EXPERIM. RESULTS
X/D SYMBOL
20.8
37.5
58.75
93.75
$\bar{T}/\bar{T}_M$
0.0
0.20
0.40
0.60
0.80
1.00
1.20
-0.50
-0.40
-0.30
-0.20
-0.10
-0.00
0.10
0.20
0.30
0.40
0.50
η = Y/X'

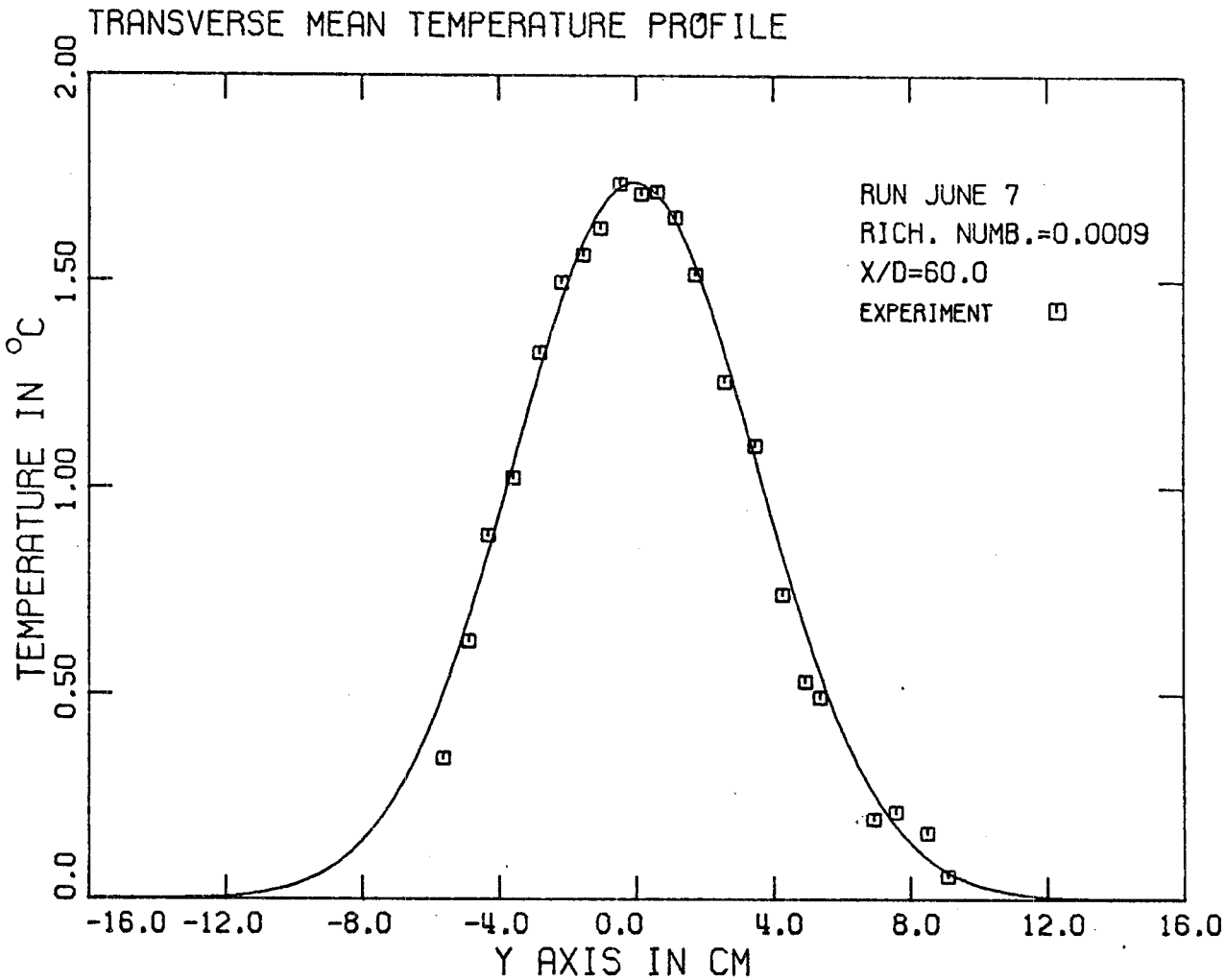
TRANSVERSE MEAN TEMPERATURE PROFILE
RUN JUNE 7
RICH. NUMB.=0.0009
X/D=60.0
EXPERIMENT
TEMPERATURE IN °C
0.0
0.50
1.00
1.50
2.00
-16.0
-12.0
-8.0
-4.0
0.0
4.0
8.0
12.0
16.0
Y AXIS IN CM

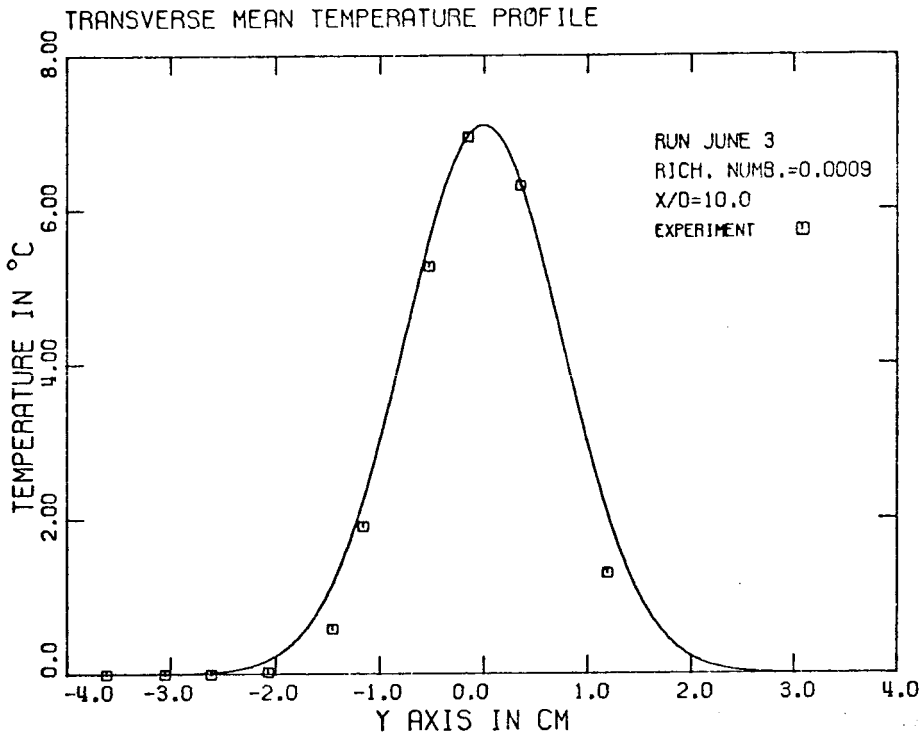
TRANSVERSE MEAN TEMPERATURE PROFILE
RUN JUNE 3
RICH. NUMB.=0.0009
X/D=10.0
EXPERIMENT
TEMPERATURE IN °C
0.0
2.00
4.00
6.00
8.00
-4.0
-3.0
-2.0
-1.0
0.0
1.0
2.0
3.0
4.0
Y AXIS IN CM

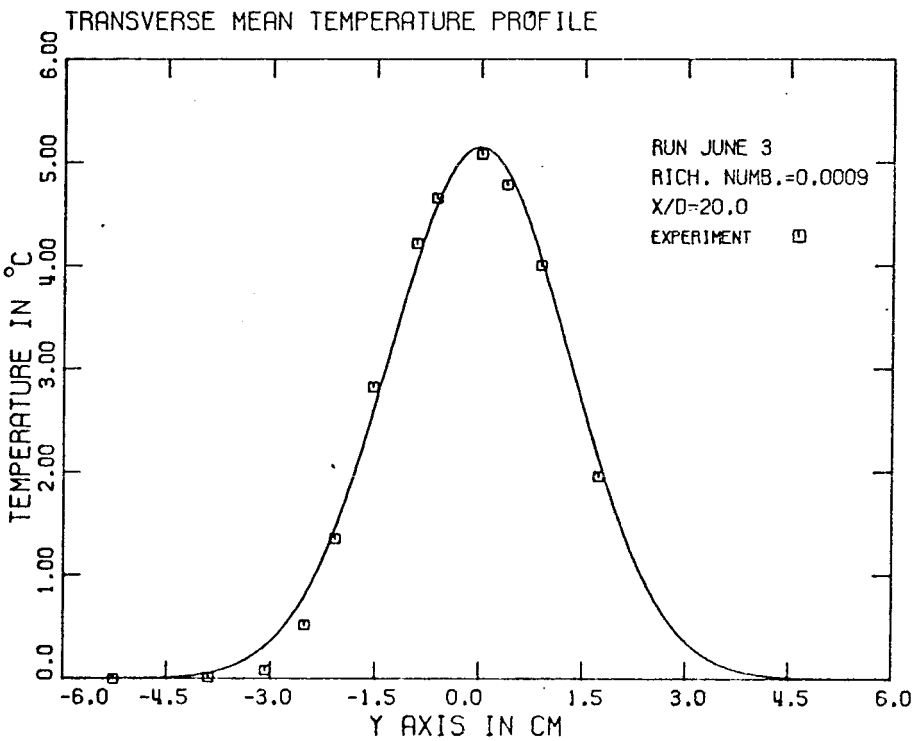
TRANSVERSE MEAN TEMPERATURE PROFILE
RUN JUNE 3
RICH. NUMB.=0.0009
X/D=20.0
EXPERIMENT
TEMPERATURE IN °C
0.0
1.00
2.00
3.00
4.00
5.00
6.00
-6.0
-4.5
-3.0
-1.5
0.0
1.5
3.0
4.5
6.0
Y AXIS IN CM

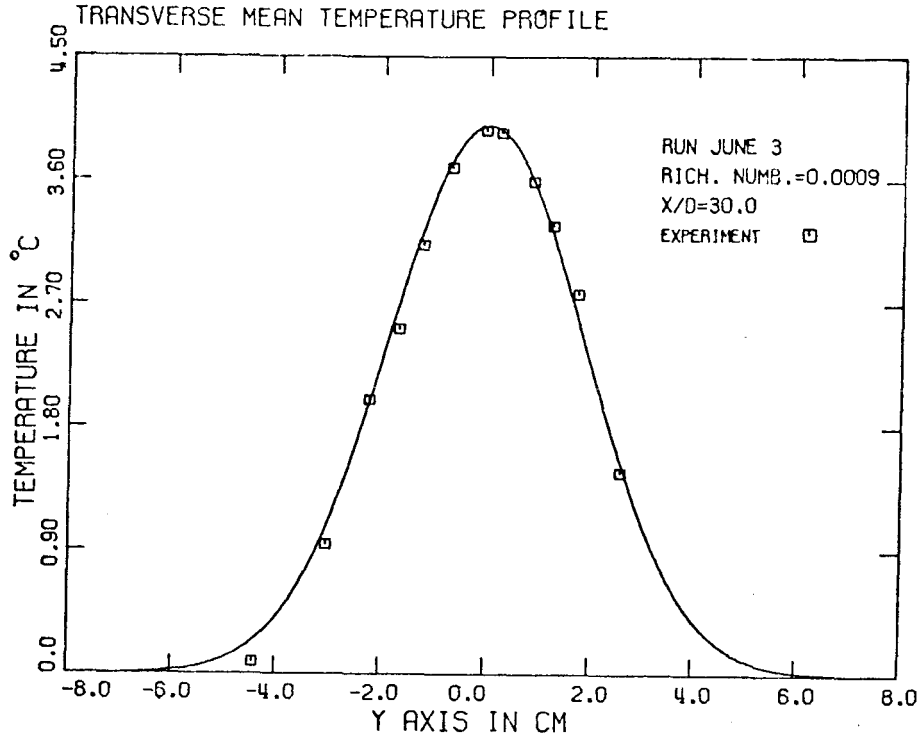
TRANSVERSE MEAN TEMPERATURE PROFILE
RUN JUNE 3
RICH. NUMB.=0.0009
X/D=30.0
EXPERIMENT
TEMPERATURE IN °C
0.0
0.90
1.80
2.70
3.60
4.50
-8.0
-6.0
-4.0
-2.0
0.0
2.0
4.0
6.0
8.0
Y AXIS IN CM

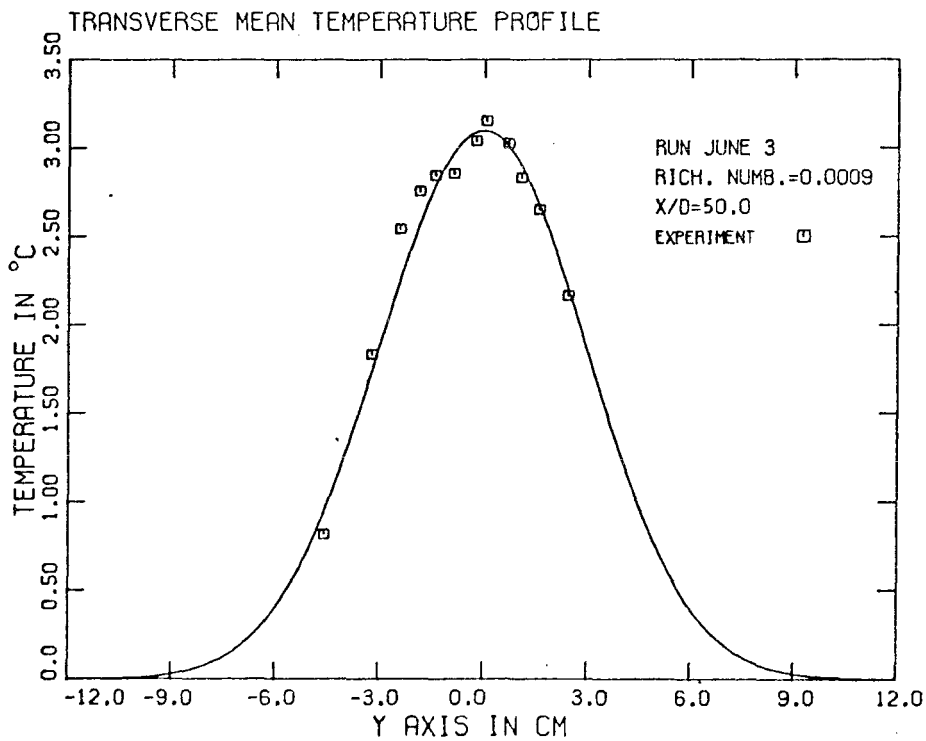
TRANSVERSE MEAN TEMPERATURE PROFILE
RUN JUNE 3
RICH. NUMB.=0.0009
X/D=50.0
EXPERIMENT
TEMPERATURE IN °C
0.0
0.50
1.00
1.50
2.00
2.50
3.00
3.50
-12.0
-9.0
-6.0
-3.0
0.0
3.0
6.0
9.0
12.0
Y AXIS IN CM

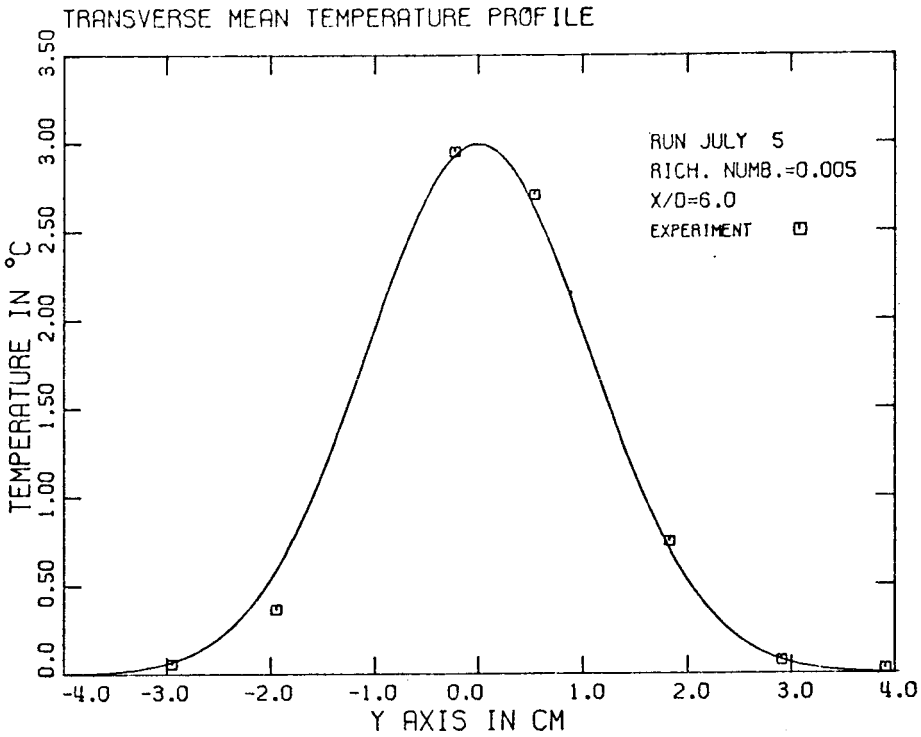
TRANSVERSE MEAN TEMPERATURE PROFILE
RUN JULY 5
RICH. NUMB.=0.005
X/D=6.0
EXPERIMENT
TEMPERATURE IN °C
0.0
0.50
1.00
1.50
2.00
2.50
3.00
3.50
-4.0
-3.0
-2.0
-1.0
0.0
1.0
2.0
3.0
4.0
Y AXIS IN CM

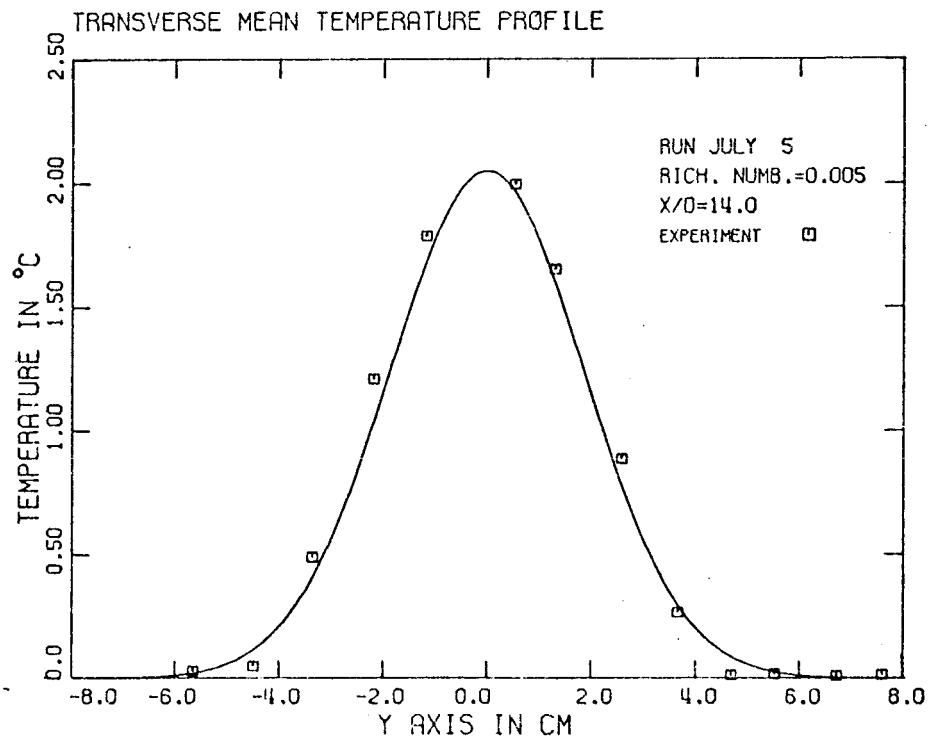
TRANSVERSE MEAN TEMPERATURE PROFILE
RUN JULY 5
RICH. NUMB.=0.005
X/D=14.0
EXPERIMENT
TEMPERATURE IN °C
0.0
0.50
1.00
1.50
2.00
2.50
-8.0
-6.0
-4.0
-2.0
0.0
2.0
4.0
6.0
8.0
Y AXIS IN CM

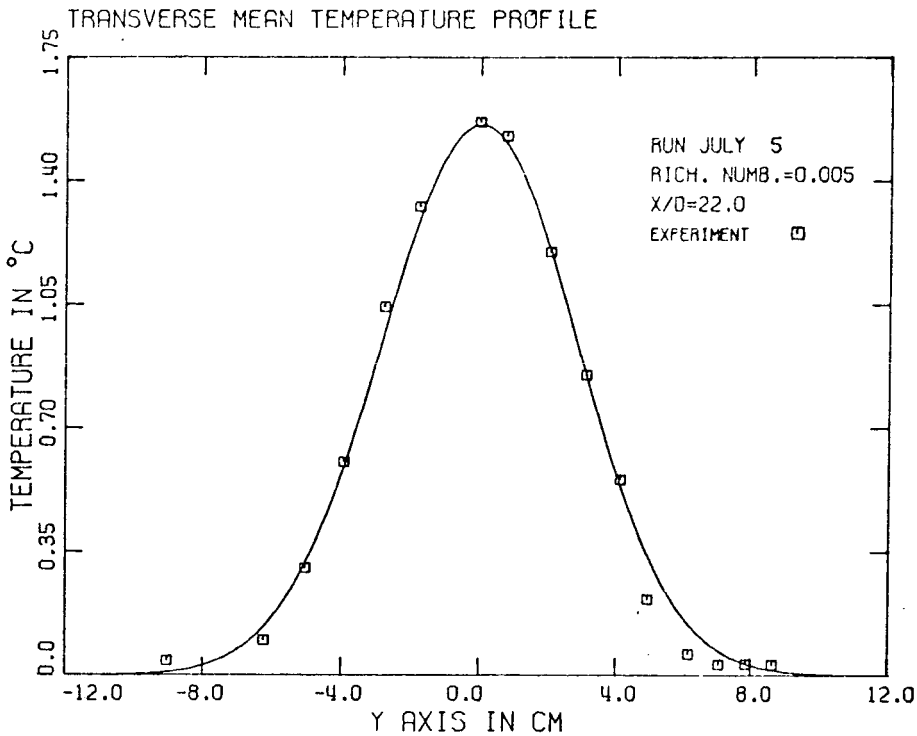
TRANSVERSE MEAN TEMPERATURE PROFILE
RUN JULY 5
RICH. NUMB.=0.005
X/D=22.0
EXPERIMENT
TEMPERATURE IN °C
0.0
0.35
0.70
1.05
1.40
1.75
-12.0
-8.0
-4.0
0.0
4.0
8.0
12.0
Y AXIS IN CM

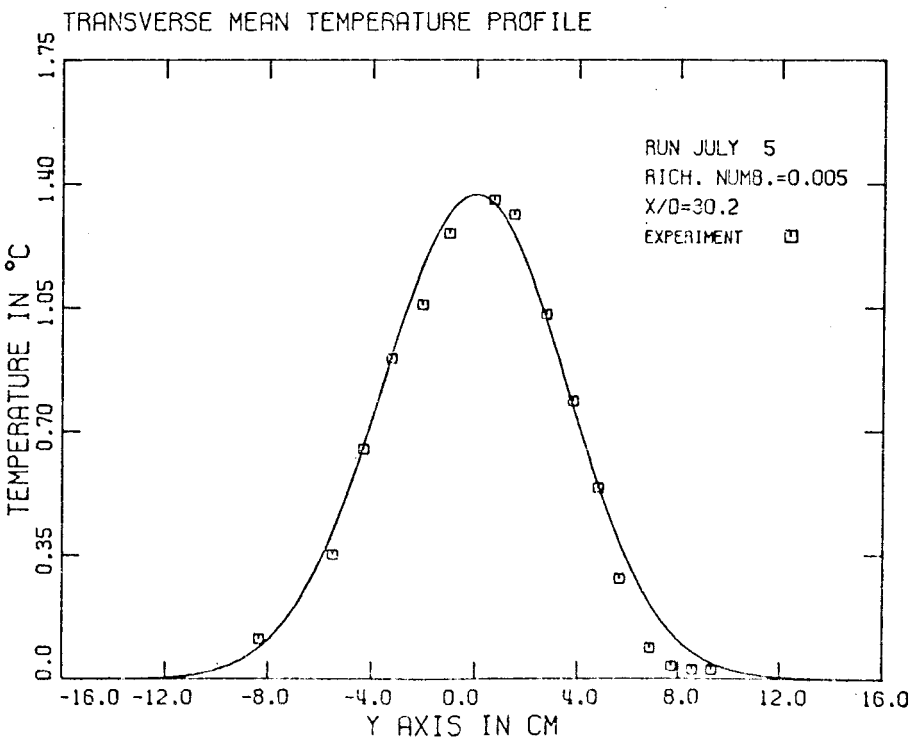
TRANSVERSE MEAN TEMPERATURE PROFILE
RUN JULY 5
RICH. NUMB.=0.005
X/D=30.2
EXPERIMENT
TEMPERATURE IN °C
0.0
0.35
0.70
1.05
1.40
1.75
-16.0
-12.0
-8.0
-4.0
0.0
4.0
8.0
12.0
16.0
Y AXIS IN CM

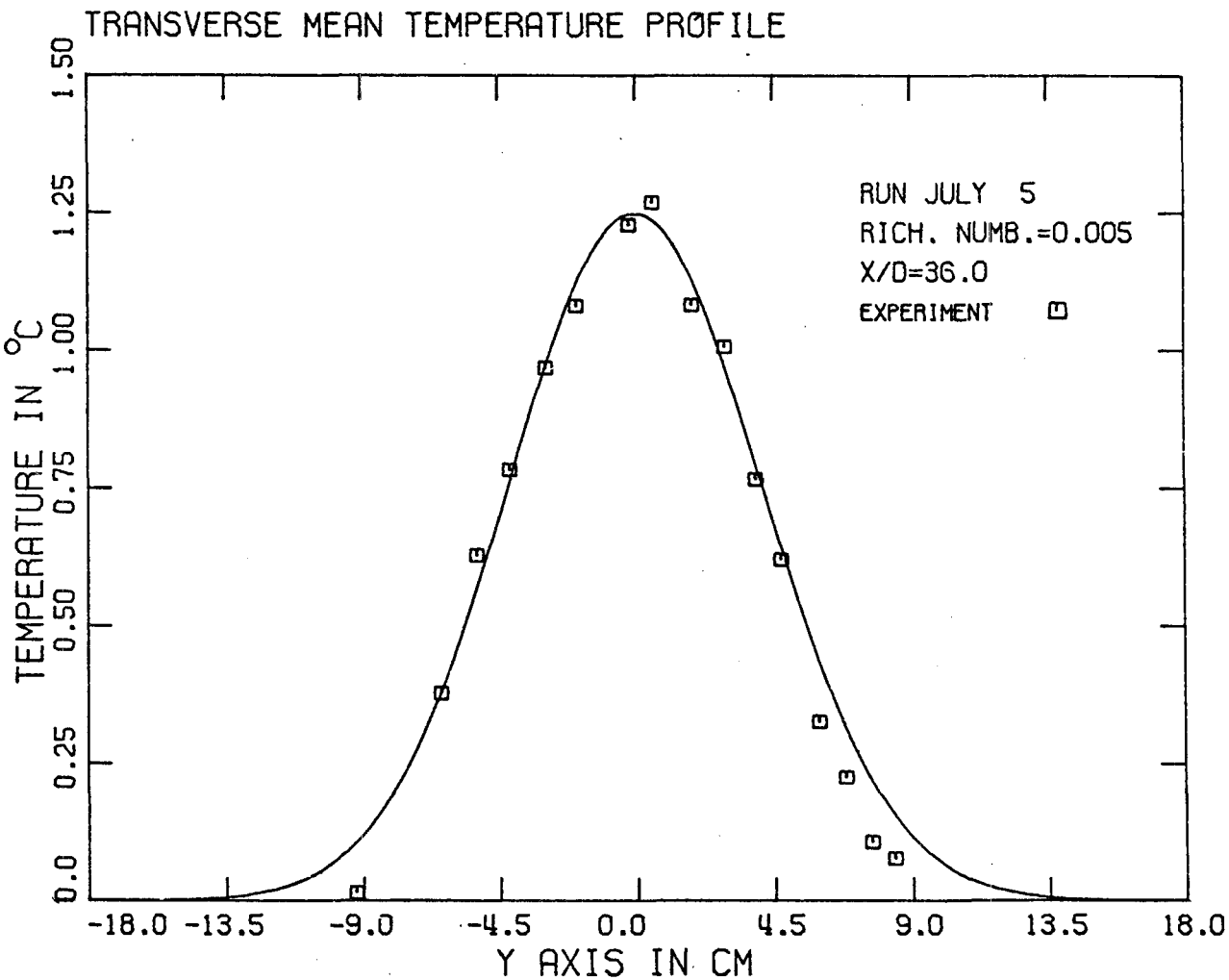
TRANSVERSE MEAN TEMPERATURE PROFILE
RUN JULY 5
RICH. NUMB.=0.005
X/D=36.0
EXPERIMENT
TEMPERATURE IN °C
0.0
0.25
0.50
0.75
1.00
1.25
1.50
-18.0 -13.5 -9.0 -4.5 0.0 4.5 9.0 13.5 18.0
Y AXIS IN CM

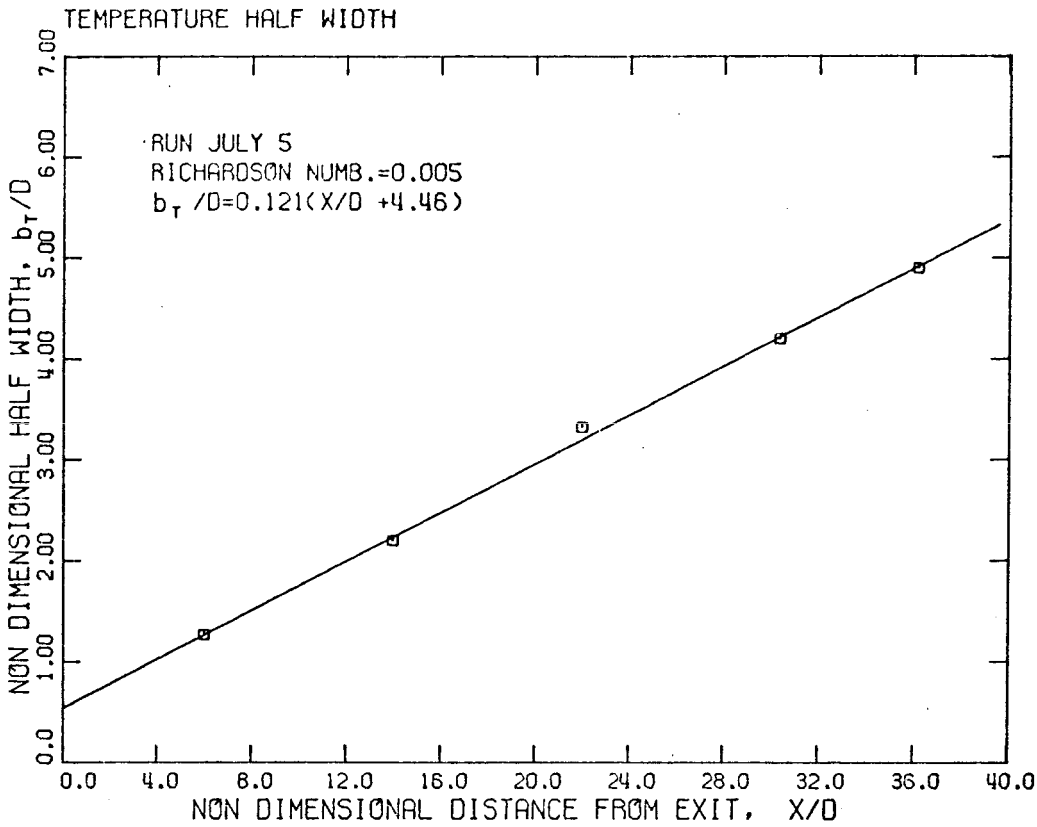
TEMPERATURE HALF WIDTH
RUN JULY 5
RICHARDSON NUMB.=0.005
$b_T/D=0.121(X/D+4.46)$
NON DIMENSIONAL HALF WIDTH, b_T/D
NON DIMENSIONAL DISTANCE FROM EXIT, X/D
0.0
1.00
2.00
3.00
4.00
5.00
6.00
7.00
0.0
4.0
8.0
12.0
16.0
20.0
24.0
28.0
32.0
36.0
40.0

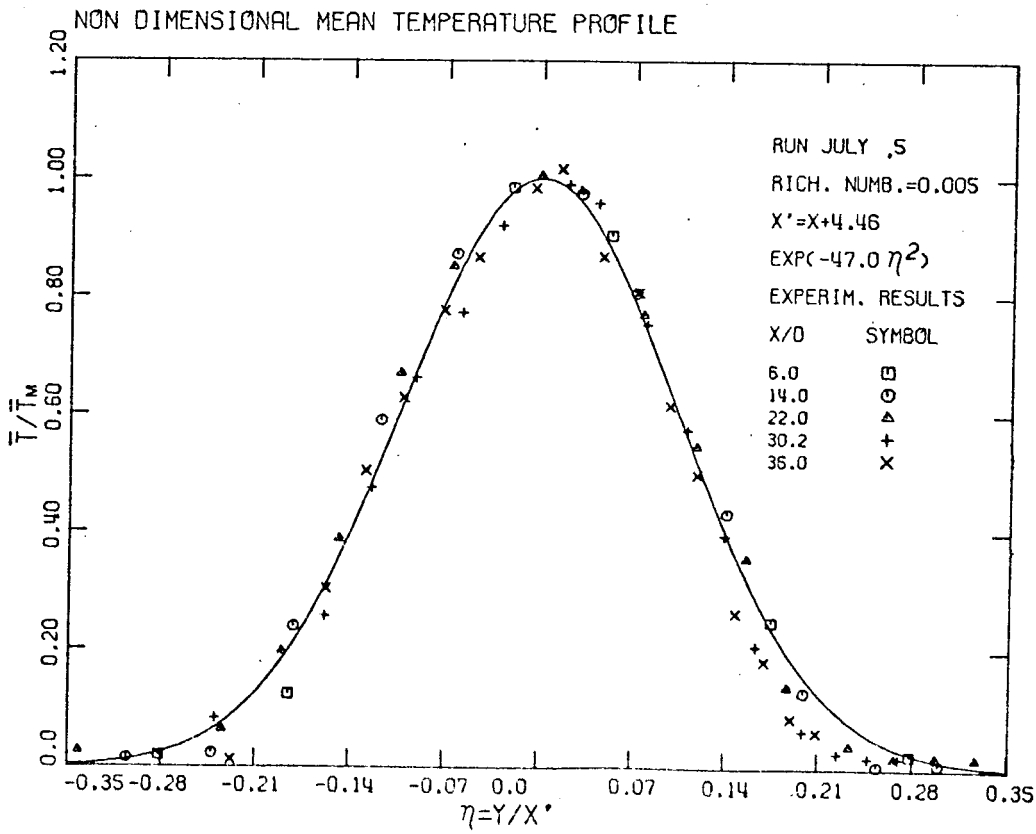
NON DIMENSIONAL MEAN TEMPERATURE PROFILE
RUN JULY ,5
RICH. NUMB.=0.005
X'=X+4.46
EXP(-47.0 η^2)
EXPERIM. RESULTS
X/D SYMBOL
6.0
14.0
22.0
30.2
36.0
$\bar{T}/\bar{T}_M$
$\eta=Y/X'$
0.0
0.20
0.40
0.60
0.80
1.00
1.20
-0.35
-0.28
-0.21
-0.14
-0.07
0.0
0.07
0.14
0.21
0.28
0.35

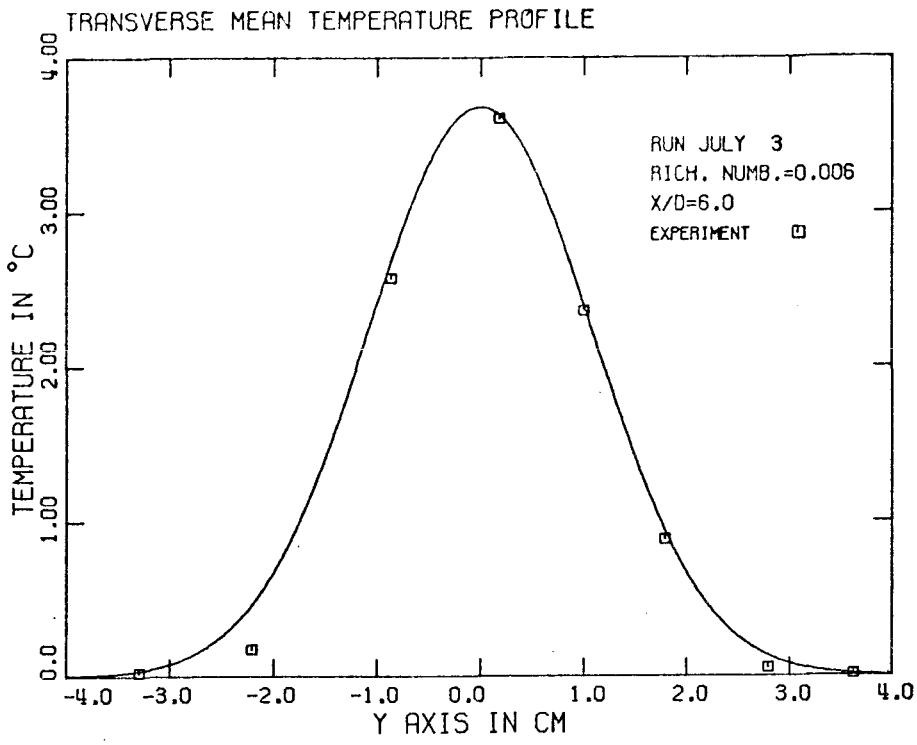
TRANSVERSE MEAN TEMPERATURE PROFILE
RUN JULY 3
RICH. NUMB.=0.006
X/D=6.0
EXPERIMENT
TEMPERATURE IN °C
0.0
1.00
2.00
3.00
4.00
-4.0
-3.0
-2.0
-1.0
0.0
1.0
2.0
3.0
4.0
Y AXIS IN CM

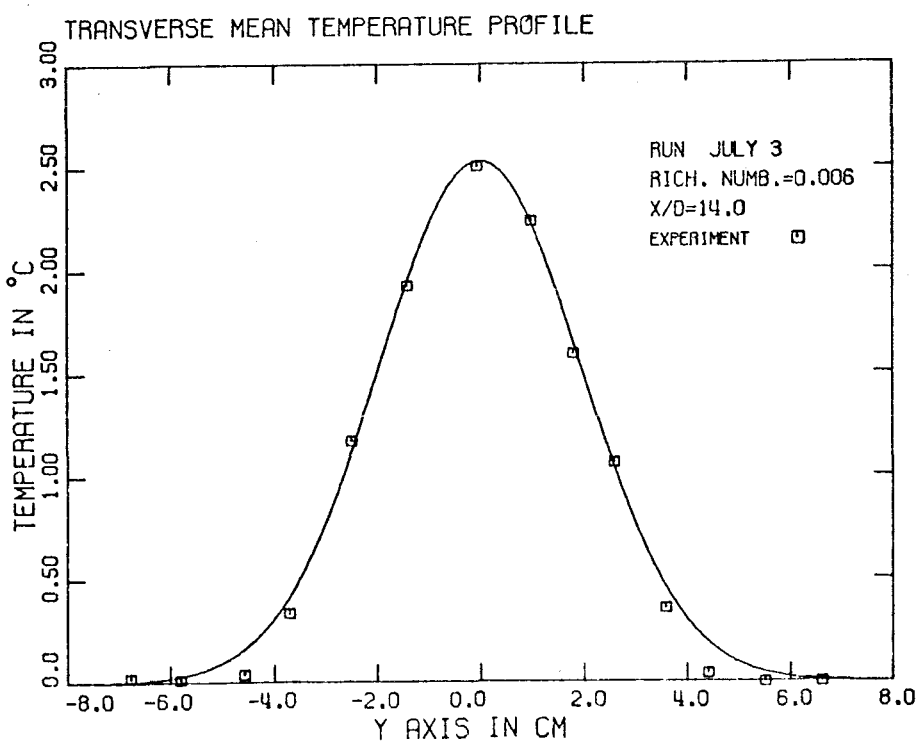
TRANSVERSE MEAN TEMPERATURE PROFILE
RUN JULY 3
RICH. NUMB.=0.006
X/D=14.0
EXPERIMENT
TEMPERATURE IN °C
0.0
0.50
1.00
1.50
2.00
2.50
3.00
-8.0
-6.0
-4.0
-2.0
0.0
2.0
4.0
6.0
8.0
Y AXIS IN CM

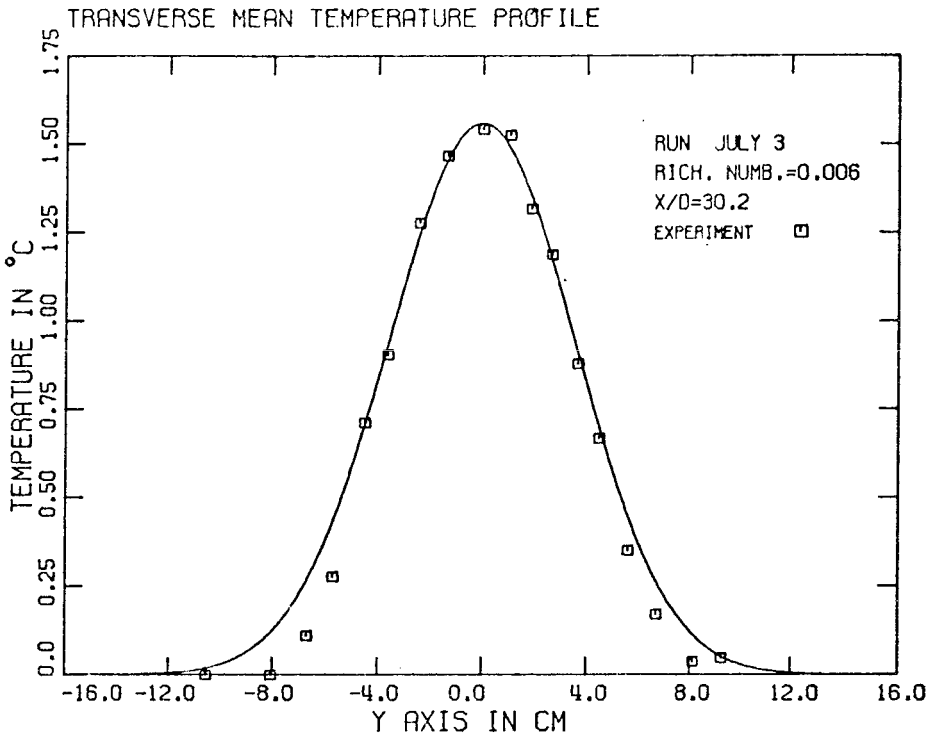
TRANSVERSE MEAN TEMPERATURE PROFILE
TEMPERATURE IN °C
0.0
0.25
0.50
0.75
1.00
1.25
1.50
1.75
-16.0 -12.0 -8.0 -4.0 0.0 4.0 8.0 12.0 16.0
Y AXIS IN CM
RUN JULY 3
RICH. NUMB.=0.006
X/D=30.2
EXPERIMENT

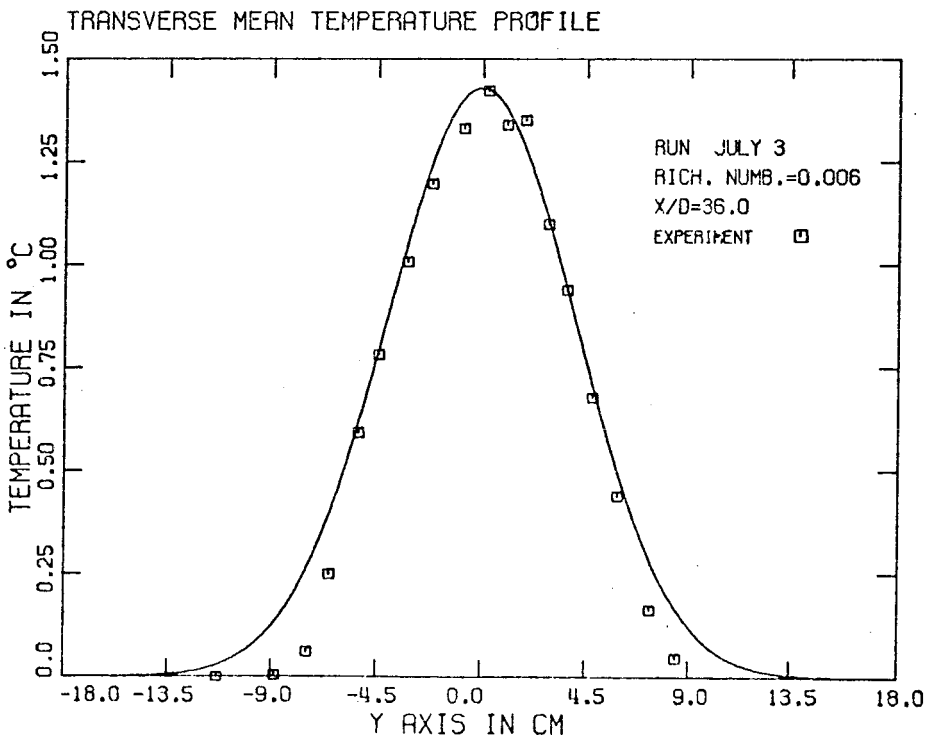
TRANSVERSE MEAN TEMPERATURE PROFILE
TEMPERATURE IN °C
0.0
0.25
0.50
0.75
1.00
1.25
1.50
-18.0 -13.5 -9.0 -4.5 0.0 4.5 9.0 13.5 18.0
Y AXIS IN CM
RUN JULY 3
RICH. NUMB.=0.006
X/D=36.0
EXPERIMENT

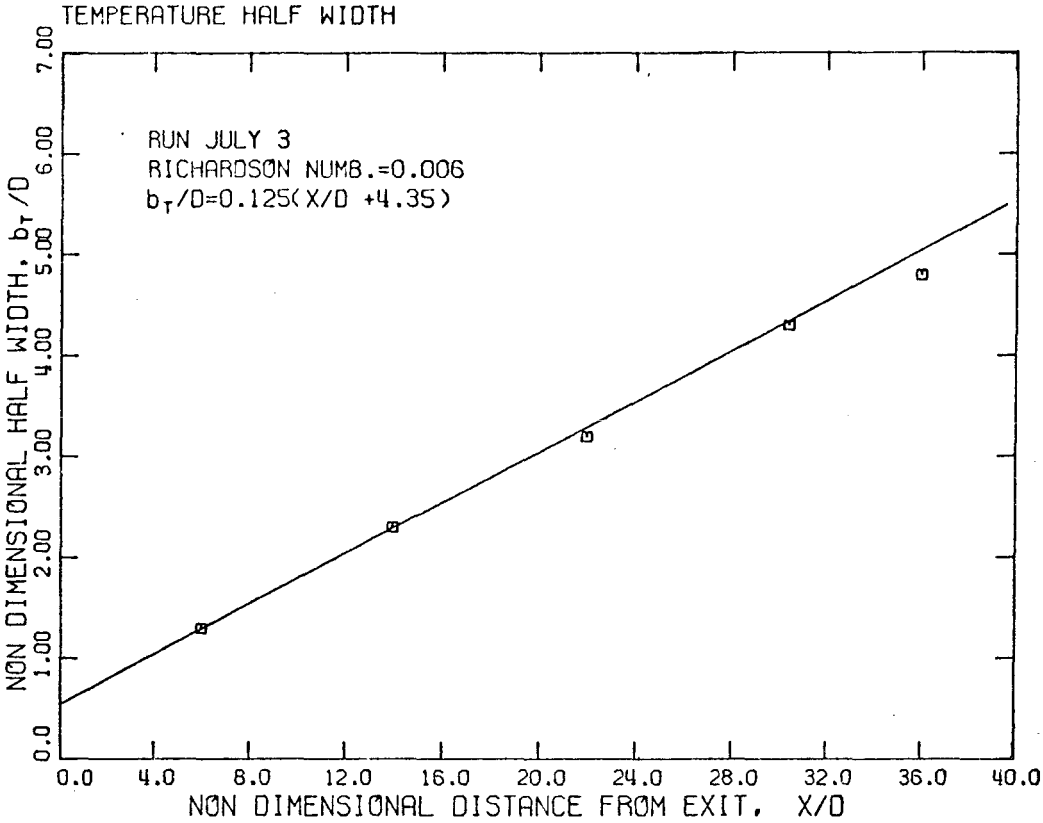
TEMPERATURE HALF WIDTH
RUN JULY 3
RICHARDSON NUMB.=0.006
$b_T/D=0.125(X/D+4.35)$
NON DIMENSIONAL HALF WIDTH, b_T/D
NON DIMENSIONAL DISTANCE FROM EXIT, X/D
0.0
1.00
2.00
3.00
4.00
5.00
6.00
7.00
0.0
4.0
8.0
12.0
16.0
20.0
24.0
28.0
32.0
36.0
40.0

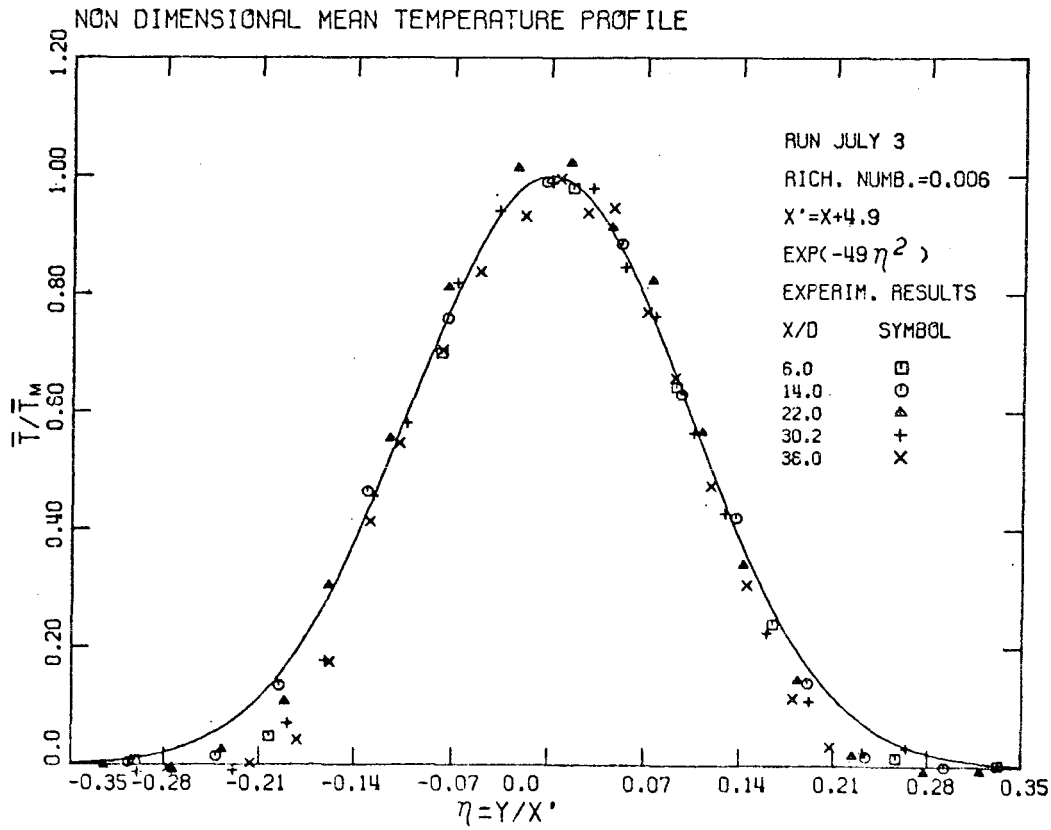
NON DIMENSIONAL MEAN TEMPERATURE PROFILE
RUN JULY 3
RICH. NUMB.=0.006
X'=X+4.9
$EXP(-49\eta^2)$
EXPERIM. RESULTS
X/D SYMBOL
6.0
14.0
22.0
30.2
36.0
$\bar{T}/\bar{T}_M$
$\eta=Y/X'$
0.0
0.20
0.40
0.60
0.80
1.00
1.20
-0.35
-0.28
-0.21
-0.14
-0.07
0.0
0.07
0.14
0.21
0.28
0.35

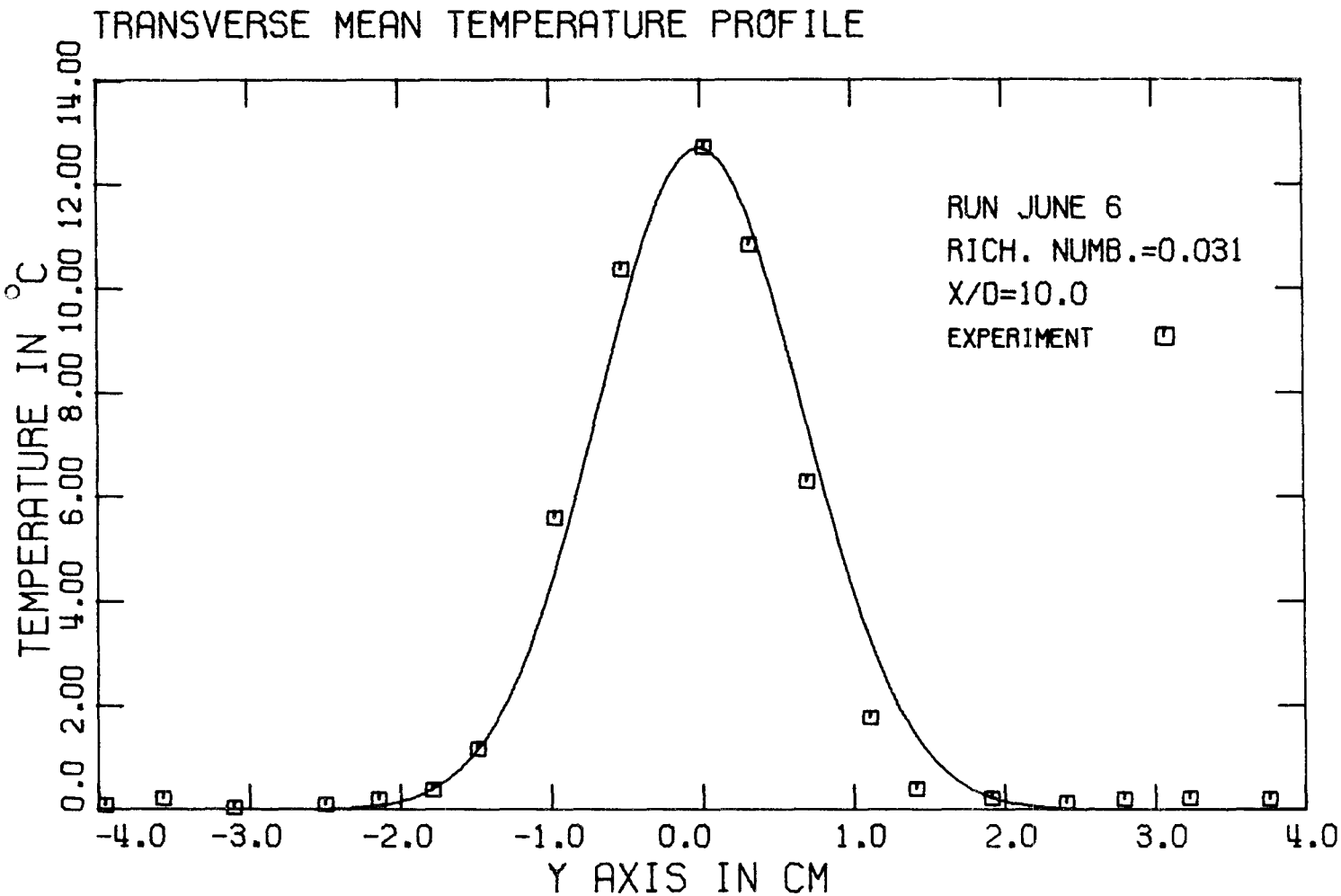
TRANSVERSE MEAN TEMPERATURE PROFILE
TEMPERATURE IN °C
0.0 2.00 4.00 6.00 8.00 10.00 12.00 14.00
-4.0 -3.0 -2.0 -1.0 0.0 1.0 2.0 3.0 4.0
Y AXIS IN CM
RUN JUNE 6
RICH. NUMB.=0.031
X/D=10.0
EXPERIMENT

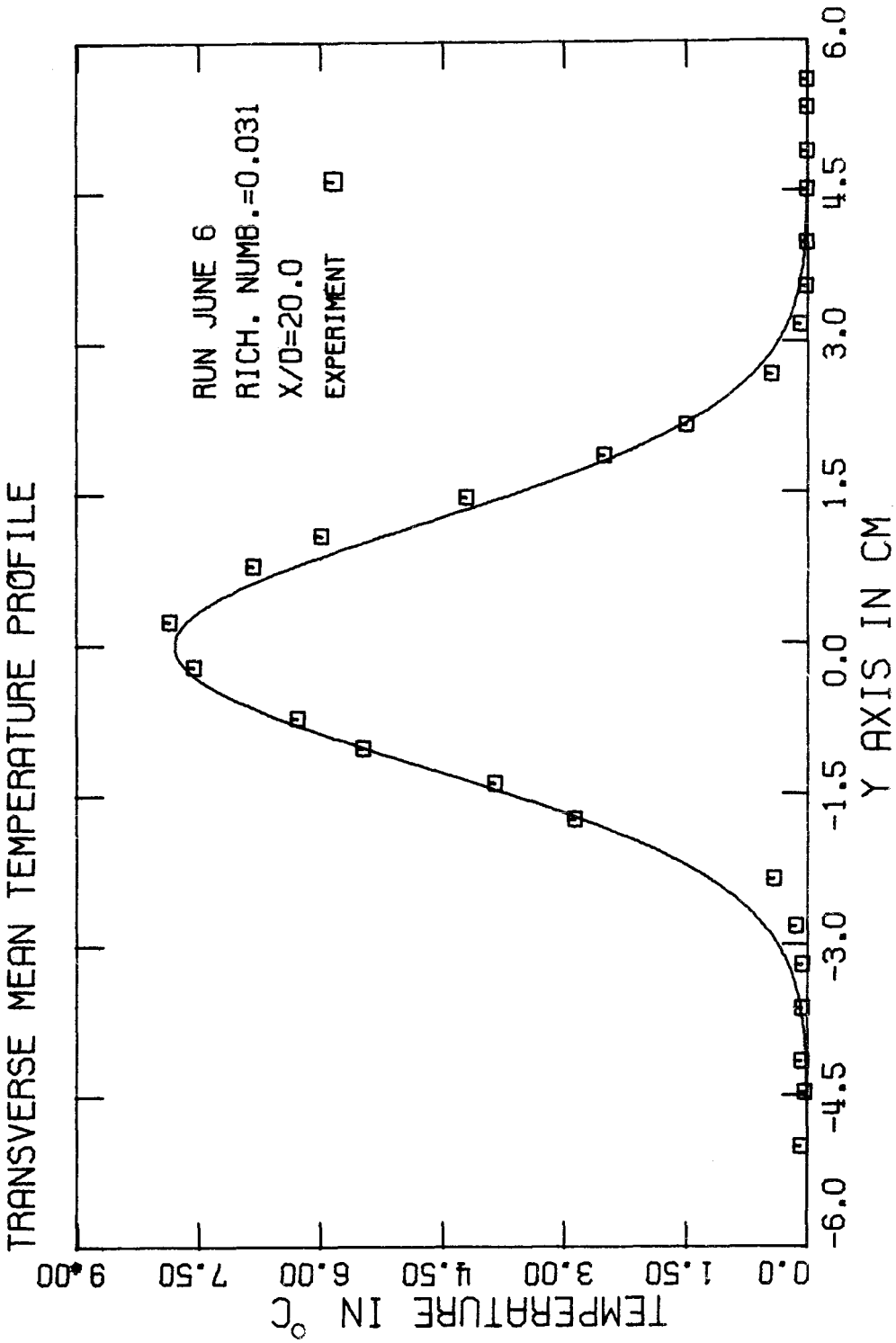
TRANSVERSE MEAN TEMPERATURE PROFILE
RUN JUNE 6
RICH. NUMB.=0.031
X/D=20.0
EXPERIMENT
TEMPERATURE IN °C
0.0
1.50
3.00
4.50
6.00
7.50
9.00
Y AXIS IN CM
-6.0
-4.5
-3.0
-1.5
0.0
1.5
3.0
4.5
6.0

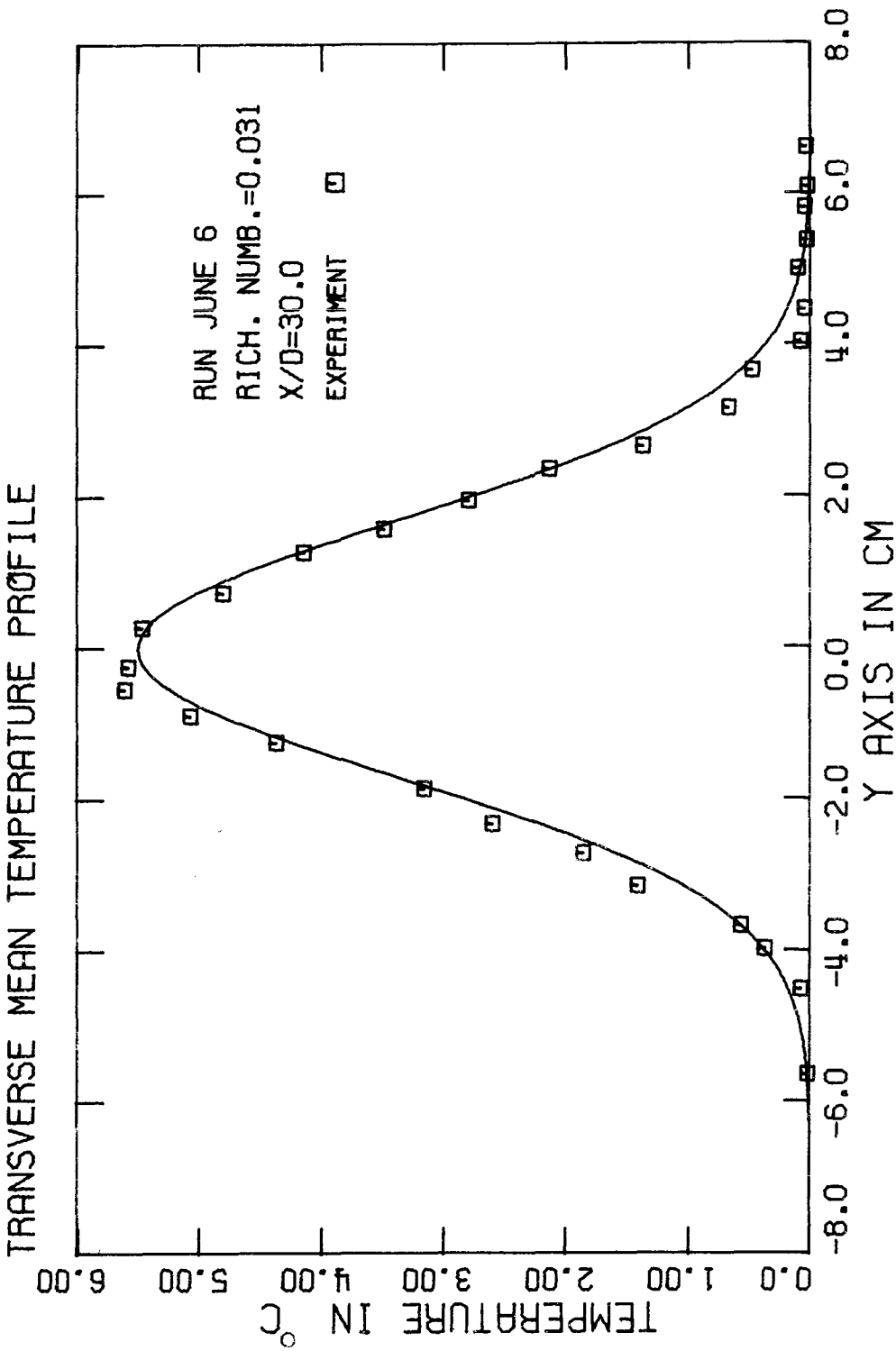
TRANSVERSE MEAN TEMPERATURE PROFILE
RUN JUNE 6
RICH. NUMB.=0.031
X/D=30.0
EXPERIMENT
TEMPERATURE IN °C
Y AXIS IN CM
0.0
1.00
2.00
3.00
4.00
5.00
6.00
-8.0
-6.0
-4.0
-2.0
0.0
2.0
4.0
6.0
8.0

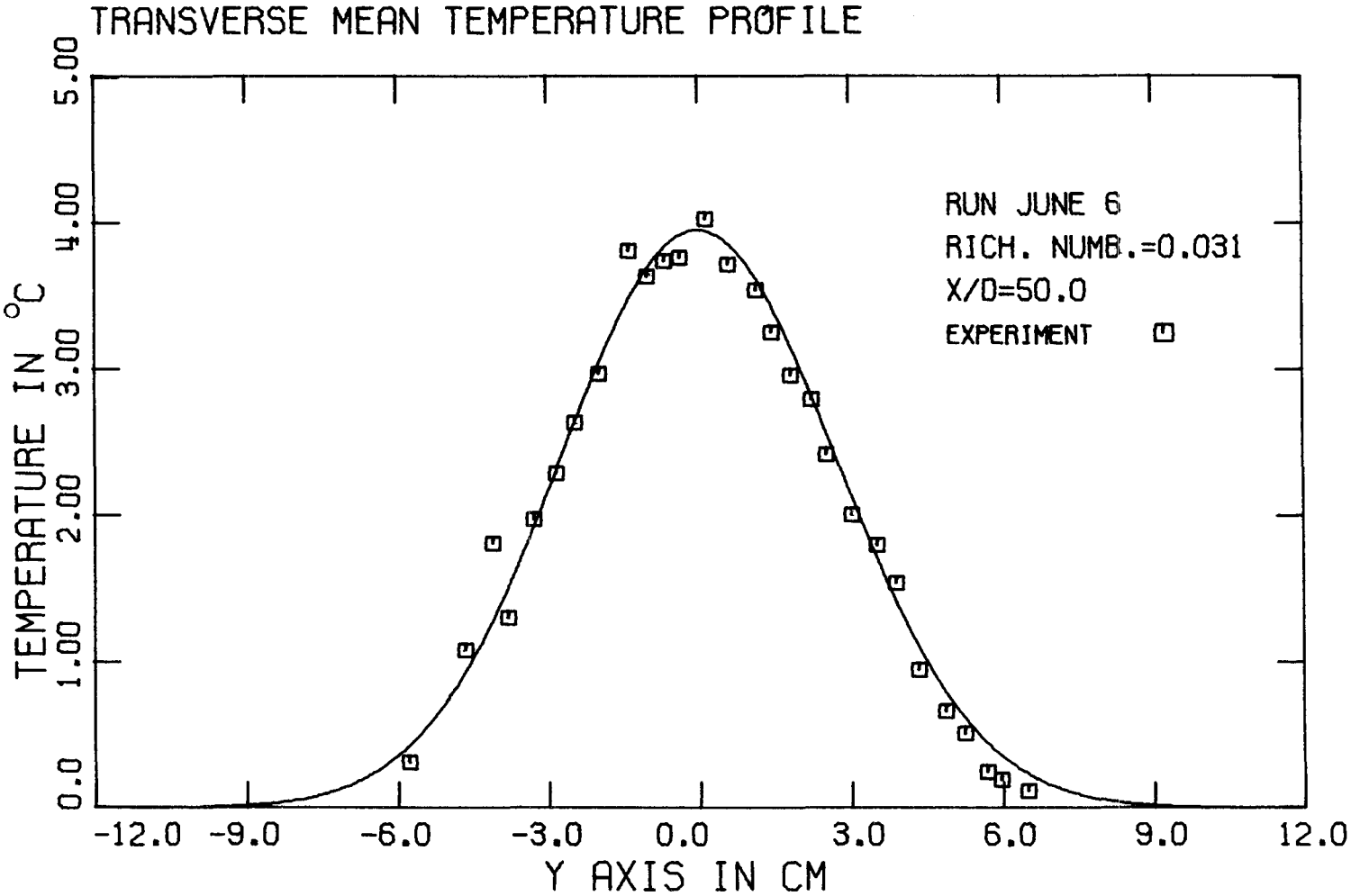
TRANSVERSE MEAN TEMPERATURE PROFILE
TEMPERATURE IN °C
0.0
1.00
2.00
3.00
4.00
5.00
-12.0
-9.0
-6.0
-3.0
0.0
3.0
6.0
9.0
12.0
Y AXIS IN CM
RUN JUNE 6
RICH. NUMB.=0.031
X/D=50.0
EXPERIMENT

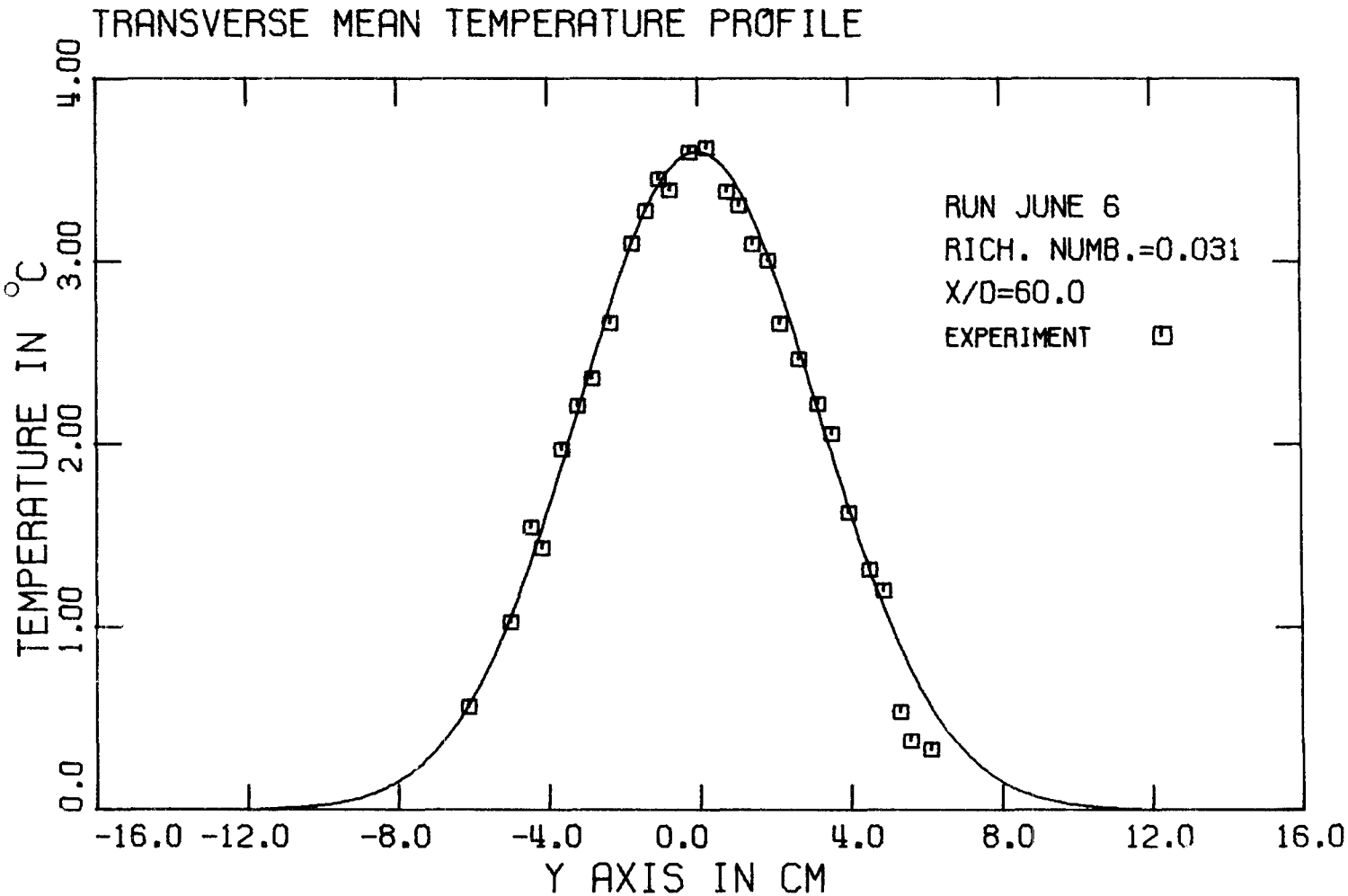
TRANSVERSE MEAN TEMPERATURE PROFILE
TEMPERATURE IN °C
4.00
3.00
2.00
1.00
0.0
-16.0 -12.0 -8.0 -4.0 0.0 4.0 8.0 12.0 16.0
Y AXIS IN CM
RUN JUNE 6
RICH. NUMB.=0.031
X/D=60.0
EXPERIMENT

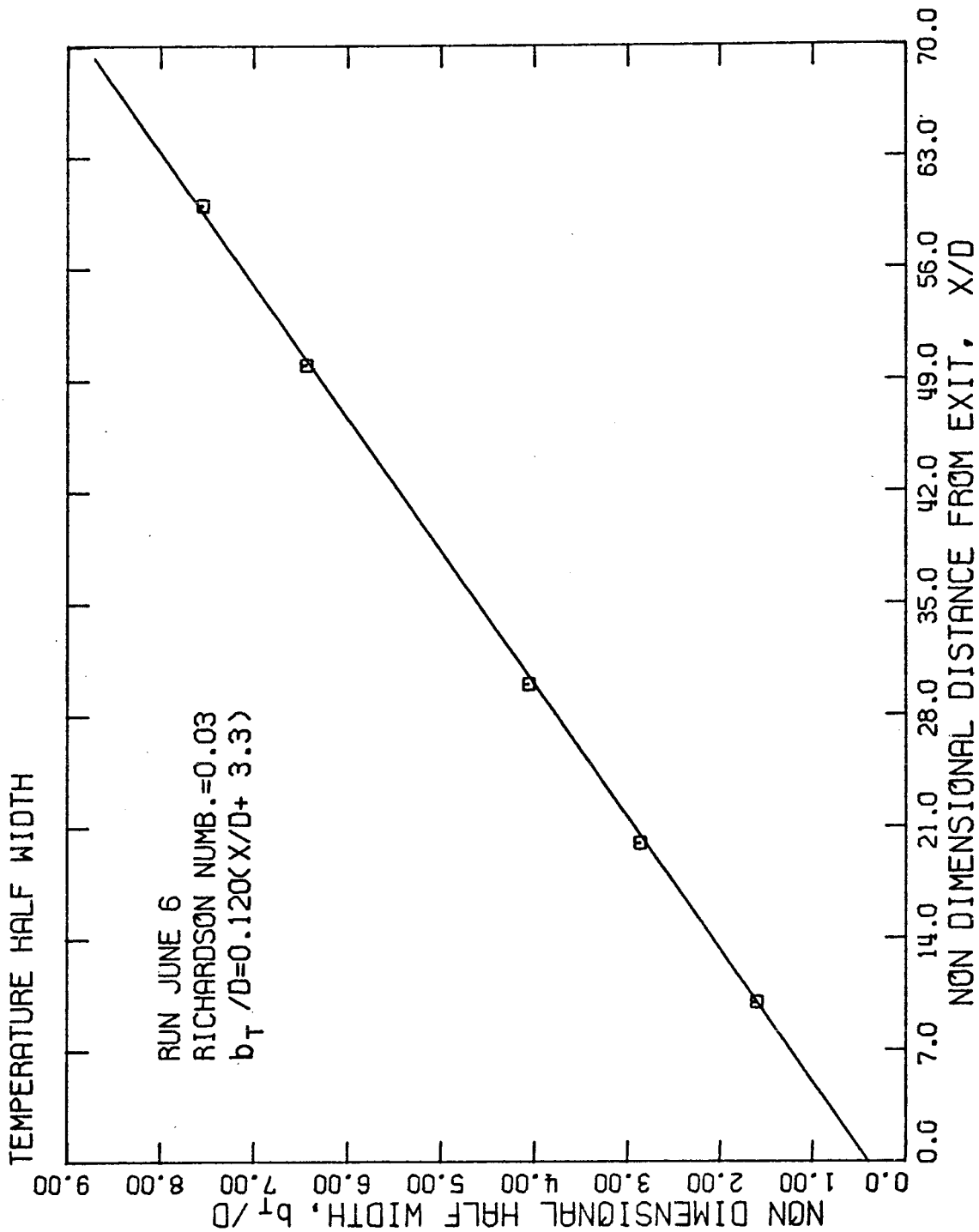
TEMPERATURE HALF WIDTH
RUN JUNE 6
RICHARDSON NUMB.=0.03
$b_T/D=0.120(X/D+3.3)$
NON DIMENSIONAL HALF WIDTH, b_T/D
0.0
1.00
2.00
3.00
4.00
5.00
6.00
7.00
8.00
9.00
NON DIMENSIONAL DISTANCE FROM EXIT, X/D
0.0
7.0
14.0
21.0
28.0
35.0
42.0
49.0
56.0
63.0
70.0

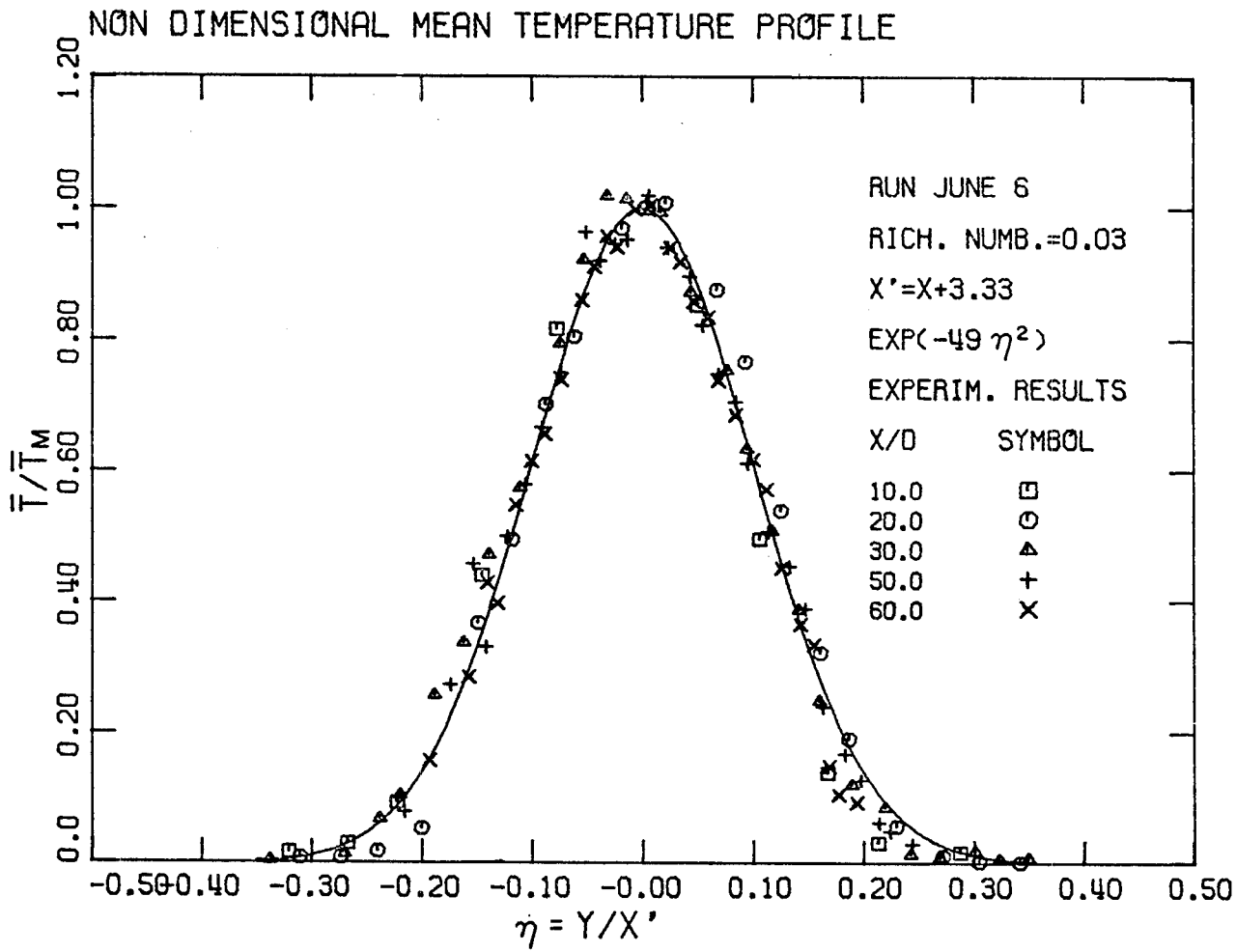
NØN DIMENSIØNAL MEAN TEMPERATURE PRØFILE
RUN JUNE 6
RICH. NUMB.=0.03
X'=X+3.33
EXP(-49 η²)
EXPERIM. RESULTS
X/D SYMBOL
10.0
20.0
30.0
50.0
60.0
T̄/T̄M
η = Y/X'
0.0
0.20
0.40
0.60
0.80
1.00
1.20
-0.50 -0.40 -0.30 -0.20 -0.10 -0.00 0.10 0.20 0.30 0.40 0.50

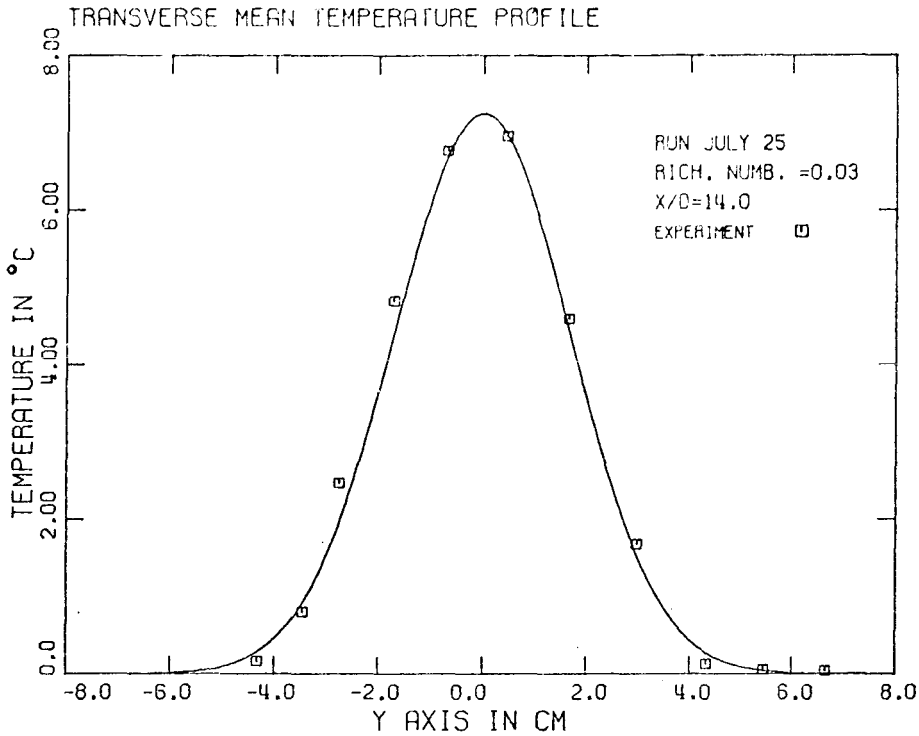
TRANSVERSE MEAN TEMPERATURE PROFILE
RUN JULY 25
RICH. NUMB. =0.03
X/D=14.0
EXPERIMENT
TEMPERATURE IN °C
0.0
2.00
4.00
6.00
8.00
-8.0
-6.0
-4.0
-2.0
0.0
2.0
4.0
6.0
8.0
Y AXIS IN CM

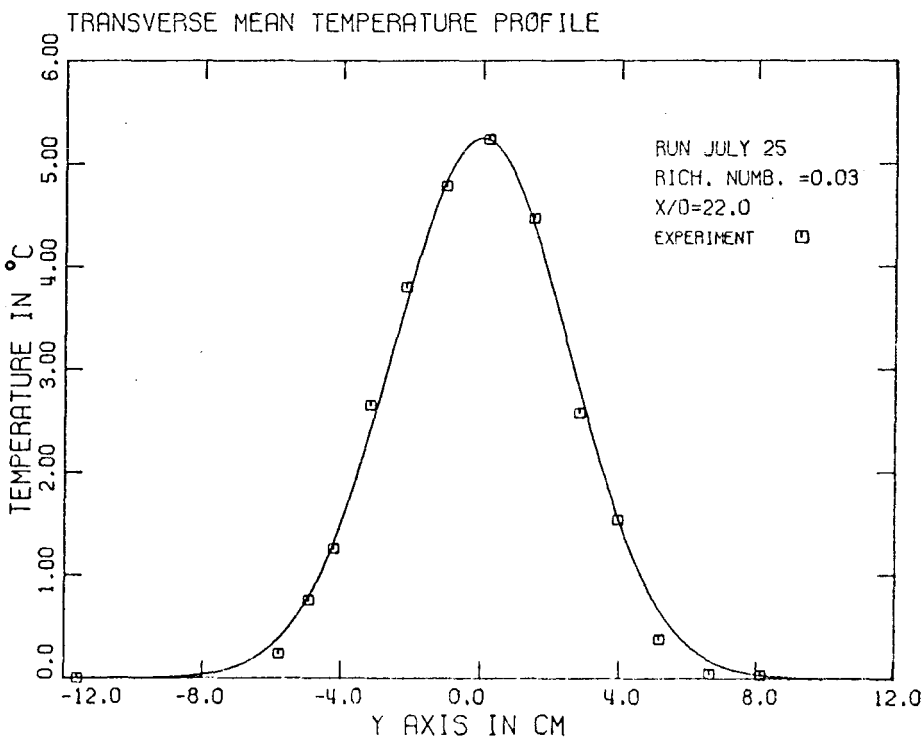
TRANSVERSE MEAN TEMPERATURE PROFILE
RUN JULY 25
RICH. NUMB. =0.03
X/D=22.0
EXPERIMENT
TEMPERATURE IN °C
0.0
1.00
2.00
3.00
4.00
5.00
6.00
-12.0
-8.0
-4.0
0.0
4.0
8.0
12.0
Y AXIS IN CM

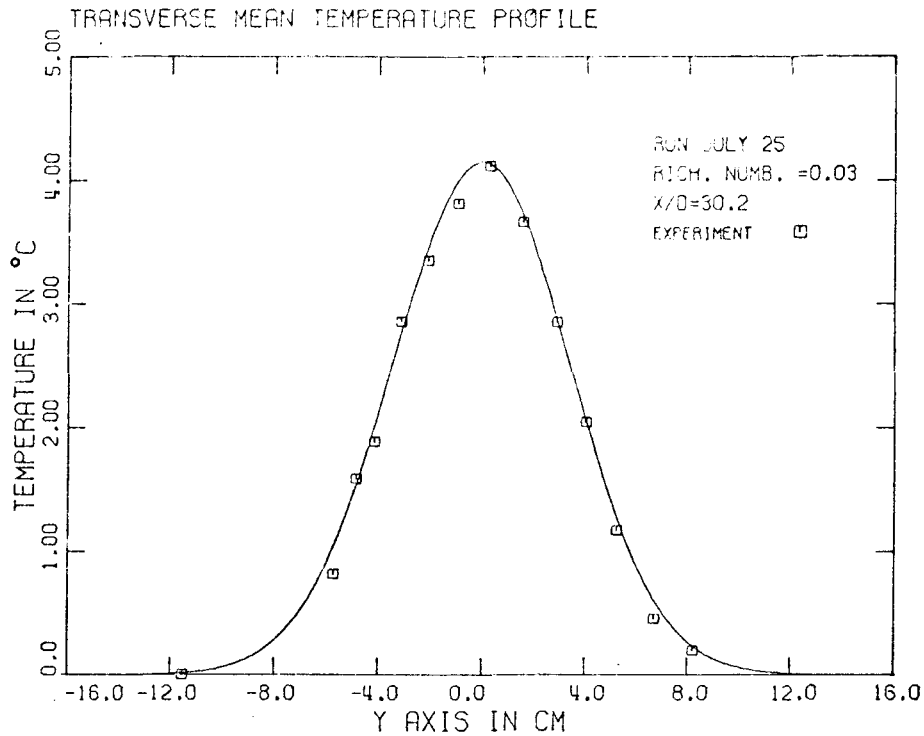
TRANSVERSE MEAN TEMPERATURE PROFILE
RUN JULY 25
RICH. NUMB. =0.03
X/D=30.2
EXPERIMENT
TEMPERATURE IN °C
0.0
1.00
2.00
3.00
4.00
5.00
-16.0 -12.0 -8.0 -4.0 0.0 4.0 8.0 12.0 16.0
Y AXIS IN CM

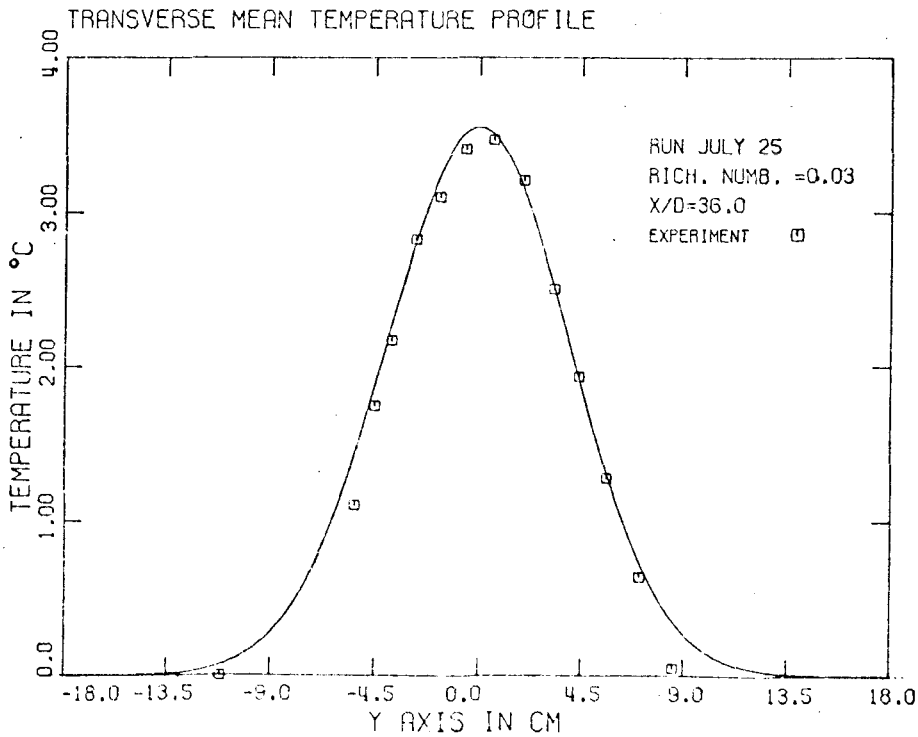
TRANSVERSE MEAN TEMPERATURE PROFILE
RUN JULY 25
RICH. NUMB. =0.03
X/D=36.0
EXPERIMENT
TEMPERATURE IN °C
0.0
1.00
2.00
3.00
4.00
-18.0 -13.5 -9.0 -4.5 0.0 4.5 9.0 13.5 18.0
Y AXIS IN CM

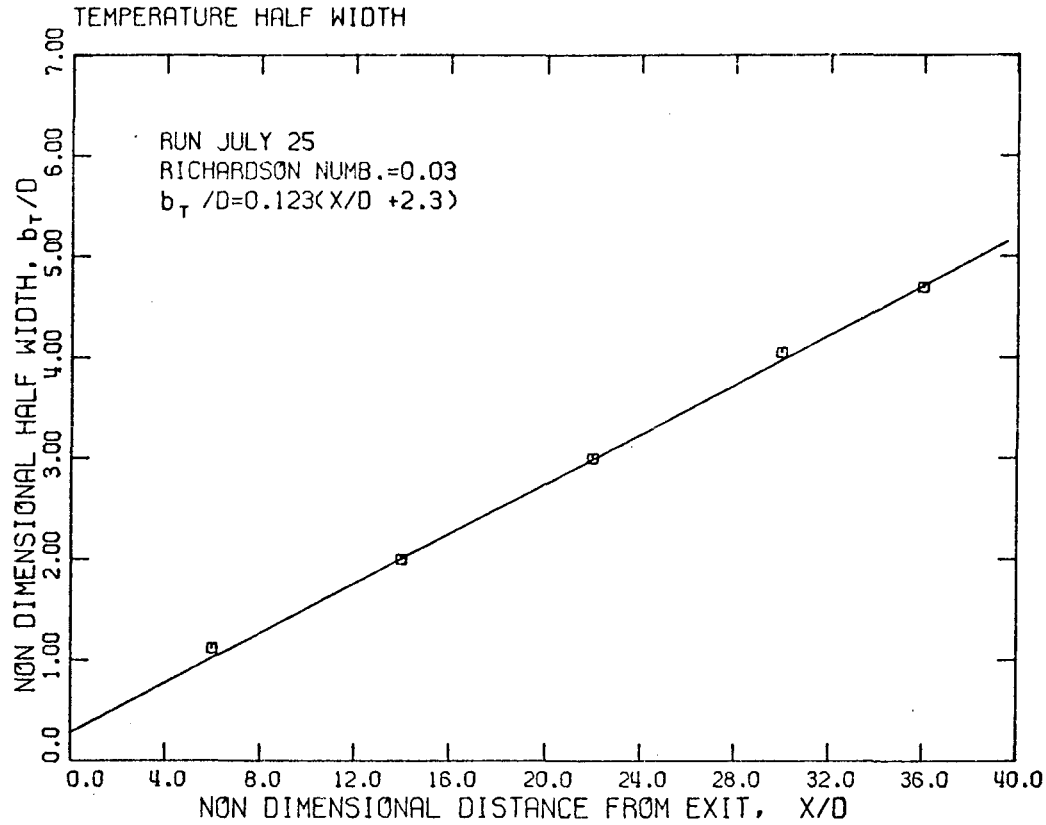
TEMPERATURE HALF WIDTH
RUN JULY 25
RICHARDSON NUMB.=0.03
b_T /D=0.123(X/D +2.3)
NON DIMENSIONAL HALF WIDTH, b_T/D
0.0
1.00
2.00
3.00
4.00
5.00
6.00
7.00
0.0
4.0
8.0
12.0
16.0
20.0
24.0
28.0
32.0
36.0
40.0
NON DIMENSIONAL DISTANCE FROM EXIT, X/D

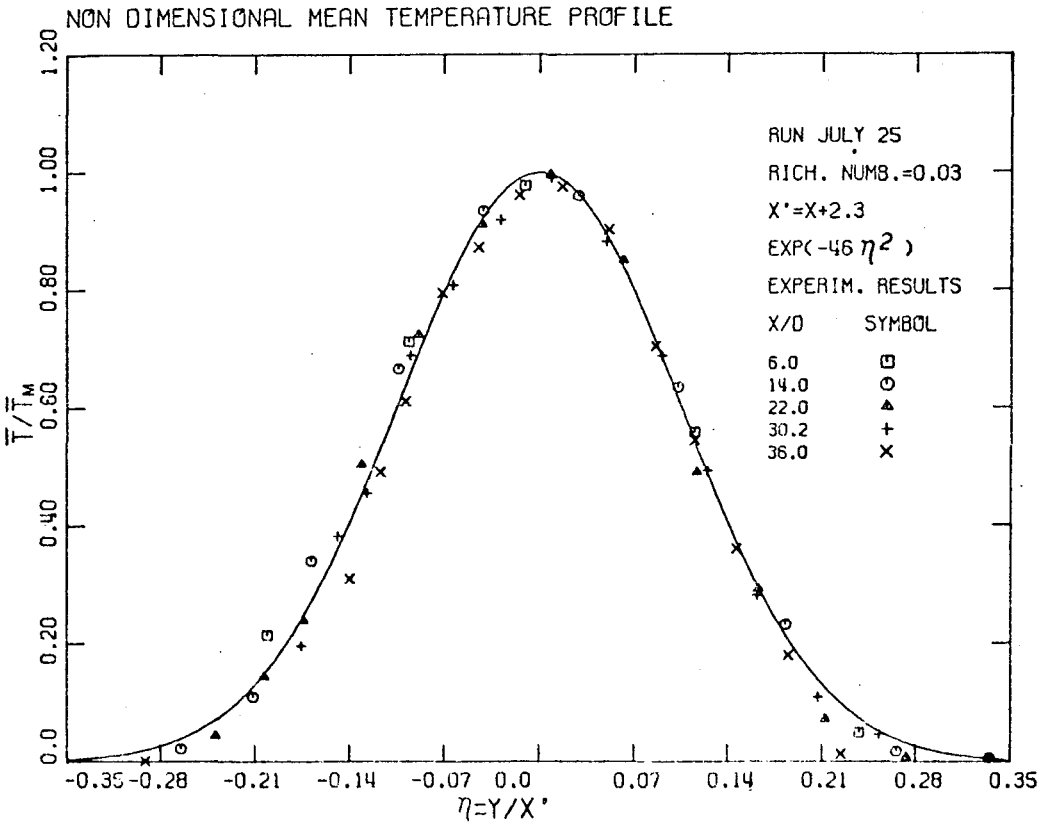
NON DIMENSIONAL MEAN TEMPERATURE PROFILE
RUN JULY 25
RICH. NUMB.=0.03
X'=X+2.3
EXP(-46 η^2)
EXPERIM. RESULTS
X/D SYMBOL
6.0
14.0
22.0
30.2
36.0
$\overline{T}/\overline{T}_M$
0.0
0.20
0.40
0.60
0.80
1.00
1.20
-0.35
-0.28
-0.21
-0.14
-0.07
0.0
0.07
0.14
0.21
0.28
0.35
η=Y/X'

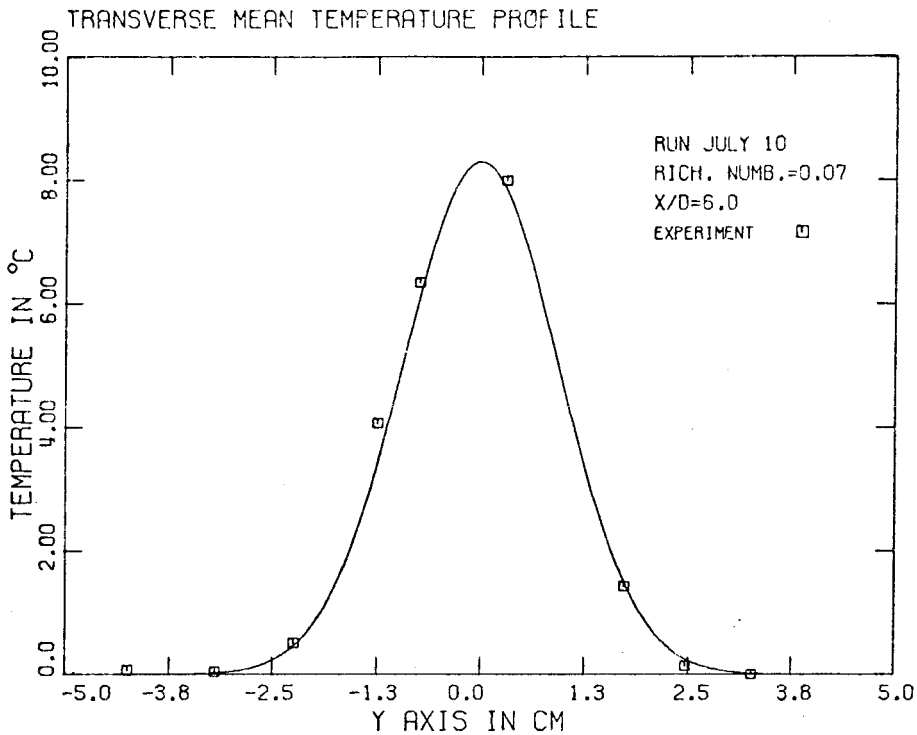
TRANSVERSE MEAN TEMPERATURE PROFILE
RUN JULY 10
RICH. NUMB.=0.07
X/D=6.0
EXPERIMENT
TEMPERATURE IN °C
0.0
2.00
4.00
6.00
8.00
10.00
-5.0
-3.8
-2.5
-1.3
0.0
1.3
2.5
3.8
5.0
Y AXIS IN CM

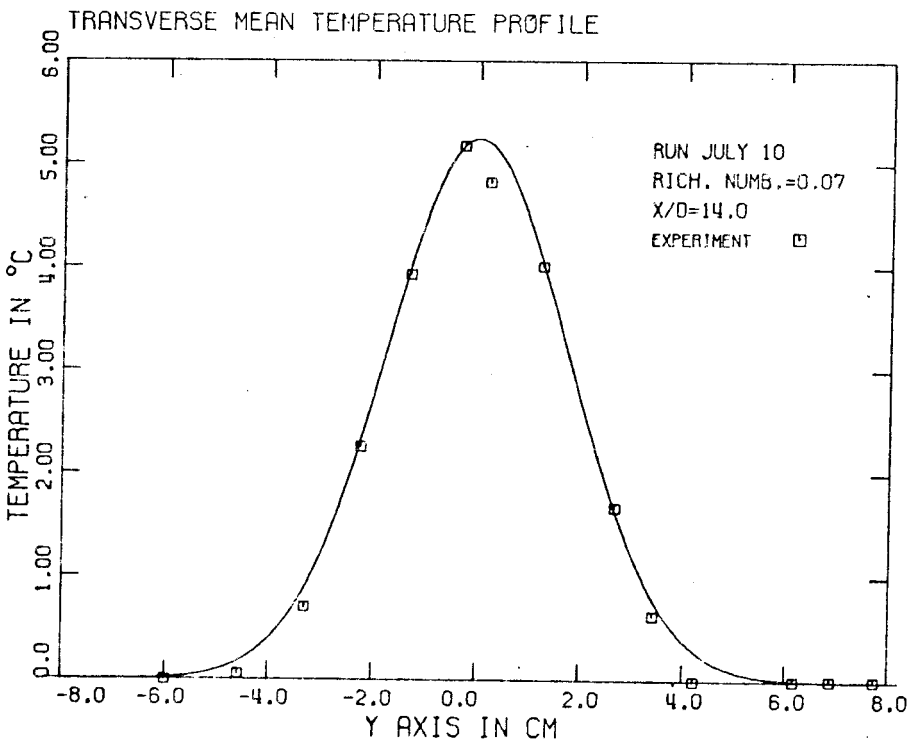
TRANSVERSE MEAN TEMPERATURE PROFILE
RUN JULY 10
RICH. NUMB.=0.07
X/D=14.0
EXPERIMENT
TEMPERATURE IN °C
0.0
1.00
2.00
3.00
4.00
5.00
6.00
-8.0
-6.0
-4.0
-2.0
0.0
2.0
4.0
6.0
8.0
Y AXIS IN CM

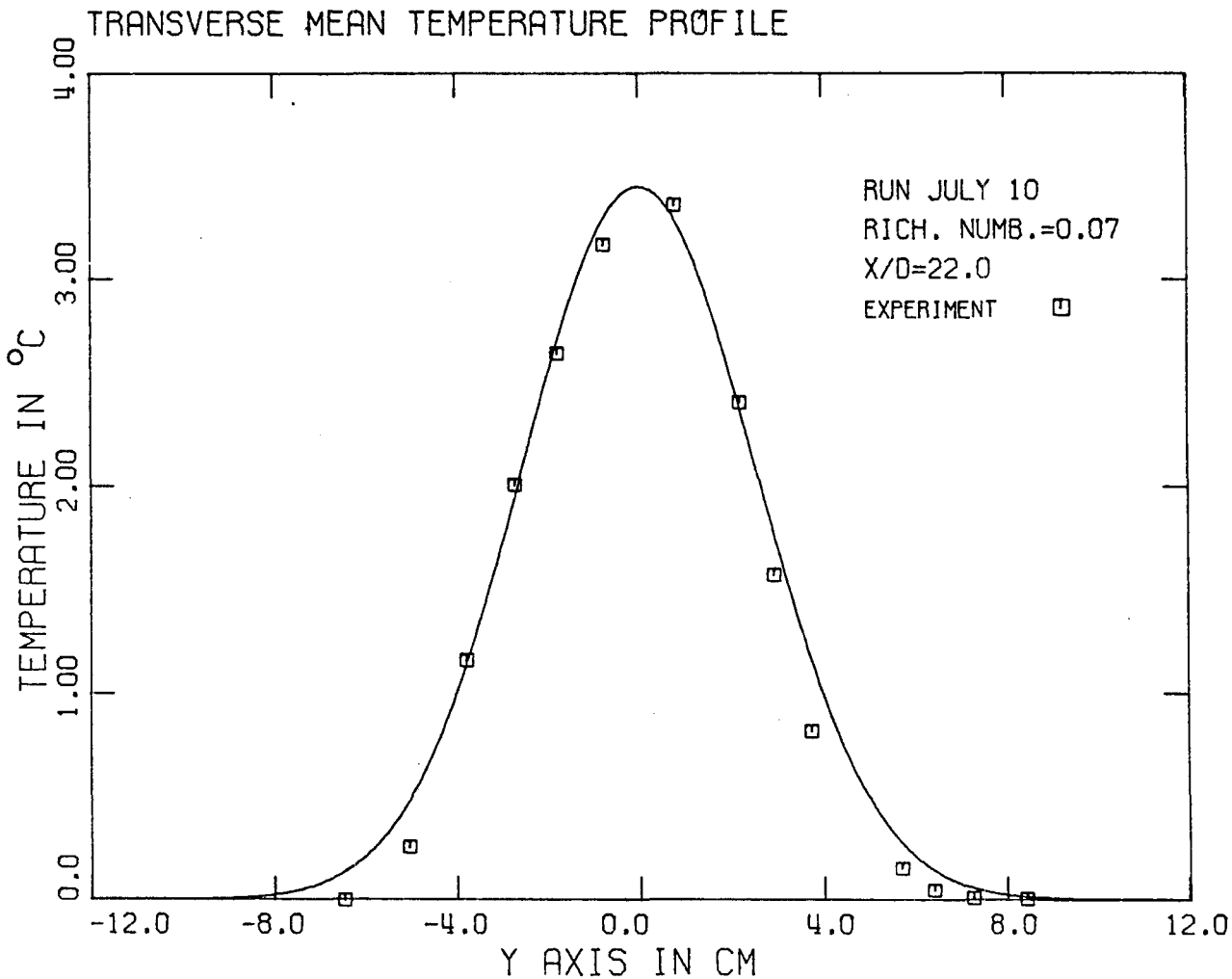
TRANSVERSE MEAN TEMPERATURE PROFILE
RUN JULY 10
RICH. NUMB.=0.07
X/D=22.0
EXPERIMENT
TEMPERATURE IN °C
0.0
1.00
2.00
3.00
4.00
-12.0
-8.0
-4.0
0.0
4.0
8.0
12.0
Y AXIS IN CM

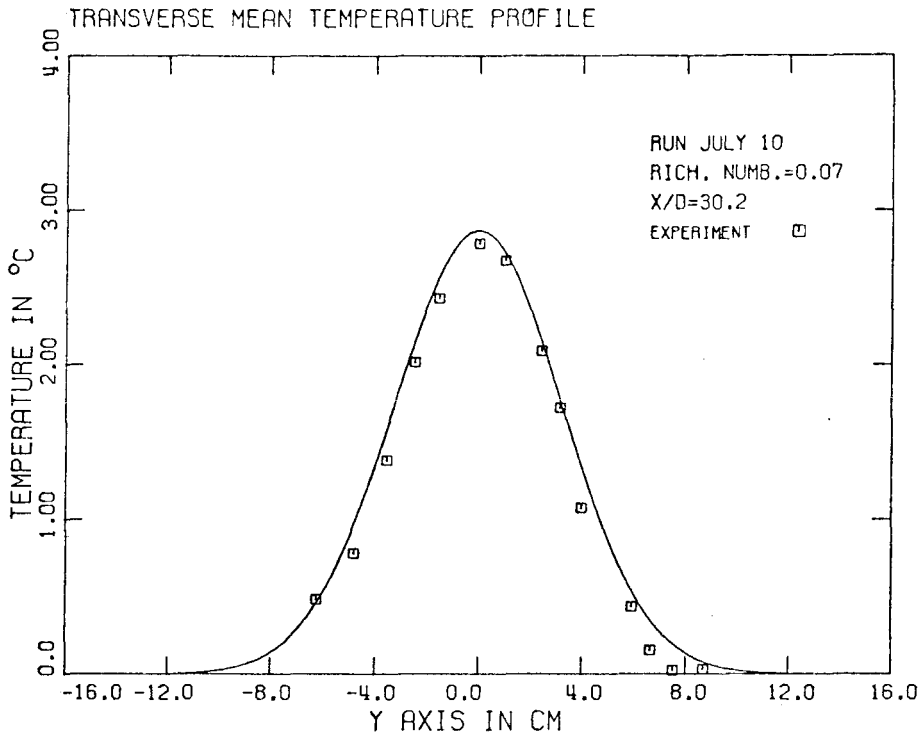
TRANSVERSE MEAN TEMPERATURE PROFILE
RUN JULY 10
RICH. NUMB.=0.07
X/D=30.2
EXPERIMENT
TEMPERATURE IN °C
0.0
1.00
2.00
3.00
4.00
-16.0 -12.0 -8.0 -4.0 0.0 4.0 8.0 12.0 16.0
Y AXIS IN CM

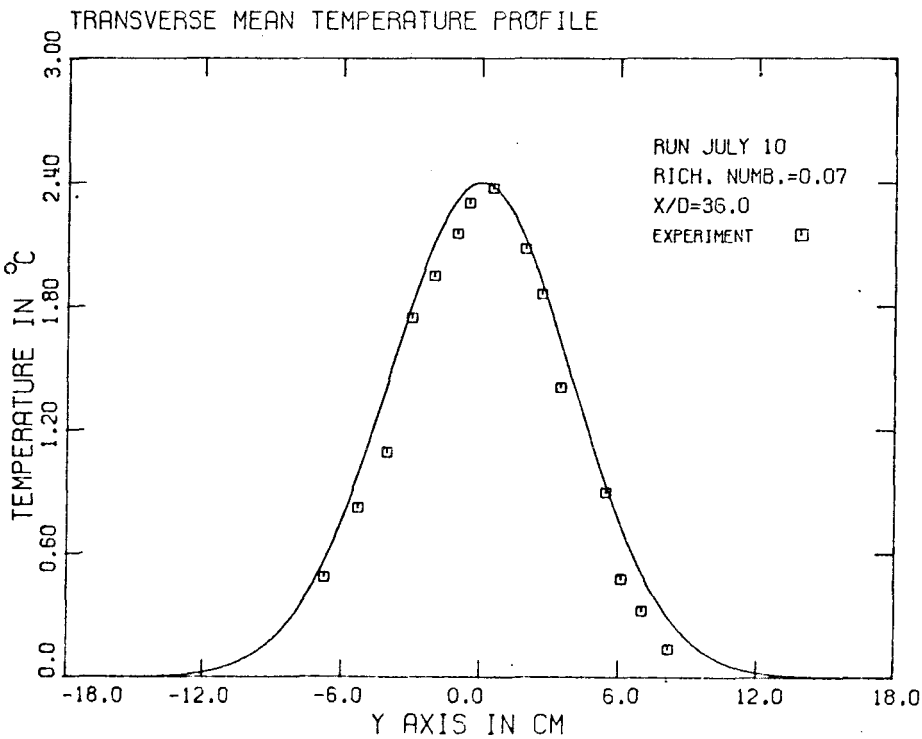
TRANSVERSE MEAN TEMPERATURE PROFILE
RUN JULY 10
RICH. NUMB.=0.07
X/D=36.0
EXPERIMENT
TEMPERATURE IN °C
0.0
0.60
1.20
1.80
2.40
3.00
-18.0 -12.0 -6.0 0.0 6.0 12.0 18.0
Y AXIS IN CM

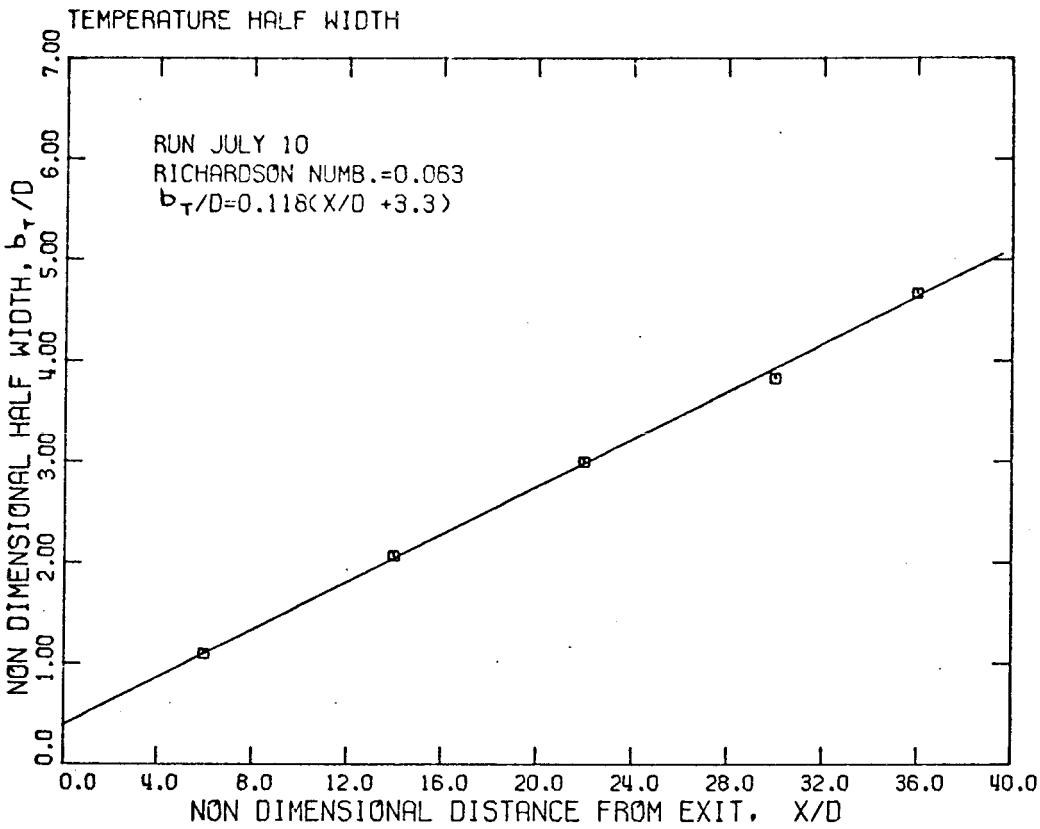
TEMPERATURE HALF WIDTH
RUN JULY 10
RICHARDSON NUMB.=0.063
$b_T/D=0.118(X/D+3.3)$
NON DIMENSIONAL HALF WIDTH, b_T/D
0.0
1.00
2.00
3.00
4.00
5.00
6.00
7.00
0.0
4.0
8.0
12.0
16.0
20.0
24.0
28.0
32.0
36.0
40.0
NON DIMENSIONAL DISTANCE FROM EXIT, X/D

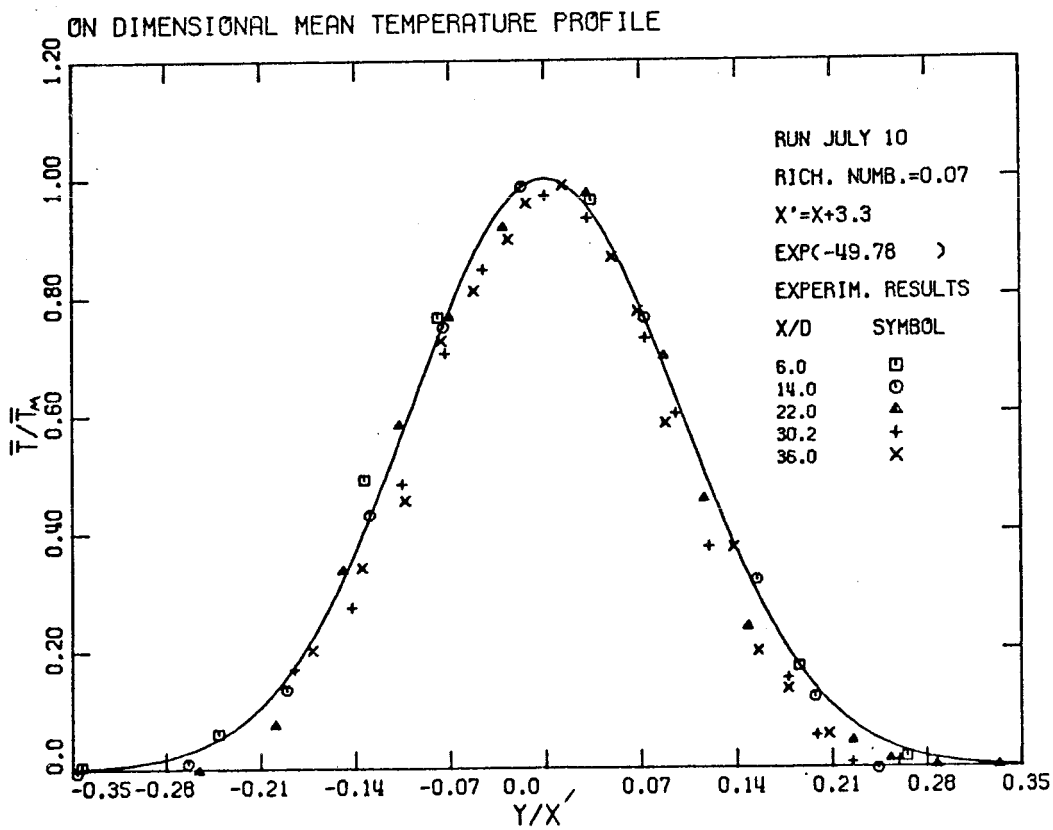
ON DIMENSIONAL MEAN TEMPERATURE PROFILE
RUN JULY 10
RICH. NUMB.=0.07
X'=X+3.3
EXP(-49.78)
EXPERIM. RESULTS
X/D SYMBOL
6.0
14.0
22.0
30.2
36.0
$\bar{T}/\bar{T}_M$
0.0
0.20
0.40
0.60
0.80
1.00
1.20
-0.35
-0.28
-0.21
-0.14
-0.07
0.0
0.07
0.14
0.21
0.28
0.35
Y/X'

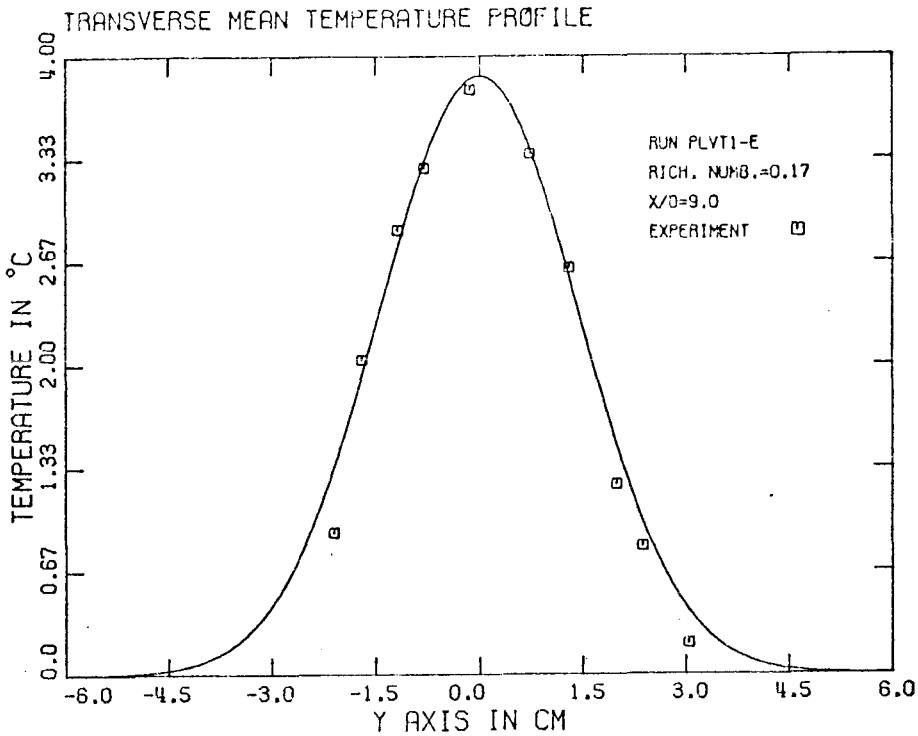
TRANSVERSE MEAN TEMPERATURE PROFILE
RUN PLVT1-E
RICH. NUMB.=0.17
X/D=9.0
EXPERIMENT
TEMPERATURE IN °C
0.0
0.67
1.33
2.00
2.67
3.33
4.00
-6.0
-4.5
-3.0
-1.5
0.0
1.5
3.0
4.5
6.0
Y AXIS IN CM

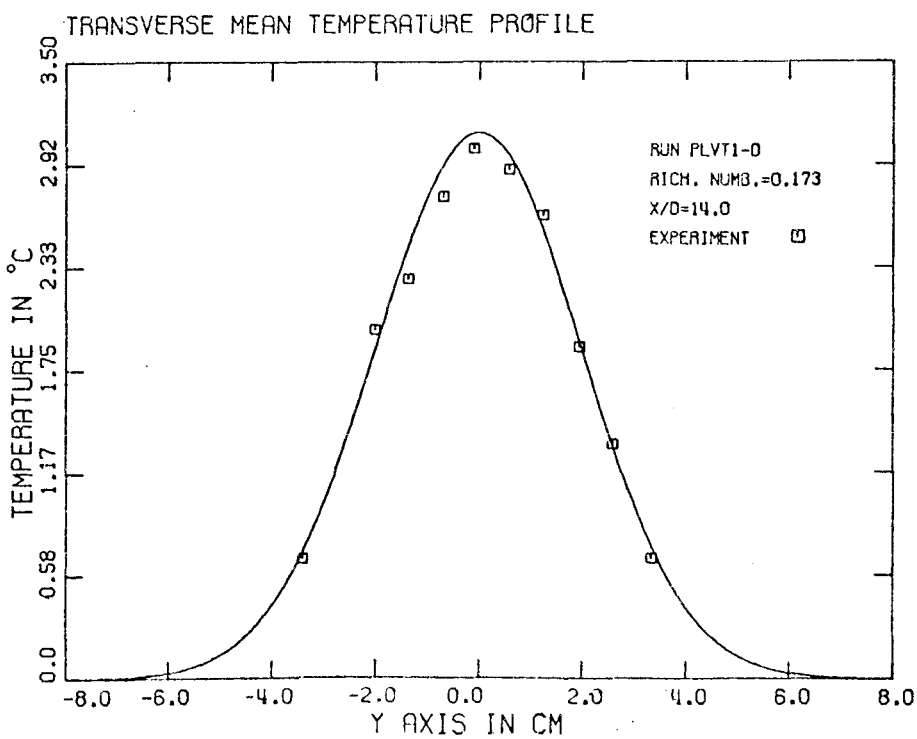
TRANSVERSE MEAN TEMPERATURE PROFILE
RUN PLVT1-D
RICH. NUMB.=0.173
X/D=14.0
EXPERIMENT
TEMPERATURE IN °C
0.0
0.58
1.17
1.75
2.33
2.92
3.50
-8.0
-6.0
-4.0
-2.0
0.0
2.0
4.0
6.0
8.0
Y AXIS IN CM

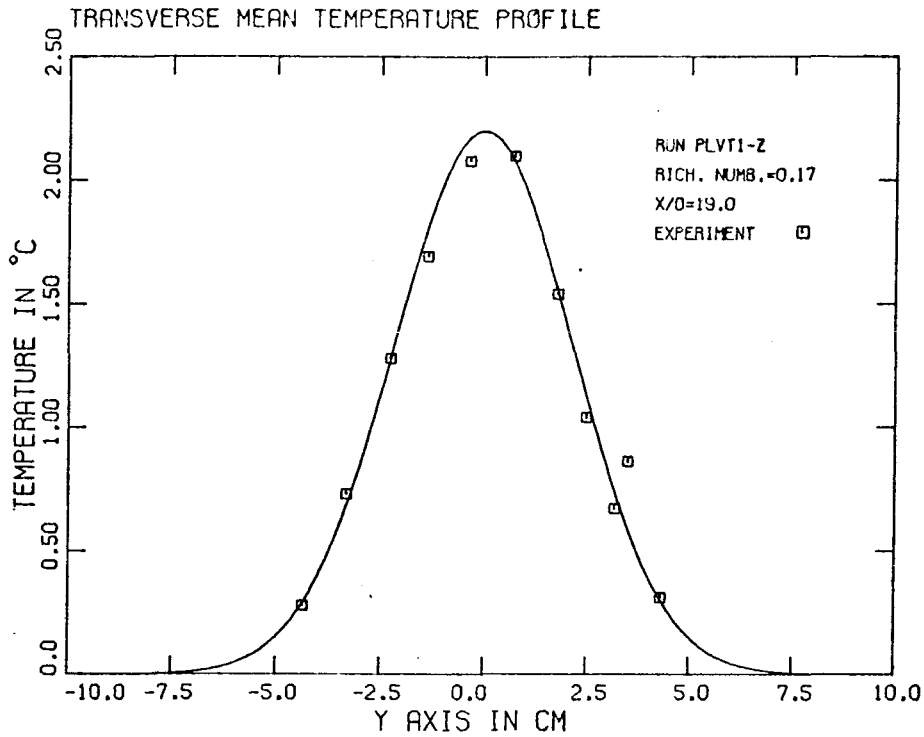
TRANSVERSE MEAN TEMPERATURE PROFILE
RUN PLVT1-Z
RICH. NUMB.=0.17
X/D=19.0
EXPERIMENT
TEMPERATURE IN °C
0.0
0.50
1.00
1.50
2.00
2.50
-10.0 -7.5 -5.0 -2.5 0.0 2.5 5.0 7.5 10.0
Y AXIS IN CM

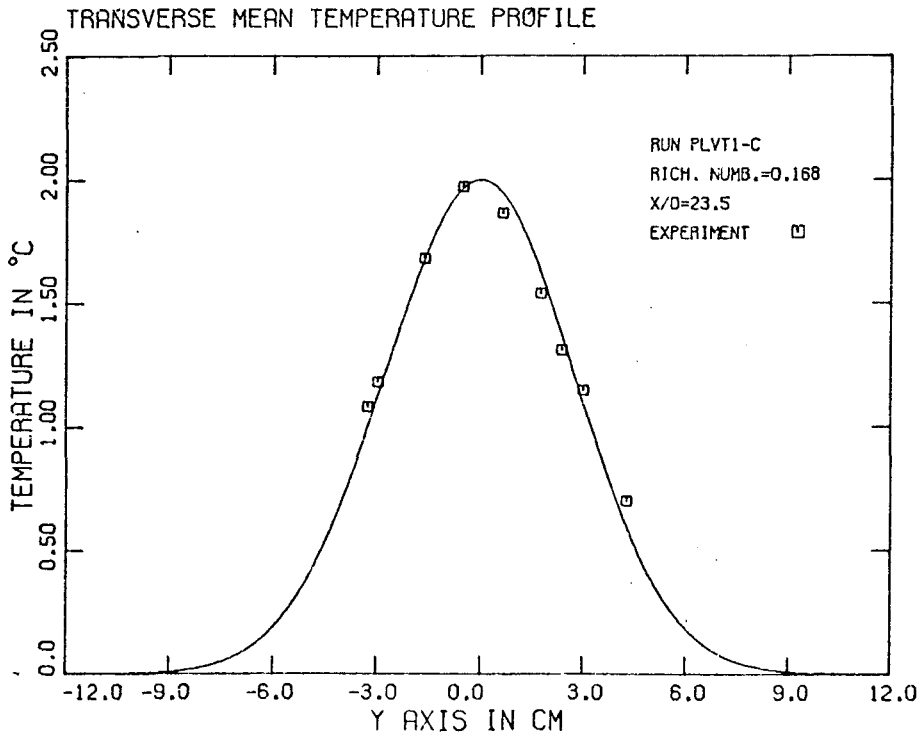
TRANSVERSE MEAN TEMPERATURE PROFILE
RUN PLVT1-C
RICH. NUMB.=0.168
X/D=23.5
EXPERIMENT
TEMPERATURE IN °C
0.0
0.50
1.00
1.50
2.00
2.50
-12.0 -9.0 -6.0 -3.0 0.0 3.0 6.0 9.0 12.0
Y AXIS IN CM

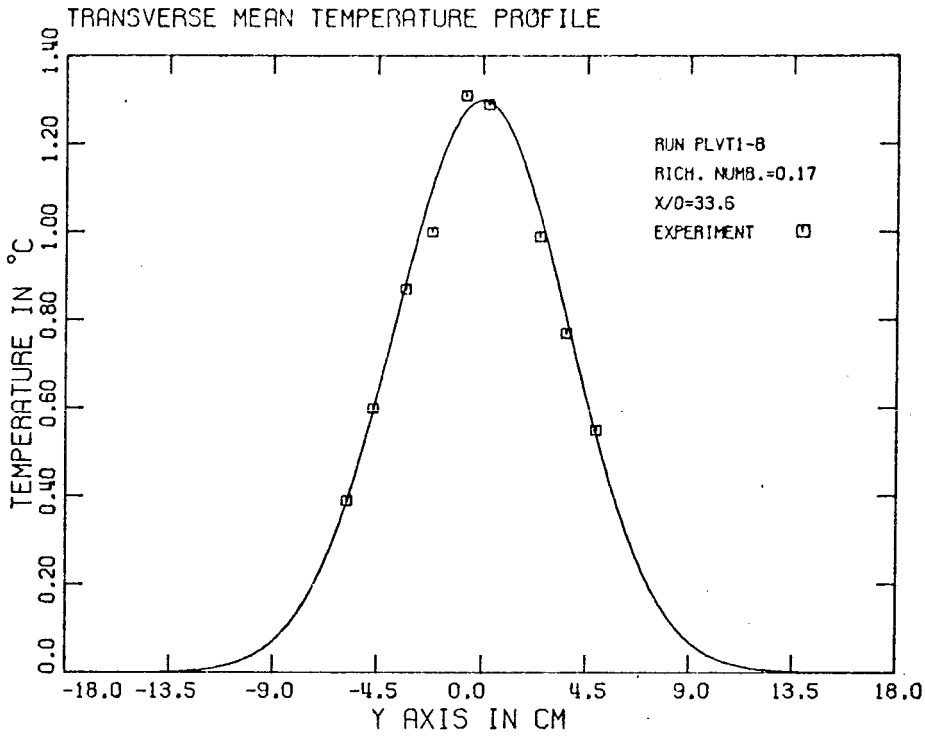
TRANSVERSE MEAN TEMPERATURE PROFILE
TEMPERATURE IN °C
0.0
0.20
0.40
0.60
0.80
1.00
1.20
1.40
-18.0 -13.5 -9.0 -4.5 0.0 4.5 9.0 13.5 18.0
Y AXIS IN CM
RUN PLVT1-8
RICH. NUMB.=0.17
X/D=33.6
EXPERIMENT

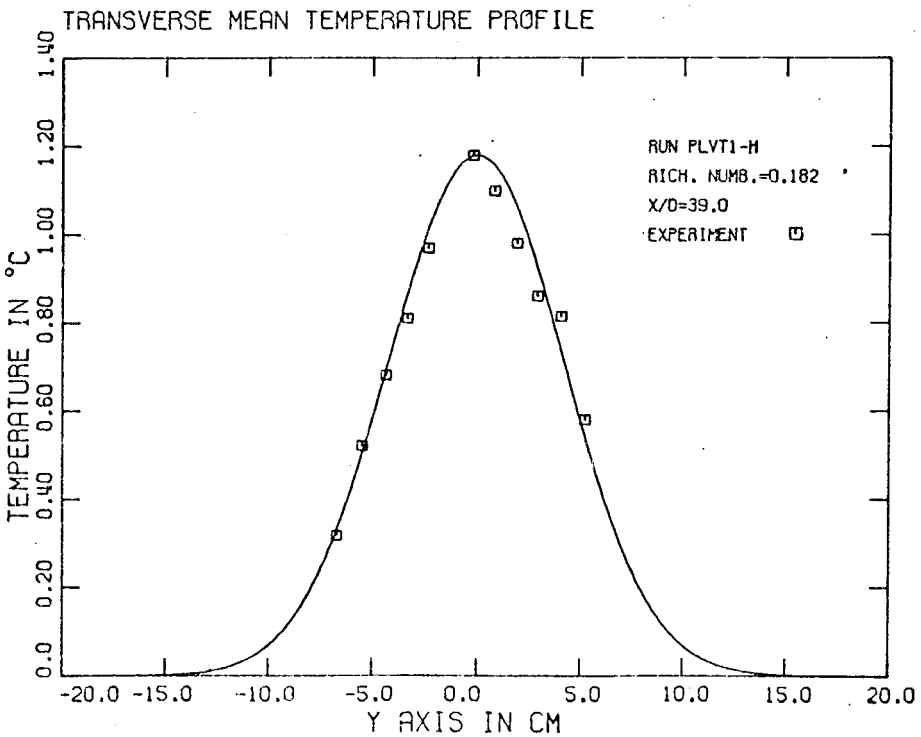
TRANSVERSE MEAN TEMPERATURE PROFILE
TEMPERATURE IN °C
0.0
0.20
0.40
0.60
0.80
1.00
1.20
1.40
-20.0 -15.0 -10.0 -5.0 0.0 5.0 10.0 15.0 20.0
Y AXIS IN CM
RUN PLVT1-H
RICH. NUMB.=0.182
X/D=39.0
EXPERIMENT

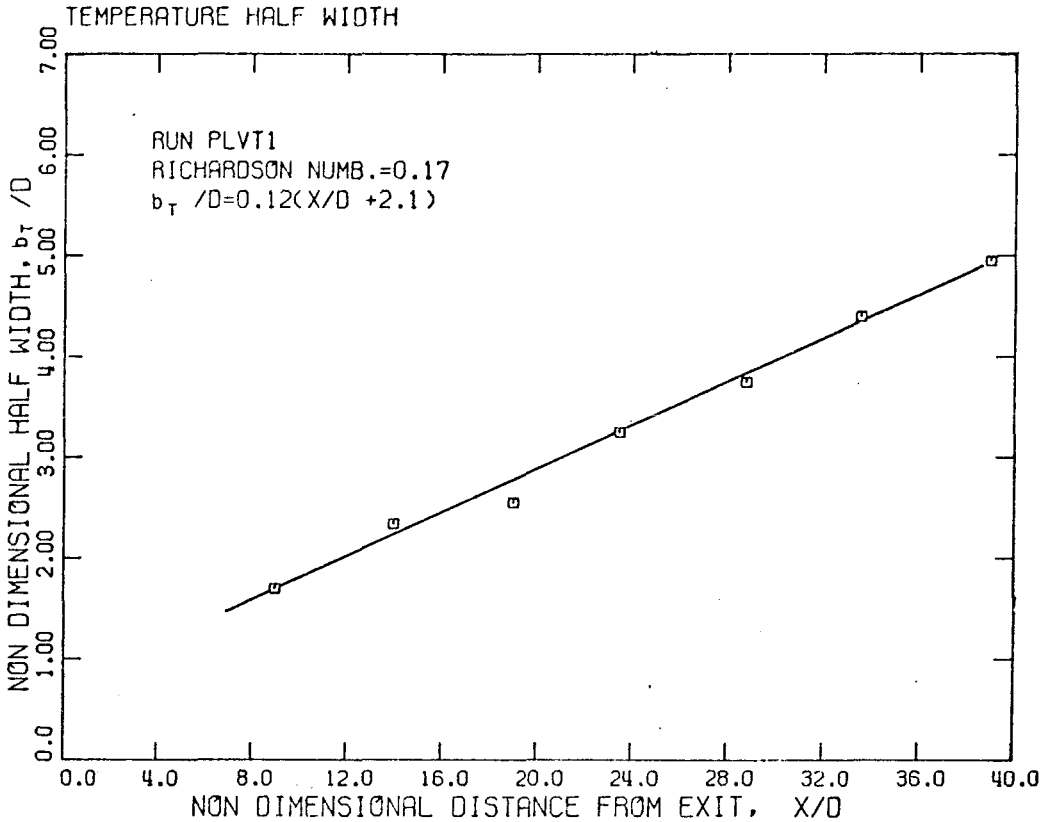
TEMPERATURE HALF WIDTH
RUN PLVT1
RICHARDSON NUMB.=0.17
b_T /D=0.12(X/D +2.1)
NON DIMENSIONAL HALF WIDTH, b_T /D
0.0
1.00
2.00
3.00
4.00
5.00
6.00
7.00
0.0
4.0
8.0
12.0
16.0
20.0
24.0
28.0
32.0
36.0
40.0
NON DIMENSIONAL DISTANCE FROM EXIT, X/D

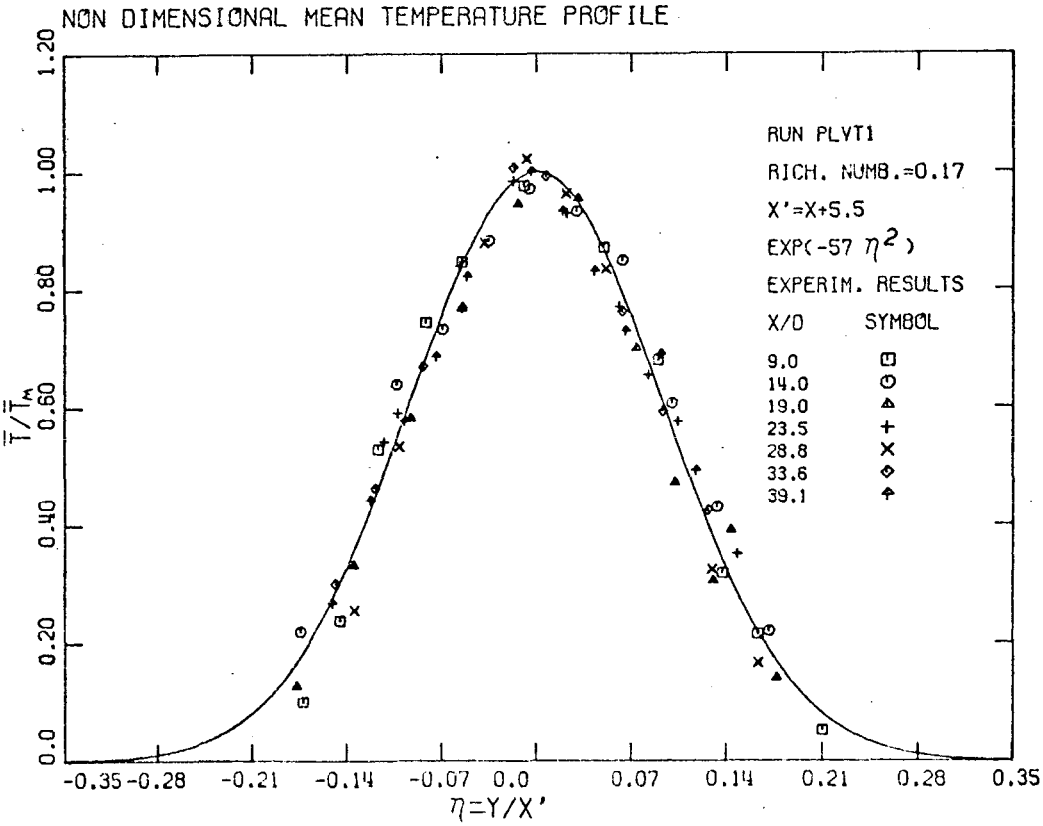
NON DIMENSIONAL MEAN TEMPERATURE PROFILE
RUN PLVT1
RICH. NUMB.=0.17
X'=X+5.5
EXP(-57 η^2)
EXPERIM. RESULTS
X/D SYMBOL
9.0
14.0
19.0
23.5
28.8
33.6
39.1
$\bar{T}/\bar{T}_m$
0.0
0.20
0.40
0.60
0.80
1.00
1.20
-0.35
-0.28
-0.21
-0.14
-0.07
0.0
0.07
0.14
0.21
0.28
0.35
η=Y/X'

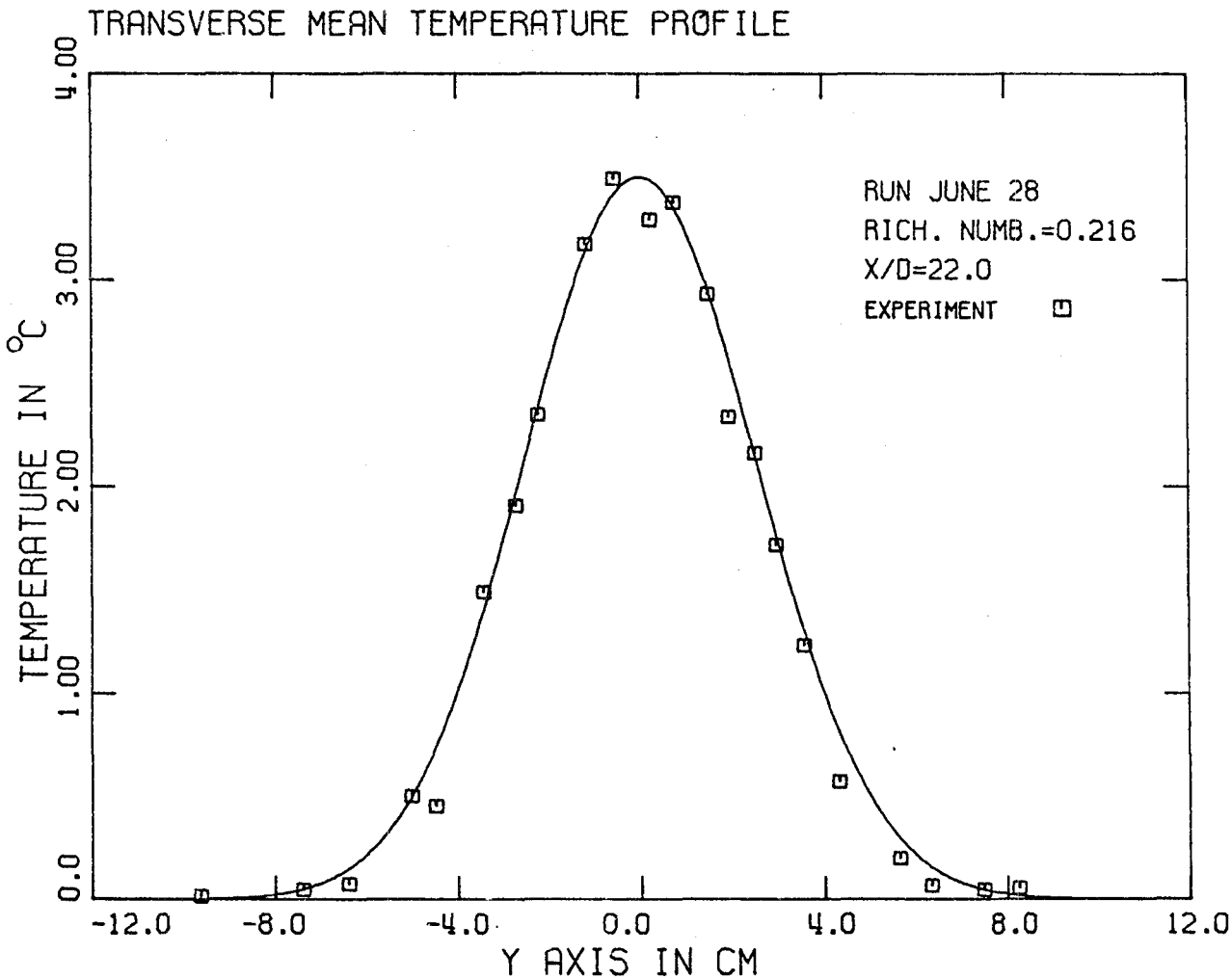
TRANSVERSE MEAN TEMPERATURE PROFILE
RUN JUNE 28
RICH. NUMB.=0.216
X/D=22.0
EXPERIMENT
TEMPERATURE IN °C
Y AXIS IN CM
0.0
1.00
2.00
3.00
4.00
-12.0
-8.0
-4.0
0.0
4.0
8.0
12.0

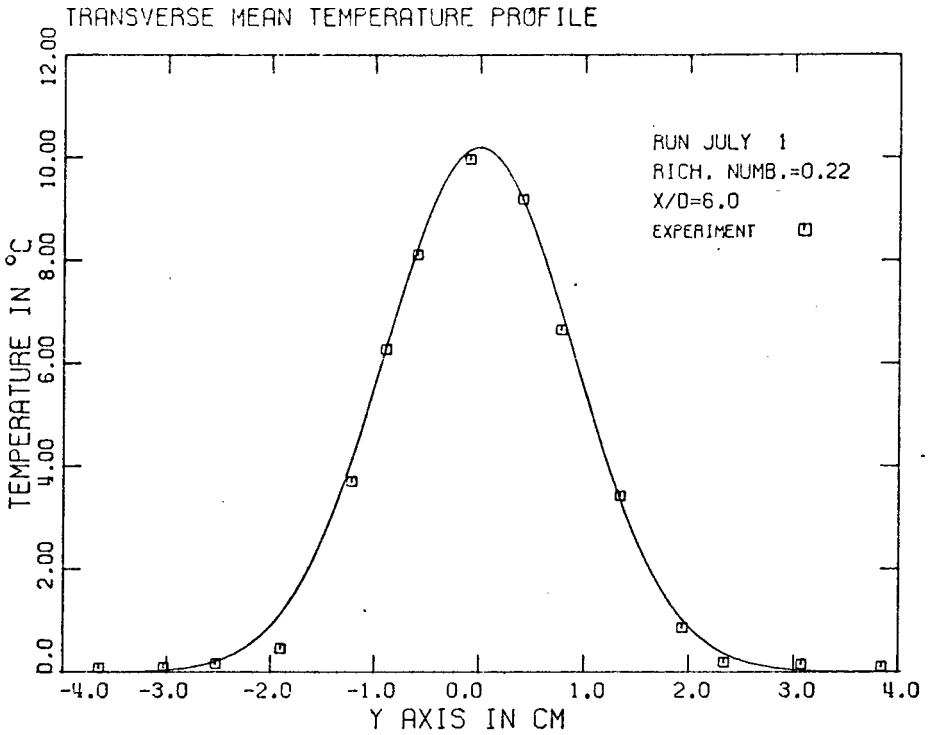
TRANSVERSE MEAN TEMPERATURE PROFILE
RUN JULY 1
RICH. NUMB.=0.22
X/D=6.0
EXPERIMENT
TEMPERATURE IN °C
Y AXIS IN CM
0.0
2.00
4.00
6.00
8.00
10.00
12.00
-4.0
-3.0
-2.0
-1.0
0.0
1.0
2.0
3.0
4.0

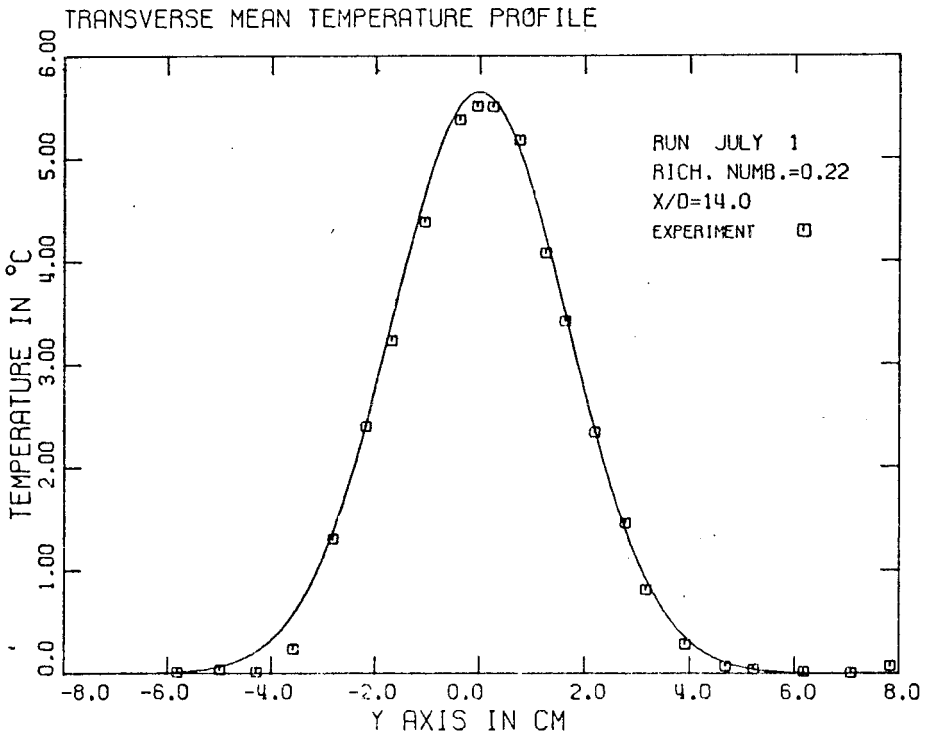
TRANSVERSE MEAN TEMPERATURE PROFILE
RUN JULY 1
RICH. NUMB.=0.22
X/D=14.0
EXPERIMENT
TEMPERATURE IN °C
Y AXIS IN CM
0.0
1.00
2.00
3.00
4.00
5.00
6.00
-8.0
-6.0
-4.0
-2.0
0.0
2.0
4.0
6.0
8.0

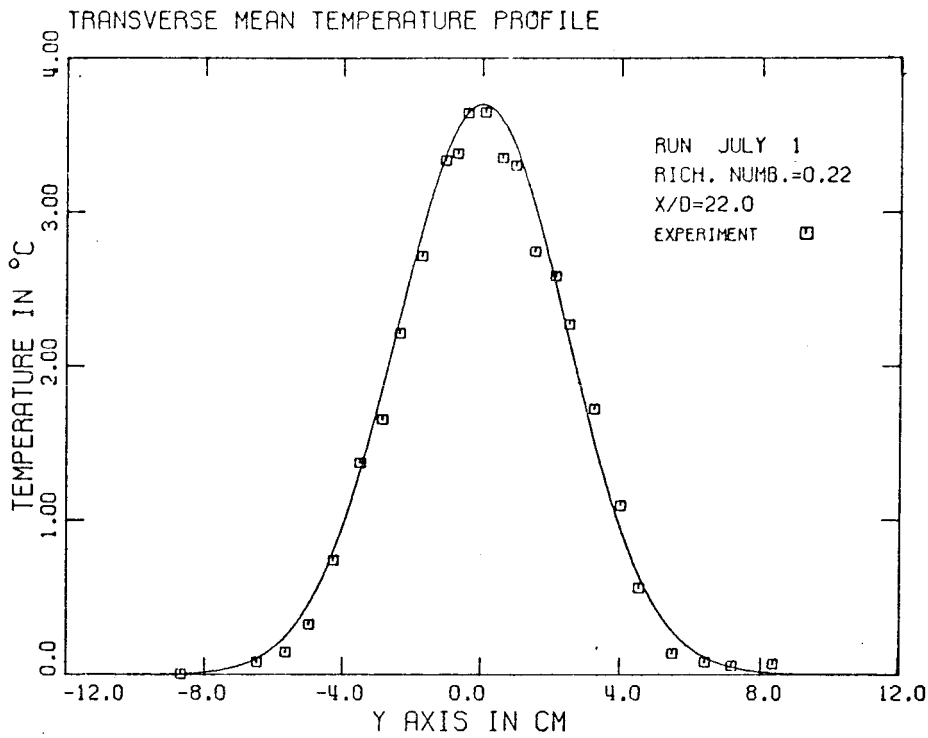
TRANSVERSE MEAN TEMPERATURE PROFILE
RUN JULY 1
RICH. NUMB.=0.22
X/D=22.0
EXPERIMENT
TEMPERATURE IN °C
Y AXIS IN CM
0.0
1.00
2.00
3.00
4.00
-12.0
-8.0
-4.0
0.0
4.0
8.0
12.0

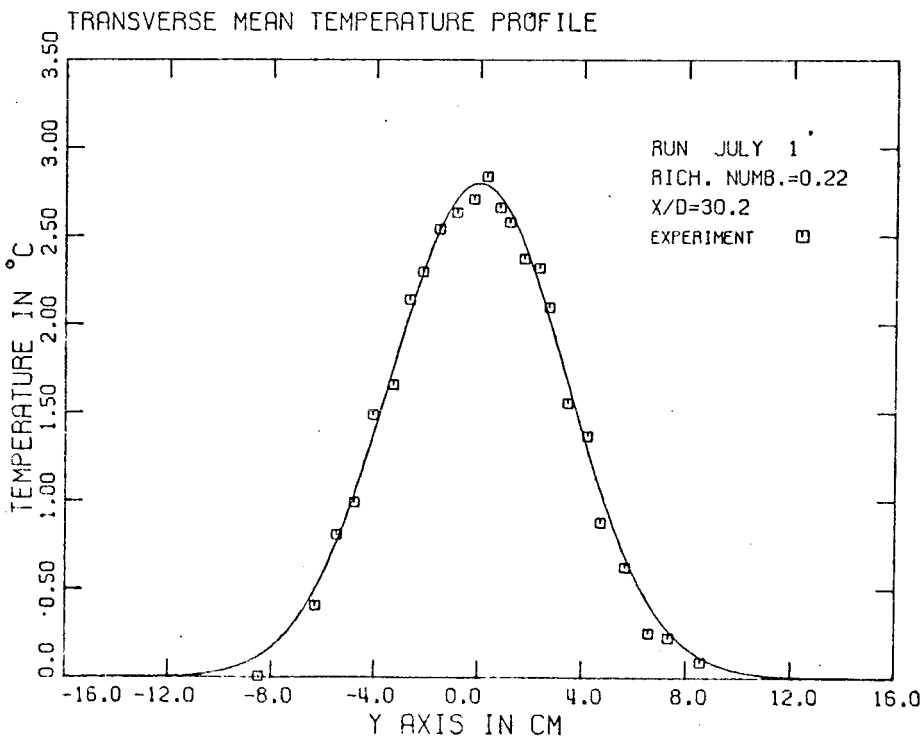
TRANSVERSE MEAN TEMPERATURE PROFILE
RUN JULY 1
RICH. NUMB.=0.22
X/D=30.2
EXPERIMENT
TEMPERATURE IN °C
Y AXIS IN CM
0.0
0.50
1.00
1.50
2.00
2.50
3.00
3.50
-16.0
-12.0
-8.0
-4.0
0.0
4.0
8.0
12.0
16.0

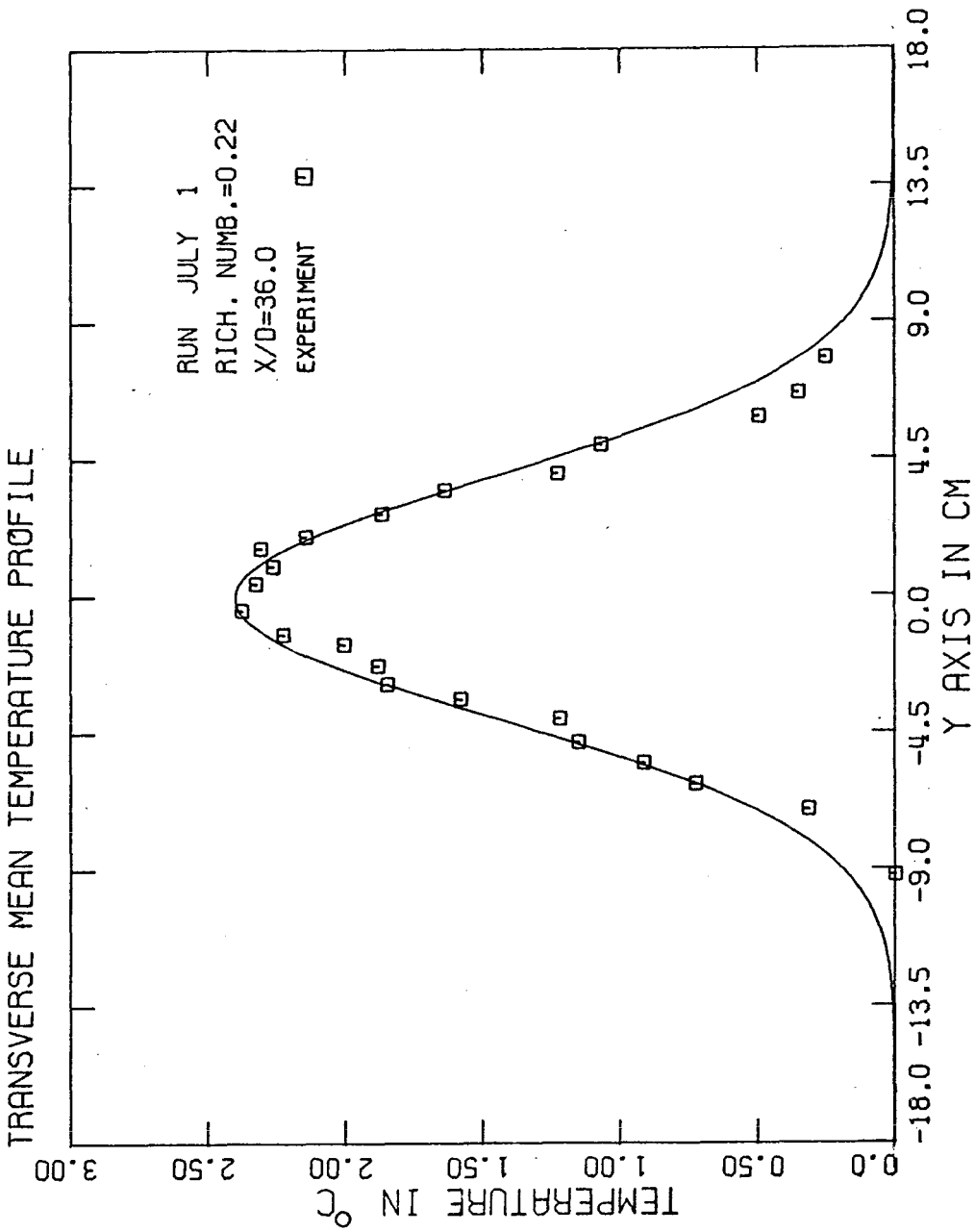
TRANSVERSE MEAN TEMPERATURE PROFILE
RUN JULY 1
RICH. NUMB.=0.22
X/D=36.0
EXPERIMENT
TEMPERATURE IN °C
0.0
0.50
1.00
1.50
2.00
2.50
3.00
-18.0
-13.5
-9.0
-4.5
0.0
4.5
9.0
13.5
18.0
Y AXIS IN CM

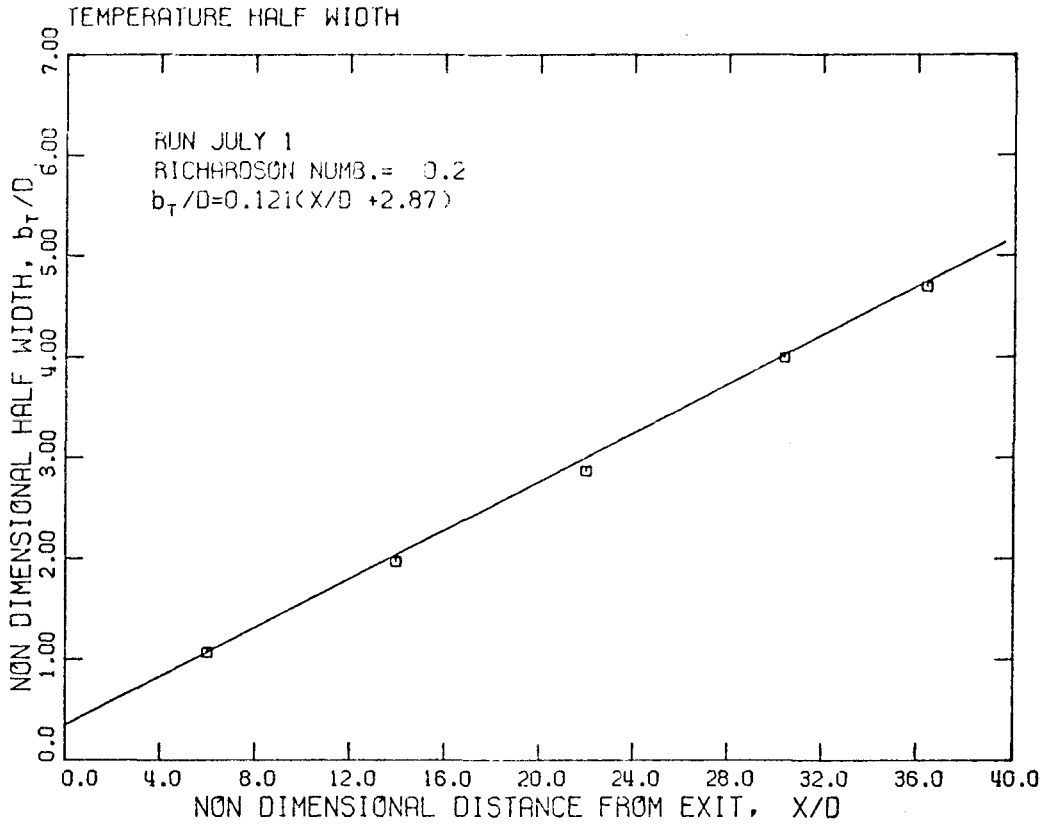
TEMPERATURE HALF WIDTH
RUN JULY 1
RICHARDSON NUMB.= 0.2
$b_T/D=0.121(X/D+2.87)$
NON DIMENSIONAL HALF WIDTH, b_T/D
NON DIMENSIONAL DISTANCE FROM EXIT, X/D
0.0
1.00
2.00
3.00
4.00
5.00
6.00
7.00
0.0
4.0
8.0
12.0
16.0
20.0
24.0
28.0
32.0
36.0
40.0

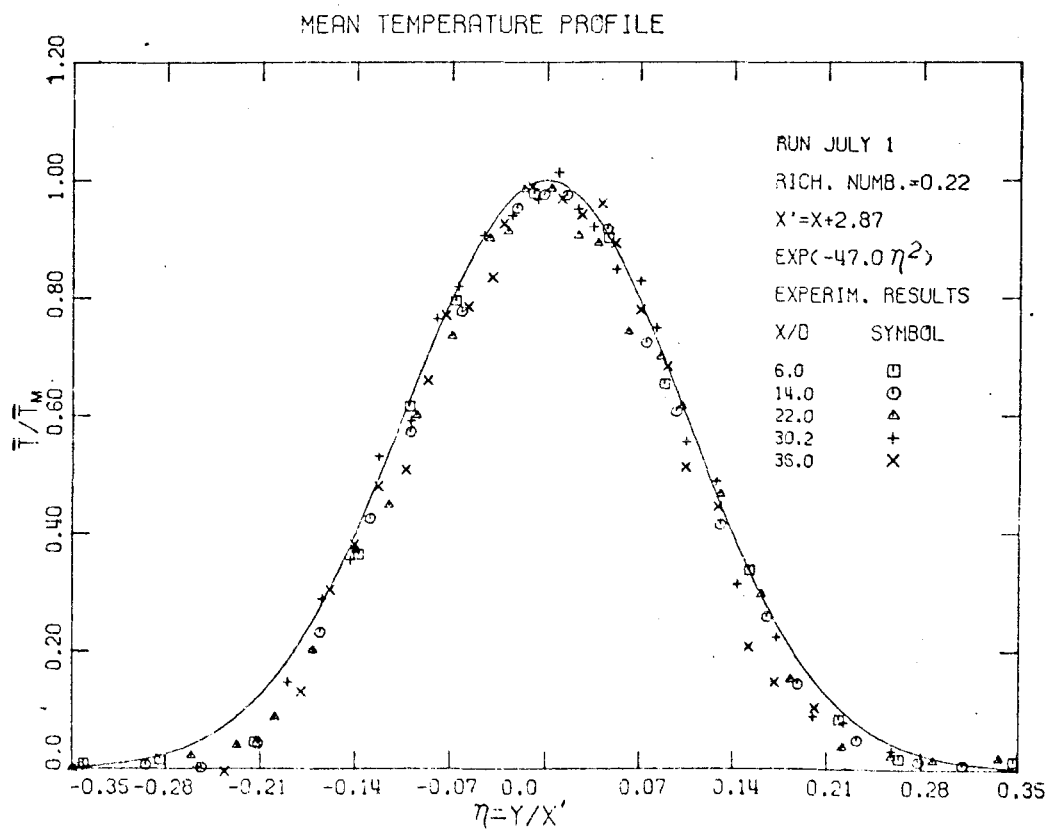
MEAN TEMPERATURE PROFILE
RUN JULY 1
RICH. NUMB.=0.22
X'=X+2.87
$EXP(-47.0\eta^2)$
EXPERIM. RESULTS
X/D SYMBOL
6.0
14.0
22.0
30.2
36.0
$\bar{T}/\bar{T}_M$
$\eta=Y/X'$
0.0
0.20
0.40
0.60
0.80
1.00
1.20
-0.35
-0.28
-0.21
-0.14
-0.07
0.0
0.07
0.14
0.21
0.28
0.35

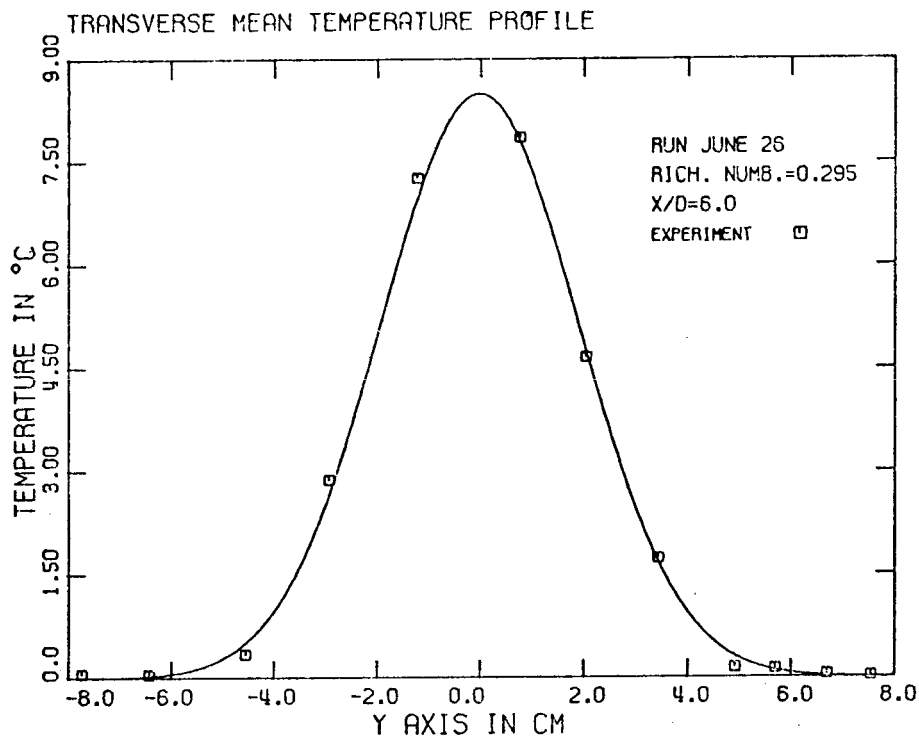
TRANSVERSE MEAN TEMPERATURE PROFILE
RUN JUNE 26
RICH. NUMB.=0.295
X/D=6.0
EXPERIMENT
TEMPERATURE IN °C
0.0
1.50
3.00
4.50
6.00
7.50
9.00
-8.0
-6.0
-4.0
-2.0
0.0
2.0
4.0
6.0
8.0
Y AXIS IN CM

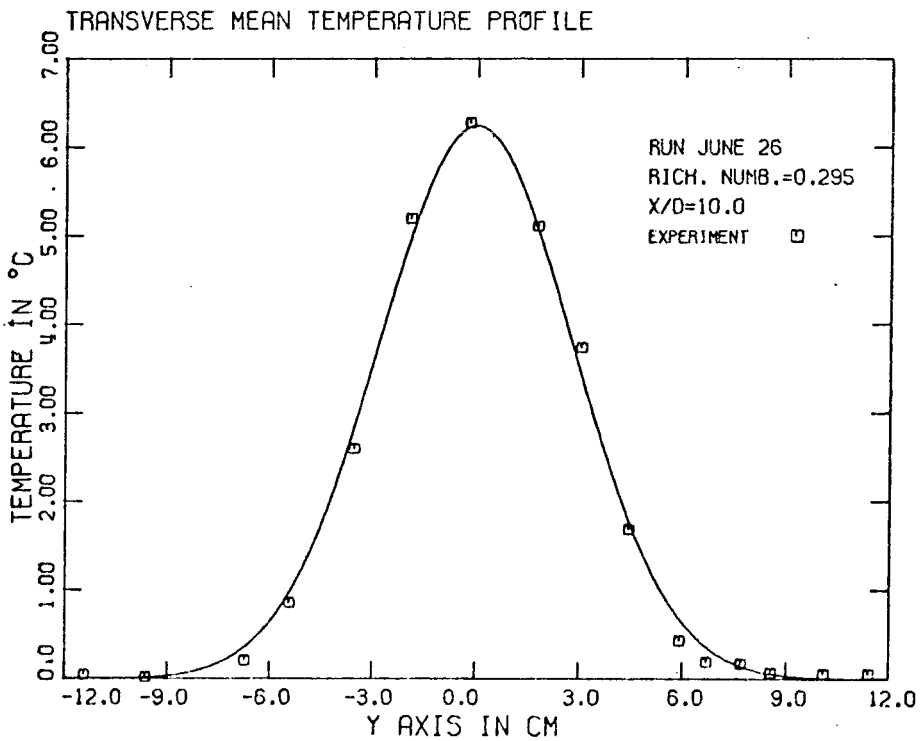
TRANSVERSE MEAN TEMPERATURE PROFILE
RUN JUNE 26
RICH. NUMB.=0.295
X/D=10.0
EXPERIMENT
TEMPERATURE IN °C
0.0
1.00
2.00
3.00
4.00
5.00
6.00
7.00
-12.0
-9.0
-6.0
-3.0
0.0
3.0
6.0
9.0
12.0
Y AXIS IN CM

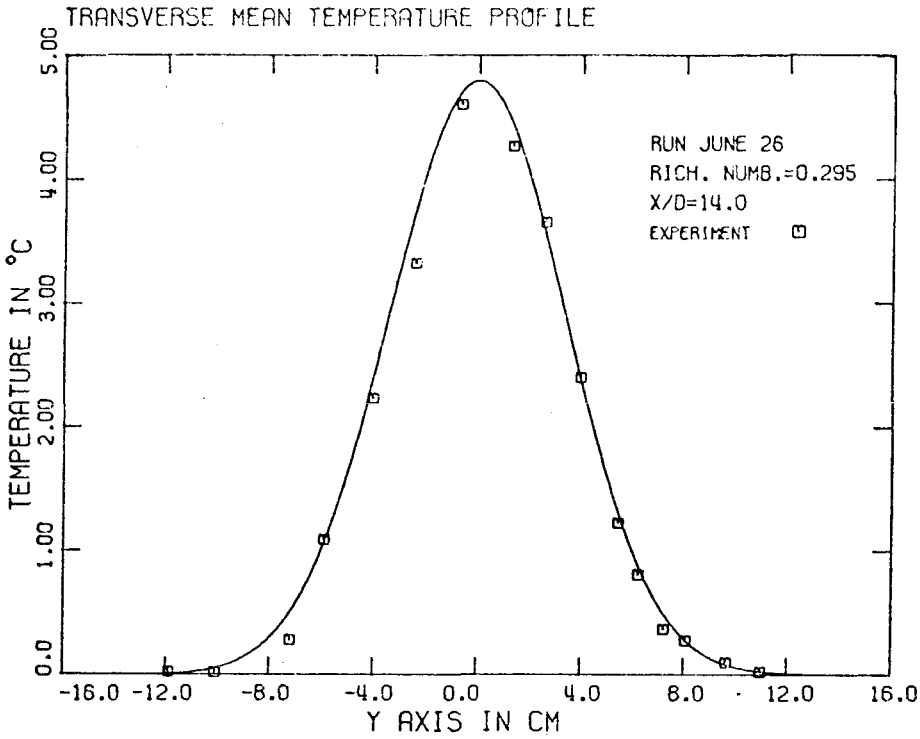
TRANSVERSE MEAN TEMPERATURE PROFILE
RUN JUNE 26
RICH. NUMB.=0.295
X/D=14.0
EXPERIMENT
TEMPERATURE IN °C
0.0
1.00
2.00
3.00
4.00
5.00
-16.0 -12.0 -8.0 -4.0 0.0 4.0 8.0 12.0 16.0
Y AXIS IN CM

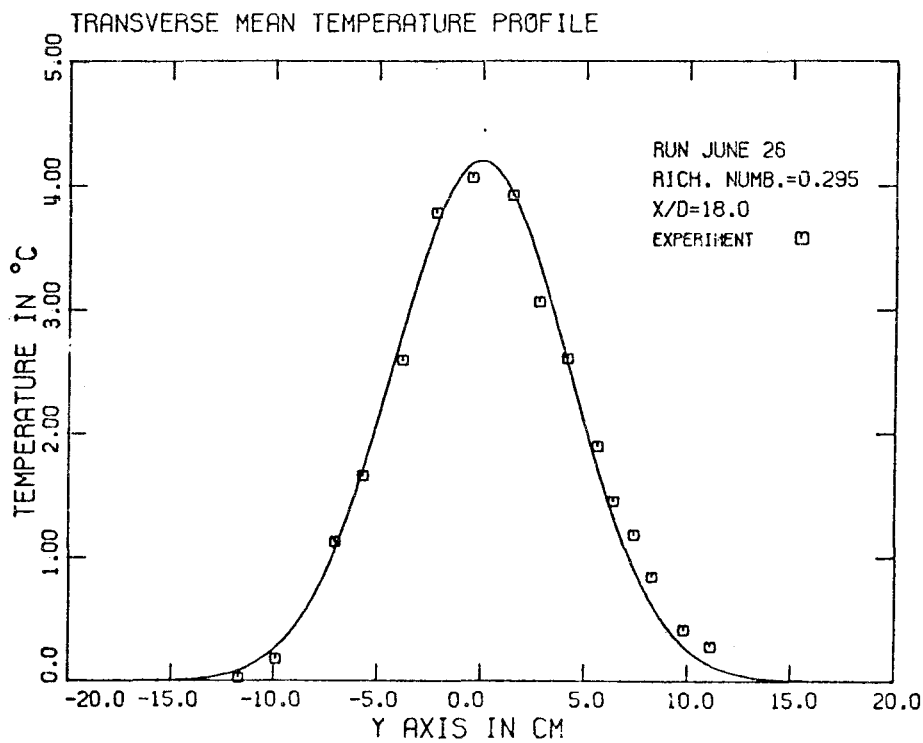
TRANSVERSE MEAN TEMPERATURE PROFILE
RUN JUNE 26
RICH. NUMB.=0.295
X/D=18.0
EXPERIMENT
TEMPERATURE IN °C
0.0
1.00
2.00
3.00
4.00
5.00
-20.0 -15.0 -10.0 -5.0 0.0 5.0 10.0 15.0 20.0
Y AXIS IN CM

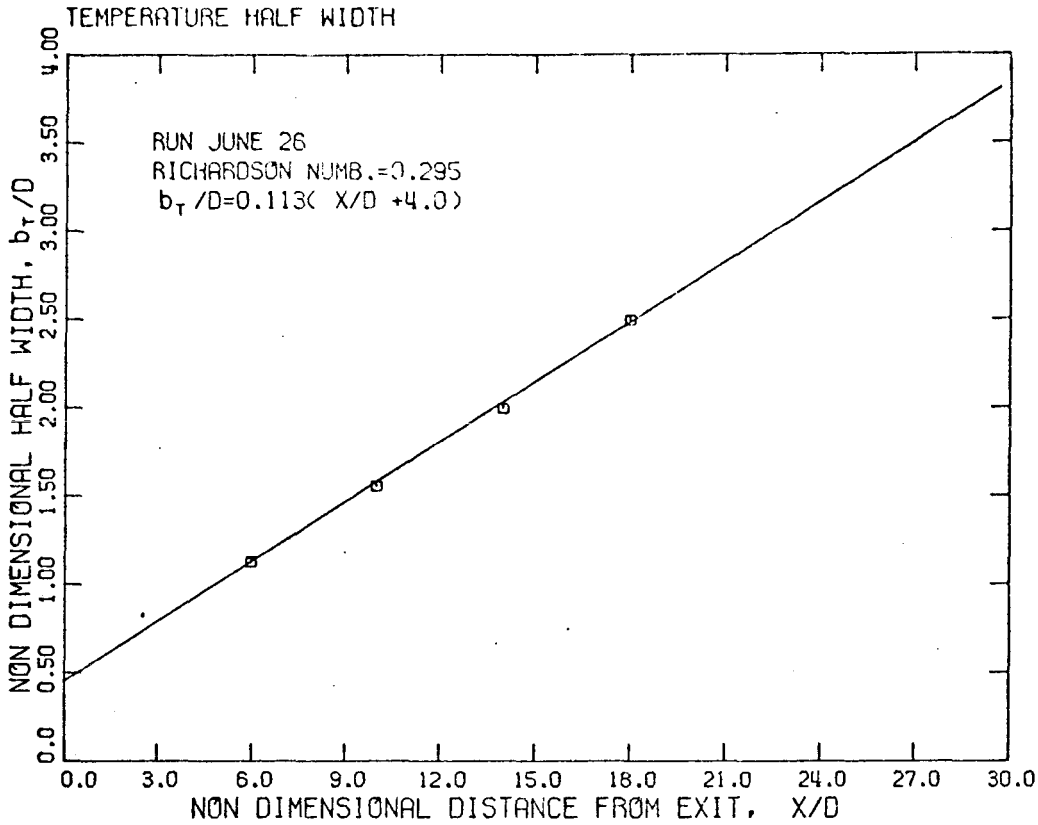
TEMPERATURE HALF WIDTH
RUN JUNE 26
RICHARDSON NUMB.=0.295
$b_T/D=0.113(X/D+4.0)$
NON DIMENSIONAL HALF WIDTH, b_T/D
0.0
0.50
1.00
1.50
2.00
2.50
3.00
3.50
4.00
0.0
3.0
6.0
9.0
12.0
15.0
18.0
21.0
24.0
27.0
30.0
NON DIMENSIONAL DISTANCE FROM EXIT, X/D

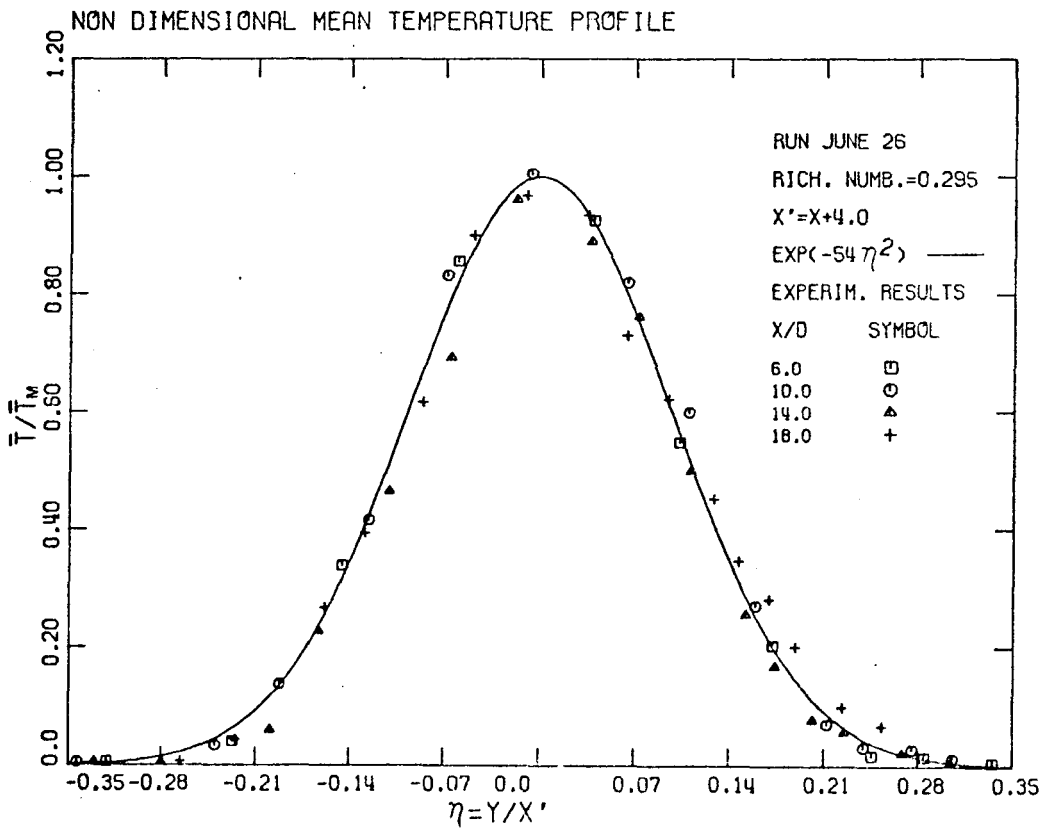
NON DIMENSIONAL MEAN TEMPERATURE PROFILE
RUN JUNE 26
RICH. NUMB.=0.295
X'=X+4.0
$EXP(-54\eta^2)$
EXPERIM. RESULTS
X/D SYMBOL
6.0
10.0
14.0
18.0
$\bar{T}/\bar{T}_M$
0.0
0.20
0.40
0.60
0.80
1.00
1.20
-0.35
-0.28
-0.21
-0.14
-0.07
0.0
0.07
0.14
0.21
0.28
0.35
$\eta=Y/X'$

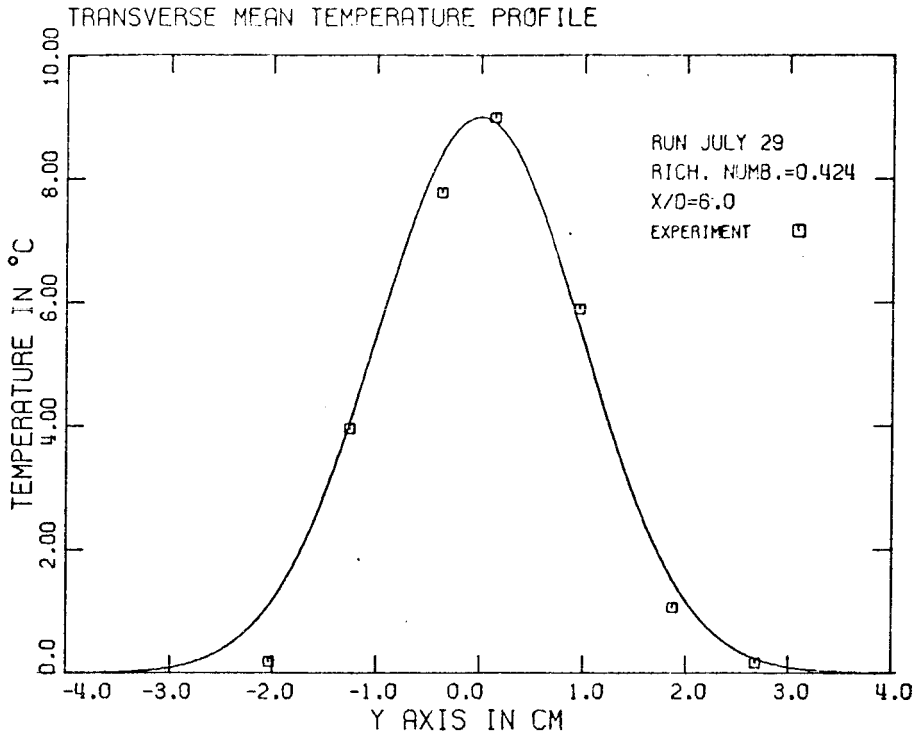
TRANSVERSE MEAN TEMPERATURE PROFILE
RUN JULY 29
RICH. NUMB.=0.424
X/D=6.0
EXPERIMENT
TEMPERATURE IN °C
0.0
2.00
4.00
6.00
8.00
10.00
-4.0
-3.0
-2.0
-1.0
0.0
1.0
2.0
3.0
4.0
Y AXIS IN CM

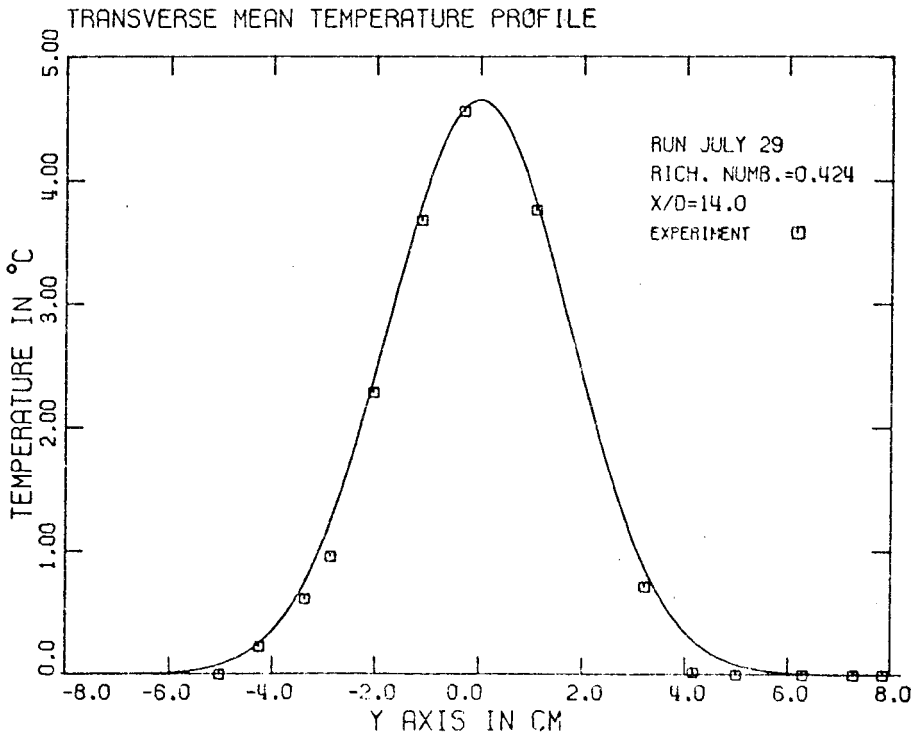
TRANSVERSE MEAN TEMPERATURE PROFILE
RUN JULY 29
RICH. NUMB.=0.424
X/D=14.0
EXPERIMENT
TEMPERATURE IN °C
0.0
1.00
2.00
3.00
4.00
5.00
-8.0
-6.0
-4.0
-2.0
0.0
2.0
4.0
6.0
8.0
Y AXIS IN CM

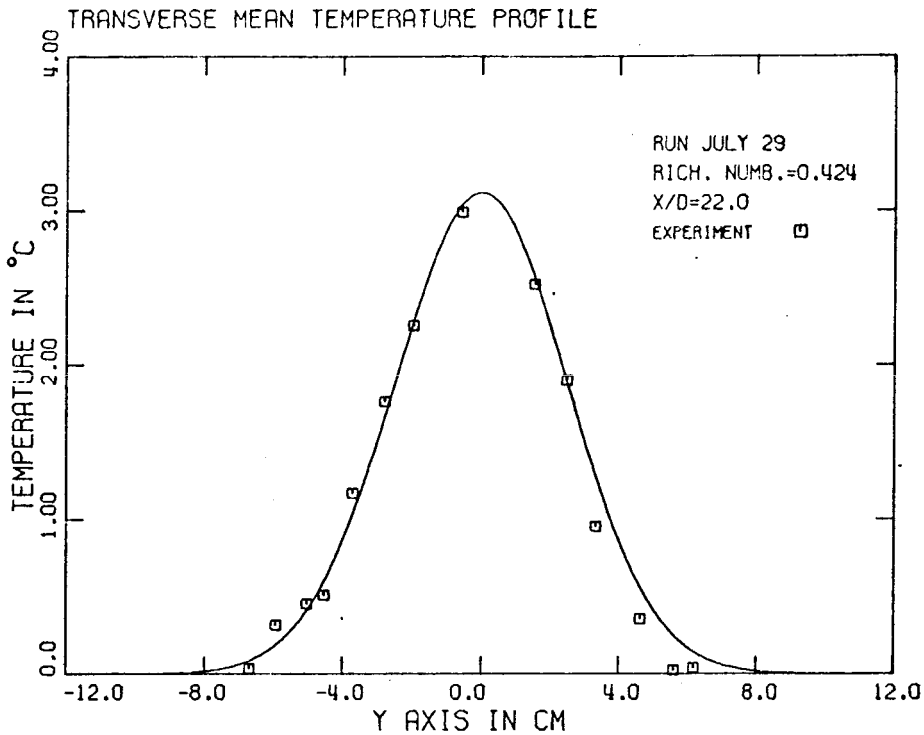
TRANSVERSE MEAN TEMPERATURE PROFILE
RUN JULY 29
RICH. NUMB.=0.424
X/D=22.0
EXPERIMENT
TEMPERATURE IN °C
0.0
1.00
2.00
3.00
4.00
-12.0
-8.0
-4.0
0.0
4.0
8.0
12.0
Y AXIS IN CM

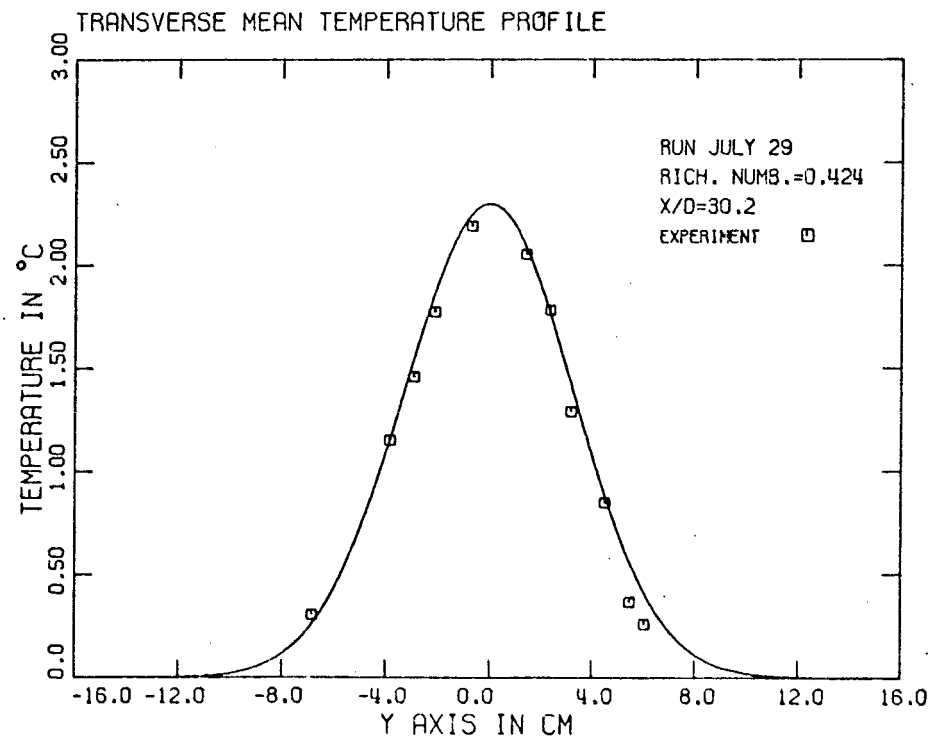
TRANSVERSE MEAN TEMPERATURE PROFILE
RUN JULY 29
RICH. NUMB.=0.424
X/D=30.2
EXPERIMENT
TEMPERATURE IN °C
0.0
0.50
1.00
1.50
2.00
2.50
3.00
-16.0
-12.0
-8.0
-4.0
0.0
4.0
8.0
12.0
16.0
Y AXIS IN CM

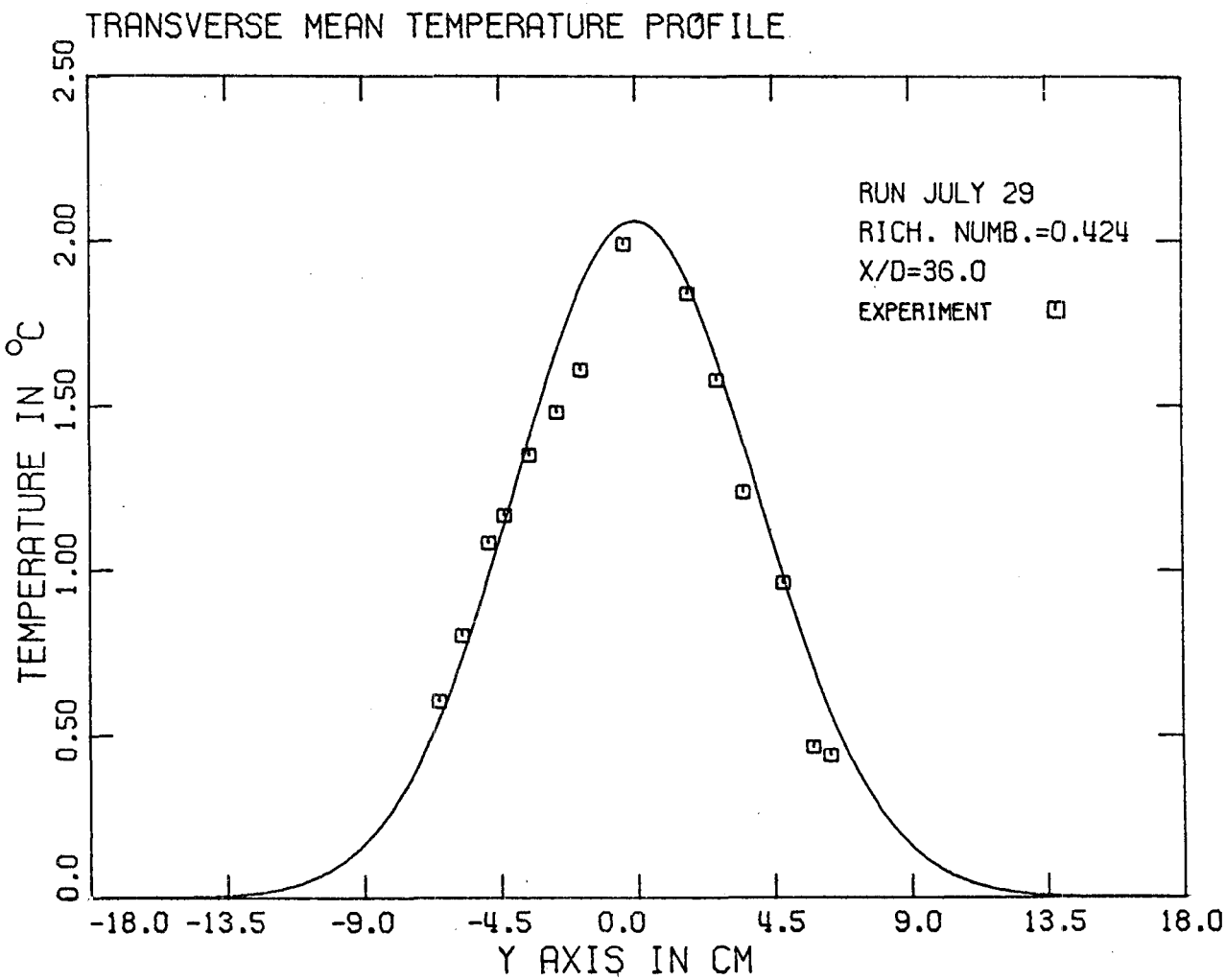
TRANSVERSE MEAN TEMPERATURE PROFILE
RUN JULY 29
RICH. NUMB.=0.424
X/D=36.0
EXPERIMENT
TEMPERATURE IN °C
0.0
0.50
1.00
1.50
2.00
2.50
-18.0 -13.5 -9.0 -4.5 0.0 4.5 9.0 13.5 18.0
Y AXIS IN CM

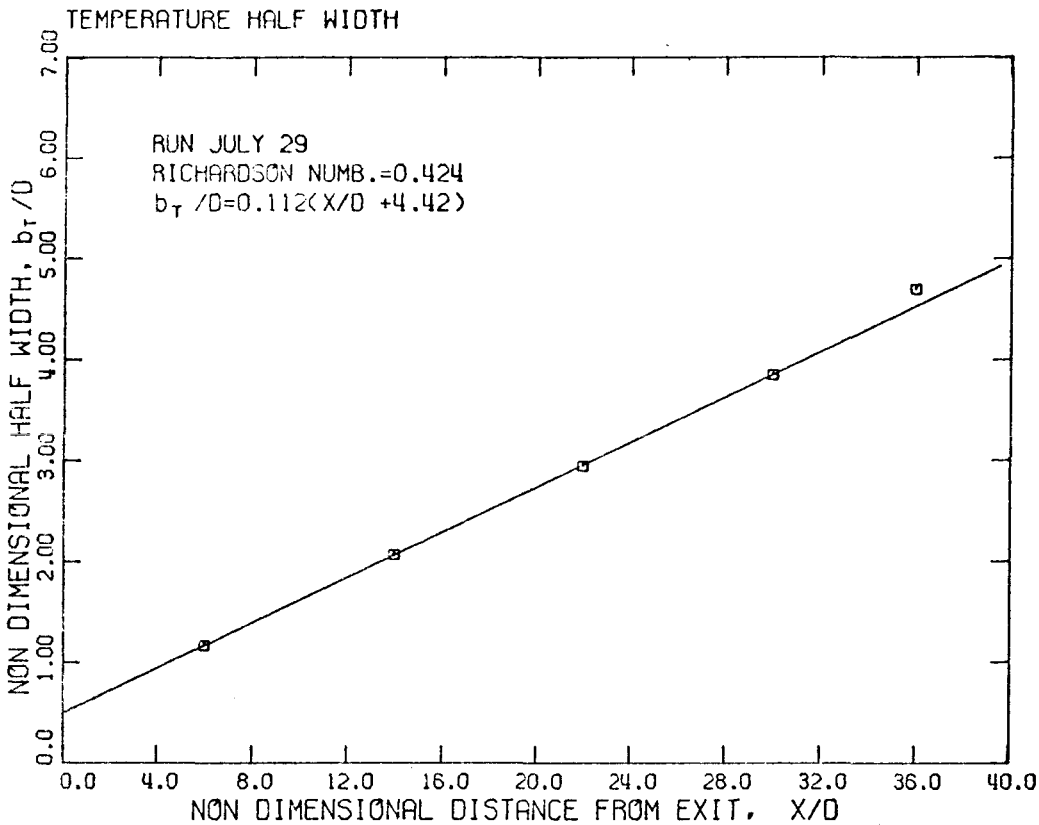
TEMPERATURE HALF WIDTH
RUN JULY 29
RICHARDSON NUMB.=0.424
$b_T/D=0.112(X/D+4.42)$
NON DIMENSIONAL HALF WIDTH, b_T/D
0.0
1.00
2.00
3.00
4.00
5.00
6.00
7.00
0.0
4.0
8.0
12.0
16.0
20.0
24.0
28.0
32.0
36.0
40.0
NON DIMENSIONAL DISTANCE FROM EXIT, X/D

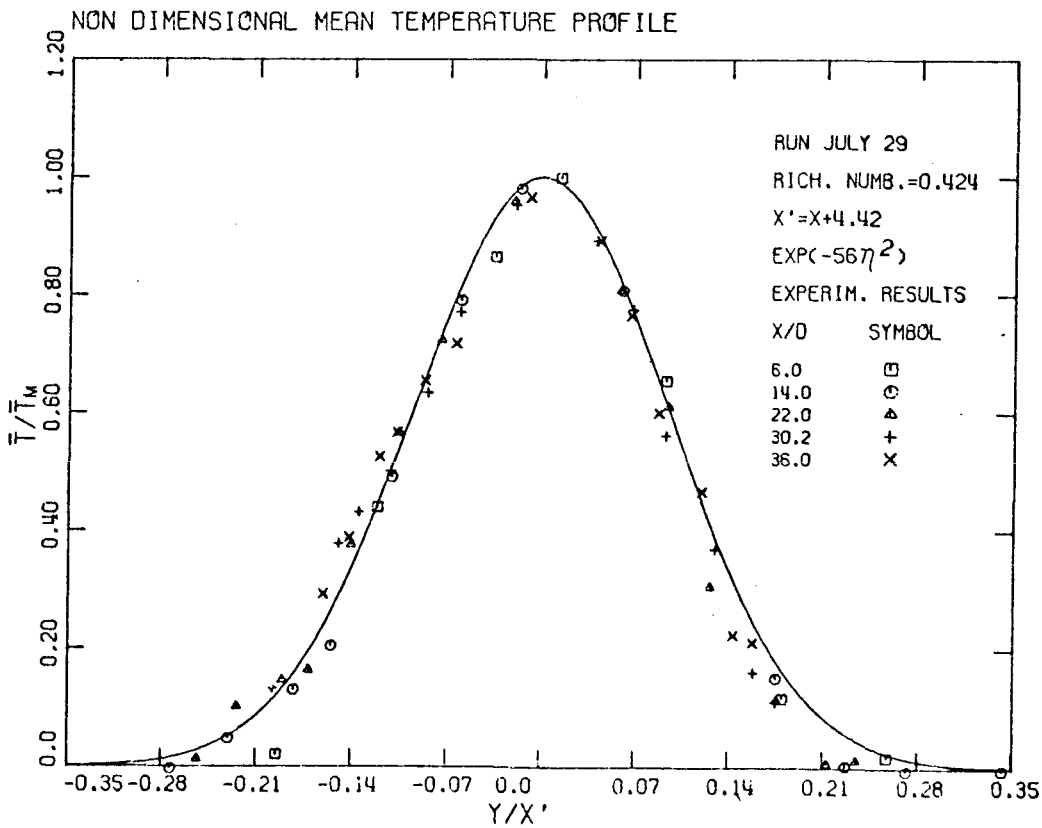
NON DIMENSIONAL MEAN TEMPERATURE PROFILE
RUN JULY 29
RICH. NUMB.=0.424
X'=X+4.42
$EXP(-56\eta^2)$
EXPERIM. RESULTS
X/D SYMBOL
6.0
14.0
22.0
30.2
36.0
$\bar{T}/\bar{T}_M$
0.0
0.20
0.40
0.60
0.80
1.00
1.20
-0.35
-0.28
-0.21
-0.14
-0.07
0.0
0.07
0.14
0.21
0.28
0.35
Y/X'

APPENDIX C

TEST OF THE TWO-DIMENSIONALITY OF THE FLOW

In this study, the two-dimensional jet (see Section 3.4) emerged out of a slot 13 cm long and D cm wide (D varied from 0.24 to 2.0 cm). The two-dimensionality of the emerging jet at x = 0 was determined by measuring the velocity $\overline{u}_o$ at the jet orifice, which was found to be in good agreement (variations of the order 1-2%) with the mean exit velocity calculated by the known volume flux μ_o, i.e.

$$\overline{u}_o = \frac{\mu_o}{WD}$$

where W is the distance between the two confining walls. In the following discussion, the Cartesian system of coordinates (x,y,z) will be considered with an origin in the plane midway between the two confining walls (see Figures 2.1.1 and 3.4.1.a).

It was considered that the two confining walls, located at $z = \pm 6.5$ cm, would serve two purposes. First, growth of the jet in the z-direction would be prevented, second, the two-dimensionality of the induced flow would be enhanced. Using dye tracers, it was found that the induced flow was approximately two-dimensional. The flow at the entrance of the two confining walls was found to be smooth and no separation effects were noticed.

The important parameter in testing the two-dimensionality of the jet is the ratio of the distance from the jet orifice X over the distance W between the two confining walls. The jet loses its two-dimensionality

for large values of the ratio X/W. For the run PLVT2, the ratio X/W was

$$0.38 < X/W < 1.7,$$

and for the run July 1

$$0.46 < X/W < 2.76.$$

Two experiments were run to test the two-dimensionality of the buoyant jet by taking measurements at different positions Y in the Z direction (parallel to the slot). The mean temperature $\overline{T}(x,y,z)$ (see Figures C.1 to C.4), the intensity of turbulent fluctuations of temperature $\overline{T'^2}(x,y,z)$ (Figures C.5 and C.6), the intermittency $\gamma(x,y,z)$ (see Figure C.7), the maximum and minimum temperature (see Figure C.8) and the frequency of the hot/cold interface crossing (see Figure C.9) were measured in a buoyant jet. We can observe that even for the largest value of X/W used in this study (X/W = 3) the flow can be considered two-dimensional over the central one-half of the distance between the two confining walls. The only exception appears to be in the frequency f_R of the hot/cold interface crossings, but we should note that the experimental determination of f_R using several probes is very delicate. On the other hand, the two-dimensionality of the large scale motions of the jet can be concluded from the Figures A.1 and A.2 of the Appendix A.

The profile of the induced flow is shown in Figure C.10. It can be seen that boundary layers have developed. This suggests why the jet temperature close to the wall is higher than the temperature over the central region between the two confining walls (see Figure C.2).

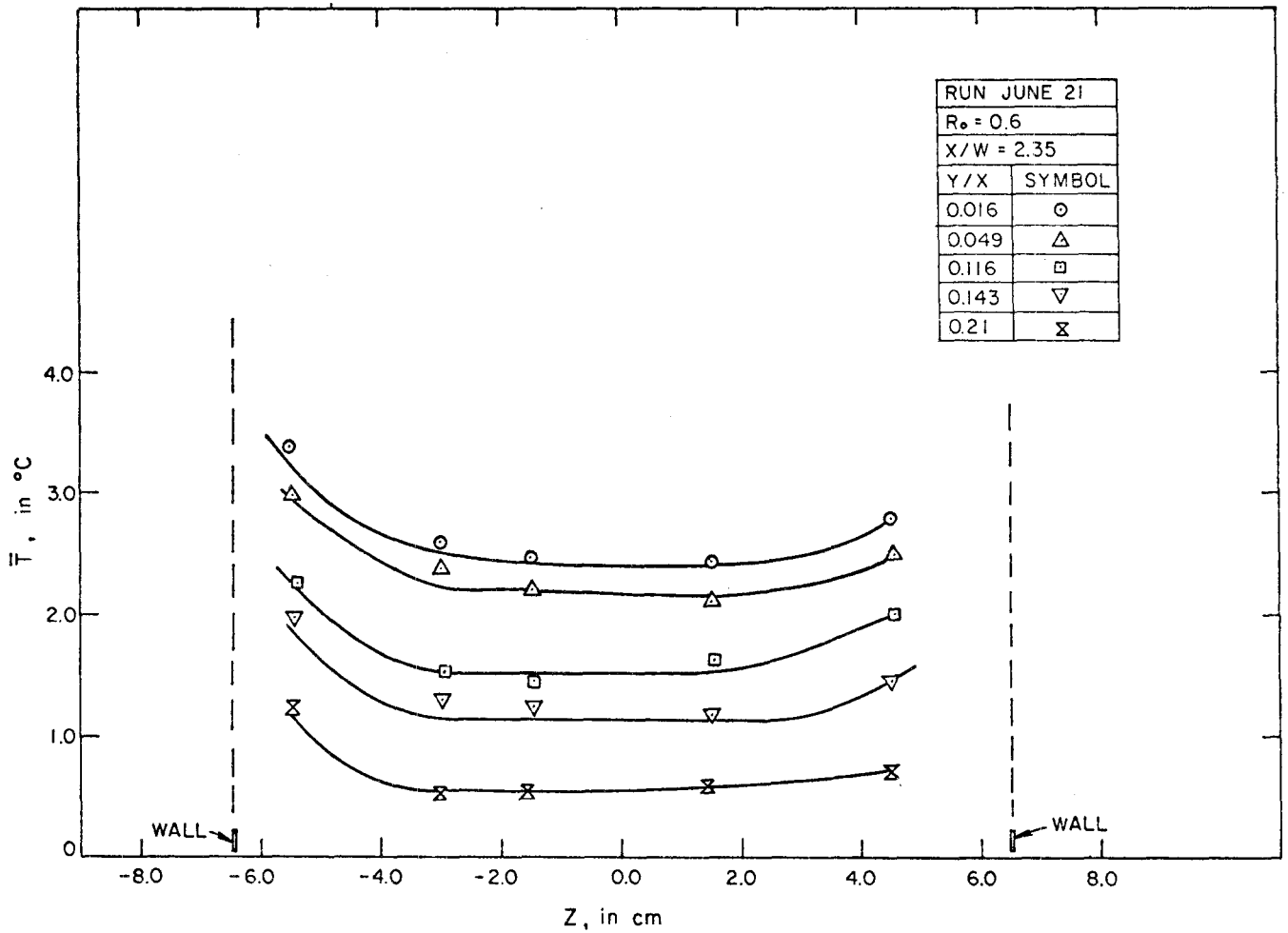

Figure C.1. Distribution of mean temperature in a direction parallel to the slot.

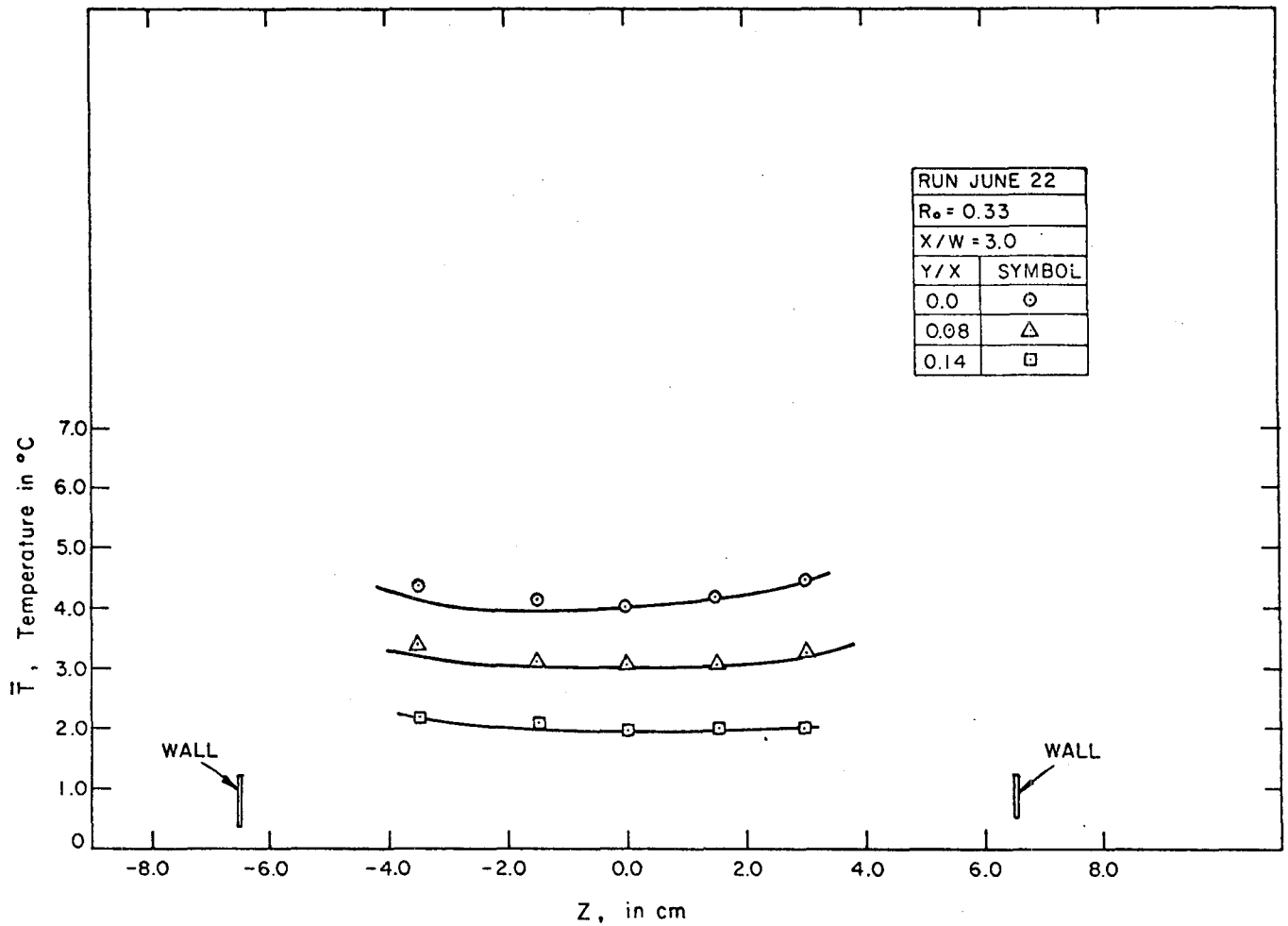

Figure C.2. Distribution of mean temperature in a direction parallel to the slot.

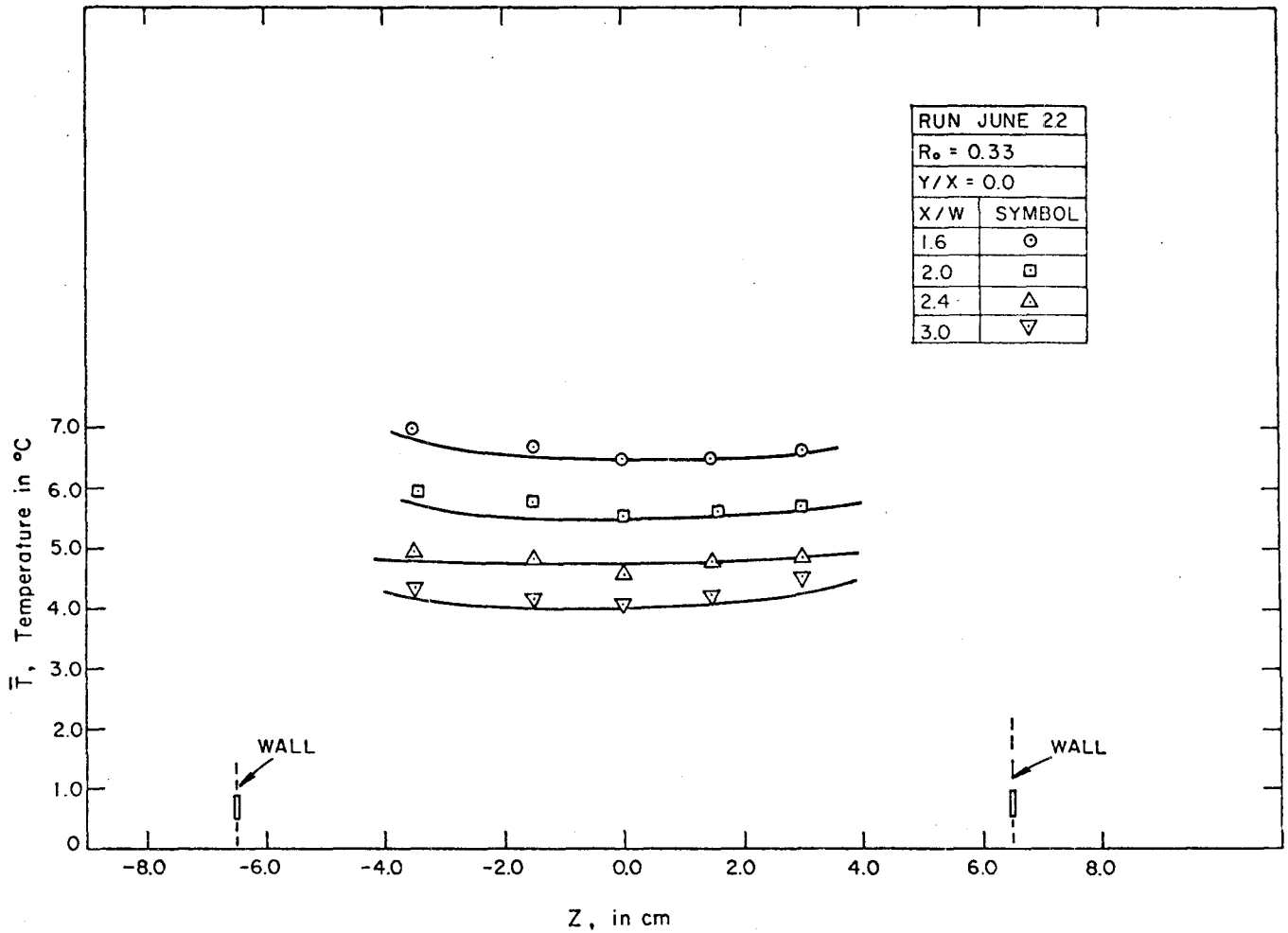

Figure C.3. Distribution of mean temperature in a direction parallel to the slot.

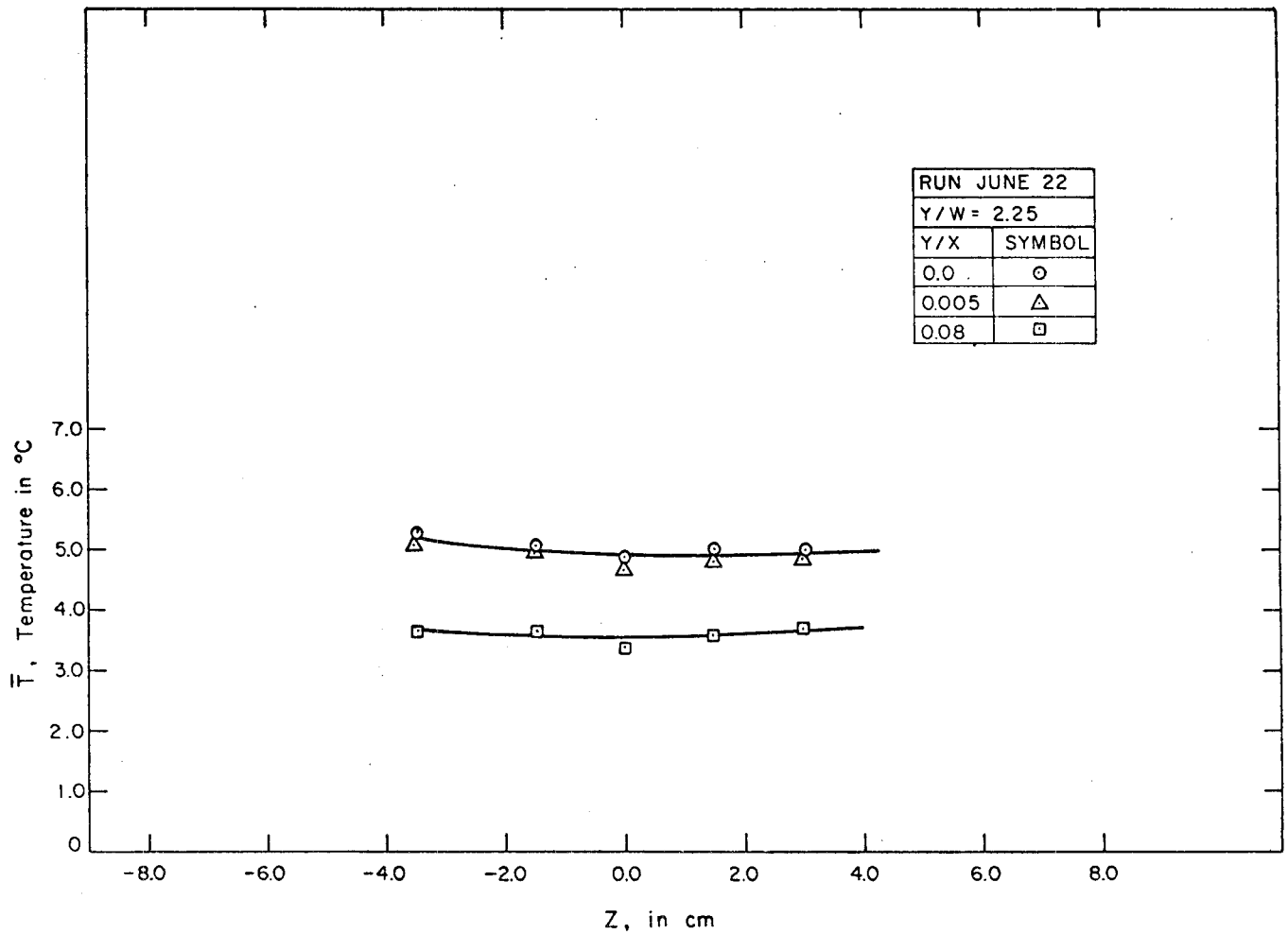

Figure C.4. Distribution of mean temperature in a direction parallel to the slot.

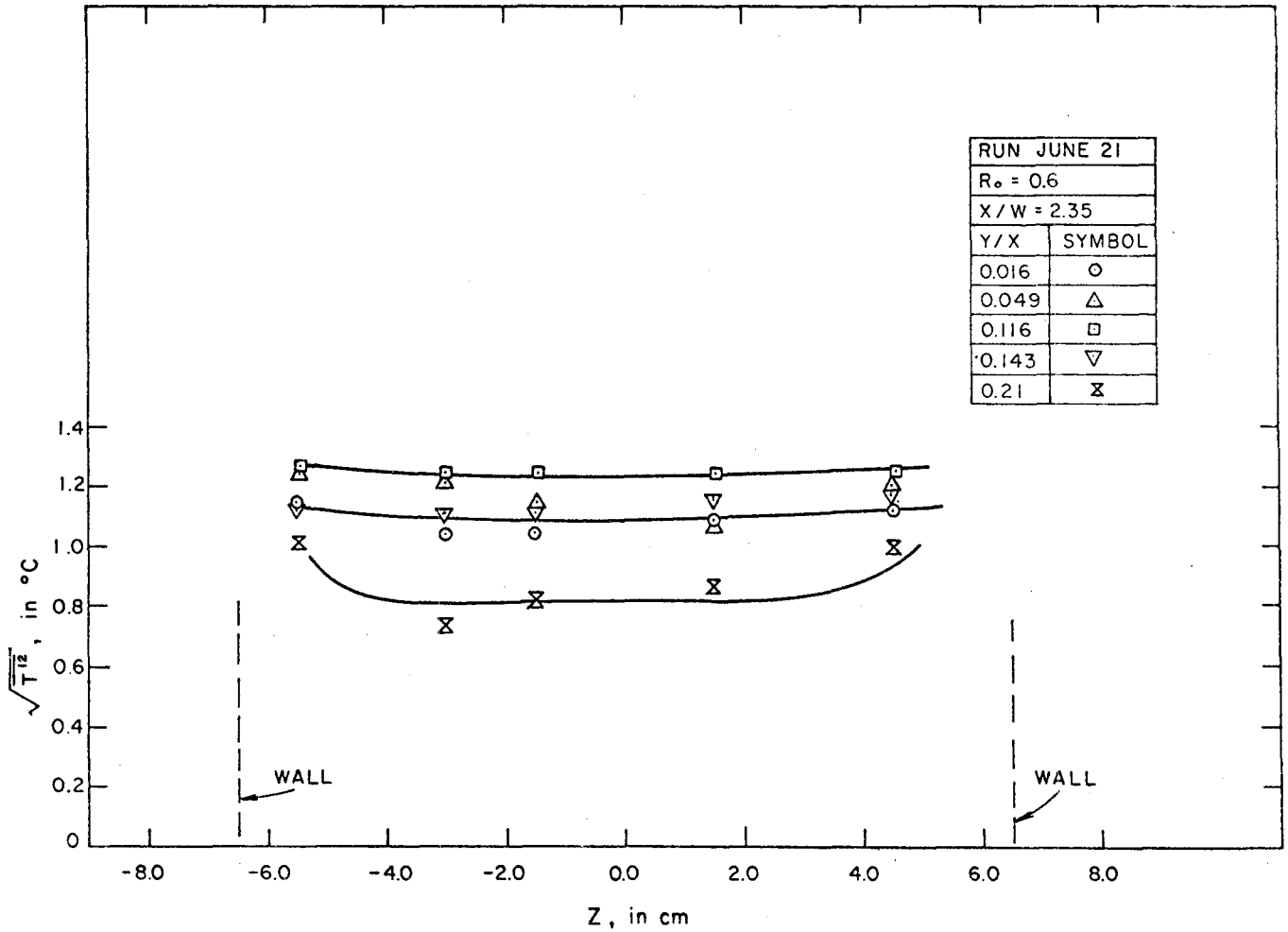

Figure C.5. Distribution of turbulence intensity in a direction parallel to the slot.

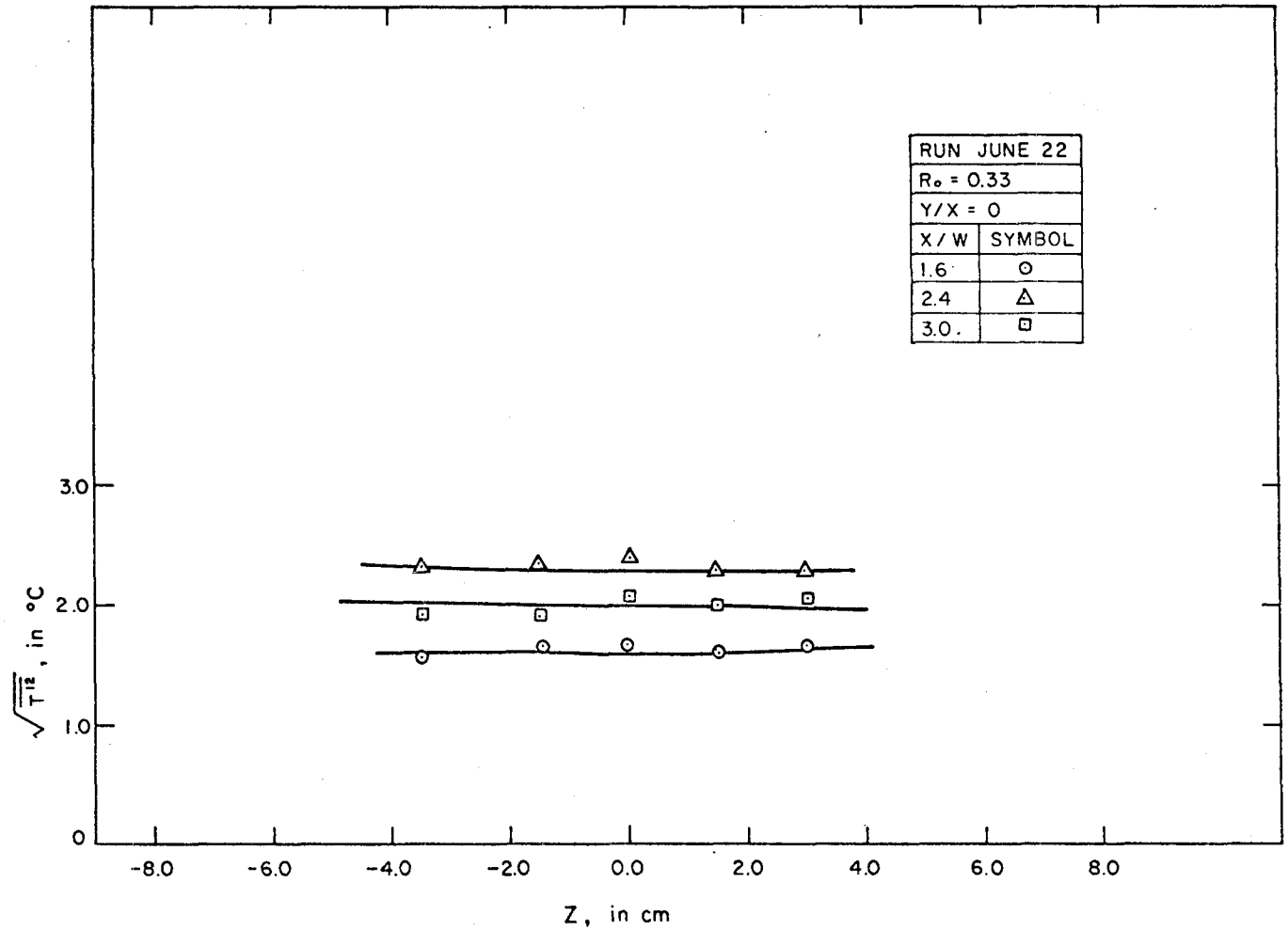

Figure C.6. Distribution of turbulence intensity in a direction parallel to the slot.

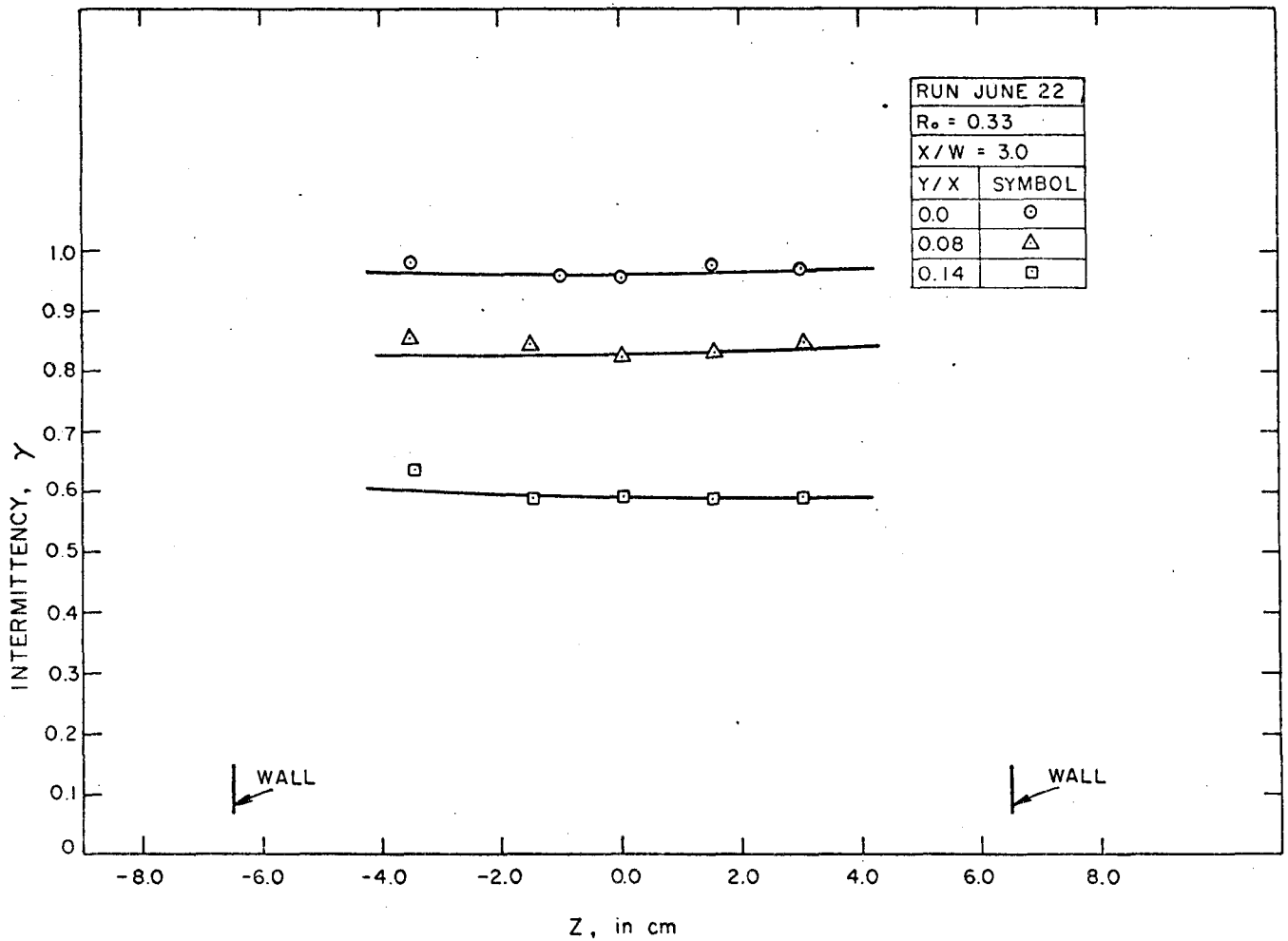

Figure C.7. Distribution of intermittency in a direction parallel to the slot.

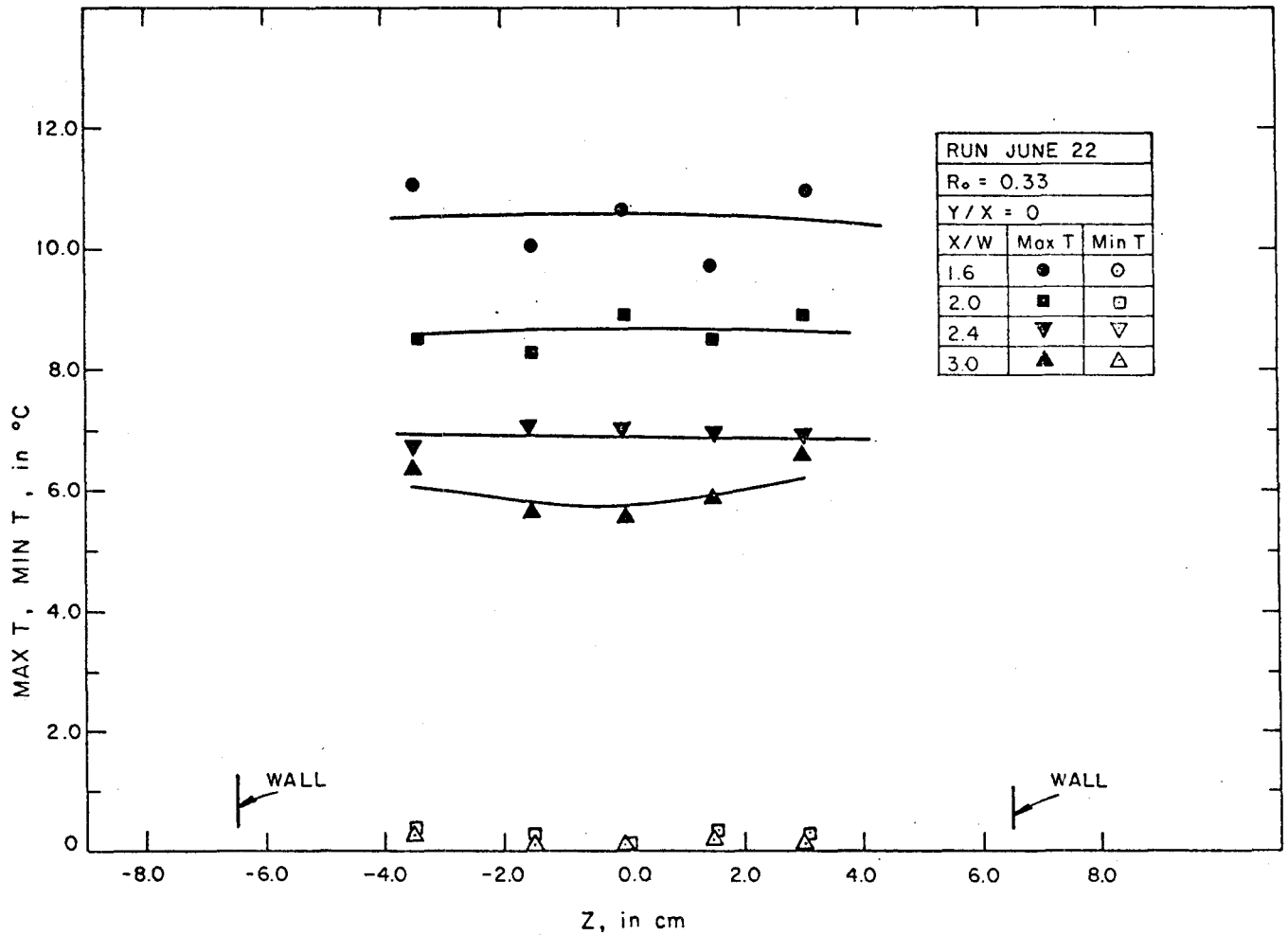

Figure C.8. Distribution of maximum and minimum temperature (see Section 4.3) in a direction parallel to slot.

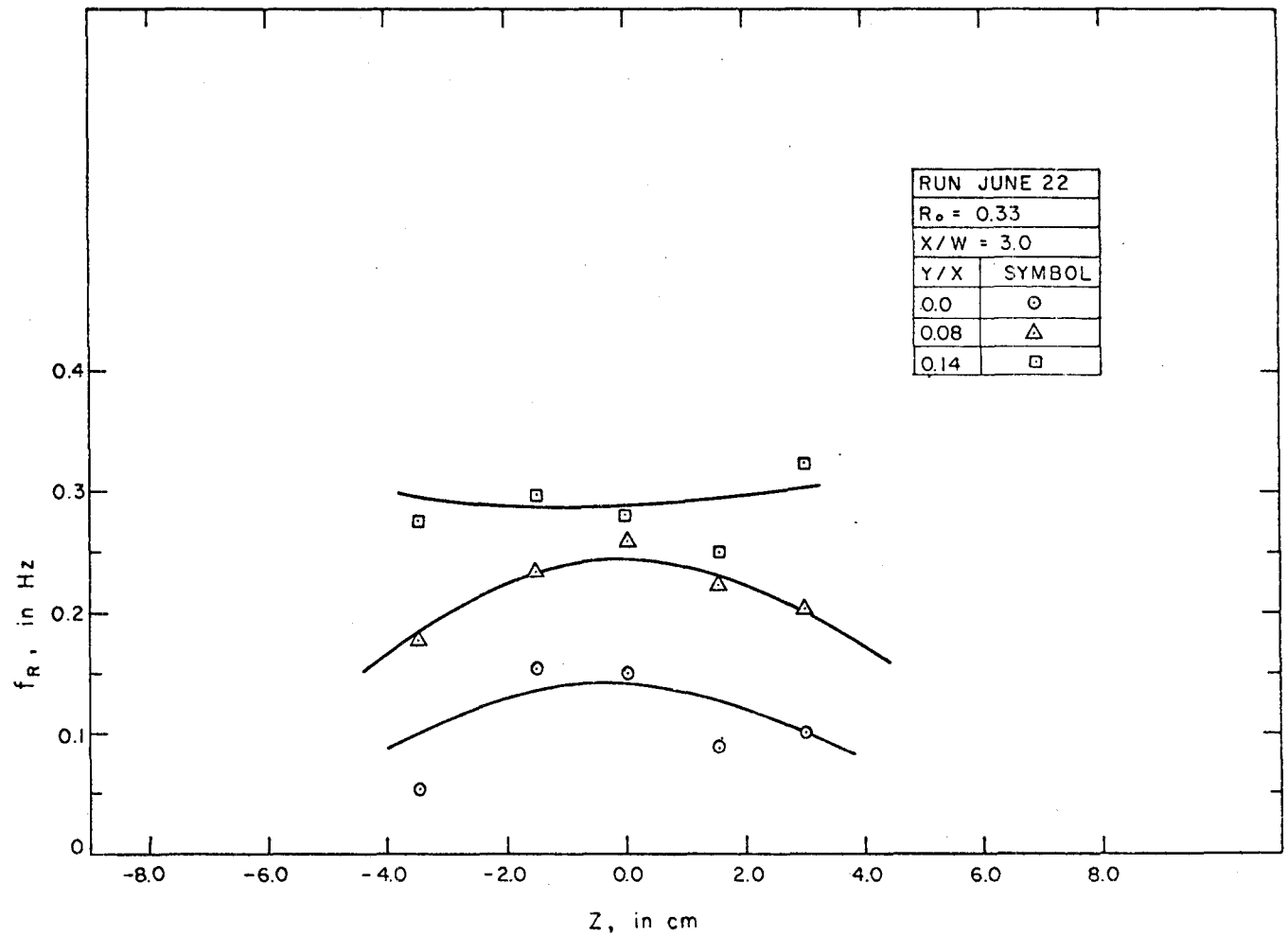

Figure C.9. Distribution of f_R (see Section 4.5) in a direction parallel to the slot.

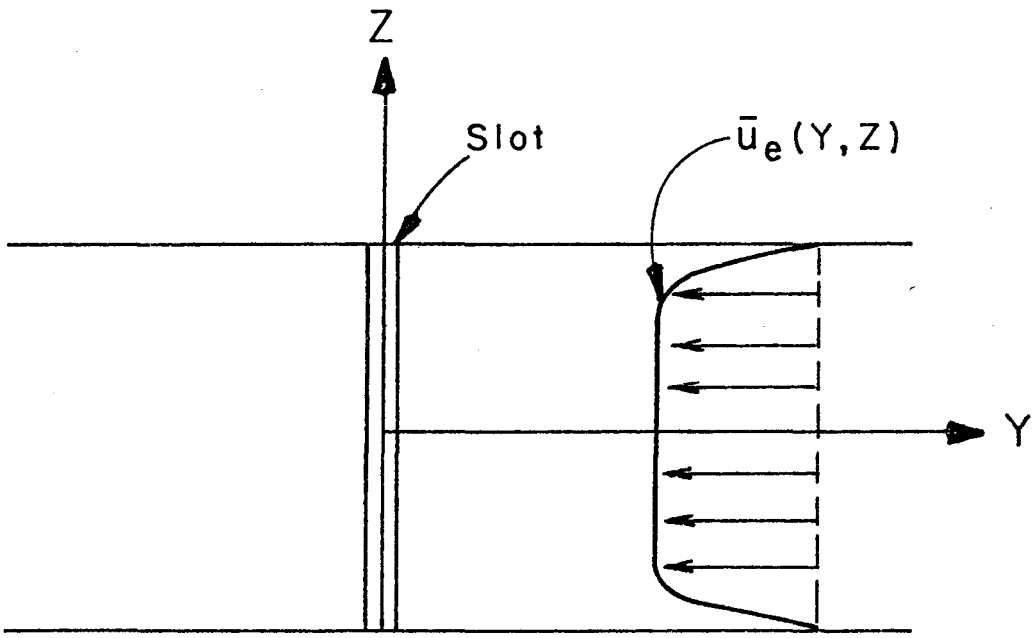

Figure C.10. Schematic of the induced flow profile between the two confining walls.

REFERENCES

1. Albertson, M. L., Dai, Y. B., Jensen, R. A., and Rouse, H. 1950. Diffusion of Submerged Jets. Transactions, ASCE, Vol. 115, pp. 639-664.

2. Bradbury, L. 1965. The Structure of Self-Preserving Turbulent Plane Jet. J. Fluid Mech., Vol. 23, pp. 31-64.

3. Förthmann, E. 1934. Uber Turbulente Strahlausbreitung. Ingenier Archiv., Vol. 5, pp. 42-54 (or translated in English (1936) NACA, TM-No. 789).

4. Flora, J., and Goldschmidt, V. 1969. Virtual Origins of a Free Plane Turbulent Jet. AIAA Journal, Vol. 7, pp. 2344-2346.

5. Heskestad, G. 1965. Hot Wire Measurements in a Plane Turbulent Jet. J. Appl. Mech., pp. 721-734, erratum, Sept. 1966, p. 710.

6. Hestroni, G., Hall, C. W., and Dhanak, A. M. 1965. Momentum Transfer in Thermally Asymmetric Turbulent Jets. Transactions ASME, Journal of Heat Transfer, Vol. 87, pp. 429-435.

7. Knystautas, R. 1964. The Turbulent Jet from a Series of Holes in Line. Aeronaut. Quart., Vol. XV, pp. 1-28.

8. Jenkins, P. E. and Goldschmidt, V. 1973. Mean Temperature and Velocity in a Plane Turbulent Jet. Transactions ASME, Journal of Fluids Eng., pp. 581-584.

9. Gartshore, I. 1966. An Experimental Investigation of the Large Eddy Equilibrium Hypothesis. J. Fluid Mech., Vol. 24, pp. 89-98.

10. Goldschmidt, V., and Eskimazi, S. 1966. Two Phase Turbulent Flow in a Plane Jet. J. Appl. Mech., pp. 735-747.

11. Mih, W. C., and Hoopes, J. A. 1972. Mean and Turbulent Velocities for Plane Jet. J. Hyd. Div., ASCE, Vol. 98, pp. 1274-1294.

12. Miller, D., and Comings, E. 1957. Static Pressure Distribution in the Free Turbulent Jet. J. Fluid Mech., Vol. 3, pp. 1-16.

13. Reichardt, H. 1942. Gesetzmassikeiten der Freien Turbulenz. VDI Forschung, Vol. 13, pp. 1-22.

14. Vulis, L. A., Kelmanson, I. A., and Platnik, I. B. 1970. Investigation of the Flow Structure in a Plane Turbulent Jet. Fluid Dynamics (Translated from Russian), Vol. 5, No. 4, pp. 684-687.

15. Vinogradov, Y. V., Gruzdev, V. N. and Talantov, A. V. 1972. Influence of Initial Turbulence on the Mixing of Plane Isothermal Jets. Soviet Aero., Vol. 15, No. 2, pp. 37-40 (Translated from Russian).

16. Van der Hegge Zijnen, B. G. 1958. Measurements of the Distribution of Heat and Matter in a Plane Turbulent Jet of Air. Appl. Sci. Res., Vol. 7, pp. 277-292.

17. Van der Hegge Zijnen, B. G. 1958. Measurements of Turbulence in a Plane Jet of Air by the Diffusion Method and by the Hot-Wire Method. Appl. Sci. Res., Vol. 7, pp. 292-313.

18. Townsend, A. A. 1956. The structure of Turbulent Shear Flow. Cambridge University Press.

19. Abraham, G. 1963. Jet Diffusion in Stagnant Ambient Fluid. Delft Hydraul. Lab. Publ. 29.

20. Morton, B., Taylor, G. I., and Turner, J. S. 1956. Turbulent gravitational convection from maintained and instantaneous sources. Proc. Royal Society, Vol. A234, 1056, pp. 1-23.

21. Rouse, H., Yih, C., and Humphreys, H. 1952. Gravitational Convection from a Boundary Source. Tellus, Vol. 4, pp. 200-210.

22. Fan, L. N., and Brooks, N. H. 1969. Numerical Solutions of Turbulent Buoyant Jet Problems. W. M. Keck Laboratory of Hydraulics and Water Resources, Report No. KH-R-18, California Institute of Technology.

23. List, E. J., and Imberger, J. 1973. Turbulent Entrainment in Buoyant Jets and Plumes. J. Hyd. Div., ASCE, Vol. 99, pp. 1461-1474.

24. Morton, B. R. 1959. Forced Plumes. J. Fluid Mech., Vol. 5, pp. 151-163.

25. Kotsovinos, N. E., and List, E. J. The Two-Dimensional Pure Plume. To be submitted for publication.

26. Ellison, T. H., and Turner, J. S. 1959. Turbulent Entrainment in Stratified Flows. J. Fluid Mech., Vol. 6, pp. 423-448.

27. Lee, S. L., and Emmons, H. W. 1961. A Study of Natural Convection above a Line Fire. J. Fluid Mech., Vol. 11, pp. 353-368.

28. Taylor, G. I. 1958. Flow Induced by Jets. J. Aero. Sci., Vol. 25, pp. 464-465.

29. Lippisch, A. 1958. Flow Visualization. Aeronau. Engrg. Rev., Vol. 36, pp. 24-32.

30. Sato, H. 1960. The Stability and Transition of a Two-Dimensional Jet. J. Fluid Mech., Vol. 7, pp. 53-80.

31. Forstrom, R. J., and Sparrow, E. M. 1967. Experiments on the Buoyant Plume above a Heated Horizontal Wire. Intern. J. Heat Mass Transfer, Vol. 10, pp. 321-331.

32. List, E. J. 1968. A Two-Dimensional Sink in a Density-Stratified Porous Medium. J. Fluid Mech., Vol. 33, pp. 529-543.

33. Batchelor, G. 1970. An Introduction to Fluid Dynamics. Cambridge University Press.

34. Hinze, J. 1959. Turbulence. McGraw-Hill Book Company.

35. Tennekes, H., and Lumley, J. 1972. A First Course in Turbulence. The M.I.T. Press.

36. Werlé, H. 1973. Hydrodynamic Flow Visualization. Ann. Rev. Fluid Mech., Vol. 5, pp. 361-382.

37. Newman, B. 1965. Turbulent Jets and Wakes in a Pressure Gradient. Symposium on the Fluid Mechanics of Internal Flow, Warren, Michigan, (Editor G. Sovran).

38. Van der Hegge Zijnen, B. G. 1957. Measurements of the Velocity Distribution in a Plane Turbulent Jet of Air. Appl. Sci. Res., Vol. 7, pp. 256-276.

39. Miller, D. 1957. Static Pressure Gradient in Turbulent Jet Mixing. Ph.D. Thesis, Purdue University.

40. Hannum, W., and Griffith, W. 1955. On the Intermittency of a Two-Dimensional Jet. J. Aeronau. Sci., Vol. 22, pp. 202-203.

41. Schorr, A. N., and Gebhart, B. 1970. An Experimental Investigation of Natural Convection Wakes above a Line Heat Source. Intern. J. Heat Mass Transfer, Vol. 13, pp. 557-571.

42. Tailland, A., Sunyach, M., and Mathiew, J. 1967. Etude d'un jet plan. Comptes Rendus Academie des Sciences, Paris, t.264, Series A, pp. 527-530.

43. Coles, D. 1962. Interfaces and Intermittency in Turbulent Shear Flow. Mechanique de la Turbulence, Colloque International, Marseille, pp. 229-250.

44. Householder, M. K., and Goldschmidt, V. W. 1968. Turbulent Diffusion of Small Particles in a Two-Dimensional Free Jet. TR FMTR 68-3, National Science Foundation, (reference in Flora and Goldschmidt [4]).

45. Tollmien, W. 1926. Die Berechung turbulenter Ausbreitungsvorgange. ZAMM 6, pp. 468-478, (NACA TM 1085, 1945).

46. Taylor, G. I. 1932. The Transport of Vorticity and Heat Through Fluids in Turbulent Motion. Proc. Roy. Soc. London, A135, pp. 685-702.

47. Schlichting, H. 1960. Boundary Layer Theory. McGraw-Hill, Fourth edition.

48. Saffman, P. G. 1970. A Model of Inhomogeneous Turbulent Flow. Proc. Roy. Soc. London, A317, pp. 417-433.

49. Laufer, J. 1975. New Trends in Experimental Turbulence Research. Ann. Rev. Fluid Mech., Vol. 7, pp. 307-326.

50. Coles, D. 1975. Private Communication.

51. Batchelor, G. 1950. Note on Free Turbulent Flows, with Special Reference to the Two-Dimensional Wake. J. Aeronau. Sci., pp. 441-445.

52. Corrsin, S., and Uberoi, M. 1950. Further Experiments on the Flow and Heat Transfer in a Heated Turbulent Air Jet. NACA Report 998.

53. Brooks, N. and Koh, R.C.Y. 1965. Discharge of Sewage Effluent from a Line Source into a Stratified Ocean. XI Congr. Int. Assoc. Hydraul. Res., Paper No. 2.19.

54. Batchelor, G. K. 1954. Heat Convection and Buoyancy Effects in Fluids. Quart. J. Roy. Meteor. Soc., Vol. 80, pp. 339-358.

55. Lee Shao-Lin. 1961. Natural Convection above a Line Fire. Ph.D. Thesis, Harvard University.

56. Magrab, E. B., and Blomquist, D. S. 1971. Measurement of Time Varying Phenomena: Fundamentals and Applications. New York, Wiley Interscience.

57. Bicknell, J. 1937. A Study of Turbulent Mixing between a Plane Jet of Fluid of Various Densities and Still Fluid. Master of Science Thesis, Massachusetts Institute of Technology.

58. Fan, L. N. 1967. Turbulent Buoyant Jets into Stratified or Flowing Ambient Fluids. W. M. Keck Laboratory of Hydraulics and Water Resources, Report No. KH-R-15, California Institute of Technology.

59. Nakaguchi, H. 1961. Jet along a Curved Wall. University of Tokyo Research Memo 4, (reference in Newman [37]).

60. Koh, R.C.Y., and Brooks, N. H. 1975. Fluid Mechanics of Waste-Water Disposal in the Ocean. Ann. Rev. Fluid Mech., Vol. 7, pp. 187-211.

61. Hanum, W. H. 1954. Intermittency of a two-dimensional jet as investigated with a Hot Wire Anemometer. Master Thesis, Princeton University.

62. Anwar, H. 1969. Experiment on an Effluent Discharging from a Slot into Stationary or Slowly Moving Fluid of Greater Density. J. Hyd. Res., 7, pp. 411-431.

63. Landau, L., and Lifshitz, E. 1959. Fluid Mechanics. Pergamon Press.

64. Stevenson, W. 1970. Optical Frequency Shifting by Means of a Rotating Diffraction Grating. Appl. Optics, Vol. 9, pp. 649-652.

65. Turner, J. S. 1973. Buoyancy Effects in Fluids. Cambridge University Press.

66. Sato, H., and Sakao, F. 1964. An Experimental Investigation of the Stability of a Two-Dimensional Jet at Low Reynolds Numbers. J. Fluid Mech., Vol. 20, pp. 337-352.

67. Brooks, N. H. 1972. Dispersion in Hydrologic and Coastal Environments. W. M. Keck Laboratory of Hydraulics and Water Resources, Report No. KH-R-29, California Institute of Technology.

68. Benjamin, T. B. 1968. Gravity Currents and Related Phenomena. J. Fluid Mech., Vol. 31, pp. 209-248.

69. Monin, A. S. and Yaglom, A. M. 1971. Statistical Fluid Mechanics, Volume 1, The MIT Press.